REPORT DOCUMENTATION PAGE

Form Approved OMB NO. 0704-0188

The public reporting burden for this collection of information is estimated to average 1 hour per response, including the time for reviewing instructions, searching existing data sources, gathering and maintaining the data needed, and completing and reviewing the collection of information. Send comments regarding this burden estimate or any other aspect of this collection of information, including suggesstions for reducing this burden, to Washington Headquarters Services, Directorate for Information Operations and Reports, 1215 Jefferson Davis Highway, Suite 1204, Arlington VA, 22202-4302. Respondents should be aware that notwithstanding any other provision of law, no person shall be subject to any oenalty for failing to comply with a collection of information if it does not display a currently valid OMB control number.
PLEASE DO NOT RETURN YOUR FORM TO THE ABOVE ADDRESS.

1. REPORT DATE (DD-MM-YYYY)	2. REPORT TYPE	3. DATES COVERED (From - To)
18-05-2021	Final Report	20-Aug-2012 - 19-Aug-2019

4. TITLE AND SUBTITLE
Final Report: Translating Biochemical Pathways to Non-Cellular Environment

5a. CONTRACT NUMBER
W911NF-12-1-0420

5b. GRANT NUMBER

5c. PROGRAM ELEMENT NUMBER
611103

6. AUTHORS

5d. PROJECT NUMBER

5e. TASK NUMBER

5f. WORK UNIT NUMBER

7. PERFORMING ORGANIZATION NAMES AND ADDRESSES

Arizona State University
ORSPA
P.O. Box 876011
Tempe, AZ 85287 -6011

8. PERFORMING ORGANIZATION REPORT NUMBER

9. SPONSORING/MONITORING AGENCY NAME(S) AND ADDRESS (ES)

U.S. Army Research Office
P.O. Box 12211
Research Triangle Park, NC 27709-2211

10. SPONSOR/MONITOR'S ACRONYM(S)
ARO

11. SPONSOR/MONITOR'S REPORT NUMBER(S)
61781-LS-MUR.61

12. DISTRIBUTION AVAILIBILITY STATEMENT

Approved for public release; distribution is unlimited.

13. SUPPLEMENTARY NOTES

The views, opinions and/or findings contained in this report are those of the author(s) and should not contrued as an official Department of the Army position, policy or decision, unless so designated by other documentation.

14. ABSTRACT

15. SUBJECT TERMS

16. SECURITY CLASSIFICATION OF:			17. LIMITATION OF ABSTRACT	15. NUMBER OF PAGES	19a. NAME OF RESPONSIBLE PERSON
a. REPORT	b. ABSTRACT	c. THIS PAGE			Hao Yan
UU	UU	UU	UU		19b. TELEPHONE NUMBER 480-727-8570

RPPR Final Report
as of 20-May-2021

Agency Code: 21XD

Proposal Number: 61781LSMUR **Agreement Number: W911NF-12-1-0420**
INVESTIGATOR(S):

Name: Hao Yan
Email: hao.yan@asu.edu
Phone Number: 4807278570
Principal: Y

Organization: **Arizona State University**
Address: ORSPA, Tempe, AZ 852876011
Country: USA
DUNS Number: 943360412 EIN: 860196696
Report Date: 19-Nov-2019 Date Received: 18-May-2021
Final Report for Period Beginning 20-Aug-2012 and Ending 19-Aug-2019
Title: Translating Biochemical Pathways to Non-Cellular Environment
Begin Performance Period: 20-Aug-2012 **End Performance Period:** 19-Aug-2019
Report Term: 0-Other
Submitted By: Hao Yan Email: hao.yan@asu.edu
Phone: (480) 727-8570
Distribution Statement: 1-Approved for public release; distribution is unlimited.

STEM Degrees: **STEM Participants:**

Major Goals: We intend to engineer and optimize nanoscale devices and systems based on important biochemical conversion pathways, where the converted species are molecules (enzymes transforming substrates into products), or energy, as is the case for photosynthesis. The use of DNA-directed assembly allows us to control and exploit the interactions between synthetic and naturally occurring bio-materials to produce highly functional biochemical conversion systems. Regarding enzyme transformations, our primary goal is to construct artificial enzyme cascades using two- and three-dimensional DNA structures as templates, and to study the ideal number of enzymes, relative distance, spatial arrangement, diffusion behavior, and reaction kinetics of the cascades in a controlled, non-cellular environment.

Regarding photosynthesis, our aim is to develop methods for translating energy conversion pathways to non-cellular environments where their functions can be more easily manipulated. The approach is to use rationally designed DNA nano-scaffolds to engineer light-harvesting networks containing synthetic pigments, interfaced with energy conversion proteins (photosynthetic reaction centers) from natural photosynthetic organisms. We intend to precisely position functional elements on the DNA scaffolds, generating energy and electron transfer pathways in which inter-molecular interactions can be predictably designed, and the local environment can be controlled. We hope to engineer systems with more uniform light absorption, efficient energy transfer and conversion, and improved photo-stability for maximum performance.

Accomplishments: We have made the following achievements under the major goals:
1. Developed reliable methods for conjugating DNA to protein enzymes and cofactors and purifying DNA conjugated proteins with exact ratios of the components;
2. Developed single-molecule characterization and predictive modeling techniques to evaluate the integrity and behavior of DNA nanostructure complexes;
3. Engineered a multi-enzyme complex utilizing a “swinging arm” to control substrate transfer between enzymes;
4. Optimized the enzymatic activity of a DNA actuator structure using single-molecule FRET;
5. Conjugated three different dye molecules to the reaction center proteins (individually) and evaluated key factors that affect energy transfer to the centers and the subsequent process of charge separation;
6. Prepared macroporous antimony-doped tin oxide (ATO) films by combining our inorganic-polymer composite gel method with the existing inverse opal templating method;
7. Engineered an artificial multi-enzyme complex to facilitate highly efficient substrate transfer and regulate the direction of enzyme reaction;
8. Constructed a 3-arm DNA complex with two spectrally distinct dye molecules attached to illustrate a step-wise multi-fluoropher light-harvesting capability;

9. Demonstrated the use of a self-assembled, spatially addressable DNA origami nanostructure to direct the precise positioning of protein enzymes onto a gold electrode to form a sub-monolayer of the enzyme-pairs on the DNA origami with designed inter-enzyme distances;
10. Established a method to co-reconstitute multiple membrane proteins in a single size specific liposome;
11. Built all-atom models of a DNA tetrahedron and a DNA octahedron to compare equilibrium structures from MD to the Finite Element framework present in CanDo;
12. Incorporated an Orange Carotenoid Protein into a DNA-templated artificial antenna system to adapt its photoprotection function for light regulation;
13. Interfaced Photosystem I from the cyanobacterium Thermosynechococcus elongatus to ultimately generate a higher redox power in our biohybrid photoelectrochemical cell;
14. Constructed two-dimensional enzyme networks to mimic multi-enzyme network organized in cells to better understand how geometry affects enzyme network behaviors;
15. Designed a self-assembled DNA crystal to assist protein organization and precise control of the protein/enzyme in the 3-dimensional manner;
16. Developed DNA nanocages for encapsulating enzymes with enhanced activity and stability;
17. Designed 2-track and 3-track DNA tiles and DNA walkers with different toehold lengths to investigate the mechanism of the walking process;
18. Used structure-based computational modeling to develop a highly programmable, rational means of controlling the targeted assembly and optical properties of excitonic circuits based on synthetic DNA;
19. Demonstrated that the mRGO LB films can be an effective electrode to achieve selective deposition of DNA nanostructures through covalent cross-linking, providing bioelectroactive and photoelectrochemical pathways;
20. Developed DNA-crowded enzyme complexes with enhanced activity;
21. Established a method to produce large sized nanodisc for Poliovirus infection study using DNA origami as modular scaffold;
22. Used single-molecule fluorescence resonance energy transfer (smFRET) to monitor a DNA tile reconfiguration process mimicking microtubules;
23. Integrated photosystem 1 into transparent, macro-porous electrodes and reducing organic compounds;
24. Linked the light-driven production of reductants by the reaction center/electrode systems with the action of a dehydrogenase enzyme (diaphorase) on DNA nanostructures.

Training Opportunities: Nothing to Report

Results Dissemination: Nothing to Report

Honors and Awards: Please see hornors and awards listed in each year's report.

Protocol Activity Status:

Technology Transfer: Nothing to Report

PARTICIPANTS:

Participant Type: PD/PI
Participant: Hao Yan
Person Months Worked: 12.00 **Funding Support:**
Project Contribution:
National Academy Member: N

Participant Type: Co PD/PI
Participant: Neal Woodbury
Person Months Worked: 12.00 **Funding Support:**
Project Contribution:
National Academy Member: N

Participant Type: Co PD/PI
Participant: Don Seo
Person Months Worked: 12.00 **Funding Support:**
Project Contribution:
National Academy Member: N

Participant Type: Co PD/PI
Participant: Mark Bathe
Person Months Worked: 12.00 **Funding Support:**
Project Contribution:
National Academy Member: N

Participant Type: Co PD/PI
Participant: William Shih
Person Months Worked: 12.00 **Funding Support:**
Project Contribution:
National Academy Member: N

Participant Type: Co PD/PI
Participant: Nils Walter
Person Months Worked: 12.00 **Funding Support:**
Project Contribution:
National Academy Member: N

Participant Type: Co PD/PI
Participant: Jinglin Fu
Person Months Worked: 12.00 **Funding Support:**
Project Contribution:
National Academy Member: N

Participant Type: Faculty
Participant: Su Lin
Person Months Worked: 12.00 **Funding Support:**
Project Contribution:
National Academy Member: N

Participant Type: Faculty
Participant: Minghui Liu
Person Months Worked: 12.00 **Funding Support:**
Project Contribution:
National Academy Member: N

RPPR Final Report
as of 20-May-2021

ARTICLES:

Publication Type: Journal Article Peer Reviewed: Y **Publication Status:** 1-Published
Journal: Nature Communications
Publication Identifier Type: DOI Publication Identifier: 10.1038/ncomms3127
Volume: 4 Issue: 0 First Page #: 0
Date Submitted: Date Published:
Publication Location:
Article Title: A DNA tweezer-actuated enzyme nanoreactor
Authors:
Keywords: Chemical Sciences, Nanotechnology
Abstract: The functions of regulatory enzymes are essential to modulating cellular pathways. Here we report a tweezer-like DNA nanodevice to actuate the activity of an enzyme/cofactor pair. A dehydrogenase and NAD+ cofactor are attached to different arms of the DNA tweezer structure and actuation of enzymatic function is achieved by switching the tweezers between open and closed states. The enzyme/cofactor pair is spatially separated in the open state with inhibited enzyme function, whereas in the closed state, enzyme is activated by the close proximity of the two molecules. The conformational state of the DNA tweezer is controlled by the addition of specific oligonucleotides that serve as the thermodynamic driver (fuel) to trigger the change. Using this approach, several cycles of externally controlled enzyme inhibition and activation are successfully demonstrated. This principle of responsive enzyme nanodevices may be used to regulate other types of enzymes and to introduce feedback or feed-fo
Distribution Statement: 1-Approved for public release; distribution is unlimited.
Acknowledged Federal Support:

Publication Type: Journal Article Peer Reviewed: Y **Publication Status:** 1-Published
Journal: Nano Letters
Publication Identifier Type: DOI Publication Identifier: 10.1021/nl304415b
Volume: 13 Issue: 2 First Page #: 0
Date Submitted: Date Published:
Publication Location:
Article Title: Super-Resolution Fingerprinting Detects Chemical Reactions and Idiosyncrasies of Single DNA Pegboards
Authors:
Keywords: Chemical imaging; DNA origami; PAINT; points accumulation for imaging in nanoscale topography; single molecule super-resolution fluorescence microscopy
Abstract: We employ the single-particle fluorescence nanoscopy technique points accumulation for imaging in nanoscale topography (PAINT) using site-specific DNA probes to acquire two-dimensional density maps of specific features patterned on nanoscale DNA origami pegboards. We show that PAINT has a localization accuracy of 10 nm that is sufficient to reliably distinguish dense (>104 features ?m–2) sub-100 nm patterns of oligonucleotide features. We employ two-color PAINT to follow enzyme-catalyzed modification of features on individual origami and to show that single nanopegboards exhibit stable, spatially heterogeneous probe-binding patterns, or “fingerprints.” Finally, we present experimental and modeling evidence suggesting that these fingerprints may arise from feature spacing variations that locally modulate the probe binding kinetics. Our study highlights the power of fluorescence nanoscopy to perform quality control on individual soft nanodevices that interact with and position reagents i
Distribution Statement: 1-Approved for public release; distribution is unlimited.
Acknowledged Federal Support:

RPPR Final Report
as of 20-May-2021

Publication Type: Journal Article Peer Reviewed: Y **Publication Status:** 1-Published
Journal: Nano Letters
Publication Identifier Type: DOI Publication Identifier: 10.1021/nl400976s
Volume: 13 Issue: 6 First Page #: 0
Date Submitted: Date Published:
Publication Location:
Article Title: Multifactorial Modulation of Binding and Dissociation Kinetics on Two-Dimensional DNA Nanostructures
Authors:
Keywords: DNA origami; DNA nanotechnology; kinetics; single molecule; single-particle FRET
Abstract: We use single-particle fluorescence resonance energy transfer (FRET) to show that organizing oligonucleotide probes into patterned two-dimensional arrays on DNA origami nanopegboards significantly alters the kinetics and thermodynamics of their hybridization with complementary targets in solution. By systematically varying the spacing of probes, we demonstrate that the rate of dissociation of a target is reduced by an order of magnitude in the densest probe arrays. The rate of target binding is reduced less dramatically, but to a greater extent than reported previously for one-dimensional probe arrays. By additionally varying target sequence and buffer composition, we provide evidence for two distinct mechanisms for the markedly slowed dissociation: direct hopping of targets between adjacent sequence-matched probes and nonsequence-specific, salt-bridged, and thus attractive electrostatic interactions with the DNA origami pegboard. This kinetic behavior varies little between individual
Distribution Statement: 1-Approved for public release; distribution is unlimited.
Acknowledged Federal Support:

Publication Type: Journal Article Peer Reviewed: Y **Publication Status:** 1-Published
Journal: Nucleic Acids Research
Publication Identifier Type: DOI Publication Identifier: 10.1093/nar/gkt1269
Volume: 42 Issue: 4 First Page #: 2159
Date Submitted: Date Published:
Publication Location:
Article Title: Structure-based model for light-harvesting properties of nucleic acid nanostructures
Authors:
Keywords: light harvesting, structural model
Abstract: Programmed self-assembly of DNA enables the rational design of megadalton-scale macromolecular assemblies with sub-nanometer scale precision. These assemblies can be programmed to serve as structural scaffolds for secondary chromophore molecules with light-harvesting properties. Like in natural systems, the local and global spatial organization of these synthetic scaffolded chromophore systems plays a crucial role in their emergent excitonic and optical properties. Previously, we introduced a computational model to predict the large-scale 3D solution structure and flexibility of nucleic acid nanostructures programmed using the principle of scaffolded DNA origami. Here, we use Förster resonance energy transfer theory to simulate the temporal dynamics of dye excitation and energy transfer accounting both for overall DNA nanostructure architecture as well as atomic-level DNA and dye chemical structure and composition. Results are used to calculate emergent optical properties including eff
Distribution Statement: 3-Distribution authorized to U.S. Government Agencies and their contractors
Acknowledged Federal Support:

RPPR Final Report
as of 20-May-2021

Publication Type: Journal Article Peer Reviewed: Y **Publication Status:** 1-Published
Journal: ACS Nano
Publication Identifier Type: DOI Publication Identifier: 10.1021/nn5011914
Volume: 8 Issue: 5 First Page #: 5132
Date Submitted: Date Published:
Publication Location:
Article Title: Virus-Inspired Membrane Encapsulation of DNA Nanostructures To Achieve
Authors:
Keywords: DNA nanotechnology, membrane encapsulation
Abstract: DNA nanotechnology enables engineering of molecular-scale devices with exquisite control over geometry and site-specific functionalization. This capability promises compelling advantages in advancing nanomedicine; nevertheless, instability in biological environments and innate immune activation remain as obstacles for in vivo application. Natural particle systems (i.e., viruses) have evolved mechanisms to maintain structural integrity and avoid immune recognition during infection, including encapsulation of their genome and protein capsid shell in a lipid envelope. Here we introduce virus-inspired enveloped DNA nanostructures as a design strategy for biomedical applications. Achieving a high yield of tightly wrapped unilamellar nanostructures, mimicking the morphology of enveloped virus particles, required precise control over the density of attached lipid conjugates and was achieved at 1 per 180 nm2. Envelopment of DNA nanostructures in PEGylated lipid bilayers conferred protection ag
Distribution Statement: 3-Distribution authorized to U.S. Government Agencies and their contractors
Acknowledged Federal Support:

Publication Type: Journal Article Peer Reviewed: Y **Publication Status:** 1-Published
Journal: ACS Nano
Publication Identifier Type: DOI Publication Identifier: 10.1021/nn500108k
Volume: 8 Issue: 6 First Page #: 5641
Date Submitted: Date Published:
Publication Location:
Article Title: DNA–Cholesterol Barges as Programmable Membrane-Exploring Agents
Authors:
Keywords: DNA-cholesterol barges
Abstract: DNA nanotechnology enables the precise construction of nanoscale devices that mimic aspects of natural biomolecular systems yet exhibit robustly programmable behavior. While many important biological processes involve dynamic interactions between components associated with phospholipid membranes, little progress has been made toward creating synthetic mimics of such interfacial systems. We report the assembly and characterization of cholesterol-labeled DNA origami “barges” capable of reversible association with and lateral diffusion on supported lipid bilayers. Using single-particle fluorescence microscopy, we show that these DNA barges rapidly and stably embed in lipid bilayers and exhibit Brownian diffusion in a manner dependent on both cholesterol labeling and bilayer composition. Tracking of individual barges rapidly generates super-resolution maps of the contiguous regions of a membrane. Addition of appropriate command oligonucleotides enables membrane-associated barges to reversi
Distribution Statement: 3-Distribution authorized to U.S. Government Agencies and their contractors
Acknowledged Federal Support:

RPPR Final Report
as of 20-May-2021

Publication Type: Journal Article Peer Reviewed: Y **Publication Status:** 1-Published
Journal: Nature Nanotechnology
Publication Identifier Type: DOI Publication Identifier: 10.1038/nnano.2014.100
Volume: 9 Issue: 7 First Page #: 531
Date Submitted: Date Published:
Publication Location:
Article Title: Multi-enzyme complexes on DNA scaffolds capable of substrate channelling with an artificial swinging arm
Authors:
Keywords: DNA nanotechnology, enzyme casecade, substrate channelling, swinging arm
Abstract: Swinging arms are a key functional component of multistep catalytic transformations in many naturally occurring multi-enzyme complexes1. This arm is typically a prosthetic chemical group that is covalently attached to the enzyme complex via a flexible linker, allowing the direct transfer of substrate molecules between multiple active sites within the complex. Mimicking this method of substrate channelling outside the cellular environment requires precise control over the spatial parameters of the individual components within the assembled complex. DNA nanostructures can be used to organize functional molecules with nanoscale precision and can also provide nanomechanical control. Until now, protein–DNA assemblies have been used to organize cascades of enzymatic reactions by controlling the relative distance and orientation of enzymatic components or by facilitating the interface between enzymes/cofactors and electrode surfaces. Here, we show that a DNA nanostructure can be used to creat
Distribution Statement: 3-Distribution authorized to U.S. Government Agencies and their contractors
Acknowledged Federal Support:

Publication Type: Journal Article Peer Reviewed: Y **Publication Status:** 1-Published
Journal: Journal of the American Chemical Society
Publication Identifier Type: DOI Publication Identifier: 10.1021/ja411843k
Volume: 136 Issue: 12 First Page #: 4599
Date Submitted: Date Published:
Publication Location:
Article Title: Reengineering the Optical Absorption Cross-Section of Photosynthetic Reaction Centers
Authors:
Keywords: Photosynthesis, reaction center, optical absorption
Abstract: Engineered cysteine residues near the primary electron donor (P) of the reaction center from the purple photosynthetic bacterium Rhodobacter sphaeroides were covalently conjugated to each of several dye molecules in order to explore the geometric design and spectral requirements for energy transfer between an artificial antenna system and the reaction center. An average of 2.5 fluorescent dye molecules were attached at specific locations near P. The enhanced absorbance cross-section afforded by conjugation of Alexa Fluor 660 dyes resulted in a 2.2-fold increase in the formation of reaction center charge-separated state upon intensity-limited excitation at 650 nm. The effective increase in absorbance cross-section resulting from the conjugation of two other dyes, Alexa Fluor 647 and Alexa Fluor 750, was also investigated. The key parameters that dictate the efficiency of dye-to-reaction center energy transfer and subsequent charge separation were examined using both steady-state and tim
Distribution Statement: 3-Distribution authorized to U.S. Government Agencies and their contractors
Acknowledged Federal Support:

RPPR Final Report
as of 20-May-2021

Publication Type: Journal Article Peer Reviewed: Y **Publication Status:** 1-Published
Journal: Journal of the American Chemical Society
Publication Identifier Type: DOI Publication Identifier: 10.1021/ja505101a
Volume: 136 Issue: 32 First Page #: 11198
Date Submitted: Date Published:
Publication Location:
Article Title: Structural DNA Nanotechnology: State of the Art and Future Perspective
Authors:
Keywords: Structural DNA nanotechnology, perspective
Abstract: Over the past three decades DNA has emerged as an exceptional molecular building block for nanoconstruction due to its predictable conformation and programmable intra- and intermolecular Watson–Crick base-pairing interactions. A variety of convenient design rules and reliable assembly methods have been developed to engineer DNA nanostructures of increasing complexity. The ability to create designer DNA architectures with accurate spatial control has allowed researchers to explore novel applications in many directions, such as directed material assembly, structural biology, biocatalysis, DNA computing, nanorobotics, disease diagnosis, and drug delivery. This Perspective discusses the state of the art in the field of structural DNA nanotechnology and presents some of the challenges and opportunities that exist in DNA-based molecular design and programming.
Distribution Statement: 3-Distribution authorized to U.S. Government Agencies and their contractors
Acknowledged Federal Support:

Publication Type: Journal Article Peer Reviewed: Y **Publication Status:** 1-Published
Journal: Inorganic Chemistry
Publication Identifier Type: DOI Publication Identifier: 10.1021/ic5023906
Volume: 5.4E+001 Issue: 3.0E+000 First Page #: 0
Date Submitted: Date Published:
Publication Location:
Article Title: Nanoporous Delafossite CuAlO
Authors:
Keywords: nanoporous materials
Abstract: Nanoporous structures of a p-type semiconductor, delafossite CuAlO(2), with a high crystallinity have been fabricated through an inorganic/polymer double-gel process and characterized for the first time via Mott-Schottky measurements. The effect of the precursor concentration, calcination temperature, and atmosphere were examined to achieve high crystallinity and photoelectrochemical properties while maximizing the porosity. The optical properties of the nanoporous CuAlO(2) are in good agreement with the literature with an optical band gap of 3.9 eV, and the observed high electrical conductivity and hole concentrations conform to highly crystalline and well-sintered nanoparticles observed in the product. The Mott-Schottky plot from the electrochemical impedance spectroscopy studies indicates a flat-band potential of 0.49 V versus Ag/AgCl. It is concluded that CuAlO(2) exhibits band energies very close to those of NiO but with electrical properties very desirable in the fabrication of p
Distribution Statement: 3-Distribution authorized to U.S. Government Agencies and their contractors
Acknowledged Federal Support:

RPPR Final Report
as of 20-May-2021

Publication Type: Journal Article Peer Reviewed: Y **Publication Status:** 1-Published
Journal: Current Nanoscience
Publication Identifier Type: DOI Publication Identifier: 10.2174/1573413711666150505223339
Volume: 1.1E+001 Issue: 6.0E+000 First Page #: 0
Date Submitted: Date Published:
Publication Location:
Article Title: Single-Molecule Sensing of Biomolecular Interactions on DNA Nanostructures
Authors:
Keywords: Biomolecular interaction
Abstract: Living systems have evolved a variety of complex nanostructures to control biomolecular interactions and biochemical reactions that are vital to the metabolism and reproduction. During the past few decades, single-molecule detection and imaging have been widely applied to interpreting biological processes in detail, which are able to observe the chemical reactions and kinetic behaviors of individual molecules. The rapid development of structural DNA nanotechnology has provided adaptable platforms to facilitate single-molecule detection and super-resolution imaging of individual biological components, as well as manipulating artificial nanosystems with molecular precision. In this review, we summarize recent exciting progress in using DNA nanostructures to sense and manipulate biomolecular interactions at the single-molecule level.
Distribution Statement: 3-Distribution authorized to U.S. Government Agencies and their contractors
Acknowledged Federal Support:

Publication Type: Journal Article Peer Reviewed: Y **Publication Status:** 1-Published
Journal: Nature Nanotechnology
Publication Identifier Type: DOI Publication Identifier: 10.1038/nnano.2015.162
Volume: 0 Issue: 0 First Page #: 0
Date Submitted: Date Published:
Publication Location:
Article Title: Complex wireframe DNA origami nanostructures with multi-arm junction vertices
Authors:
Keywords: DNA nanostructure
Abstract: Structural DNA nanotechnology and the DNA origami technique5, in particular, have provided a range of spatially addressable two- and three-dimensional nanostructures. These structures are, however, typically formed of tightly packed parallel helices. The development of wireframe structures10, 11 should allow the creation of novel designs with unique functionalities, but engineering complex wireframe architectures with arbitrarily designed connections between selected vertices in three-dimensional space remains a challenge. Here, we report a design strategy for fabricating finite-size wireframe DNA nanostructures with high complexity and programmability. In our approach, the vertices are represented by n?×?4 multi-arm junctions (n?=?2–10) with controlled angles, and the lines are represented by antiparallel DNA crossover tiles of variable lengths. Scaffold strands are used to integrate the vertices and lines into fully assembled structures displaying intricate architectures. To demonstr
Distribution Statement: 3-Distribution authorized to U.S. Government Agencies and their contractors
Acknowledged Federal Support:

RPPR Final Report
as of 20-May-2021

Publication Type: Journal Article Peer Reviewed: Y **Publication Status:** 1-Published
Journal: Bioconjugate Chemistry
Publication Identifier Type: DOI Publication Identifier: 10.1021/acs.bioconjchem.5b00194
Volume: 0 Issue: 0 First Page #: 0
Date Submitted: Date Published:
Publication Location:
Article Title: DNA Nanostructures as Programmable Biomolecular Scaffolds
Authors:
Keywords: DNA nanotechnology
Abstract: This Review focuses on how to use DNA nanostructures as scaffolds to organize biological molecules. First, we introduce the use of structural DNA nanotechnology to engineer rationally designed nanostructures. Second, we survey approaches used to generate protein–DNA conjugates. Third, we discuss studies exploring DNA scaffolds to create DNA nanodevices to analyze protein structures, to engineer enzyme pathways, to create artificial light-harvesting systems, and to generate nanomachines in vitro and in vivo. Future challenges and perspectives of using DNA nanostructures as programmable biomolecular scaffolds are addressed at the end.
Distribution Statement: 3-Distribution authorized to U.S. Government Agencies and their contractors
Acknowledged Federal Support:

Publication Type: Journal Article Peer Reviewed: Y **Publication Status:** 1-Published
Journal: ACS Nano
Publication Identifier Type: DOI Publication Identifier: 10.1021/acsnano.5b01841
Volume: 9.0E+000 Issue: 7.0E+000 First Page #: 0
Date Submitted: Date Published:
Publication Location:
Article Title: Electron Microscopic Visualization of Protein Assemblies on Flattened DNA Origami
Authors:
Keywords: DNA nanotechnology, EM
Abstract: DNA provides an ideal substrate for the engineering of versatile nanostructures due to its reliable Watson-Crick base pairing and well-characterized conformation. One of the most promising applications of DNA nanostructures arises from the site-directed spatial arrangement with nanometer precision of guest components such as proteins, metal nanoparticles, and small molecules. Two-dimensional DNA origami architectures, in particular, offer a simple design, high yield of assembly, and large surface area for use as a nanoplatform. However, such single-layer DNA origami were recently found to be structurally polymorphous due to their high flexibility, leading to the development of conformationally restrained multilayered origami that lack some of the advantages of the single-layer designs. Here we monitored single-layer DNA origami by transmission electron microscopy (EM) and discovered that their conformational heterogeneity is dramatically reduced in the presence of a low concentration o
Distribution Statement: 3-Distribution authorized to U.S. Government Agencies and their contractors
Acknowledged Federal Support:

RPPR Final Report
as of 20-May-2021

Publication Type: Journal Article Peer Reviewed: Y **Publication Status:** 1-Published
Journal: Nature Biotechnology
Publication Identifier Type: DOI Publication Identifier: 10.1038/nbt.3246
Volume: 3.3E+001 Issue: 7.0E+000 First Page #: 0
Date Submitted: Date Published:
Publication Location:
Article Title: Kinetic fingerprinting to identify and count single nucleic acids
Authors:
Keywords: Kinetic fingerprinting, single molecule
Abstract: MicroRNAs (miRNAs) have emerged as promising diagnostic biomarkers. We introduce a kinetic fingerprinting approach called single-molecule recognition through equilibrium Poisson sampling (SiMREPS) for the amplification-free counting of single unlabeled miRNA molecules, which circumvents thermodynamic limits of specificity and virtually eliminates false positives. We demonstrate high-confidence, single-molecule detection of synthetic and endogenous miRNAs in both buffer and minimally treated biofluids, as well as >500-fold discrimination between single nucleotide polymorphisms.
Distribution Statement: 3-Distribution authorized to U.S. Government Agencies and their contractors
Acknowledged Federal Support:

Publication Type: Journal Article Peer Reviewed: Y **Publication Status:** 1-Published
Journal: Archives of Toxicology
Publication Identifier Type: DOI Publication Identifier: 10.1007/s00204-014-1357-9
Volume: 8.8E+001 Issue: 1.1E+001 First Page #: 0
Date Submitted: Date Published:
Publication Location:
Article Title: Single-molecule tools for enzymology, structural biology, systems biology and nanotechnology: an update
Authors:
Keywords: Single molecule enzymology
Abstract: Toxicology is the highly interdisciplinary field studying the adverse effects of chemicals on living organisms. It requires sensitive tools to detect such effects. After their initial implementation during the 1990s, single-molecule fluorescence detection tools were quickly recognized for their potential to contribute greatly to many different areas of scientific inquiry. In the intervening time, technical advances in the field have generated ever-improving spatial and temporal resolution and have enabled the application of single-molecule fluorescence to increasingly complex systems, such as live cells. In this review, we give an overview of the optical components necessary to implement the most common versions of single-molecule fluorescence detection. We then discuss current applications to enzymology and structural studies, systems biology, and nanotechnology, presenting the technical considerations that are unique to each area of study, along with noteworthy recent results. We als
Distribution Statement: 3-Distribution authorized to U.S. Government Agencies and their contractors
Acknowledged Federal Support:

RPPR Final Report
as of 20-May-2021

Publication Type: Journal Article Peer Reviewed: Y **Publication Status:** 1-Published
Journal: Angewandte Chemie International Edition
Publication Identifier Type: DOI Publication Identifier: 10.1002/anie.201603183
Volume: 55 Issue: 26 First Page #: 7483
Date Submitted: 7/21/16 12:00AM Date Published: 6/1/16 7:00AM
Publication Location:
Article Title: Directional Regulation of Enzyme Pathways through the Control of Substrate Channeling on a DNA Origami Scaffold
Authors: Guoliang Ke, Minghui Liu, Shuoxing Jiang, Xiaodong Qi, Yuhe Renee Yang, Shaun Wootten, Fei Zhang
Keywords: enzyme cascade, DNA nanotechnology
Abstract: Artificial multi-enzyme systems with precise and dynamic control over the enzyme pathway activity are of great significance in bionanotechnology and synthetic biology. Herein, we exploit a spatially addressable DNA nanoplatform for the directional regulation of two enzyme pathways (G6pDH–MDH and G6pDH–LDH) through the control of NAD+ substrate channeling by specifically shifting NAD+ between the two enzyme pairs. We believe that this concept will be useful for the design of regulatory biological circuits for synthetic biology and biomedicine.
Distribution Statement: 3-Distribution authorized to U.S. Government Agencies and their contractors
Acknowledged Federal Support: **Y**

Publication Type: Journal Article Peer Reviewed: Y **Publication Status:** 1-Published
Journal: ChemBioChem
Publication Identifier Type: DOI Publication Identifier: 10.1002/cbic.201600103
Volume: 17 Issue: 12 First Page #: 1097
Date Submitted: 7/21/16 12:00AM Date Published: 6/1/16 12:00AM
Publication Location:
Article Title: A Three-Enzyme Pathway with an Optimised Geometric Arrangement to Facilitate Substrate Transfer
Authors: Minghui Liu, Jinglin Fu, Xiaodong Qi, Shaun Wootten, Neal W. Woodbury, Yan Liu, Hao Yan
Keywords: enzyme cascade, DNA nanotechnology
Abstract: Cascade reactions drive and regulate a variety of metabolic activities. Efficient coupling of substrate transport between enzymes is important for overall pathway activity and also controls the depletion of intermediate molecules that drive the reaction forward. Here, we assembled a three-enzyme pathway on a series of DNA nanoscaffolds to investigate the dependence of their activities on spatial arrangement. Unlike previous studies, the overall activity of the three-enzyme pathway relied less on inter-enzyme distance and more on the geometric patterns that arranged them within a relatively small range of 10–30?nm. Pathway intermediate detection demonstrated that the assembled enzyme systems quickly depleted the intermediate molecules through efficient reaction coupling.
Distribution Statement: 3-Distribution authorized to U.S. Government Agencies and their contractors
Acknowledged Federal Support: **Y**

RPPR Final Report
as of 20-May-2021

Publication Type: Journal Article Peer Reviewed: Y **Publication Status:** 1-Published
Journal: Nature Communications
Publication Identifier Type: DOI Publication Identifier: 10.1038/ncomms10619
Volume: 7 Issue: First Page #: 10619
Date Submitted: 7/21/16 12:00AM Date Published: 2/1/16 7:00AM
Publication Location:
Article Title: Nanocaged enzymes with enhanced catalytic activity and increased stability against protease digestion
Authors: Zhao Zhao, Jinglin Fu, Soma Dhakal, Alexander Johnson-Buck, Minghui Liu, Ting Zhang, Neal W. Wooc
Keywords: Enzyme encapsulation, Nanocage
Abstract: Cells routinely compartmentalize enzymes for enhanced efficiency of their metabolic pathways. Here we report a general approach to construct DNA nanocaged enzymes for enhancing catalytic activity and stability. Nanocaged enzymes are realized by self-assembly into DNA nanocages with well-controlled stoichiometry and architecture that enabled a systematic study of the impact of both encapsulation and proximal polyanionic surfaces on a set of common metabolic enzymes. Activity assays at both bulk and single-molecule levels demonstrate increased substrate turnover numbers for DNA nanocage-encapsulated enzymes. Unexpectedly, we observe a significant inverse correlation between the size of a protein and its activity enhancement. This effect is consistent with a model wherein distal polyanionic surfaces of the nanocage enhance the stability of active enzyme conformations through the action of a strongly bound hydration layer. We further show that DNA nanocages protect encapsulated enzymes aga
Distribution Statement: 3-Distribution authorized to U.S. Government Agencies and their contractors
Acknowledged Federal Support: **Y**

Publication Type: Journal Article Peer Reviewed: Y **Publication Status:** 1-Published
Journal: Nanoscale
Publication Identifier Type: DOI Publication Identifier: 10.1039/C5NR07263H
Volume: 8 Issue: 5 First Page #: 3125
Date Submitted: 7/21/16 12:00AM Date Published:
Publication Location:
Article Title: Rational design of DNA-actuated enzyme nanoreactors guided by single molecule analysis
Authors: Soma Dhakal, Matthew R. Adendorff, Minghui Liu, Hao Yan, Mark Bathe, Nils G. Walter
Keywords: DNA tweezers, enzyme regulation
Abstract: The control of enzymatic reactions using nanoscale DNA devices offers a powerful application of DNA nanotechnology uniquely derived from actuation. However, previous characterization of enzymatic reaction rates using bulk biochemical assays reported suboptimal function of DNA devices such as tweezers. To gain mechanistic insight into this deficiency and to identify design rules to improve their function, here we exploit the synergy of single molecule imaging and computational modeling to characterize the three-dimensional structures and catalytic functions of DNA tweezer-actuated nanoreactors. Our analysis revealed two important deficiencies – incomplete closure upon actuation and conformational heterogeneity. Upon rational redesign of the Holliday junctions located at their hinge and arms, we found that the DNA tweezers could be more completely and uniformly closed. A novel single molecule enzyme assay was developed to demonstrate that our design improvements yield significant, indepe
Distribution Statement: 3-Distribution authorized to U.S. Government Agencies and their contractors
Acknowledged Federal Support: **Y**

RPPR Final Report
as of 20-May-2021

Publication Type: Journal Article Peer Reviewed: Y **Publication Status:** 1-Published
Journal: Nano Letters
Publication Identifier Type: DOI Publication Identifier: 10.1021/acs.nanolett.5b04608
Volume: 16 Issue: 1 First Page #: 736
Date Submitted: 7/21/16 12:00AM Date Published: 1/1/16 7:00AM
Publication Location:
Article Title: DNAzyme-Based Logic Gate-Mediated DNA Self-Assembly
Authors: Cheng Zhang, Jing Yang, Shuoxing Jiang, Yan Liu, Hao Yan
Keywords: DNA origami; DNA self-assembly; DNAzyme; logic gates
Abstract: Controlling DNA self-assembly processes using rationally designed logic gates is a major goal of DNA-based nanotechnology and programming. Such controls could facilitate the hierarchical engineering of complex nanopatterns responding to various molecular triggers or inputs. Here, we demonstrate the use of a series of DNAzyme-based logic gates to control DNA tile self-assembly onto a prescribed DNA origami frame. Logic systems such as “YES,” “OR,” “AND,” and “logic switch” are implemented based on DNAzyme-mediated tile recognition with the DNA origami frame. DNAzyme is designed to play two roles: (1) as an intermediate messenger to motivate downstream reactions and (2) as a final trigger to report fluorescent signals, enabling information relay between the DNA origami-framed tile assembly and fluorescent signaling. The results of this study demonstrate the plausibility of DNAzyme-mediated hierarchical self-assembly and provide new tools for generating dynamic and responsive self-assembl
Distribution Statement: 3-Distribution authorized to U.S. Government Agencies and their contractors
Acknowledged Federal Support: **Y**

Publication Type: Journal Article Peer Reviewed: Y **Publication Status:** 1-Published
Journal: PLOS ONE
Publication Identifier Type: DOI Publication Identifier: 10.1371/journal.pone.0154865
Volume: 11 Issue: 5 First Page #:
Date Submitted: 7/21/16 12:00AM Date Published: 5/1/16 12:00AM
Publication Location:
Article Title: A Hidden Transhydrogen Activity of a FMN-Bound Diaphorase under Anaerobic Conditions
Authors: John Collins, Ting Zhang, Scott Huston, Fangfang Sun, Y.-H. Percival Zhang, Jinglin Fu, Feng Liang
Keywords: Hydrides, Curve fitting, Argon, Oxidation-reduction reaction, Adenine, Dehydrogenases, Enzyme assays, Cofactors
Abstract: Redox cofactors of NADH/NADPH participate in many cellular metabolic pathways for facilitating the electron transfer from one molecule to another in redox reactions. Transhydrogenase plays an important role in linking catabolism and anabolism, regulating the ratio of NADH/NADPH in cells. The cytoplasmic transhydrogenases could be useful to engineer synthetic biochemical pathways for the production of high-value chemicals and biofuels.A transhydrogenase activity was discovered for a FMN-bound diaphorase (DI) from Geobacillus stearothermophilus under anaerobic conditions. The DI-catalyzed hydride exchange were monitored and characterized between a NAD(P)H and a thio-modified NAD+ analogue. This new function of DI was demonstrated to transfer a hydride from NADPH to NAD+ that was consumed by NAD-specific lactate dehydrogenase and malic dehydrogenase.We discover a novel transhydrogenase activity of a FMN-DI by stabilizing the reduced state of FMNH2 under anaerobic conditions. FMN-DI was de
Distribution Statement: 3-Distribution authorized to U.S. Government Agencies and their contractors
Acknowledged Federal Support: **Y**

RPPR Final Report
as of 20-May-2021

Publication Type: Journal Article Peer Reviewed: Y **Publication Status:** 1-Published
Journal: Journal of Chemical Theory and Computation
Publication Identifier Type: DOI Publication Identifier: 10.1021/acs.jctc.5b00965
Volume: 12 Issue: 1 First Page #: 261
Date Submitted: 7/21/16 12:00AM Date Published: 1/1/16 7:00AM
Publication Location:
Article Title: Computing Nonequilibrium Conformational Dynamics of Structured Nucleic Acid Assemblies
Authors: Reza Sharifi Sedeh, Keyao Pan, Matthew Ralph Adendorff, Oskar Hallatschek, Klaus-Jürgen Bathe, Ma
Keywords: Nucleic acids, molecular dynamics, DNA origami, DNA nanostructures
Abstract: Synthetic nucleic acids can be programmed to form precise three-dimensional structures on the nanometer-scale. These thermodynamically stable complexes can serve as structural scaffolds to spatially organize functional molecules including multiple enzymes, chromophores, and force-sensing elements with internal dynamics that include substrate reaction-diffusion, excitonic energy transfer, and force–displacement response that often depend critically on both the local and global conformational dynamics of the nucleic acid assembly. However, high molecular weight assemblies exhibit long time-scale and large length-scale motions that cannot easily be sampled using all-atom computational procedures such as molecular dynamics. As an alternative, here we present a computational framework to compute the overdamped conformational dynamics of structured nucleic acid assemblies and apply it to a DNA-based tweezer, a nine-layer DNA origami ring, and a pointer-shaped DNA origami object, which consis
Distribution Statement: 3-Distribution authorized to U.S. Government Agencies and their contractors
Acknowledged Federal Support: **Y**

Publication Type: Journal Article Peer Reviewed: Y **Publication Status:** 1-Published
Journal: Inorganic Chemistry
Publication Identifier Type: DOI Publication Identifier: 10.1021/acs.inorgchem.6b00712
Volume: 55 Issue: 13 First Page #: 6574
Date Submitted: 7/21/16 12:00AM Date Published: 7/1/16 7:00AM
Publication Location:
Article Title: Unusual Changes in Electronic Band-Edge Energies of the Nanostructured Transparent n-Type Semiconductor Zr-Doped Anatase TiO
Authors: Daniel G. Mieritz, Adèle Renaud, Dong-Kyun Seo
Keywords: Nanoporous materials, scanning electron microscopy, transmission electron microscopy, nitrogen gas sorption measurements, UV/vis spectroscopies, and Mott–Schottky measurements
Abstract: By the establishment of highly controllable synthetic routes, electronic band-edge energies of the n-type transparent semiconductor Zr-doped anatase TiO2 have been studied holistically for the first time up to 30 atom % Zr, employing powder X-ray diffraction, scanning electron microscopy, transmission electron microscopy, nitrogen gas sorption measurements, UV/vis spectroscopies, and Mott–Schottky measurements. The materials were produced through a sol–gel synthetic procedure that ensures good compositional homogeneity of the materials, while introducing nanoporosity in the structure, by achieving a mild calcination condition. Vegard's law was discovered among the homogeneous samples, and correlations were established between the chemical compositions and optical and electronic properties of the materials. Up to 20% Zr doping, the optical energy gap increases to 3.29 eV (vs 3.19 eV for TiO2), and the absolute conduction band-edge energy increases to ?3.90 eV (vs ?4.14 eV). The energy c
Distribution Statement: 3-Distribution authorized to U.S. Government Agencies and their contractors
Acknowledged Federal Support: **Y**

RPPR Final Report
as of 20-May-2021

Publication Type: Journal Article Peer Reviewed: Y **Publication Status:** 1-Published
Journal: Journal of Solid State Chemistry
Publication Identifier Type: DOI Publication Identifier: 10.1016/j.jssc.2016.02.007
Volume: Issue: First Page #:
Date Submitted: 7/21/16 12:00AM Date Published: 2/1/16 7:00AM
Publication Location:
Article Title: Accessing alkali-free NASICON-type compounds through mixed oxoanion sol–gel chemistry: Hydrogen titanium phosphate sulfate, H1?xTi2(PO4)3?x(SO4)x (x=0.5–1)
Authors: Daniel Mieritz, Stephen K. Davidowski, Dong-Kyun Seo
Keywords: Sol-gesynthesis; NASICON-type oxides; Mixed oxoanion; Battery material
Abstract: We report a direct sol–gel synthesis and characterization of new proton-containing, rhombohedral NASICION-type titanium compounds with mixed phosphate and sulfate oxoanions. The synthetic conditions were established by utilizing peroxide ion as a decomposable and stabilizing ligand for titanyl ions in the presence of phosphates in a strong acidic medium. Thermogravimetric analysis (TGA), powder X-ray diffraction (PXRD), induction-coupled plasma optical emission spectroscopic (ICP-OES) elemental analysis, and Raman and 1H magic angle spinning nuclear magnetic resonance (MAS-NMR) spectroscopic studies have determined the presence of sulfate and proton ions in the structure, for which the compositional range has been found to be H1?xTi2(PO4)3?x(SO4)x (x=0.5–1). The particulate products exhibit a nanocrystalline nature observed through characterization with scanning electron microscopy (SEM) and transmission electron microscopy (TEM). The N2 sorption isotherm measurements and subsequent Br
Distribution Statement: 3-Distribution authorized to U.S. Government Agencies and their contractors
Acknowledged Federal Support: **Y**

Publication Type: Journal Article Peer Reviewed: Y **Publication Status:** 1-Published
Journal: Nature Chemistry
Publication Identifier Type: DOI Publication Identifier: 10.1038/nchem.2472
Volume: 8 Issue: 5 First Page #: 476
Date Submitted: 7/21/16 12:00AM Date Published: 3/1/16 7:00AM
Publication Location:
Article Title: Self-assembly of size-controlled liposomes on DNA nanotemplates
Authors: Yang Yang, Jing Wang, Hideki Shigematsu, Weiming Xu, William M. Shih, James E. Rothman, Chenxia
Keywords: lipids, molecular self-assembly, organizing materials with DNA, self-assembly
Abstract: Artificial lipid-bilayer membranes are valuable tools for the study of membrane structure and dynamics. For applications such as the study of vesicular transport and drug delivery, there is a pressing need for artificial vesicles with controlled size. However, controlling vesicle size and shape with nanometre precision is challenging, and approaches to achieve this can be heavily affected by lipid composition. Here, we present a bio-inspired templating method to generate highly monodispersed sub-100-nm unilamellar vesicles, where liposome self-assembly was nucleated and confined inside rigid DNA nanotemplates. Using this method, we produce homogeneous liposomes with four distinct predefined sizes. We also show that the method can be used with a variety of lipid compositions and probe the mechanism of templated liposome formation by capturing key intermediates during membrane self-assembly. The DNA nanotemplating strategy represents a conceptually novel way to guide lipid bilayer format
Distribution Statement: 3-Distribution authorized to U.S. Government Agencies and their contractors
Acknowledged Federal Support: **Y**

RPPR Final Report
as of 20-May-2021

Publication Type: Journal Article Peer Reviewed: Y **Publication Status:** 1-Published
Journal: Journal of the American Chemical Society
Publication Identifier Type: DOI Publication Identifier: 10.1021/jacs.5b13107
Volume: 138 Issue: 13 First Page #: 4439
Date Submitted: 7/21/16 12:00AM Date Published: 4/1/16 7:00AM
Publication Location:
Article Title: A Programmable DNA Origami Platform to Organize SNAREs for Membrane Fusion
Authors: Weiming Xu, Bhavik Nathwani, Chenxiang Lin, Jing Wang, Erdem Karatekin, Frederic Pincet, William Sh
Keywords: SNARE, cellular communication, trafficking, DNA nanostructure
Abstract: Soluble N-ethylmaleimide-sensitive factor attachment protein receptor (SNARE) complexes are the core molecular machinery of membrane fusion, a fundamental process that drives inter- and intracellular communication and trafficking. One of the questions that remains controversial has been whether and how SNAREs cooperate. Here we show the use of self-assembled DNA-nanostructure rings to template uniform-sized small unilamellar vesicles containing predetermined maximal number of externally facing SNAREs to study the membrane-fusion process. We also incorporated lipid-conjugated complementary ssDNA as tethers into vesicle and target membranes, which enabled bypass of the rate-limiting docking step of fusion reactions and allowed direct observation of individual membrane-fusion events at SNARE densities as low as one pair per vesicle. With this platform, we confirmed at the single event level that, after docking of the templated-SUVs to supported lipid bilayers (SBL), one to two pairs of SN
Distribution Statement: 3-Distribution authorized to U.S. Government Agencies and their contractors
Acknowledged Federal Support: **Y**

Publication Type: Journal Article Peer Reviewed: Y **Publication Status:** 1-Published
Journal: Nature Communications
Publication Identifier Type: DOI Publication Identifier: 10.1038/ncomms9634
Volume: 6 Issue: First Page #: 8634
Date Submitted: 7/21/16 12:00AM Date Published: 11/1/15 7:00AM
Publication Location:
Article Title: Scalable amplification of strand subsets from chip-synthesized oligonucleotide libraries
Authors: Thorsten L. Schmidt, Brian J. Beliveau, Yavuz O. Uca, Mark Theilmann, Felipe Da Cruz, Chao-Ting Wu,
Keywords: Biological sciences Biotechnology Molecular biology Nanotechnology
Abstract: Synthetic oligonucleotides are the main cost factor for studies in DNA nanotechnology, genetics and synthetic biology, which all require thousands of these at high quality. Inexpensive chip-synthesized oligonucleotide libraries can contain hundreds of thousands of distinct sequences, however only at sub-femtomole quantities per strand. Here we present a selective oligonucleotide amplification method, based on three rounds of rolling-circle amplification, that produces nanomole amounts of single-stranded oligonucleotides per millilitre reaction. In a multistep one-pot procedure, subsets of hundreds or thousands of single-stranded DNAs with different lengths can selectively be amplified and purified together. These oligonucleotides are used to fold several DNA nanostructures and as primary fluorescence in situ hybridization probes. The amplification cost is lower than other reported methods (typically around US$ 20 per nanomole total oligonucleotides produced) and is dominated by the use
Distribution Statement: 3-Distribution authorized to U.S. Government Agencies and their contractors
Acknowledged Federal Support: **Y**

RPPR Final Report
as of 20-May-2021

Publication Type: Journal Article Peer Reviewed: Y **Publication Status:** 1-Published
Journal: Nature Nanotechnology
Publication Identifier Type: DOI Publication Identifier: 10.1038/nnano.2015.190
Volume: 10 Issue: 10 First Page #: 892
Date Submitted: 7/21/16 12:00AM Date Published: 8/1/15 7:00AM
Publication Location:
Article Title: Routing of individual polymers in designed patterns
Authors: Jakob Bach Knudsen, Lei Liu, Anne Louise Bank Kodal, Mikael Madsen, Qiang Li, Jie Song, Johannes E
Keywords: Bioconjugate chemistry Conjugated polymers Organizing materials with DNA
Abstract: Synthetic polymers are ubiquitous in the modern world, but our ability to exert control over the molecular conformation of individual polymers is very limited. In particular, although the programmable self-assembly of oligonucleotides and proteins into artificial nanostructures has been demonstrated, we currently lack the tools to handle other types of synthetic polymers individually and thus the ability to utilize and study their single-molecule properties. Here we show that synthetic polymer wires containing short oligonucleotides that extend from each repeat can be made to assemble into arbitrary routings. The wires, which can be more than 200?nm in length, are soft and bendable, and the DNA strands allow individual polymers to self-assemble into predesigned routings on both two- and three-dimensional DNA origami templates. The polymers are conjugated and potentially conducting, and could therefore be used to create molecular-scale electronic or optical wires in arbitrary geometries
Distribution Statement: 3-Distribution authorized to U.S. Government Agencies and their contractors
Acknowledged Federal Support: **Y**

Publication Type: Journal Article Peer Reviewed: Y **Publication Status:** 1-Published
Journal: Advanced Science, Engineering and Medicine
Publication Identifier Type: DOI Publication Identifier: 10.1166/asem.2015.1807
Volume: 7 Issue: 12 First Page #: 1007
Date Submitted: 7/22/16 12:00AM Date Published: 12/1/15 7:00AM
Publication Location:
Article Title: <I>A Special Issue on</I> How Can We Learn from Biology to Create New Functional Materials?
Authors: Jinglin Fu, Bryce Sadtler, Ian Wheeldon, Zhuangqun Huang
Keywords: biosynthesis, self-assembly, spatial organization
Abstract: Biology evolves biosynthetic pathways to fabricate complex materials with advanced functionalities. Bioinspired materials are chemically synthetic or bioproduced molecules, compounds, complexes, and superstructured materials whose composition, properties and synthetic strategies are reverse engineered from functional components in natural biosystems. Since biology has developed a blueprint for translating atomic and nanoscale elements into mesoscale materials, a major focus of this interdisciplinary field is to uncover the secrets of these natural processes (e.g., composition, synthesis pathways, mechanisms of self-assembly, and hierarchical and spatial organization), and apply this information to synthesize novel materials with new functions and properties. Bioinspired concepts are increasingly adapted into materials and devices intended for a variety of practical applications in the consumer industry, health care, and energy conversion. In this special issue of Advan
Distribution Statement: 3-Distribution authorized to U.S. Government Agencies and their contractors
Acknowledged Federal Support: **Y**

RPPR Final Report
as of 20-May-2021

Publication Type: Journal Article Peer Reviewed: Y **Publication Status:** 1-Published
Journal: Advanced Science, Engineering and Medicine
Publication Identifier Type: DOI Publication Identifier: 10.1166/asem.2015.1809
Volume: 7 Issue: 12 First Page #: 1019
Date Submitted: 7/22/16 12:00AM Date Published: 12/1/15 7:00AM
Publication Location:
Article Title: DNA-Directed Assembly of Conductive Nanomaterials
Authors: Ting Zhang, John Collins, Georgia A. Arbuckle-Keil, Jinglin Fu
Keywords: Conductive Nanomaterial, DNA Nanostructures, DNA-Templated Metallization, Nanoparticles, Conductive Polymer, Carbon Nanotube.
Abstract: Nanoelectronic devices are believed to have broad future applications, such as high-performance computer processors, high-capacity memory storage, optoelectronic devices, energy transformation and diagnostic sensors. They require the fabrication and manipulation of electronic components with nanoscale resolution, where materials exhibit different properties from traditional bulk devices. Over the past few decades, the rapid development of structural DNA nanotechnology has enabled the design and fabrication of complex nanostructures with prescribed 1D, 2D and 3D patterns. Selfassembled DNA nanostructures can thereby serve as templates to direct and control the synthesis of conductive materials at the nanoscale. In this review, we summarize recent exciting progress in the DNA-templated synthesis of a variety of conductive nanomaterials, including metal nanowires, nanoparticles, polymers, and carbon nanotubes.
Distribution Statement: 3-Distribution authorized to U.S. Government Agencies and their contractors
Acknowledged Federal Support: **Y**

Publication Type: Journal Article Peer Reviewed: Y **Publication Status:** 1-Published
Journal: ACS Applied Materials & Interfaces
Publication Identifier Type: DOI Publication Identifier: 10.1021/acsami.6b07940
Volume: 8 Issue: 38 First Page #: 25104
Date Submitted: 8/31/17 12:00AM Date Published: 9/1/16 7:00AM
Publication Location:
Article Title: Photocurrent Generation by Photosynthetic Purple Bacterial Reaction Centers Interfaced with a Porous Antimony-Doped Tin Oxide (ATO) Electrode
Authors: Anne-Marie Carey, HaoJie Zhang, Daniel Mieritz, Alex Volosin, Alastair T. Gardiner, Richard J. Cogdell,
Keywords: antimony-doped tin oxide (ATO); cytochrome c, electron transfer, photocurrent, porous electrode, reaction center
Abstract: The ability to exchange energy and information between biological and electronic materials is critical in the development of hybrid electronic systems in biomedicine, environmental sensing, and energy applications. While sensor technology has been extensively developed to collect detailed molecular information, less work has been done on systems that can specifically modulate the chemistry of the environment with temporal and spatial control. The bacterial photosynthetic reaction center represents an ideal photonic component of such a system in that it is capable of modifying local chemistry via light-driven redox reactions with quantitative control over reaction rates and has inherent spectroscopic probes for monitoring function. Here a well-characterized model system is presented, consisting of a transparent, porous electrode (antimony-doped tin oxide) which is electrochemically coupled to the reaction center via a cytochrome c molecule. Upon illumination, the reaction center perform
Distribution Statement: 3-Distribution authorized to U.S. Government Agencies and their contractors
Acknowledged Federal Support: **Y**

RPPR Final Report
as of 20-May-2021

Publication Type: Journal Article Peer Reviewed: Y **Publication Status:** 1-Published
Journal: J. Mater. Chem. A
Publication Identifier Type: DOI Publication Identifier: 10.1039/C6TA10458D
Volume: 5 Issue: 13 First Page #: 6038
Date Submitted: 8/31/17 12:00AM Date Published:
Publication Location:
Article Title: A highly stable and scalable photosynthetic reaction center–graphene hybrid electrode system for biomimetic solar energy transduction
Authors: Haojie Zhang, Anne-Marie Carey, Ki-Wan Jeon, Minghui Liu, Travis D. Murrell, Joshua Locsin, Su Lin, H
Keywords: reaction center, mercapto reduced graphene oxide
Abstract: A photosynthetic reaction center (RC)-based electrode system is one of the most promising biomimetic approaches for solar energy transduction which is a renewable and environment-friendly source of energy. However, the instability of RCs in a non-cellular environment and the unfeasible scalability of electrode materials hamper the promising application of these systems. Herein, we report a highly stable and scalable RC-electrode system in which RCs are directly immobilized on a flexible and transparent mercapto reduced graphene oxide (mRGO) electrode. RCs immobilized on a mRGO film retain their photoactivity after twenty-week storage under darkness and even after 24 h continuous illumination at room temperature under aerobic conditions. The remarkable stability and mechanical flexibility of our system offer great potential for the development of a flexible RC-based biomimetic device for solar energy transduction.
Distribution Statement: 3-Distribution authorized to U.S. Government Agencies and their contractors
Acknowledged Federal Support: **Y**

Publication Type: Journal Article Peer Reviewed: Y **Publication Status:** 1-Published
Journal: ACS Applied Materials & Interfaces
Publication Identifier Type: DOI Publication Identifier: 10.1021/acsami.6b04985
Volume: 8 Issue: 33 First Page #: 21539
Date Submitted: 8/31/17 12:00AM Date Published: 8/1/16 7:00AM
Publication Location:
Article Title: Equipment-Free Deposition of Graphene-Based Molybdenum Oxide Nanohybrid Langmuir–Blodgett Films for Flexible Electrochromic Panel Application
Authors: Haojie Zhang, Ki-Wan Jeon, Dong-Kyun Seo
Keywords: electrochromic materials; electrodes; hybrid materials; Langmuir?Blodgett; molybdenum
Abstract: The potential electrochromic application of graphene-based nanohybrids is hampered by the challenges in interfacing the electrochromic nanoparticles with graphene at atomic scale and in fabricating their thin film on the substrate through a scalable method. In an effort to overcome these challenges, we demonstrate a highly dispersible graphene-based molybdenum oxide nanohybrid (mRGO-MoO3–x) for flexible electrochromic application. With only a squeeze pipet, mRGO-MoO3–x could be deposited with a high coverage on various substrates through a scalable equipment-free Langmuir–Blodgett film deposition method. By taking advantage of high transmittance benefited from its remarkable thinness, the mRGO-MoO3–x Langmuir–Blodgett film shows a superior reversible electrochromic property with high coloration efficiency on both hard and flexible substrates.
Distribution Statement: 3-Distribution authorized to U.S. Government Agencies and their contractors
Acknowledged Federal Support: **Y**

RPPR Final Report
as of 20-May-2021

Publication Type: Journal Article Peer Reviewed: Y **Publication Status:** 1-Published
Journal: Journal of Power Sources
Publication Identifier Type: DOI Publication Identifier: 10.1016/j.jpowsour.2017.01.057
Volume: 343 Issue: First Page #: 197
Date Submitted: 8/31/17 12:00AM Date Published: 3/1/17 7:00AM
Publication Location:
Article Title: New hydrogen titanium phosphate sulfate electrodes for Li-ion and Na-ion batteries
Authors: Ran Zhao, Daniel Mieritz, Dong-Kyun Seo, Candace K. Chan
Keywords: CathodeLithium batteryNASICONPolyanionSodium batteryTitanate
Abstract: NASICON-type materials with general formula AxM2(PO4)3 (A = Li or Na, M = Ti, V, and Fe) are promising candidates for Li- and Na-ion batteries due to their open three-dimensional framework structure. Here we report the electrochemical properties of hydrogen titanium phosphate sulfate, H0.4Ti2(PO4)2.4(SO4)0.6 (HTPS), a new mixed polyanion material with NASICON structure. Micron-sized HTPS aggregates with crystallite grain size of ca. 23 nm are synthesized using a sol-gel synthesis in an acidic medium. The properties of the as-synthesized HTPS, ball-milled HTPS, and samples prepared as carbon composites using an in-situ glucose decomposition reaction are investigated. A capacity of 148 mAh g?1 corresponding to insertion of 2 Li+ per formula unit is observed in the ball-milled HTPS over the potential window of 1.5–3.4 V vs. Li/Li+. Lithiation at ca. 2.8 and 2.5 V is determined to occur through filling of the M1 and M2 sites, respectively. Powder X-ray diffraction (PXRD), scanning electron
Distribution Statement: 3-Distribution authorized to U.S. Government Agencies and their contractors
Acknowledged Federal Support: **Y**

Publication Type: Journal Article Peer Reviewed: Y **Publication Status:** 1-Published
Journal: Langmuir
Publication Identifier Type: DOI Publication Identifier: 10.1021/acs.langmuir.7b00761
Volume: 33 Issue: 25 First Page #: 6410
Date Submitted: 8/31/17 12:00AM Date Published: 6/1/17 7:00AM
Publication Location:
Article Title: Tracking Single DNA Nanodevices in Hierarchically Meso-Macroporous Antimony-Doped Tin Oxide Demonstrates Finite Confinement
Authors: Daniel Mieritz, Xiang Li, Alex Volosin, Minghui Liu, Hao Yan, Nils G. Walter, Dong-Kyun Seo
Keywords: DNA nanostructures, ATO
Abstract: Housing bio-nano guest devices based on DNA nanostructures within porous, conducting, inorganic host materials promise valuable applications in solar energy conversion, chemical catalysis, and analyte sensing. Herein, we report a single-template synthetic development of hierarchically porous, transparent conductive metal oxide coatings whose pores are freely accessible by large biomacromolecules. Their hierarchal pore structure is bimodal with a larger number of closely packed open macropores (?200 nm) at the higher rank and with the remaining space being filled with a gel network of antimony-doped tin oxide (ATO) nanoparticles that is highly porous with a broad size range of textual pores mainly from 20?100 nm at the lower rank. The employed carbon black template not only creates the large open macropores but also retains the highly structured gel network as holey pore walls. Single molecule fluorescence microscopic studies with fluorophore-labeled DNA nanotweezers reveal a detailed v
Distribution Statement: 3-Distribution authorized to U.S. Government Agencies and their contractors
Acknowledged Federal Support: **Y**

RPPR Final Report
as of 20-May-2021

Publication Type: Journal Article Peer Reviewed: Y **Publication Status:** 1-Published
Journal: Nano Letters
Publication Identifier Type: DOI Publication Identifier: 10.1021/acs.nanolett.6b04846
Volume: 17 Issue: 2 First Page #: 1174
Date Submitted: 8/31/17 12:00AM Date Published: 1/1/17 7:00AM
Publication Location:
Article Title: Orange Carotenoid Protein as a Control Element in an Antenna System Based on a DNA Nanostructure
Authors: Alessio Andreoni, Su Lin, Haijun Liu, Robert E. Blankenship, Hao Yan, Neal W. Woodbury
Keywords: artificial light-harvesting; DNA nanotechnology; energy transfer; fluorescence spectroscopy; Orange carotenoid protein; photoprotection
Abstract: Taking inspiration from photosynthetic mechanisms in natural systems, we introduced a light-sensitive photo protective quenching element to an artificial light-harvesting antenna model to control the flow of energy as a function of light intensity excitation. The orange carotenoid protein (OCP) is a nonphotochemical quencher in cyanobacteria: under high-light conditions, the protein undergoes a spectral shift, and by binding to the phycobilisome, it absorbs excess light and dissipates it as heat. By the use of DNA as a scaffold, an antenna system made of organic dyes (Cy3 and Cy5) was constructed, and OCP was assembled on it as a modulated quenching element. By controlling the illumination intensity, it is possible to switch the direction of excitation energy transfer from the donor Cy3 to either of two acceptors. Under low-light conditions, energy is transferred from Cy3 to Cy5, and under intense illumination, energy is partially transferred to OCP as well. These results demonstrate t
Distribution Statement: 3-Distribution authorized to U.S. Government Agencies and their contractors
Acknowledged Federal Support: **Y**

Publication Type: Journal Article Peer Reviewed: Y **Publication Status:** 1-Published
Journal: Nature Protocols
Publication Identifier Type: DOI Publication Identifier: 10.1038/nprot.2016.139
Volume: 11 Issue: 11 First Page #: 2243
Date Submitted: 8/31/17 12:00AM Date Published: 10/1/16 7:00AM
Publication Location:
Article Title: Assembly of multienzyme complexes on DNA nanostructures
Authors: Jinglin Fu, Yuhe Renee Yang, Soma Dhakal, Zhao Zhao, Minghui Liu, Ting Zhang, Nils G Walter, Hao Y
Keywords: Multienzyme complexes Nanobiotechnology Nanostructures Organizing materials with DNA
Abstract: In nature, the catalytic efficiency of multienzyme complexes highly depends on their spatial organization. The positions and orientations of the composite enzymes are often precisely controlled to facilitate substrate transport between them. Self-assembled DNA nanostructures hold great promise for organizing biomolecules at the nanoscale. Here, we present detailed protocols for exploiting DNA nanostructures as assembly scaffolds that organize the spatial arrangements of multienzyme cascades with control over their relative distance, compartmentalization and substrate diffusion paths. The protocol describes the preparation and purification of DNA-conjugated enzymes and cofactors, along with the assembly of these prepared complexes on DNA nanostructures. The architecture of assembled enzyme complexes is then readily characterized using a broad selection of techniques from routine gel electrophoresis to advanced single-molecule imaging. We also describe methods of purifying these nano-ass
Distribution Statement: 3-Distribution authorized to U.S. Government Agencies and their contractors
Acknowledged Federal Support: **Y**

RPPR Final Report
as of 20-May-2021

Publication Type: Journal Article Peer Reviewed: Y **Publication Status:** 1-Published
Journal: Nucleic Acids Research
Publication Identifier Type: DOI Publication Identifier: 10.1093/nar/gkx378
Volume: 45 Issue: 11 First Page #: 6284
Date Submitted: 8/31/17 12:00AM Date Published: 6/1/17 7:00AM
Publication Location:
Article Title: Structure and conformational dynamics of scaffolded DNA origami nanoparticles
Authors: Keyao Pan, William P. Bricker, Sakul Ratanalert, Mark Bathe
Keywords: DNA origami
Abstract: Synthetic DNA is a highly programmable nanoscale material that can be designed to self-assemble into 3D structures that are fully determined by underlying Watson–Crick base pairing. The double crossover (DX) design motif has demonstrated versatility in synthesizing arbitrary DNA nanoparticles on the 5– 100 nm scale for diverse applications in biotechnology. Prior computational investigations of these assemblies include all-atom and coarse-grained modeling, but modeling their conformational dynamics remains challenging due to their long relaxation times and associated computational cost. We apply all-atom molecular dynamics and coarse-grained finite element modeling to DX-based nanoparticles to elucidate their fine-scale and global conformational structure and dynamics. We use our coarsegrained model with a set of secondary structural motifs to predict the equilibrium solution structures of 45 DX-based DNA origami nanoparticles including a tetrahedron, octahedron, icosahedron, cuboctahe
Distribution Statement: 3-Distribution authorized to U.S. Government Agencies and their contractors
Acknowledged Federal Support: **Y**

Publication Type: Journal Article Peer Reviewed: Y **Publication Status:** 1-Published
Journal: Nature Communications
Publication Identifier Type: DOI Publication Identifier: 10.1038/ncomms15654
Volume: 8 Issue: First Page #: 15654
Date Submitted: 8/31/17 12:00AM Date Published: 5/1/17 7:00AM
Publication Location:
Article Title: Oligolysine-based coating protects DNA nanostructures from low-salt denaturation and nuclease degradation
Authors: Nandhini Ponnuswamy, Maartje M. C. Bastings, Bhavik Nathwani, Ju Hee Ryu, Leo Y. T. Chou, Mathias
Keywords: oligolysine, DNA origami, nuclease degradation
Abstract: DNA nanostructures have evoked great interest as potential therapeutics and diagnostics due to ease and robustness of programming their shapes, site-specific functionalizations and responsive behaviours. However, their utility in biological fluids can be compromised through denaturation induced by physiological salt concentrations and degradation mediated by nucleases. Here we demonstrate that DNA nanostructures coated by oligolysines to 0.5:1 N:P (ratio of nitrogen in lysine to phosphorus in DNA), are stable in low salt and up to tenfold more resistant to DNase I digestion than when uncoated. Higher N:P ratios can lead to aggregation, but this can be circumvented by coating instead with an oligolysine-PEG copolymer, enabling up to a 1,000-fold protection against digestion by serum nucleases. Oligolysine-PEG-stabilized DNA nanostructures survive uptake into endosomal compartments and, in a mouse model, exhibit a modest increase in pharmacokinetic bioavailability. Thus, oligolysine-PEG
Distribution Statement: 3-Distribution authorized to U.S. Government Agencies and their contractors
Acknowledged Federal Support: **Y**

RPPR Final Report
as of 20-May-2021

Publication Type: Journal Article Peer Reviewed: Y **Publication Status:** 1-Published
Journal: Angewandte Chemie International Edition
Publication Identifier Type: DOI Publication Identifier: 10.1002/anie.201607050
Volume: 55 Issue: 41 First Page #: 12832
Date Submitted: 8/31/17 12:00AM Date Published: 10/1/16 7:00AM
Publication Location:
Article Title: 3D Framework DNA Origami with Layered Crossovers
Authors: Fan Hong, Shuoxing Jiang, Tong Wang, Yan Liu, Hao Yan
Keywords: DNA origami framework
Abstract: Designer DNA architectures with nanoscale geometric controls provide a programmable molecular toolbox for engineering complex nanodevices. Scaffolded DNA origami has dramatically improved our ability to design and construct DNA nanostructures with finite size and spatial addressability. Here we report a novel design strategy to engineer multilayered wireframe DNA structures by introducing crossover pairs that connect neighboring layers of DNA double helices. These layered crossovers (LX) allow the scaffold or helper strands to travel through different layers and can control the relative orientation of DNA helices in neighboring layers. Using this design strategy, we successfully constructed four versions of two-layer parallelogram structures with well-defined interlayer angles, a three-layer structure with triangular cavities, and a 9- and 15-layer square lattices. This strategy provides a general route to engineer 3D framework DNA nanostructures with controlled cavities and opportunit
Distribution Statement: 3-Distribution authorized to U.S. Government Agencies and their contractors
Acknowledged Federal Support: **Y**

Publication Type: Journal Article Peer Reviewed: Y **Publication Status:** 1-Published
Journal: Nature Materials
Publication Identifier Type: DOI Publication Identifier: 10.1038/nmat5033
Volume: 17 Issue: 2 First Page #: 159
Date Submitted: 10/12/18 12:00AM Date Published: 11/1/17 7:00AM
Publication Location:
Article Title: Programmed coherent coupling in a synthetic DNA-based excitonic circuit
Authors: Étienne Boulais, Nicolas P. D. Sawaya, Rémi Veneziano, Alessio Andreoni, James L. Banal, Toru Kond
Keywords: DNA circuits, light-harvesting systems
Abstract: Natural light-harvesting systems spatially organize densely packed chromophore aggregates using rigid protein scaffolds to achieve highly efficient, directed energy transfer. Here, we report a synthetic strategy using rigid DNA scaffolds to similarly program the spatial organization of densely packed, discrete clusters of cyanine dye aggregates with tunable absorption spectra and strongly coupled exciton dynamics present in natural light-harvesting systems. We first characterize the range of dye-aggregate sizes that can be templated spatially by A-tracts of B-form DNA while retaining coherent energy transfer. We then use structure-based modelling and quantum dynamics to guide the rational design of higher-order synthetic circuits consisting of multiple discrete dye aggregates within a DX-tile. These programmed circuits exhibit excitonic transport properties with prominent circular dichroism, superradiance, and fast delocalized exciton transfer, consistent with our quantum dynamics pred
Distribution Statement: 3-Distribution authorized to U.S. Government Agencies and their contractors
Acknowledged Federal Support: **Y**

RPPR Final Report
as of 20-May-2021

Publication Type: Journal Article Peer Reviewed: Y **Publication Status:** 1-Published
Journal: Coatings
Publication Identifier Type: DOI Publication Identifier: doi:10.3390/coatings8040128
Volume: 8 Issue: 128 First Page #:
Date Submitted: 10/12/18 12:00AM Date Published: 4/2/18 7:00AM
Publication Location:
Article Title: Thickness-Dependent Bioelectrochemical and Energy Applications of Thickness-Controlled Meso-Macroporous Antimony-Doped Tin Oxide
Authors: Daniel Mieritz, Runli Liang, Haojie Zhang, Anne-Marie Carey, Shaojiang Chen, Alex Volosin, Su Lin, Ne
Keywords: : thick coatings; hierarchically porous; meso-macroporous; biomacromolecule; TCO; ATO; nanomaterials; carbon black
Abstract: Coatings of hierarchically meso-macroporous antimony-doped tin oxide (ATO) enable interfacing adsorbed species, such as biomacromolecules, with an electronic circuit. The coating thickness is a limiting factor for the surface coverage of adsorbates, that are electrochemically addressable. To overcome this challenge, a carbon black-based templating method was developed by studying the composition of the template system, and finding the right conditions for self-standing templates, preventing the reaction mixture from flowing out of the mask. The thicknesses of as-fabricated coatings were measured using stylus profilometry to establish a relationship between the mask thickness and the coating thickness. Cyclic voltammetry was performed on coatings with adsorbed cytochrome c to check whether the entire coating thickness was electrochemically addressable. Further, bacterial photosynthetic reaction centers were incorporated into the coatings, and photocurrent with respect to coating thick
Distribution Statement: 3-Distribution authorized to U.S. Government Agencies and their contractors
Acknowledged Federal Support: **Y**

Publication Type: Journal Article Peer Reviewed: Y **Publication Status:** 1-Published
Journal: ChemSusChem
Publication Identifier Type: DOI Publication Identifier: DOI : 10.1002/cssc.201701390
Volume: 10 Issue: 22 First Page #: 4457
Date Submitted: 10/12/18 12:00AM Date Published: 9/19/17 2:00PM
Publication Location:
Article Title: Enhancing photocurrent generation in photosynthetic reaction center-based photoelectrochemical cells with biomimetic DNA antenna
Authors: Anne-Marie Carey,HaoJie Zhang, Minghui Liu, Daiana Sharaf, Natalie Akram, Hao Yan, Su Lin, Neal W
Keywords: artificial photosynthesis, DNA, energy transfer, light harvesting, photoelectrochemical cells
Abstract: Three? to four?times higher performance of biohybrid photoelectrochemical cells with photosynthetic reaction centers (RC) has been achieved by using a DNA?based biomimetic antenna. Synthetic dyes Cy3 and Cy5 were chosen and strategically placed in the anntena in such a way that they can collect additional light energy in the visible region of the solar spectrum and transfer it to RC through Förster resonance energy transfer (FRET). The antenna, a DNA templated multiple dye system, is attached to each Rhodobacter sphaeroides RC near the primary donor, P, to facilitate the energy transfer process. Excitation with a broad light spectrum (approximating sunlight) triggers a cascade of excitation energy transfer from Cy3 to Cy5 to P, and also directly from Cy5 to P. This additional excitation energy increases the RC absorbance cross?section in the visible and thus the performance of the photoelectrochemical cells. DNA?based biomimetic antennas offer a tunable, modular light?harvesting system
Distribution Statement: 3-Distribution authorized to U.S. Government Agencies and their contractors
Acknowledged Federal Support: **Y**

RPPR Final Report
as of 20-May-2021

Publication Type: Journal Article Peer Reviewed: Y **Publication Status:** 1-Published
Journal: ACS Applied Materials & Interfaces
Publication Identifier Type: DOI Publication Identifier: 10.1021/acsami.8b07101
Volume: Issue: First Page #:
Date Submitted: 10/12/18 12:00AM Date Published: 6/13/18 7:00AM
Publication Location:
Article Title: Redox Engineering of Cytochrome c using DNA Nanostructure-Based Charged Encapsulation and Spatial Control
Authors: Zhilei Ge, Zhaoming Su, Chad R. Simmons, Jiang Li, Shuoxing Jiang, Wei Li, Yang Yang, Yan Liu, Wah
Keywords: cytochrome c; DNA tetrahedron; framework nucleic acids; protein engineering
Abstract: Three-dimensional (3D) DNA nanostructures facilitate the directed self-assembly of various objects with designed patterns with nanometer scale addressability. Here, we report the enhancement of cytochrome c (cyt c) redox activity by using a designed 3D DNA nanostructure attached to a gold electrode to spatially control the position of cyt c within the tetrahedral framework. Charged encapsulation and spatial control result in the significantly increased redox potential and enhanced electron transfer of this redox protein when compared to cyt c directly adsorbed on the gold surface. Two different protein attachment sites on one double stranded edge of a DNA tetrahedron were used to position cyt c inside and outside of the cage. Cyt c at both binding sites show similar redox potential shift and only slight difference in the electron transfer rate, both orders of magnitude faster than the cases when the protein was directly deposited on the gold electrode, likely due to an effective electr
Distribution Statement: 3-Distribution authorized to U.S. Government Agencies and their contractors
Acknowledged Federal Support: **Y**

Publication Type: Journal Article Peer Reviewed: Y **Publication Status:** 1-Published
Journal: Nature Nanotechnology
Publication Identifier Type: DOI Publication Identifier: 10.1038/s41565-018-0130-2
Volume: 13 Issue: 8 First Page #: 723
Date Submitted: 10/12/18 12:00AM Date Published: 5/1/18 7:00AM
Publication Location:
Article Title: Exploring the speed limit of toehold exchange with a cartwheeling DNA acrobat
Authors: Jieming Li, Alexander Johnson-Buck, Yuhe Renee Yang, William M. Shih, Hao Yan, Nils G. Walter
Keywords: DNA-based nanomachines, DNA walker, stepping rate
Abstract: Dynamic DNA nanotechnology has yielded nontrivial autonomous behaviours such as stimulus-guided locomotion, computation and programmable molecular assembly. Despite these successes, DNA-based nanomachines suffer from slow kinetics, requiring several minutes or longer to carry out a handful of operations. Here, we pursue the speed limit of an important class of reactions in DNA nanotechnology—toehold exchange—through the single-molecule optimization of a novel class of DNA walker that undergoes cartwheeling movements over a field of complementary oligonucleotides. After optimizing this DNA ‘acrobat’ for rapid movement, we measure a stepping rate constant approaching 1 s?1, which is 10- to 100-fold faster than prior DNA walkers. Finally, we use single-particle tracking to demonstrate movement of the walker over hundreds of nanometres within 10 min, in quantitative agreement with predictions from stepping kinetics. These results suggest that substantial improvements in the operating rates
Distribution Statement: 3-Distribution authorized to U.S. Government Agencies and their contractors
Acknowledged Federal Support: **Y**

RPPR Final Report
as of 20-May-2021

Publication Type: Journal Article Peer Reviewed: Y **Publication Status:** 1-Published
Journal: ChemBioChem
Publication Identifier Type: DOI Publication Identifier: 10.1002/cbic.201700613
Volume: 19 Issue: 3 First Page #: 212
Date Submitted: 10/12/18 12:00AM Date Published: 2/1/18 7:00AM
Publication Location:
Article Title: 2D Enzyme Cascade Network with Efficient Substrate Channeling by Swinging Arms
Authors: Yuhe R. Yang, Jinglin Fu, Shaun Wootten, Xiaodong Qi, Minghui Liu, Hao Yan, Yan Liu
Keywords: DNA nanotechnology, enzyme cascade, scaffold, redox intermediate
Abstract: In living cells, compartmentalized or membrane?associated enzymes are often assembled into large networks to cooperatively catalyze cascade reaction pathways essential for cellular metabolism. Here, we report the assembly of an artificial 2D enzyme network of two cascade enzymes—glucose?6?phosphate dehydrogenase (G6PDH) and lactate dehydrogenase (LDH)—on a wireframe DNA origami template. Swinging arms were used to facilitate the transport of the redox intermediate of NAD+/NADH between enzyme pairs on the array. The assemblies of 2D enzyme networks were characterized by gel electrophoresis and visualized by atomic force microscopy (AFM). The spatial arrangements of multiple enzyme pairs were optimized to facilitate efficient substrate channeling by exploiting the programmability of DNA origami to manipulate the key parameters of swinging arm length and stoichiometry. Compared with a single enzyme pair, the 2D organized enzyme systems exhibited higher reaction efficiency due to the promo
Distribution Statement: 3-Distribution authorized to U.S. Government Agencies and their contractors
Acknowledged Federal Support: **Y**

Partners

,

I certify that the information in the report is complete and accurate:
Signature: Hao Yan
Signature Date: 5/18/21 1:42PM

Translating Biochemical Pathways to Non-Cellular Environments

Principal Investigator: Hao Yan[1]
Co-PIs: Don Seo[1], Neal Woodbury[1], Mark Bathe[2], William Shih[3], Nils Walter[4]
[1]Arizona State University, [2]MIT, [3]Harvard University, [4]U of Michigan

Reporting period: 2012-2019

Translating Biochemical Pathways to Non-Cellular Environments

Principal Investigator: Hao Yan[1]
Co-PIs: Don Seo[1], Neal Woodbury[1], Mark Bathe[2], William Shih[3], Nils Walter[4]
[1]Arizona State University, [2]MIT, [3]Harvard University, [4]U of Michigan

Reporting period: 8/20/12-7/31/13

I. Scientific and Technical Objectives

We intend to engineer and optimize nanoscale devices and systems based on important biochemical conversion pathways, where the converted species are molecules (enzymes transforming substrates into products), or energy, as is the case for photosynthesis. The use of DNA-directed assembly allows us to control and exploit the interactions between synthetic and naturally occurring bio-materials to produce highly functional biochemical conversion systems. Regarding enzyme transformations, our primary goal is to construct artificial enzyme cascades using two- and three-dimensional DNA structures as templates, and to study the ideal number of enzymes, relative distance, spatial arrangement, diffusion behavior, and reaction kinetics of the cascades in a controlled, non-cellular environment. Towards this goal, we initially focused on a representative DNA-templated GOx/HRP enzyme cascade. We will apply the results of the initial study toward the design of more complex, bioelectroactive, NAD dependent dehydrogenase pathways, with the ultimate goal of interfacing our systems with external conductive materials. We aimed to achieve the following objectives during this reporting period: (1) understand the factors influencing site-specific, hybridization dependent immobilization of enzymes and cofactors on addressable DNA nanostructures, (2) systematically evaluate DNA-scaffolded enzyme activity in various conditions (3) investigate the mechanism of local diffusive transport of a "swinging" single stranded DNA arm functionalized with an enzyme cofactor, (4) investigate the conformational changes that occur in a DNA tweezer structure used for modulating enzyme activity, at the single-molecule and bulk levels, (5) characterize the yield of enzyme encapsulation and retention in 3-dimensional DNA nanocages, (6) engineer the formation of liposomes on the outside of our DNA structures to limit substrate/intermediate's escape. Our findings will ultimately be used to enhance local diffusion behavior, reaction kinetics, and the optical and electrical properties within the proposed devices, behavior that can be extended to other systems of interest to the DoD.

Regarding photosynthesis, our aim is to develop methods for translating energy conversion pathways to non-cellular environments where their functions can be more easily manipulated. The approach is to use rationally designed DNA nano-scaffolds to engineer light-harvesting networks containing synthetic pigments, interfaced with energy conversion proteins (photosynthetic reaction centers) from natural photosynthetic organisms. We intend to precisely position functional elements on the DNA scaffolds, generating energy and electron transfer pathways in which inter-molecular interactions can be predictably designed, and the local environment can be controlled. We hope to engineer systems with more uniform light absorption, efficient energy transfer and conversion, and improved photo-stability for maximum performance. Here, artificial light harvesting pigments and the photosynthetic reaction center protein of purple non-sulfur bacteria are being co-assembled on a DNA nanostructure. The ideal

number of light-harvesting molecules, relative distance, spatial arrangement, and their spectral properties were varied to optimize the performance of the system. We are also comparing the experimental outcomes with the results of computational modeling in an effort to predict and improve upon the behavior of our model system. Due to the prospect of using sun light as an energy source for bio-electroactive and photo-electrochemical bio-pathways, ideal materials that are transparent and electrically conducting, either fabricated as a film or coated on an electrode, are also being developed. Toward this end, two different types of materials were utilized: nanoporous transparent metal oxides and functionalized reduced graphene oxides. In line with DoD goals, the proposed research will increase our understanding of nanoscale energy transfer processes and aid in the development of robust strategies for the synthesis, characterization, and assembly of synthetic biochemical pathways for application in high-efficiency photo-energy generation, energy storage devices, sensors, or completely new capabilities that enhance war fighter and battle system capabilities.

II. Concise Accomplishments

Enzyme Pathway – We have: (a) developed reliable methods for conjugating DNA to protein enzymes and cofactors and purifying DNA conjugated proteins with exact ratios of the components, (b) developed single-molecule characterization and predictive modeling techniques to evaluate the integrity and behavior of DNA nanostructure complexes, (c) engineered a multi-enzyme complex utilizing a "swinging arm" to control substrate transfer between enzymes, (d) optimized the enzymatic activity of a DNA actuator structure using single-molecule FRET, and (e) constructed two 3D-DNA tunnel structures for facilitated substrate diffusion by directed substrate channeling and compartmentalization.

.

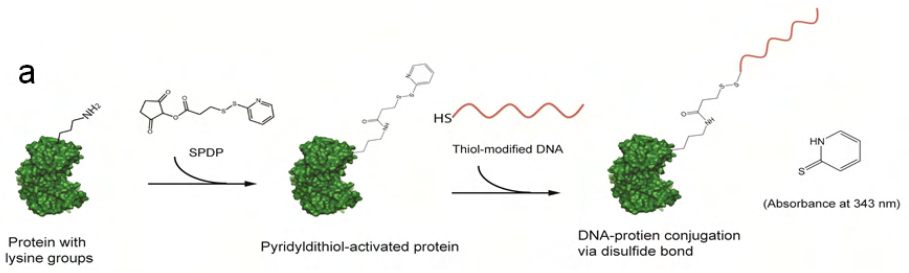
Photosynthetic Pathway – We have: (a) obtained a *Rhodobacter sphaeroides* reaction center mutant that has cysteine residues appropriately placed for DNA and/or dye conjugation, (b) developed a consistent process to grow the mutant cells and isolate the reaction center proteins, with optimized yields and stabilities, (c) conjugated three different dye molecules to the reaction center proteins (individually) and evaluated key factors that affect energy transfer to the centers and the subsequent process of charge separation, (d) developed spectroscopic protocols for characterizing the function of the assembled nanostructure complexes, (e) achieved high (up to 70%) yield of energy transfer between a dye specifically attached to the reaction center protein and the reaction center cofactors, (f) demonstrated that upon energy transfer, charge separation within the reaction center takes place, with a yield approaching unity, (g) constructed a 3-arm DNA complex with 2 dyes attached to it. This will be covalently conjugated to the reaction center protein to further extend the light-harvesting capability of the system, (h) implemented an excitonic model of dye-conjugated DNA-based nanostructures for calculation of light-harvesting and photonic properties, (i) prepared macroporous antimony-doped tin oxide (ATO) films by combining our inorganic-polymer composite gel method with the existing inverse opal templating method, (j) discovered and perfected two thionation methods that metathetically functionalize graphene oxides with thiols while simultaneously achieving chemical reduction, and (k) prepared Langmuir-Blodgett films of the thionated reduced graphene oxides with different thicknesses through a simple self-assembly process at the air-water interface.

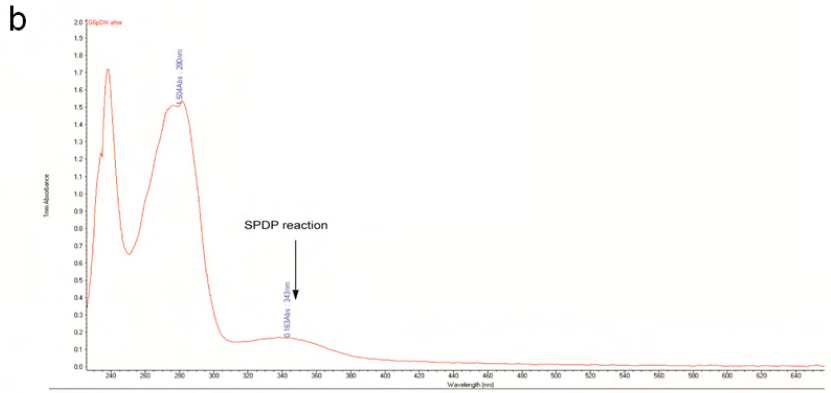
III. Expanded Accomplishments

Enzyme Pathway

Bio-conjugation strategies for coupling DNA to proteins and enzyme cofactors

1. Chemical conjugation of DNA to proteins:





c

Name	A260/A280	A260	A280	Ratio (oligo/protein)	Protein conc. (μM)	A260/A280 (oligo)	Extinc.(260)	Extinc.(280)	A260/A280 (G6pDH)	Extinc.(260)	Extinc.(280)
G6pDH-oligo	0.84	0.81	0.97	0.86	5.1	1.34	115200	85970	0.52	61594	118450

Figure 1. Protein-DNA conjugation using an SPDP crosslinker. (a) A schematic illustration of the conjugation chemistry; (b) Quantification of the protein-SPDP modification via absorbance spectra. G6pDH-SPDP conjugation: ΔA343 before and after SPDP conjugation is ~ 0.16 (extinction coefficient: 8080 M-1 cm-1), corresponding to 20 μM SPDP coupled to 13 μM G6pDH (ε=115200 M-1 cm-1 at 280 nm for G6pDH). (c) Quantification of a purified DNA-conjugated G6pDH: an A260/A80 ratio of 0.84 corresponds to ~ 0.86 DNA per protein, with a DNA-conjugated protein concentration of ~ 5.1 μM.

We developed an SPDP (*N*-Succinimidyl 3-(2-pyridyldithio)-propionate) crosslinking chemistry for attaching oligonucleotides to proteins. As shown in Figure 1, SPDP was used to crosslink GOx and HRP to DNA probe strands. For a typical conjugation, 100 μl of 40 μM enzyme solution was first reacted with a 20-fold excess of SPDP in 10 mM HEPES buffer (pH 8.5) for one hour, allowing amine-reactive *N*-hydroxysuccinimide (NHS) esters to react with the lysine residues on the protein surface. Excess SPDP was removed by washing, and filtered using Amicon, 30 kD cutoff filters.

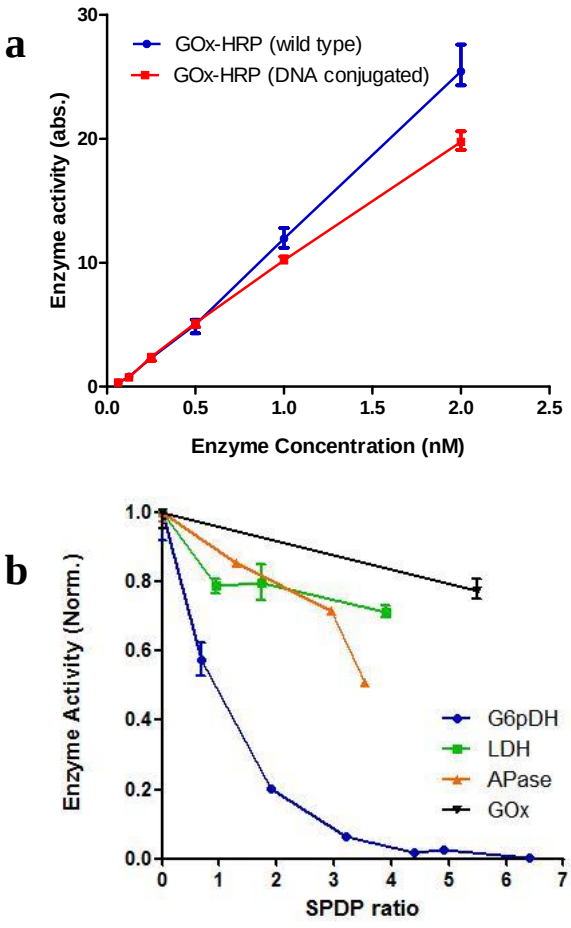


Figure 2. Activities of DNA-protein conjugates Protein-DNA conjugation (A) Enzyme activity vs. concentration for both DNA-modified GOx/HRP cascades and unmodified enzymes. (B) Activities vs. SPDP ratio for G6pDH, LDH, APase and GOx. using a SPDP crosslinker.

Next, SPDP-modified protein was conjugated to thiol-modified DNA (10-fold excess) through a disulfide bond exchange of the activated pyridyldithiol group. The reaction mixture was incubated in 1 × PBS (pH 8.5) for two hours. The coupling efficiency was evaluated by monitoring the increase in absorbance at 343 nm due to the release of pyridine-2-thione (extinction coefficient: 8080 M^{-1} cm^{-1}). Finally, the excess DNA was removed by washing, and filtered using Amicon 30 kD cutoff filters. The enzymatic activities of DNA-modified GOx and HRP were ~ 75% of the activities of the unmodified enzymes as shown by Figure 2A. The activity of several DNA-modified enzymes including Glucose 6-phosphate dehydrogenase (G6pDH), Lactate dehydrogenase (LDH), Alkaline Phosphatase (APase) and Glucose Oxidase (GOx) are shown in Figure 2B *vs.* the average number of SPDP molecules per protein. Over labeling the proteins with multiple SPDP molecules reduces their activity, especially for G6pDH.

2. <u>Purification of DNA-protein conjugates with exact stoichiometric ratios</u>: To achieve more precise control of the protein-DNA nanostructures, we had to develop a method of purification that produced conjugates with exact ratios of DNA and protein molecules. Figure 3 shows the purification of DNA conjugated protein by ionic-exchange fast protein liquid chromatography (FPLC). 500 ul of 50 µM G6pDH-TTTTTCCCTCCCTCC solution with an average ratio of ~ 2 DNA molecules per protein was loaded into the FPLC equipped with an anion exchange column, using an elution gradient from 20% 50 mM sodium phosphate, 1 M NaCl to 55% 50 mM sodium phosphate, 1 M NaCl (Figure 3 and Figure 4). Multiple peaks from the purification chromatogram were collected, including unmodified protein, protein bound to one DNA molecule, protein bound to two DNA molecules, protein bound to three DNA molecules, protein bound to four DNA molecules, and free DNA.

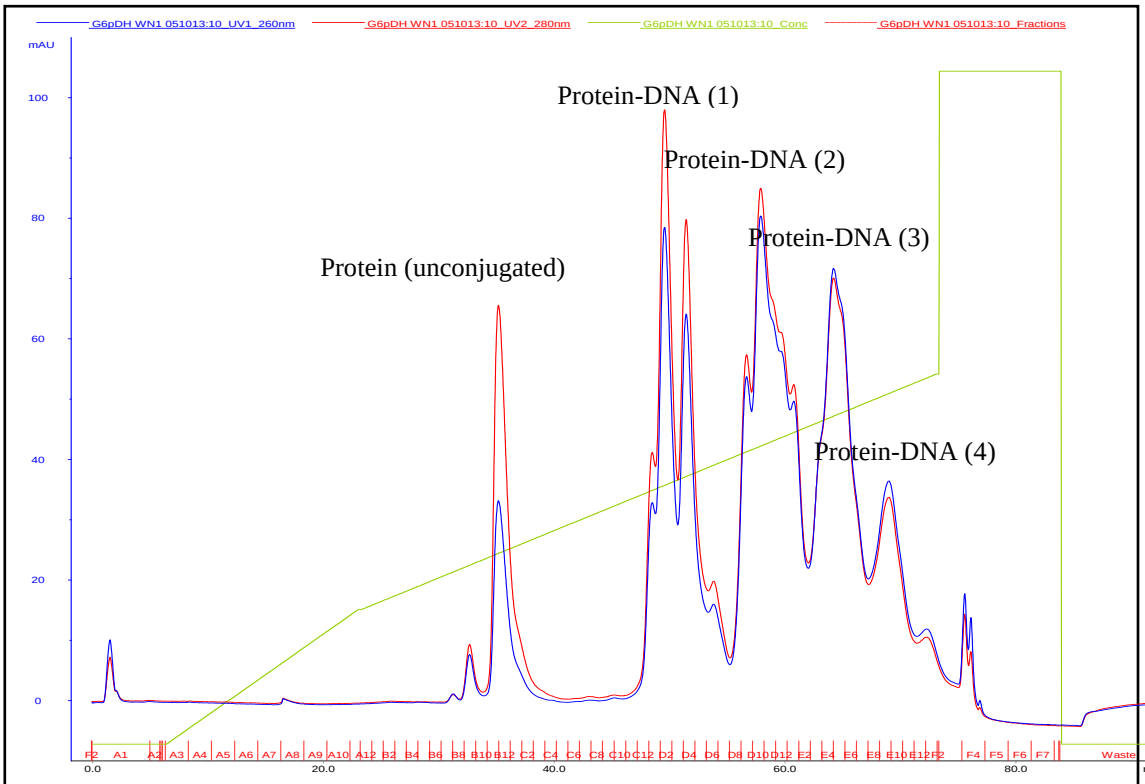


Figure 3. Anion-exchange FPLC to purify DNA conjugated G6pDH with 0, 1, 2, 3, and 4 DNA molecules attached. Condition: buffer A - 50 mM sodium phosphate (pH7.5); buffer B - 50 mM sodium phosphate, 1 M NaCl (pH 7.5).

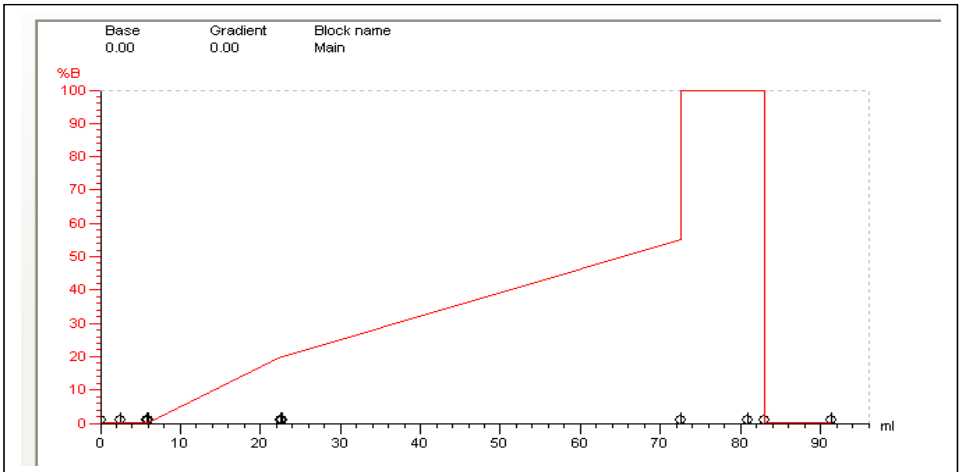


Figure 4. Elution gradient for anion-exchange chromatography. Buffer A - 50 mM sodium phosphate (pH 7.5); buffer B - 50 mM sodium phosphate and 1 M NaCl pH 7.5).

3. Developing site-specific conjugation of oligonucleotides to proteins:

Site-specific conjugation of oligonucleotides to proteins was envisioned through N-terminal modification. Proteins bearing solvent accessible N-terminal amino acids can be derivitized to pyruvamides by treatment with pyridoxal-5′-phosphate (PLP) and then coupled to hydroxylamines to afford the conjugated oxime (Figure 5).

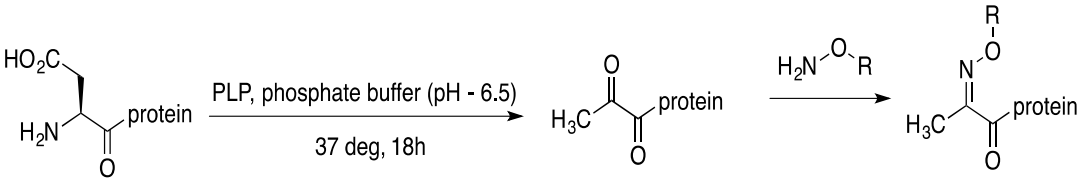


Figure 5. Optimizing the length of the DNA conjugated to GOx/HRP for driving protein assembly onto DNA nanostructures.

Initial efforts were directed toward the development of a protein bearing an azide at its N-terminus (via the chemistry described above) as well as an oligonucleotide probe strand derivitized with a strained alkyne capable of coupling to the azide via copper free click chemistry. The 22-mer poly T alkyne modified DNA probe strand was prepared by standard automated oligonucleotide synthesis, purified by RP-HPLC and characterized by MALDI-TOF MS (Figure 6).

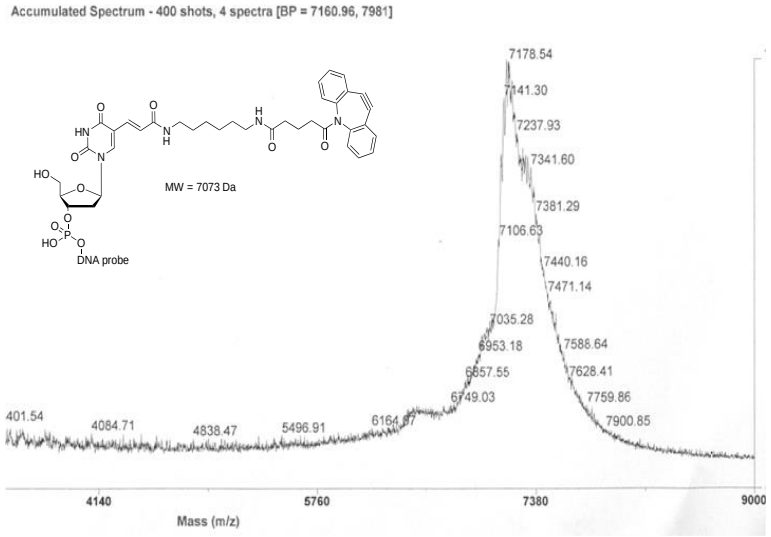


Figure 6. MALDI-TOF MS characterization of 22-mer poly T bearing strained alkyne.

The N-terminus of Azurin was converted to its pyruvamide derivative **2** by treatment with PLP in phosphate buffer. **2** was then coupled with N_3-O-PEG-O-NH_2 via oxime formation affording **3** bearing the required azide for coupling to the alkyne modified DNA probe strand **1** and characterized via MALDI-TOF MS (Figure 7).

For the future work, we plan to perform an in gel digestion of the protein. Analysis of the peptides resulting from tryptic digestion will demonstrate unambiguously where the modification/coupling has occurred.

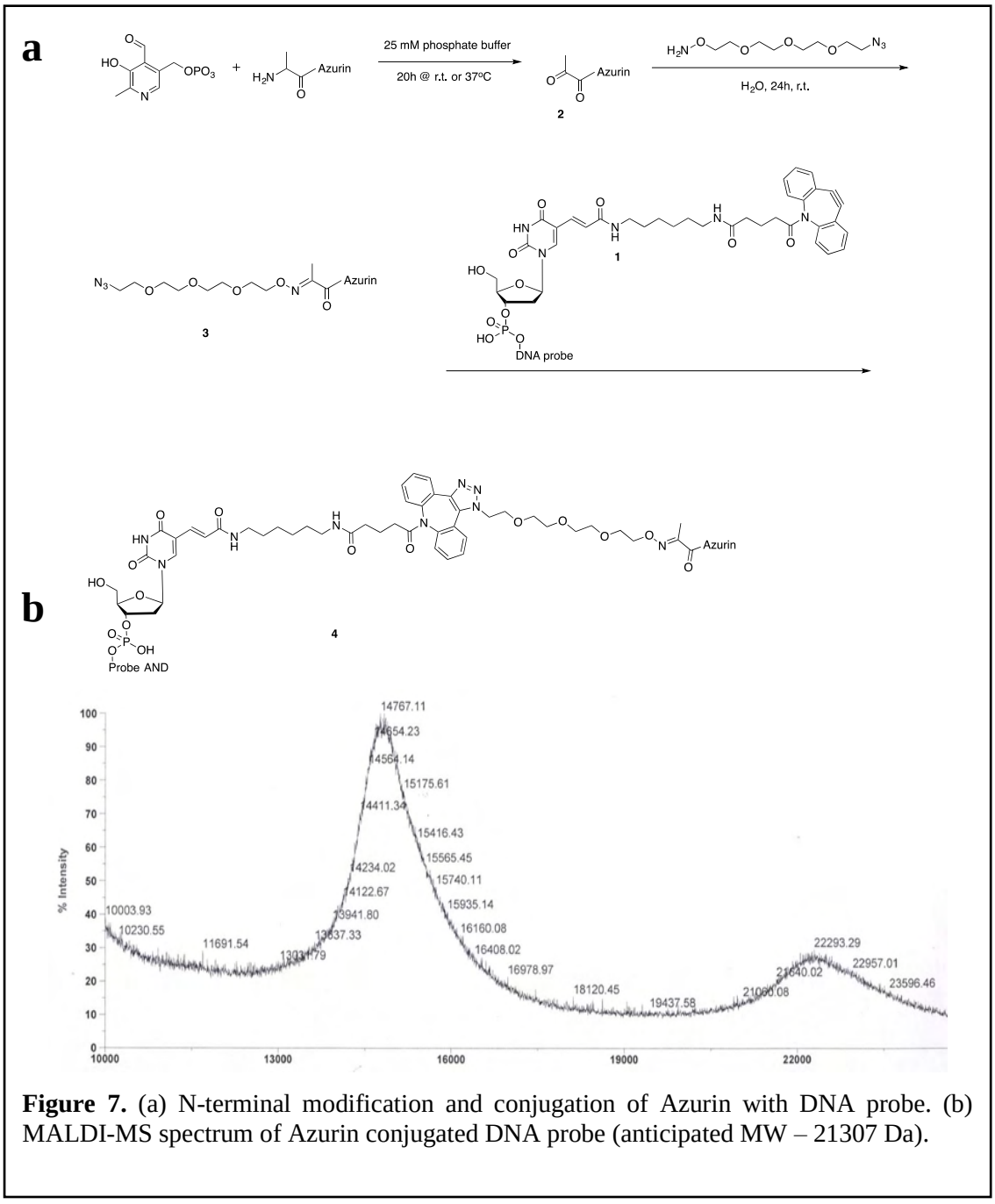


Figure 7. (a) N-terminal modification and conjugation of Azurin with DNA probe. (b) MALDI-MS spectrum of Azurin conjugated DNA probe (anticipated MW – 21307 Da).

4. Attaching cofactors to DNA scaffolds:

Figure 8 shows the conjugation of 6AE-NAD+ to single-stranded DNA. 200 µL of 100 µM 5'amine-modified oligo was first immobilized on a 200 µL anion-exchange DEAE-Sepharose resin by charge absorption. The unbound oligo and water was removed by washing and filtering the resin with DMF in a Sigma Prep Spin column (7-30 µm). 200 µL of 150 mM DSS was prepared in DMF with 2 %(v/v) DIPEA. The oligo-bound resin was incubated with DSS for one hour. Excess DSS crosslinker was removed by washing the resin with DMF. To couple NAD+ to an oligo, a 10- fold excess of 6AE-NAD+ was incubated with oligo-bound resin in 1 M HEPES, pH8 for one hour. After the reaction, the oligo-bound resin was spun down at 3000 rpm to remove any unreacted 6AE-NAD+. The purification of 6AE-NAD+ was performed using

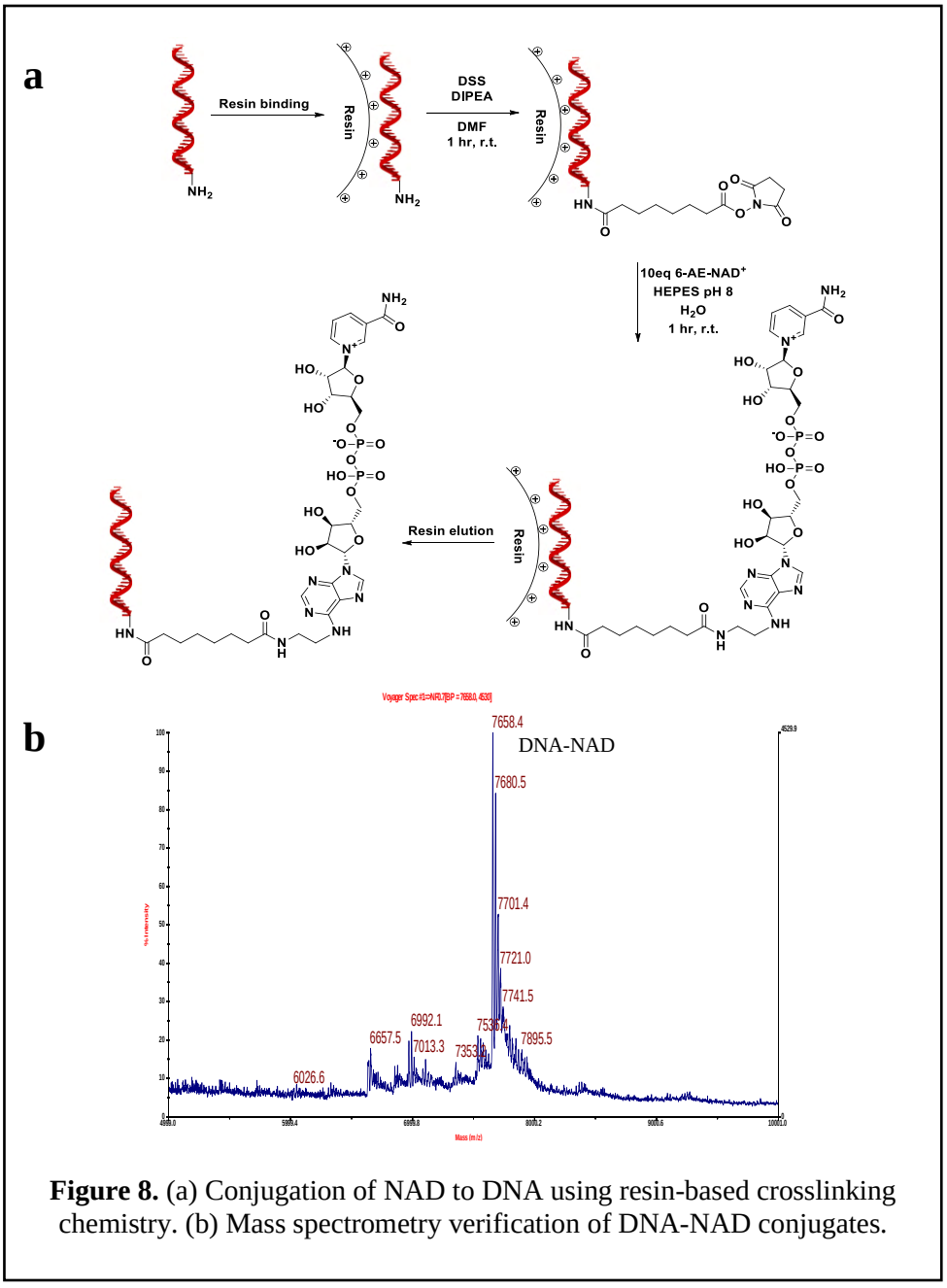


Figure 8. (a) Conjugation of NAD to DNA using resin-based crosslinking chemistry. (b) Mass spectrometry verification of DNA-NAD conjugates.

HPLC and the product was characterized by MALDI-TOF Mass Spectrometry. The thermal stability of the NAD+-coupled oligo was measured as shown in Figure 9. NAD+ maintained most of its activity after incubation at temperatures less than 75 ˚C, while NAD+ activity quickly decreased after incubation at temperatures higher than 85 ˚C.

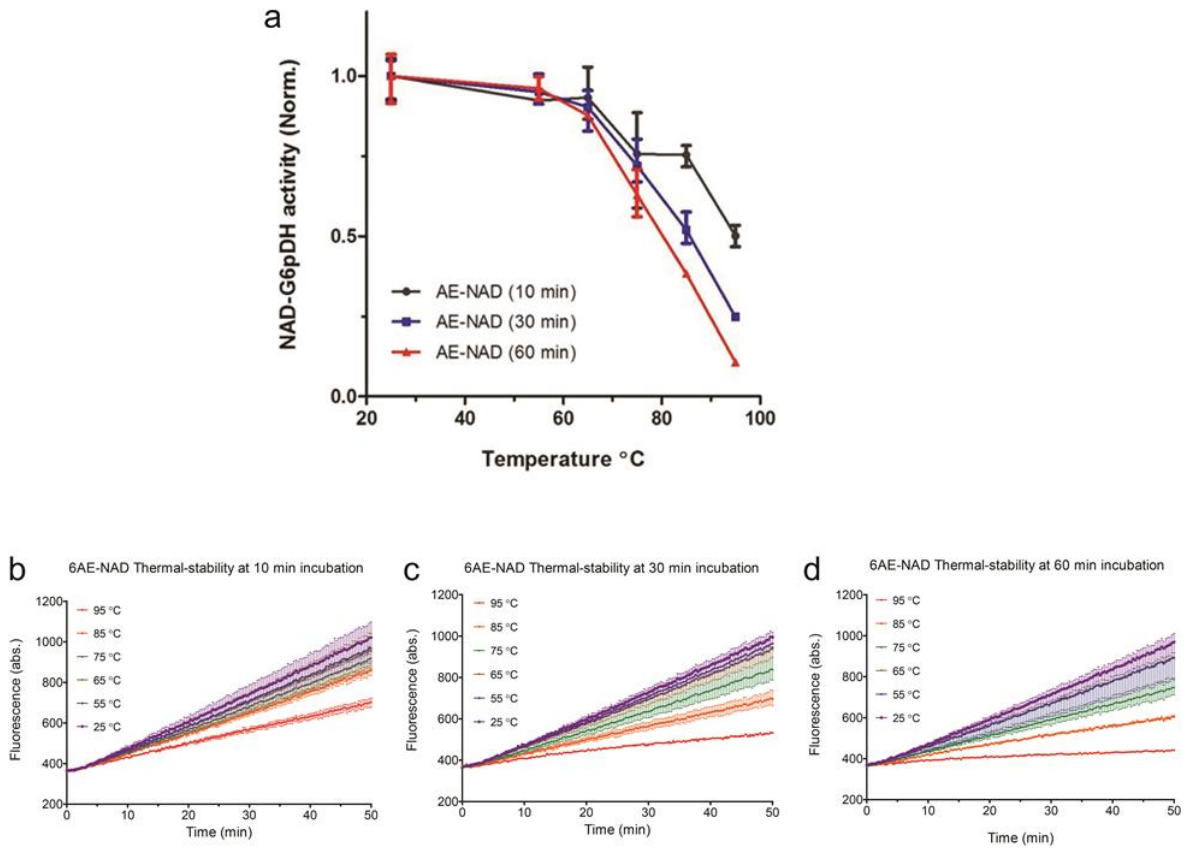


Figure 9. Evaluation of the thermal stability of amino-modified NAD. (a) Normalized G6pdH/NAD activities after incubation at various temperatures. Amino-modified NAD (AE-NAD+) was incubated at a series of temperatures ranging from 25 to 95 ˚C for 10 min (black), 30 min (blue) and 60 min (red), respectively. All the thermal activities were normalized to the sample incubated at 25 ˚C. (b) Raw activity traces for G6pDH/AE-NAD with 10 min incubation at a series of temperatures ranging from 25 to 95 ˚C. (c) Raw activity traces for G6pDH/AE-NAD with 30 min incubation at a series of temperatures ranging from 25 to 95 ˚C. (d) Raw activity traces for G6pDH/AE-NAD with 60 min incubation at a series of temperatures ranging from 25 to 95 ˚C. AE-NAD activity was evaluated via the reduction of NAD+ to NADH by G6pDH, followed by a coupled PMS-catalyzed resazurin reaction. The enzyme activities were characterized by analyzing the slopes of the product-time traces which were obtained by fitting the raw traces with linear regression. Assay conditions: 50 nM G6pDH, 50 µM AE-NAD+, 1 mM glucose-6 phosphate, 200 µM PMS and 400 µM resazurin in 1×TBS with 1 mM MgCl2 at pH 7.5, room temperature. The results show that after 10 minutes, AE-NAD+ activity is significantly reduced for temperatures higher than 70 ˚C. This indicates that thermal annealing programs with very short incubation times at high temperature are required.

Single-molecule characterization and predictive modeling to evaluate the integrity and behavior of DNA nanostructure complexes

1. Imaging site-specific and density-dependent kinetics and thermodynamics of oligonucleotide binding to DNA nanostructures by fluorescence microscopy:

The site-specific attachment of external molecules to DNA nanostructures by hybridization is a fundamental part of our approach to constructing multi-enzyme complexes. To better understand this phenomenon, we extended the points accumulation for imaging in nanoscale topography (PAINT) technique using site-specific DNA probes to acquire two-dimensional density maps of features patterned on ~90 x 60 nm rectangular DNA origami. We showed that PAINT has a localization accuracy of ~10 nm which is sufficient to reliably distinguish dense (>104 features μm−2), sub-100 nm patterns of oligonucleotide features. We also used two-color PAINT to monitor the enzymatic modification of these features and to show that single origami tiles exhibit stable, spatially heterogeneous probe-binding patterns, or "fingerprints" (Figure 10a). Finally, we presented experimental and modeling evidence that these fingerprints may arise from variations in the spacing of features that locally modulate the probe binding kinetics. This work highlights some important design considerations for the dense assembly of components on DNA nanostructures, and provides us with a technique for detailed characterization of such assemblies.

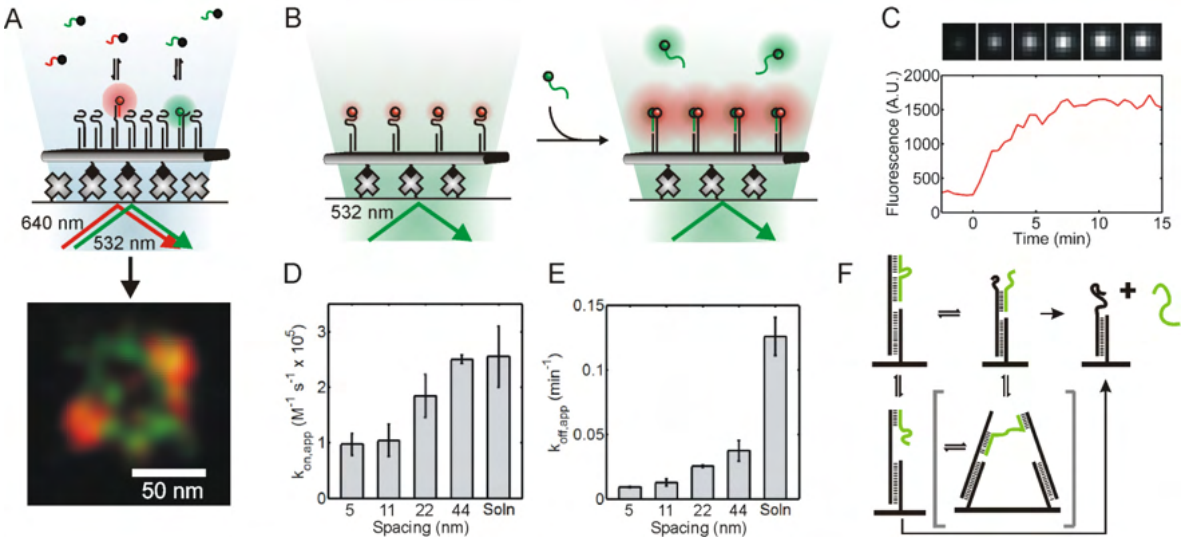


Figure 10. (a) Scheme for DNA PAINT imaging of probe binding to DNA origami (top) and two-color PAINT image showing the distribution of probe binding to one rectangular origami tile. (b) Scheme for single-origami FRET assays of hybridization kinetics. (c) FRET readout of oligonucleotide binding to a single origami tile. (de) Kinetics of binding (d) and dissociation (e) of a ssDNA target to DNA origami bearing probes spaced by different distances or in solution (Soln). (f) Proposed model for the retention of an ssDNA target by "hopping" between adjacent surface-bound probes.

To further investigate the attachment of features to DNA origami by hybridization, we developed a single-particle fluorescence resonance energy transfer (spFRET) assay to study the kinetics and thermodynamics of hybridization between origami-bound probes and complementary targets in solution (Figure 10 b, c). By systematically varying the spacing of probes, we demonstrated that two-dimensional crowding slows the rate of hybridization by as much as 2.5-fold at the highest probe densities tested (Figure 10d). Intriguingly, the effect of probe density on dissociation

reactions was highly dependent on the target sequence, decreasing by up to ~10-fold at the smallest spacing. By varying target sequence and buffer composition, we found evidence for two distinct mechanisms for this enhanced retention: direct hopping of targets between adjacent probes of the same sequence (Figure 10f) and nonsequence-specific, electrostatic salt-bridge interactions with the DNA origami. This kinetic behavior varies little between individual copies of a given array design, suggesting a robust set of phenomena that should be considered in the future design of complexes based on DNA origami.

2. Dynamic conformational and diffusivity measurements of DNA nanostructures:

To predict the dynamic conformational and diffusivity behavior of the type of DNA nanostructures we are utilizing here, we developed a bead-based model of hydrodynamics that is integrated into the finite element model CanDo. This model enables the calculation of translational and rotational diffusivities of DNA tiles and origami structures. In addition, the model enables the calculation of time-dependent conformational fluctuations of DNA tiles and origami structures that may be key to their chemical and light-harvesting properties, which occur on shorter time-scales for which conformational fluctuations may be rate-limiting.

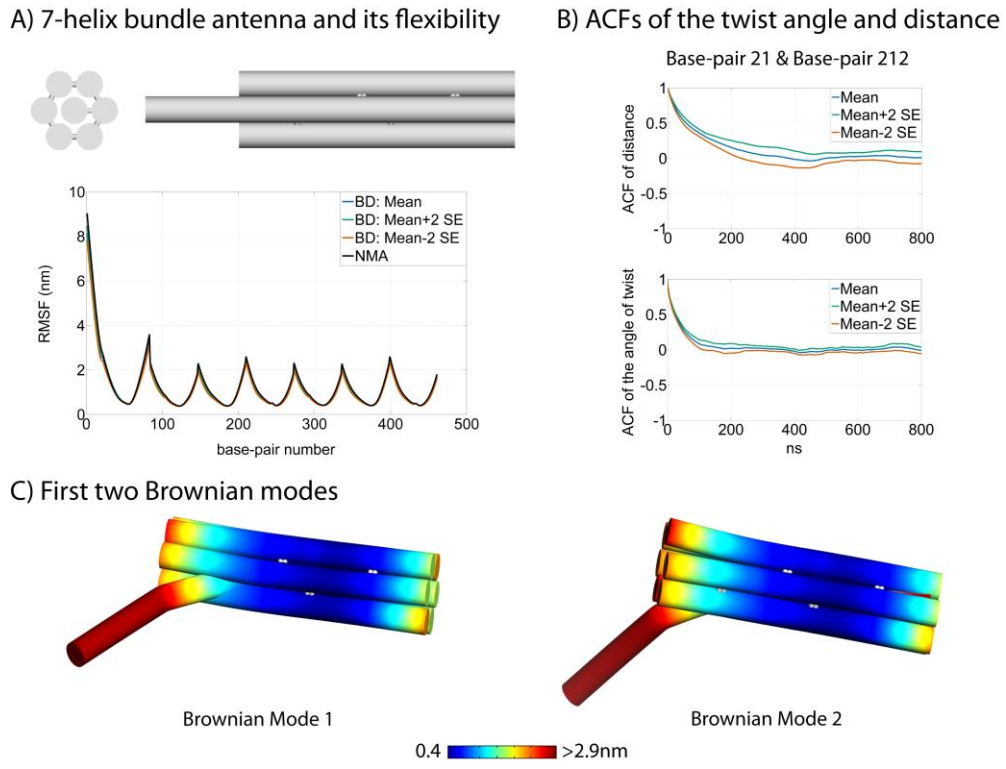
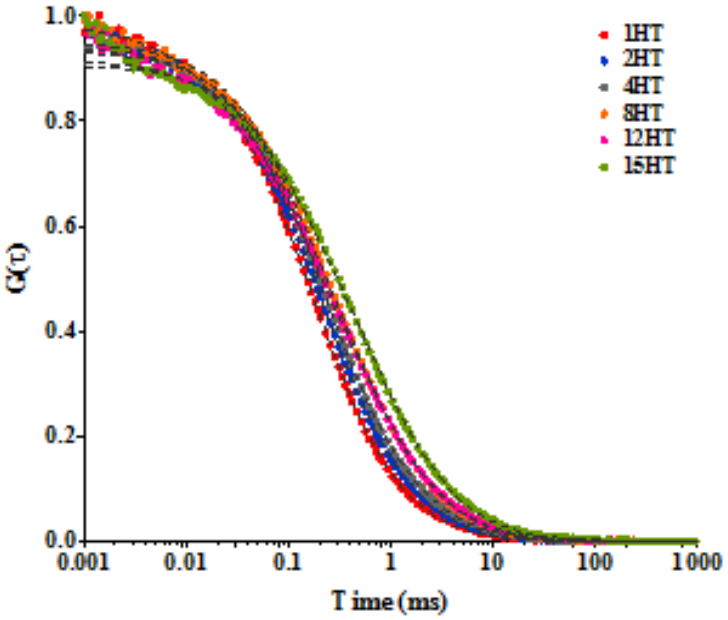


Figure 11. (a) Root-mean-square-fluctuations of the 7-helix bundle computed using Brownian Dynamics as a function of base-pair number in the structure. Peaks show highly flexible regions and troughs show relatively rigid regions located near crossovers. (b) Temporal Auto-correlation Functions (ACFs) of the twist angle and distance between individual base-pairs 21 and 212 show the temporal relaxation of the nanostructure is on the order of 200 nanoseconds. (c) The first two Brownian Modes illustrate that they are dominated by the high degree of flexibility of the central helix.

As an example of the latter, Brownian Dynamics approach, we applied the method to calculate the conformational dynamics of the 7-helix light-harvesting antenna studied previously by the Yan and Woodbury groups (Figure 11b). Results of the Brownian Dynamics simulation show that the equilibrium, long time-scale (equilibrium) conformational dynamics of the antenna is reproduced by the model (a), and also illustrate the temporal relaxation time-scale of the antenna, which is on the order of 200 nanoseconds (b). This long-time scale dynamical conformational response of the antenna is not accessible to standard, all-atom simulation methods such as Molecular Dynamics, which may reach at most tens of nanoseconds for large-scale structures such as these. Further, this model is generally applicable to higher molecular weight DNA origami structures that relax on considerably longer time-scales and are completely outside of reach of atomistic models. This model may be used together with a multi-FRET light-harvesting model discussed elsewhere in this report to compute the time-dependent excitonic properties that depend on its conformational dynamics.

Fluorescence Correlation Spectroscopy (FCS) was performed on several representative DNA tile structures (HT) to investigate the diffusivity of DNA scaffolds and validate the bead-based model described above. The experimental results are shown in Figure 12. The data are normalized at 0.001 ms for comparison. It is clear from the raw data points that the diffusion decay time increases with the size of the nanostructure. By fitting the data with Equation 1 the diffusion time was extracted and the diffusion coefficient (*D*) was subsequently calculated. The values of *D* for each HT structure are presented in Table 1: as expected from the raw data, the diffusion coefficient decreases as the size of the DNA structure increases. These results match the predicted values (Figure 13), therefore validating the bead-based



Structure	D (μm²/s)
1 HT	59 (±9)
2 HT	53 (±3)
4 HT	42 (±5)
8 HT	30 (±1)
12 HT	27 (±2)
15 HT	22 (±1)

Figure 12. Fluorescence Correlation Data for 1, 2, 4, 8, 12, and 15 HT. Colored circles correspond to raw data points and the grey dashed lines are fits from Equation 1. Data were normalized to 1 at 0.001 ms.

model used to simulate the c
of DNA in solution, and its
the solvent molecules.

By means of FCS it was pos
the translational diffusion co
nanostructures with differen
ratios. The experimental va
FCS match the predicted
simulations performed by th
thus, further validate the bea
predict the physical prop
nanostructures. FCS reveale
powerful and versatile tool fc
rotational diffusion coeffici
structures, therefore allowi
complete validation of the the
of DNA properties.

Work is now in progress
measurements to DNA origar
higher molecular weight. DNA origami have more elaborated 3D shapes than HT structures and it is important to be able to predict their behavior in solution: this will add to our knowledge of the physical properties of DNA and will also be useful to determine the general applicability of the modeling system that is currently implemented.

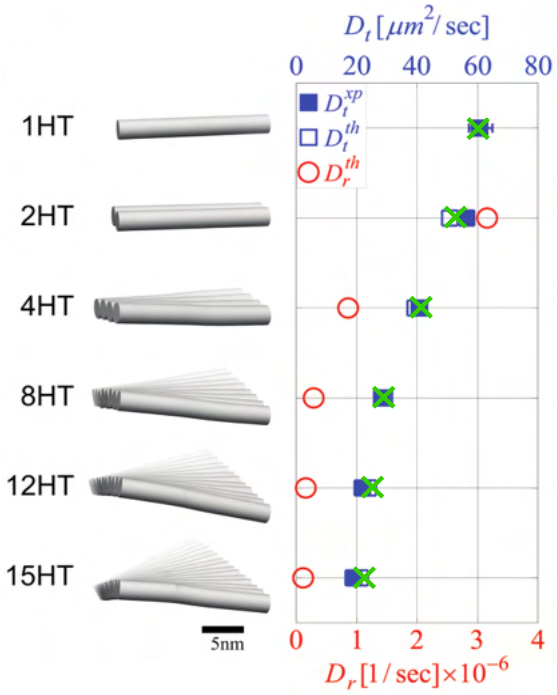


Figure 13. Theoretical calculations of the translational and rotational diffusion coefficients of the HT DNA structures based on a DNA bead-based model. The empty squares are the theoretical values of the translational diffusion coefficients, the green crosses are the experimental values of the translational diffusion coefficient as determined by FCS and the empty circles are the calculated rotational diffusion rates.

Engineering a DNA scaffolded multi-enzyme complex utilizing a "swinging arm" to control substrate transfer between enzymes

1. Assembly of DNA-swinging arm-enzyme complexes:

Swinging arms are key functional components of multi-step, catalytic transformations in many multi-enzyme complexes. In such systems, these flexible prosthetic groups couple enzyme active sites via facilitated substrate channeling for high catalytic efficiency and specificity. Engineering systems with this kind of structural and mechanistic complexity is a grand challenge in the area of biomimetic nanotechnology. Here we report the design and assembly of a multi-enzyme complex based on a DNA nanostructure, in which an artificial swinging arm is used to channel hydride transfer between two coupled dehydrogenase enzymes. By exploiting the programmability of DNA nanostructures, it was possible to optimize key parameters including orientation, stoichiometry and inter-enzyme distance for maximal activity.

The general design of the swinging arm nanostructure complex is shown in Figure 14a, where a two-enzyme cascade consisting of glucose-6 phosphate dehydrogenase (G6pDH) and malic dehydrogenase (MDH) is displayed on a DNA double crossover (DX) tile scaffold. G6pDH catalyzes the oxidation of glucose-6 phosphate and the reduction of NAD^+ to NADH. Subsequently, MDH catalyzes the reduction of oxaloacetate to malic acid using the NADH produced by G6pDH. To facilitate the efficient channeling of NADH between G6pDH and MDH, an NAD^+-functionalized poly $(T)_{20}$ oligonucleotide was attached to the DNA tile surface half-way between G6pDH and MDH. Figure 14b shows a native polyacrylamide gel electrophoresis (PAGE) analysis of the assembled enzyme complex, together with various sub-complexes. Both the gel and size-exclusion chromatography results demonstrate the assembly of the G6pDH-NAD^+-MDH swinging arm cascade with >70% yield. Assembly of the complete complex was also confirmed by atomic force microscopy (AFM) (Figure 14c), where the presence of the enzymes is signified by differences in height ("brightness") compared to the surface of the DNA tile.

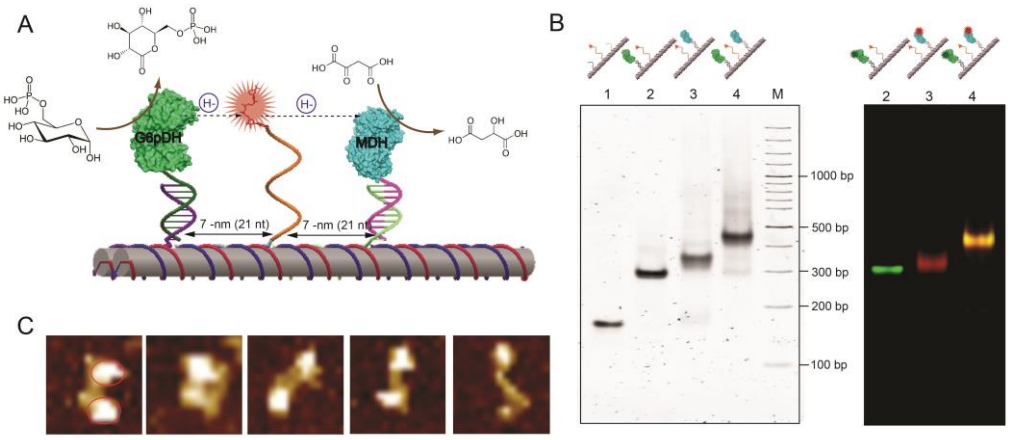


Figure 14. Design and characterization of an NAD+-modified swinging arm providing restricted diffusion of NAD+/NADH between two dehydrogenases. (a) Schematic illustration of the nanostructure complex consisting of glucose-6 phosphate dehydrogenase (G6pDH) and malic dehydrogenase (MDH) organized on a DNA DX tile. The NAD+-modified single-stranded poly(T)20 is positioned half-way between the two enzymes, facilitating the transfer of hydrides. (b) Left: Native PAGE (3%) characterization of the assembled swinging arm enzyme complex: (1) a DNA tile with the NAD+-modified arm; (2) G6pDH-NAD+ complex; (3) MDH-NAD+ complex; (4) fully assembled G6pDH-NAD+-MDH swinging arm structure. Right: fluorescence gel image of an Alexa 555-labeled G6pDH-NAD+ structure (lane 2), an Alexa 647-labeled MDH-NAD+ structure (lane 3), and a dual color image of a G6pDH (Alex a555 labeled)-NAD+-MDH(Alexa 647 labeled) swinging arm structure (lane 4). M: double stranded DNA ladder. (c) AFM imaging of the G6pDH-NAD+-MDH swinging arm structures.

2. Single-molecule characterization of local transport by the swinging arm:

To understand the mechanism of transport by the swinging arm in more detail, we designed a model system in which the cofactor and enzyme are replaced by complementary ssDNA probes. By attaching fluorescent labels to the ssDNA probes, we were able to monitor the transport of a probe to nearby target sites on individual complexes using single-molecule FRET, providing strong evidence that the swinging arm is functioning as designed (Figure 15). In this model, a Cy3 reporter dye takes the place of NAD^+ on the single-stranded poly$(T)_{20}$ arm, whereas a BHQ fluorescence quencher and a Cy5 energy transfer acceptor dye replace one or both enzymes on selected probe positions surrounding the swinging arm (Figure 15a). To mimic the binding of NAD^+/NADH to the dehydrogenase enzymes, an oligonucleotide sequence (5'-(TT)TTTCACTAT) was extended from the 5' end of the poly$(T)_{20}$ sequence, allowing the arm to transiently hybridize to the probes that each bear the complementary sequence (ATAGTGAAA(TT)-3'). The relative motion of the swinging arm was then monitored by single molecule fluorescence resonance energy transfer (smFRET,) between the attached reporter and either the quencher (obliterating the reporter fluorescence) or the acceptor (yielding a distinct red acceptor signal) using Total Internal Reflection Microscopy (TIF). In Figure 15a, the Cy3-

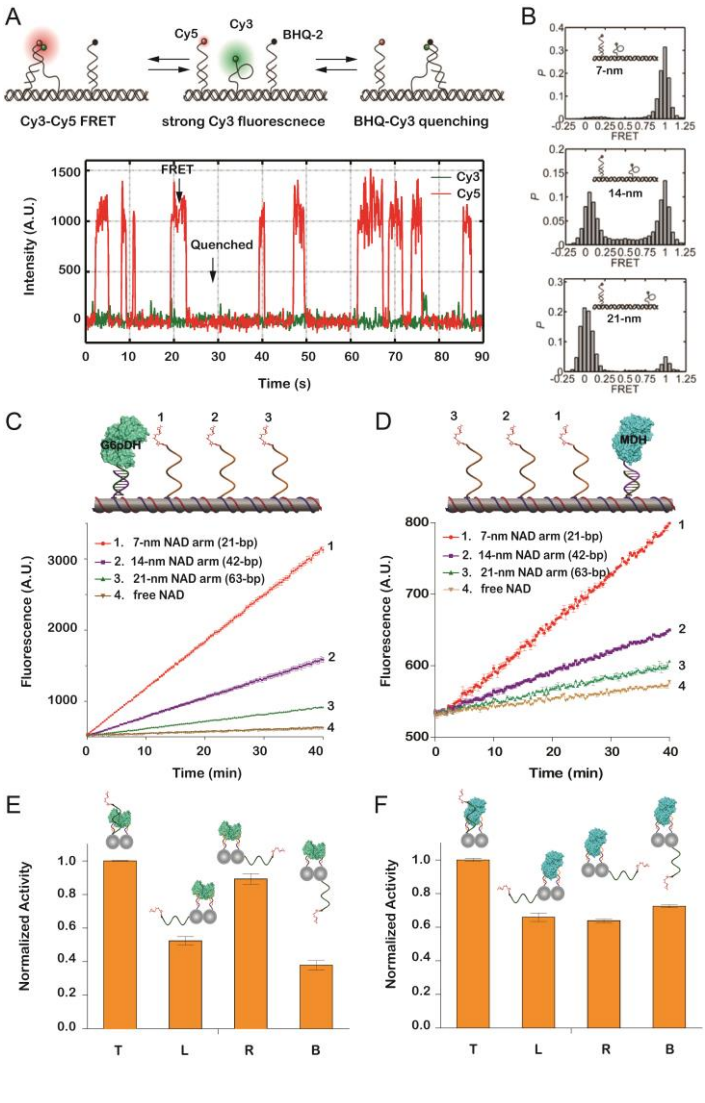


Figure 15. Characterization of the NAD+-modified swinging arm. (a) Single-molecule fluorescence resonance energy transfer (smFRET) characterization of the restricted diffusion of a single-stranded poly (T)20- arm between two DNA probes anchored at either side of the structure. Top: Cy3-labeled poly(T)20 with a 5' sticky end extension assembled between two capture probes that are modified with Cy5 (energy acceptor) and BHQ-2 (Black Hole Quencher®), respectively, with ~ 7nm distance from the anchor position of the arm. The Cy3-Cy5 FRET signal (red emission) is observed when the arm swings and binds to the Cy5-labeled capture probe, while a Cy3-BHQ interaction quenches the fluorescence when the arm swings and binds to the BHQ-labeled capture probe. Bottom: smFRET monitoring the swinging poly(T)20 arm with alternating Cy3-BHQ quenching and Cy3-Cy5 FRET events. CCD integration time: 0.1 s. (b) smFRET characterization of the distance-dependent hybridization of the poly(T)20 arm, with 7 nm (top), 14 nm (middle) and 21 nm (bottom) enzyme-NAD-modified arm distances. (c & d) Distance dependent enzyme activity for complexes in which the NAD+-modified arm is coupled to either G6pDH (c) or MDH (d) with enzyme-NAD+-modified arm distances of 7-nm, 14-nm and 21-nm. (e & f) Orientation dependent enzyme activity for complexes in which the NAD+-modified arm is coupled to either G6pDH (e) or MDH (f) at various angles between the enzyme and arm attachment sites on the DNA scaffold. Angles of ~ parallel 0˚ (T), ~ left 90˚ (L), ~ right 90˚(R) and ~ bottom 180˚ (B) were investigated.

labelled poly$(T)_{20}$ swinging arm is positioned halfway between the quencher and acceptor. In the resulting smFRET time traces, the fluorescence signal alternates between Cy3-BHQ quenching and Cy3-Cy5 energy transfer, indicating that the poly$(T)_{20}$ arm is swinging between the two probes and transiently hybridizing to them. The absence of observable low-FRET intermediates (Cy3 signal only) shows that the transient movement of the swinging arm between bound states occurs rapidly compared to the 100-ms time resolution of our single molecule measurement. To characterize the distance dependent binding mediated by the swinging arm motion using smFRET, we chose a design in which a single Cy5-labeled probe was placed at one of three, topologically accessible, distances from the Cy3-labeled arm: 7 nm (21 base pairs), 14 nm (42 base pairs) and 21 nm (63 base pairs). As shown in Figure 15b, the most efficient capture by the hybridization probe was observed at 7 nm, where ~94% of all individual swing arms were consistently associated with the Cy5 probe (leading to high FRET). As the distance increased, the efficiency of swinging arm capture decreased to ~58% of the sample at 14 nm and only ~10% at 21 nm, consistent with a theoretical considerations based on a recent coarse-grained model of the ssDNA poly$(T)_{20}$ arm. Titrating in free, unlabeled ssDNA (5'-AATTTCACTAT-$(T)_{20}$) to directly compete with the swinging arm for hybridization to the capture probe allowed us to also determine the effective local concentration of the swinging arm, ~250 μM for the 7-nm design and ~1 μM for the 14 nm construct, which demonstrated a steep distance dependence. Based on these observations we predicted that the swinging arm enzyme complex would show similar distance dependent activities. Intriguingly, we also have preliminary evidence that stretching a DNA arm close to its contour length can accelerate the dissociation of a complex by exerting an entropic force. In addition to helping interpret and explain the bulk activity assays on multi-enzyme complexes constructed using the swinging ssDNA arm, these findings should provide valuable insight into many systems in which a flexible arm is used to engineer interactions between surface-tethered components, including similar natural systems. In the future, we will refine the accuracy and generality of our model to describe the control of binding thermodynamics and kinetics by swinging DNA arms of varying lengths, distances, and flexibility (i.e., flexible single-stranded arms vs. rigid double-stranded arms). This should yield a predictive framework for unprecedented control over bimolecular reactions using DNA nanostructures.

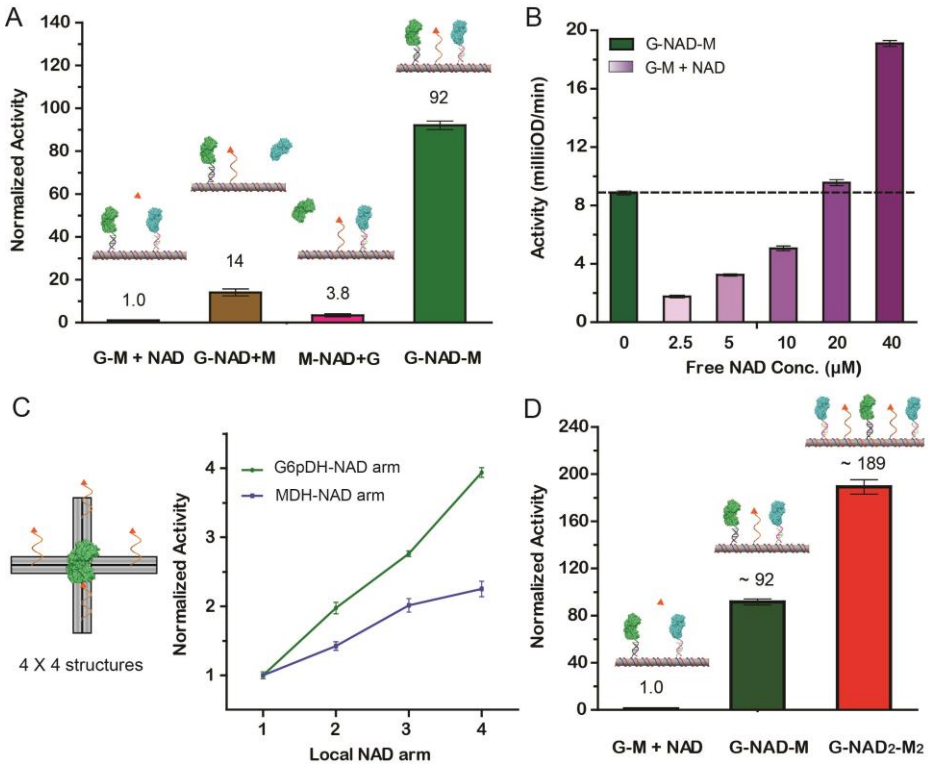


Figure 16. Characterization of enzymatic activity in the G6pDH-NAD+-MDH swinging arm structures. (a) Normalized overall pathway activities for G6pDH-MDH assembly with free NAD+ (G-M + NAD, blue), G6pDH-NAD+ semi-assembly with free MDH (G-NAD + M, brown), MDH-NAD+ semi-assembly with free G6pDH (M-NAD + G, pink) and the fully assembled G6pDH-NAD+-MDH swinging arm structure (G-NAD-M, red). Total enzyme structure and NAD+ concentration: 100 nM. Substrate conditions: 1 mM glucose-6 phosphate and 1 mM malic acid in 100 mM HEPES buffer (pH 8). (b) Titrating the effective concentration of freely diffusing NAD+ into the G6pDH-MDH assembly with equivalent activity to the swinging arm structure of G6pDH-NAD+-MDH assembly: 100 nM G6pDH-MDH assemblies with free aminoethyl modified NAD+ (AE-NAD) at 2.5, 5, 10, 20 and 40 μM. All NAD+ used in the assay refers to aminoethyl modified NAD+. (c) Relative stoichiometric dependence of enzyme activity as the number of NAD+-modified arms on a 4 × 4 DNA tile increases from 1 to 4. (d) Improving the catalytic efficiency by adjusting the relative number of G6pDH and MDH molecules.

3. Measuring and optimizing enzymatic activity facilitated by the swinging arm:

Next, we evaluated the ability of an NAD^+-modified swinging arm to enhance dehydrogenase activity in a one enzyme-NAD^+ arm assembly (Figure 15b and c). The activities of the two enzymes were measured individually in bulk solution for three swinging arm-enzyme distances (7, 14 and 21 nm) using phenazine methosulfate (PMS) catalyzed resazurin fluorescence assays. As predicted, the 7-nm distance resulted in the highest activity for both G6pDH and MDH. At this distance from the NAD^+-modified swinging arm, G6pDH-NAD^+ assembly showed an activity enhancement of ~30-fold compared to an enzyme system with the same concentration of 100 nM freely diffusing NAD^+. Conversely, this enhanced activity by a swinging arm

corresponds to the activity generated in the presence of ~5-10 µM freely diffusing NAD^+. Similarly, MDH-NAD^+ assembly exhibited a ~7-fold activity enhancement at 7 nm, corresponding to the activity at ~2.5-5 µM freely diffusing NAD^+. Notably, the effective local concentration of the NAD^+-coupled swinging arm determined by enzyme catalysis (~5 µM at 7 nm) is significantly lower than the swinging arm concentration estimated from competitive binding (~200 µM at 7 nm). We suggest that this difference may be due to the orientation and steric constraints associated with binding of the tethered NAD^+ to the active site of the enzymes, higher binding affinity for oligo-hybridization (~ 0.4 µM k_d) than NAD^+/dehydrogenase (> 10 µM k_d), and/or to active-site binding differences between NAD^+ and NADH, as G6pDH binds to NADH much more weakly than to NAD^+. In order to further examine the orientation effects, we varied the angle between the NAD^+-modified arm and the enzyme attachment site to maintain a distance of ~ 6-8 nm (Figure 15e and f) and found the highest activity when the arm was attached to the top surface of the DNA nanostructure at an angle parallel to that of the enzyme.

Using the optimized distance and orientation parameters, a G6pDH-NAD^+-MDH swinging arm structure was constructed with the NAD^+-modified arm positioned centrally, 7 nm from either enzyme. In Figure 16, the activity of this complete two-enzyme nanostructure is compared to that of the partially assembled structures including a G6pDH-MDH assembly with freely diffusing

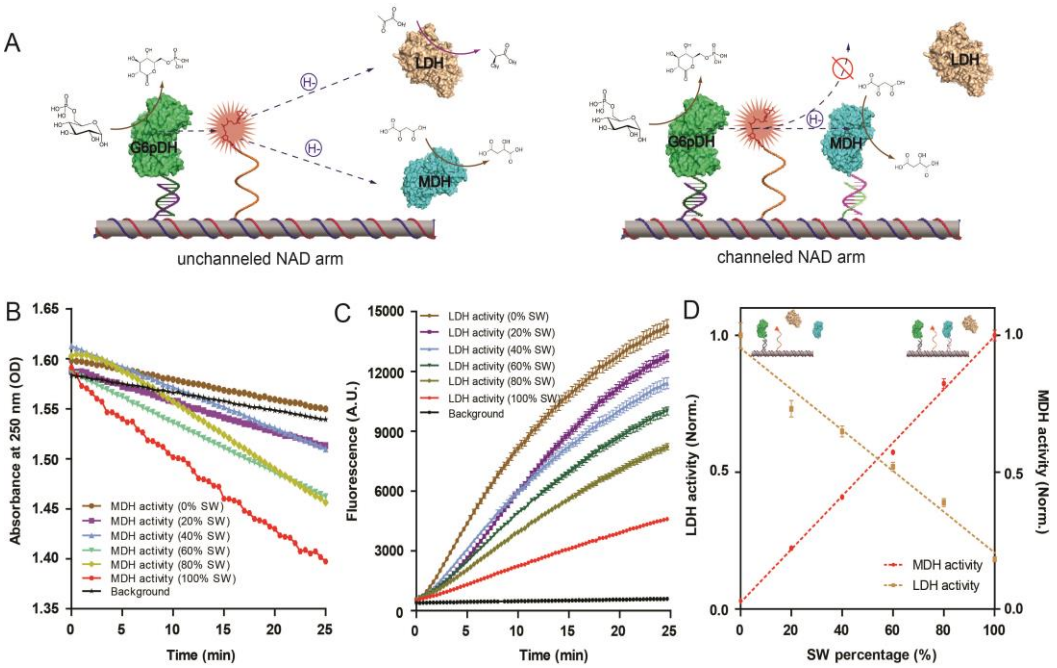


Figure 17. Specificity of the G6pDH-NAD+-MDH swinging arm structure when LDH is introduced to compete for the NADH produced by G6pDH. (a) Schematic illustration of LDH competition in G6pDH-NAD+ swinging arm half structures with free MDH (left) and fully assembled G6pDH-NAD+-MDH swinging arm structures (right). (b) MDH activity vs. the fraction of fully assembled enzyme/arm complexes. (c) LDH activity vs. the fraction of fully assembled complexes. (d) Normalized LDH and MDH activities as a function of the fraction of assembled complexes. Assay conditions: 100 nM G6pDH-NAD+-MDH structures (total concentration including the half and fully assembled swinging arm structures); 100 nM LDH; 1 mM glucose-6 phosphate, 1 mM malic acid, 1 mM sodium pyruvate in 100 mM HEPES buffer (pH8).

NAD^+, a G6pDH-NAD^+ arm assembly with freely diffusing MDH, and an MDH-NAD^+ arm assembly with freely diffusing G6pDH. For the same total NAD^+ and enzyme concentration (100 nM), the activity of the complete swinging arm structure is ~ 90-fold higher than that obtained with the similar two-enzyme assembly but freely diffusing NAD^+ system. Semi-assembled swinging arm complexes with only one enzyme attached (G6pDH-NAD^+ or MDH-NAD^+ structures) and the other enzyme freely diffusing in solution also resulted in higher activities than the enzyme complexes without NAD^+-modified arms (~14-fold for G6pDH-NAD^+, and ~4-fold for MDH-NAD^+), but were still considerably less active than the complete G6pDH-NAD^+-MDH enzyme cascade. The effective local NAD^+ concentration for G6pDH-NAD^+-MDH was determined to be ~20 μM, by titrating free NAD^+ to G6pDH-MDH assembly until the activity was equivalent to that of G6pDH-NAD^+-MDH assembly(Figure 16b).

In natural multi-enzyme complexes, the relative stoichiometry of the enzymes is optimized to maximize their catalytic efficiency. Toward this end, we investigated the dependence of enzymatic activity on the number of surrounding NAD^+-modified swinging arms on a DNA-scaffolded 4 × 4 tile (Figure 16c). For the G6pDH-NAD^+ structure, the activity increased almost linearly as the number of NAD^+-modified arms increased from 1 to 4. By comparison, the enzymatic activity of the MDH-NAD^+ structure only improved 2-fold as the number of NAD^+-modified arms increased from 1 to 4. Kinetic measurements found ~10-fold higher turnover number (k_{cat}) for the isolated G6pDH than MDH, indicating that MDH is the rate-limiting enzyme in the G6pDH-MDH cascade. To maximize the catalytic efficiency we therefore engineered structures in which two MDH molecules surrounded a single G6pDH molecule, channeled by two NAD^+-modified arms (G6pDH-NAD^+_2-MDH_2) as shown in Figure 16d. As expected, this enzyme cascade exhibited an additional ~2-fold activity enhancement compared to G6pDH-NAD^+-MDH. Another important advantage of an enzyme cascade with a central swinging arm is the increased reaction specificity that results from restricting the diffusion of intermediates. To explore this idea, free lactate dehydrogenase (LDH) was added to compete for NADH with the malic dehydrogenase on the G6pDH-NAD^+-MDH nanostructure. The presence of LDH is expected to consume a fraction of the NADH generated by G6pDH and, thus, should interfere with the enzyme cascade, leading to decreased malic acid production. Figure 17 shows the results of using various mixtures of G6pDH-MDH complexes, with and without the swinging arm, in competition with LDH for NADH. As expected, for the G6pDH-NAD^+ assembly with freely diffusing MDH and LDH, we found strong competition between the two free enzymes so that the coupled activity of the G6pDH-MDH pathway was very low. As the percentage of G6pDH-NAD^+-MDH increased in the mixture (keeping the total enzyme concentrations constant), the MDH activity increased accordingly, indicating that the fully assembled G6pDH-NAD^+-MDH complex was effectively channeling NADH from G6pDH to MDH, avoiding the competition from free LDH. The activity of LDH behaved in the opposite manner, exhibiting much lower activity as the amount of the fully assembled G6pDH-NAD^+-MDH increased (Figure 17b). Figure 17c presents the normalized activities of MDH and LDH against the fraction of assembled complexes.

In summary, we designed and constructed artificial “swinging arm”-channeled multi-enzyme complexes with NAD^+-modified molecular arms to transfer hydrides between two dehydrogenase enzymes. The swinging arm not only significantly enhances enzymatic activity, but also affords high specificity in a complex environment. The concept of a flexible molecular arm-channeled reaction should be applicable to the design and assembly of other multi-enzyme

systems. For example, a similar approach can be used to construct swinging arm enzyme cascades based on other reactive cofactors such as FAD, CoA, ATP, lipoic acid, biotin or pantetheine that are used in naturally occurring multi-enzyme complexes to carry intermediates. Artificial swinging arm structures may also lead to new approaches for regulating enzyme activities by incorporating mechanisms for controlling the diffusion and motion of the arm. In a simple demonstration, we exchanged a ssDNA arm for a double-stranded DNA-arm (dsDNA-arm) by introducing a poly(A)$_{22}$ oligonucleotide into solution to hybridize with the NAD$^+$-poly(T)$_{20}$ arm. We observed an almost 50% decrease in enzyme activity for the enzyme complex with the dsDNA-arm compared to the ssDNA-arm, likely due to the slower diffusion and increased structural rigidity of dsDNA. The underlying DNA nanostructure scaffolds provide programmable frameworks for creating more complex enzymatic circuitry, and will find utility in the development of functional catalytic systems for the synthesis of high-value chemicals, generation of energy, conversion of materials and bioenergy, and as regulatory biological circuits for diagnostic and therapeutic applications.

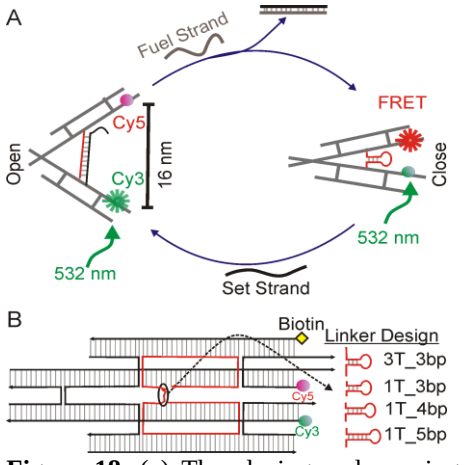


Figure 18. (a) The closing and opening cycles of DNA tweezers monitored by single-molecule fluorescence resonance energy transfer (smFRET). (b) Schematic detail of the DNA tweezers and different linker designs used in this study.

Optimizing the enzymatic activity of a DNA actuator structure using single-molecule FRET

A dynamic nanodevice called "DNA tweezers" has recently been used to coordinate the activity of an enzyme/cofactor pair by juxtaposing the enzyme and cofactor on opposite arms of the tweezers. Initial studies focused on bulk properties of the tweezers-mediated reactions, and hence lacked insight into how these tweezers behave at the single-molecule level. We used site-specifically fluorophore-labeled DNA tweezers to monitor the FRET efficiency at the single-molecule level to achieve the following two major goals: (1) quantitatively characterize the conformational changes of DNA tweezers during their operation at the single-molecule level, and (2) improve the design of DNA tweezers based on feedback from single-molecule studies to achieve superior control over the activity of the enzyme/cofactor pair. The basic operational principle of the DNA tweezers is shown in Figure 18. The addition of specific DNA oligonucleotides (Fuel and Set) provides the thermodynamic driving force to

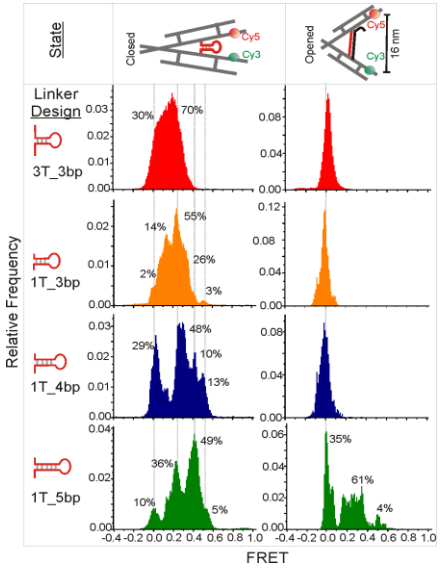


Figure 19. smFRET histograms of the DNA tweezers with different linker designs. Experiments were performed in 1X TAE buffer containing 12.5 mM Mg^{2+}. The conformations were switched in solution by incubating the tweezers with excess set/fuel strands before injecting into the microscope slides.

trigger conformational changes in the tweezers. To directly monitor the closing/opening cycles, a pair of FRET fluorophores (Cy3 as a donor and Cy5 as an acceptor) were incorporated near the ends of two arms (Figure 18). Tweezers were immobilized on streptavidin-coated microscope slides via a single biotin label (Figure 18b). The FRET was calculated by recording the fluorescence intensity of both Cy3 and Cy5 while Cy3 was illuminated at 532 nm.

First, we characterized the DNA tweezers design containing a hairpin linker with a 3T spacer and 3-bp stem (3T_3bp, Figure 18b). This design showed only partial closing of tweezers, with a Cy3-Cy5 distance of ~7 nm in the closed state. We hypothesized that replacing this linker sequence by one containing a longer hairpin could increase enzyme activity by bringing the enzyme and cofactor in closer proximity. To this end, we reduced the spacer to a single thymine (1T) and varied the stem length from 3 to 5bp (1T_3bp, 1T_4bp and 1T_5bp, Figure 18b). Our single-molecule experiments showed that all of the hairpin designs except 1T_5bp permit switching between open and closed states with nearly 100% efficiency (Figure 19); we surmise that the stability of the 5bp stem prevents efficient reopening of the tweezers. Therefore, we chose 1T_4bp as a candidate for further testing in the promotion of enzymatic reactions as described recently by the Yan group. To directly test whether the new design further enhances enzyme activity, the ratio in activity between the open and closed states of the initial 3T_3bp design was compared with that of 1T_4bp. The preliminary results suggest that the new design increases the enzyme activity by ~10 fold compared to only ~5 fold in the original design, a significant improvement made possible by feedback from our single molecule experiments. Surprisingly, single-molecule studies show multiple populations with distinct FRET values (highlighted by vertical dotted lines in Figure 19) for all designs except for the original 3T_3bp. Studies are ongoing to probe the cause of these distinct FRET populations.

Currently, we are attempting to detect enzymatic turnover at the single-molecule level to enable activity assays of individual pairs of DNA tweezers. A primary challenge is the in situ detection of the fluorescent product, resorufin, as it rapidly escapes from the evanescent field. We are currently exploring the use of bovine serum albumin as a crowding agent to slow the diffusion of resorufin.

3D-DNA nanostructures for facilitated substrate diffusion by directed substrate channeling and compartmentalization

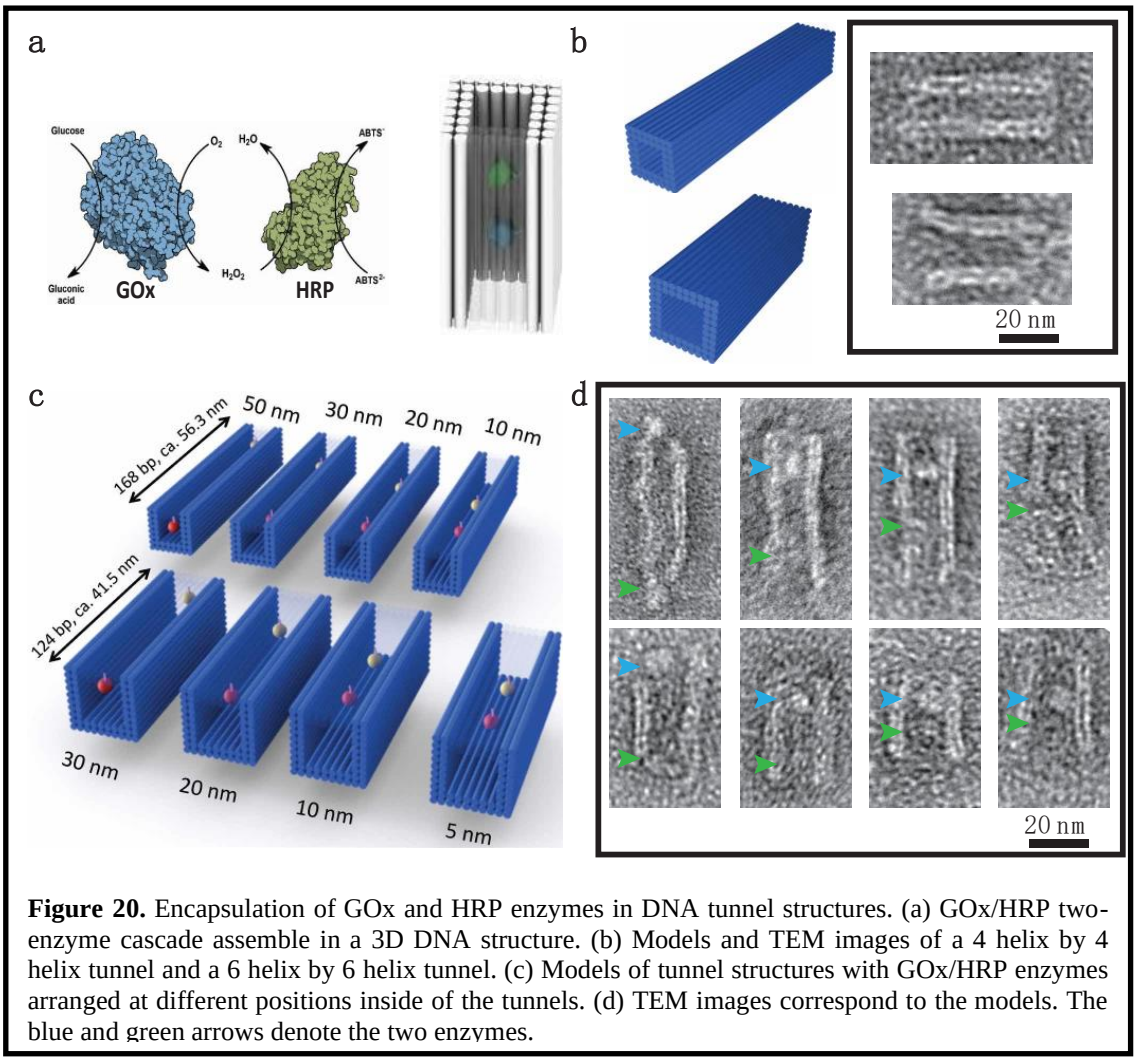


Figure 20. Encapsulation of GOx and HRP enzymes in DNA tunnel structures. (a) GOx/HRP two-enzyme cascade assemble in a 3D DNA structure. (b) Models and TEM images of a 4 helix by 4 helix tunnel and a 6 helix by 6 helix tunnel. (c) Models of tunnel structures with GOx/HRP enzymes arranged at different positions inside of the tunnels. (d) TEM images correspond to the models. The blue and green arrows denote the two enzymes.

1. Engineering 3D DNA-origami structures:

One of the most attractive features of DNA nanostructures for the study of enzymatic reactions is that they can be engineered to incorporate external elements that impart certain desired properties, at very specific positions. It is possible to simulate and explore substrate channeling by modifying the path between the enzymes with molecules that generate favorable electrostatic or hydrophobic interactions with the intermediates to direct their travel along the path.

3D DNA origami is a suitable method for encapsulating the model GOx/HRP enzyme cascade with controllable ratio, orientation, and distance between enzymes. We designed and assembled two tunnel structures (Figure 20). One is 168 bp (56 nm) long, and contains a 4 helix by 4 helix (10 nm by 10 nm) cavity. The other is 124 bp (42 nm) in length, and contains a 6 helix by 6 helix (15 nm by 15 nm).

2. Systematically evaluating the immobilization of GOx and HRP enzymes:

The two-tunnel structures were used for systematically testing the immobilization efficiency of

GOx and HRP enzymes, and for demonstrating position control of the enzymes. Our results showed the two enzymes could be precisely connected to the inside of the 4 helix by 4 helix tunnel with 10 nm, 20 nm, 30 nm, and 50 nm meter inter-molecular distances. When immobilized on the inside of a 6 helix by 6 helix tunnel, the distances between the two enzymes were engineered as 5 nm, 10 nm, 20 nm, 30 nm (Figure 20c and d). Our result showed the enzyme-occupancy efficiencies of the 4 helix by 4 helix tunnel were significantly lower than for the 6 helix by 6 helix tunnel. Therefore, the 6 helix by 6 helix tunnel was used for the following experiments

3. Constructing a reel-shaped DNA structure for liposome encapsulation:

Formation of liposomes using DNA structures as templates could potentially further limit the escape of substrates/intermediates, and thus increase the efficiency of an artificial enzyme cascade. Towards this goal, we design a reel-shaped DNA structure. We plan to use previously described methods to form liposomes around the outside of the structure. The reel-shaped design consists of three parts, each of which is composed of DNA origami. Two disc-shaped DNA origami (diameters ~ 60 nm) were designed to connect to a 6 helix by 6 helix tunnel (Figure 21). The disc and the tunnel were assembled and purified separately. The assembly of the reel-shaped structures was done through multimerization between the discs and the tunnels. We test different magnesium chloride concentrations, temperatures, connector strand designs, and mixing ratios of disc/tunnel, for the multimerization process. Our results show the multimerization was most efficient under the following conditions: 10 mM magnesium chloride concentration, 30 degrees Celsius, 24 nucleotide connector strands, and a 4 to 1 ratio of disc:tunnel. In the future, after successfully demonstrating the encapsulation of the enzymes, we further propose to construct a gated structure for dynamic control over a multi-protein pathway.

4. Future direction:

Our goal remains to limit diffusional escape of reaction intermediates in enzyme cascades using lipid membranes as reflecting walls. Because the yield of our tunnel design has been low we have decided to change architectures. We are currently working with stacked-ring cylinder DNA nanostructures referred to as "o-bricks". We are examining o-bricks with outer diameters of 30 nm, 60 nm, and 90 nm, and corresponding inner diameters that are 12 nm less than the outer diameter. Our goal is to capture lipid nanotubes on the inside or outside of these structures, and then to capture the metabolic enzymes (glucose oxidase and horse radish peroxidase) on the inside of the lipid nanotubes. We will strive to create openings on the lipid nanotubes to allow free diffusion in and out of substrate and product.

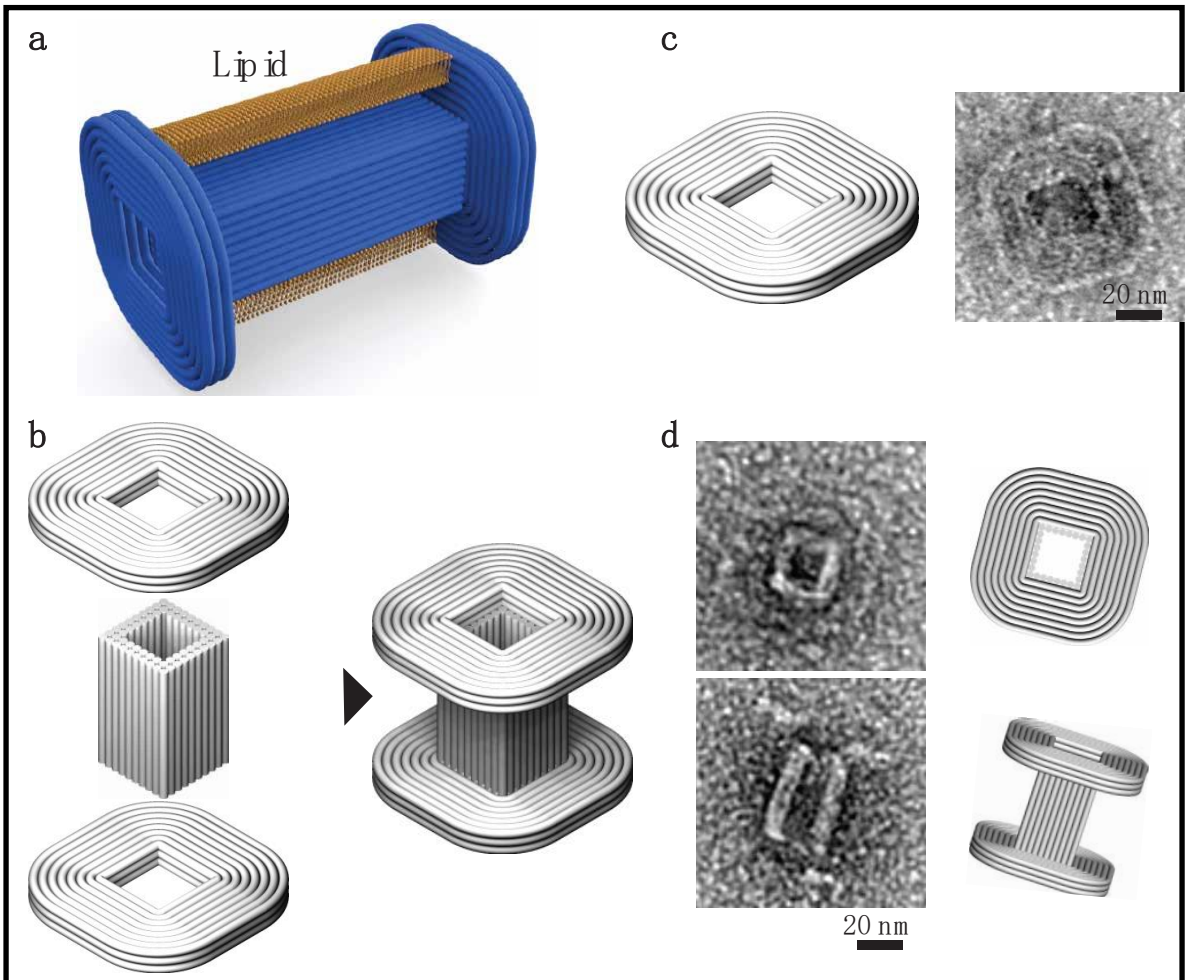


Figure 21. Hierarchical assembly of a reel-shaped DNA structure. (a) A model of liposome formed on the outside of a reel-shaped DNA structure. (b) The DNA structure is formed by a 6 helix by 6 helix tunnel and two disc-shaped DNA structures. (c) A model and a TEM image of the three-layer DNA disc structure. (d) TEM images of the reel-shaped DNA structure. The two 3D models on the right show similar orientation as the DNA structures in TEM images.

Photosynthetic Pathway

Design of the photosynthetic pathway

1. Global system components:

The proposed artificial photosynthetic pathway will contain three different elements (Figure 22): (1) a DNA scaffold to arrange the components. These origami structures will be modified with light harvesting pigments to allow unidirectional (downhill) energy transfer to the reaction center protein. (2) Light harvesting pigments for the initial absorption of energy. Two fluorophores, absorbing light between 600 - 750 nm, will be incorporated into the nanostructure. Additional fluorophores can be added to span the entire visible to near IR region, resulting in a more continuous absorption and/or to make it tunable for different applications (adapted to different light conditions). The selected fluorophores will be arranged such that dyes with higher excited state energies (absorbing at shorter wavelength) are distal to the reaction center and those with lower energies (longer wavelength) are proximal. (3) The photosynthetic reaction center from the purple non sulfur photosynthetic bacterium *Rhodobacter sphaeroides* will be used to perform charge separation. The reaction center is a pigment-protein complex that uses light energy to power a series of electron transfer reactions resulting in a charge-separated state that ultimately drives trans-membrane proton translocation in natural systems.

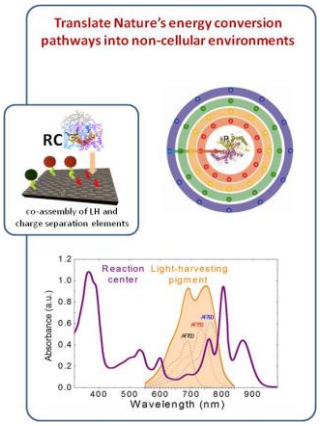


Figure 22. Design concept: (upper-left) engineer a light-harvesting system using nanostructured DNA scaffolds by placing antenna molecules and a photosynthetic reaction center complex at specific positions for precise geometric control. (Upper-panel) one of the proposed arrangements. Colors represent the excited state energies of the dye molecules in each ring from higher energy (blue) to lower energy (red) allowing the absorbed photons to be funneled to the reaction center protein located at the center of the ring. (Lower panel) an example of the absorption spectra of selected dye molecules, relative to that of the reaction center. This should result in greater spectral coverage of light harvesting.

2. Initial system components:

The design of the artificial light harvesting system should facilitate spectrally uniform light absorption, efficient energy conversion and improved photo-stability, as compared to the natural system. While the ultimate goal is to place a set of fluorophores in known positions relative to the photosynthetic reaction center using a nanostructured DNA scaffold, it is necessary to first characterize the light-harvesting functions of individual dye molecule with different spectral properties and excited state lifetimes working in conjunction with the reaction center. First, several different dye molecules were attached directly to the reaction center protein individually. The distance and average orientation of the dye molecule to reaction center cofactors are identical in all cases, making it possible to probe the effects of spectral overlap and the inherent excited state lifetime of each dye. The results of this study will guide the design of a more complex DNA-templated multiple dye light-harvesting system. Towards this end, a simple DNA-templated light-harvesting antenna system utilizing 2 different dye molecules is shown on the right of Figure 23.

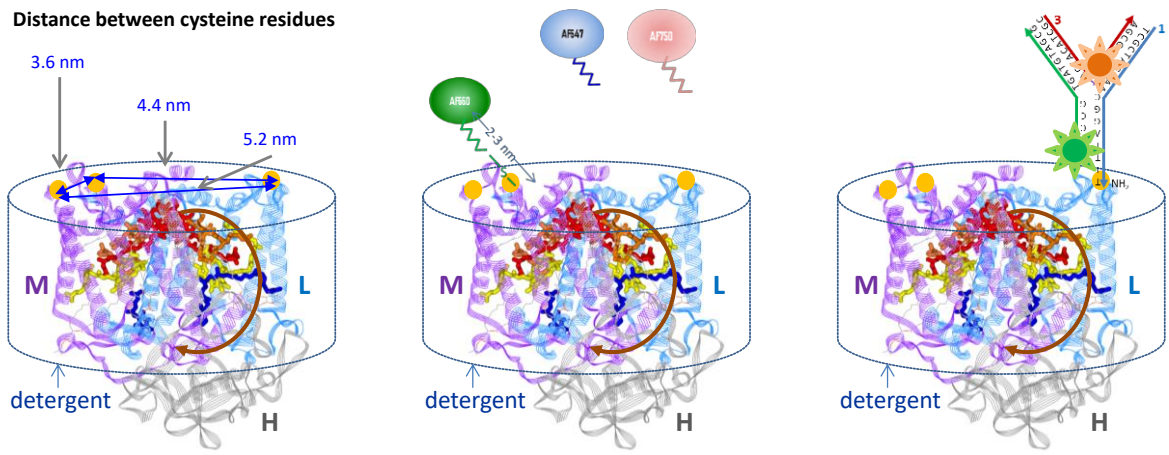


Figure 23. A systematic approach for building a photosynthetic light harvesting system.(a) The reaction center protein from the purple nonsulfur photosynthetic bacterium *Rhodobacter sphaeroides* is genetically mutated to have only 3 cysteine residues on the protein surface for attaching artificial antenna molecules or complexes at specific positions. All 3 cysteine residues are located close to the primary electron donor (P). The arrow indicates the electron transfer pathway for light energy conversion once the cofactor P receives the photon energy. (b) Attaching dye molecules to the available sites. (c) Attaching DNA-templated dye complexes to the reaction center with multiple dyes of different colors. These both increases the cross section of light absorption and the size of the spectral region over which light can be absorbed resulting in a step-wise energy transfer.

Once the bacteriochlorophyll dimer, P, is excited either directly or via energy transfer from the surrounding light harvesting molecules, it transfers an electron via a monomer bacteriochlorophyll (BA) to a bacteriopheophytin (HA) in a few picoseconds. This is followed by a 200-ps electron transfer to the first of two quinones, QA, and finally to a second quinone, QB, in 200 μs. The back reactions of each step are 2 – 4 orders of magnitude slower than the forward reactions, resulting in a quantum yield of charge separation that is near unity. One advantage of this system is that each intermediate state in the energy and electron transfer process can be clearly distinguished from the others using time-resolved spectroscopic techniques.

3. Engineering reaction center protein-dye conjugates:

The primary focus of this work is the design and construction of an energy conversion system with broad spectral coverage. The key parameters for achieving spectrally uniform light absorption are the relative geometry (distance and orientation) of the components and the spectral coverage of the light harvesting components. Regarding the direct attachment of individual dyes to the reaction center, the geometry should be very similar for all 3 dyes examined in this study. The dyes have similar molecular weights and the same covalent linkage for the dye-protein conjugation.

We used a triple mutant of the *Rhodobacter sphaeroides* strain 2.4.1 (PDB 1AIG) reaction center for this work. This genetically modified reaction center contains three cysteine residues at positions M100, L72 and L274, which are used for conjugation with selected maleimide-modified fluorophores. The 3 cysteine residues are located on the surface of the reaction center protein, 3 – 5 nm from the primary electron donor P in the reaction center. This is important as the efficiency of energy transfer has an inverse sixth power relationship to the distance between the donor and acceptor. The short donor-acceptor distance makes it possible to achieve high energy transfer yields. Energy transfer efficiency is also orientation dependent. Here, the

transition dipole direction is not rigidly fixed and the dyes rotate nearly freely, resulting in an average of efficiencies over almost all possible orientations.

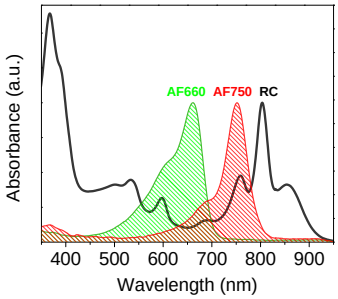


Figure 24. Absorption spectra of the reaction center protein (blue), Alexa Fluor 660 (green) and Alexa Fluor 750 (red).

By selecting various dye molecules from a large variety of commercially available dyes, the spectral range over which light is absorbed can be tuned. Figure 24 shows the absorption spectra of 2 selected dyes, Alexa Fluor 660 ($\lambda_{max,abs}$ = 660 nm, $\lambda_{max,emi}$ = 690 nm) and Alexa Fluor 750 ($\lambda_{max,abs}$ = 752 nm, $\lambda_{max,emi}$ = 780 nm), both of which absorb in the region where the reaction center absorbs very weakly. Their fluorescence spectra (not shown) overlap well with the absorption bands of the reaction center cofactors in the Q_Y transition region (the degree of overlap between the fluorescence spectrum of the donor, the dye in this case, and the absorbance spectrum of the acceptor, the reaction center, is one of the factors in determining energy transfer efficiency). The fluorescence quantum yields determined experimentally are 37% and 12% for Alexa Fluor 660 and Alexa Fluor 750 in solution, respectively. Both have reasonably long excited state lifetimes (see below), facilitating the energy transfer process.

The fluorophores were conjugated to the reaction center protein using maleimide chemistry. To accomplish this, the reaction center protein was treated with a 5-fold molar excess of Tris(2-carboxyethyl)phosphine hydrochloride to reduce the disulfide bonds, then it was purified in phosphate buffer (1Xphosphate-buffered saline, 0.025% N,N-dimethyl-dodecylamine N-oxide, pH 7.2) using a 50,000 dalton Amicon molecular weight cutoff filter. The reaction center protein was then mixed with a 15-fold molar excess of dye (15 mM in dimethylsulfoxide) containing a reactive maleimide group (purchased from Invitrogen), and left for 6 hours at 4^0C. The excess dye molecules were then removed by purification using Amicon filters (50,000 dalton molecular weight cutoff) followed by purification using a Ni-sepharose column (the reaction centers used in this study contain a poly-histidine tag that binds to the nickel column). All the Alexa Fluor dyes were conjugated to reaction center with an average ratio of 2.1 – 2.5 dyes-per-reaction center.

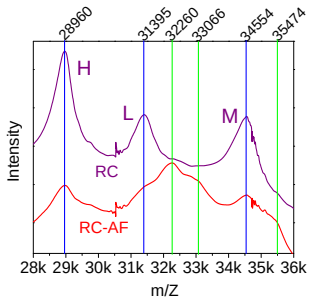


Figure 25. MALDI-TOF spectra of reaction centers (purple) and reaction n centers conjugated with Alexafluor 660 (red). The reaction centers spectrum shows three peaks corresponding to the H, L and M subunits. In contrast, the Alexafluor reaction center-dye spectrum has two additional peaks associated with the L protein subunit and one associated with M, signifying selective conjugation of the dye to the reaction center.

The covalent bonds between the dye molecules and the reaction center proteins were confirmed by matrix-assisted laser desorption ionization time-of-flight (MALDI-TOF) measurements (Applied Biosystem Voyager System 4320). Figure 25 compares the MALDI spectra of reaction center proteins with and without Alexa Fluor 660. The unconjugated reaction center shows three distinct peaks corresponding to its three protein subunits (H, L and M), whereas the reaction center-Alexa Fluor 660 conjugate exhibits two additional peaks associated with the L-subunit and one

additional peak associated with the M-subunit. This result confirms that the conjugation of the dye molecule to the reaction center protein was selective and specific.

Characterization of the initial dye-reaction center constructs

1. Calculating the number of dye molecules/protein using ground state absorbance spectra: Functional characterization of the assembled system was performed using several spectroscopic methods. Ground state absorbance spectra were used to calculate the number of dye molecules attached to each reaction center protein. The left panels of Figure 26 compare the absorption spectra of reaction center-Alexa Fluor 647 conjugates ($\lambda_{max,abs}$ = 649 nm, $\lambda_{max,emi}$ = 667 nm, upper panel), reaction center-Alexa Fluor 660 conjugates (middle panel) and reaction center-Alexa Fluor 750 conjugates (bottom panel) to that of the reaction center alone. There is a large absorption increase in the 550 nm to 800 nm wavelength region for the dye-conjugated reaction centers. Dye-to-reaction center ratios of 2.5, 2.1 and 2.2 were calculated from the absorption

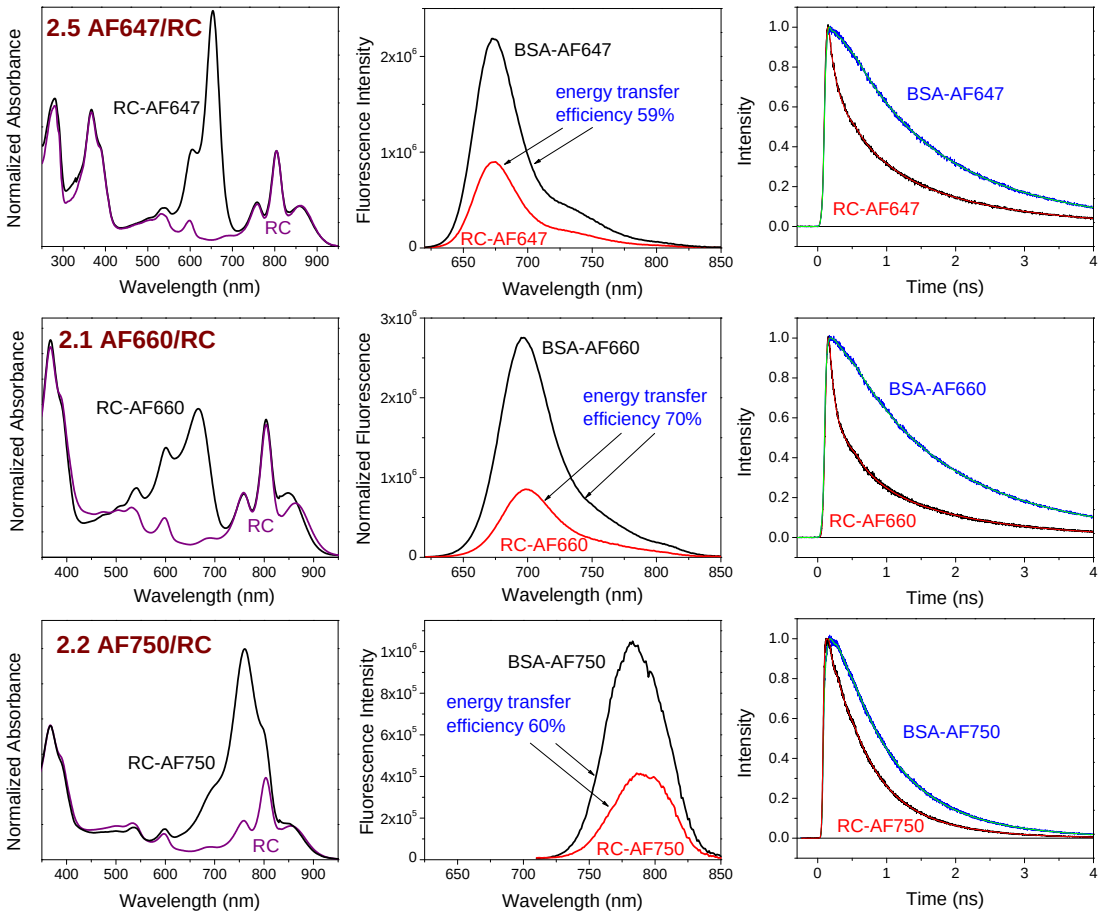


Figure 26. (Left to right) Absorption spectra of reaction center (purple) and reaction center conjugated with Alexa Fluor (black), fluorescence emission spectra of Alexa Fluor conjugated to BSA (black) and to reaction center (red), and fluorescence decay profile of Alexa Fluor conjugated to BSA (blue), and to reaction center (red) using TCSPC techniques . The upper row of data correspond to Alexa Fluor 647 (excitation wavelength 600 nm, decay kinetics monitored at 670 nm), the middle row of data corresponds to Alexa Fluor 660 (excitation wavelength 600 nm, decay kinetics monitored at 698 nm) and the bottom row of data corresponds to Alexa Fluor 750 (excitation wavelength 710 nm, decay kinetics monitored at 780 nm).

spectra for reaction centers conjugated with Alexa Fluor 647, Alexa Fluor 660 and Alexa Fluor 750, respectively.

2. Determining the efficiency of energy transfer to the reaction center:

To better mimic the spectral and kinetic properties of Alexa Fluor dyes in a protein environment without an energy acceptor, the dye molecules were conjugated to bovine serum albumin (BSA) and examined by steady-state and time-resolved fluorescence spectroscopic. BSA has a cysteine residue on the protein surface which can be conjugated to the dye molecules. However, there are no energy acceptors, making it a good control for measuring the intrinsic excited state lifetime of the dye.

The middle column in Figure 26 shows the steady-state fluorescence spectra of each sample. The spectra for Alexa Fluor 647 (upper), Alexa Fluor 660 (middle) dyes and Alexa Fluor 750 (bottom) coupled to either BSA or the reaction center are compared. The first two dyes were excited at 600 nm and the last dye was excited at 700 nm. The fluorescence intensity of each dye is quenched when conjugated to the reaction center relative to the BSA controls. The Förster resonance energy transfer (FRET) efficiencies, calculated from the relative fluorescence intensities of the reaction center-conjugated vs. BSA-conjugated dyes were estimated to be 59%, 70% and 60% for Alexa Fluor 647, Alexa Fluor 660 and Alexa Fluor 750, respectively.

Consistent with this interpretation, there is a decrease in the fluorescence lifetime of the reaction center conjugated dyes, observed using time correlated single photon counting. The kinetic traces shown in the right column in Figure 26 (Alexa Fluor 647, upper panel; Alexa Fluor 660, middle panel; and Alexa Fluor 750, bottom panel) compare the excited state population changes of dye conjugated with BSA and with reaction centers. Excitation in these studies was at 600 nm (monitored at 670 nm), 600 nm (monitored at 698 nm) and 710 nm (monitored at 780 nm) for Alexa Fluor 647, Alexa Fluor 660 and Alexa Fluor 750, respectively. As one would expect for efficient energy transfer, the fluorescence decay lifetimes are much shorter when the dye molecules are attached to the reaction center proteins. Fitting of the fluorescence decay to a sum of exponential decay terms for the BSA-Alexa Fluor 660 conjugate results in three exponential components with lifetimes (amplitudes) of 0.10 ns (13.2%), 0.81 ns (25.5%) and 1.81 ns (61.3%). The average lifetime is 1.33 ns (calculated from the integral under the curve divided by the initial amplitude). The decay lifetimes (amplitudes) resulting from a similar fit of the time-resolved fluorescence from the reaction center-Alexa Fluor 660 conjugate are 0.04 ns (67.9%), 0.31 ns (16.1%) and 1.46 ns (16%) with an average

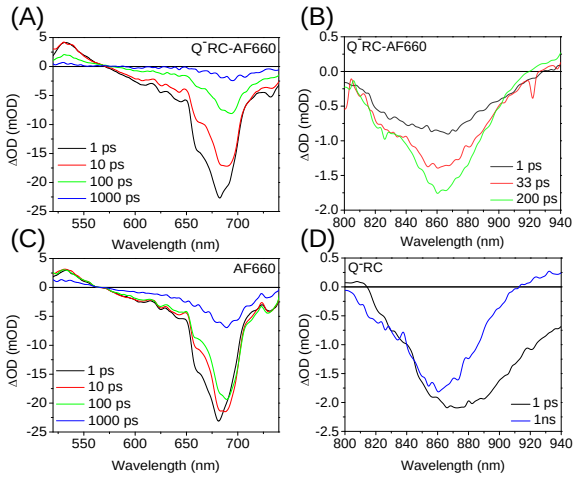


Figure 27. Time-resolved spectra. (a) reaction centers conjugated with Alexa Fluor 660 near the dye absorbance peak. (b) same as (A) except in the spectral region near the maximal ground state absorbance of the reaction center cofactor P. (c) Alexa Fluor 660 in solution and (d) unconjugated reaction centers.

lifetime of 0.31 ns. The presence of large contributions from a short lifetime component (0.04 ns) signifies a very efficient energy transfer from the dye to the reaction center cofactors. The integral over the decay kinetics indicates a 55% energy transfer efficiency compared to that of the BSA-Alexa Fluor 660 conjugate. Similar to the BSA-Alexa Fluor 660 conjugate, fitting the fluorescence from Alexa Fluor 750 conjugated BSA results in lifetimes (amplitudes) of 0.12 ns (11.7%), 0.73 ns (76.0%) and 1.63 ns (12.3%), with an average lifetime of 0.77 ns. The lifetimes (amplitudes) for reaction center-Alexa Fluor 750 conjugates are 0.06 ns (40.0%), 0.38 ns (34.6%) and 0.85 ns (25.4%) with an average of 0.37 ns, corresponding to a 33% energy transfer efficiency compared to the decay integral of BSA-AlexaFluor 750. The lifetimes for BSA-Alexa Fluor 647 fluorescence decay profile are 0.05 ns (30.8%), 0.64 ns (19.8 %) and 1.73 ns (49.4%) with an average lifetime of 0.99 ns. The lifetimes for reaction center-Alexa Fluor 647 are 0.07 ns (62.9%), 0.46 ns (16.2%) and 1.61 ns (20.9%) with an average lifetime of 0.45 ns. The energy transfer efficiency calculated from the decay integrals is 44%. (Note that calculating the energy transfer efficiencies from the integrals of the time resolved fluorescence data has the advantage over steady-state measurements that normalization for concentration is not necessary; by normalizing at time zero, concentration differences are accounted for).

3. Observation of charge separation:

To directly observe the excitation energy transfer from the dye molecules to the reaction center cofactors and the subsequent charge separated state formation by the reaction center, ultrafast transient absorbance spectroscopy was used to study the reaction center-Alexa Fluor 660 conjugate sample. Bleaching of both the dyes ground state absorbance (650 – 750 nm), and the ground state absorbance of the reaction center initial electron donor, P, (800 – 940 nm peaking at 860 nm) were monitored. The transient absorption spectra were recorded over a large wavelength region at different time delays following excitation at 650 nm, where Alexa Fluor 660 represents more than 80% of the sample absorbance.

Figure 27 shows the absorbance change spectra recorded at various delay times following excitation. For the dye-conjugated reaction centers, the bleaching signal in the 650 – 750 nm region appeared instantaneously and then decreased as a function of delay time (Figure 27a), indicating the disappearance of the excited state population of Alexa Fluor 660. The bleaching signal of P in the 800 – 940 nm region (Figure 27b) increased with time as energy and then electron transfer occurred. For these measurements, the quinone molecules were removed from the reaction centers, and the charge separated state is $P^+H_A^-$, which lives for nanoseconds (longer than the measurement time used here). Figure 27c shows the transient absorption spectra of the signal from the unconjugated dye in solution recorded over the same time period as in (a). Unlike Figure 27a, the amplitude of the dye alone does not decay significantly during the initial 100 ps, presumably due to the lack of energy transfer acceptors. Figure 27d shows electron transfer in the reaction center upon direct excitation at 650 nm. The spectrum at 1 ns has the same profile as that obtained from the dye-conjugated reaction centers, consistent with formation of the charge separated state $P^+H_A^-$. However, the 1-ps spectrum is significantly different from the dye-conjugated reaction center. The large bleaching signal on the longer wavelength of the P band (near 900 nm) is due to the excited state of P (stimulated emission), resulting from the direct excitation of the reaction centers. The lack of P* in Figure 27b indicates that there is little direct excitation of P, but instead only a low steady state population produced via energy transfer from the dye. Energy transfer from Alexa Fluor 660 to P takes place in roughly tens of ps, while the

conversion of P* to P^+ takes only 3 ps. Thus, the P* population is small at all times. Detailed numbers are provided below based on fits to kinetic models.

4. Kinetic analysis of transient dye absorbance:

Figure 28a compares the kinetics of ground state bleaching of unconjugated dye and Alexa Fluor 660 dye conjugated to the reaction center. In agreement with the single photon counting measurements shown in Figure 26, the excited state lifetime of the dye molecules in the reaction center-Alexa Fluor 660 complex is much shorter that in solution, again supporting the conclusion that substantial energy transfer to the reaction center is taking place. A decay lifetime of 25-ps is resolved from the transient absorption spectral measurement that is not observed in the single photon counting data. This is due to the higher time resolution available in transient absorbance measurements compared to time correlated single photon counting (0.1 ps vs. 40 ps). An average lifetime of 328 ps and 611 ps for reaction center-Alexa Fluor 660 and Alexa Fluor 660 in solution, respectively, were determined based on the transient absorption measurement. BSA-Alexa Fluor 660 was measured with an average lifetime of 792 ps. Using excitation at 650 nm, where reaction center absorbs weakly, roughly a 2.5-fold increase in P^+ formation was observed in the reaction center-Alexa Fluor 660 conjugate compared to the reaction center alone at the same concentration (Figure 28b). This is roughly what one would expect given the increase in absorbance at 650 nm and the observed energy transfer efficiency. Figure 28c compares the dye decay kinetics of the dye ground state bleaching at 700 nm with P^+ formation kinetics at 870 nm in the reaction center-Alexa Fluor 660 conjugate. The normalized traces show a fast decay of the dye and a concomitant formation of the P^+ signal, indicative of energy transfer followed by electron transfer in the reaction center. In contrast, the kinetic trace from the reaction center alone exhibits instantaneous formation of the P bleaching signal due to the direct excitation of the reaction center when there is no Alexa Fluor 660 conjugated to the reaction center protein.

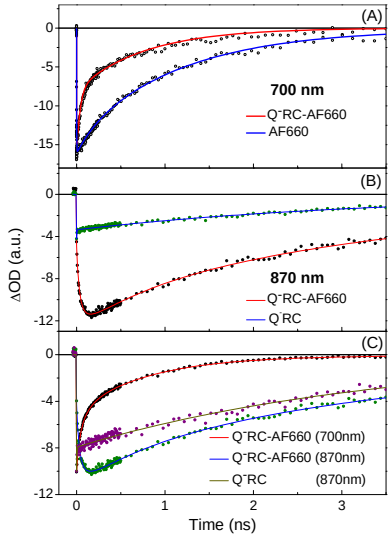


Figure 28. Transient absorbance kinetics of (a) Alexafluor 660 (AF660) in solution (blue) and the reaction center-Alexafluor 660 (RC-AF660) conjugate (red) , (b) P^*/P^+ signal in reaction centers alone (blue) and the reaction center-Alexafluor 660 conjugate (red), (c) normalized Alexafluor 660 (red) and P^+ in the reaction center-Alexafluor 660 conjugate (blue) and in the unconjujgated reaction center (purple). Excitation is at 650 nm.

The spectroscopic data provides compelling evidence of enhanced light-harvesting in the dye-conjugated photosynthetic reaction center (i.e., larger functional absorbance cross section for charge separation at wavelengths that the dye absorbs). In addition, the energy transfer efficiency in the reaction center-Alexa Fluor 750 complex was lower than that in the reaction center-Alexa Fluor 660 complex, primarily due to the shorter inherent excited state lifetime of the Alexa Fluor 750 dye (0.55 ns vs 1.1 ns), even though Alexa Fluor 750 has a better spectral overlap with the reaction center than does Alexa Fluor 660. This type of data begins to provide quantitative design guidelines for future work in the selection of light-harvesting dyes.

5. Future direction:

To illustrate the possibility of using DNA scaffolds for the construction of a multi-dye-reaction center complex, a simple 3-arm DNA-structured antenna system (Figure 23) is being constructed and conjugated to the reaction center. Three different 3-arm DNA structures have been created, one with both Alexa Fluor 660 and Alexa Fluor 750, and the other two containing only one dye, either Alexa Fluor 660 or Alexa Fluor 750. In initial experiments, a single stranded DNA is being conjugated to the reaction center and then two additional DNA strands are being hybridized to the conjugated strand. This aspect of the work is still in progress.

Predictive modeling of energy transfer efficiency

1. CanDo – a predictive modeling tool for the design of DNA origami:

We sought to perform computational modeling to understand the effect of position and dye linker flexibility on energy transfer efficiency for a model, 7-helix 3-dye system. We developed the first predictive computational modeling tool for the design of DNA origami (CanDo, Computer-aided engineering for DNA origami, http://cando.dna-origami.org). This software uses the finite element method to compute the actual 3-D shape of DNA origami. In the past year we extended this model to construct atomic structures of DNA nanoassemblies, including dye positions and orientations, based on ONR funding in related work. This model was further developed in the MURI project to model excitonic properties of the resulting dye-DNA assembly using a multi-FRET model. The model is capable of simulating the time-dependent photonic properties of DNA-dye assemblies consisting of up to 10,000 dye molecules, which may be used in the next research phase to design and evaluate large-scale DNA-based light harvesting antenna constructs.

2. Model validation:

To validate our model, we applied it to analyze the 7-helix bundle light-harvesting antenna previously published. Photon adsorption and exciton funneling from attached Pyrene (donors) to Cy3 (bridge), and to an AF647 (acceptor) ensure its light-harvesting capability. Following our modeling workflow, Figure 29a, from left to right, shows the structure of the 7-helix bundle DNA antenna (7HB) at equilibrium as obtained from CanDo output, the atomic structure of this antenna, as obtained by introducing atomic base pairs into the DNA, as well as the center positions and AV of dyes attached to the DNA.

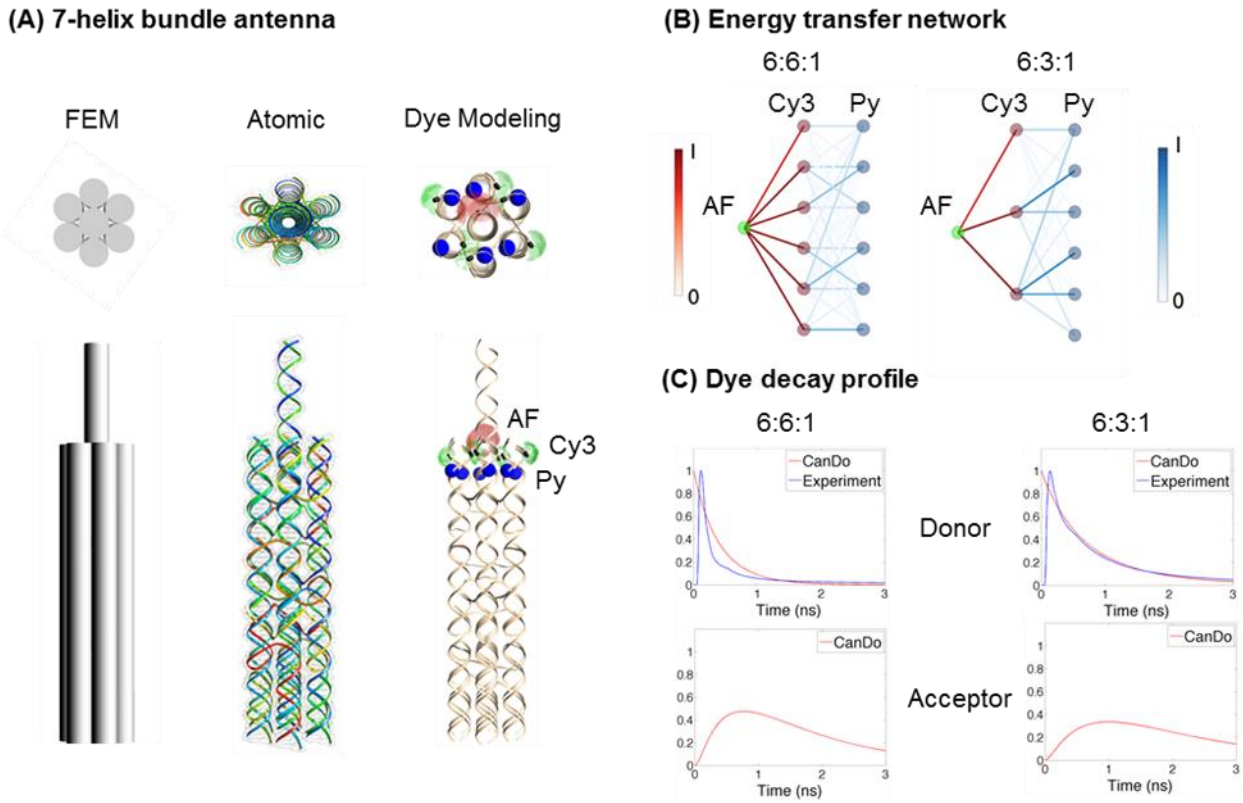


Figure 29. Validating the model CanDo to predict the excitonic properties of the dye-DNA nanostructure assemblies (a) The structure of the 7-helix bundle DNA antenna (7HB) at equilibrium as obtained from CanDo output, the atomic structure of this antenna as obtained by introducing atomic base pairs into the DNA, and the center positions and AV of dyes attached to the DNA, respectively. (b) Calculating the pair wise energy transfer networks for the two different settings (6:6:1 and 6:3:1). (c) Simulation results for the decay profile of donors (Py) and acceptor (AF) for each of the 6:6:1 and 6:3:1 compared to the published experimental data.

Previous work describes and compares different arrangements of the dyes on the 7HB, which lead to different energy absorption and funneling characteristics. A first configuration, labeled 6:6:1 is composed of 6 Py donors, 6 Cy3 bridge and 1 AF647 acceptor. A second, 6:3:1 configuration is also studied. From the time-resolved fluorescence measurement from Py, Dutta et al. deduce the antenna effect (A_{exp}) of each construct. Their results show a much higher antenna effect for the 6:6:1 construct (85%) compared to the 6:3:1 (43%), as reproduced by our model. This value represents the ratio of the fluorescence intensity when the acceptor AF dye is excited following the excitation of the Py donor dyes relative to the intensity when AF is directly excited. In particular, Dutta et al. excite selectively Py and AF647 using respectively a wavelength of 380 nm and 620nm. The antenna effects introduced by Dutta et al. is thus an empirical measure of the light-harvesting efficiency of the system, and is proportional to the energy transfer efficiency T, and to the ratio of the total molar extinction of the donors relative to the acceptors, at the specific wavelengths at which each measurement is taken. In particular, in our case:

$$A_{sim} = T \frac{N_D \Xi_{Py}^{380nm}}{\Xi_{AF647}^{620nm}}$$

where $N_D$is the number of Py molecules (per acceptor), Ξ_{Py}^{380nm} is the molar extinction of Py at 380nm, and Ξ_{AF647}^{620nm} is the molar extinction of AF647 at 620nm. Our simulation results, shown in Table 1, are in good agreement with the experimental values for the (6:6:1) configuration, although the efficiency is overestimated for the 6:3:1 construct (71% vs 43%).

Table 1 - 7 Helix Bundle Light Harvesting Antenna

Configuration (Py:Cy3:AF)	Antenna Effect (experimental)	Antenna Effect (simulation)	Efficient absorption cross-section (nm^2)	Transferred power under sunlight (fW)
6:6:1	0.85	2.38 (1.46)	1.22×10^{-2}	4.9×10^{-3}
6:3:1	0.43	2.06 (1.26)	1.05×10^{-2}	2.4×10^{-3}

Our modeling also allows calculating the pair wise energy transfer networks for the two different settings (6:6:1 and 6:3:1), as shown in Figure 29b. In the first configuration, the network shows both energy transfer pathways along the helix and across the helix from Py to Cy3. In the second, the network shows stronger energy transfer pathways from Py to Cy3 across the DNA helix than along the helix. Strong energy transfer pathways are always observed from Cy3 to AF in both settings. Our modeling framework hence satisfactorily captures with exciton transfer in the 7HB antenna. In addition, Figure 29c compares our simulation results for the decay profile of donors (Py) and acceptor (AF) for each of the 6:6:1 and 6:3:1 with the published experimental data. Results show a general agreement between the curves.

It is important to note that transfer efficiency alone cannot account for the performance of a light-harvesting system. For an irradiation wavelength that is only absorbed by the donors (Py), in addition to the antenna effect, the efficient cross-section is also a useful concept that can characterize the power transferred from the donors to the final acceptor. This cross-section is calculated in Table 1 for each of the construct.

3. Future direction:

In subsequent applications to the design of novel light-harvesting systems, such devices will typically be designed to absorb sunlight, which comprises photons of different energies at a specific ratio. To calculate the total power transferred to the final acceptor under this condition, the efficient cross-section must be calculated at every wavelength and be weighted by the spectral irradiance of the sun. Note that while at short wavelength only the Py is excited, at longer wavelength, initial excitation occurs in Py, Cy3, and even AF, with a ratio given by their relative cross-section at that specific wavelength. The power transferred to the AF acceptor under sunlight is reported in Table 1. In a complete light-harvesting system that would include a photosynthetic reaction center (RC) in addition to the antenna unit, that total transferred power should have to be matched to the transformation rate of the RC in order to yield the most efficient design.

Toward the production of materials to transfer bioelectroactive and photoelectrochemical pathways to external platforms

1. Fabrication of nanoporous transparent metal oxide (TCO) films:

Nanoporous materials are three-dimensional architectures with high internal surface areas that are ideal to house DNA origami nanostructures *if* they satisfy the stringent requirements for the proposed applications: they must be transparent so they do not obstruct irradiation of the (photo)electrochemically active nanostructures, possess relatively large pore sizes to accommodate various DNA nanostructures, be mechanically rigid, have good electrical conductivity, possess surfaces that can be easily functionalized by organic cross-linkers, and be inexpensive to manufacture in large quantities.

By extending an existing method that is based on formation of interpenetrating inorganic-polymer composite gel networks, we intended to produce macroporous TCOs using CuI nanoparticles as hard templates. Despite the initial successes we did not pursue this route as it was prohibitively difficult to produce uniformly sized CuI nanoparticles, and also because it required rather strict chemical conditions to maintain the chemical stability of CuI and would eventually limit the scope of the synthetic method. Subsequently, we discovered that self-assembled opal structures of poly(methyl methacrylate) (PMMA) beads[2] are robust templates that are compatible with our previously reported inorganic-polymer composite gel method. In parallel, we explored the use of nanoporous anodized alumina (AAO) membranes as templates, an alternative method that did not produce satisfactory results.

Figure 30 illustrates how the macroporous ATO has been synthesized on a conducting substrate such as indium tin oxide (ITO) or fluorine-doped tin oxide (FTO) glass. Highly monodispersed PMMA beads were first synthesized through emulsifier free emulsion polymerization in a four-necked round-bottom flask equipped with an electric stirrer with a Teflon stir blade, a water condenser, a pipet connected to a source of nitrogen, and a thermocouple probe. Sphere sizes of approximately 200 nm were adjusted by controlling the stirring rate, monomer concentration, reaction temperature, and amount of initiator.

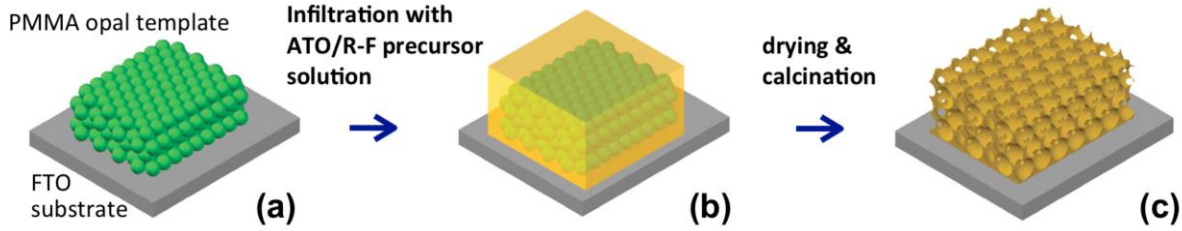


Figure 30. Scheme for fabrication of macroporous ATO films on FTO glass. (a) Layers of the PMMA beads are stacked onto an FTO substrate through a gravitational sedimentation method to form opal structures. (b) An ethanol/water solution of $SbCl_3$, $SnCl_4 \cdot 5H_2O$, resorcinol and formaldehyde precursors are poured into the PMMA template and subjected to an inorganic-polymer composite gel formation process. (c) The materials are dried and calcined at 500 °C to burn off all the organic materials and the PMMA opal template to obtain a macaroporous ATO film with an inverse opal structure.

Layers of the PMMA beads were then stacked onto an FTO substrate through a gravitational sedimentation method to form opal structures (Figure 30a). An ethanol/water solution of $SbCl_3$, $SnCl_4 \cdot 5H_2O$, resorcinol and formaldehyde precursors were poured into the PMMA template and subjected to an inorganic-polymer composite gel formation process (Figure

30b). To obtain a macroporous ATO film with an inverse opal structure, the material was then dried and calcined at 500 °C to burn off all the organic materials, as well as the PMMA opal template (Figure 30c). A scanning electron microscopy (SEM) image of the surface of the films (Figure 31) shows a nanostructure with ordered pores of ~200 nm diameter (where the PMMA spheres were originally located). Importantly, the macropores are well connected with large windows between them to facilitate ample diffusion of the DNA nanostructures during the incorporation phase. Further work is in progress to optimize the synthetic conditions to achieve greater homogeneity in the films.

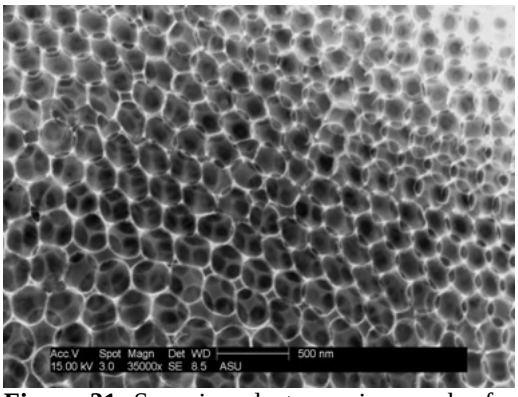


Figure 31. Scanning electron micrograph of a macroporous ATO film. Scale bar = 500 nm.

2. Fabrication of thionated reduced graphene oxides and their films:

Reduced graphene oxides are emerging as electrically conducting nanomaterials that are promising for transparent displays and other optoelectronic devices. Recent work has suggested that chemically modified graphene is an excellent substrate material for adsorption and spatial patterning of DNA origami structures. We devised two different chemical methods that can produce reduced graphene oxides with thiol functional groups directly attached to the graphene sheet (called "reduced graphene oxysulfide (RGOS)"; Figure 32). Typical C:O:S ratios are ~20:1:1, and more than 90% of the sulfur atoms exist as thiols that can participate in disulfide bond formation (based on the Ellman essay). Those thiol functional groups can be linked to DNA nanostructures through disulfide bond formation or thiol-ene(yne) click chemistry. Meanwhile, the oxygen functional groups on the sheets are mainly hydroxyl groups which can be used in crosslinking with metal oxide surfaces.

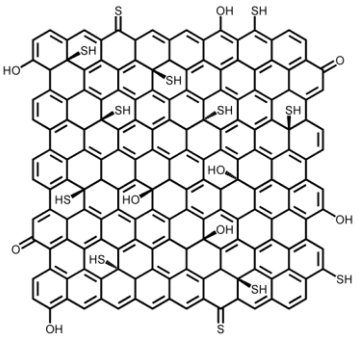


Figure 32. Schematic diagram of reduced graphene oxysulfide (RGOS).

Figure 33 shows a schematic diagram of DNA nanostructures crosslinked to an ITO substrate through RGOS sheets, using the thiols and hydroxyl groups as the sites of crosslinking. This architecture is somewhat similar to a previously developed 2D gold electrode surface. In fact, the optical transparency of the system in Figure 33 makes it uniquely positioned to serve as a link between a 2D gold electrode system and the 3D nanoporous TCO electrode system.

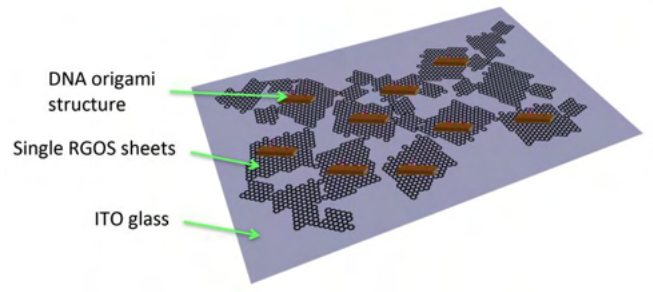


Figure 33. DNA nanostructures on a transparent conducting ITO substrate anchored through single RGOS sheets.

The thin film preparation procedure is schematically presented in Figure 34. An RGOS dispersion in an

ethanol/DMF solvent mixture was added drop wise onto the surface of water in a petri dish (Figure 34a). RGOS sheets gather at the air-water interface, and an RGOS Langmuir film was visible after adding several drops of the dispersion (Figure 34b). The film was collected from the substrate by scooping and dried in air to give an RGOS Langmuir-Blodgett (LB) film on the substrate (Figure 34c). Figures 35a and 35b show the UV-Vis spectra of the RGOS LB films on glass and an AFM image of a thick RGOS LB film on mica, respectively. The RGOS LB films on glass exhibit optical transmittance values of 92 and 81% at 550 nm, which correspond to 4 and 8 layers of the graphene sheets on average, respectively. However, the AFM image indicates that the graphene sheets are severely winkled or folded when the films are thick. Current efforts are geared to produce thinner films by optimizing the concentration and volume of the RGOS dispersions, as well as the average size of the RGOS sheets. Preliminary results indicate that RGOS sheets no larger than ~1μm show a much lower degree of folding and agglomeration.

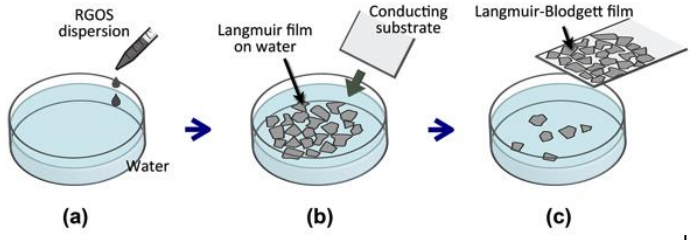


Figure 34. Scheme for fabrication of RGOS thin films on a 2D flat substrate. The size of the RGOS sheets (<1 ~ 500 μm) is exaggerated in the figure for clarity. (a) An ethanol/DMF solvent mixture is added drop wise onto the surface of water in a petri dish. (b) RGOS sheets gather at the air-water interface, and an RGOS Langmuir film is visible after adding several drops of the dispersion (c) The film is collected from the substrate by scooping and dried in air to give an RGOS Langmuir-Blodgett (LB) film.

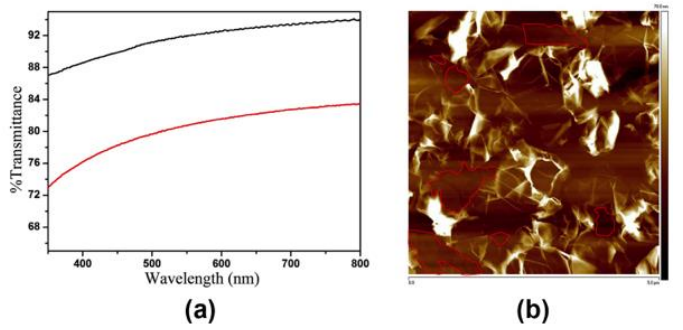


Figure 35. (a) UV-Vis spectra of two RGOS LB films on glass and (b) AFM image (5×5 μm^2) of a thick RGOS film on mica (height range = 0 – 70 nm). The areas circled in red are single sheets of RGOS.

3. Future Direction:

Despite the initial success in fabricating macroporous ATO coatings, the coatings are still not adequate as they sometimes peel away from the FTO substrate. One reason could be that the ATO surface is not nanoscopically flat, but corrugated with 100 – 500 nm-sized FTO crystalline grains. This will not allow a good contact between the substrate surface and the PMMA beads, especially if the latter is highly packed. The problem may be mitigated by employing ITO substrates instead of FTO, as they exhibit much smoother surfaces. As alternatives, we will explore the synthesis of other macroporous metal oxides using spinodal decomposition or ice templating. The former appears to be particularly compatible with our synthetic method, although it may not provide ordered pores. The latter can provide highly oriented sheet-like pore structures with a higher porosity. Regarding the subproject on RGOS, we will continue to refine our procedure to produce more uniform RGOS LB films, while working on crosslinking DNA origami structures on the deposited RGOS films.

Translating Biochemical Pathways to Non-Cellular Environments

Principal Investigator: Hao Yan[1]
Co-PIs: Don Seo[1], Neal Woodbury[1], Mark Bathe[2], William Shih[3], Nils Walter[4]
[1]Arizona State University, [2]MIT, [3]Harvard University, [4]U of Michigan

Reporting period: 8/01/13-7/31/14

I. Scientific and Technical Objectives

We intend to engineer and optimize nanoscale devices and systems based on important biochemical conversion pathways, where the converted species are molecules (enzymes transforming substrates into products), or energy, as is the case for photosynthesis. The use of DNA-directed assembly allows us to control and exploit the interactions between synthetic and naturally occurring bio-materials to produce highly functional biochemical conversion systems. Regarding enzyme transformations, our primary goal is to construct artificial enzyme cascades using two- and three-dimensional DNA structures as templates, and to study the ideal number of enzymes, relative distance, spatial arrangement, diffusion behavior, and reaction kinetics of the cascades in a controlled, non-cellular environment. Towards this goal, we initially focused on a representative DNA-templated GOx/HRP enzyme cascade. We will apply the results of the initial study toward the design of more complex, bioelectroactive, NAD dependent dehydrogenase pathways, with the ultimate goal of interfacing our systems with external conductive materials. We aimed to achieve the following objectives during this reporting period: (1) understand the factors influencing site-specific, hybridization dependent immobilization of enzymes and cofactors on addressable DNA nanostructures, (2) systematically evaluate DNA-scaffolded enzyme activity in various conditions (3) investigate the mechanism of local diffusive transport of a "swinging" single stranded DNA arm functionalized with an enzyme cofactor, (4) investigate the conformational changes that occur in a DNA tweezer structure used for modulating enzyme activity, at the single-molecule and bulk levels, (5) characterize the yield of enzyme encapsulation and retention in 3-dimensional DNA nanocages, (6) engineer the formation of liposomes on the outside of our DNA structures to limit substrate/intermediate's escape. Our findings will ultimately be used to enhance local diffusion behavior, reaction kinetics, and the optical and electrical properties within the proposed devices, behavior that can be extended to other systems of interest to the DoD.

Regarding photosynthesis, our aim is to develop methods for translating energy conversion pathways to non-cellular environments where their functions can be more easily manipulated. The approach is to use rationally designed DNA nano-scaffolds to engineer light-harvesting networks containing synthetic pigments, interfaced with energy conversion proteins (photosynthetic reaction centers) from natural photosynthetic organisms. We intend to precisely position functional elements on the DNA scaffolds, generating energy and electron transfer pathways in which inter-molecular interactions can be predictably designed, and the local environment can be controlled. We hope to engineer systems with more uniform light absorption, efficient energy transfer and conversion, and improved photo-stability for maximum performance. Here, artificial light harvesting pigments and the photosynthetic reaction center protein of purple non-sulfur bacteria are being co-assembled on a DNA nanostructure. The ideal

number of light-harvesting molecules, relative distance, spatial arrangement, and their spectral properties were varied to optimize the performance of the system. We are also comparing the experimental outcomes with the results of computational modeling in an effort to predict and improve upon the behavior of our model system. Due to the prospect of using sun light as an energy source for bio-electroactive and photo-electrochemical bio-pathways, ideal materials that are transparent and electrically conducting, either fabricated as a film or coated on an electrode, are also being developed. Toward this end, two different types of materials were utilized: nanoporous transparent metal oxides and functionalized reduced graphene oxides. In line with DoD goals, the proposed research will increase our understanding of nanoscale energy transfer processes and aid in the development of robust strategies for the synthesis, characterization, and assembly of synthetic biochemical pathways for application in high-efficiency photo-energy generation, energy storage devices, sensors, or completely new capabilities that enhance war fighter and battle system capabilities.

II. Concise Accomplishments

Enzyme Pathway – We have: (a) developed reliable methods for specifically conjugating DNA oligos to the N- or C- terminus of several target dehydrogenases and purifying DNA conjugated proteins with optimal ratios of the components and activity, (b) engineered an artificial multi-enzyme complex to facilitate highly efficient substrate transfer and regulate the direction of enzyme reactions, and (c) developed a bioelectroactive methanol dehydrogenase pathway organized by DNA nanostructure.

Photosynthetic Pathway – We have (a) constructed a 3-arm DNA complex with two spectrally distinct dye molecules attached to illustrate a step-wise multi-fluoropher light-harvesting capability (2 different pairs of dyes were tested to demonstrate spectral tunability), (b) conjugated the DNA-dye complex to the reaction center protein to extend the light-harvesting capability of the system, (c) characterized the enhancement of the light-harvesting function of the DNA-dye-RC nanostructure assembly using the previously developed spectroscopic protocols from year-1, (d) achieved high (up to 70%) yield of energy transfer between the two dye molecules specifically arranged in the DNA structure that attached to the reaction center protein, and demonstrated that upon energy transfer to the reaction center, charge separation occurs that is enhanced by an amount corresponding to the increase in overall energy transfer efficiency, (e) designed a 2D DNA array (4x4 tile array) for programmable geometric arrangement of multiple dyes and reaction center proteins at specific places based on model calculations of light-harvesting and photonic properties (by Bathe's group), (f) constructed the 2D DNA array a assembled 1 – 3 reaction center proteins at the desired locations on, resulting in optimized protocols for assembly of membrane proteins on DNA nanostructures, (g) designed and constructed mutant light-harvesting proteins from purple nonsulfur bacteria (LH1) as part of a LH1-RC system that include an appended zine finger that binds to a specific sequence in the DNA structure for facile assembly, (h) attached the LH1-RC complexes to a DNA tile and developed a protocol to optimize the conjugation and purification of the assembly, (i) characterized the fluorescence decay kinetics from individual LH1-RC complexes conjugated with DNA.

III. Expanded Accomplishments

Enzyme Pathway

Site-specific bio-conjugation strategies for coupling DNA to protein enzymes

1. Gene cloning into Halo-tag vectors:

Protein sequences of Alcohol dehydrogenase (ADH), Formaldehyde dehydrogenase (FALDH) and Formate dehydrogenase (FDH) were obtained from GenBank with the accession numbers CAA80989, P46154 and P33160 respectively. DNA sequences encoding for these three proteins

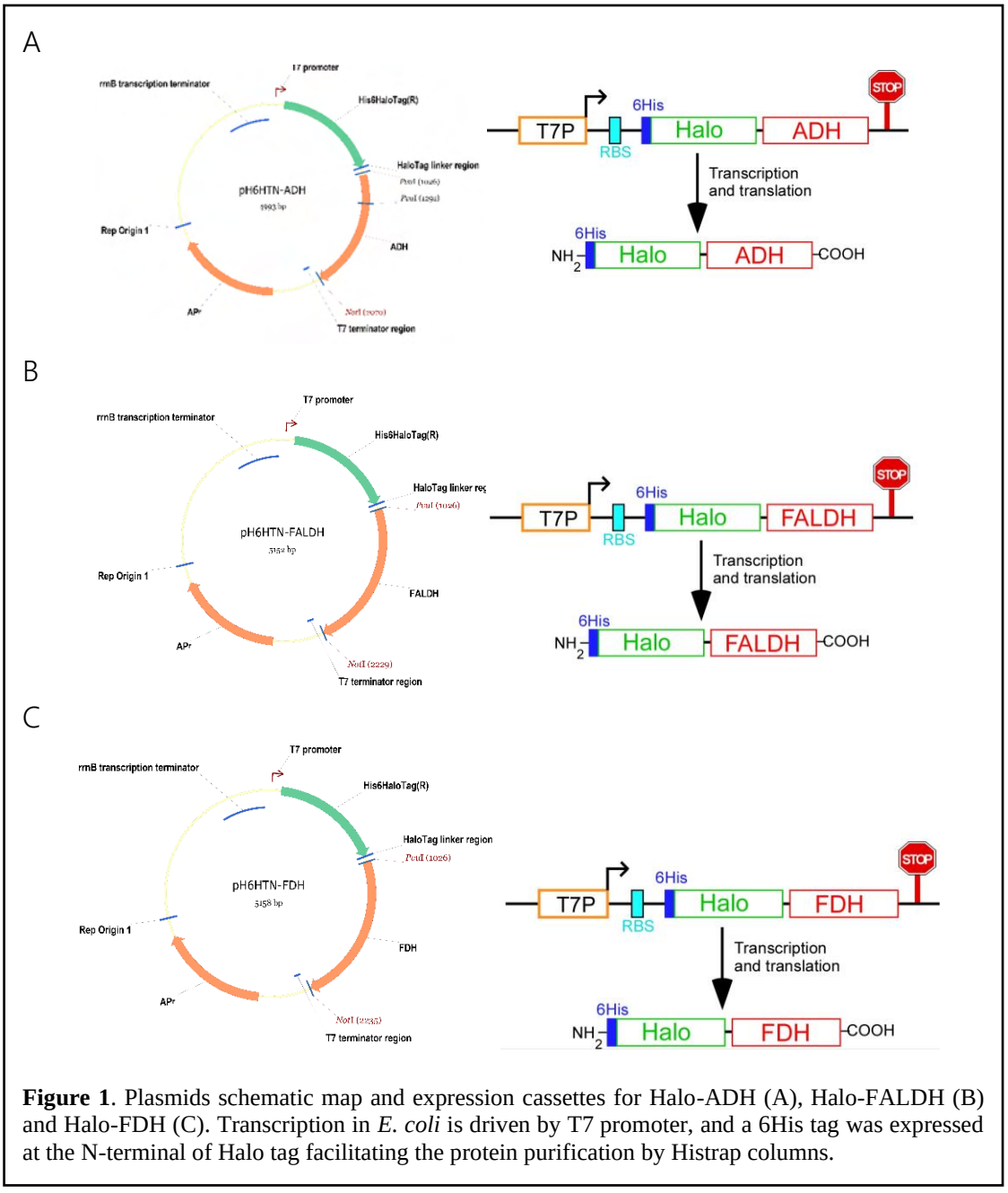


Figure 1. Plasmids schematic map and expression cassettes for Halo-ADH (A), Halo-FALDH (B) and Halo-FDH (C). Transcription in *E. coli* is driven by T7 promoter, and a 6His tag was expressed at the N-terminal of Halo tag facilitating the protein purification by Histrap columns.

were purchased from Genscript with codons optimized for E. coli expression. ADH, FALDH and FDH genes were digested with the restriction enzymes PvuI and NotI (New England Biolabs) and cloned into pH6HTN vector (Promega) digested by the same enzymes. Ligation reactions were performed by mixing the digested gene and vector with a 3:1 molar ratio in 1X ligation buffer and 1U T4 DNA ligase (New England Biolabs) at room temperature for 2 hours. Ligation products were transformed into the NEB 5-alpha competent cells (New England Biolabs) and the correct clones were confirmed by DNA sequencing. The pH6HTN vector and gene plasmids maps were shown in Figure 1.

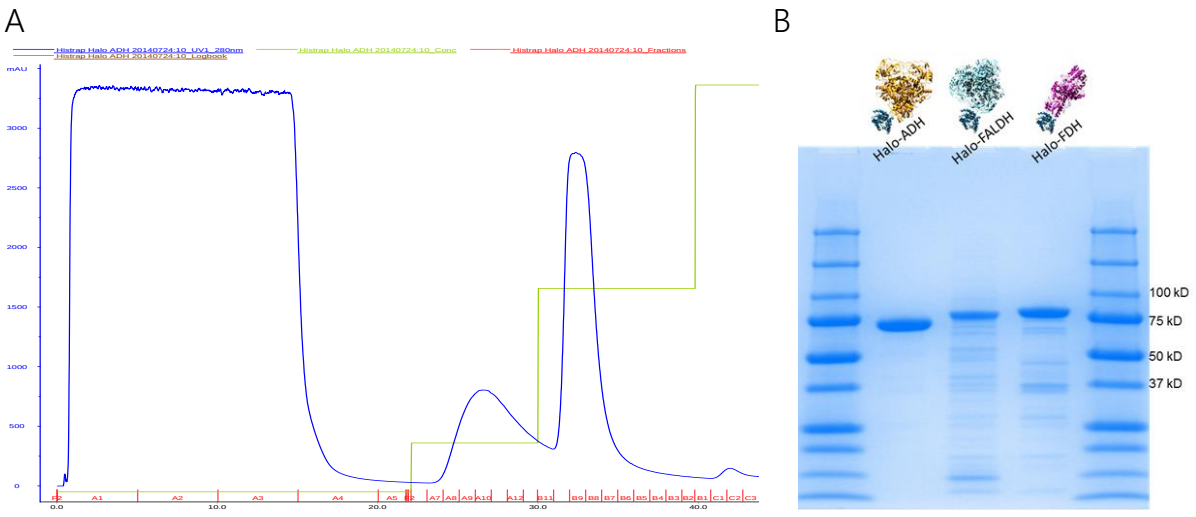


Figure 2. Halo tag enzymes purification. (**A**) Halo-ADH Histrap HP FPLC chromatography. (**B**) SDS-PAGE of three enzymes after Histrap purification. The theoretical molecular weight of these three enzymes are 73 kDa, 78 kDa and 80 kDa respectively.

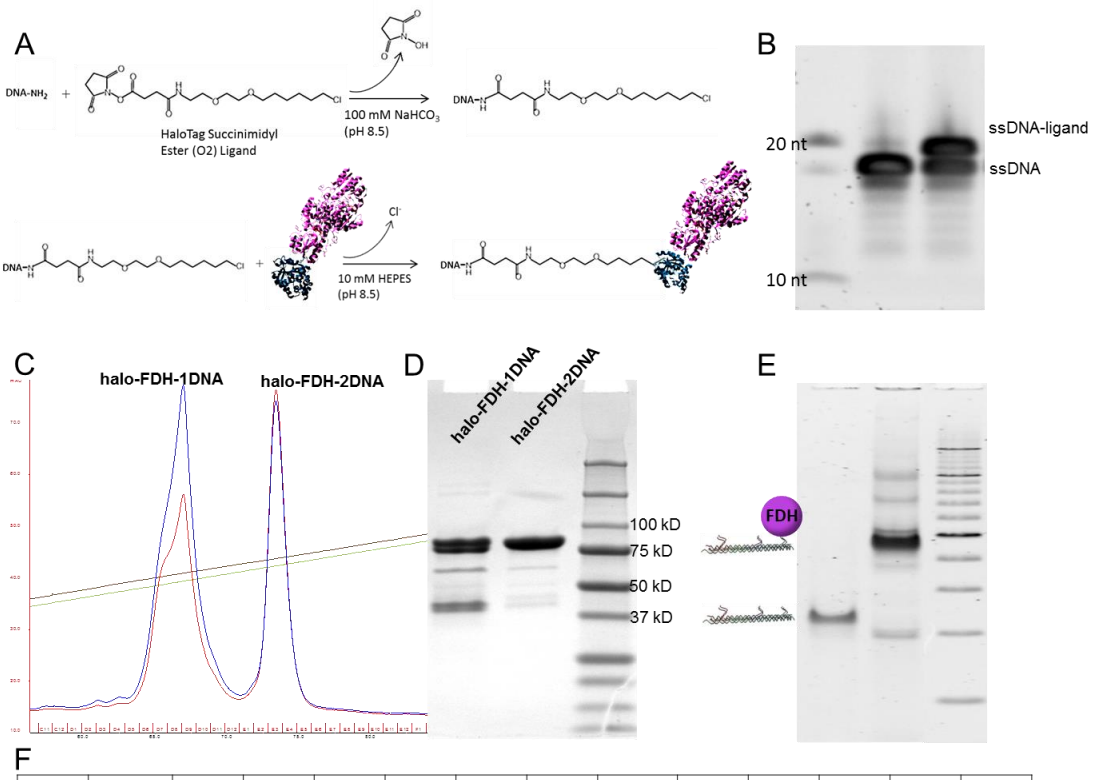
2. <u>Halo-tagged enzyme expression and purification:</u>

Plasmids pH6HTN-ADH, pH6HTN-FALDH and pH6HTN-FDH were transformed into E. coli NEB T7 express LysY competent cells (New England Biolabs). A single colony was inoculated into 10 ml LB medium and grown at 37°C with constant shaking for overnight. The 10 ml overnight culture was then inoculated into 1 L LB medium and incubated in a 37°C shaking incubator. Isopropyl-β-D-thiogalactopyranoside (IPTG) was added to a final concentration of 0.5 mM after OD600 reached 0.6. E. coli cells were pelleted down 3 hours after IPTG induction by centrifugation at 7,000xg for 15 min. Cells were then resuspended in 20 ml of lysis buffer (20 mM Sodium Phosphate pH 7.5, 0.5 M NaCl, 20 mM imidazole and 0.3 mM TCEP supplemented with 1X Complete Protease Inhibitor Cocktails [Roche Diagnostics]) and lysed with sonication. The cell lysate was clarified by centrifugation at 20,000xg for 30 min at 4°C and the supernatant was filtered through a 0.22 µM membrane. The cell lysate containing 6XHis tagged Halo fusion proteins were loaded onto the Histrap HP chromatography (GE Healthcare) under the manufacturer's instructions (Figure 2A). The Histrap column was then washed with 10 ml buffer containing 70 mM imidazole in the lysis buffer and Halo tagged proteins were eluted with 10 ml 250 mM imidazole buffer. The purity of the three enzymes from the elution fractions were

verified by 4-15% Mini-PROTEAN TGX Stain-free SDS-PAGE gel (Figure 2B). Different fractions containing the desired proteins were pooled and subjected for the DNA conjugation.

3. Conjugating DNA to Halo-tagged proteins:

Previously, we developed SPDP (N-Succinimidyl 3-(2-pyridyldithio)-propionate) crosslinking chemistry for attaching oligonucleotides to Lysine residue on protein surface. Due to presence of multiple lysine residues on the surface of dehydrogenases, the reaction products are mixtures of unique conjugates with different number of DNAs attached. To isolate enzymes modified with different numbers of DNA oligonucleotides, we developed purification method using anionic-exchange chromatography by AKTA fast-protein liquid chromatography (FPLC, GE Healthcare). It is important to be noted here after FPLC purification we got conjugates with the same average



F

DNA	A260/A280	ε^{260} (M^{-1} cm^{-1})	ε^{280} (M^{-1} cm^{-1})	Protein	A260/A280	ε^{260} (M^{-1} cm^{-1})	ε^{280} (M^{-1} cm^{-1})	Conjugates	A260/A280	A260	A280	DNA - to-Protein Ratio	Protein Conc. (uM)
WN2	1.60	130100	81313	**halo-FDH**	0.63	147609	234300	**wildtype**	0.63	7.938	12.60	0.00	53.78
WN2	1.60	130100	81313	**halo-FDH**	0.63	147609	234300	**labeled with 2DNA**	0.97	3.8412	3.96	1.56	10.98

Figure 3. Site-specific Halo-tagged protein-DNA conjugation. (A) A schematic illustration of the conjugation process; (B) 14% denaturing gel of unmodified single-stranded DNA (ssDNA, lane 1) and ssDNA-ligand conjugates (lane 2), yield is estimated to be ~50% from band intensity; (C) Anion-exchange FPLC purification of Halo-Formate dehydrogenase (FDH)-DNA conjugates. Condition: buffer A, 50 mM sodium phosphate (pH7.5); buffer B, 50 mM sodium phosphate, 1 M NaCl (pH 7.5). (D) SDS PAGE of 1 DNA labeled Halo-FDH and 2 DNA labeled Halo-FDH; (E) 3% Native PAGE characterization of DNA tile-protein assembly. Lane 1: DNA tile, lane 2: tile assembled with with purified Halo-FDH labeled with 2 DNAs; (F) Quantification of a purified DNA-conjugated Halo-FDH: an A260/A80 ratio of 1.6 corresponds to ~ 1.6 DNA per protein, with a DNA-conjugated protein concentration of ~ 11 µM.

number of DNAs per protein, but the site of DNA labeling may vary. It was not a site-specific conjugation method.

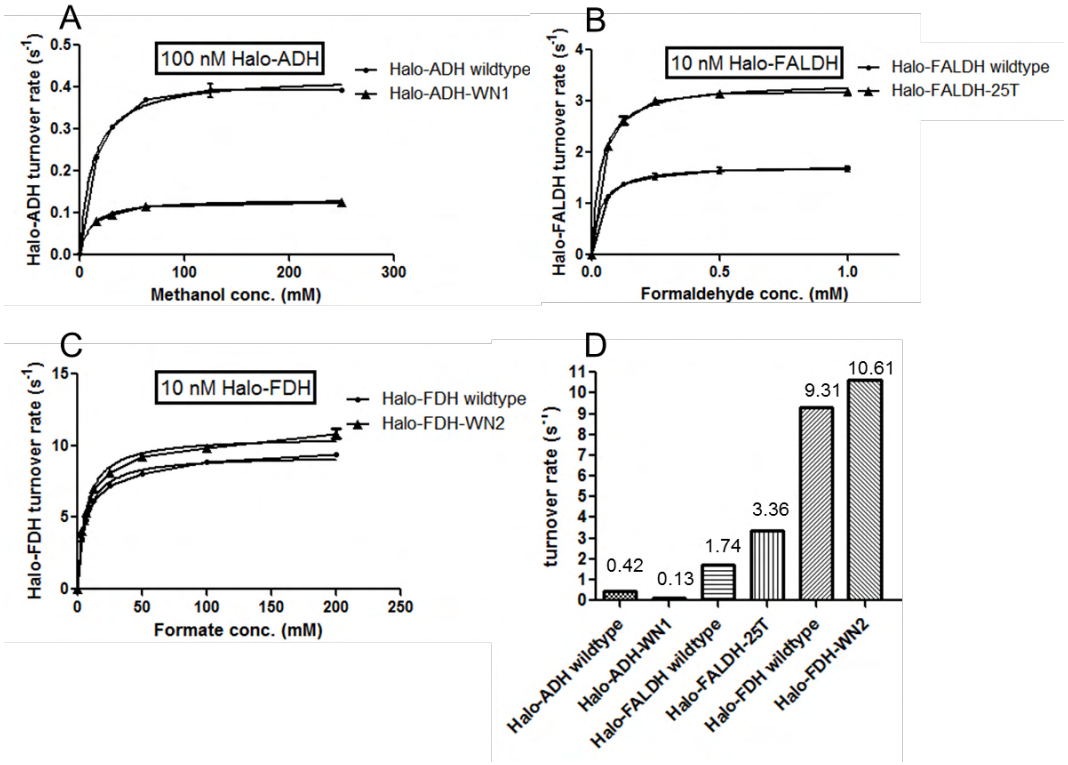


Figure 4. Michaelis-Menten plot of halotagged protein-DNA conjugates of alcohol dehydrogenase (ADH), Formaldehyde dehydrogenase (FALDH) and formate dehydrogenase (FDH). (A) Halo-ADH-DNA conjugates activity compared with wildtype Halo-ADH with respect to methanol; (B) Halo-FALDH-DNA conjugates activity compared with wildtype Halo-FALDH with respect to formaldehyde; (C) Halo-FDH-DNA conjugates activity compared with wildtype Halo-FDH with respect to sodium formate; (D) turnover rates of all protein samples. Assay condition: 100 nM Halo-ADH-DNA conjugates with 15.6 - 250 mM of methanol and 1 mM NAD+ in 50 mM Sodium phosphate (pH 8.5); 10 nM Halo-FALDH-DNA with 0.0625 - 1 mM of formaldehyde and 1 mM NAD+ in 50 mM Sodium phosphate (pH 8.5); 10 nM Halo-FDH-DNA conjugates with 3.125 - 200 mM of sodium formate and 1 mM NAD+ in 50 mM Sodium phosphate (pH 8.5).

To achieve more accurate control over the orientation and decrease the activity lose after SPDP modification we developed a site-specific Halo-tagged protein-DNA conjugation method (Figure 3). First step, 100 µL of 10 mM HaloTag ® Succinimidyl Ester (O2) Ligand (purchased form Promega) was prepared in DMSO. 500 µL of 100 µM 5'amine-modified oligo was incubated with 20 fold excess Halo tag ligand in 100 mM NaHCO3 (pH 8.5) for 2h. After reaction, excess Halotag-ligand was removed by washing with Amicon, 3 kD cutoff filters. Halotag-ligand conjugated DNA was characterized by 14% denaturing gel as shown in Figure 1B. The reaction yield was estimated to be ~50% from the band intensity between ssDNA and ssDNA-ligand conjugates. Second step, 500 µL of 40 µM enzyme solution was incubated with DNA-ligand conjugates in 10 mM sodium HEPES (pH 8.5) at room temperature for one hour, allowing Halo tag ligand reacting with Halo-tagged protein forming a covalent linkage. For Halo-FDH-DNA

conjugation, a 2-fold excess of ssDNA-ligand was used, while Halo-ADH/ FALDH-DNA conjugation used a 2-fold excess of ssDNA-ligand.

To get enzyme modified with exact number of labeled oligonucleotides, the Halo-tagged protein-DNA conjugates obtained in the above procedures were then purified with anionic-exchange chromatography using ionic-exchanged FPLC as shown in Figure 3C (Same buffer and gradient as the purification method we used for SPDP conjugation). 2 peaks from the corresponding chromatogram were collected, including protein functionalized with 1 DNA and protein functionalized with 2 DNAs. The filtered protein-oligo solution was quantified by absorbance at 260 and 280 nm (Figure 3F). SDS PAGE (Figure 3D) showed single band of Halo-FDH-2DNA since both two monomers has DNA conjugated on Halo tag, while Halo-FDH labeled with 1 DNA showed 2 bands, the higher one corresponds to DNA conjugated monomer and the lower band corresponds to monomer without DNA conjugation. Assembly of protein on DNA for Halo-FDH-DNA were evaluated by 3% native PAGE (Figure 3E). Halo-FDH labeled with two DNA molecules gave the correct assembly of one protein per DNA structures with more than 80% yield.

4. Evaluating the enzymatic activity of Halo-tagged protein-DNA conjugates:

The activities of purified Halo-protein-DNA were evaluated and compared with the activities of wild type Halo-proteins, as shown in Figure 4. The activity of all dehydrogenases (ADH, FALDH and FDH) was evaluated by the rate of reduction of NAD^+ to NADH as monitored by the change in absorbance at 340 nm (NADH production). Assay condition: 100 nM Halo-ADH-DNA conjugates with 15.6 - 250 mM methanol and 1 mM NAD+ in 50 mM Sodium phosphate (pH 8.5); 10 nM Halo-FALDH-DNA with 0.0625 - 1 mM of formaldehyde and 1 mM NAD+ in 50 mM Sodium phosphate (pH 8.5); 10 nM Halo-FDH-DNA conjugates with 3.125 - 200 mM of sodium formate and 1 mM NAD+ in 50 mM Sodium phosphate (pH 8.5).

Michaelis-Menten plot is analyzed to for determine the k_{cat} and K_m value of wild type Halo-tagged proteins and Halo-protein-DNA conjugates. For all 3 dehydrogenases, K_m value remains the same comparing before and after DNA conjugation: Halo-ADH (11.9 mM) and Halo-ADH-DNA (10.5 mM); Halo-FALDH (32.6 μM) and Halo-FALDH-DNA (35.2 μM); Halo-FDH (6.1 mM) and Halo-FDH-DNA (6.0 mM), which indicated that DNA labeling using Halo tag method doesn't inhibit or increase the binding affinity of substrate and 2 dehydrogenases. However, k_{cat} varied differently with different proteins (Figure 4D). For Halo-ADH, after DNA conjugation, the activity only remained ~ 30% of wild type while Halo-FALDH-DNA doubled the activity of wild type Halo-FLADH and for FDH, DNA labeling didn't change the activity at all. The reason of different activity change with different proteins is unknown for now, comparing the activity of 3 proteins in cascades, FDH is 3 fold faster than FALDH, and both of them are more than 10 fold faster than ADH.

Single-Molecule Characterization and analysis of the integrity and behavior of DNA nanostructure complexes

1. Single-molecule characterization of biomimetic membrane-bound DNA barges:

Natural photosynthetic antenna systems undergo functionally relevant dynamic rearrangements within lipid membranes in response to environmental cues, such as changes in light intensity. To investigate the potential of DNA nanotechnology to mimic aspects of these systems, we constructed DNA "barges," cholesterol-labeled DNA origami platforms that are designed to dynamically associate with synthetic lipid bilayers. In work summarized in a 2014 *ACS Nano* publication (Figure 5), we used single-particle fluorescent tracking to demonstrate that the barges associate with synthetic lipid bilayers in a cholesterol-dependent fashion, and can be induced to dissociate by exposure to appropriate signals (i.e., DNA molecules of a particular sequence). We also showed that the barges can freely diffuse in two dimensions while associated with the bilayer, permitting them to

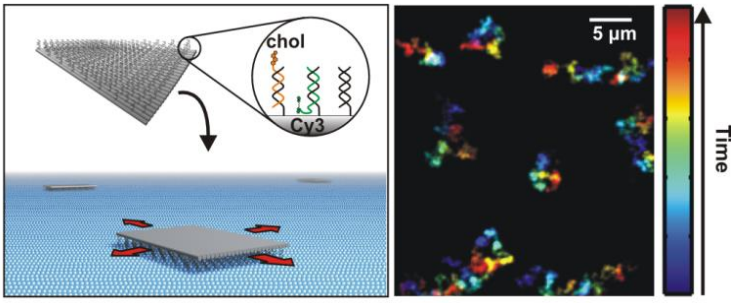


Figure 5. Rectangular DNA origami "barges" (left) are labeled with cholesterol to permit association with synthetic lipid bilayers. Fluorescent labels (Cy3) permit the monitoring of the two-dimensional movement of single DNA barges within synthetic lipid bilayers by fluorescence microscopy (right).

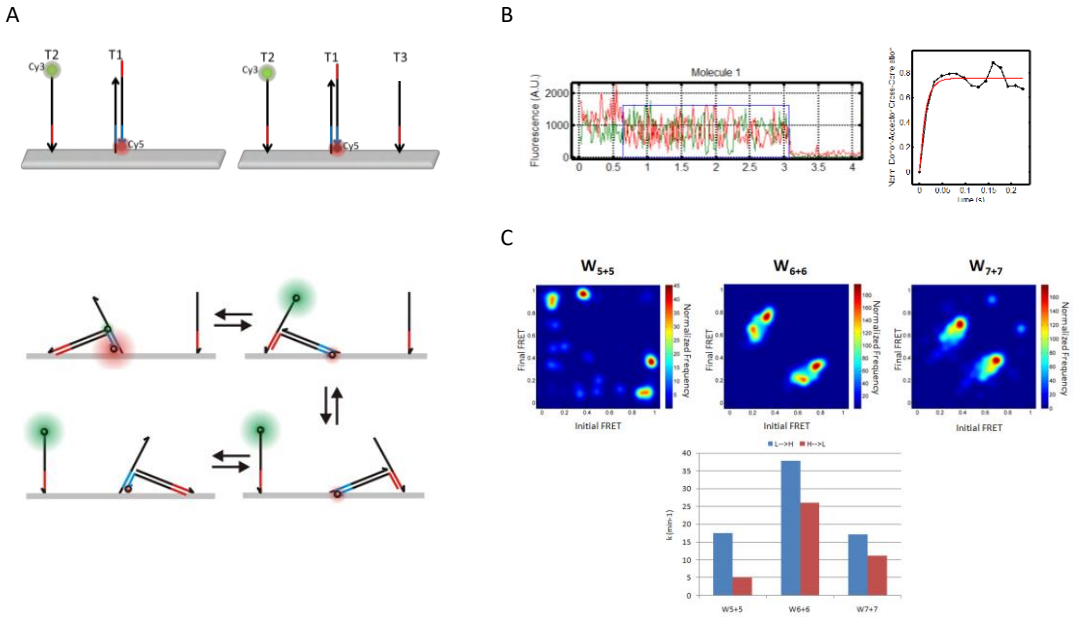


Figure 6. (A) Scheme for 2-track and 3-track walking systems (top panel) and mechanism of walking through toehold exchange (bottom panel). (B) smFRET characterization of 2-track walker for stepping dynamics. (C) Kinetics of stepping rates of 3-track walkers with different toehold lengths. The trend in stepping rate is not monotonic; the walker with 6-nt toeholds exhibits the most rapid stepping rate of the designs studied.

assemble into larger complexes upon addition of appropriate signal DNA molecules. This work lays a foundation for the development of new photosynthetic mimics that utilize dynamic environmental cues.

2. A DNA walker utilizing toehold exchange:

Several DNA walkers have been reported previously with translocation rates of ~1 nm/min, which is over 1,000 times slower than natural protein motors. In order to improve the walking speed for practical applications such as long-range enzyme substrate channeling, we designed a DNA walker system for rapid, directionless transport based on a toehold exchange mechanism. A single-stranded DNA (ssDNA) walker alternatively associates with adjacent ssDNA binding sites on the track to achieve fast movement (Figure 6A). By attaching fluorescent labels to both the ssDNA walker and one of the track binding sites, we could monitor the system's kinetic behavior by single-molecule fluorescence resonance energy transfer (smFRET). Both 2-track and 3-track systems were studied, and a few parameters, including the domain length, linker length and buffer were optimized to yield the most rapid stepping rate. smFRET measurements showed evidence of walking behavior on 2- and 3-track systems. The processed data also suggested that branch migration equilibrated on a timescale of less than 20 ms while the stepping took seconds, indicating that toehold binding and/or dissociation kinetics are the rate-limiting step. Among the parameters tested here, only the toehold length showed a significant influence on the stepping rate; in contrast, varying linker length from 3T to 6T or using Na+ instead of Mg2+ in the reaction buffer showed little influence. Of the designs we studied, the walker with a 6-nucleotide toehold exhibits the most rapid stepping rate of ~0.5-1 s-1, corresponding to an average speed of 210-420 nm/min, a ~100-fold improvement over previously reported walker designs. In the future, we will further refine the design by varying the inter-track spacing and branch migration domain length to realize a more efficient walker. We will also explore longer track geometries and alternative scaffolds as well as coupling the walker system with multi-enzyme pathway for further applications.

3. Step photobleaching analysis of enzyme encapsulation in DNA nanocages:

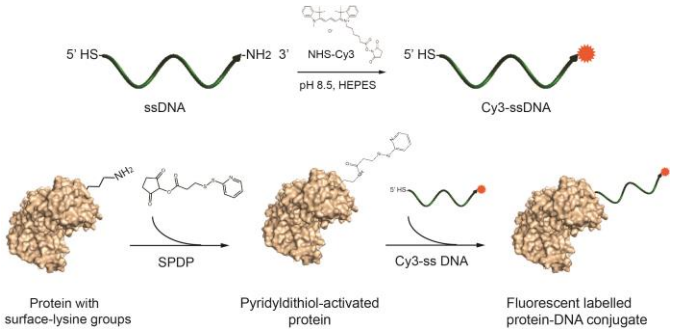


Figure 7. Fluorescent labelling of Protein-DNA conjugate. Top: A single-stranded DNA (ssDNA) with 5' thiol modification and 3'amine modification reacts with NHS-Cy3 to modify the fluorophore on the 3'end of the ssDNA. Bottom: The protein reacts with the Cy3-ssDNA via SPDP chemistry.

In order to characterize single-molecule enzyme activity, it is required to label the enzyme-DNA conjugate with fluorophores for imaging purpose. In Figure 7, a single-stranded DNA (ssDNA) with 5' thiol modification and 3'amine modification first reacts with NHS-Cy3 to modify the fluorophore on the 3'end of the ssDNA. Then, the Cy3-ssDNA is conjugated to the protein *via* previously developed SPDP chemistry. The Cy3-labelled protein-DNA conjugate is purified with ionic-exchange HPLC and the unmodified protein and fluorescently labelled protein-DNA are separated and collected.

Using fluorescence microscopy to measure step photobleaching of single fluorophores, we estimated the average number of enzymes associated with each DNA nanocage. This analysis

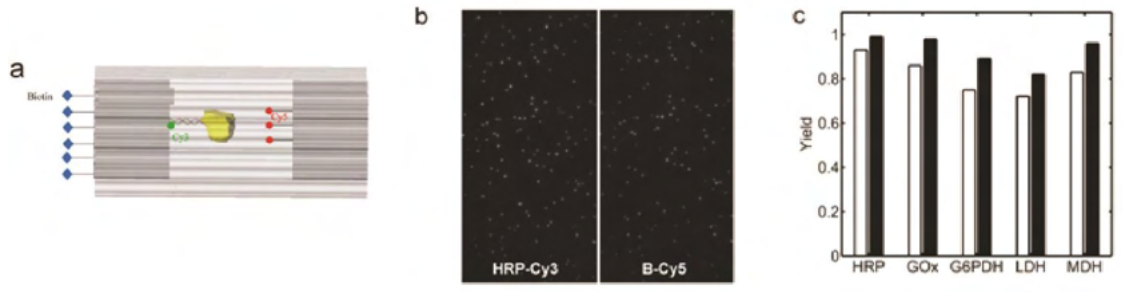


Figure 8. TIRF co-localization analysis of enzyme encapsulation inside the DNA cage assembly. (a) The DNA cage constructs were dual fluorescently labeled for characterization of the localization of enzymes inside the DNA cage by single molecule fluorescence imaging using TIRF. The DNA origami cage was labeled with Cy5 dye (inside the cavity), while the enzymes (HRP, GOx, G6pD, LDH and MDH) were covalently labeled with Cy3, individually. The DNA cage, encapsulating with enzyme was anchored on streptavidin coated glass through biotin modified on one of the half cage structure. (b) A representative field of view from the nanocage-encapsulated HRP sample. The left and right pictures showed the TIRF images of the same area in two channels (Cy3 channel for the left picture, and Cy5 channel for the right picture). Each of the bright spot represents one DNA cage structure. Co-localization of the two dyes was observed for most of the bright spots. (c) Yield of DNA cage assembly (white bars) and enzyme encapsulation (black bars) for the five enzymes studied. DNA cage assembly yield and DNA cage enzyme encapsulation yield were quantified using the following equations: $Y_{assembly} = \frac{Ncoloc}{NCy3}$, $Y_{encapsulation} = \frac{Ncoloc}{NCy5}$. ($N_{Cy3}$ = number of molecules with Cy3 > 150 counts; N_{Cy5} = number of molecules with Cy5 > 150 counts; N_{coloc} = number of molecules with both Cy3 and Cy5). For each measurement, >190 particles from 2-3 fields of view were used.

indicates that ~85% of occupied nanocages contain only 1 copy of glucose-6-phosphate dehydrogenase (G6pDH) enzyme, which will inform subsequent kinetic analyses of nanocage-encapsulated enzymes.

Fluorescence Correlation Spectroscopy Measurements on DNA Nanostructures

Fluorescence Correlation Spectroscopy (FCS) measurements on DNA nanostructures were used for the determination of their translational diffusion coefficient. New experiments were performed to improve both the performance of the measuring technique, as well as to deepen the level of detail of our knowledge on the physical properties of DNA nanostructures. The most relevant aspects investigated are the following:

- Alternative fluorescent dyes to the classical ones used for FCS
- Influence of cation concentration on the structure diffusivity properties
- Rotational Dynamics of the structures

1. <u>Alternative Fluorescent Dyes:</u>

Fluorescence Correlation Spectroscopy experiments on DNA nanostructure aimed at the determination of their translational diffusion coefficient, were performed by using tetramethylrhodamine (TMR) as a fluorescent dye. This dye was classically used for internal labeling of DNA for fluorescence studies. However, TMR, despite being a well-characterized dye, has several drawbacks such as low absorption cross-section, moderate hydrophobicity, and

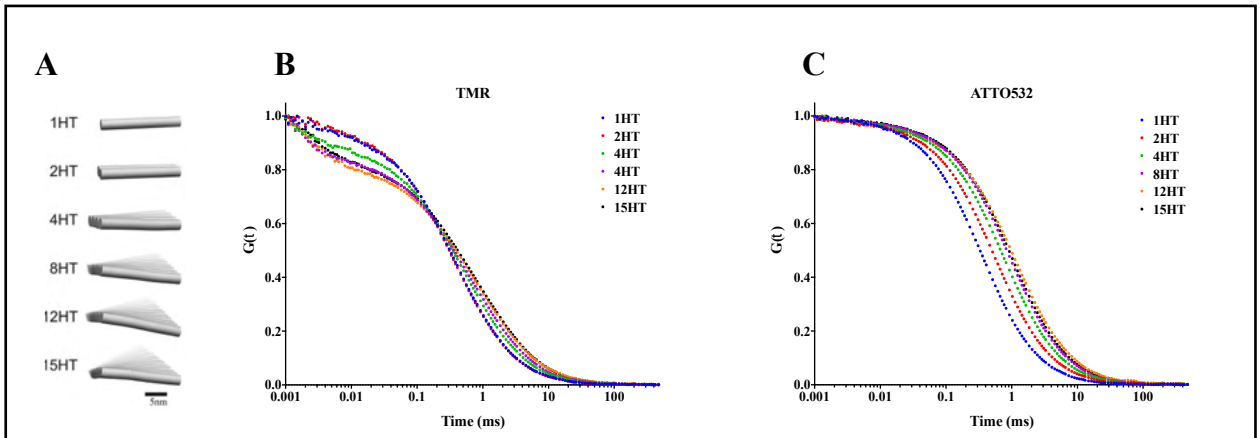


Figure 9. (A) DNA nanostructures selected for diffusivity studies. (B) FCS data obtained by labeling the DNA with the fluorescent label TMR. (C) FCS data obtained by incorporating ATTO532-labeled DNA oligos in the structures presented in panel A.

low photostability. New fluorescent dyes are now available that can overcome these issues and drastically improve the performance of the measurements, as well as ease the analysis and interpretation of the data.

As an alternative to TMR, the dye ATTO532 was used for FCS experiments aimed at the determination of the diffusion coefficient of selected DNA nanostructures, in particular the HT tiles structures depicted in Figure 9A. The dye shows brighter signal than TMR, no interactions with the DNA double helix, and allow easier data evaluation. FCS traces of DNA nanostructures recorded with TMR and ATTO532 are presented in Figure 9, panel B and C respectively. It is noticeable that with ATTO532 the shift in the diffusion decay is clearer with increasing size of the structures. This is due to the fact that at shorter time scale, below 0.1 ms, no other decay that interferes with the diffusion decay appears. This yields more reliable data and an easier fitting procedure. A comparison of the values obtained with the two different dyes is presented in **Table** 1.

Structure	**TMR**	**ATTO532**
1HT	30 (±4)	43 (±5)
2HT	28 (±3)	33 (±1)
4HT	20 (±2)	26 (±6)
8HT	16.5 (±0.2)	19 (±1)
12HT	13.4 (±0.6)	17 (±1)
15HT	13.3 (±0.2)	17 (±1)

Table 1: Translational diffusion coefficients of the HT tiles structures measured by FCS. The values obtained with the two different dyes described in the main text, TMR and ATTO532, are compared.

These studies provided a useful new tool for accurate data acquisition by means of FCS. Furthermore, together with improving the quality and interpretation of the data, the use of ATTO532 opened the possibility of using FCS to investigate larger nanostructures such as DNA

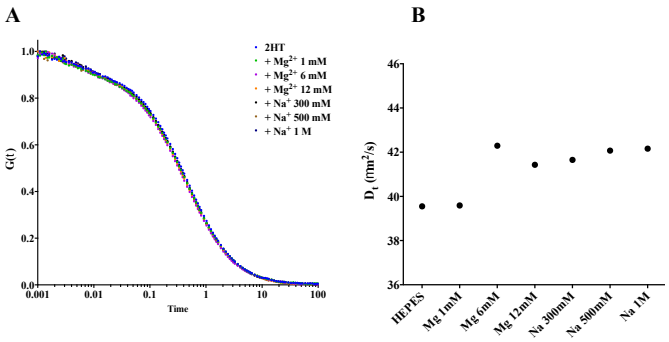


Figure 10. (A) FCS data of the structure 2HT recorded in different buffers containing an increasing amount of either mono or divalent cations. (B) Diffusion coefficient of 2HT obtained by fitting the FCS data presented in panel A.DNA oligos in the structures presented in panel A.

origami: TMR, in fact, revealed to be unsuitable for this task due to its properties. Investigations in this direction are in progress.

2. Cation Concentration Studies:

Mono- and divalent cations play an important role in the annealing of DNA nanostructures, as well as in maintaining their structure in solution. In the present work we show the use of FCS to observe the effect of cations on the physical properties of nanostructures in solution. By measuring the diffusion coefficient of the selected DNA tiles, it is possible to estimate their apparent hydrodynamic radius: this relates directly with how compact a structure is, and therefore would allow evaluating its structural properties in solution. In Figure 10A the FCS data obtained for the structure 2HT in different buffer conditions are presented. The structure diffusivity properties were measured either in a buffer solution with no salt, or in presence of Magnesium or Sodium ions at increasing concentration. The differences between the FCS traces are revealed by fitting the data: the diffusion coefficient of 2HT is extracted for each condition and plotted in Figure 10B. It is evident from these data that in presence of high concentration of mono- or divalent cations the structure diffuses faster than in a buffer solution with no salt. FCS can therefore be used to investigate the physical properties of DNA nanostructures in a variety of solution conditions for a more detailed insight on their structural properties.

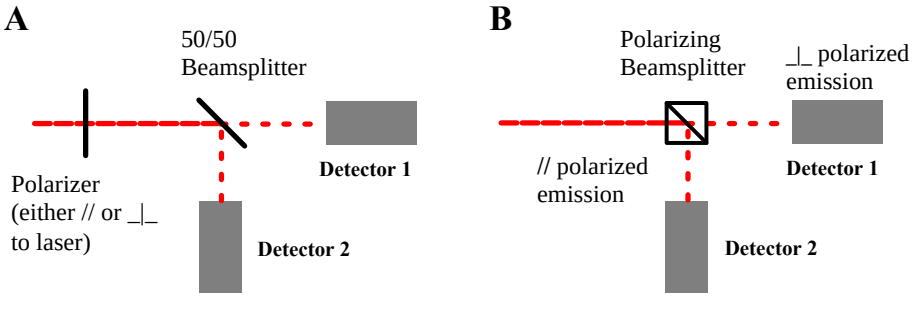


Figure 11. Panel A and B show the possible configurations of the detection path of the FCS measuring setup for polarized detection. The combinations of excitation and detection polarization are listed at the bottom of the figure: for each configuration is possible to record a separate FCS dataset that will be used for the analysis of the molecular rotation of the HT tiles.

3. Rotational Dynamics Measured by FCS:

Fluorescence Correlation Spectroscopy can be applied to study fast dynamics of molecules in solution otherwise not accessible by other techniques. Molecular rotation is one of these properties, and it is very interesting due to its intrinsic connection to the shape and dimensions of the object of interest. A simple modification of the FCS setup allows to measure the polarization of the fluorescent signal emitted by the sample (Figure 11). The decay of the polarization observed in the FCS traces can be transformed into a measure of the rotation rate of the molecule along its axes.

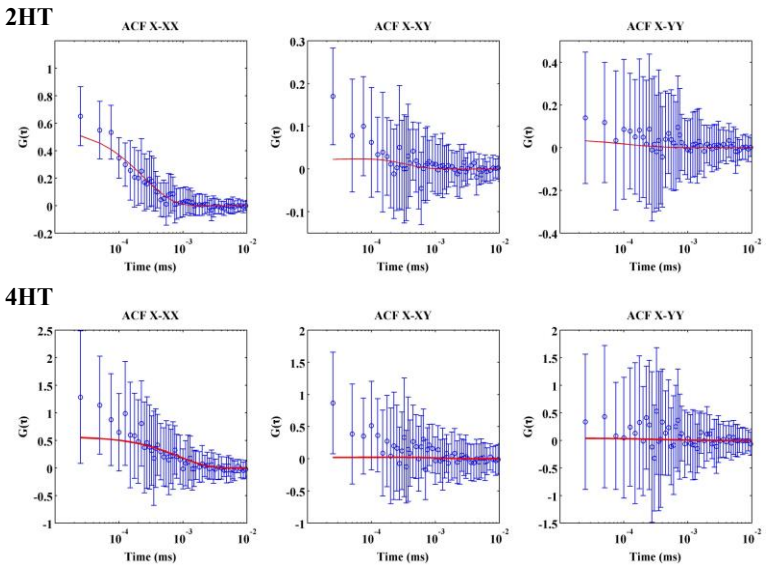


Figure 12. Examples of polarized FCS traces for some of the HT tiles structures. Top row: 2HT. Bottom row: 4HT. From left to right the panels show the data obtained with the excitation-detection scheme X-XX, X-XY, X-YY, respectively. The blue circles are the data, the error bars represent the standard deviation and the red line is the fit to a model for a totally anisotropic molecule.

The rotational diffusion coefficient of the HT tiles used in the present study was calculated based on the model developed by the Bathe's lab at MIT. FCS traces of each structure were then recorded with different polarization configurations. To analyze the data, a new theoretical approach was needed: the HT tiles are an example of totally anisotropic rotor that was not approached before by means of FCS measurements. The new theoretical approach was developed in collaboration with Prof. Joerg Enderlein, George-August University (Göttingen, Germany) and it allows to fit the rotational

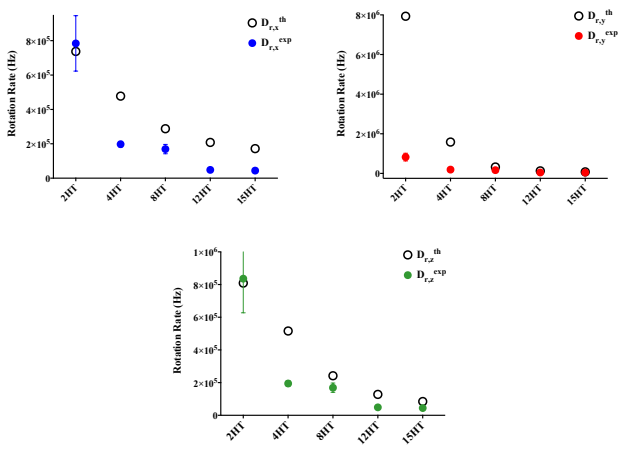


Figure 13. Rotation rates of the HT tiles structures obtained by polarized FCS measurements. On each plot are presented: the data from three replicates (full circles), the error bars representing the standard deviation, and the theoretical values based on the model developed by the Bathe's lab at MIT (empty circles). From the top left panel, moving clockwise, the plots show the rotation rate along the *x*, *y*, and *z* molecular axes, respectively

correlation data and extract the diffusion coefficient along each of the molecular axes of the structures.

An example of the data with the fit to the newly developed model is presented in Figure 12. In Figure 13, the experimental values of the rotation rates for each HT tile structure are compared against the calculated values based on the model developed in the Bathe's lab at MIT. These are preliminary data, and need further analysis and refinement. Nevertheless, similarities in the trends of the theoretical and experimental values are observed. Matches between values are also found: further experiments are in progress to validate the accuracy of the experimental data.

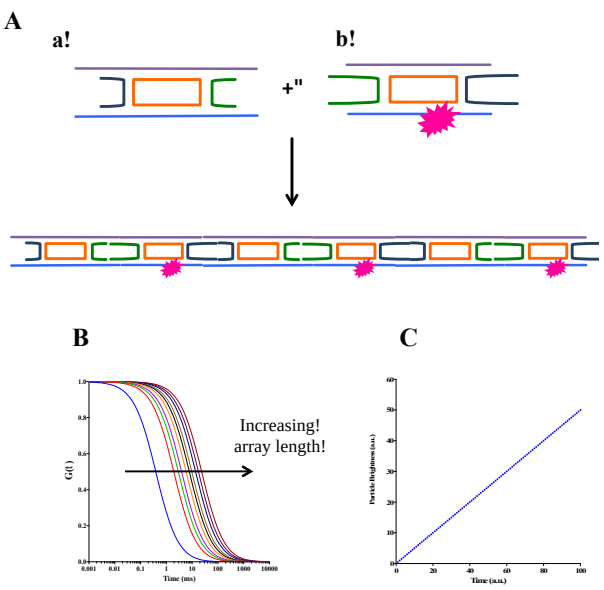


Figure 14. (A) 1D array composed by two DAE tiles, a and b, with complementary sticky ends. Tile b is fluorescently labeled. Any incorporation of either of the two tiles increases the overall size. Any incorporation of tile b increases the brightness of the array. (B) By measuring FCS traces at regular interval of times starting from the seeding of the array, it is possible to follow the changes in the diffusion coefficient of the species in solution. (C) It might be possible to follow the changes of brightness of the diffusing particles as a function of time due to the increase in brightness after any incorporation of tile b in the array.

4. Future directions:

FCS has been used to experimentally evaluate the model provided by the Bathe's lab to predict the physical properties of DNA nanostructures in solution. Correlation Spectroscopy revealed to be a useful and flexible tool for this purpose, providing measurements of the translational as well as the rotational diffusion coefficients of the HT tiles structures. As previously mentioned, the most recent experiments on the usage of different dye labels for FCS measurements identified a new candidate, ATTO532, to be used to tag DNA nanostructures. Furthermore, due to its properties, ATTO532 seems to be ideal for investigations on DNA origami that were so far hindered by the unfavorable qualities of TMR.

Besides structural investigations, it is possible to use FCS for kinetic investigation as well. It is very important to understand the processes involved in the self-assembly of nanostructures to be able to correctly design networks of interconnected elements. The assembly of enzymes on DNA tiles, or the assembly of different tiles to form 1, 2, or 3D arrays are just an example.

Here we propose the use of FCS to follow the growth of DNA tile arrays in solution by looking at the changes in the diffusion coefficient, as well as brightness of the particles monitored. In Figure 14, panel A, the process of growth of a 1D DNA tile array is schematically depicted. The system is composed by two tiles, a and b, exposing complementary sticky end to one another. Tile b is fluorescently labeled: this allows monitoring the changes in size that occur during the growth of the array. In panel B, an example of how the FCS data may look like is provided: by measuring traces at regular intervals of time after mixing together the two tiles will allow to

observe the changes in the diffusion coefficient, and therefore have kinetic information on the process. In Figure 14, panel C, the evolution of the particle brightness in time is depicted: any incorporation of tile b in the array will increase both size and brightness of the resulting array particle, and therefore the specific brightness per particle may also be used to gather kinetic information about the process.

Engineering a three-enzyme pathway with channeled substrate transfer

1. Pathway design and rationale:

Malate dehydrogenase (MDH) is capable of catalyzing the oxidation of malate to oxaloacetate (OAA) using the reduction of NAD^+ to NADH which is part of biological metabolic pathways, including the citric acid cycle. MDH alone in solution, however, is measured to have much higher preference for the reduction of oxaloacetate to malate which is a reversed reaction direction (Figure 5B). In the last reaction of the citric acid cycle, NAD^+-linked malate dehydrogenase catalyzes the oxidation of malate to oxaloacetate. The equilibrium of this reaction lies far to the synthesis of malate rather than oxaloacetate under standard thermodynamic conditions, but in cells oxaloacetate is continually removed by downstream citrate synthase reaction which is highly exergonic. This keeps the concentration of oxaloacetate in the cell extremely low, pulling the MDH reaction toward the unfavorable direction. Nature has evolved to efficiently transfer intermediates to direct reaction pathways and reach high yield and speed.

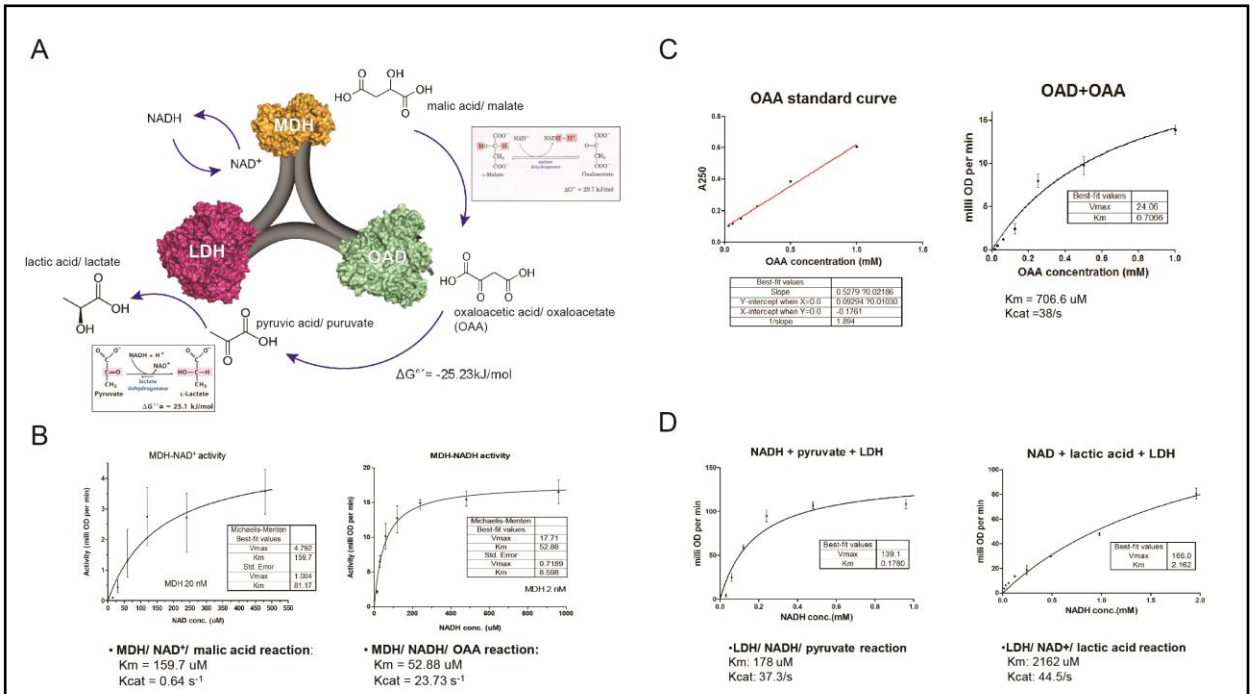


Figure 15. Design of three-enzyme pathway and theoretical thermodynamic and kinetic favorability. (A) Scheme for MDH-OAD-LDH pathway to facilitate ultilizing of malic acid by MDH. The overall strandard free energy is -20.63 kJ/mol which indicates the thermodynamic favorability. (B) Kinetic parameters of MDH on both reaction directions. In solution, the NADH-OAA direction is 112-fold more efficient than the malate-NAD^+ direction. (C) Standard curve of OAA concentraion vs. absorbance at 250 nm and kinetics parameters of OAD on OAA oxidation (D) Kinetics of LDH on both reaction directions. The pyruvate-NADH direction is 14.5-fold more efficient than the lactate-NAD^+ direction.

In this work, taking the advantage of spatially controllable DNA nanostructures, we aim to construct an artificial enzyme complex, integrating a circular enzyme pathway to regulate the reaction direction of enzymes (Figure 15A).

The two downstream enzymes are oxaloacetate decarboxylase (OAD) and lactate dehydrogenase (LDH). MDH oxidizes malate to oxaloacetate with the reduction of NAD^+ to NADH. Oxaloacetate is then converted to pyruvate and can be reduced to lactate by LDH with the oxidation of NADH back to NAD^+. In solution, although the NADH-OAA direction for MDH is 112-fold more efficient than the malate-NAD^+ direction (Figure 15B), OAD only catalyzes the decarboxylation of oxaloacetate to pyruvate due to the low concentration of CO_2 (Figure 15C) and for LDH the pyruvate-NADH direction is 14.5-fold more efficient than the lactate-NAD^+ direction (Figure 15D). Theoretically, we may drive the reaction of MDH towards the unfavorable direction for two reasons: (1) the overall standard free energy is calculated -20.63 kJ/mol so by coupling the two downstream enzyme pathways we may overcome the energy barrier (-29.7 kJ/mol) of malate oxidation by MDH; (2) comparing the catalytic efficiency of three enzymes, the second enzyme OAD is working more efficiently than MDH and LDH is more efficient than OAD so this allows intermediates to be efficiently comsumed by the following enzyme in this pathway.

2. Design of DNA nanostructure and characterization of three-enzyme assembly:

To assemble the three-enzyme pathway, we designed a three-arm DNA nanostructure, named three-point star. Each arm has two anchoring single-stranded region that can hybridize with the DNA probes modified on protein surface. The calculated distance between each neighboring anchoring points is ~11.8 nm. The sequences detail and gel confirmation are shown in Figure 16A.

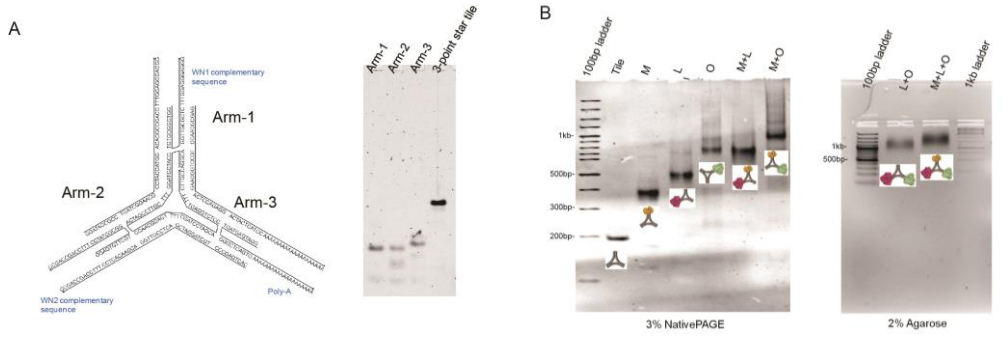


Figure 16. Design and characterization of assembled enzyme complex. (A) Design of three-point star tile with three anchoring positions (left) and native PAGE gel of structure assembly (right) (B) Assembly of multi-enzyme complex on DNA tiles.

Three proteins were labeled with different DNA oligos that can specifically target different arms. As shown in Figure 16B, upon the binding of enzymes, there is a significant band shift which indicates the formation of a larger complex. The center strand is modified with biotin so any assembled two-enzyme or three-enzyme complex can be purified using monomeric avidin resin. The protocol of biotin-avidin purification was previously reported.

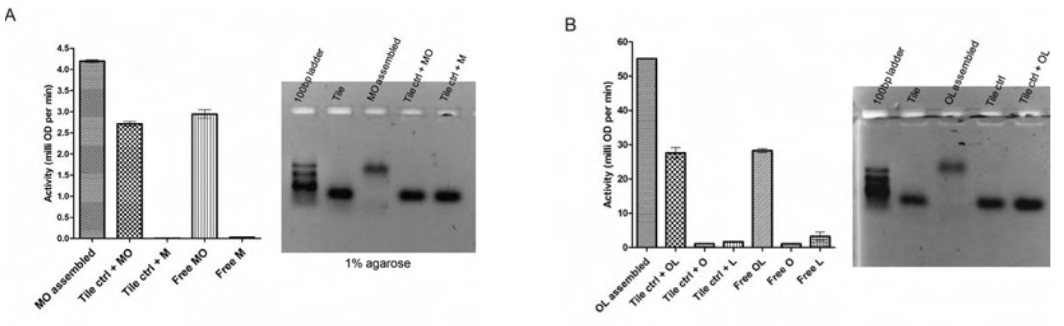


Figure 17. Characterization of enzymatic activity in the MDH-OAD and OAD-LDH enzyme pair. (A) Raw activity and gel of MDH-OAD assembled on 3-point star structure, MDH and OAD with free DNA control, MDH only with free DNA control, free MDH and OAD, Free MDH only. Measured concentration: 10 nM. Substrate conditions: 1 mM malic acid and 1 mM NAD^+ in 100 mM HEPES buffer (pH 8). (B) Raw activity and gel of OAD-LDH assembled on 3-point star structure, OAD and LDH with free DNA control, OAD only with free DNA control, LDH only with free DNA control, free OAD and LDH, Free OAD only, free LDH only. Measured concentration: 10 nM. Substrate conditions: 1 mM oxaloacetic acid and 1 mM NADH in 100 mM HEPES buffer (pH 8).

3. Characterization of two-enzyme pair assembled on DNA nanostructures:

MDH-OAD pair (Figure 17A) and OAD-LDH pair (Figure 17B) were constructed purified and evaluated, respectively. NADH level in both measurements were monitored with time. Any single enzyme in solution is catalyzing at a very low level and the overall activity is significantly enhanced with the addition of a second enzyme. In the MDH-OAD pathway, NAD^+ is continually reduced by MDH due to the efficient removal of oxaloacetate by OAD so NADH is accumulated during the measurement. Similarly, in the OAD-LDH pathway, NADH is kept been oxidized by LDH so the level of NADH is decreasing with time. Compared with free enzyme systems, assembled two-enzyme complexes demonstrate a more rapid accumulation of NADH in MDH-OAD pair and consumption in OAD-LDH pair and either the activity of two-enzyme pair or single enzyme is not affected by the addition of DNA environment.

4. Characterization of three-enzyme pathway assembled on DNA nanostructures:

The scheme for evaluating the three-enzyme pathway is shown in Figure 18A, where a coupled assay using lactate oxidase (LOX), horseradish peroxidase (HRP) and Amplex Red is used to detect the final product lactate of this MDH-OAD-LDH pathway. Lactate oxidase catalyzes the oxidation of lactate to pyruvate and produced H_2O_2 can be utilized by HRP. In the presence of HRP, the Amplex Red reagent reacts with H_2O_2 in a 1:1 stoichiometry to produce the red-fluorescent oxidation product, resorufin. Resorufin can be excited at 540 nm and emission signal is monitored at 590 nm. Because the oxidation of lactate will increase the level of pyruvate which is involved in the three-enzyme pathway, the lactate has to be separated from the assembled complex before quantification. A stop time assay was designed for removal of large

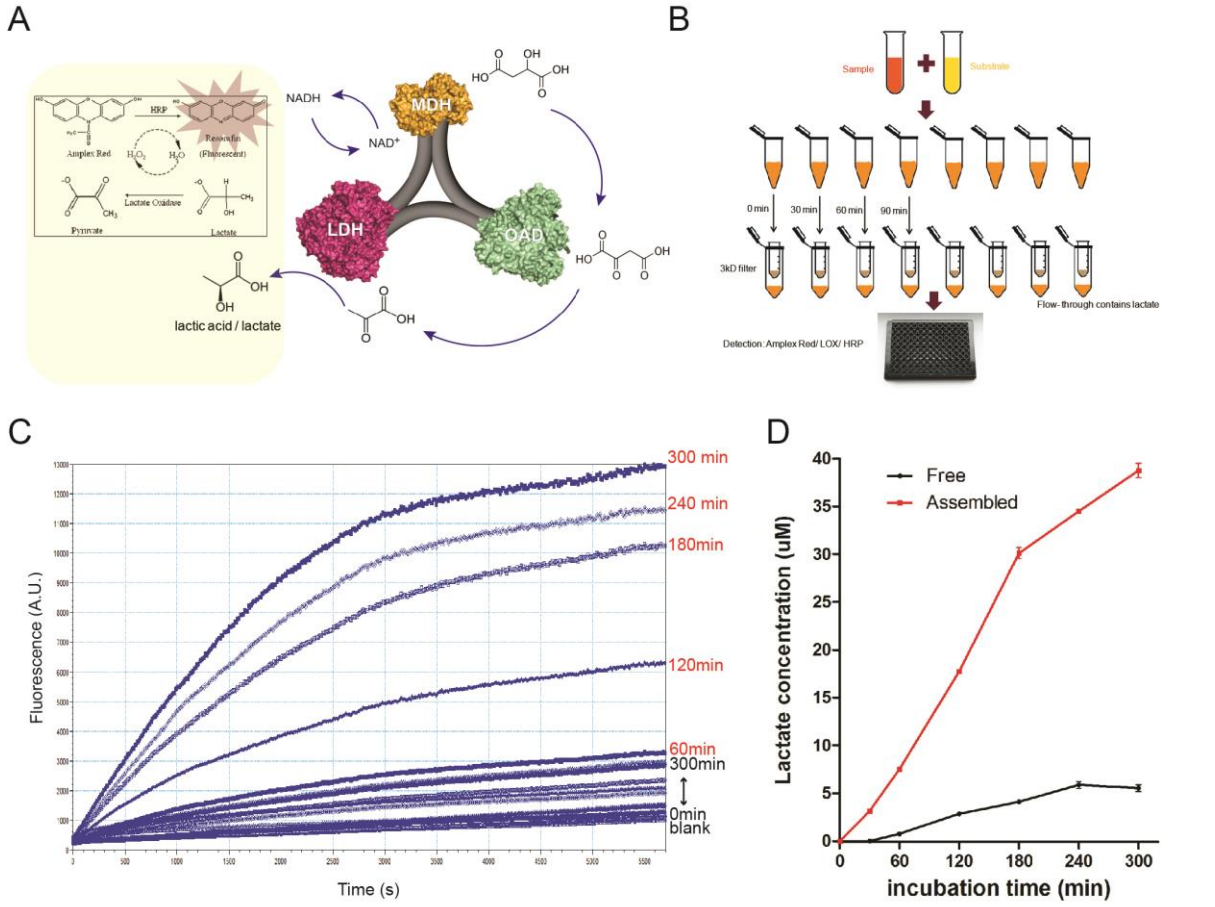


Figure 18. Characterization of assembled three-enzyme pathway. (A) Schematic illustration of lactate detection using LOX/HRP/Amplex Red assay. (B) Scheme for stop time assay for separating final enzyme complex from lactate. (C) Raw data collected from assembled complex (red) and control group with free enzymes (black). Fluorescent signal comes from resorufin which can be correlated to the lactate concentration. (D) Lactate accumulation with incubation time. Data was normalized from (C) after two-step subtractions and lactate standard curve. Stop time assay conditions: 5 nM MDH-OAD-LDH assembled or free control; 1 mM malic acid, 1 mM NAD^+ in 100 mM HEPES buffer (pH8). Coupled assay conditions: 1 nM LOX, 1 nM HRP, 300 uM Amplex Red.

complex after reaction (Figure 18B). 10 nM samples (assembled complex or free enzyme control group) and substrates (2mM malic acid and 2mM NAD^+) were mixed with 1: 1 volume ratio. After mixing the sample and substrates, the mixture was quickly aliquoated equally into several tubes. Each tube was incubated at room temperature for different length time. The reaction in the first tube was passed through a 3kD cut-off filter and the enzymes and DNA nanostructures were trapped in the top column so the reaction is stopped and this time point was defined as 'Time Zero'. Other tubes were later stopped at different time points until the last tube was processed. The flow-through containing lactate was later quantified using plate reader with the coupled LOX/HRP/Amplex Red assay.

As raw data shown in Figure 18C, the fluorescent signal was monitored for a certain time period until the velocity of the coupled assay gets slower and close to the velocity of blank group which indicates the full consumption of lactate. The increasing fluorescence in blank group comes from the oxidation of Amplex Red by HRP with the oxygen in buffer and the increased fluorescence should be subtracted from all experimental groups. After the first step of subtraction, the fluorescence increased in 'Time Zero' group was subtracted from all the other groups to obtain normalized result shown in Figure 18D. Normalized fluorescence was converted to exact lactate concentration using lactate standard curve and plotted with incubation time. According to Figure 8D, we can estimate the overall turnover rate of the assembled complex to be ~ 0.55 per second which is close to the turnover rate (0.64 per second) of the first enzyme MDH in consuming malic acid. This indicates in the assembled pathway, the MDH is the slowest and thus the rate-limiting enzyme and the downstream enzymes can efficiently remove the products by MDH almost at the same time when they are produced.

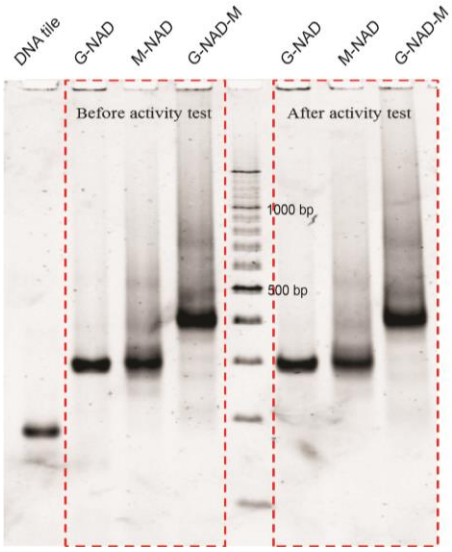


Figure 19. Native PAGE (3%) characterization of the stability of swinging-arm structures before and after the catalytic reaction. Left: the structures of G-NAD, M-NAD and G-NAD-M before running the reaction. Right: the structures of G-NAD, M-NAD and G-NAD-M after running the reaction. Reaction conditions: 1 mM G6pDH and OAA were incubated with 100 nM enzyme structures for one hour in the pH 7.5 HEPES buffer.

5. Future directions:

Work is now in progress to (a) increase the fold enhancement between assembled pathway and free control by decreasing the measurement concentration; (b) determine the effective concentration of assembled complex and (c) evaluate the change to equilibrium of MDH reactions with the addition of the downstream OAD and LDH.

Engineering a DNA scaffolded multi-enzyme complex utilizing a "swinging arm" to control substrate transfer between enzymes

Previously we have reported engineering a multi-enzyme complex utilizing a "swinging arm" to control substrate transfer between enzymes. This work was published on 2014 *Nature Nanotechnology* journal. Here we evaluated the stability of assembled complex and optimized the swinging arm complex by adding a poly $(A)_{15}$ spacer to the arm.

1. Stability of tile-enzyme assembled structure:

The stability of assembled swinging-arm structures was characterized by Native PAGE (3%). After incubating the assembled DNA-protein complexes in substrates and buffer: 1 mM G6p and OAA in the pH 7.5 HEPES buffer for one hour, structure still remain the same compared to freshly prepared samples (Figure 19).

2. Regulation of enzyme complex activity by conversion of the ssDNA arm to dsDNA:

Here we achieved regulation of the activity of the G6pDH-NAD^+ semi-swinging arm and

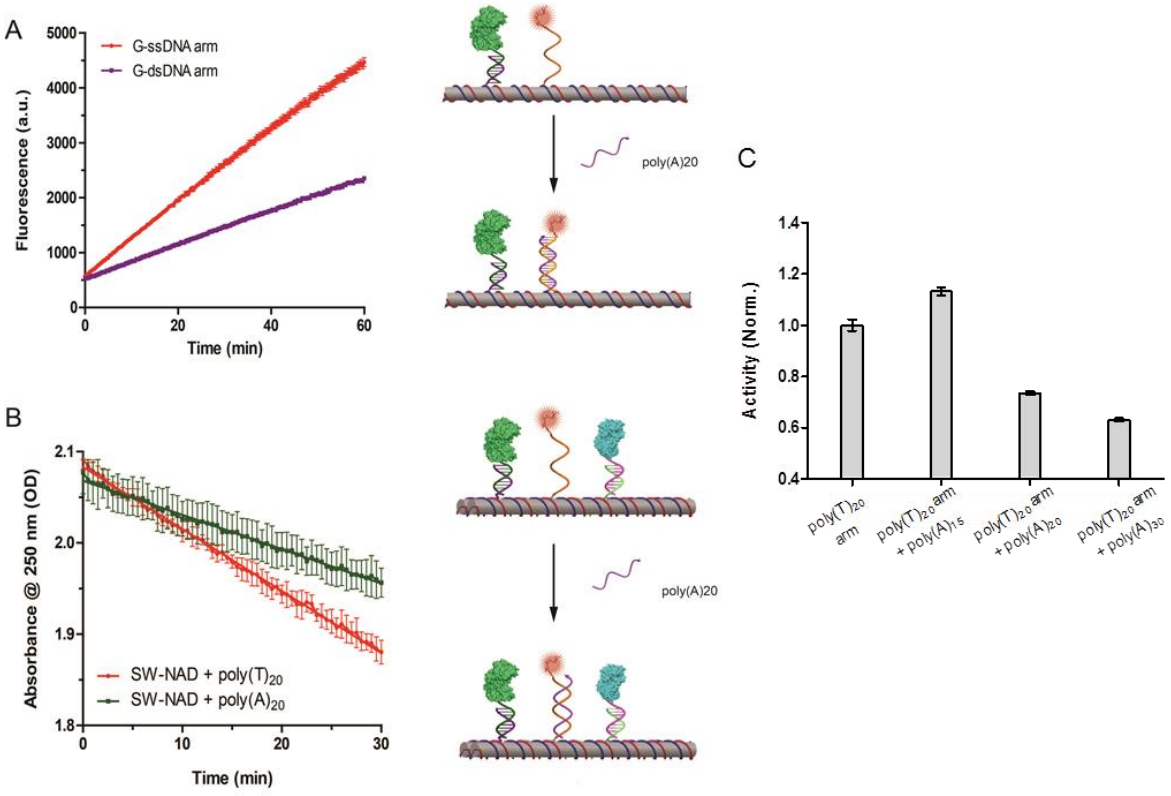


Figure 20. Regulation of enzyme complex activity by conversion of the ssDNA arm to dsDNA. (A) Regulating the activity of the G6pDH-NAD^+ semi-swinging arm structure by adding a poly$(A)_{20}$ strand to hybridize with the NAD^+-poly$(T)_{20}$ arm. The formation of a double-stranded arm results in a ~50% drop in activities, likely by slowing down the diffusion of NAD^+ and decreasing the flexibility of the arm (and hence its freedom to explore the space near the enzyme). (B) Regulating the activity of the G6pDH-NAD^+-MDH swinging arm structures by adding a poly$(A)_{20}$ strand to hybridize with the NAD^+-poly$(T)_{20}$ arm. For control reactions in (A) and (B), an equal concentration of poly(T)20 (which is unable to hybridize with the swinging arm) is added to the sample. Assay conditions: a 10-fold excess of poly(A)20 is added into solution with 100 nM swinging arm complex and incubated for 30 min at room temperature (to allow hybridization to reach equilibrium) before the activity assay. (C) The dependence of swinging arm complex activity on the length of added complementary strands.

G6pDH-NAD^+-MDH swinging arm structures by adding a poly$(A)_{20}$ strand to hybridize with the NAD^+-poly$(T)_{20}$ arm. The formation of a double-stranded arm results in a ~50% drop in activities, likely by slowing down the diffusion of NAD^+ and decreasing the flexibility of the arm (and hence its freedom to explore the space near the enzyme). For control reactions in (Figure 20AB) , an equal concentration of poly$(T)_{20}$ (which is unable to hybridize with the swinging arm) is added to the sample. Assay conditions: a 10-fold excess of poly$(A)_{20}$ is added into solution with 100 nM swinging arm complex and incubated for 30 min at room temperature (to allow hybridization to reach equilibrium) before the activity assay.

The activity of the swinging arm decreases as the length of the complements increases, suggesting that the increased rigidity of the double-stranded DNA reduces activity. However, the partially double-stranded arm consisting of poly$(T)_{20}$ and poly$(A)_{15}$ is slightly more active (15%) than the single-stranded poly$(T)_{20}$, suggesting that a partially double-stranded DNA may more effectively present the NAD to the enzyme. The observed the effect of double-stranded DNA rigidity on inhibiting the efficient interaction between the enzyme and the cofactor, is consistent with a previous study that the inhibition and activation of an enzyme-inhibitor complex were regulated by switching the linker between an enzyme and an inhibitor from a single-stranded DNA to a double-stranded DNA. Reaction conditions: 100 nM G6pDH-NAD semi-swinging arm structure was incubated with 1 µM poly(A) complementary strands, and assayed with 500 µM resazurin and PMS in pH 7.5 HEPES buffer.

Developing logic-gated multi-enzyme pathway circuits

We started to design and engineer swinging arms to channel intermediate in multi-enzyme pathways. A logic-gated circuit is incorporated to control the release and activation of swinging arms. In this way, the pathway activity and specificity is regulated by input DNA strands that trigger the activation of the logic-gated system. Figure 21A shows a locked NAD swinging arm whose release is controlled by an 'AND' logic gate. The structure consists of two domains labeled I and II. The open domain, I, is achieved by adding a key strand, I', that is fully complementary to the lock strand in both the blue and the green regions, and is driven by thermodynamically favored strand displacement. Then, the opening of domain II requires another key strand, II', which is fully complementary to the blue and pink regions, and releases an NAD-modified single strand for participating reactions. In this design, an 'AND' logic gate is used to control the release and activation of the swinging arm, requiring both key strands, I' and II'. In Figure 21B, we used FRET to characterize the release of swinging arm by the logic gate. In the locked arm, FRET was observed between Cy3 and Cy5, while the opened arm exhibited very little FRET between Cy3 and Cy5.

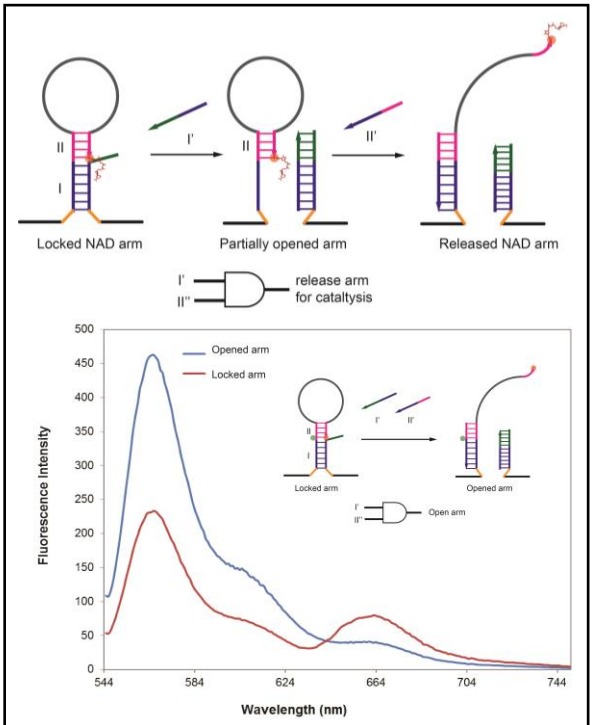


Figure 21. (A) A 'AND' gate-controlled swinging arm. (B) Characterization of the logic gate-regulated swinging arm by FRET. In the locked arm, FRET between Cy3 and Cy5 is observed, while the opened arm shows little FRET.

Developing artificial electron-transport chains

Energy transfer pathways play a key role in energy transformations in biological systems. For instance, nature uses electron-transport chains to couple the electron transfer between a series of donors and acceptors that are able to extract chemical energy from photosynthesis, carry out redox reactions in mitochondrion and regulate bioenergy conversions. We started to apply the organizational power of DNA nanotechnology to the challenges of engineering artificial electron-transport chains with controlled electron flow. In Figure 22A, we used DNA scaffolds to template a synthetic electron-transport chain consisting of glucose 6 phosphate dehydrogenase (G6pDH)-NADH-diaphorase (DI)-electrical mediator (e.g. methylene blue). The electrons derived from the oxidation of alcohol will be spontaneously transferred to the conductive electrode surface along an increased redox potential ($\Delta G^{\circ}<0$). This electron-transport structure can be applied to complex, bioelectroactive multienzyme pathway for bioelectricity applications. In Figure 22B, the electron transfer between NADH and DI was confirmed by measuring the absorbance spectrum of cofactors. The oxidation of NADH to NAD^+ resulted in a decreased absorbance at 350 nm. DI is a FMN-binding protein. The reduction of FMN to $FMNH_2$ with receiving electrons from NADH induced an absorbance decrease at 450 nm. Figure 22B clearly shows the electron transfer from NADH to FMN-binding DI. However, the reduced $FMNH_2$-DI is not stable under the environmental oxygen. To improve the guided electron transport, oxygen needs to be removed from the solution system.

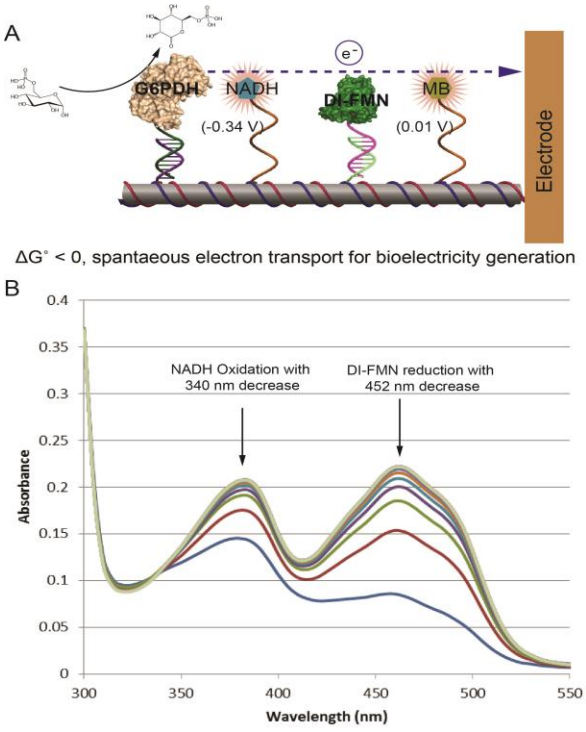


Figure 22. (A) Schematic illustration of an artificial electron transport pathway organized by DNA nanoscaffolds facilitating the electron transfer along a redox potential gradient. (B) Spectrum characterization of the electron transport between NADH and DI.

Optimizing the enzymatic activity of a DNA actuator structure and single-molecule detection of enzyme activity

1. <u>Optimization for enhanced enzyme activity using single-molecule FRET:</u>

Switchable nanomachines provide a universal platform to control dynamic systems by altering distances at the nanoscale on demand. Recently, a tweezers-like DNA device has been used to control the activity of an enzyme/cofactor pair juxtaposed on the two arms of the tweezers. Initial studies focused on bulk properties of the tweezers-mediated reactions, and hence lacked insight into the mechanism of enzymatic activation. Here, we used site-specifically fluorophore-labeled DNA tweezers and monitored the arm-to-arm distance through single-molecule fluorescence

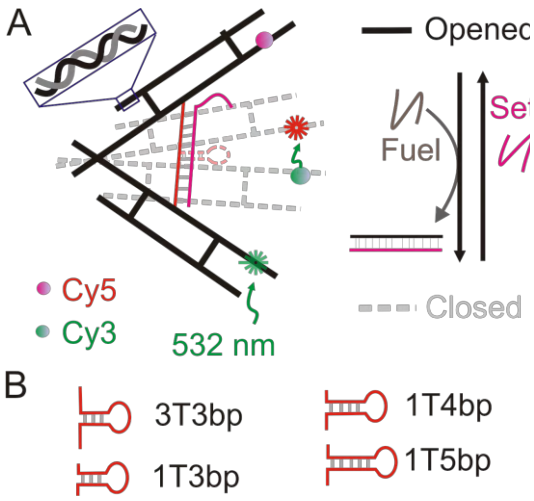


Figure 23. (A) The closing and opening cycles of DNA tweezers as monitored by single-molecule fluorescence resonance energy transfer (smFRET). (B) The four different hairpin sequences used in this study.

resonance energy transfer (smFRET). These tweezers are composed of DNA double-helix arms joined by a Holliday junction 'hinge'. To control the arm-to-arm distance, a DNA strand called 'linker strand' that can cycle between hairpin and double helical structures through a strand-displacement reaction is incorporated between the arms. First, we characterized the original DNA tweezers containing a hairpin linker with a 3T spacer and 3-base pair (bp) stem (3T3bp, Fig. Walter3) and found that these tweezers are only partially (to an arm-to-arm distance of ~6.5 nm) closed even in the "closed" state. Varying the hairpin length from 3 to 5 bp, we demonstrated an improved closing and enhancement on enzyme-activity by using a hairpin containing 1T spacer and 4-bp stem "1T4bp" tweezers (Figure 23).

In addition to the linker strand, Holliday junction (HJ1) could also play significant role on closing/opening of the tweezers (Figure 24A). Holliday junctions are known to switch between two isomers (iso-i and iso-ii) at the millisecond time scale with the relative occupancy of the isomers depending on the inner-core sequence. To determine the relative abundance of the isomers at HJ1, we monitored the isomer ratio on the isolated junction HJ1 after proper labeling of fluorophores (labeling scheme 1 and 2, Figure 24A). Since the rate of isomer transition depends on the Mg^{2+} concentration, we were able to resolve the isomer transition after increasing the Mg^{2+} concentration to 100 mM. We revealed that the ratio of iso-i to iso-ii is 1:3. The isomer ratio was consistent in the complementary labeling scheme. These experiments suggested that the "correct" isomer-I needed to close these tweezers is relatively disfavored, rationalizing the only partial closing of the tweezers. Since the closing of tweezers could be improved by choosing a correct inner-core sequence to favorably bias a desired isomer, we used this knowledge to further improve the closing. Towards this goal, we rationally redesigned either only HJ1 or all five HJs (HJ1 to HJ5), empirically or using published junction sequences (Seeman's iso-i & ii) (Figure 24B). Among these junction sequences, all of the redesigned sequences are expected to improve closing except for Seeman's iso-ii. Our smFRET measurements of these redesigned constructs (Figure 24B, right) revealed that tweezers with corrected HJ1 (iso-i) favored closing. The construct with all five HJs corrected demonstrated the best closing as reflected by high FRET states (0.60 FRET state, 80% and 0.95, 20%). These results demonstrated that the DNA nanostructures can be rationally improved. Currently Yan lab (ASU) is working on measuring the bulk enzyme activity of this construct after juxtaposing an enzyme glucose-6-phosphate dehydrogenase (G6pDH) and its cofactor NAD^+ on the tweezers arms.

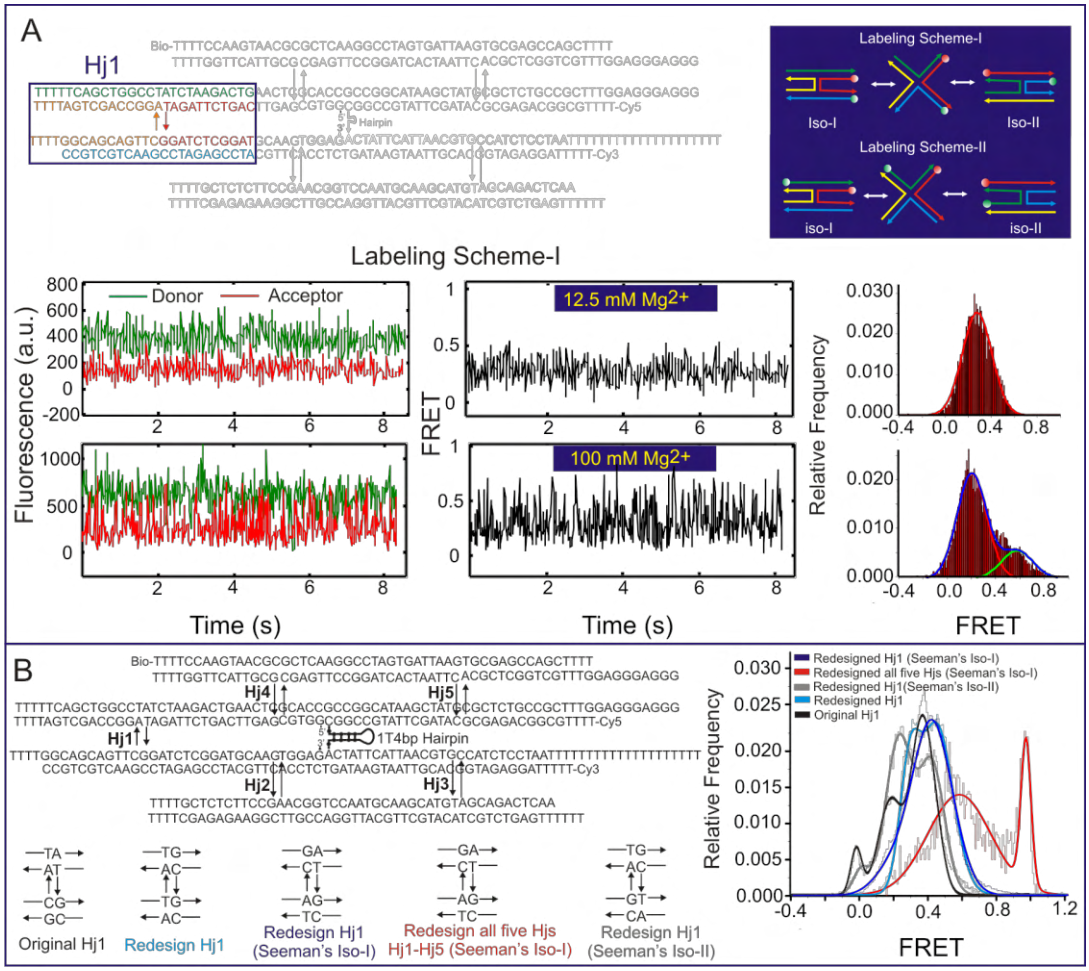


Figure 24. (A) smFRET measurement of an isolated Holliday Junction (HJ1). Only the region of interest is highlighted. Two labeling schemes used for smFRET measurements of HJ1 are shown on the right. (B) Typical FRET traces and corresponding smFRET histograms for labeling scheme-I at 12.5 and 100 mM Mg^{2+}. Two isomers (iso-i and iso-ii) were clearly observed at 100 mM Mg^{2+} whereas a weighted average population was observed at 12.5 mM Mg^{2+}. (B) Redesigning of the HJ(s) to improve closing. The inner-core sequences used to redesign the HJ(s) are provided. Seeman's isomer is referring to the Holliday junction sequence in the DNA crystal of PDB ID 3GBI. smFRET measurements of these redesigned constructs are compared on the right.

2. <u>Molecular Dynamics Simulation of the Full DNA Tweezer:</u>

Single-molecule Förster Resonance Energy Transfer (smFRET) measurements of the conformational dynamics of the DNA tweezer, performed by the Walter Lab, have revealed a sub-optimal "closed" state in which the tweezer arms are further apart than expected. This observation is important because close proximity of the multiple enzymes that are tethered by the DNA tweezer is required to maximize substrate throughput in the design.

In order to generate possible molecular-level explanations for this observation, the Bathe lab built an all-atom model of the DNA tweezer and simulated it using molecular dynamics. The model was built in explicit solvent with monovalent and divalent ions matching experimental conditions, and simulated in the isothermal-isobaric ensemble at 300 K and 1 atm for 100 nanoseconds. The simulated structure deviates significantly from an idealized model consisting of parallel cylinders (Figures 25-27). Snapshots of the dynamics indicate that the system does not

adopt a planar conformation but rather exhibits a global twisting along with relative bending of the arms away from one another. One source of this out-of-plane bending and twisting is postulated to be the isomer state adopted by the four-way Holliday Junction (4WJ) at the base of the tweezer holding the two arms together, Junction 1.

3. Molecular Dynamics Simulation of Junction 1:

Having identified that Junction 1, the four-way Holliday Junction (4WJ) at the base of the tweezer, plays an important role in determining the overall conformation of the tweezer, we focused additional molecular dynamics simulations on Junction 1 isolated from the remainder of the tweezer. In isolation, it is known that immobile 4WJs may adopt one of two alternate conformational isomeric states, which were postulated to potentially drive the tweezer into an open conformation. Further, it is known that the DNA base composition at the 4WJ has an important effect on the propensity of the junction to adopt one over the other isomeric state. To explore the conformational mobility and stability of each isomer of Junction 1, they were separately simulated in isolation in the same conditions as the full tweezer, including explicit solvent. Simulation results of the two isomers are then compared with one another as well as their conformation in the full tweezer simulation.

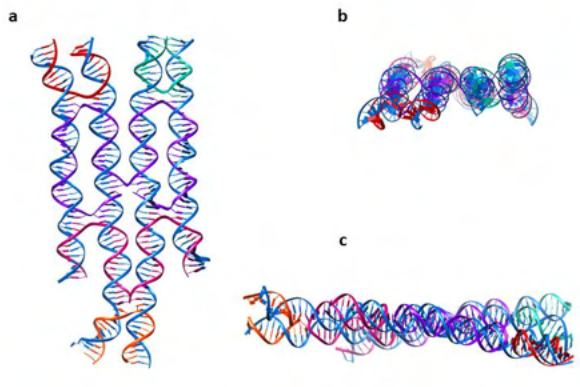


Figure 25. Molecular dynamics model of the DNA tweezer. (a) Top-, (b) front- and (c) side-view of the system after 30 ns of molecular dynamics.

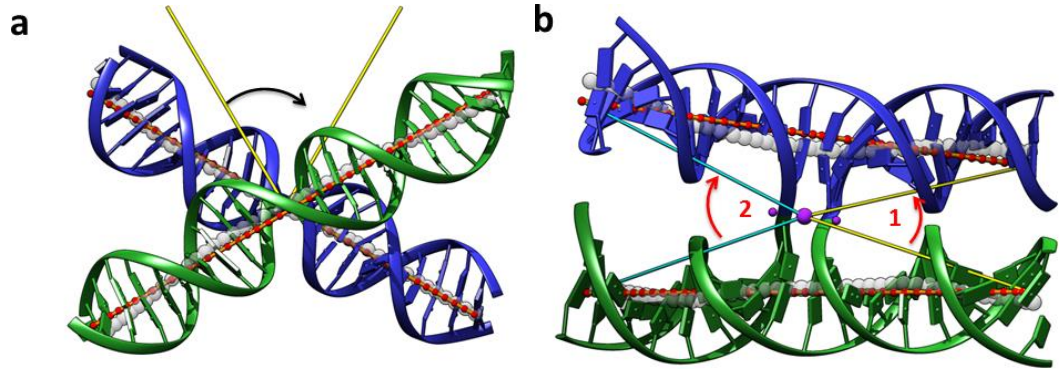


Figure 26. Definition of 4WJ conformational metrics. (a) The Jtwist angle represents the scissor motion of the duplex arms. (b) The interduplex angles (IDA) indicate bending of the duplex arms.

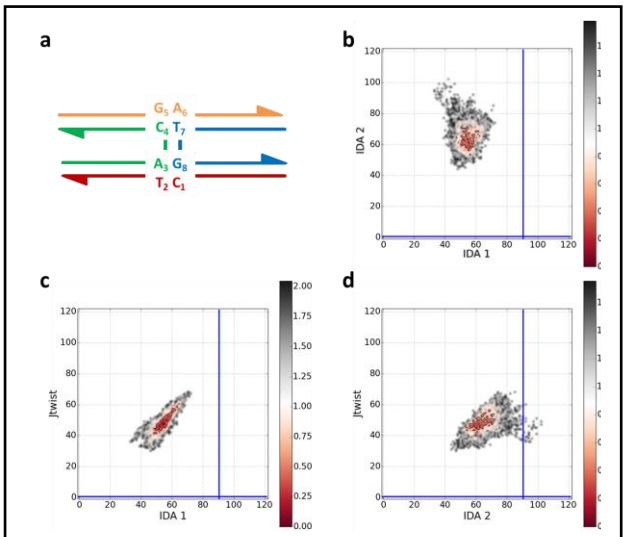


Figure 27. IDA and Jtwist distributions of isolated Junction 1, Isomer I. (a) Sequence topology of Isomer I of the isolated Junction 1 system. (b) The 2D distribution of the two IDA values. (c) The 2D distribution of Jtwist vs. IDA 1. (d) The 2D distribution of Jtwist vs. IDA 2. The color maps indicate relative energies in kcal/mol, with contours at 0.5 kcal/mol to emphasize minima.

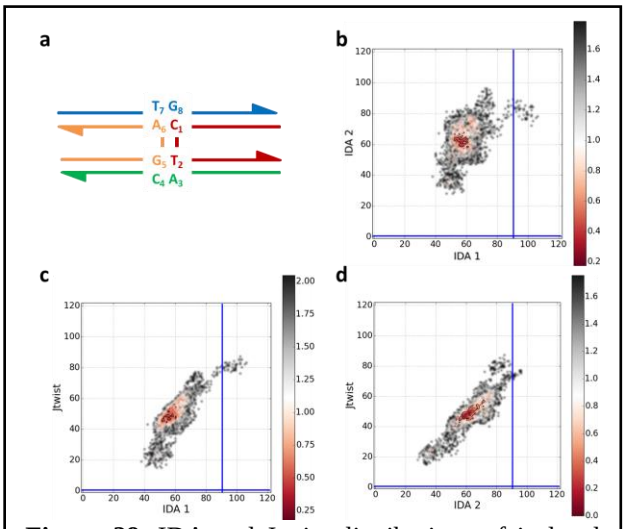


Figure 28. IDA and Jtwist distributions of isolated Junction 1, Isomer II. (a) Sequence topology of Isomer II of the isolated Junction 1 system. (b) The 2D distribution of the two IDA values. (c) The 2D distribution of Jtwist vs. IDA 1. (d) The 2D distribution of Jtwist vs. IDA 2. The color maps indicate relative energies in kcal/mol, with contours at 0.5 kcal/mol to emphasize minima.

Analysis of the dynamical data includes monitoring the large-scale motions of the two isomers using the interduplex angle (IDA) and Jtwist angle (Figure 26). IDAs indicate intraduplex bending of the two arms, and Jtwist represents the scissor-like motion of the duplex arms relative to one another. Preliminary results indicate that the value of Jtwist in situ is reduced significantly compared with the isolated junction result, purportedly due to structural constraints that are imposed on the junction by the remainder of the tweezer structure (Figures 27 and 28). These 2D probability landscapes for the two IDAs of Junction 1 reveal distinct free energy landscapes for the two isomers that we are in the process of interpreting. Additional conformational analysis at the base-pair level suggests that bases are displaced along the x-axis (orthogonal to the helical axis). The detailed distributions of these parameters may allow us to gain further insight into the origins of the distinct Jtwist/IDA conformational landscapes to explain the origin of the atomic-level interactions for the stability or instability of the 4WJ in each isomeric state. This analysis suggested alternative sequence designs to test the hypothesis experimentally that the core sequence is responsible for the observed opening of the tweezer.

4. Single-molecule detection of enzyme activity on dynamic DNA tweezer:

Biological pathways are controlled at the molecular level by rate-limiting enzymatic reactions. While the mechanism of enzyme activation is poorly understood, recent single-molecule methods have discovered nonuniform behavior of enzymes. Single-molecule methods can give access to nonuniform kinetic behavior as well as transient and rare states that are impossible to study in bulk. Along this line, to further investigate the enzymatic behavior of single G6pDH molecules, Walter lab developed an assay to detect G6pDH/NAD^+ turnover for individual DNA tweezers. DNA tweezers are suitable tools to actuate the enzyme activity by opening and closing the tweezers with protein/cofactor juxtaposed on two arms of the tweezers (Yan lab, ASU). Using a novel fluorescence based assay, we demonstrated that G6pDH/NAD^+ activity can be

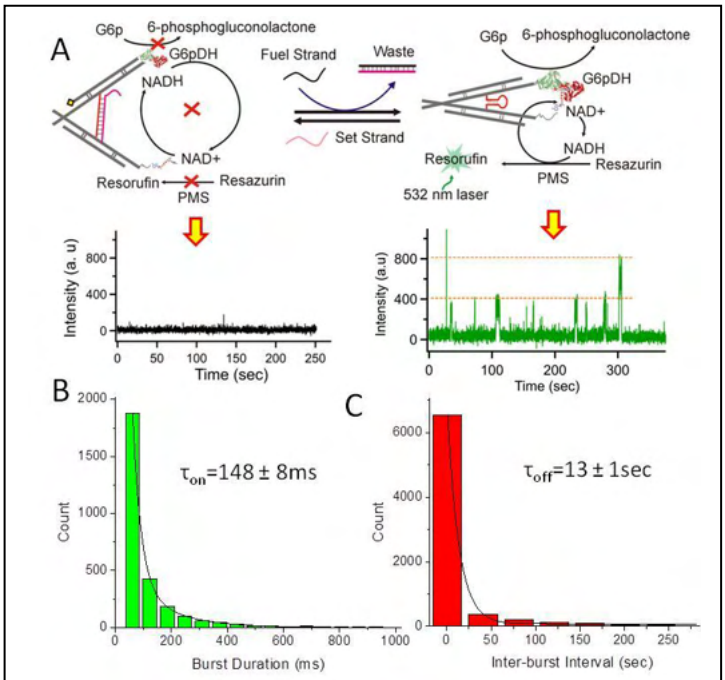


Figure 29. (A) Top panel: Modulation of G6pDH activity by dynamic DNA tweezers. Bottom panel: Typical Intensity-time traces from enzymatic reaction in open and closed DNA tweezers. Only background intensity was observed for opened tweezers (left). By contrast, fluorescent bursts of varying intensity (highlighted by red dotted lines) and inter-burst intervals were observed for closed tweezers (right). (B) The distribution of apparent burst life times (τ_{on}). (C) The distribution of apparent inter-burst intervals (τ_{off}). Black curve in (B) & (C) are single-exponential fits. Experiments were performed in 1xTBE buffer in presence of 1 mM Mg^{2+}, 1 mM G6P, 25 nM resazurin, 125 uM PMS and 10% PEG 8000. Data were collected at 62 ms time resolution.

detected in situ with the aid of an enzyme cascade reaction (Figure 29). The detection is based on the conversion of fluorogenic substrate 'resazurin' to the fluorescent 'resorufin' due to the enzyme cascade reaction (Figure 29). G6pDH activity was measured separately for open and closed tweezers after immobilizing the tweezers on a microscope slide. While opened tweezers prevented enzymatic activity, the fluorescence time traces for individual closed tweezers showed variations in bursts intensity (dotted red lines) and inter-burst intervals, suggesting a stochastic behavior of the enzyme. In addition, from the dwell time analysis of bursts and inter-burst intervals, we determined an average burst life time (τon) of 148 ± 8 ms and an inter-burst life time (τoff) of 13 ± 1 sec. These findings will provide invaluable insight into the molecular behavior of G6pDH. In the future, we will refine the accuracy and generality of our single-molecule assay to make it applicable to other systems such as DNA nanocage-enzyme complexes.

3D-DNA Origami lipid complex for facilitated substrate diffusion

1. Systematic evaluation of assembly of lipid bilayer with DNA nanostructures:

We constructed two different types of DNA Origami, Octahedron shaped nanostructure (80nm in diameter) and stacked-ring cylinder structures, including Candlestick (30nm in diameter) and Cactus (90 nm in diameter), to assemble with lipid bilayer, either inside or outside DNA structure. According to our recently published method, lipid conjugates could be attached to DNA Origami to direct vesicle reconstitution from lipid-detergent micelles. With the same protocol, we have tested the envelopment of DNA Octahedron or Candlestick (30nm in diameter and 120 nm in length), and TEM results showed that only DNA Octahedron can be wrapped with lipid bilayer very tightly (Figure 30), while Candlestick liposome complex is not uniform, which might result from Candlestick's asymmetric structure. At the same time, Cactus Origami, with 87 nm diameter and 20 nm length had also been tested to assemble with liposome inside cavity, and TEM proved that liposome could tightly fit into Cactus inner cavity, achieving high yield. In future, to better control inner assembled liposome dimension, we are planning to make

polymerized Cactus in 1D to form tubular structures as templates to assemble liposomal tubes on the inside.

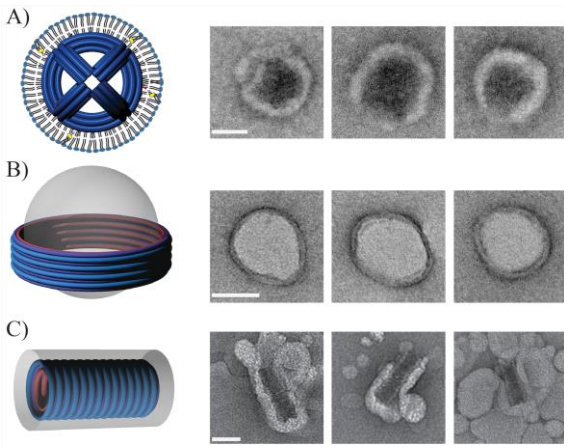


Figure 30. Liposome assembly with DNA Origami. (a) Model and TEM images for liposome wrapped Octahedron Origami, with 80nm in diameter. (b) Model and TEM images for liposome assembled inside Cactus Origami, which has 87 nm diameter and 20 nm length. (c) Model and TEM images for liposome wrapped outside Candlestick Origami, which has 30 nm diameter and 120 nm length. (Scale bar: 50 nm)

DNA brick crystal:

Previously, Ke et al. constructed large DNA array using 3D DNA bricks. Here we tried to use DNA brick crystal as template to organize cascade enzymes. In our design, DNA brick unit cell has dimensions of 45 nm × 42 nm ×10 nm, which assembled with one pair of HRP, GOx enzymes. From the TEM image, we could observe enzymes assembled in lines on crystal structure and the measured distance of adjacent lines is around 40 nm, which fits our design very well. Our result (Figure 32) proved that DNA crystal can be used to organize enzymes with high yield, and in future we will study cascade enzyme activity on DNA crystal template, with controllable distance and ratio.

4. Future directions:

Our goal is to limit diffusional escape of reaction intermediates in enzyme cascades using lipid membrane as reflecting walls. As

2. Cascade enzyme assembled inside DNA Octahedron origami, wrapped with lipid bilayer:

Lipid bilayer wrapped DNA Octahedron was used to limit the escape of intermediates to increase cascade enzyme efficiency. To achieve this goal, we firstly tested cascade enzymes, HRP and GOx could be assembled inside Octahedron cavity, proved by TEM images (Figure 31). Secondly Octahedron enzyme complex was wrapped with lipid bilayer, and enzyme activity was monitored after purification. Our result showed that after wrapped with lipid bilayer, internalized enzyme activity decreased 3 fold, which proved that lipid bilayer could efficiently block substrate diffusion. In future, to ensure substrate transportation, outer membrane protein f (Ompf), a channel protein, will be placed on lipid bilayer to create transportation channel.

3. Immobilization of cascade enzyme onto

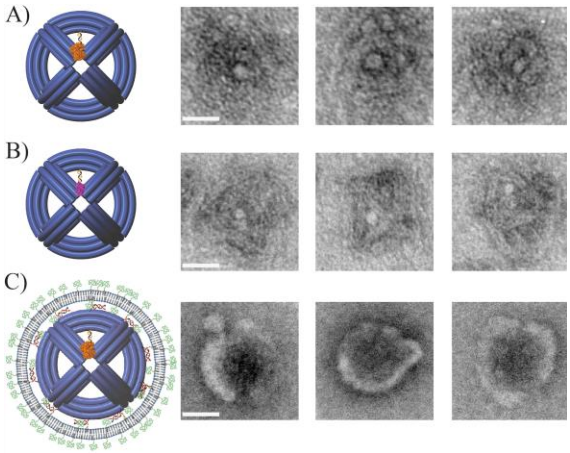


Figure 31. Octahedron shaped DNA Origami as template to assemble with HRP, GOx enzyme and liposome. (a) Model and TEM images for Octahedron assembled with GOx enzyme. (b) Model and TEM images for Octahedron with HRP enzyme. (c) Model and TEM images for Octahedron assembled with both GOx enzyme and liposome. (Scale bar: 50 nm)

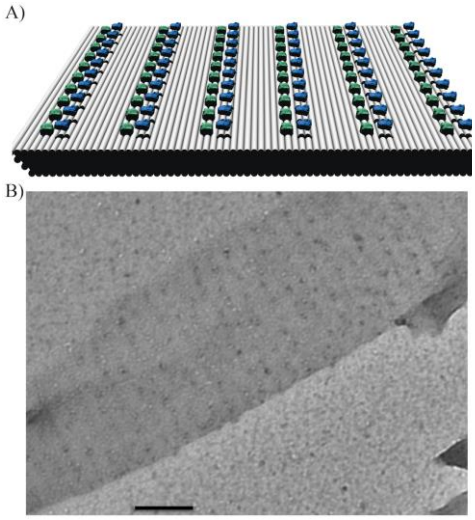


Figure 32. Model and TEM image for DNA brick crystal organized cascade enzymes, HRP and GOx. (Scale bar: 100 nm)

we have demonstrated, enzymes can be assembled inside a DNA octahedron, covered with lipid bilayer outside, which can prevent substrate from free diffusion. Our next challenge is to site specifically construct a membrane channel in the liposome for controlled substrate and product diffusion in and out, while restricting escape of intermediates prior to enzymatic processing. At the same time, we will continue to explore liposome assembly with polymerized Cactus origami to form tubular shaped liposomes.

A bioelectroactive methanol dehydrogenase pathway organized by DNA nanostructure

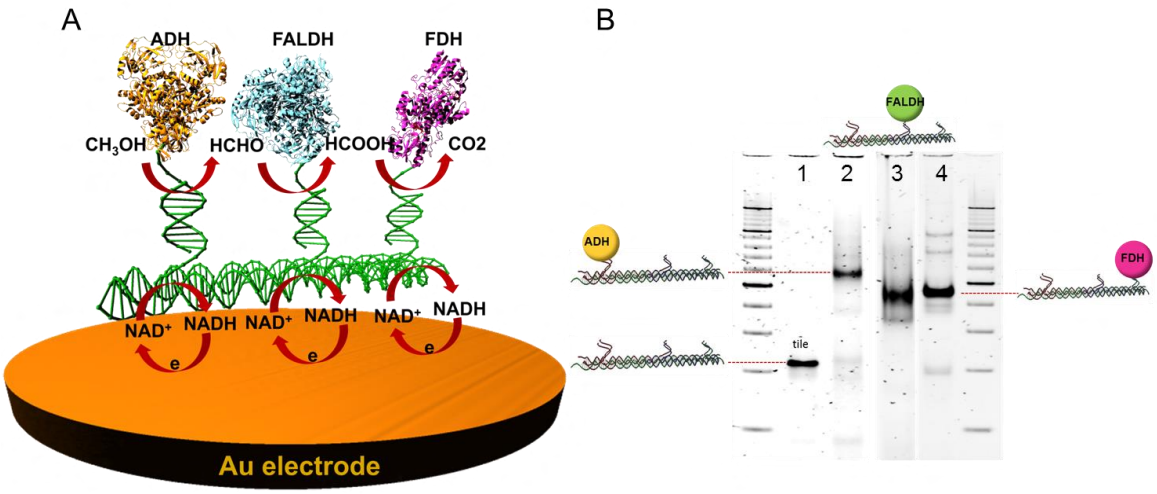


Figure 33. Design and characterization of an. (A) Schematic illustration of the nanostructure complex consisting of alcohol dehydrogenase (ADH), Formaldehyde dehydrogenase (FALDH) and formate dehydrogenase (FDH) organized on a DNA DX tile. The center to center distances between each protein is designed to be 14 nm. (B) Native PAGE (3%) characterization of the assembled dehydrogenase-tile structure: (1) DNA tile; (2) ADH-tile assembled complex; (3) FALDH-tile assembled complex; (4) FDH-tile assembled complex.

Here we developed a bioelectroactive NAD-dependent methanol pathway which involves three dehydrognenase enzymes: alcohol dehydrogenase (ADH), Formaldehyde dehydgrogenase (FALDH) and formate dehydrogenase (FDH). The pathway fully oxidizes methanol to carbon dioxide and simultaneously reduces NAD^+ to NADH. As shown in Figure 33A, ADH catalyzes

the oxidation of methanol to formaldehyde with the concurrent reduction of NAD^+ to NADH.Subsequently, FALDH oxidizes formaldehyde to formate. The final enzyme of the cascade, FDH oxidizes formate to CO_2. Summarizing the overall reaction cascade, the full oxidation of one mole of methanol to CO_2 leads to the reduction of NAD^+ to form 3 moles of NADH. By organizing 3 enzymes by a double helix (DX) tile, the center to center distances between each enzyme is designed to be 14 nm, which significantly facilitates intermediates diffusion, therefore increase overall pathway activity. By building this protein-DNA complex enzymatic biofuel cell, we aim to achieve fully transferring the chemical energy released upon the redox reactions to electrical power.

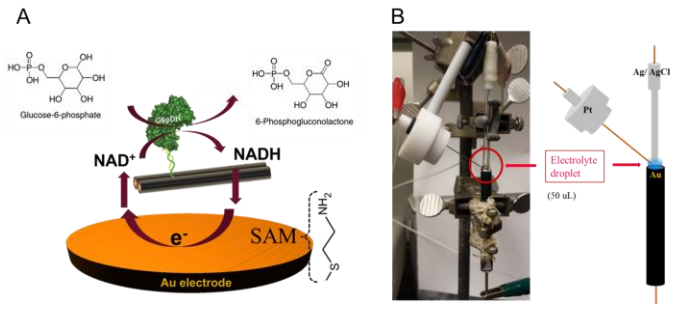


Figure 34. (A) A scheme illustrating model system with glulcose-6-phosphate dehydrogenase (G6pDH) assembled on DNA tile and producing NADH molecules which is converted back by electrode; (B) Three electrodes system including working electrode (Au), reference electrode (saturated Ag/ AgCl) and counter electrode (Pt). 50 µL droplet held by 3 electrodes contains electrolytic buffer (100 mM sodium phosphate, pH 8.0) with enzyme and substrates.

1. <u>Optimizing electron transfer from NADH to Au electrode:</u>

In this methanol dehydrogenase cascades, every enzyme produces NADH molecule which carries 2 electrons and pass those electrons to Au electrode. To study the electron-transfer reactivity between NADH molecule and Au electrode, Cyclic voltammograms (CV) and Amperometric response (I-t) versus different concentration of NADH were measured. All electrochemical measurements were performed with a CHI 660 electrochemical workstation (CH Instruments Inc., Ausin, TX). A conventional three-electrode configuration was employed all through the experiment, including a gold working electrode, an Ag/AgCl reference electrode, and a platinum counter electrode. Instead of using a traditional glass cell with several mL of electrolytic buffer, we placed a droplet of 50 µL containing all electrolytic buffer and samples between 3 electrodes to minimize the volume and prevent wasting the DNA and enzyme materials (Figure 34B). All potentials were referred to the Ag/AgCl (3 M KCl) electrode, and all measurements were carried out at a scan rate of 100 mV/s.

With the Cystamine forming self-assembled monolayer by covalent thiol-Au bond, electrode fouling was prevented, and well-defined oxidation peak of NADH molecule was exhibited on Cyclic voltammograms (Figure 35A) at 0.75V. Peak current increased linearly with higher NADH concentration (0, 100, 200, 300, 400, 500 µM). Amperometric detection of NADH was performed at a fixed potential of 0.75V. From the I-t curve, current was stable with the same concentration of NADH and immediately increase when adding higher concentration of NADH (200, 400, 600, 800, 1000 µM).

Amperometric response of both free enzyme and enzyme-DNA tile assembled structures were tested with the presence of saturated level of substrates (1mM NAD^+, 10 mM glucose 6-phosphate in 100 mM sodium phosphate buffer, pH 8.0. Current remained close to 0 when adding both NAD^+ and G6p and started increasing immediately adding 20 nM free G6pDH/

G6pDH-tile, total volume was 50 µL. With same concentration of free G6pDH and G6pDH-tile complex, comparable level of current was obtained, indicating that with single enzyme, DNA tile assembly didn't inhibit enzyme activity. Current was maintained at same level for at least 2000s.

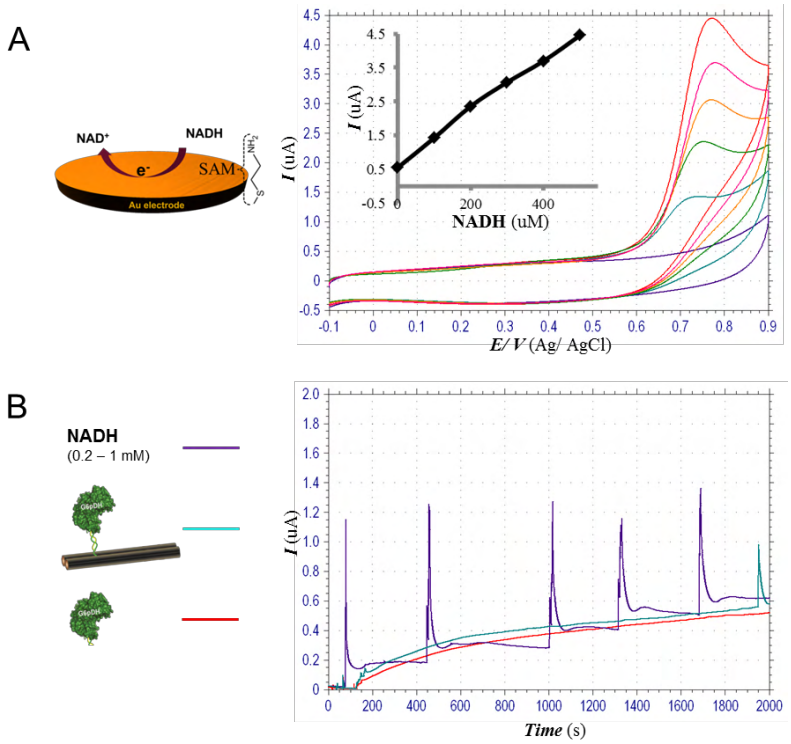


Figure 35. Electrochemical measurements of NADH molecule and G6pDH-DNA complex on Au electrode. (A) Cyclic voltammograms with different NADH concentration (0, 100, 200, 300, 400, 500 µM), the peak around 0.75 V corresponding to oxidation of NADH. Inset shows the corresponding calibration plot. Buffer: 100 mM $NaNO_3$, pH 7.5; (B) I-t curve adding different concentration (200, 400, 600, 800, 1000 µM) of NADH (purple), I-t curve with 20 nM of free G6pDH, 1mM NAD+ and 1 mM G6p (glucose 6-phosphate) (red), and I-t curve with 20 nM of G6pDH-DNA complex,1mM NAD+ and 10 mM G6p (saturated substrates). Buffer: 100 mM sodium phosphate, pH 8.0.

2. Assembly of DNA tile-methanol pathway dehydrogenases complexes:

ADH, FALDH and FDH –DNA conjugates were purified as described above (Figure 3). The assembly of single enzyme-tile complexes was evaluated by 3% native gel (Figure 33B). Yield of ADH, FALDH and FDH- tile assembly was estimated to be > 80% from band intensity.

2. Summery and Future Direction:

We have succeeded in detecting electron transfer with model system (G6pDH-tile) on gold electrode. Site-specific DNA conjugation on expressed Halo-ADH, Halo-FALDH and Halo-FDH was developed and purity was tested. We measured the activity of each enzyme and successfully assembled the DNA labeled proteins with DX tile. For the future plan, assembly of enzyme pair and all 3 enzymes need to be optimized. Then we will be able to compare assembled 3 enzyme cascade versus free system by electrochemistry and conventional activity measurement.

Photosynthetic Pathway

Construction of the photosynthetic pathway

1. Design concept:

We are constructing artificial photosynthetic pathways that contain three different elements (Figure 36): (1) a DNA scaffold to arrange the components. These origami structures are designed so that light harvesting and electron transfer components can be attached in specific positions. (2) Light harvesting pigments for the initial absorption of energy. Typically, we incorporate two fluorophores that absorb light between 600 - 750 nm into the nanostructure. Additional fluorophores can be added to span the entire visible to near IR region, resulting in a more continuous absorption and/or to make it tunable for different applications (adapted to different light conditions). The selected fluorophores are normally arranged such that dyes with higher excited state energies (absorbing at shorter wavelength) are distal to the reaction center and those with lower energies (longer wavelength) are proximal. (3) The photosynthetic reaction center from the purple non sulfur photosynthetic bacterium *Rhodobacter sphaeroides* is also attached to perform charge separation. The reaction center is a pigment-protein complex that uses light energy to power a series of electron transfer reactions resulting in a charge-separated state that ultimately drives trans-membrane proton translocation in natural systems.

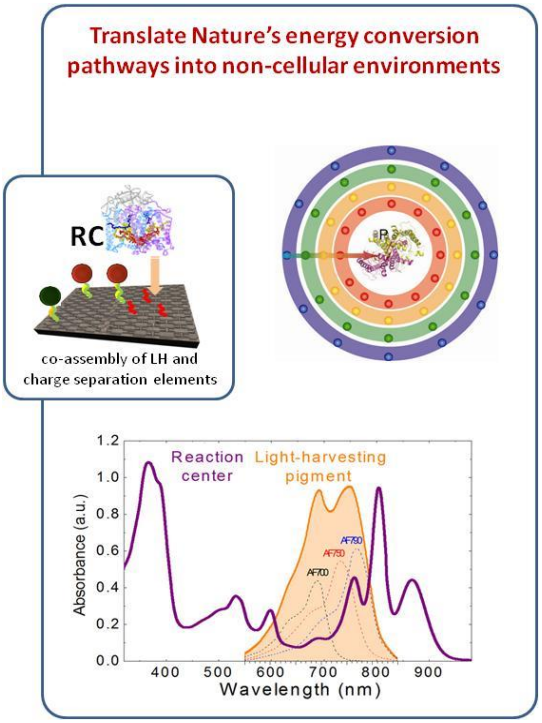


Figure 36. Design concept: (upper-left) engineer a light-harvesting system using nanostructured DNA scaffolds by placing antenna molecules and a photosynthetic reaction center complex at specific positions for precise geometric control. (Upper-panel) one of the proposed arrangements. Colors represent the excited state energies of the dye molecules in each ring from higher energy (blue) to lower energy (red) allowing the absorbed photons to be funneled to the reaction center protein located at the center of the ring. (Lower panel) an example of the absorption spectra of selected dye molecules, relative to that of the reaction center. This should result in greater spectral coverage of light harvesting.

2. Assembled a DNA-templated light-harvesting system which contains multiple dyes and is capable of efficient energy transfer (three-arm-DNA-dye):

This goal of this subproject is to create an ideal artificial light harvesting system that facilitates spectrally uniform light absorption, efficient energy transfer and improved photo-stability, as compared to the natural system. While the ultimate objective is to place a set of fluorophores in known positions relative to the photosynthetic reaction center using a nanostructured DNA scaffold to form a network, we first constructed an antenna complex assembled with a pair of dyes attached to a DNA structure that enhances the spectral coverage (in terms of absorbance cross-section). Two different pairs of DNA-conjugated chromophores are used in this study: either Cy3 and Cy5, or Alexa Fluor 660 and Alexa Fluor 750. Cy3 acts as the donor and Cy5 as the acceptor in the first pair, and AF660

acts as the donor and AF750 as the acceptor in the second pair. The fluorophores were chosen so that there is significant spectral overlap between the emission of the dyes and the absorption of the RC to facilitate efficient energy transfer, and so that there is a substantial increase in the absorption cross section in the spectral regions where the absorbance of RC alone is low. The three-arm DNA structure was designed to assemble the two dye molecules in a geometrically defined manner and to avoid chemical modification of any DNA strands with more than one dye (to reduce cost and synthetic complexity). Two of the strands (Strand-2 and -3, Figure 37) in the three-arm DNA contain the dye molecules, and the other one (Strand-1, Figure 37) is designed to conjugate to the RC through a covalent cross-link.

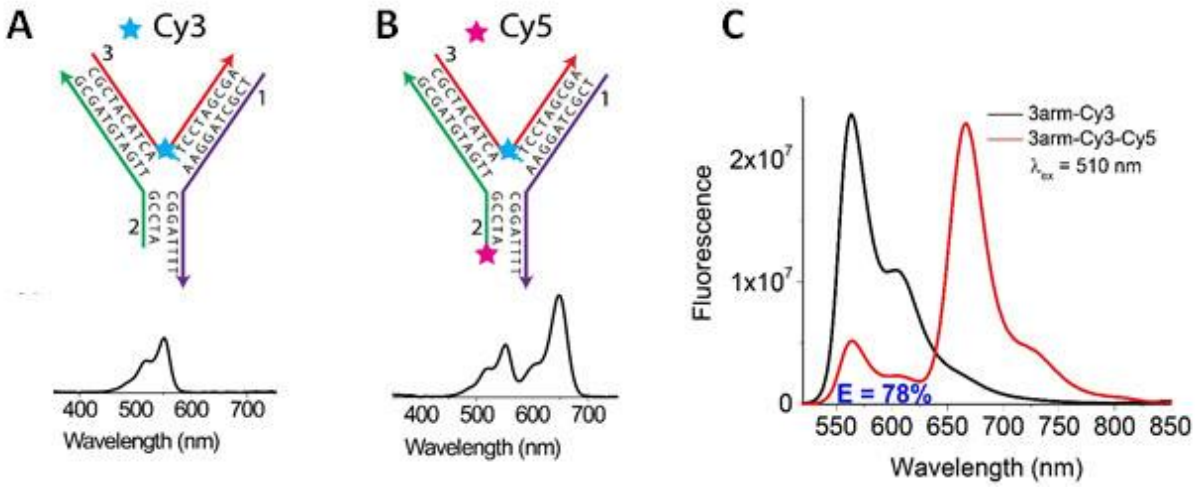


Figure 37. An assembly of DNA-dye complexes and the absorption spectra for samples (A) with only Cy3 dye molecule, (B) with Cy3 and Cy5 molecules. (C) fluorescence emission spectra of assembly (A, black)) and (B, red) shown efficient energy transfer from Cy3 to Cy5. Excitation is at 510 nm, which excites Cy3 exclusively.

Figure 37 illustrates the structure of DNA-templated dye complexes with (panel A) Cy3 alone and (panel B) both Cy3 and Cy5 dyes**.** Figure 37 (panel C) compares the fluorescence emission spectra from the constructs in panels (A) and (B), both using excitation of Cy3 exclusively (510 nm). An efficient energy transfer from Cy3 to Cy5 of nearly 80% is shown. These results from the three-arm DNA nanostructure show the ability of a DNA scaffold to organize multiple dye molecules, resulting in a geometrically programmable model system mimicking a natural photosynthetic light harvesting apparatus.

3. Engineering reaction center protein-DNA-dye conjugates (DNA-dye-RC):

The primary focus of this work is the design and construction of an energy conversion system based on a photosynthetic reaction center, but using additional dye molecules to achieve broad spectral coverage (improve the spectral range of the absorbance cross-section). The enhancement of light-harvesting using the 3arm-DNA-multi-dye complex as an antenna was examined by monitoring charge separation in the reaction center, which can use excitation energy received from the light harvesting DNA-dye complex to drive charge separation with a quantum efficiency of nearly 100%.

Conjugation of the reaction center protein to the DNA-dye nanostructure is shown in Figure 38

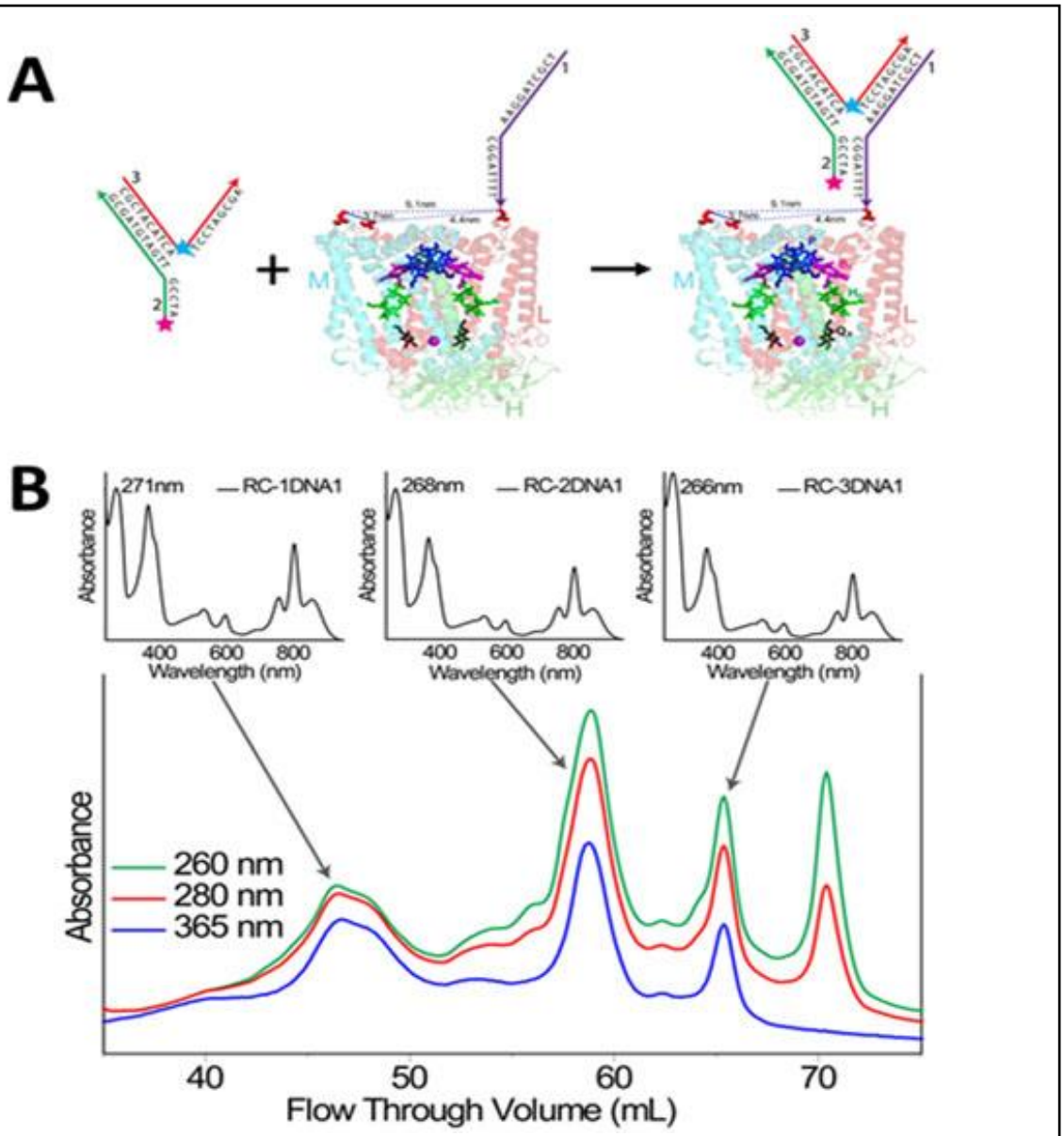


Figure 38. (A) Assembly of DNA-dye and reaction center conjugates. (B) FPLC chromatographic trace of DNA (Strand-1) conjugated RCs. Chromatographs at 260 nm (green), 280 nm (red) and 365 nm (blue) are shown. The absorbance bands at 260 nm and 280 nm are from both RC and DNA, whereas the absorbance band at 365 nm is from the RC only. The fractions from each of the peaks were collected separately and their respective absorbance spectra measured. The UV absorbance maxima for the first, second and third peaks in the chromatograph are at 271 nm, 268 nm and 266 nm, respectively, with a relative increase in the absorbance intensity (compared to the absorbance peak at 800 nm), which shows that there are different ratios of DNA conjugated to the RC (DNA:RC = 1:1, 2:1 and 3:1). The right-most peak in the chromatograph has no absorbance at 365 nm, indicating it is free ssDNA.

(panel A). We used the same triple mutant of the *Rhodobacter sphaeroides* strain 2.4.1 (PDB 1AIG) reaction center as the one used for direct dye-reaction center conjugation reported in 2013 (REF). The genetically modified reaction center contains three cysteine residues at positions M100, L72 and L274, all located on the surface of the reaction center protein and available for conjugating with DNA-strand-1 (Figure 38, panel A). The 3'-Amine modified Strand-1 was conjugated to these Cys residues of the RC using a SPDP (N-succinimidyl 3-(2-pyridyldithio)

propionate) cross-linker, and the conjugate was subsequently purified by fast protein liquid chromatography (FPLC). The first three peaks on the FPLC trace shown in Figure 38 (panel B) represent conjugates with different DNA/protein ratios, i.e. one, two or three DNA strands conjugated to the RC, respectively. This assignment was based on the UV-VIS absorbance spectra of the fractions and the extinction coefficients of the DNA and the RC. The last peak in the chromatograph has no absorbance at 365 nm (the Soret absorbance band of the RC), indicating that it is likely excess free ssDNA. Dye-labeled Strand-2 and -3 are then allowed to hybridize to the purified Strand 1-conjugated-RC to create 3arm-RC conjugates with one, two or three 3-arm junctions on each RC. The DNA with either Cy3 dye alone or Cy3 and Cy5 dyes and the ratio of DNA-to-reaction center are listed in Table 2.

Dye	Sample	Abbreviation	3arm/RC
Cy3/Cy5	3arm-Cy3-RC(1DNA)	1C	0.75 ±0.05
	3arm-Cy3-RC(2DNA)	2C	1.65 ±0.05
	3arm-Cy3-RC(3DNA)	3C	2.35 ±0.05
	3arm-Cy3-Cy5-RC(1DNA)	1CC	0.8 ±0
	3arm-Cy3-Cy5-RC(2DNA)	2CC	1.65 ±0.05
	3arm-Cy3-Cy5-RC(3DNA)	3CC	2.2 ±0.1
AF660/AF750	3arm-660-RC(1DNA)	1-6	0.85 ±0.15
	3arm-660-RC(2DNA)	2-6	1.6 ±0
	3arm-660-RC(3DNA)	3-6	2.15 ±0.05
	3arm-660-750-RC(1DNA)	1-6-7	0.9 ±0.1
	3arm-660-750-RC(2DNA)	2-6-7	1.65 ±0.05
	3arm-660-750-RC(3DNA)	3-6-7	2.0 ±0.1

Table 2. DNA-to-RC ratio of different constructs

Characterization of Excitation Energy Transfer in DNA-dye-reaction center constructs

1. Absorption cross-section of reaction center complexes enhanced by the addition of DNA-dye light-harvesting antenna:

The total absorbance cross section of the reaction center is greatly enhanced by attaching the DNA-dye complexes to the reaction center. Figure 39 illustrates the increase in absorbance in the visible region of the spectrum where the dye molecules absorb strongly. DNA conjugated with one dye (upper panels) and two dyes (lower panels) are compared.

This work demonstrates that using DNA as a template, multiple dye molecules can be incorporated into an antenna complex to serve as an external light-harvesting complex to collect light with a desired spectral distribution.

2. Energy transfer efficiency in different DNA-dye-reaction center constructs:

The Förster resonance energy transfer process for each construct was investigated using both steady-state and time-resolved fluorescence spectroscopy. The free 3arm-DNA constructs with their respective dye(s) attached (without the RC) were used as reference samples for these

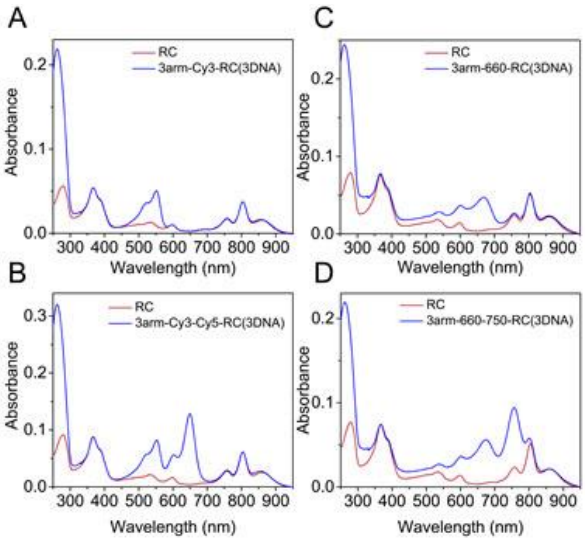


Figure 39. Absorption spectra of the 3arm-dye-RC constructs. (A) 3arm-Cy3-RC(3DNA) or **3C**, (B) 3arm-Cy3-Cy5-RC(3DNA) or **3CC**, (C) 3arm-660-RC(3DNA) or **3-6** and (D) 3arm-660-750-RC(3DNA) or **3-6-7**. Abbreviations are defined in Table 2. The spectrum of RC alone (red trace) is included in each panel for comparison.

experiments. Upon exciting **1C** at 510 nm (see Table 2 for the definition of abbreviations), 42% of the Cy3 emission was quenched compared to that of 3arm-Cy3, presumably due to energy transfer from Cy3 to the RC. In the case of **1CC**, there was an 83% decrease in Cy3 emission intensity compared to that of 3arm-Cy3. The greater decrease in fluorescence of Cy3 when Cy5 was present is attributed to the summation of multiple energy transfer pathways, which include a direct energy transfer from Cy3 to RC and a stepwise energy transfer from Cy3 to Cy5 to the RC. The same construct shows a 51% decrease in total fluorescence intensity integrated from 520 nm to 850 nm, compared with that of the 3arm-Cy3-Cy5 alone with no RC (Figure 40). On excitation of Cy5 at 620 nm, the direct FRET efficiency of Cy5 to the RC is 58%, using the emission of the 3arm-Cy3-Cy5 as a reference with the same excitation.

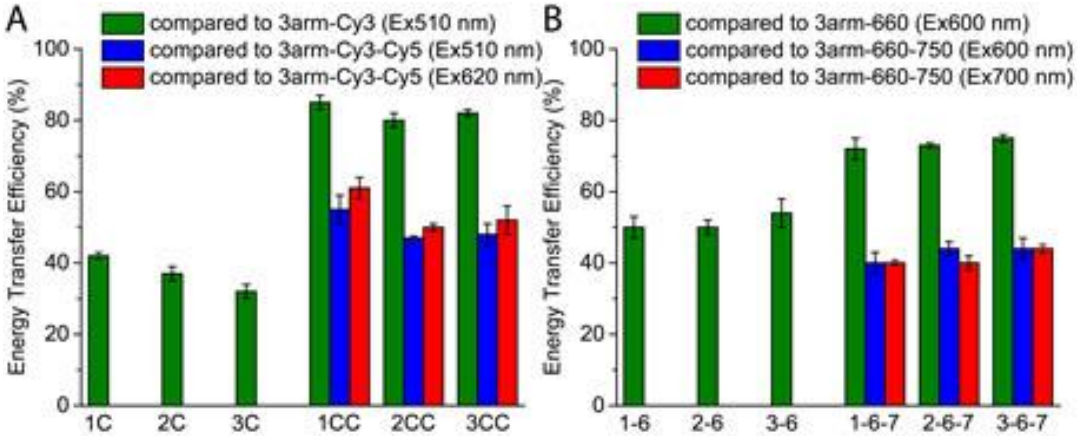


Figure 40. Energy transfer efficiency of 3arm-DNA conjugated RCs calculated from steady-state data. (A) **1C**, **2C**, **3C**, **1CC**, **2CC** and **3CC**. (B) **1-6**, **2-6**, **3-6**, **1-6-7**, **2-6-7** and **3-6-7**. (See Table 1 for a definition of the abbreviations.) The green bars show energy transfer efficiency calculated by comparing fluorescence from the RC containing complex with that from the 3arm-DNA consisting of only the initial energy transfer donor, which is either Cy3 or AF660. The blue and red bars are energy transfer values calculated using the 3arm-DNA consisting both the dyes (Cy3-Cy5 or AF660-AF750) without the RC attached as the fluorescence reference. The Blue bar results from direct excitation of the initial energy transfer donor (Cy3 or AF660). The red bar results from direct excitation of the intermediate energy transfer dye (Cy5 or AF750).

Similar experiments were performed on all the other 3arm-dye-RC constructs, and the energy

transfer efficiency values are shown in Figure 40. Samples with different ratios of 3arm-dye conjugate to RC (such as 1C, 2C and 3C, or 1-6, 2-6 and 3-6) all yielded similar energy transfer efficiency values. This is due to the fact that although there are multiple dye molecules on the assembled structures, the probability of exciting more than one dye associated with a RC at a time is very low due to the continuous nature and low intensity of the excitation light. Moreover, as expected, the efficiency of energy transfer from AF650 to the RC is higher than the efficiency of Cy3 transfer to the RC. This is presumably due to the greater spectral overlap between the emission of AF660 and the absorbance of the RC compared to Cy3. However, even though AF750 has a greater spectral overlap with the RC than does Cy5, it has lower energy transfer efficiency to the RC than Cy5 does, and this results in a higher overall energy transfer efficiency of the Cy3-Cy5 pair to the RC than the AF660-AF750 pair. We have observed similar phenomena earlier, and the reason is the low intrinsic lifetime of AF750 compared to that of Cy5.

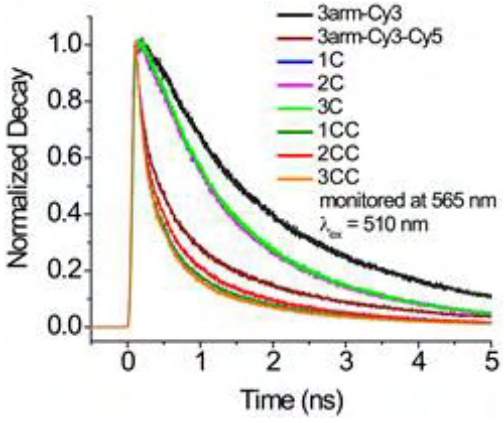


Figure 41. Cy3 fluorescence decay profile of free 3arm-DNA and 3arm-DNA conjugated to the RC in various ratios, with either constructs containing Cy3 alone (**1C**, **2C**, **3C**) or constructs with both Cy3 and Cy5 (**1CC**, **2CC**, **3CC**), monitored at 565 nm (λ_{ex} = 510 nm).

Time-resolved fluorescence analysis was performed using time-correlated single-photon counting (TCSPC) (Figure 41) excited by a pulsed laser and fitted with a multi-exponential decay function. The amplitude-weighted average lifetimes that resulted were 1.79 ns for Cy3, 1.65 ns for Cy5, 1.68 ns for AF660, and 0.64 ns for AF750. A substantial increase in the fluorescence decay rate is seen with the RC conjugates (average lifetimes of 3C and 3CC are ~1.17 ns and ~0.25 ns, respectively). This follows the same trend as the steady-state energy transfer measurements and again implies that a significant amount of energy transfer takes place from the dye to the RC. Similar decay patterns were observed for the Alexa Fluor dye sets. Starting with the lifetime data for the dyes alone (without RCs) or one dye with the RC, the rate constants for the various component processes can be determined as described in the supplemental material. In particular, the rate constant for the decay of Cy3 in the absence of Cy5 or the RC is 0.55 ns-1, the rate constant for energy transfer from Cy3 to the RC is 0.39 ns-1, and the rate constant for energy transfer from Cy3 to Cy5 is calculated to be 1.45 ns-1. If one uses the rate constants for these individual processes to predict the decay lifetime of Cy3 in the fully assembled complex (1CC), it is calculated to be 0.42 ns, whereas the experimental average lifetime is 0.28 ns. Similarly for 1-6-7, the calculated decay lifetime of AF660 is 0.92 ns, whereas the experimentally observed lifetime is 0.90 ns. The approximate agreement of the decay times for the full nanostructures based on the kinetic constants estimated for individual component reactions indicates that the experimental measurements are internally consistent with each other, and consistent with an overall picture of step-wise energy transfer.

Further evidence of a stepwise energy transfer process is provided by the rise in the emission of Cy5 and AF750 in the TCSPC experiment, upon excitation of Cy3 and AF660, respectively, in the two-dye complexes. This is due to the energy transfer from the initial donor (Cy3 or AF660)

to the intermediate dye (Cy5 or AF750), which results in an initial increase in the excited-state population of the intermediate. A comparison of the average lifetimes of the dyes in the 3arm-RC constructs vs. that in the 3arm-only constructs result in estimated energy-transfer efficiencies from the dye to the RC, which are in reasonable agreement with the results obtained from the steady-state fluorescence intensity measurements. Like the steady-state measurements, similar energy-transfer efficiencies are observed for samples with different numbers of DNA-dye constructs per RC. Again, in the case of time-resolved measurements, higher energy-transfer efficiency is observed for constructs that contain Cy5 compared to AF750, even though the fluorescence spectrum of AF750 overlaps better with the absorbance of the RC than does Cy5. This is because AF750 has a shorter excited state lifetime (0.64 ns) than does Cy5 (1.64 ns), giving the Cy5 excited state a greater probability of transferring energy to the RC before decaying by other pathways. Similar results were obtained previously when dye molecules with different lifetimes were conjugated directly to the RC.

3. Characterization of formation of the charge separated state:

Once the bacteriochlorophyll dimer, P, is excited either directly or via energy transfer from the surrounding light harvesting molecules, it transfers an electron via a monomer bacteriochlorophyll (BA) to a bacteriopheophytin (HA) in a few picoseconds. This is followed by a 200-ps electron transfer to the first of two quinones, QA, and finally to a second quinone, QB, in 200 μs. Because charge separation in the RC has almost unity yield, the amount of charge separation that takes place correlates with the energy transfer efficiency. The relative amount of charge separation in the RC was investigated by measuring the light-minus-dark difference absorbance spectra of the different dye-DNA-RC complexes. The light-minus-dark difference spectra were obtained by subtracting the absorbance spectrum of a sample taken in the dark from the absorbance spectrum taken under continuous illumination at 550 nm (Cy3 abosrbance peak, 10 nm bandwidth). The light intensity at 550 nm was kept low enough to ensure the light-minus-dark signals changed linearly with the light energy absorbed.

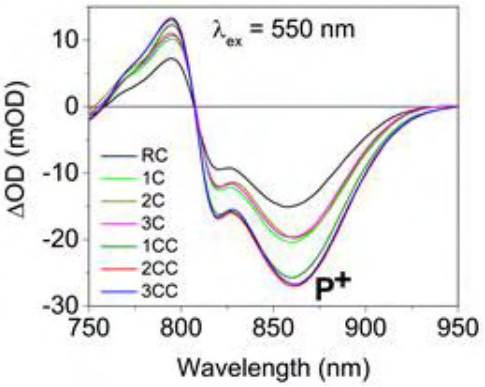


Figure 42. Light-minus-dark difference absorbance spectra of RCs with and without conjugation to a 3arm DNA nanostructure-dye complex.

A 1.3 fold absorbance change at 862 nm (reflecting P^+ formation) was observed for **3C** compared to the RC alone, implying enhanced charge separated state formation due to the increased absorbance cross section at 550 nm, confirming that photons absorbed by Cy3 result in energy transfer to RC cofactors (Figure G). Similarly, **3CC** shows a 1.8 fold enhancement in P^+ formation over unconjugated RCs. The enhanced P^+ formation in **3CC** compared to **3C** presumably results from the higher efficiency of energy transfer from Cy3 to Cy5 to RC compared to direct Cy3 to RC transfer (Figure 42). The insertion of Cy5 between Cy3 and the reaction center results in two relatively efficient transfer steps (better spectral overlap and shorter distance) compared to the single Cy3 to RC transfer. Like the energy transfer efficiency results obtained from both the steady state and the time resolved fluorescence measurements, the relative intensity of P^+ formation is similar for samples with different numbers of 3arm DNA

nanostructures conjugated to each RC (i.e., **1C**, **2C** and **3C** vs. **1CC**, **2CC** and **3CC**).

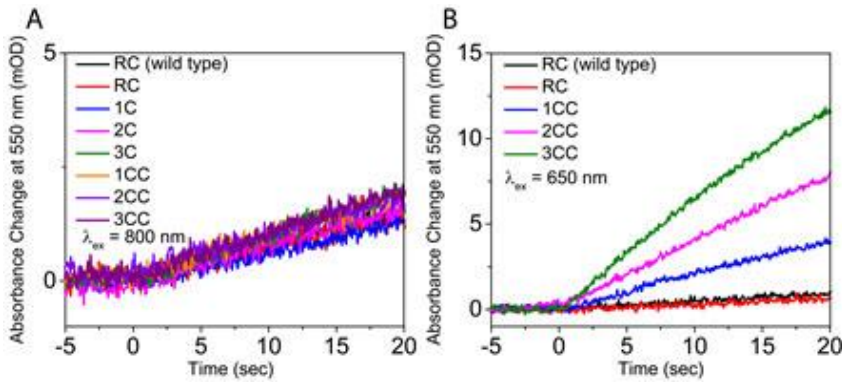


Figure 43. Cytochrome *c* oxidation monitored at 550 nm (where the difference in absorbance between reduced and oxidized cytochrome *c* is maximal) after exciting the RC directly at 800 nm (A) or Cy5 directly at 650 nm (B). Each of the samples shows very similar kinetics upon excitation at 800 nm, which indicates that the presence of the DNA structure on the RC does not affect the ability of cytochrome *c* to transfer electrons to the RC, at least when the cytochrome is in excess. In contrast, excitation at 650 nm where Cy5 absorbs, results in a rate of cytochrome *c* oxidation that depends on the number of Cy5 molecules (and thus the absorption cross-section at 650 nm) associated with the complex, with the rate for **3CC** being greatest.

In the natural system, the RC operates in conjunction with the cytochrome bc_1 complex, cytochrome c_2, and a quinone pool, to convert light energy into a proton motive force. In this process, the oxidized initial electron donor of the RC, P^+, that is formed upon light-driven electron transfer is subsequently reduced by cytochrome c_2, which docks to the periplasmic face (P side) of the RC. In our artificial antenna system, the 3arm-DNA structures are located on the P side of RC, and so one might expect that this conjugation of DNA close to the docking site of cytochrome would hinder cytochrome binding as well as the electron transfer process from cytochrome to P^+. To explore this possibility, a 10-fold molar excess of reduced cytochrome *c* and a 100-fold molar excess of decylubiquinone were added into a solution of 3arm DNA-dye-RC constructs, and the absorbance intensity change at 550 nm (an absorbance decrease at this wavelength reflects the oxidation of cytochrome *c*) was measured, while either exciting the RC directly or the dye directly. Using 800 nm excitation (direct excitation of the RC), where both the Cy3 and Cy5 have no absorbance, the wild type RC, the Cys-modified RC , and the RC conjugated with the DNA-dye construct all showed similar rates of cytochrome *c* oxidation (Figure 43 (panel A**)**). Apparently, DNA conjugation does not hinder the rate of cytochrome electron transfer to the RC, at least at these concentrations. Moreover, upon 650 nm excitation (Cy5 excitation peak), the DNA-dye conjugated RC showed a much faster rate of oxidation then did the Cys-modified RC or wild type RC, both of which have very low absorbance at 650 nm (Figure 43 (panel B)). Under these conditions, the oxidation rate of cytochrome *c* depends on the number of dye molecules in the construct. This presumably results from the enhanced absorbance cross-section of the light harvesting antenna that increases the number of photons absorbed per unit time by the 3arm DNA-dye-RC complex. Since the spectrum of reduced cytochrome *c* overlaps strongly with that of Cy3, similar measurements using 550 nm excitation were not attempted as they would have been ambiguous.

In summary, a DNA nanostructure with dyes attached at specific positions was conjugated to a RC to serve as a geometrically defined light harvesting antenna. This extended the absorbance cross section of the complex into a spectral range where the RC has only weak absorbance. A combination of placement, spectral properties and excited state kinetic properties of the dyes used are important in determining the efficiency of the antenna in energy transfer. At low light

flux, the rate of photon capture by the complex is proportional to the number of dye molecules in the complex that absorb at the excitation wavelength; thus increasing the number of DNA-dye constructs attached to the reaction center increases the functional cross section but does not greatly change the energy transfer efficiency. The complexes explored in this work provide useful model systems for future applications in nanophotonics.

Construction of antenna-reaction center network on large DNA arrays

1. Design and assembly of a photosynthetic network using dye molecules as the light-harvesting components:

To facilitate nanoscale photonic applications more broadly, the construction of artificial antenna systems that provide controllable geometry and stoichiometry represent the next objective of this research, i.e. assemble an antenna network. The ultimate goal is to develop a network with high efficiency of photon collection and energy transfer to the reaction center. The Bathe group has performed simulations that provide guidelines and insights for the design of such systems (Figure 48).

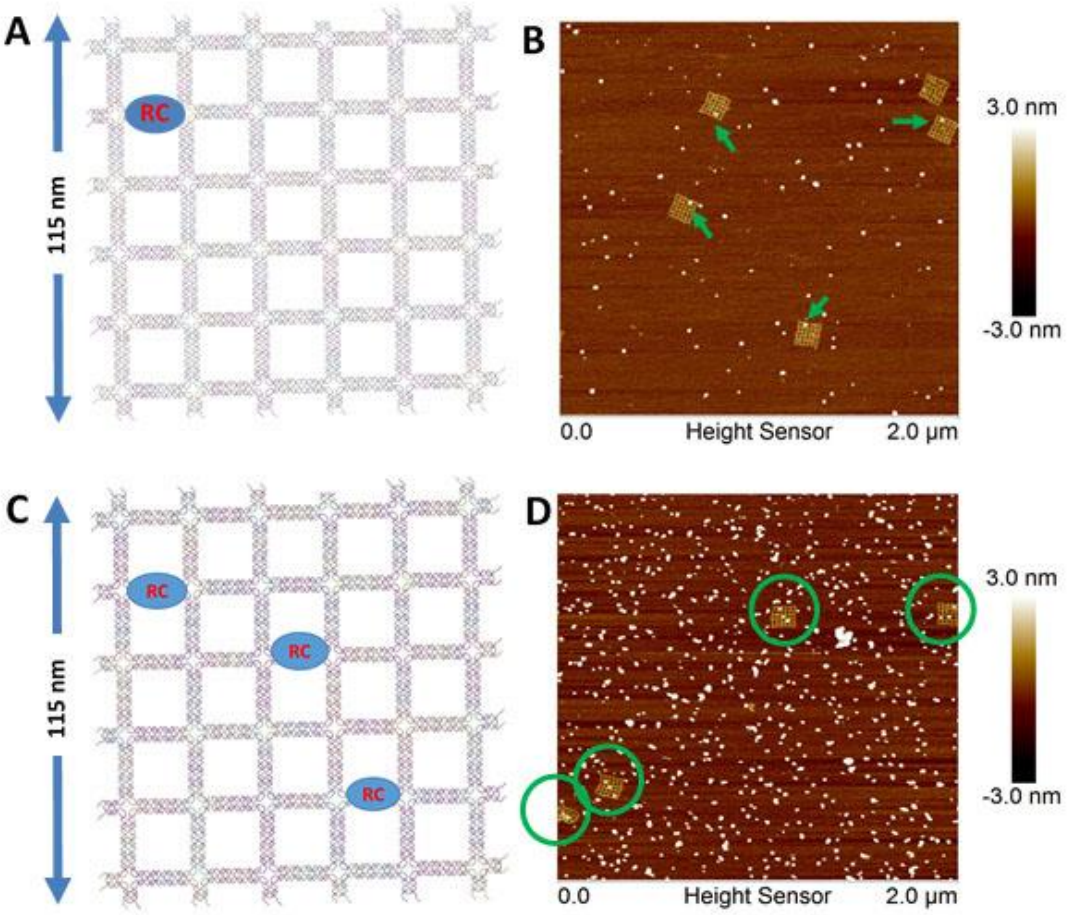


Figure 44. Schematic of origami with location(s) of RC binding probe for (A) single RC-origami construct and (C) triple RC-origami construct. Origami dimension is 115 nm X 115 nm. (B) AFM images of (C) Ni-affinity column purified single RC-origami conjugate and (D) Ni-affinity column purified triple RC-origami conjugate. All the images are 2um x 2um in dimension.

The first step of this project is to design a large DNA tile, which can be used as the foundation to affix the reaction center protein and dye molecules to in order to explore the effect of specific arrangements on light-harvesting function.

We first constructed a 2D DNA origami comprised of 4x4 tiles, which is used as a template to organize reaction center proteins. Initially, to optimize the conditions for RC-origami conjugation and to optimize the purification method, we designed both a single and a triple RC-origami construct (Figure 44A and B). An amine modified ssDNA (5'-TCGCTAGGAACGGATTTT-amine-3') was first conjugated to the RC using SPDP chemistry and then the RC-DNA construct was conjugated to the origami having probe strand complementary to the one on RC. For single RC and triple RC constructs we have one and three probes, respectively at designed location.

The quality of the assembled systems was characterized by Atomic Force Microscope (AFM), as shown in Figure 44C and D) for single and triple reaction center constructs, respectively. The AFM image of the purified DNA origami alone shows very high yield (more than 60%), and the structure has the desired shape and size. Upon conjugation with the RC, the single RC-origami construct shows significant yield, but the sample contains free origami and free RC, which must be removed before spectroscopy can be reliably performed. We attempted this by using a Ni-sepharose affinity column. The Ni^{2+} binds to a poly-histidine tag incorporated in the RC, so both the free RC and the RC-origami conjugate are separated from free origami. We also studied a triple RC-origami construct, and after purification we observed that all of the origami has RCs specifically associated with them (indicated by green arrows in Figure 44 (panel C) for one RC/DNA tile, and green circles for three RCs/DNA tile in Figure 44 (panel D)). But for both the cases, single and triple RC-origami constructs, we observed excess of free RC, which can interfere in future experiments. To remove the excess RC, we propose to use a biotin-conjugated DNA tile for purification. Five biotin molecules will be incorporated into the origami, and after removing free origami using the Ni-sepharose approach described above, we will use avidin to bind to and purify the RC/DNA tiles away from free RCs resulting in pure RC-origami constructs.

2. <u>Assembling hybrid light-harvesting systems containing both natural antenna complexes and dye molecules:</u>

Another project designed to create a light-harvesting system with enhanced capability involves constructing a hybrid structure using both a nature antenna and selected dye molecules, organized on a DNA scaffold. This approach should provide a broader range of antenna components than either a purely biological and purely artificial light harvesting approach.

(1) Modifying the natural light harvesting /reaction center (LH1-RC) complex for attachment to the DNA tile: the main aim of this project is use a DNA directed assembly to show that we can provide nanoscale control over the position, orientation and organization of light harvesting components. This should allow us to better study and understand the process of light capture as well as build more complex arrays of multiple LH components. To date, detailed investigations into the function of natural light harvesting systems are limited by the geometries that Nature provides; the detailed positions of the complexes in relation to each other is not under our control.

The objective is to build a DNA structure that will allow us to explore in more detail how the geometry of these light-harvesting components affects the ability to capture and transfer light energy.

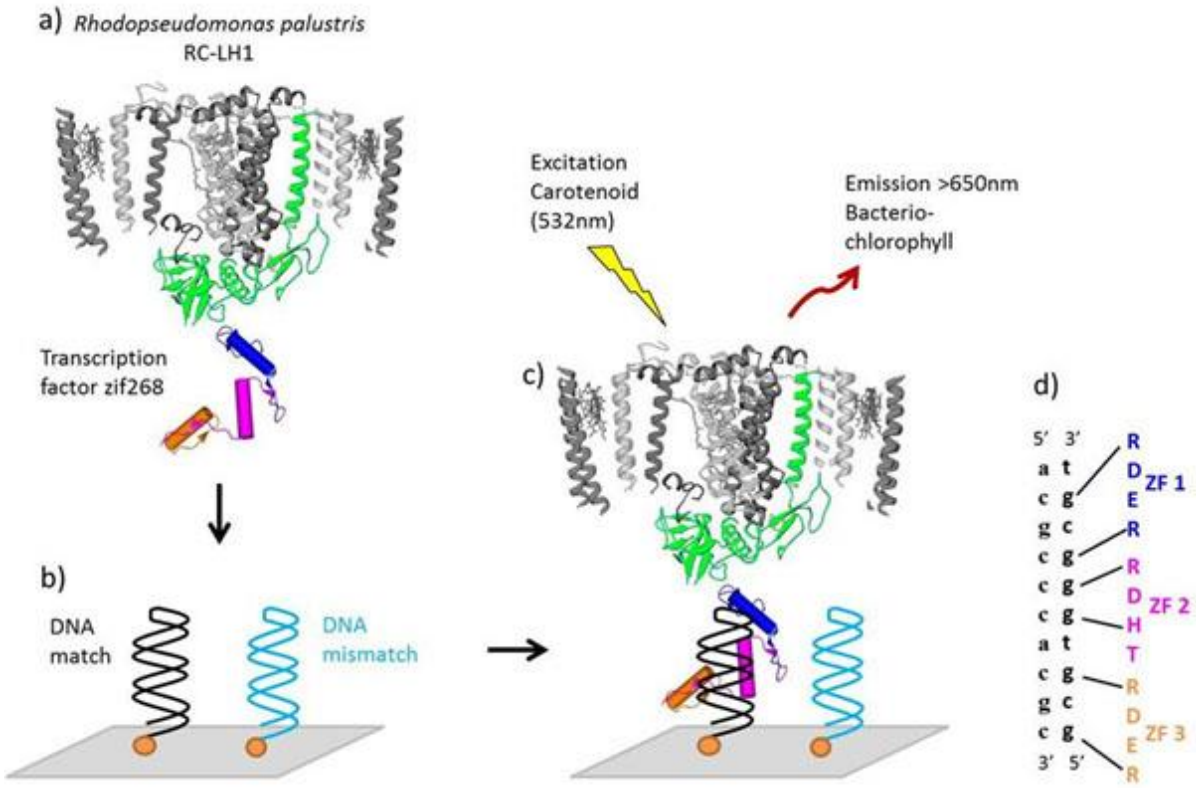


Figure 45. (a) Structure of the RC-LH1 from Rps. Palustris (shown in grey) with the H-subunit highlighted in green within the plane of the membrane. The 3 zinc finger (ZF) motifs of zif268 are shown in blue, pink and orange and are attached to the H-subunit by a short linker sequence of 39bp (linker not shown). (b) Immobilization of dsDNA by the formation of a triazole between cyclooctyne modified-DNA and an azide-modified surface. (c) Excitation Energy Transfer was measured between the carotenoid and bacteriochlorophyll pigments. (d) The 11bp DNA ZF recognition sequence and the residues for each ZF motif which form attachments.

A modified photosynthetic reaction center which includes a DNA binding zinc finger motif was constructed by our collaborators in Prof. Richard Cogdell's Lab in the University of Glasgow, UK (Figure 45). The zinc finger motif binds a 12bp nucleotide sequence on a DNA nanostructure which can be immobilized on a surface (Figure 45). Our first objective following this result is to demonstrate selective binding of the complete RC-LH1 complex (RC-LH1) to more complex DNA nanostructures. For this work a DNA origami tile has been designed and made containing 3 DNA probes able to bind the RC-LH1. In Prof. Richard Cogdell lab, University of Glasgow, a strain of *Rhodopsuedomonas (Rps.) palustris* was constructed in which a DNA binding domain was added to the H-subunit of the RC. This DNA binding domain confers binding to dsDNA with a specific sequence (Figure 46).

(2) Arranging multiple Light-Harvesting (LH) complexes and dye molecules on DNA nanostructure: the objective for this part of the project is to arrange multiple Light-Harvesting

(LH) complexes with different spectroscopic properties at defined positions and distances in relation to each other (Figure 46). This will allow us to engineer directionality of the energy transfer down an energy gradient towards the reaction center. Dyes and fluorophores could also be incorporated to expand the spectrum available for light-harvesting.

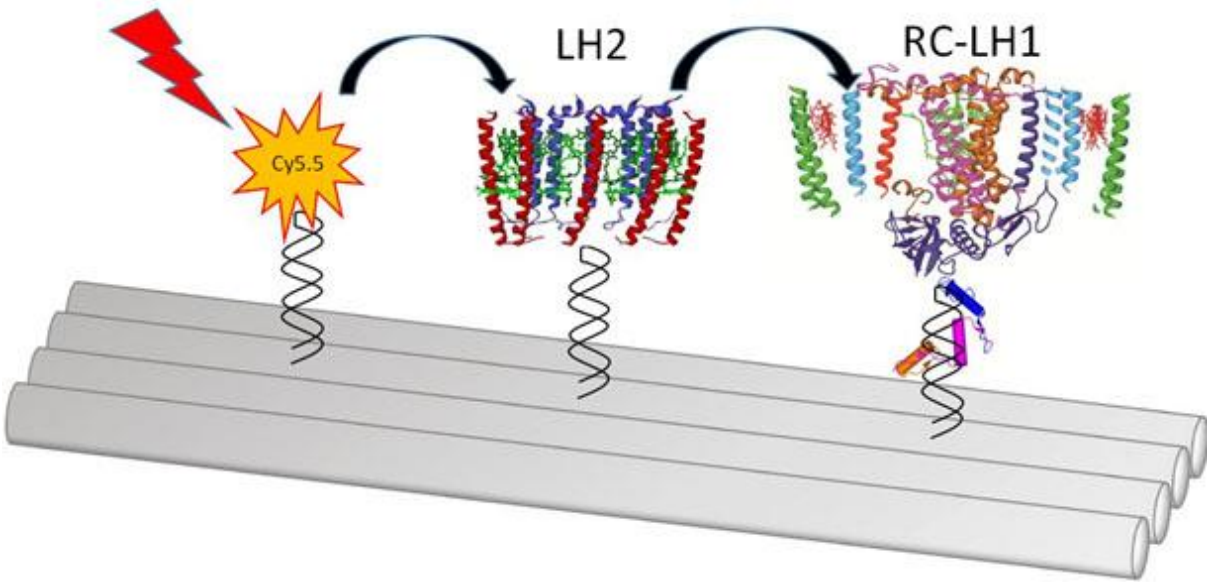


Figure 46. The RC-LH1 is attached to DNA though the addition of a DNA binding domain (transcription factor zif268) which selectively binds to a specific 12 bp nucleotide sequence (see Figure K for more detail). The LH2 complexes will be attached to the DNA by either a polyhistidine tag or by incorporating a specific cysteine (depending on the complex used). This allows for arrays to be engineered in which the distance, orientation and ratio of complexes to be controlled with nanoscale precision. It will also be possible to incorporate fluorophores and artificial dyes for the purpose of increasing the spectrum for light capture, if necessary.

Currently work is underway to make new strains of purple photosynthetic bacteria in which the LH2 complexes are modified with either a polyhistidine tag or an accessible cysteine for assembly into the complex. Two different LH2 complexes have been selected for use that have different absorption spectra in order to build an array of multiple LH complexes. The strains are created by making a tagged copy of the wild type gene which is cloned into a suicide vector. This vector is then transferred into the purple bacterial cells by conjugation and the tagged LH2 gene swapped into the genome replacing the wild type gene through homologous recombination. Currently three new strains are being made; LH2 with Bchl absorption peaks at 800 and 850 (B800-B850) from *Rhodobacter sphaeroides*, LH2 with Bchl peaks at 800 and 820 nm (B800-B820) from *Rps. palustris*, and a RC-LH1 complex that does not contain carotenoid from *Rps. Palustris.*

(3) Constructing a large scale antenna network and extending it to three dimensions: we are further extending the photosynthetic networks described above toward a design that mimics the stacked biological membranes of Nature. To accomplish this, we intend to assemble a DNA-directed photosynthetic structure in 3 dimensions. Presently photosynthetic arrays have only been built in 2D by organizing LH complexes onto surfaces, limiting the amount of photons able to be captured in a single structure. One way to increase the potential for light harvesting would be to build an ordered system in 3 dimensions, organizing the LH complexes in layers. There are

two strategies for this, either DNA origami layers, or a self-assembling DNA tile.

To test the binding of the protein to a higher order DNA assembly, we have designed and constructed a 4x4 DNA origami grid which has been modified to introduce a DNA probe containing the 12bp recognition sequence for the zinc-finger modified RC-LH1 shown in Figure K. The DNA has been visualized by AFM (Figure 47). Currently the focus is on optimizing the binding and purification of the RC-LH1 complex. The complexes created will be analyzed using the kinds of spectroscopic approaches described above that have been applied to the simpler systems constructed thus far.

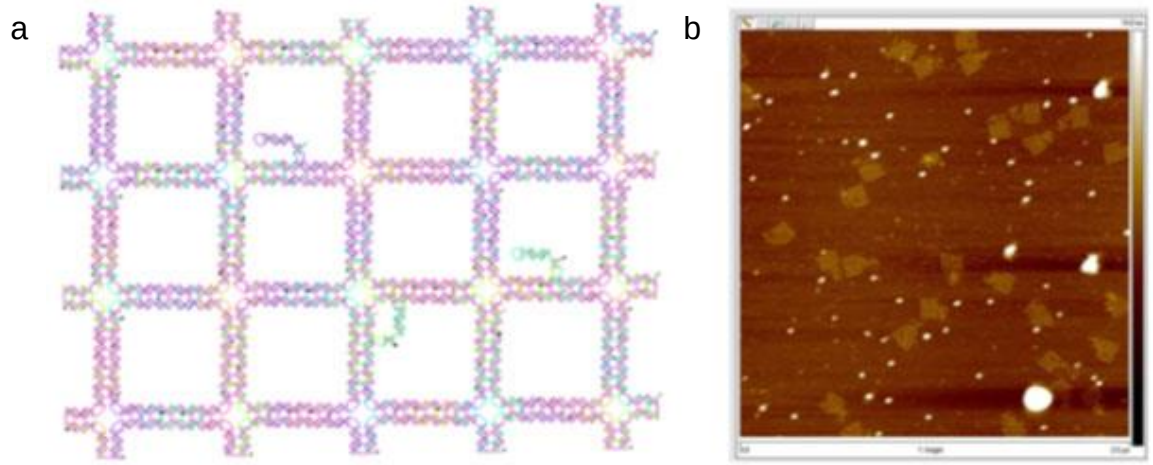


Figure 47. (a) Schematic diagram of the DNA origami 4x4 structure containing the 3 DNA binding probes for the attachment of the RC-LH1 complex. Each square within the origami grid is ~20nm on a side, roughly matching the diameter of the RC-LH1 complex. (b) An AFM showing the DNA structure. Optimization of RC-LH1 binding is on-going.

Computational Design and Simulation of Light-harvesting Antennas

1. Lattice-based model for the optimization of light-harvesting antenna:

Building on the multi-FRET-based computational modeling tool previously developed and published within the MURI project, we sought to understand and optimize the energy funneling and transfer from a collection of dyes and reaction center disposed on an addressable crystal lattice made from DNA that acts as a molecular pegboard. This tool provides the capability to rationally design light-harvesting antennas by suggesting optimal compositions and spatial arrangements of chromophores needed to maximize energy transfer to the reaction center under given irradiation conditions. The software optimizes the exciton transfer to the reaction center by iteratively choosing dyes from a library provided by the user and positioning them on the DNA lattice. A Monte-Carlo minimization scheme is used to explore the search space and optimize the geometry and composition of the dyes assembly (Figure 48a and b).

Results show that the optimal configuration of dyes around the reaction center strongly depends on the irradiation spectrum and lattice geometry. Interestingly, optimal configurations include funneling features that are also presents in natural light-harvesting antenna systems such as the

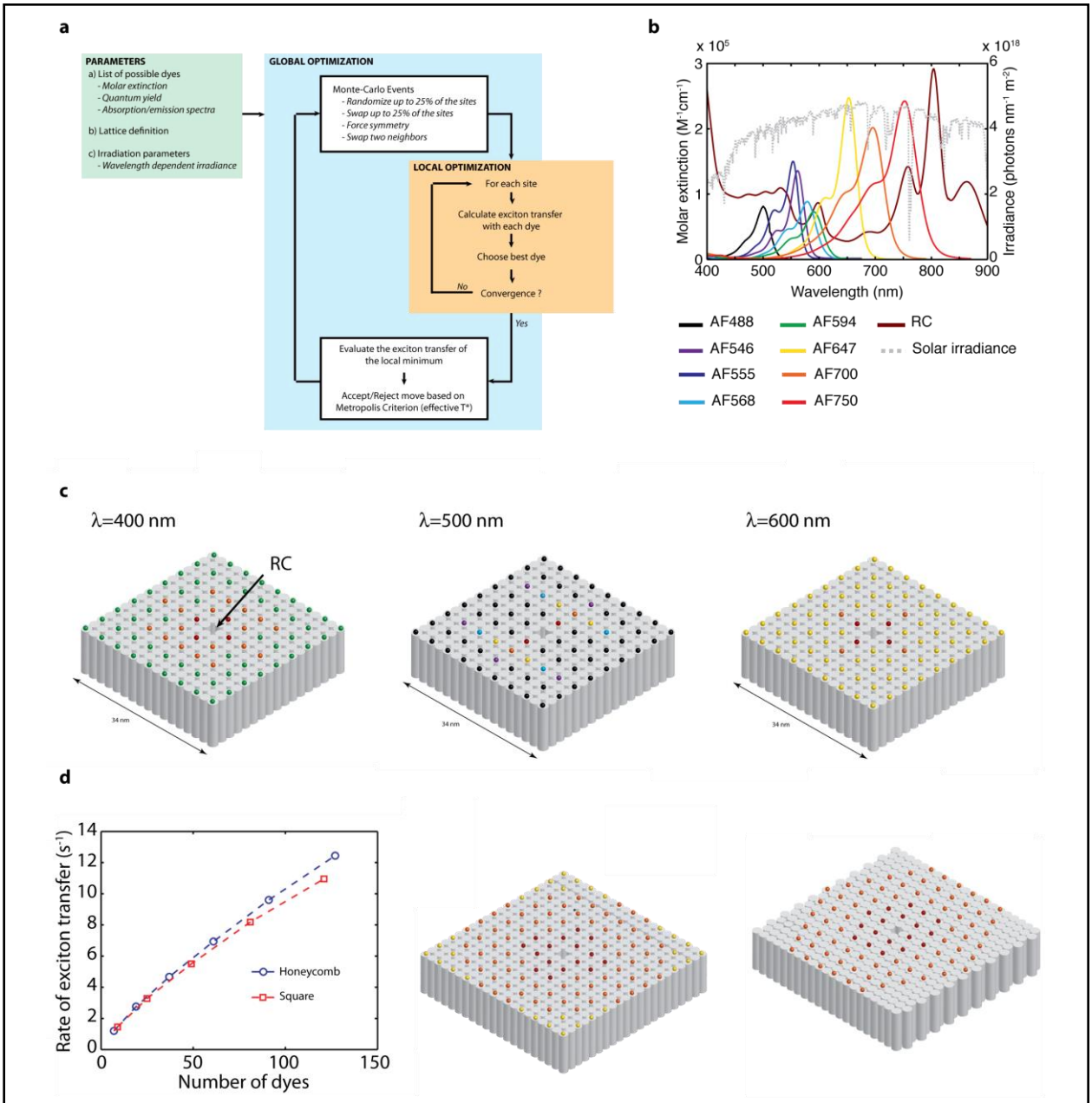


Figure 48. Lattice-based model for designing light-harvesting antenna. (a) Optimization algorithm. (b) Dye library used for the study. Solar irradiance spectrum is shown in light grey. (c) Optimal design on square lattice for 3 different irradiation wavelengths. (d) Optimal design yielding a rate of exciton transfer that matches the reaction center turn-around time. The irradiation spectrum corresponds to the solar spectrum, with a total irradiance of 4 W/m^2.

purple bacterium photosynthetic complex (Figure 48c). Total irradiance also affects the theoretical optimal design if we require the rate of exciton transfer to match the reaction center turn-around time (~100 ms). The optimal configuration maximizes the transfer efficiency as the number of dyes is increased to reach the absorption cross-section required to meet the prescribed exciton transfer rate. Results show that a hexagonal lattice offers better performance compared with a square lattice because it of the correspondingly higher packing density of chromophores (Figure 48d).

Next steps include the incorporation of multiple reaction centers on the lattice, as well as extending the model to more complex 3D designs. In addition, as experimental data from the lattice-based antenna becomes available, the present model can be used to help understand which aspects of the experimental system are performing according to design specifications, which will offer feedback to the multi-chromophore antenna design. Further, extension of this computationally efficient lattice-based model to the investigation of the organization of individual protein-dyes complexes such as the LH1 and LH2 systems from purple bacterium on DNA lattices will offer the opportunity to study excitonic energy transfer in hybrid protein-DNA multi-chromophore systems.

2. Computational modeling of highly packed DNA-dye complexes:

Natural light-harvesting antennas are typically composed of high-density chromophore assemblies that are highly organized structurally (position and orientation) at the nanometer-scale. The corresponding small inter-dye distances involve the emergence of quantum effects that strongly influence the optical and exciton transfer properties of these multi-chromophore dye assemblies. Recent studies on natural light-harvesting systems suggest that these quantum effects contribute substantially to their high efficiency. Thus, in order to maximize the energy transfer efficiency and light-harvesting capacity of DNA-based antennas our modeling needs to capture energy transfer physics that accounts for these highly packed chromophore organizations.

The preceding FRET-based model is unable to capture exciton dynamics for such systems. Thus, we are developing an open quantum-system based QM/MM framework to calculate exciton transfer in high-density DNA-dyes assemblies (Figure 49). This model is based on an extension to the 3D structural modeling tool CanDo (Computer-aided engineering for DNA origami, http://cando.dna-origami.org), which employs the finite element method to efficiently predict 3D structure of high molecular weight DNA origami assemblies.

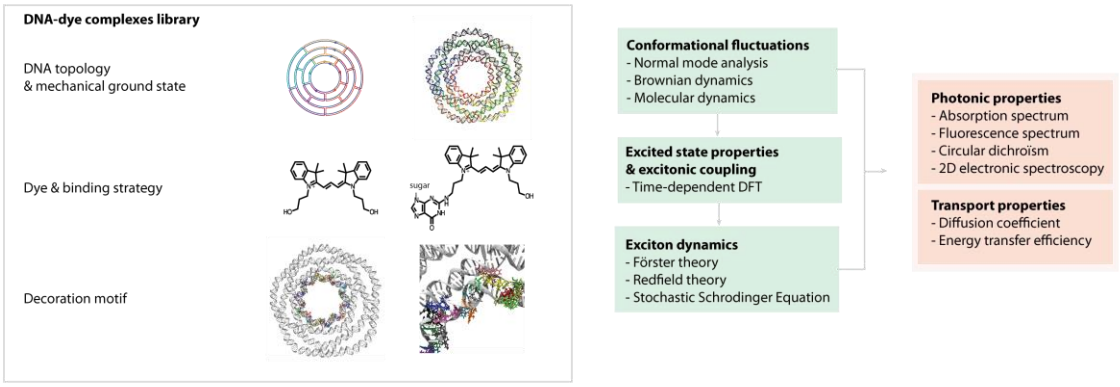


Figure 49. Structure-based excitonic modeling framework for densely packed multi-chromophore DNA-scaffolded assemblies

Molecular mechanics is used to dock and covalently attach dyes to the DNA scaffold, which is subsequently relaxed accounting for detailed atomic interactions. Long time-scale conformational fluctuations of the DNA-dye complexes are computed using a combination of normal mode analysis, a Brownian Dynamics simulation platform previously developed in the MURI project, and all-atom molecular dynamics. Quantum chemistry methods including TD-

DFT (Time Dependent Density Functional Theory), is used to calculate the excited-state properties of each dye and their inter-dye couplings. Exciton transport is subsequently calculated using methods derived from open quantum theory, including the Redfield and stochastic Schrödinger equations. Resulting spectroscopic and transport properties are finally then computed (Figure 49).

As a pilot project to validate our framework, we are currently studying the excitonic properties of (1) a short 19 bases DNA duplex scaffolded with six dyes and (2) a 4-ring DNA origami with a size comparable to the LH2 natural light-harvesting system. Preliminary results illustrate the onset of quantum coherence effects when Cy3-modified guanine bases are included at strategic places in the DNA origami structure. Further studies are required to fully characterize these structures.

In addition to completing the preceding validation study, future steps include experimental validation of the computational model on the wire system and extension to other DNA-dyes complexes aside from the four-ring structure that mimics the LH1/LH2 ringlike chromophore arrangements in purple bacterium. Our objective is to generate a library of distinct DNA origami structures, dyes, binding strategies, and binding motifs to explore in silico optimal multi-chromophore organizations that best mimic natural multi-chomophore organizations and their light-harvesting properties. This framework will provide our experimental collaborators with rapid feedback on the identification of interesting candidate assemblies to pursue synthesis and characterization of, as well as to interpret corresponding results.

Toward the production of materials to transfer bioelectroactive and photoelectrochemical pathways to external platforms

1. Fabrication of nanoporous transparent metal oxide (TCO) films:

Nanoporous materials are three-dimensional architectures with high internal surface areas that are ideal to house DNA origami nanostructures *if* they satisfy the stringent requirements for the proposed applications: they must be transparent so they do not obstruct irradiation of the (photo)electrochemically active nanostructures, possess relatively large pore sizes to accommodate various DNA nanostructures, be mechanically rigid, have good electrical conductivity, possess surfaces that can be easily functionalized by organic cross-linkers, and be inexpensive to manufacture in large quantities.

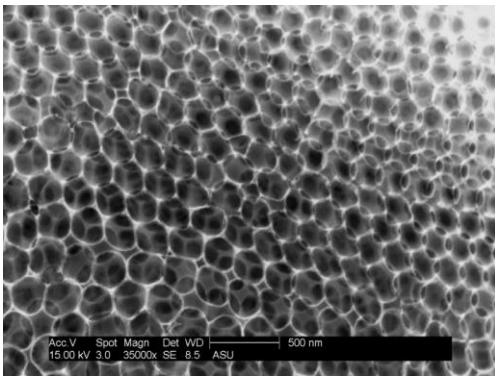


Figure 50. Scanning electron micrograph of a macroporous ATO film. Scale bar = 500 nm.

Despite the availability of diverse synthetic methods for nanoporous metal oxides in the literature, successful application of those methods for our purpose has been hampered by the fact that they employ a relatively "dilute" aqueous solution of the metal precursors, and that such a synthetic condition frequently results in pore closing at the top surface of the films and also severe cracking and peeling-off of the entire film layers, during later synthetic steps of drying

and calcination. These problems were particularly challenging for the inverse opal methods where self-assembled opal structures of polymer nanobeads are used as macropore templates. Despite our initial success described in the last year's report (Figure 50), the method has not resulted in sturdy films of transparent conducting Sb-doped tin oxide (ATO).

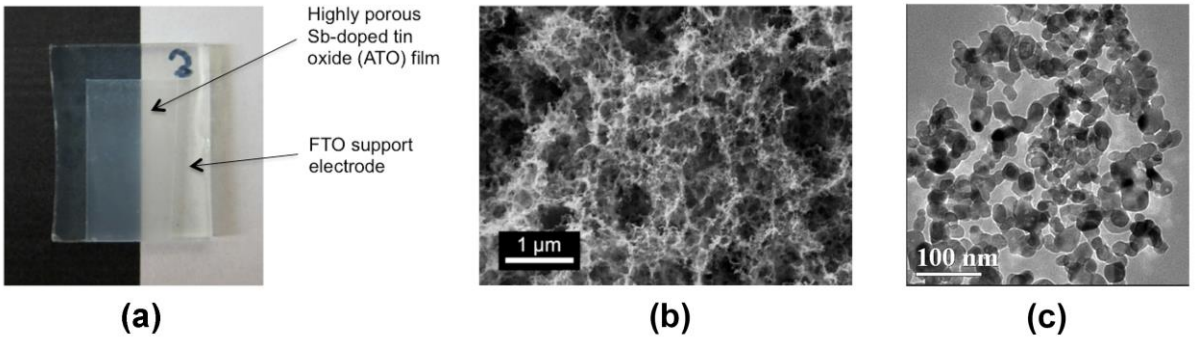


Figure 51. (a) Photograph and (b) scanning electron micrograph of the crack-free large-area ATO film (~1×2 cm^2) on FTO glass, which was produced by using carbon black shown in (c) as a hard template.

The breakthrough came about recently when we employed carbon black nanoporous aggregates as a "crack-preventing" hard template for macroporous TCO films. The rigid fractal structure of carbon black particles provides the precursor solution a viscosity required for doctor-blading, upon mixing. When the particles are controlled to be physically in contact, the resulting three-dimensional network structure of the fractal particles retains its structural rigidity, withstanding the capillary pressure during drying. Furthermore, the textural mesopores within the carbon black aggregates act as the structural template for the three-dimensional macroporous structure of the final metal oxide film. In Figure 51a, the photograph of the film indicates the uniformity of the film on the FTO backing electrode. The film is somewhat transparent but becomes much more transparent in aqueous solutions due to a better refractive index matching. The scanning electron micrograph in Figure 51b shows the nature of the random three-dimensional porous structure of the film in which textural pores in the range from 100 nm to a micron are aplenty for impregnation of DNA-enzyme cascades. Finer structural features in the network are the nature of the negative replica of the mesopore network of the carbon black template shown in Figure 51c.

2. <u>Fabrication of thionated reduced graphene oxides and their films</u>:

We have continued to explore the chemistry of thiol-functionalized reduced graphene oxides (called "mercapto reduced graphene oxides (m-RGOs)" hereafter; shown in Figure 52 and to examine the electrochemical properties of m-RGO Langmuir-Blodgett (LB) films. The high theoretical surface area (close to 2600 m^2/g), chemically modifiable surfaces and structural flexibility of graphene monolayers are quite attractive in effectively accommodating a large number of DNA structures. Unlike the typical RGOs which contain only oxygen-functional groups, the m-RGOs contain a large number

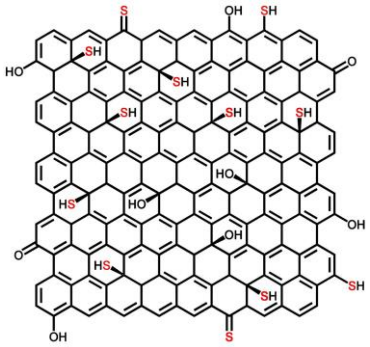


Figure 52. Schematic diagram of mercapto reduced graphene oxides (m-RGOs).

of free thiols (about one SH group per nm^2 on each side of graphene sheet) and those thiols can participate in cross-linking reactions in a mild aqueous environment as demonstrated in our previous work.

As indicated in the last year's report, we were able to develop a rapid fabrication method for m-RGO LB films and demonstrated high electrical conductivities of their transparent films (transmittance > 90%). By expanding the developments, we have fabricated large-area LB films on Au electrode substrate, as shown in Figure 53a, and covalently functionalized the m-RGO surface with ferrocene (Figure 53b), a redox molecule. Importantly, the cross-linking reaction between ferrocenecarboxylic acid and the m-RGOs was found to be effective even without the need of any catalyst in the aqueous buffer solution. Cyclovoltammetric studies (Figure 53c) of the functionalized electrode indicate that there is an effective electron transfer between the covalently-bound ferrocene and the Au electrode through the m-RGO LB film. It is anticipated that the m-RGO LB films can serve as a robust charge transport medium that can covalently immobilize DNA nanostructures.

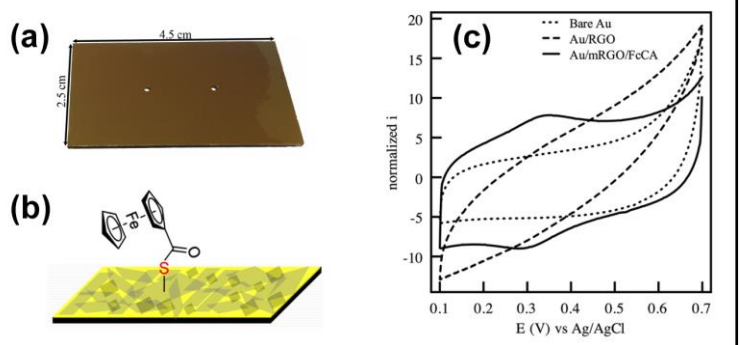


Figure 53. (a) Photograph of large-area m-RGO LB film on Au electrode. (b) Schematic diagram of ferrocene-functionalized m-RGO LB film on Au electrode and (c) the cyclovoltammograms of the film and the corresponding references (bare Au and RGO LB films on Au).

3. Future direction:

Having developed synthetic protocols for robust macroporous ATO films, Seo lab is currently examining their effectiveness in incorporation of DNA structures through collaborations with Yan's and Walter's labs. Our preliminary results indicate that the Mg^{2+} ions in the buffer solution may favorably affect the surface charge on the ATO surface, promoting the DNA adsorption. By using the recently acquired Zetasizer, we will perform systematic studies on the surface charge and point of zero charge (PZC) of the ATO as a function of Mg^{2+} ion concentration. The results will lead us to new information on the surface properties of ATO in a realistic solution environment where the DNA-enzyme cascades will function.

Deposition of DNA structures on m-RGO LB films on various substrates are in progress with the emphasis on possibility of selective binding of the DNA structures with the m-RGOs. Our preliminary results indicate that m-RGO sheets are strongly favored against soda glass, fused silica, silicon wafer and polymer but similar affinities were found for indium-doped tin oxide (ITO) and mica surface. Further studies will be carried out by using DNA structures functionalized with redox molecules and the result will elucidate the electron transferability through DNA nanostructures. To construct electrically conducting three-dimensional high-surface area structure of m-RGO/DNA nanostructures, we will also examine hybridization of the DNA structure and m-RGO single sheets in dispersion.

Translating Biochemical Pathways to Non-Cellular Environments

Principal Investigator: Hao Yan[1]
Co-PIs: Don Seo[1], Neal Woodbury[1], Mark Bathe[2], William Shih[3], Nils Walter[4], Jinglin Fu[5]

[1]Arizona State University, [2]MIT, [3]Harvard University, [4]U of Michigan, [5]Rutgers University

Reporting period: 8/01/14-7/31/15

I. Scientific and Technical Objectives

We intend to engineer and optimize nanoscale devices and systems based on important biochemical conversion pathways, where the converted species are molecules (enzymes transforming substrates into products), or energy, as is the case for photosynthesis. The use of DNA-directed assembly allows us to control and exploit the interactions between synthetic and naturally occurring bio-materials to produce highly functional biochemical conversion systems. Regarding enzyme transformations, our primary goal is to construct artificial enzyme cascades using two- and three-dimensional DNA structures as templates, and to study the ideal number of enzymes, relative distance, spatial arrangement, diffusion behavior, and reaction kinetics of the cascades in a controlled, non-cellular environment. Towards this goal, we initially focused on a representative DNA-templated GOx/HRP enzyme cascade. We will apply the results of the initial study toward the design of more complex, bioelectroactive, NAD dependent dehydrogenase pathways, with the ultimate goal of interfacing our systems with external conductive materials. We aimed to achieve the following objectives during this reporting period: (1) systematically evaluate DNA-scaffolded enzyme networks and pathways in various conditions, (2) investigate the conformational changes that occur in a DNA tweezer structure used for modulating enzyme activity, at the single-molecule and bulk levels, (3) organize proteins in 3D self-assembled DNA crystal lattice with precise position and orientation control, (4) characterize the yield of enzyme encapsulation and retention in 3-dimensional DNA nanocages, (5) engineer an artificial electron transport pathway organized by DNA nanoscaffolds facilitating the electron transfer via an increased redox potential gradient, (6) construct 3D-DNA nanostructure scaffolded lipid compartment as nanoscale reaction chambers. Our findings will ultimately be used to enhance local diffusion behavior, reaction kinetics, and the optical and electrical properties within the proposed devices, behavior that can be extended to other systems of interest to the DoD.

Regarding photosynthesis, our aim is to develop methods for translating energy conversion pathways to non-cellular environments where their functions can be more easily manipulated. The approach is to use rationally designed DNA nano-scaffolds to engineer light-harvesting networks containing synthetic pigments, interfaced with energy conversion proteins (photosynthetic reaction centers) from natural photosynthetic organisms. We intend to precisely position functional elements on the DNA scaffolds, generating energy and electron transfer pathways in which inter-molecular interactions can be predictably designed, and the local environment can be controlled. We hope to engineer systems with more uniform light absorption, efficient energy transfer and conversion, and improved photo-stability for maximum performance. Here, we have created an artificial light harvesting platform designed specifically to provide carefully controllable geometry and stoichiometry of dyes in an array format. The goal of this effort is to simulate, build and test

specific dye arrangements, and in this way iteratively develop the theoretical models needed to guide the design of more complex photonic systems in the future. We are also exploring ways to effectively interface the light-induced redox potentials generated by photosynthetic reaction centers from purple bacteria with novel nano and meso-structured electrode materials. Due to the prospect of using sun light as an energy source for bio-electroactive and photo-electrochemical bio-pathways, ideal materials that are transparent and electrically conducting, either fabricated as a film or coated on an electrode, are also being developed. Toward this end, two different types of materials were utilized: nanoporous transparent metal oxides and functionalized reduced graphene oxides. In line with DoD goals, the proposed research will increase our understanding of nanoscale energy transfer processes and aid in the development of robust strategies for the synthesis, characterization, and assembly of synthetic biochemical pathways for application in high-efficiency photo-energy generation, energy storage devices, sensors, or completely new capabilities that enhance war fighter and battle system capabilities.

II. Concise Accomplishments

Enzyme Pathway – We have: (a) constructed two-dimensional enzyme networks to mimic multi-enzyme network organized in cells to better understand how geometry affects enzyme network behaviors, (b) engineered an artificial multi-enzyme complex to facilitate highly efficient substrate transfer and regulate the direction of enzyme reactions, (c) designed a self-assembled DNA crystal to assist protein organization and precise control of the protein/enzyme in the 3-dimensional manner, (d) developed DNA nanocages for encapsulating enzymes with enhanced activity and stability, (e) developed a bioelectroactive electron-transport pathway organized by DNA scaffolds, (f) Rationally designed DNA tweezer for enhanced enzyme activity guided by single-molecule and computational analysis, (g) designed 2-track and 3-track DNA tiles and DNA walkers with different toehold lengths to investigate the mechanism of the walking process, and (h) constructed 3D-DNA nanostructure scaffolded lipid compartments.

Photosynthetic Pathway – We have (a) constructed DNA nanostructured photonic systems that enhance the light-harvesting capability of photosynthetic reaction centers, (b) constructed a photosynthetic network on a 2D DNA platform is to help simulate, build and test specific dye arrangements, and in this way iteratively develop the theoretical models needed to guide the design of more complex photonic systems, (c) effectively interfaced the light-induced redox potentials generated by photosynthetic reaction centers from purple bacteria with novel nano and meso-structured electrode materials, (d) explored experimental conditions required for optical control of a small orange carotenoid binding protein dissociation, and incorporating this proten into our DNA nanostructured phonic devices as a regulatory element, (e) used structure-based computational modeling to develop a highly programmable, rational means of controlling the targeted assembly and optical properties of excitonic circuits based on synthetic DNA, (f) demonstrated that the mRGO LB films can be an effective electrode to achieve selective deposition of DNA nanostructures through covalent cross-linking, providing bioelectroactive and photoelectrochemical pathways.

III. Expanded Accomplishments

Enzyme Pathway

Swinging arm channeled 2D protein array

1. Introduction:

Previously we have engineered a multi-enzyme complex utilizing a "swinging arm" to control substrate transfer between enzymes. Here we use the swinging arm system has a model to study

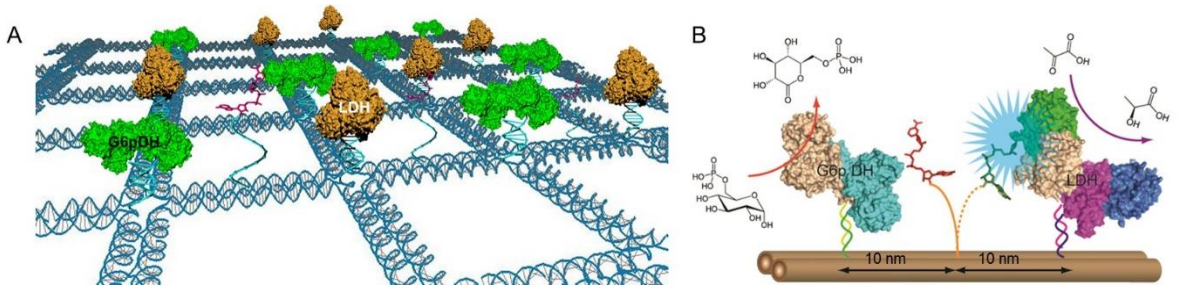


Figure 1. Schematic figure of (A) swinging arm based protein array using a square lattice like DNA origami. (B) single-particle swinging arm enzyme cascades consist of Glucose 6-phosphate dehydrogenase (G6pDH) and Lactate dehydrogenase (LDH).

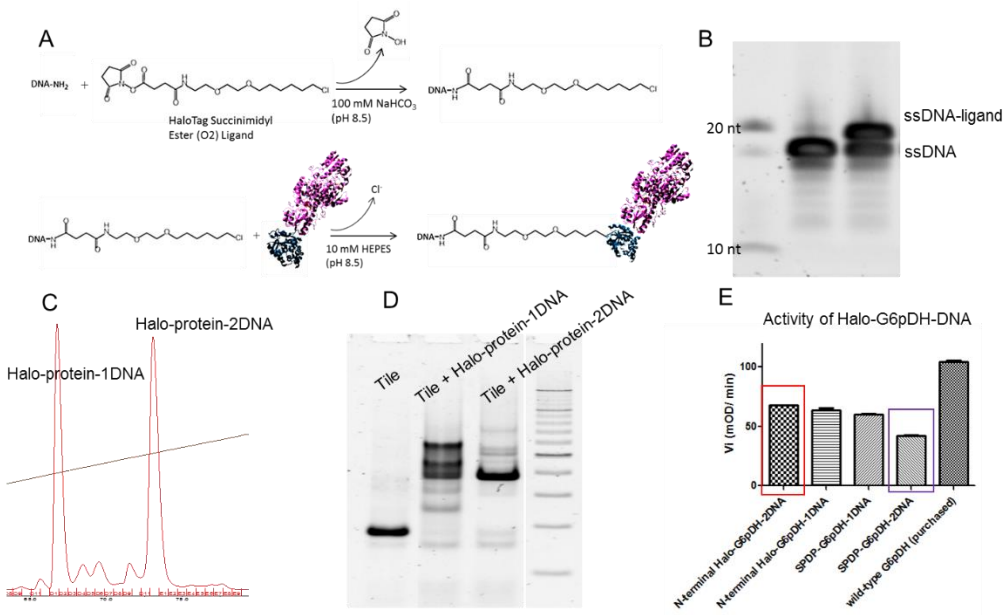


Figure 2. Site-specific Halo-tagged protein-DNA conjugation. (A) General scheme: First step, 100 µL of 10 mM HaloTag ® Succinimidyl Ester (O2) Ligand (purchased form Promega) was prepared in DMSO. 500 µL of 100 µM 5'amine-modified oligo was incubated with 20 fold excess Halotag ligand in 100 mM NaHCO3 (pH 8.5) for 2h. After reaction, excess Halotag-ligand was removed by washing with Amicon, 3 kD cutoff filters. The reaction yield was estimated to be ~50% from the band intensity between ssDNA and ssDNA-ligand conjugates. Second step, 500 µL of 40 µM enzyme solution was incubated with DNA-ligand conjugates in 10 mM sodium HEPES (pH 8.5) at room temperature for one hour, allowing halotag ligand reacting with Halotagged protein forming a covalent linkage; (B) 14% denaturing gel of unmodified single-stranded DNA (ssDNA, lane 1) and ssDNA-ligand conjugates (lane 2), yield is estimated to be ~50% from band intensity. (C) Anion-exchange FPLC purification of G6pDH-DNA conjugates. (D) Native gel characterization of DNA tile-protein assembly. Lane 1 to 3 of 3% native gel: DNA tile, tile assembled with purified G6pDH labeled with 1 DNA, and tile assembled with purified G6pDH labeled with 2 DNA. (E) Activity comparison of SPDP DNA-protein conjugation and halotagged protein-DNA conjugation of G6pDH. Assay condition: 2 nM G6pDH-DNA conjugates with 1 mM G6p and 1 mM NAD+ in 100 mM HEPES (pH 8).

how enzyme 2D network behaves compare to single-particle system, how does geometry affect the 2D enzyme network. Scaling up of the engineered multi-enzyme complexes better mimics the cell organization of multi-enzyme network.

2. Design and assembly of Swinging arm channeled 2D protein array:

We use a square latticed DNA origami recently developed by Yan lab as a scaffold, 8 of each proteins are assembled in the structure, NAD molecules are positioned between each protein, therefore 4 NAD arms are surrounding one protein instead of one in the single tile swinging arm design (Figure 1A). The anchor point of NAD swinging arm to both proteins are designed to be 10 nm. This origami with finite size is applied to mimic the infinite 2D array, but with better quantitate control. A DX DNA tile is used to assemble the single-particle swinging arm system, with the same distances between each components in the 2D system (Figure 1B)

To avoid the heterogeneity generated by multiple NAD-ssDNA conjugation, a double-stranded swinging arm is used with 30T hybridized with 25A, 5 A is used as ssDNA linker to give enough flexibility. As previously reported, the activity of the G6pDH-NAD^+ semi-swinging arm is enhanced after adding a $poly(A)_{15}$ strand to hybridize with the NAD^+-$poly(T)_{20}$ arm, so dsDNA swinging arm will not restrict the swinging.

To assemble the proteins we used the previously developed site-specific Halo-tagged protein-DNA conjugation. Figure 2A is a schematic illustration of the conjugation process. The N-terminal site-specific halotagged method achieved higher activity compared to random SPDP labeling. The assembly yield of origami-enzyme-NAD complex is characterized by both agarose gel and AFM imaging. The origami is purified to remove extra helper and then react with 5 fold excess enzymes and poly(T)25-NAD annealed at 37℃ for 30 mins. From the gel, band shift clearly showed the difference between origami, origami with G6pDH only, origami with both G6pDH and LDH (Figure 3A). Although the number of each enzyme on one origami scaffold is hard to quantify. Number of enzymes can be calculated from AFM imaging comparing origami with proteins and without, in average 7 to 8 enzymes are assembled on the

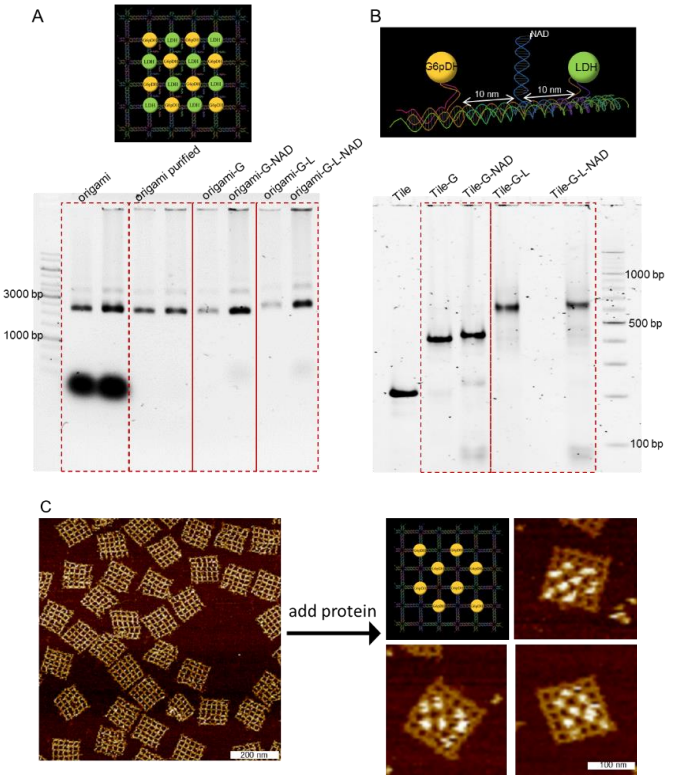


Figure 3. Assembly characterization of origami-enzyme-NAD and tile-enzyme-NAD complex. (A) 0.75% agarose gel of the assembled origami with 32 probes for 16 proteins (8 G6pDH and 8 LDH, 2 probes for each protein). (B) 3% nave PAGE of the tile assembled with G6pDH and LDH. (C) AFM imaging of origami scaffold only and origami assembled with 8 G6pDH. After adding one of the proteins it's possible to tell the assemble yield is acceptable (7 to 8 proteins on one origami).

scaffold (Figure 3C). The tile-enzyme-NAD complex is characterized with 3% native PAGE as previously described (Figure 3B).

3. Activity of Swinging arm channeled 2D protein array:

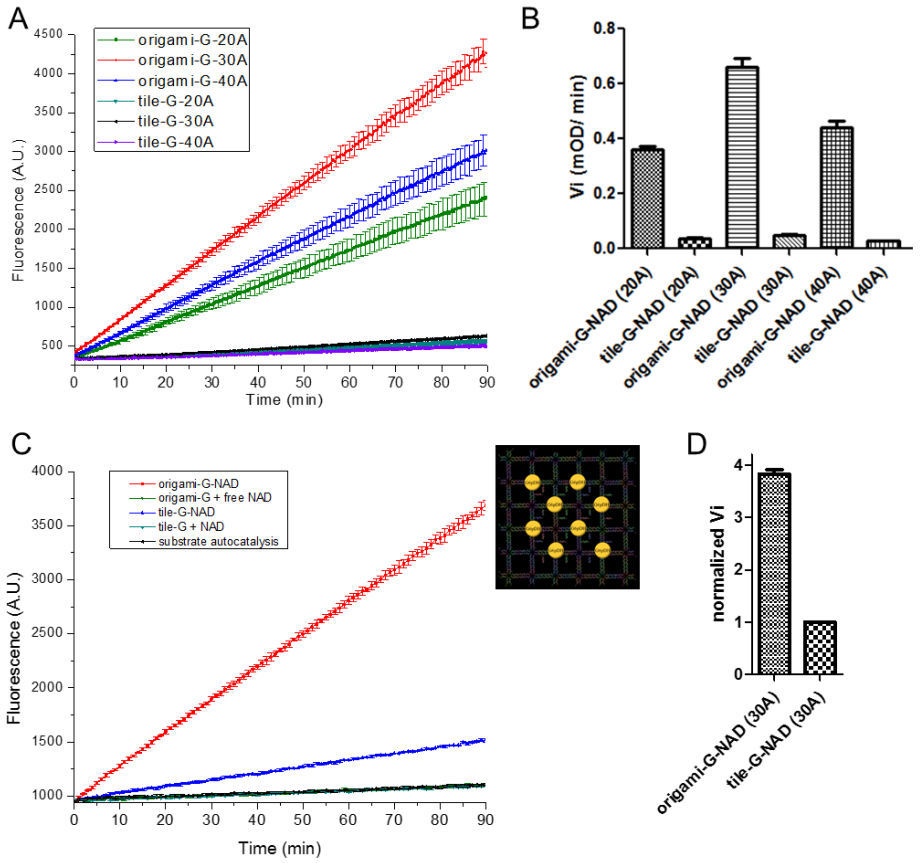


Figure 4. (A) Enzyme activity for origami and tile complexes in which the NAD+-modified arm is coupled to G6pDH with enzyme-NAD+-modified arm lengths of polyA$_{20}$-T$_{15}$, polyA$_{30}$-T$_{25}$, polyA$_{40}$-T$_{35}$, corresponding to 7 nm, 10 nm, and 13 nm; (B) histogram of activity; (C)Activity of origami compare to tile with optimal NAD arm length (~ 10 nm); (D) normalized activity shows 2D array has ~ 4 fold activity compared to single tile complex. Activity assayed with 500 µM resazurin and PMS in 1 × TBS buffer pH 7.5.

First, we evaluated the length dependency of both the 2D array system and single-tile system. The activities of the two designs were measured individually in bulk solution for three swinging arm lengths (polyA20-T15, polyA30-T25, polyA40-T35) using phenazine methosulfate (PMS) catalyzed resazurin fluorescence assays (Figure 4AB). As predicted, the arm with poly(A)30 resulted in the highest activity for both origami and tile, because the length matches the distance between enzymes and swinging arm (10 nm). With the optimal arm length, NAD+-modified swinging arm, origami-G6pDH-NAD+ assembly showed an activity enhancement of ~4-fold compared to tile-G6pDH-NAD+ with the same concentration of enzymes at 8 nM (Figure 4CD). The control samples with freely diffusing NAD+ shows little activity (almost same as substrate autocatalysis).

Next, using the optimized distance and parameters, a G6pDH-NAD$^+$-LDH swinging arm structure was constructed. The activity of this complete two-enzyme nanostructure is compared to that of

the partially assembled structures including a G6pDH-LDH assembly with freely diffusing NAD^+, a G6pDH-NAD^+ arm assembly with freely diffusing LDH (Figure 5A). For the same total NAD^+ and enzyme concentration (8 nM), the activity of the complete swinging arm structure is ~ 50-fold higher than Semi-assembled swinging arm complexes with G6pDH-NAD^+ attached and the LDH freely diffusing in solution, confirming the LDH harm arm also works. Kinetic measurements found ~5-fold higher turnover number (k_{cat}) for the isolated G6pDH than LDH, indicating that LDH is the rate-limiting enzyme in the G6pDH-LDH cascade (Figure 5B).

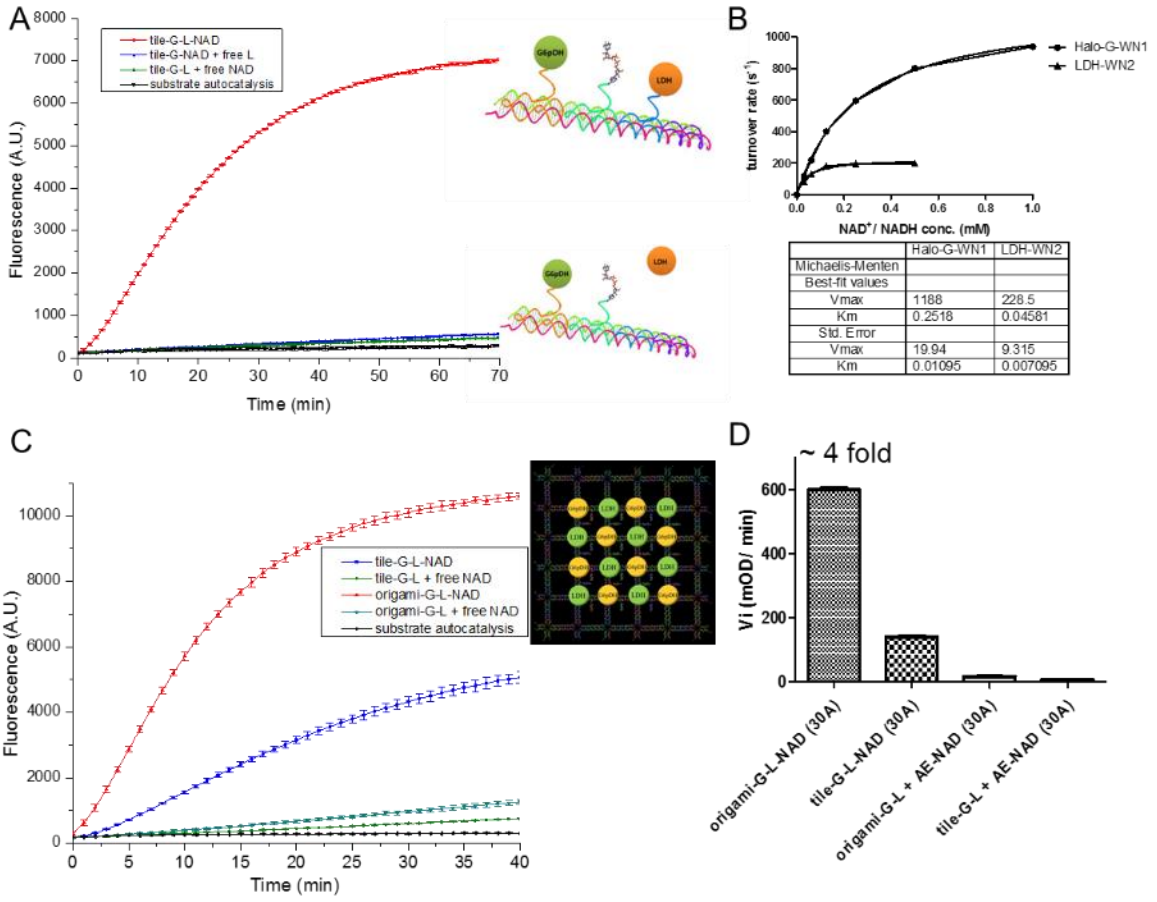


Figure 5. (A) G6pDH-NAD^+-LDH swinging arm activity compare to that of the partially assembled structure G6pDH-NAD^+ arm assembly with freely diffusing LDH. (B) Michaelis-Menten plot for G6pDH and LDH activity (turnover rate) *vs.* NAD^+ concentration. Kcat of G6pDH is roughly 5 fold higher than the LDH. (C&D) Overall pathway activities for origami-G6pDH-LDH-NAD compared to tile-G6pDH-LDH-NAD, with same concentration of enzymes (8 nM), about 4 fold activity is observed. Substrate conditions: 1 mM glucose-6 phosphate and 1 mM pyruvate in 100 mM HEPES buffer (pH 8).

Finally, we compared the 2D network with single particle of the complete origami/ tile-G6pDH-LDH-NAD complex. Overall pathway activities for origami-G6pDH-LDH-NAD compared to tile-G6pDH-LDH-NAD, with same concentration of enzymes (8 nM), showed about 4 fold activity enhancement. Indicating the network effect of enzyme cascades do benefit the overall pathway efficiency, potentially due to the accessibility of multiple swinging arms and downstream enzymes in a close distance compared to single-particle systems (Figure 5CD).

For future plans, we plan to investigate the dependence of enzymatic activity on the number of surrounding NAD^+-modified swinging arms on a DNA-scaffolded 4 × 4 tile (Figure 6A). Since in the 2D network, for each enzyme, there is 4 arms and 4 enzymes around it locally. Titration from 1 to 4 G6pDH around one LDH, and 1 to 4 LDH around one G6pDH will be tested. To father investigate the geometry dependence of the enzyme networks using a different scaffold with 3-arm junction instead of 4-arm junction (Figure 6B). In this scaffold, 3 NAD arms and enzymes will be surrounding one enzyme, different activity is expected compared to the 4 NAD arm system.

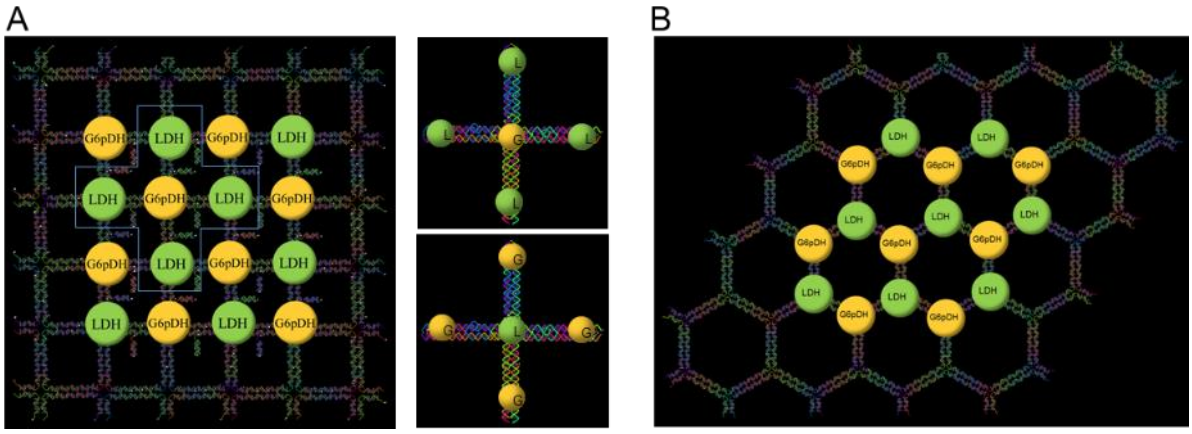


Figure 6. Future experiments including (A) titrating different number of swinging arms and enzymes around one enzyme, mimicking the local environment in the 2D enzyme network, (B) test the geometry dependence of the enzyme networks using a different scaffold with 3-arm junction instead of 4-arm junction.

In summary, we designed and constructed artificial "swinging arm"-channeled multi-enzyme 2D network with NAD^+-modified molecular arms and compared to the previously developed single particle swinging arm. The benefits of enzyme networks have been discovered. To further study the network effects, 3D scaffolding with DNA crystals to organize enzymes is a promising direction

Engineering a three-enzyme pathway with channeled substrate transfer

1. Design and characterization of assembled pathway:

Malate dehydrogenase (MDH) is capable of catalyzing the oxidation of malate to oxaloacetate (OAA) using the reduction of NAD^+ to NADH which is part of biological metabolic pathways, including the citric acid cycle. MDH alone in solution, however, is measured to have much higher preference for the reduction of oxaloacetate to malate which is a reversed reaction direction (Figure 5B). In the last reaction of the citric acid cycle, NAD^+-linked malate dehydrogenase catalyzes the oxidation of malate to oxaloacetate. The equilibrium of this reaction lies far to the synthesis of malate rather than oxaloacetate under standard thermodynamic conditions, but in cells oxaloacetate is continually removed by downstream citrate synthase reaction which is highly exergonic. This keeps the concentration of oxaloacetate in the cell extremely low, pulling the MDH reaction toward the unfavorable direction. Nature has evolved to efficiently transfer intermediates to direct reaction pathways and reach high yield and speed. In this work, taking the advantage of spatially controllable DNA nanostructures, we aim to construct an artificial enzyme complex,

integrating a circular enzyme pathway to regulate the reaction direction of enzymes (Figure 7A). Gel and AFM characterization are shown in Figure 7B and 7C separately.

2. Evaluation of assembled three-enzyme pathway and channeled substrate transfer:

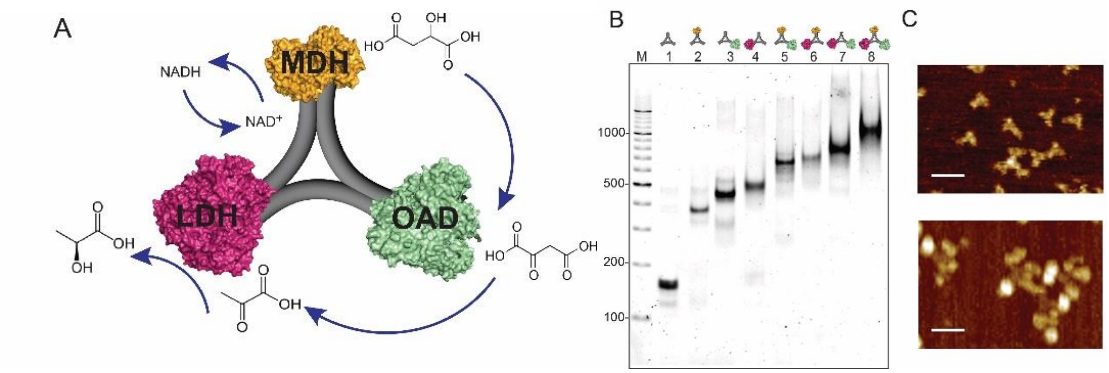


Figure 7. Design and characterization of assembled pathway. (A) illustration of assembled three-enzyme pathway. (B) Polyacrylamide gel characterization of assembly. (C) AFM characterization of DNA nanostructure only (top) and assembled three enzymes (bottom). Scale bar: 50nm.

Previously we have reported the design and rationale of engineering malate dehydrogenase (MDH), oxaloacetate decarboxylase (OAD) and lactate dehydrogenase (LDH) on a three-point star DNA nanostructures. We also evaluated the assembled pathway compared with free enzymes. Our results demonstrated great enhancement on regulation of enzyme reaction direction with assembled enzyme pathways on DNA nanostructure. Here we further evaluated the assembled three-enzyme pathway upon lactate production via stop time assay as previously described and rule out the activity enhancement by DNA nanostructure (shown in Figure 8A). We also evaluated

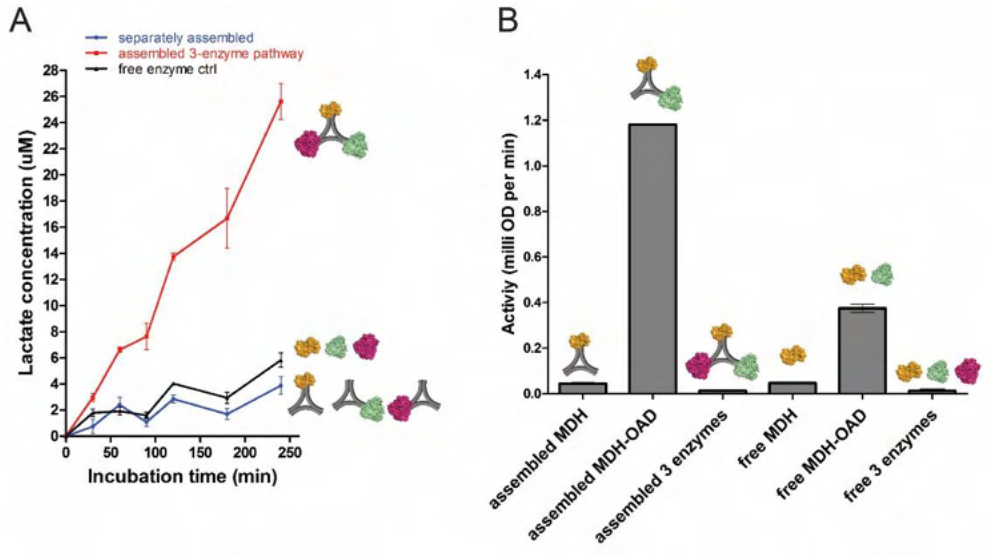


Figure 8. Evaluation of assembled three enzyme pathway on DNA nanostructure by lactate production and NADH depletion. (A) Lactate accumulation with time for three enzymes, free enzymes and separately assembled enzymes. (B) NADH accumulation and depletion by different enzyme pathways.

intermediate depletion by monitoring NADH level between MDH-OAD pathway and MDH-OAD-LDH pathway (Figure 8B).

In the stop time assay (Figure 8A), we quantified lactate production with time using Amplex Red/ horseradish peroxidase (HRP)/ lactate oxidase (LOx) system. Lactate oxidase catalyzes the oxidation of lactate to pyruvate and produced H_2O_2 can be utilized by HRP. We compared assembled three enzyme pathway, separately assembled three enzymes and free enzymes within an incubation time of up to 4 hours with 30 minutes intervals. Red curve showed that 1.5nM assembled three enzymes demonstrated greater lactate production with time and accumulated ~ 26uM lactate after 4 hours while non-assembled groups including free enzyme group and separately assembled group only showed very limited level of lactate production. According to Figure 8A, we can estimate the overall turnover rate of the assembled complex to be ~1.2 per second which is close to the NAD^+ turnover rate (1.074 per second) of MDH with 1mM NAD^+ and malic acid as the substrates.

As shown in Figure 8B, we also evaluated intermediate depletion by measuring NADH level between multiple enzyme pathways. In the overall three-enzyme pathway, MDH oxidizes malic acid with the reduction of NAD^+ to NADH but at a very low level so free MDH and assembled MDH showed similar low activity on NADH production. As the second enzyme OAD added in which works more efficiently removing oxaloacetate and inhibit NADH depletion by MDH, both free and assembled MDH-OAD pairs demonstrated a great enhanced activity. When assembled on DNA nanostructure, the distance between two anchoring positions is ~11.8 nm and two enzymes were brought to a close proximity that can greatly facilitate intermediate transfer between MDH and OAD and thus produce higher level of NADH compared with free enzyme pairs. With the addition of third enzyme LDH that has greater catalytic efficiency MDH and OAD, it works rapidly on NADH oxidation and maintain NADH at a minimum level which inhibits MDH to compete with OAD on oxaloacetate reduction. Given 1mM NAD^+ in the system and NADH maintained almost close to zero, the NAD^+/ NADH ratio in solution is kept extremely low and will facilitate MDH to work on the direction of malic acid oxidation. Assembled LDH demonstrated greater ability on removal of accumulated NADH compared with free enzyme system.

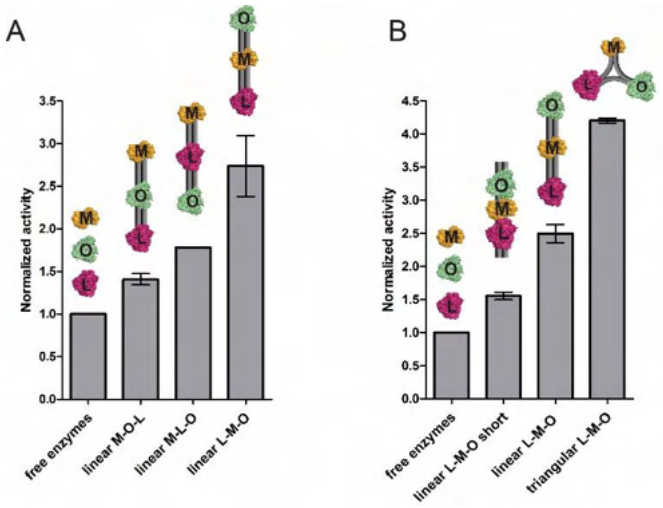


Figure 9. Evaluation of assembled three enzyme pathway on DNA nanostructure by lactate production and NADH depletion. (A) Lactate accumulation with time for three enzymes, free enzymes and separately assembled enzymes. (B) NADH accumulation and depletion by different enzyme pathways.

2. <u>A study of linear geometry and distance effects:</u>

To assemble the three-enzyme pathway, we designed a three-arm DNA nanostructure, named three-point star. The sequences and gel confirmation were shown in last year's report. On the

three-point star structure, the distance between each neighboring enzyme pairs is the same (~11.8 nm). In reality, due to different turnover rates of three enzymes and diffusion ability of intermediates, we would assume that the efficiency of assembled pathway variates with distance and patterns. As shown in Figure 9A, in order to explore more on the geometry effects, here we designed a linear DX tile and assembled three enzymes in 3 different orders: M-O-L, M-L-O and O-M-L. In this design, the distance between two enzymes is 14nm. When OAD is placed in the middle in the scenario of M-O-L, the traveling distance for oxaloacetate from MDH to OAD is 14nm and 28nm for NADH to be transferred from MDH to LDH. Similarly, in the scenario of M-L-O when LDH is placed in the middle the distance for NADH to reach LDH from MDH is 14nm and oxaloacetate has to travel 28nm to get to OAD. Only when MDH is placed in the middle, both oxaloacetate and NADH travel the shortest paths to OAD and LDH. According to the activity assay, L-M-O demonstrated highest activity compared to free enzymes, M-O-L and M-L-O. This could be explained by the shortest transferring distance for products (oxaloacetate and NADH) from MDH which is the rate-limiting enzyme in the three-enzyme pathway.
We further investigated distance effect for linear L-M-O pattern and also compare with our original three-point star design in which three enzymes are placed in a triangular pattern that each enzyme pair has equal distance in between (Figure 9B). We observed that on DX tiles, 14nm inter-enzyme distance yields higher activity than 7nm (linear L-M-O short) and this is due to existing steric hindrance which may prevent the binding of MDH between OAD and LDH. The original three-point star design is demonstrated better geometry pattern compared with linear design and showed more than 4-fold enhancement to free enzymes.

In summary, combined with part of last year's report, we have designed and constructed an artificial three-enzyme pathway that mimic part of citric acid cycle to facilitate substrate transfer between enzymes. The artificial enzyme pathway not only significantly enhances overall enzymatic activity, but also efficiently removes intermediates to drive enzyme pathway towards unfavorable direction. The concept we demonstrated here can be applied to construct more complex enzyme pathways that will help conquer existing energy barrier and facilitate rapid substrate transfer. Structural DNA nanotechnology provide programmable scaffolds for controllable distance, geometry and ratios, and will find utility in development of both mass conversion and regulatory systems.

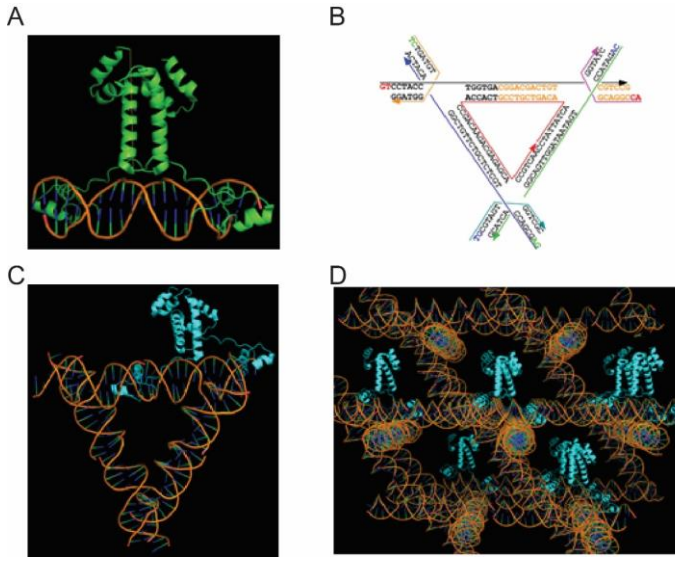


Figure 10. Self-assembled Gal4-DNA crystal design. (A) Crystal structure of Gal4 with its binding DNA (adapt from crystal structure 3COQ). (B) Tensegrity triangle crystal asymmetric design with Gal4 binding sequence (highlighted as yellow). (C) Model of Gal4 docking in a DNA triangle monomer. (D) Docking of Gal4 in the tensegrity triangle crystal lattice.

3D self-assembled DNA crystal assisted protein organization

1. <u>Self-assembled DNA crystal design with Gal4 binding site:</u>

The 3D self-assembled DNA crystal assisted protein organization will facilitate the precise position and orientation control of the protein/enzyme in the 3-dimensional manner. Based on this study, we will be able to build the enzyme cascade pathways in the three dimensional space for a more accurate control towards distance and direction. We have achieved the DNA binding protein (Gal4) organization in the 3D DNA crystals. Other enzyme molecules can be fused to the N- or C-terminal of Gal4 as a functional fusion protein. Gal4-DNA specific binding will facilitate the enzyme organization inside the crystal.

Gal4 protein is a yeast transcription factor, which binds with a specific 17bp double-stranded DNA. The truncated Gal4 (1-94) contains a DNA binding domain and a dimerization domain, which is sufficient for specific DNA binding (Figure 10A). Here we designed a self-assemble DNA crystal embedded with Gal4 recognition sequence, allowing Gal4 to be precisely organized in the 3D DNA crystal lattice. The DNA tensegrity triangle crystal was previous described by Dr. Seeman's group (Zheng et al. 2009 Nature). To accommodate Gal4 protein binding in the crystal cavity, the 3-turn triangle design was employed which contains sufficient space. The original 3-turn triangle design was modified to be asymmetric with 3 different sets of sticky ends and Gal4 binding sequence was also incorporated (Figure 10BCD).

2. Gal4 protein (1-94) expression and purification:

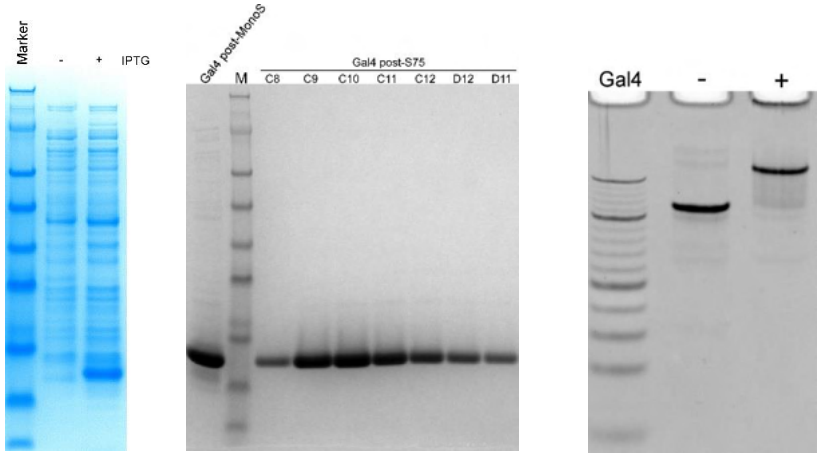


Figure 11. Expression and purification of Gal4 and its binding with the triangle monomer. (A) SDS-PAGE of *E. coli* whole cell protein with and without IPTG induction. The Gal4 (1-94) protein was overexpressed with IPTG induction. (B) SDS-PAGE of Gal4 after MonoS column (the lane left to the marker) and after Superdex 75 column (lanes right to the marker). (C) Gel mobility shift assay (EMSA) of triangle DNA with Gal4 protein. The triangle DNA was annealed as a single band (Gal4- lane) and binds with Gal4 (1-94) protein (Gal4+ lane, with a band shift).

The plasmid encoding Gal4 (1-94) was received as a gift from Dr. Michael Carey (UCLA), and transformed into *E. coli* Express I^q strain (New England Biolabs). A single colony was inoculated into 10 ml LB medium and grown at 37°C with constant shaking for overnight. The 10 ml overnight culture was then inoculated into 1 L LB medium. The *E. coli cells* were grown at 37°C to an OD600 of ~0.6, induced with 0.5 mM IPTG and 0.1 mM $Zn(OAc)_2$ and grown for an additional 3 hrs (Figure 11A). The cell pellet was recovered by centrifugation at 5,000xg for 15 min and sonicated in lysis buffer containing 20 mM HEPES (pH 7.5), 150 mM NaCl, 10 uM $Zn(OAc)_2$, 1 mM DTT, and supplemented with 1X Complete Protease Inhibitor Cocktail (Roche). The cell lysate was clarified by centrifugation at 18,000xg for 30 min at 4°C and the supernatant was filtered through a 0.22 uM membrane. The supernatant was loaded on a MonoS column (GE Healthcare Life Sciences) and eluted with a 0.15 M to 1 M NaCl gradient in the lysis

buffer (Figure 11B). The peak fractions containing Gal4 (1-94) were pooled and concentrated using an Amicon 5K concentrator. The concentrated Gal4 was loaded onto a Superdex 75 gel filtration column (GE Healthcare). The resulting peak fractions were collected and concentrated to 0.5 mM and stored at -80°C. The purified Gal protein was tested to bind with triangle DNA (Figure 11C).

3. DNA crystallization and Gal4 binding:

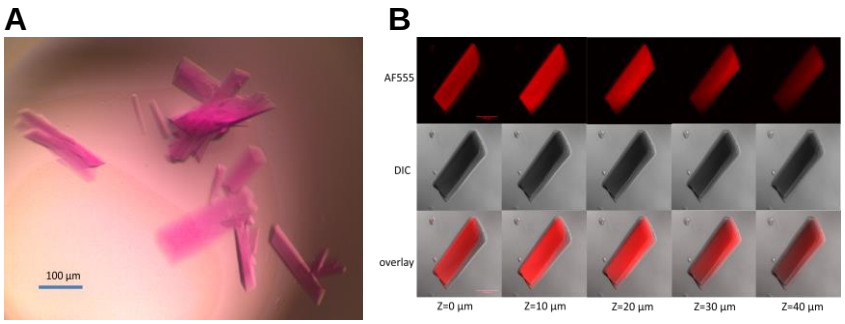


Figure 12. Gal4/DNA crystallization and analysis. (A) Rhombohedral-shaped crystals were obtained by slow annealing. AF555 labeled Gal4 protein was added to the crystal drop and the crystal was labeled with Gal4 showing as pink color. (B) Confocal images of Rhombohedral-shaped crystal soaked with AF555 labeled Gal4. The first row shows AF555 fluorescent images, and DIC indicates differential interference contrast (bright light images). The last row shows the overlay images. The fluorescence was evenly observed at different Z axis indicating the AF555 labeled Gal4 was successfully soaked inside of the crystal.

The DNA crystal was prepared by mixing all seven strands (Figure 10B) at equal molar concentration (final concentration as ~40 uM). Crystals were grown by mixing 4.5 ul DNA solutions with 2.25 ul of TA/Mg buffer (40 mM Tris-Acetate pH 7.0, 7.5 mM $MgCl_2$) in a 24 well crystallization plate, equilibrated against a 0.5 ml reservoir of 0.4 M ammonium sulfate. The crystallization plate was incubated at 60°C for 1 hour, and the temperature was slowly decreased to 25°C with a cooling rate of 0.3°C per hour. The crystals were obtained at the end of cooling step, and Gal4 protein was added the crystal drop. To visualize the soaking step, the purified Gal4 protein was labeled with fluorescent dye Alexa Fluor 555 (AF555) NHS ester following the manufacturer's instruction (Life technologies). The soaking of AF555 labeled Gal4 to the crystal was observed by microscope (Figure 12A) and confirmed by Confocal Microscope (Figure 12B).

Nano-caged Enzymes with Enhanced Activity and Stability

1. Design DNA nanocages to efficiently encapsulate enzyme targets:

As shown in Figure 13a, our approach for enzyme encapsulation within DNA nanocages involves two steps: 1) the attachment of an individual enzyme into an open half-cage and 2) the assembly of two half-cages into a full (closed) nanocage. DNA half-cages were constructed by folding a full-length M13 viral DNA into the indicated shape based on a honeycomb lattice using the DNA origami technique; a shape with two open sides was chosen to improve accessibility of the internal cavity to large proteins. Two half-cages were then linked into a full-cage by adding 24 short bridge DNA strands that hybridize with the complementary ssDNA sequences extending from the edges of either half-cage. The DNA full-cage is ~54 nm × 27 nm × 26 nm with designed inner cavity dimensions of 20 nm × 20 nm × 17 nm. By design, 42 small nanopores (each ~2.5 nm in diameter) were introduced on each of the top and bottom surfaces of the DNA nanocage to permit the diffusion of small molecules (e.g., enzyme substrates) across the DNA walls.

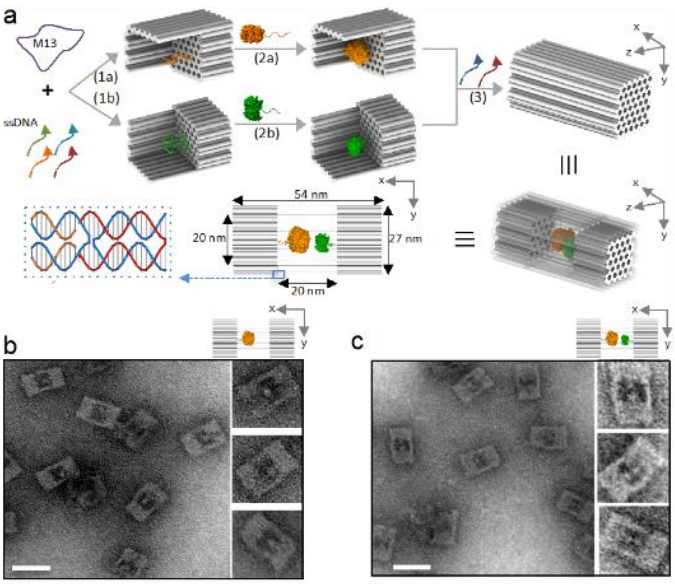


Figure 13. Design and characterization of DNA nanocage encapsulated enzymes with controlled stoichiometry. **a**, Schematics of the assembly of a DNA nanocage encapsulating a pair of GOx (yellow) and HRP (orange) enzymes. Individual enzymes were first attached to half-cages, followed by the addition of linker strands (red) to combine the two halves into a full-cage. Small pores of honeycomb shape (~2.5 nm d.i.) were designed on the bottom of cages to facilitate the diffusion of substrate molecules in an out of the cage. **b,** Negatively stained TEM images of DNA cages containing a single GOx (shown as less stained dots) and **c,** a pair of GOx and HRP (shown as less stained dots). Scale bar: 50 nm.

The formation of half and full DNA nanocages first was characterized using transmission electron microscopy (TEM) and gel electrophoresis, which indicate a nearly 100% yield for half-cages and a more than 90% yield for full-cages. To capture target enzymes into a half-cage, a previously reported succinimidyl 3-(2-pyridyldithio) propionate (SPDP) chemistry was used to crosslink a lysine residue on the protein surface to a thiol-modified oligonucleotide. Two anchor probes of complementary sequence were displayed on the bottom of the half-cage cavity to capture a DNA-modified enzyme via sequence-specific DNA hybridization. As a demonstration of an enzyme cascade, a glucose oxidase (GOx)-attached half-cage was incubated with a horseradish peroxidase (HRP)-attached half–cage at a stoichiometric ratio of ~1:1, followed by the addition of bridge strands into solution to assemble a full DNA nanocage containing a GOx/HRP pair. The inner cavity of a full nanocage is of sufficient size to encapsulate this enzyme pair (GOx is ~10 nm and HRP ~5 nm in diameter). Unencapsulated enzyme and excess short DNA strands were removed using agarose gel electrophoresis (AGE).

2. <u>Characterization of enzyme encapsulation</u>**:**

To verify the presence of both enzymes within a DNA nanocage, the co-localization of a Cy3-labeled GOx (green emission) and a Cy5-labeled HRP (red emission) was quantified by dual-color fluorescence gel electrophoresis where a gel band with overlapped green and red color was identified as shown in Figure 14. By comparison, the GOx-containing half-cage (Half [GOx]) shows the presence of only Cy3 (green), whereas a HRP-half-cage (Half [HRP]) shows the presence of only Cy5 (red). In addition, negatively-stained TEM images were used to visualize DNA cages upon stoichiometrically controlled encapsulation of a single GOx (Figure 13b) or a single GOx/HRP pair (Figure 13c), where GOx and HRP were visible as brighter spots within the cage. To quantitatively analyze the yield of DNA nanocage encapsulation,

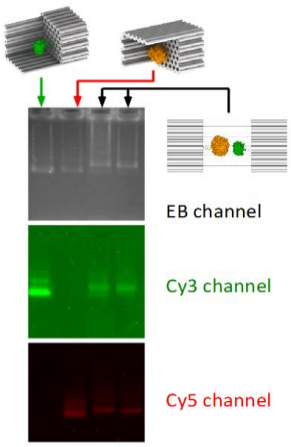


Figure 14. Native AGE characterization of a DNA nanocage encapsulating a GOx/HRP pair. GOx and HRP were conjugated with Cy3 and Cy5, respectively.

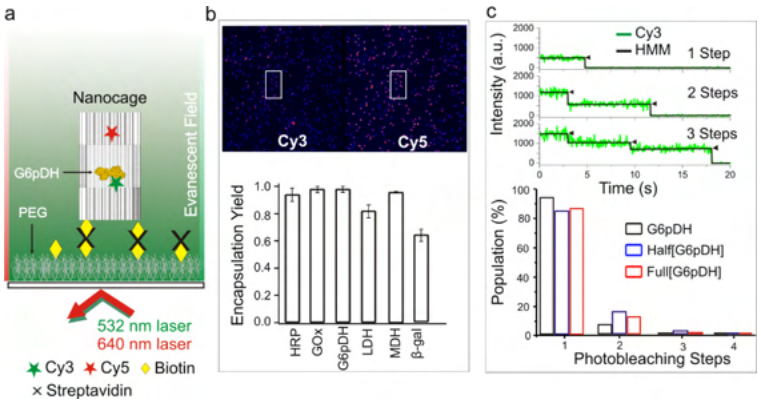


Figure 15. Single molecule fluorescence characterization of enzyme encapsulation. a, Schematic illustration of single-molecule fluorescence co-localization of Cy3-labeled protein with Cy5-labeled cage using TIRF microscopy. DNA cages were captured on the surface by biotin-streptavidin interaction. b, Top: representative field of view of enzyme-encapsulating cages under TIRF microscope. Examples of Cy3-Cy5 co-localization are highlighted using a pair of rectangles. Bottom: quantified encapsulation yield for six different enzymes. c, Top: Fluorophore photobleaching trajectories with one, two, and three photobleaching steps. Photobleaching steps were quantitatively analyzed by fitting the trajectories by hidden-Markov Modeling (HMM) in QUB program. Bottom: Photobleaching statistics for Cy3-labeled proteins encapsulated within half-cages (Half[G6pDH]) or full-cages (Full[G6pDH]), as well as for an unencapsulated protein control (G6pDH).

two-color total internal reflection fluorescence (TIRF) microscopy (Figure 15a) was used to characterize the fluorescence co-localization of a Cy3-labeled enzyme and a Cy5-labeled nanocage (Figure 15b, top panel). Six different enzymes were tested and characterized for encapsulation, ranging from the smallest HRP (~44 kD), malic dehydrogenase (MDH, ~70 kD), glucose 6-phosphate dehydrogenase (G6PDH, ~100 kD), lactic dehydrogenase (LDH, ~140 kD) and GOx (~160 kD) to the largest β-galactosidase (β-Gal, ~450 kD). All six enzymes were successfully encapsulated within full DNA nanocages with high yields, ranging from 64-98% (Figure 15b). The relatively low yield of β-Gal (64%) may be due to its large size (~17 nm in diameter), which is comparable to the inner diameter of the nanocage (~20 nm), likely resulting in steric hindrance for encapsulation. To evaluate how many copies of the same enzyme were encapsulated per DNA nanocage, single-molecule fluorescence photobleaching (SMPB) was used to count the number of photobleaching of Cy3 fluorophores per cage (Figure 15c). The number of copies of each enzyme per cage was estimated by normalizing the number of Cy3 fluorophores per DNA nanocage with the average number of Cy3 labels per free enzyme (see Materials and Methods in Supplementary Information). A majority of nanocage-encapsulated enzymes showed only one- or two-step photobleaching of Cy3, similar to the photobleaching of single free enzymes (Figure 15c). These results suggest that most nanocages (~90%) contain exactly one enzyme per cage, as expected (Figure 15c).

3. <u>Activity characterization of the nano-caged enzymes:</u>

To evaluate the effect of DNA nanocages on enzyme activity, we first tested an encapsulated GOx/HRP pair (Figure 16a). This pair of enzymes catalyzes a reaction cascade beginning with the oxidation of glucose by GOx to generate hydrogen peroxide (H_2O_2). H_2O_2 is subsequently used by HRP to oxidize ABTS, producing a strong colorimetric signal. As shown in Figure 16b, the overall activity of a co-assembled GOx/HRP cage (Full[GOx/HRP]) is ~8-fold higher than that of a control enzyme pair at the same concentration without encapsulation. In order to analyze the pure effect of DNA nanocage on encapsulated enzymes, it is necessary to exclude the possible activity enhancement by substrate channeling due to the close proximity of the two enzymes in a cascade reaction. Control experiments showed an increased activity also for DNA nanocages

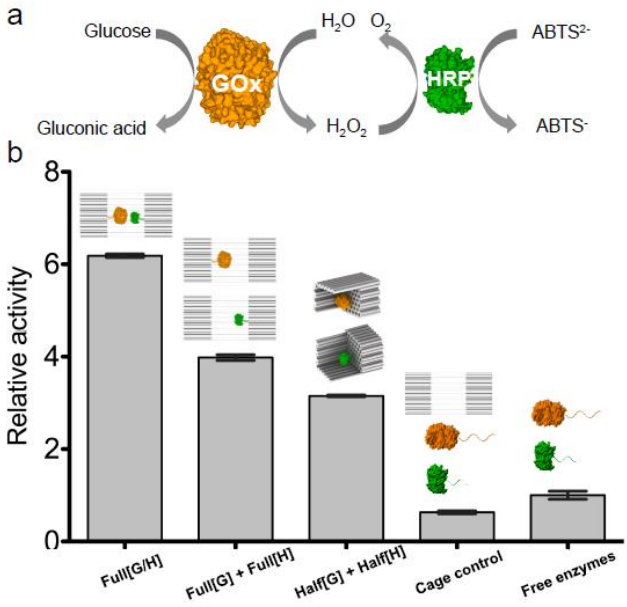


Figure 16. Activity characterization of encapsulated GOx/HRP pairs. a. Schematic of the GOx/HRP cascade. b. Normalized cascade activities for a GOx/HRP pair encapsulated within a full-cage (Full[GOx/HRP]), two individual full-cages (Full[GOx] + Full[HRP]), and two individual half-cages (Half[GOx] + Half[HRP]), as well as unencapsulaed enzyme pairs with and without the presence of DNA cages. Assay conditions: 1 nM enzyme or 1 nM enzyme-DNA cage, 1 mM Glucose and 2 mM ABTS in TBS buffer (pH 7.5), and monitoring absorbance at 410 nm.

encapsulating only a single GOx or HRP enzyme, which clearly do not result in substrate channeling between enzymes. For example, an equimolar mixture of two separate nanocages encapsulating either a single GOx or a single HRP (Full[GOx]+Full[HRP]) exhibited an ~4-fold increase in overall activity compared to the unencapsulated control enzymes. Similarly, an equimolar mixture of two half-cages encapsulating either a single GOx or a single HRP already showed an increase in overall activity by ~3-fold. Since there was no proximity effect in the case of two enzymes encapsulated into two different nanocages, the local environment modified by a DNA nanocage appears to be more important for the observed activity enhancement. Similarly, a half-cage was almost as effective in activity enhancement (3-fold) as a full nanocage, suggesting that enzyme access to substrate does not play a role in this enhancement. Interestingly, a similar enhancement was reported previously upon conjugation of enzymes to a giant multibranched DNA scaffold, without further explanation.

To test the generality of our observations, we evaluated the activity of six different enzymes upon encapsulation within DNA nanocages. As shown in Table 1, five of them (GOx, HRP, G6PDH, MDH and LDH) exhibited higher activity in nanocages than the free enzyme, with enhancements ranging from 3- to 10-fold. Detailed kinetic analyses showed that the K_m (the Michaelis constant) varies little between encapsulated and free enzyme for most substrates (ranging from 0.5 to 2.4-fold of the free enzyme), which suggests uninterrupted and efficient diffusion of substrates through the designed pores of the DNA nanocage. In contrast, a large increase in turnover number (k_{cat}) was observed for these five enzymes (ranging from 3.5- to 9.6-fold of the free enzyme), suggesting an inherently higher catalytic activity of the proteins. Strikingly, an inverse correlation was observed between enhanced turnover and size of the encapsulated enzyme. That is, the smaller HRP (44 kD) and MDH (70 kD) exhibited relatively large increases in turnover number of 9.6±0.4 and 9.0±0.7 fold, respectively, whereas the larger enzymes G6PDH, LDH, and GOx exhibited smaller enhancements of 4.7±0.1 fold, 4.1±0.1 fold, and 5.4±0.2 fold, respectively. No correlation was observed between enhancement and isoelectric point (pI), despite the wide range of pI values for these enzymes (ranging from 4.2 to 10.0). In contrast to these five enzymes, β-Gal is strongly inhibited upon encapsulation, possibly due to its large size (~16 nm in diameter) that is comparable to the inner cavity diameter (~20 nm) of the DNA nanocage. Alternatively, the β-Gal orientation may be unfavorable and block binding of substrate to the active site. Notably, in a control

experiment polyphosphate inhibited the activity of β-Gal, suggesting that the local high density of backbone phosphates of the DNA nanocage might be responsible for the decrease in activity of β-Gal.

Enzyme	pI	Molecular Weight	Substrate	Free enzymes		Encapsulated enzymes	
				K_m (μM)	k_{cat}(s^{-1})	K_m (μM)	k_{cat}(s^{-1})
GOx	4.2	160 kD	glucose	6200±900	240±10	3000±600	1300±50
HRP	8.8	44 kD	H_2O_2	2.3±0.5	32±1	4.3±0.6	290±5
			*ABTS	2600±400	59±5	2500±200	560±20
G6pDH	4.3	100 kD	glucose-6 phosphate	220±20	130±3	310±30	460±10
			NAD^+	510±50	100±3	590±40	480±10
MDH	10.0	70 kD	NADH	180±50	51±5	270±50	460±30
LDH	5.0	140 kD	NADH	7.2±1.3	46±2	17.0±1.5	190±5
β-Gal	4.1	465 kD	RBG	58.7±16.0	*8.5±0.6	95.5±18.9	*1.6±0.1

Table 1. Enzyme kinetic data (values of K_m and k_{cat}) for each individual enzyme encapsulated inside a DNA full-cage in comparison with the values for the free enzymes in solution. (The Michaelis-Menten plots of each enzyme and the conditions of the enzyme activity measurements, can be found the SI. The pI values of the enzymes were obtained from brenda-enzymes.org).

4. Single-molecule kinetics of nanocage-encapsulated enzymes:

To gain more detailed mechanistic insight into the enhancement of catalytic turnover, Walter lab applied a novel single-molecule fluorescence assay to characterize the activity of individual enzymes with and without encapsulation (Figure 17). As shown in Figure 17A, we used TIRF microscopy to record the repetitive turnover of substrates by individual G6pDH enzymes over time; coupling with a PMS/resazurin reaction allowed us to detect stochastic fluctuations of enzyme turnover rates via transient spikes in intensity from the generation of the fluorescent product resorufin (Figure 17B,C). Such fluctuations have been observed for various enzymes before and are thought to be induced by the conformational switching between more and less active sub-states. Compared to a control without substrate, more frequent fluorescent spikes were observed with the addition of glucose-6-phosphate substrate (Figure 17B, C). The average spike frequency increased from 0.016±0.001 s-1 for unencapsulated enzymes, to 0.019±0.001 s-1 for the half-cage and 0.026±0.002 s-1 for the full-cage (Figure 17D, left). Further analysis suggested that the fraction of active enzyme encapsulated within DNA nanocages was ~1.5 fold higher than that of unencapsulated enzymes ((Figure 17D, middle). Taken together, the higher spike frequency and the increase in the fraction of active enzyme yielded an ~3-fold higher G6pDH activity for the encapsulated compared to the unencapsulated enzyme ((Figure 17D, right), comparable to the ~4-

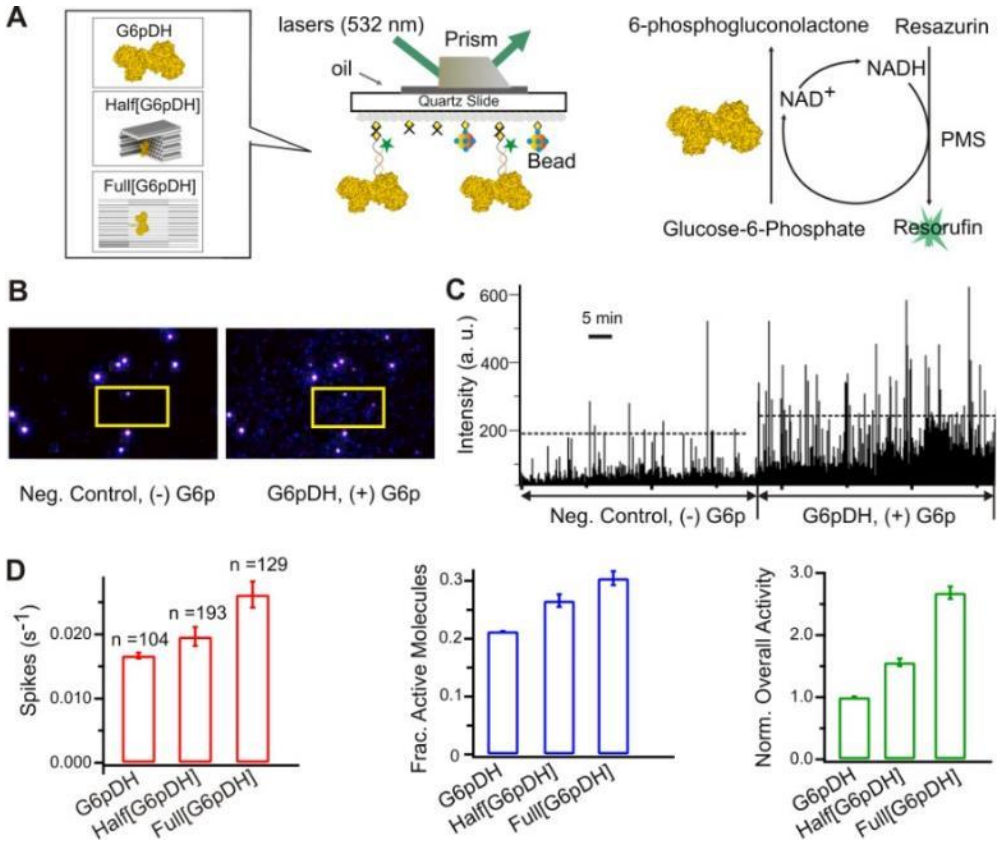


Figure 17. Single-molecule kinetics of nanocage-encapsulated enzymes. (A) Schematic of the experimental TIRF set up for characterizing G6pDH encapsulated within a full-cage (Full[G6pDH]) and a half-cage (Half[G6pDH]), as well as an unencapsulated control. Right: A PMS/resazurin-coupled fluorescence assay used to characterize the activity of G6pDH. (B) TIRFM snapshots captured before (left) and after (right) the injection of substrate glucose-6-phosphate (G6p). In presence of G6p, the field of view showed increased fluorescence due to the formation of resorufin (compare the boxed regions in the left and right panels). Fluorescent beads (very bright spots present in both +G6p and –G6p images) were used as reference markers to correct for the drift. (C) Real-time traces of fluorescence spikes (resorufin production) for enzymes without and with the addition of G6p substrate. Ten single-molecule traces for each condition were concatenated. (D) Statistics of spike frequency (left), fraction of active molecules (middle), and overall observed enzyme activity (right) for G6pDH. The number of active molecules analyzed is denoted by 'n'. All experiments were carried out at room temperature in 1× TBS buffer, pH 7.5 in 1 mM Mg^{2+} and 10% (w/v) PEG 8000.

fold enhancement observed in the bulk assay reported in Figure 16. Conversely, a similar analysis of β-Gal activity showed an ~3-fold lower activity of the full-cage enzyme (2.3±0.5 fold lower in spike frequency compared to free enzyme, whereas the fractions of active enzymes (~65%) were similar) compared to unencapsulated enzyme, also consistent with the bulk measurement reported in Figure 16.

5. Protection of enzymes under complex biological conditions:

Self-assembled DNA nanostructures previously were found to be more resistant against nuclease degradation than single- or double-stranded DNA molecules. Similarly, DNA nanocages should protect encapsulated enzymes from deactivation and aggregation under challenging biological conditions. As shown in Figure 18, encapsulated GOx/HRP was highly resistant to digestion by trypsin, and retained more than 95% of its initial activity after incubation with trypsin for 24 h. In

contrast, free GOx/HRP only retained ~50% of its initial activity after a similar incubation with trypsin. This result demonstrated the potential utility of DNA nanocages for protecting encapsulated proteins from biological degradation.

6. Conclusions:

DNA nanocages may serve as a molecular tool to precisely sculpt the properties of the local environment of enzymes in smart-material and biotechnological application. DNA nanocages also demonstrated their value in protecting encapsulated enzymes from biological degradation through proteases. In the future, it may be feasible to construct precisely controlled, programmable DNA nanocages for theranostic nanodevices as therapeutic agents.

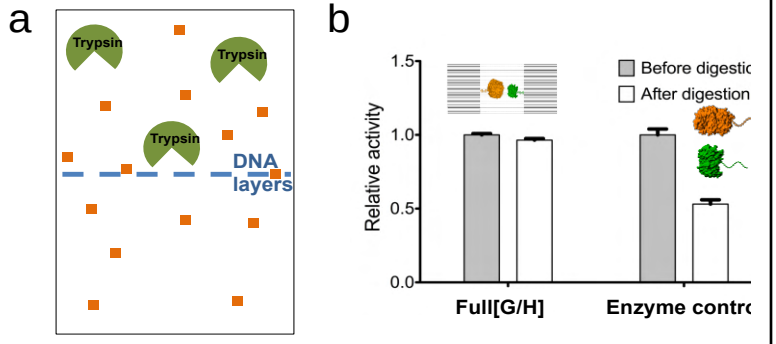


Figure 18. Protection of nano-caged enzymes against protease-mediated degradation and aggregation. a. Schematic illustrating how a DNA cage may block access of big proteins such as a protease to the interior of the cage, but still allow the penetration of small molecules. b. Relative enzyme activity of encapsulated GOx/HRP pairs (left, Full[GOx/HRP]) and free GOx/HRP pairs (right, GOx/HRP free) before and after the addition of trypsin. Trypsin digestion conditions: enzyme or enzyme-DNA cage was incubated with 1000 times excess Trypsin for 24h at 37 °C. Assay conditions: 0.5 nM enzyme or 0.5 nM enzyme-DNA cage, incubation with 1 mM Glucose and 2 mM ABTS in TBS buffer (pH 7.5), and monitoring absorbance at 410 nm.

Developing artificial electron-transport chains

1. Design of artificial electron-transport chains:

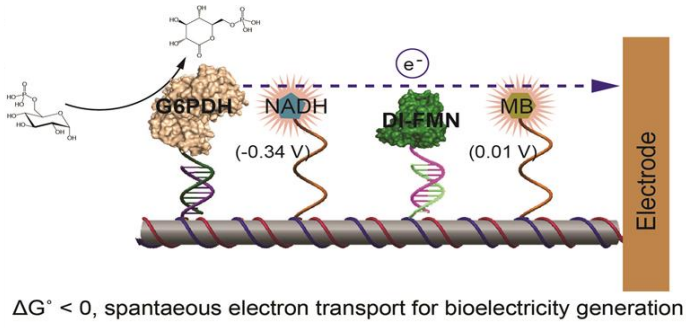


Figure 19. Schematic illustration of an artificial electron transport pathway organized by DNA nanoscaffolds facilitating the electron transfer via an increased redox potential gradient.

Energy transfer pathways play a key role in energy transformations in biological systems. For instance, nature uses electron-transport chains to couple the electron transfer between a series of donors and acceptors that are able to extract chemical energy from photosynthesis, carry out redox reactions in mitochondria, and regulate bioenergy conversions. We have started to apply the organizational power of DNA nanotechnology to the challenges of engineering artificial electron-transport chains (ETC) with controlled electron flow. As shown in Figure 19, the spontaneous electron-transport chain is designed to consist of a

series of redox molecules: NAD^+ (-0.32 V), FMN-incorporated diaphorase (DI-FMN) (-0.15 V), and methylene blue (0.01 V). NAD(H) is a natural dehydrogenase cofactor participating in many biochemical reactions. However, NAD(H) is difficult to interface directly with electrodes due to the energy barrier of two-electron transfer, resulting in a high overvoltage. Flavin mononucleotide (FMN) is a redox mediator with the FMN/FMNH* (accepting one electron) state ~ -0.15 V, and FMNH */$FMNH_2$ (accepting two electron) state ~ -0.30 V. Due to its close redox potential to NADH, the electron transfer between NADH and FMN is quite efficient and reversible. In many bioelectroactive systems, FMN-bound diaphorase (DI-FMN) is used to catalyze the electron transfer between NADH and MB or other redox mediators. Here, FMN is not freely diffused but is tightly incorporated into a DI monomer for serving as a redox center. Methylene blue (MB ~ 0.01 V) has been known to actively interact with electrodes, and thus is used as the final step of the electron-transport pathway. The alternative mediator can be NHS-activated Nile Blue (-0.1 V). The spontaneous electron transfer from reduced NADH to FMN-DI and MB is driven by the increased redox potentials.

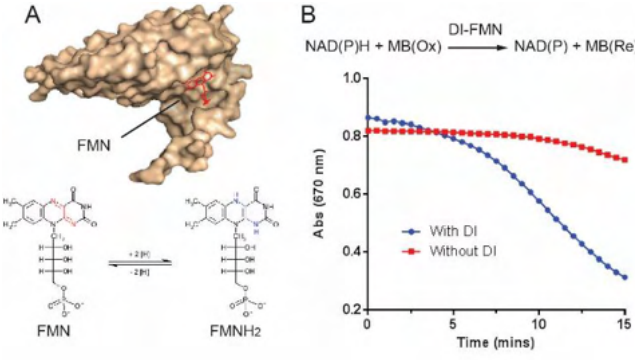


Figure 20. (A) Structure of Diaphorase (DI) incorporating a FMN cofactor. DI-FMN is reduced to DI-$FMNH_2$ by accepting two electrons. (B) DI catalyzes the electron transfer from NAD(P)H to methylene blue (MB).

A model system of an artificial ETC will be initiated by a glucose 6 phosphate dehydrogenase (G6PDH) oxidizing a substrate of glucose 6 phosphate. Then, electrons will be transferred from a glucose to the electrode through a facilitated pathway with an increased redox potential gradient of NADH-FMN/DI-MB-electrode. The thermodynamic energy that drives the electron transfer along the redox potential gradient can be estimated by the Nernst equation:

$$\Delta G^\circ = - nF\Delta E^\circ \qquad (1)$$

where ΔG° is the standard change of Gibbs free energy, n is the number of transferred electrons, F is the Faraday constant and ΔE° is the standard difference in the redox potential.

2. <u>Diaphorase-FMN as a key redox protein for electron transfer</u>:

The Fu lab characterized a diaphorase (DI) from Geobacillus stearothermophilus to catalyze the electron transfer between NADH and other cofactors (e.g. methylene blue, vitamin K_3). As shown in Figure 20A, FMN (flavin mononucleoide) is tightly incorporated into the protein and serves as a redox center. Oxidized DI-FMN has a strong absorbance at 452 nm, and can

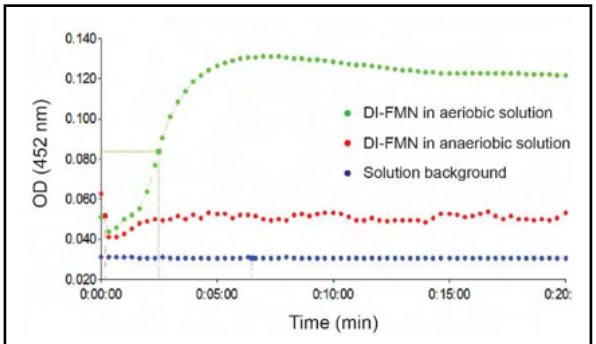


Figure 21. The oxidation state of DI-FMN under aerobic and anaerobic condition. 7 μM FMN-DI is incubated with 100 uM NADH in pH 7.4, 1 × TBS buffer, with monitoring the absorbance at 452 nm under aerobic condition (green) and anaerobic condition (red).

be reduced to DI-FMNH$_2$ by accepting two electrons. Because FMN also accepts one electron to become semiquinone (FMNH•), it can serve as a mediator to couple the electron transfer between NAD(P)H and other redox molecules, such as methylene blue shown in Figure 20B. Our recent studies have shown that bioelectroactive redox reactions will be affected by the dissolved oxygen molecule in solution, reducing the electron-transfer efficiency. For example, as shown in Figure 21, DI-FMN is oxidized by oxygen under aerobic condition, resulting in a high 452 nm absorbance. This oxidized DI-FMN participates in a side reaction of oxidase to produce H_2O_2, which competes with the target electron-transfer pathway of NADH to methylene blue.

By removing oxygen in solution, DI-FMN was also found to work similarly as a transhydrogenase to catalyze the reversible hydride transfer between NADPH and NADH. To characterize this activity, we used a thio-NAD analogue that showed an increased absorbance at 400 nm upon the reduction to thio-NADH. As shown in Figure 22, DI-FMN can catalyze the electron transfer from NADH to thio-NADH. For the control reaction without adding DI-FMN, the hydride transfer between NADH and thio-NAD is more than 200-fold slower. The above results demonstrated that DI-FMN can serve as a key redox component to couple the electron transfer in the artificial ETC.

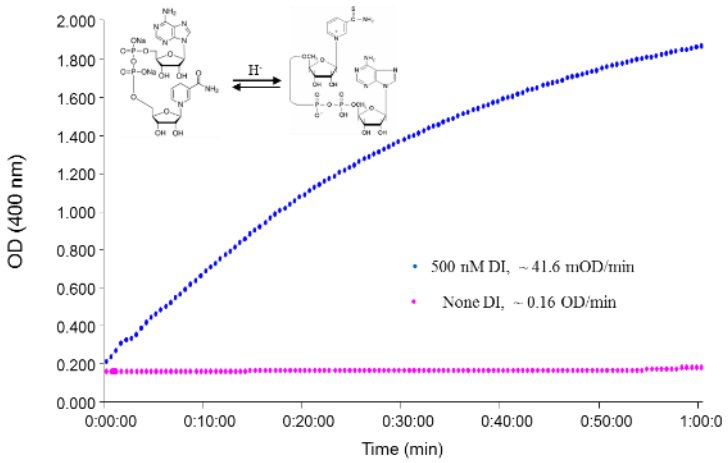


Figure 22. Characterization of the transhydrogenase activity of DI-FMN under anaerobic condition using thio-NAD analogue. The successful hydride transfer from NADH to thio-NAD is monitored by the absorbance increase at 400 nm.

3. Future directions:

We will apply the results of above initial study of artificial ETCs toward the design of a bioelectroactive, NAD-dependent dehydrogenase pathway (e.g. the proposed ADH-ALDH-FDH pathway in MURI), with the ultimate goal of interfacing this system with an external conductive surface for bioelectricity production. The artificial ETC represents a new protein immobilization technology that will potentially improve the performance of immobilized enzymes.

Electron microscopic visualization of protein assemblies on flattened DNA origami

DNA nanostructures are promising platforms for the site-directed spatial arrangement of guest components such as proteins, metal nanoparticles, and small molecules. Two-dimensional DNA origami architectures in particular offer a simple design, high yield of assembly, and large surface area for use as nano-platform. However, such single-layer DNA origami are structurally polymorphous due to their high flexibility, leading to the development of conformationally restrained multi-layered origami that lack some of the advantages of the single-layer designs. In work summarized in a 2015 *ACS Nano* publication, the Walter lab monitored single-layer DNA

origami (prepared in the Yan Lab, ASU) by transmission electron microscopy (EM) and discovered that their conformational heterogeneity is lost in the presence of a low concentration of dimethyl sulfoxide (DMSO), allowing for an efficient flattening onto the carbon support of an EM grid (Figure 23). We further demonstrated that streptavidin and a biotinylated target protein (cocaine esterase – CocE) can be captured at pre-designated sites on these flattened origami while maintaining their functional integrity. Our demonstration that protein assemblies can be constructed with high spatial precision (within ~2 nm of their predicted position on the platforms) by using strategically flattened single-layer origami improves our approaches for exploiting the well-defined guest molecule assemblies for biochemistry and nanotechnology applications proposed under this MURI project.

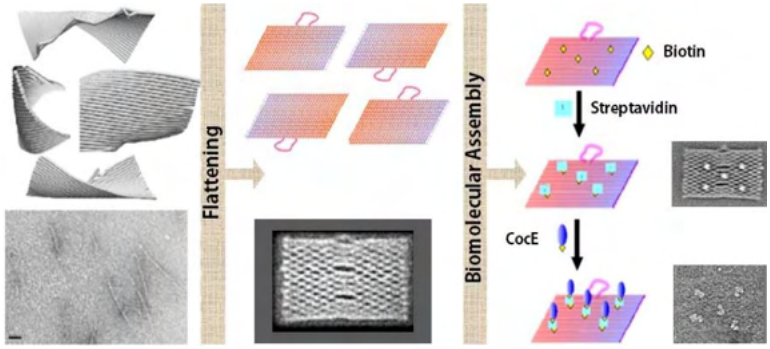


Figure 23. Flexibility of 2D DNA origami rectangles as predicted by computational modeling and visualized by EM (Left). Surface flattening of 2D DNA origami in 2% (v/v) DMSO (middle). Visualization of streptavidin and biotinylated cocaine—estarage (CocE) binding to DNA origami.

Rational design of DNA tweezer for enhanced enzyme activity guided by single-molecule and computational analysis

1. <u>Rational design of hairpin actuator and Holliday junctions in the DNA tweezers:</u>

The control of enzymatic reactions using DNA tweezers offers a powerful application of DNA nanotechnology uniquely derived from actuation. However, previous characterization of enzymatic reaction rates using bulk biochemical assays (Yan Lab, ASU) reported suboptimal tweezer function. To gain mechanistic insight into this deficiency and to identify key design rules to achieve optimal function, we exploited the synergy of single molecule imaging (Walter lab, UM), bulk measurement of enzyme activity (Yan lab, ASU), and explicit solvent molecular dynamics (MD), Bathe lab, MIT) to characterize the three-dimensional structures and catalytic functions of DNA tweezer-actuated nanoreactors. In a manuscript submitted to Nature Chemistry (currently under peer review), we reported that the original DNA tweezer containing a hairpin linker with a 3T spacer and 3-base pair (bp) stem (3T3bp, Figure 24) is only partially closed (to an arm-to-arm distance, IADFRET of ~6.5 nm) even in the "closed" state. Increasing the hairpin length from 3 to 4 bp and shortening the spacer from 3T to 1T, the Walter lab demonstrated an improved closing of the tweezer (Figure 24). The closing was further improved by rationally

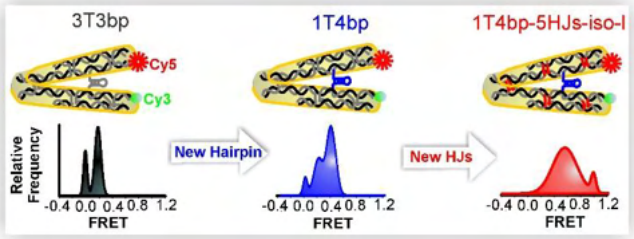


Figure 24. Optimization of tweezer closing by rational design of hairpin actuator and Holliday junctions (HJs). In the top panel, the optimized hairpin and five HJs are highlighted in blue and red respectively. The bottom panel shows the corresponding FRET histograms for each tweezer design.

redesigning (guided by single-molecule and computational analysis) of all five Holliday junctions (1T4bp-5HJs-iso-I) to adopt the desired conformational isomer (Figure 24). Molecular design principles that emerged from this quantitative computational-experimental study have broad implications for the design of multi-enzyme nanoscale systems.

2. MD characterization and optimization:

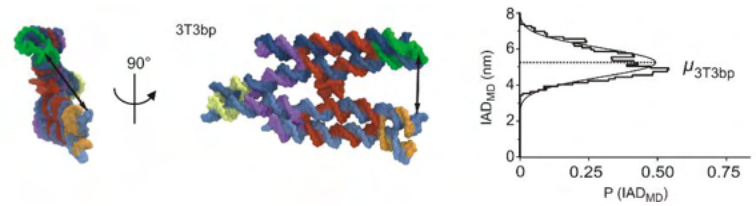


Figure 25. MD characterization of the 3D structure of the 3T3bp tweezer system. Two representative orthogonal views of a typical molecular conformation from MD, corresponding to an IAD_{MD} of 5.3 nm (left) and the probability distribution of mean, μ_{3T3bp} (right). The IAD_{MD} of 5.3 nm is highlighted by double-sided arrows in the orthogonal views of the tweezer.

To gain sequence-level insight into possible structural origins for the large IADFRET in the closed-state, Bathe lab performed all-atom MD of a model 3T3bp tweezer in solution under experimental conditions. Results revealed that the tweezer arms splay in a three-dimensional manner that is facilitated by the long and flexible three-thymine spacers that bridge the actuating hairpin, resulting in a predicted mean IADMD of 5.3 nm (Figure 25). This structural origin of the observed incomplete closure offered a straightforward explanation for the limited bulk activity enhancement observed for the scaffolded enzyme system. To force more complete closure of the tweezer, the 3T3bp architecture was redesigned by eliminating the thymine spacers and the hairpin entirely in a 0T0bp construct. While this redesign was anticipated to bring the tweezer arms into the closest possible proximity upon closure, smFRET characterization (Walter lab) revealed worse closure (IADFRET = 6.8 ± 0.1 nm) that MD simulations indicated is due to inter-arm twisting in this square-lattice design (IADMD = 4.7 nm, Figure 25). To relieve this lattice strain single-thymine spacers were introduced between each tweezer arm of the actuating hairpin. MD simulation confirmed improved closure of a tweezer containing single-thymine spacers (1T0bp) that relieved inter-arm distortion present in the 0T0bp construct (Figure 25).

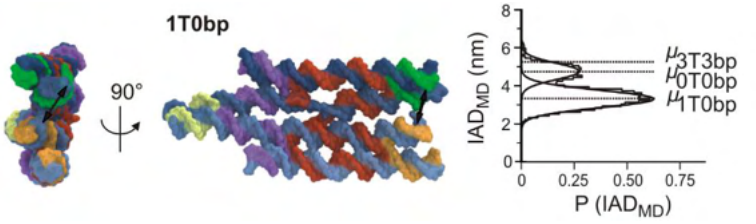


Figure 26. Effects of modifying the hairpin actuator element explored with MD. Two orthogonal views of a typical conformation corresponding to the mean IAD_{MD} of 3.3 nm of the lower subpopulation (highlighted by double-sided arrows) and the full IAD_{MD} distribution (right), predicted using MD of the tweezer with only a single-thymine spacer and no hairpin (1T0bp), showing a substantially reduced IAD_{MD} compared with the three-thymine spacer (3T3bp) and zero-thymine (0T0bp) spacer.

Walter lab previously reported that using a 1T3bp tweezer redesign confirmed substantial improvement of the closed-state; however, a significant low-FRET population in the closed-state remained. 1T4bp and 1T5bp constructs were tested with both resulting in improved closure, though both exhibited several distinct IADFRET populations. In order to elucidate the origin of the distinct states observed using smFRET, Bathe lab investigated the conformational dynamics of the 1T3bp tweezer (Figure 26) as a model system.

Results of MD simulations indicated that the inclusion of explicit thymine dye linker tails had a noticeable effect on the IAD due to their non-specific interactions involving hydrogen bonding and partial base pairing and stacking, resulting in two sub-populations centered at 2.7 nm and 3.6 nm respectively. Simulation of the same construct excluding these tails resulted in IADMD sub-populations with mean values of 3.6 nm and 4.3 nm, supporting the hypothesis that interactions involving these linkers might stabilize conformational sub-states observed experimentally. A redesign of all five HJs to the canonical Seeman J1 sequence resulted in an additional substantial

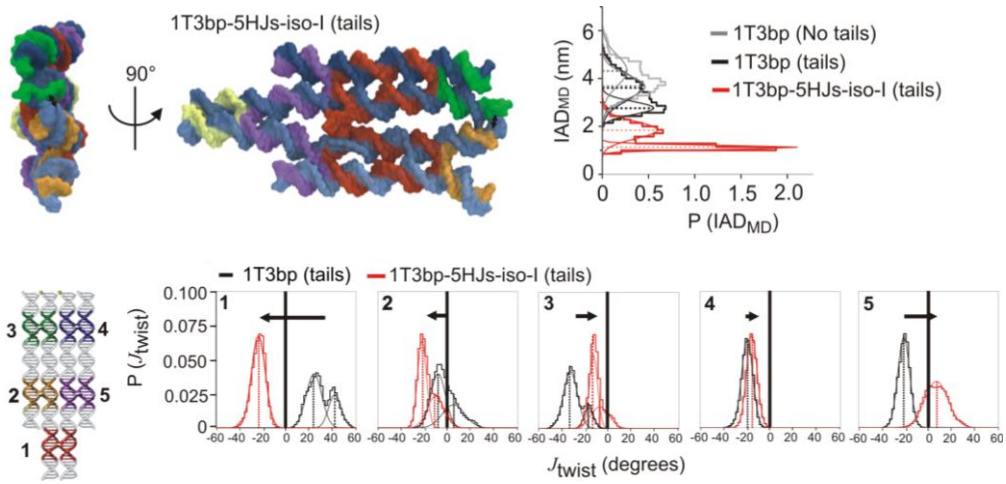


Figure 27. Redesigned Holliday junctions improve tweezer closure. (Top) Two orthogonal views of a typical conformation corresponding to the mean IAD_{MD} of 1.1 nm of the lower subpopulation (highlighted by double-sided arrows) of the '1T3bp-5HJs-iso-I' tweezer (left) and the corresponding IAD_{MD} distributions (right; dotted lines represent mean values, μ). (Bottom) Reduction in individual J_{twist} angles in tweezer 1T3bp-5HJs-iso-I (red) compared with the original junction design 1T3bp (black; dotted lines represent the means, μ, and solid, thick black lines highlight a J_{twist} angle of 0˚. which correspond to the planar conformation). Compared with the original design, the mean J_{twist} angles of all but HJ2 are shifted (arrows) closer to 0˚ in the redesigned tweezer.

shift towards higher mean FRET (the IADFRET decreased to 4.4 ± 0.2 nm). MD simulation indicated that redesign of all five HJs resulted in a planar tweezer conformation that also brought the arms into closer proximity (IADMD values of 1.1 nm and 1.8 nm, Figure 27). This flattening correlates with Jtwist values for the junctions adopting distributions that are on average closer to zero. MD simulations additionally suggested that the dye-linked dT tails play an important role in stabilizing the high-FRET conformation via an inter-tail interaction across the arms. This interaction was enhanced in the construct with the redesigned HJs, suggesting cooperativity with flattening of the overall tweezer conformation.

3. Characterization of optimized enzyme nanoreactors:

To investigate how the preceding structural improvements impact their intended application, the two arms of three representative tweezer designs – 3T3bp (original), 1T4bp (actuator-optimized), and 1T4bp-5HJs-iso-I (1T4bp with all five HJs redesigned to adopt iso-I) is coupled with the enzyme glucose-6-phosphate dehydrogenase (G6pDH) and its cofactor NAD+ to generate DNA-tweezer actuated nanoreactors. Utilizing a PMS/resazurin coupled reaction Yan labmonitored the G6pDH activity in bulk solution by fluorescence (Figure 28A) and found that 1T4bp improved enzymatic actuation by ~2-fold, whereas 1T4bp-5HJs-iso-I further enhanced the nanoreactor performance by ~3-fold over the original 3T3bp design (Figure 28B). To probe the mechanism underlying these enhancements, Walter lab optimized the fluorescent assay to reach single

molecule sensitivity when detected by TIRFM and able to observe single fluorescence spikes as an indication of individual substrate turnovers (Figure 28C). Compared to a control without substrate, the fluorescence spikes were noticeably more frequent (Figure 28C). After applying an empirical intensity threshold to distinguish from noise, showing that only a subset (~20%) of 3T3bp nanoreactors was active (Figure 28D). This observation is likely due to heterogeneity in enzyme orientation on the tweezer arm due to non-specific lysine-DNA conjugation. Accordingly, increasing numbers of nanoreactors became active with improved closure: 28% for 1T4bp and 32% for 1T4bp-5HJs-iso-I.

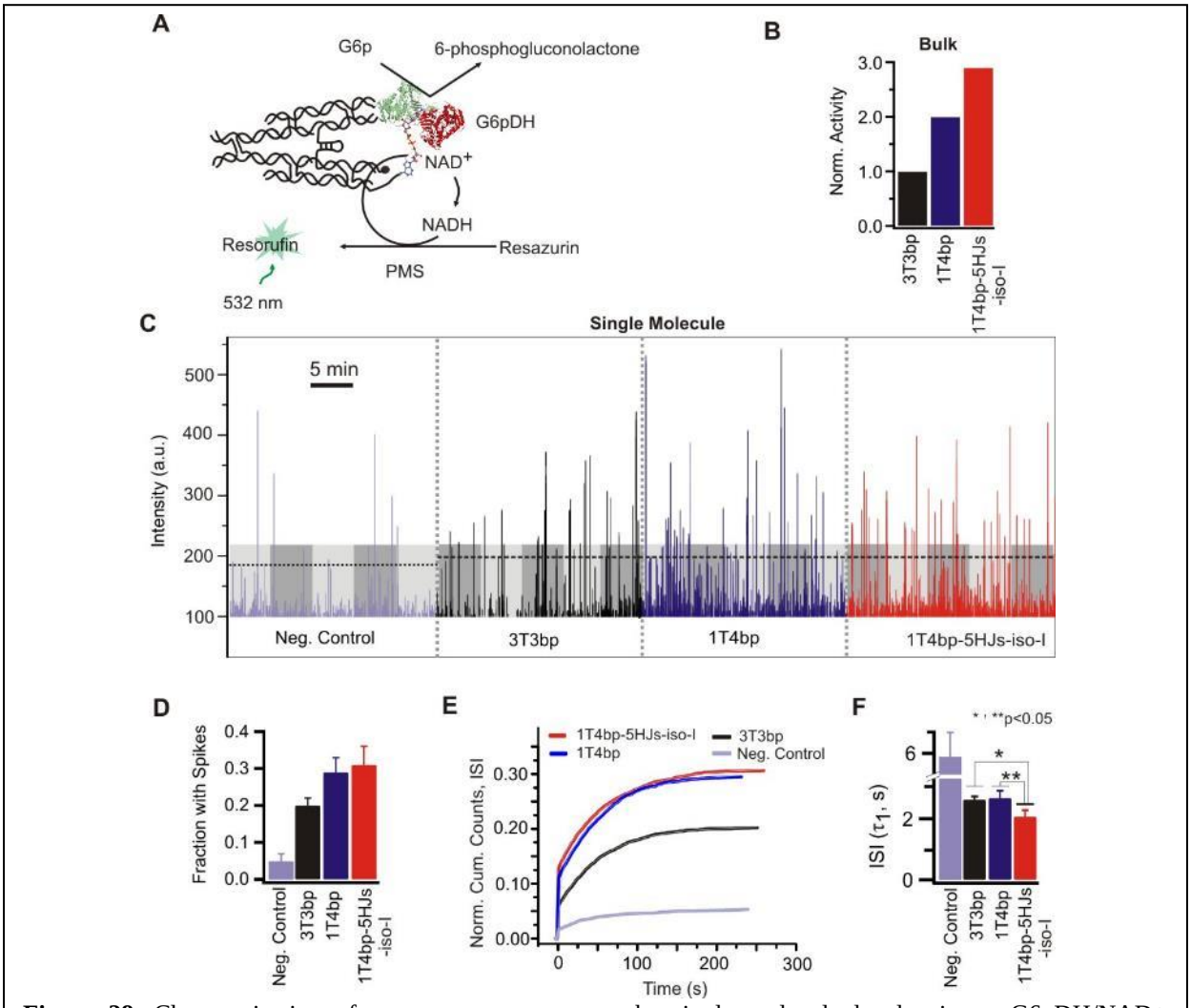


Figure 28. Characterization of enzyme nanoreactor at the single molecule level using a G6pDH/NAD+ enzyme/cofactor pair. (A) Detection of enzyme activity is enabled by a PMS/resazurin coupled assay (B) Relative bulk activity of the G6pDH/NAD+-coupled original (3T3bp), linker-optimized (1T4bp), and junction-redesigned (1T4bp-5HJs-iso-I) tweezers. (C) Time traces for single nanoreactors with different tweezer designs. Each resorufin conversion leads to a single fluorescent spike. The alternating gray and light-gray pattern highlights individual molecules in the concatenated traces. The horizontal dotted-lines represent an intensity threshold (chosen as mean + 8 × standard deviation, SD). (D) Fraction of all enzyme nanoreactors of a particular tweezer design producing fluorescent spikes above the background. The "Neg. Control" is lacking G6p. (E) Cumulative frequency of the inter-spike interval (ISI). These data are best fitted with double-exponential increase functions, yielding two time constants (τ1 and τ2). (F) Comparison of the short ISIs (τ1) extracted from the plot in panel E.

Further a bursting behavior of these single-turnover spikes that we dissected by spike train analysis, plotting the cumulative population distribution of inter-spike intervals (ISIs) for each tweezer design normalized to the total fraction of active nanoreactors (Figure 28E). These data were best fitted with double-exponentials, revealing (at least) two populations: one with a relatively short average ISI ($\tau 1$), the other with a relatively longer average ISI ($\tau 2$). In accord with previous single molecule studies of enzymes, these two populations were interpreted as distinct enzyme conformational sub-states. The population with short ISIs corresponds to enzymes in an optimal catalytic conformation, whereas the population of longer ISIs corresponds to enzymes in non-optimal, catalytically less active conformations. Strikingly, the mean short ISI ($\tau 1$), or wait time between catalytic events of highly active enzymes, did not change from the 3T3bp to the 1T4bp tweezer, but decreased significantly with the redesigned HJs of 1T4bp (Figure 28F). The single molecule observations thus suggest that we have discovered two independent mechanisms for improving nanoreactor performance: (i) a greater number of nanoreactors reach the critical IAD distance needed for activating their coupled enzyme with its cofactor due to improved closure upon optimized design of the actuator element; and (ii) more frequent substrate turnover is achieved when stabilizing interarm tail-tail interactions are implemented based on the straighter tweezer arms resulting from optimized HJs. In summary, the design features of the DNA tweezer identified here are general to many other DNA nanostructures so that we anticipate that our work establishes a roadmap for the rational optimization of the performance of nanodevices including reactors, chemical and biological sensors, as well as programmable nanomaterials.

A DNA walker utilizing toehold exchange

Ever since the step-by-step (hand-over-hand) movement of molecular motors such as dynein, myosin and kinesin super families was mechanistically characterized, attempts have been made to mimic their dynamic behavior in the form of synthetic molecular walkers. Several DNA-based molecular walkers have been synthesized, motivated by a long-term goal of controlling molecular transport processes with the programmability and structural robustness of DNA nanotechnology. Previous studies have shown that DNA walkers can walk directionally along a track upon sequential addition of a DNA strand as chemical "fuel". Despite all this progress, the DNA walkers reported so far have been constrained by slow translocation rates, which are typically on the order of a few nm/min. By comparison, natural protein motors have translocation rate of ~1μm/s under saturating ATP conditions, a 3~4 orders of magnitude faster rate. It is desirable to reduce this gap if synthetic DNA walkers are to serve as useful agents of molecular transport.

Based on prior investigations, the translocation rate of many DNA walkers is believed to be limited by slow catalytic steps or the release of cleavage products. In contrast, the displacement of one strand in a DNA duplex by another can be catalyzed by the nucleation of short single-strand overhangs, or "toeholds", a process that can be very rapid when the reagents are present at high concentrations. Since DNA scaffolds can be used to generate local effective reagent concentrations in excess of 100 μM in bimolecular reactions, a DNA walker using toehold exchange reactions for locomotion may be able to realize higher translocation rates than previously reported DNA walkers.

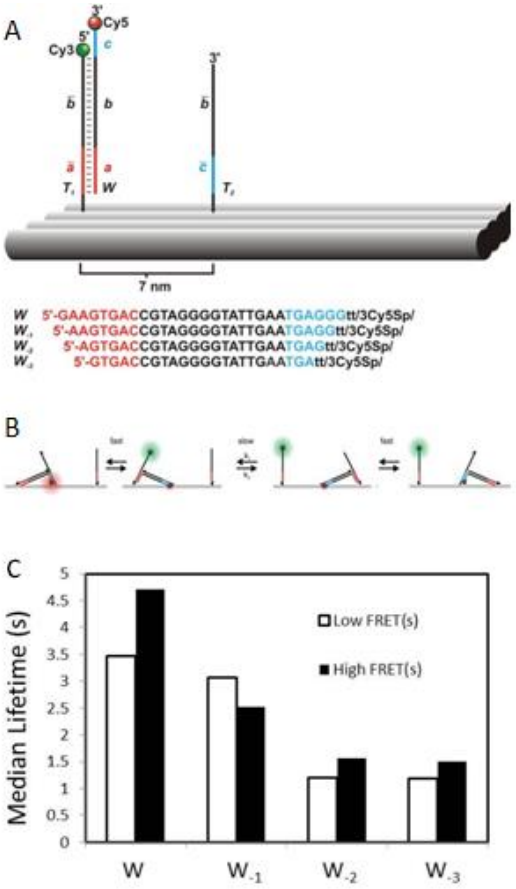


Figure 29. (A) Design of toehold exchange walker and track. Track strands T_1 and T_2 are 5′ and 3′ extensions of ssDNA strands within the 4-helix tile (gray cylinders). (B) Model of walking on a three-stranded track. (C) Median lifetimes in the high- and low-FRET states for walkers with varying toehold lengths.

To this end, we have designed 2-track and 3-track DNA tiles (Figure 29A) and DNA walkers with different toehold lengths. We used smFRET characterization to investigate the mechanism of the walking process. So far, the fastest rate constant of stepping approaches 1 s^{-1}, which is ~100-fold higher than typical DNA-based transporters. We present evidence that the walking occurs via a rapid branch migration step that may be treated as a rapid equilibrium process, followed by slower dissociation and rebinding of toehold sequences (Figure 29B). Consistent with this model, we show that the rate constant of stepping between adjacent track sites is dependent on the length of the toehold sequences. That is, the dwell time spent in low-FRET state and high-FRET states measuring the distance between the walker and a terminal track strand decreases when the toehold becomes shorter (Figure 29C). In the 3-track system, thus, the fastest FRET transitions are observed for a short-toehold W_{-2} walker, with median lifetimes of 1.2 s and 1.5 s in the low- and high-FRET states, respectively. In summary, we have created a rapid, directionless single-stranded DNA walker that utilizes a toehold exchange mechanism to repeatedly traverse oligonucleotide tracks in a head-over-heels fashion.

3D-DNA nanostructure scaffolded lipid compartment as nanoscale reaction chambers

1. <u>DNA barrel origami templated reconstruction of lipid compartment with controllable size:</u>

Cellular compartment is one of the machanism nature developed to ensure high efficiency and specificity of chemical reaction and signaling transduction, as it will provide high local concentration of both protein/enzyme and substrate, prevent toxic intermediate escaping and reduce competing reaction availability. To transfer cellular reaction to in vitro system for better understanding native cellular strategies of spatial organization, here we apply spatial addressable DNA nanostructures as scaffold to direct lipid compartment reconstitution as nanoscale reaction chambers to mimic nature system.

To mimic cellular compartment, our lab have developed a method to reconstruct lipid bilayer compartment using DNA nanostructure template. The general idea is to decorate origami surface with hydrophobic lipid molecules, through complementary hybridization of handles extruding from DNA nanostructure with lipid-DNA conjugates in the presence of detergent, followed by mixing with liposome, and after dialysis to get rid of detergent, lipid compartment can be formed

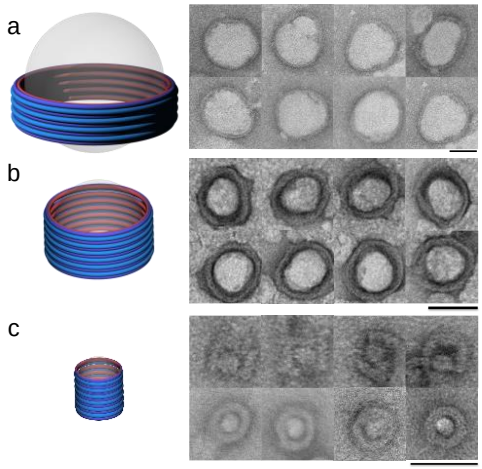


Figure 30. DNA barrel origami scaffolded lipid compartment with controllable size, 90 nm (a), 60 nm (b) and 30 nm (c). (Scale bar: 50 nm)

on DNA nanostructure template. To demonstrate this idea, a group of barrel shaped origami with 90 nm, 60 nm and 30 nm diameter were computationally designed and constructed. By decorating lipid-DNA conjugates onto the inner surface, different sized lipid compartment can be formed, proved by negative stained TEM images (Figure 30). In Figure 30a, white membrane structure found inside 90nm diameter DNA barrel origami with very uniform size. As the height of this DNA origami is around 20 nm, only one conformation, in which origami sit on the surface, was observed under 2D projected TEM images. The same thing happen for 60 nm in diameter DNA barrel shown in Figure 30b, and the diameter of inner lipid structure is also very uniform. For 30 nm diameter DNA barrel, as the height is around 30 nm, two conformations observed under TEM, including origami sitting on surface and lay the side onto surface, in which spherical lipid structure was observed, as shown in Figure 30c.

2. <u>DNA nanostructure scaffolded nonspherical lipid compartment:</u>

As some cellular compartments are not spherical, we are also curious to see whether our method can construct nonspherical lipid compartment, such as tubular shape liposome. To make tubular shaped lipid compartment, a tubular shaped DNA nanostructure was constructed by stacking DNA barrel origami together through complementary hybridization. As shown in Figure 31a, TEM image confirmed the formation of origami tube, with very uniform diameter and length can be up to 2 um. By decorating lipid-DNA conjugates onto inner surface of DNA tube, tubular shaped lipid nanostructure had been made, with very uniform diameter and the lipid tube length can be as long as 1 um. We also established a new type DNA nanostructure, called DNA brick crystal, developed by Ke et al, to template reconstruction of nonspherical lipid nanostructure, as shown in Figure 31b. Three different DNA crystal structures, two with parallel grove (20 nm and 30 nm grove diameter) and the last one has cross shaped grove with 20 nm in diameter, had been constructed. Using the same strategy, by assembling DNA-lipid conjugates onto the bottom of DNA grove, different sized parallel and cross-shaped lipid nanotubes had been successfully fabricated. In summary, we can utilize spatial addressable DNA nanostructures as container to direct lipid compartment reconstitution with controllable size and geometry.

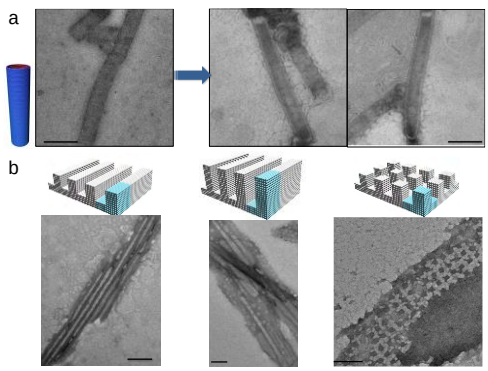


Figure 31. DNA nanostructure scaffolded nonspherical lipid compartment. (a) illustration and TEM image of stacked barrel origami tube before and after liposome reconstitution. (b) three different DNA brick crystal designs and TEM images after liposome reconstitution inside crystal grove. (Scale bar: 100 nm)

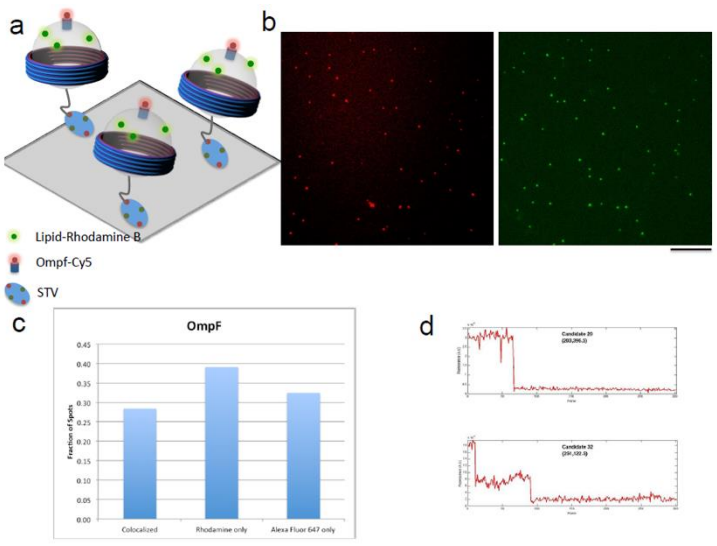


Figure 32. Surface immobilization and fluorescence microscopy imaging to characterize membrane protein assembled onto origami-liposome system. (a) Schematics show DNA Origami-liposome-Ompf immobilization on glass surface. (b) Micrographs of typical sample (Scale bar: 5um). (c) Static analysis of fluorescence co-localized events. (d) Photobleaching of typical Ompf-Cy5.

3. Membrane channel protein reconstitution:

Because the lipid bilayer of organelle membrane is impermeable to most hydrophilic molecules, the membrane of each organelle mush contain membrane transport proteins that can import and export of metabolites. To mimic cellular compartment, we need not only to make lipid compartment, but also to assemble membrane channel protein onto lipid membrane to transport metabolites. Here a channel protein, outer membrane protein f (Ompf) was applied as model to be reconstituted onto DNA nanostructure scaffolded lipid compartment. Ompf was added together with liposome after lipid decoration step, and reconstituted together with lipid bilayer membrane through dialysis process. To quantitatively analyze the yield of Ompf reconstitution, two-color total internal reflection fluorescence (TIRF) microscopy (Figure 32) was used to characterize the fluorescence co-localization of a Rhodamine-labeled liposome and an Alexa Fluor 647-labeled Ompf (Figure 32b). Around 40% origami-liposome complex had been reconstituted with Ompf, and photo-bleaching data showed one or two Ompf was reconstituted on each liposome surface.

4. Future directions:

Work in now in progress to (a) improve Ompf reconstitution efficiency; (b) assembly cascade enzymes into origami template lipid compartment; (c) apply single molecular enzymology method to characterize DNA origami scaffolded lipid compartment (Ompf) encapsulated enzyme activity;

Photosynthetic Pathway

Construction of DNA nanostructured photonic systems that enhance the light-harvesting capability of photosynthetic reaction centers.

The primary focus of this work is the design and construction of an energy conversion system based on a photosynthetic reaction center, using additional dye molecules to achieve broad spectral coverage that increases the absorbance cross-section at wavelengths that the reaction center does not normally absorb light. For this effort DNA templates have been used to achieve precise placement of the photonic components involved. Specifically, a 3arm-DNA-multi-dye complex was used as an antenna and attached to the reaction center via specific cysteine residues. The resulting photophysical and photochemical properties were then examined by monitoring energy transfer in the DNA-bound dye molecules and charge separation in the reaction center. Figure 33A shows the three elements of the nanostructured photonic system: (1) a DNA scaffold to arrange the components at specific positions; (2) light-harvesting pigments for the initial absorption of energy and to serve as energy transfer donors and acceptors. (3) The photosynthetic reaction center from the purple non sulfur photosynthetic bacterium *Rhodobacter sphaeroides*; the reaction center is a pigment-protein complex that uses light energy to power a series of electron transfer reactions resulting in a charge-separated state.

We have incorporated two fluorophores that absorb light between 450 - 700 nm into the nanostructure. The selected fluorophores are normally arranged such that dyes with higher excited state energies (absorbing at shorter wavelengths) are distal to the reaction center and those with lower energies (absorbing longer wavelengths) are proximal. Two pairs of dye molecules were used to show the generality of the design, either Cy3 and Cy5, or Alexa Fluor 660 and Alexa Fluor 750. Cy3 acts as the donor and Cy5 as the acceptor in the first pair, and AF660 acts as the donor and AF750 as the acceptor in the second pair. The fluorophores were chosen so that there is significant spectral overlap between the emission of the dyes and the absorption of the RC to facilitate efficient energy transfer, and so that there is a substantial increase in the absorption cross section in the spectral regions where the

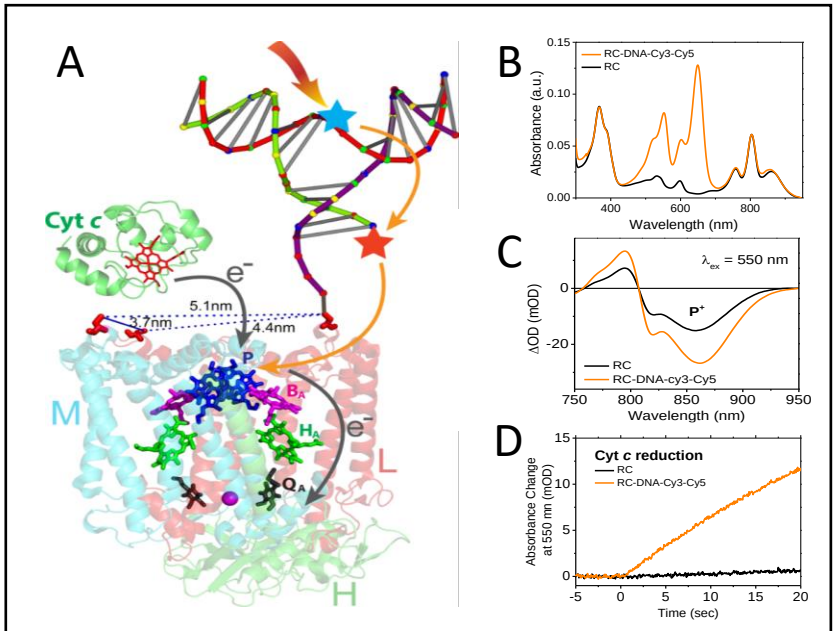


Figure 33. (A) Assembly of 3arm DNA-dye-RC complexes. The excitation energy transfer pathways are marked with orange arrows and the electron transfer pathways are marked with dark gray arrows. (B) absorption spectra of RC only (black) and the assembly (orange) shown in A. (C) light-minus-dark spectra of the assembly (orange) and RC alone (black) and (D) Cyt c reduction as a function of time. C and D: illustrate the energy conversion enhancement of RCs with the additional light-harvesting capability in B.

absorbance of RC alone is low. The enhancement of absorption cross section of the RC-DNA-Cy3-Cy5 complex over that of the RC alone is illustrated in Figure 33B.

The relative amount of charge separation in the RC was investigated by measuring the light-minus-dark difference absorbance spectra of the different dye-DNA-RC complexes. The light-minus-dark difference spectra were obtained by subtracting the absorbance spectrum of a sample taken in the dark from the absorbance spectrum taken under continuous illumination at 550 nm (Cy3 abosrbance peak, 10 nm bandwidth). A 1.8 fold enhancement in P^+ formation over RCs with no dye molecules conjugated was observed at limiting light intensities (Figure 33C). The oxidized initial electron donor, P^+, can be subsquentially reduced by cytochrome c_2, which docks to the periplasmic face (P side) of the RC. The rate of the oxidation of cytochrome *c* was monitored by measuring the absorption intensity changes at 550 nm. Upon 650 nm excitation (Cy5 excitation peak), the DNA-dye conjugated RC showed a much faster rate of oxidation than did the RC alone (Figure 33D). This presumably results from the enhanced absorbance cross-section provided by the light harvesting antenna, increasing the number of photons absorbed per unit time by the 3arm DNA-dye-RC complex. Since the spectrum of reduced cytochrome *c* overlaps strongly with that of Cy3, similar measurements using 550 nm excitation were not attempted as the results would have been difficult to interpret quantitatively.

In summary, a DNA nanostructure with dyes attached at specific positions was conjugated to a RC to serve as a geometrically well-defined light harvesting antenna. This extended the absorbance cross section of the complex into a spectral range where the RC has only weak absorbance. A combination of placement, spectral properties and excited state kinetic properties of the dyes used are important in determining the efficiency of the antenna in energy transfer. The complexes explored in this work provide useful model systems for future applications in nanophotonics. The result was published in the *Journal of American Chemistry* in 2014.

Construction of DNA nanostructured photonic system with a light-harvesting network on a 2-dimensional DNA array

1. Design concept of a photosynthetic network on a 2D DNA platform:

The three arm-DNA junction attached to the reaction center described above provided a good model for understanding the transfer of excitation energy into the reaction center, but as a nanostructured antenna system, it lacked the flexibility to explore in detail different arrangements of dye molecules in order to understand the most efficient energy transfer geometries. Towards this end, the Lin, Yan, Woodbury and Bathe labs have created an artificial light harvesting platform designed specifically to provide carefully controllable geometry and stoichiometry of dyes in an array format. The goal of this effort is to simulate, build and test specific dye arrangements, and in this way iteratively develop the theoretical models needed to guide the design of more complex photonic systems in the future. We have stated with the fundamental design and construction of paired donor-accepter molecules at known distances and with defined linkages to provide the initial experimental data needed to calibrate the theoretical simulations. This will be used as the basis for structures involving larger numbers of dyes covering a broader spectral range in the future.

2. Assembly of a DNA-templated 2D light-harvesting platform:

We are using an addressable 8x8 cubic DNA structure developed previously by Yan's lab. The crystal lattice made from this DNA origami acts as a molecular pegboard onto which dyes can be attached in specific positions. Compared to other DNA nanostructures, the cubic 3D origami used here is relatively rigid (see TEM images in Figure 34A). On one surface of the cube, defined by the ends of helices, there are 8×8 = 64 unique positions to attach dye molecules providing a plethora of different possible geometries (Figure 34B and C). The center-to-center distances between the helices range from 2 to 16 nm. However, detailed modeling has shown that the actual distances based on the helical structure of double-stranded DNA depend on the position and mode of attachment and can actually be less than 1 nm.

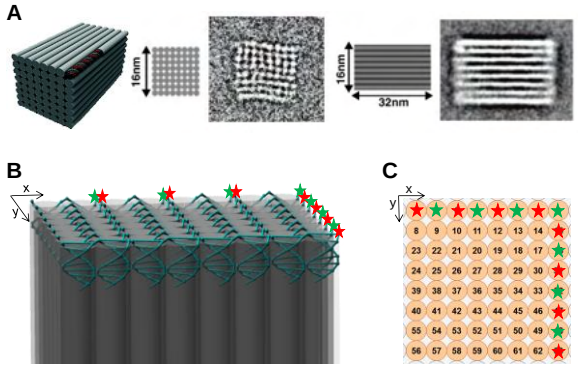


Figure 34. (A) Schematic figure of the 8×8 DNA origami. From left to right: the 3D structure of 8×8 DNA origami, top view schematic showing the dimensions, top view AFM image, side view schematic showing the dimensions, and side view AFM image. (B) Perspective view and **C.** top schematic of DNA helices on the end of the 8×8 DNA origami structure showing the possible positions to for attachment of the dyes.

Recently, we have designed and constructed a version of this structure using a cy3-cy5 FRET pair in 3 geometric arrangements. For the closest distance (neighboring helices), 2 geometric layouts

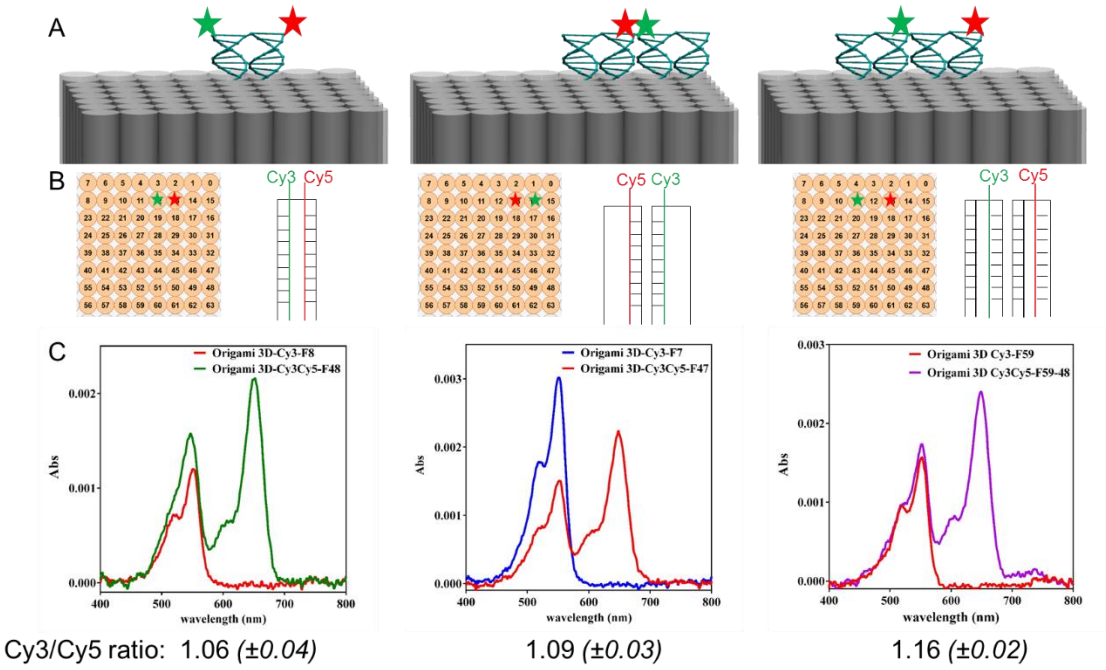


Figure 35. (A/B) Schematic structure of the three origami-Cy3-Cy5 constructs: neighboring helices in same loop (Cy3Cy5-X2C, left), neighboring helices with different loop (Cy3Cy5-X2, center), and alternating helices (Cy3Cy5-X4, right). (C) Absorption spectra of the three origami-Cy3-Cy5 constructs overlaid with the corresponding spectrum of the Cy3-only construct. Scattering due to the large size of the DNA origami was corrected by subtracting a Rayleigh scattering function. The numbers under each absorption spectrum indicate the Cy3:Cy5 ratios calculated from that spectrum.

are possible, i.e. cy3 and cy5 dyes attached either to the helper strands that share the same M13 scaffold loop (called Cy3Cy5-X2C, Figure 34A/B, left), or the two dyes attached to different M13 loops (Cy3Cy5-X2, Figure 34A/B, center). (Helper strands are the pieces of DNA used to pair to the long, single-stranded M13 DNA at specific places and fold it into a defined structure). While the center to center distance between two helices is 2 nm, the exact distances for these two constructs are difficult to estimate precisely due to the flexibility of the structures (see below). A third design was also constructed in which alternating helices have dyes attached. In this case, the distance between cy3 and cy5 molecules is estimated to be ~4 nm (Cy3Cy5-X4, Figure 34A/B, right).

In all samples, Cy3 and Cy5 dyes are covalently attached to either the 3' or 5' ends of the DNA helper strands and positioned at the end of helices with an unpaired TT linker to prevent stacking on the double-stranded DNA. After annealing, all samples are purified using a 100 kD amicon filter to remove extra helper strands. Figure 36 shows the characterization of the complex using a 1% agarose gel. Three bands are visible representing the DNA structure with different dyes attached (Cy3 only (green), Cy5 only (red), and Cy3 Cy5 overlapping (orange). There are no free helper strands detectable on the gel.

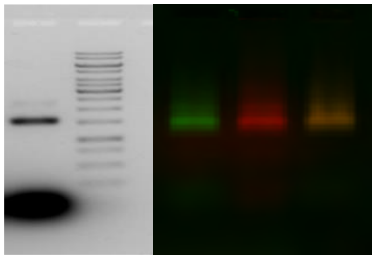


Figure 36. 1% Agarose gel of the unpurified origami structure (left), and purified origami structure (right) including Cy3 only band (green), Cy5 only band (red), and Cy3 Cy5 overlapping band (orange).

The absorption spectra of the 3 different two-dye geometries (Cy3Cy5-X2C, Cy3Cy5-X2, and Cy3Cy5-X4 in Figure 35A/B) are shown in Figure 35C**.** Extinction coefficients provided by the dye manufacturer (ε = 150 $mM^{-1}cm^{-1}$ for Cy3, and ε = 250 $mM^{-1}cm^{-1}$ for Cy5) were used to calculate the concentration of the dyes, and subsequently their ratio for each of the double labeled origami constructs. In each case, the ratio very close to 1:1 for the two dyes (Figure 35C), indicating near stoichiometric assembly of the structures with the dye-labeled DNA helper strands

3. <u>Energy transfer efficiency characterized by steady state fluorescence emission spectroscopy:</u>

Steady state fluorescence emission spectra were measured for the 3 doubly labeled DNA origami structures of Figure 35 and the results are shown in Figure 37. The Cy3 dye was excited directly at 520 nm. The same structure with only the Cy3 dye was also measured as a reference. The amount of FRET was calculated based on the decrease in emission intensity of Cy3 in the presence of the acceptor Cy5, compared to that of the Cy3-only sample, using the equation:

$$E = 1 - \frac{A_D}{A_{DA}}\frac{I_{DA}}{I_D} \qquad (2)$$

Here, I_D, and A_D are the emission and absorbance, respectively, of the donor in the absence of the acceptor; and I_{DA}, and A_{DA} are the corresponding emission and absorbance of the donor in the presence of the acceptor. The resulting FRET efficiencies are given below each plot in Figure 37, and the error shown is the standard deviation of the value derived from three measurements of each sample.

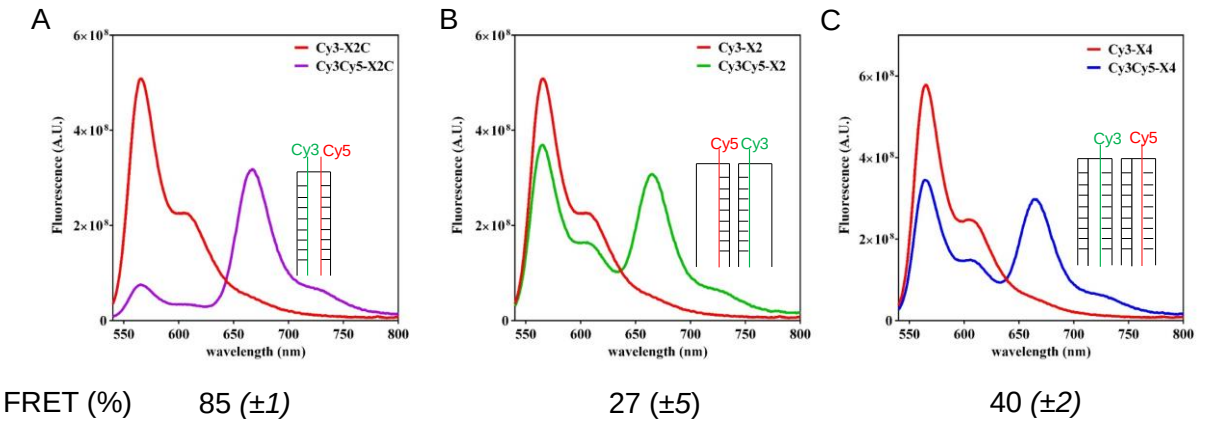


Figure 37. Steady state emission spectra of dye-labeled DNA origami structures with different designs for the position of Cy3 and Cy5. In all the plots, the red curve shows the emission of the Cy3-only structure used for the calculation of FRET efficiency. The spectra were normalized based on the measured concentration of Cy3 in each sample. The FRET efficiency reported below each plot is calculated based on the decrease of the emission of the donor dye (Cy3) in the presence of the acceptor, compared to its emission in the absence of the latter. (A) Structure with both dyes on neighboring helices connected by an M13 loop (Cy3Cy5-X2C). (B) Structure with dyes on neighboring helices where each helix belongs to a different loop of the M13 scaffold (Cy3Cy5-X2). (C) Structure with dyes on alternate helices (Cy3Cy5-X4).

It is worth noting that the two samples with dyes on neighboring helices result in a very different energy transfer efficiencies (85% and 27% for Cy3Cy5-X2C and Cy3C5-X2, respectively). The main difference between these two constructs is whether the dye-labeled helper strands are both associated with one loop of the M13 DNA or cross between two M13 DNA loops. The first design is predicted to result in a more rigid structure than the second and the specific attachment points within the helices are also different, as illustrated in Figure 35A. This is exactly the kind of experimental information that is needed to create and validate our theoretical models for energy transfer in these nanostructured systems.

4. Energy transfer efficiency characterized by time-correlated single photon counting (TCSPC) techniques:

The energy transfer processes for each construct was also investigated using time-resolved fluorescence spectroscopy. Fluorescence decay kinetics were measured between 550 and 700 nm at 10 nm intervals, covering the fluorescence emission bands of both Cy3 and Cy5. Excitation was performed with a pulsed laser at 520 nm which predominantly excites Cy3. The rate of the decay of the excited state of Cy3 should increase as the efficiency of Cy3 to Cy5 energy transfer increases, and the rise time of the Cy5 excited state fluorescence signal should be observed correspondingly. As shown in Figure 38A, the decay of the fluorescence from each of the three test constructs (red, green, and blue traces) was faster than the corresponding Cy3-only sample (black trace). Figure 38B shows an example of the corresponding rise time in the fluorescence at 680 nm from the Cy5 excited state in the Cy3Cy5-X2 construct. As can be seen, the rise is not instantaneous, presumably because it is accepting energy from Cy3 over time.

The fluorescence from the three constructs was collected as a function of both time and wavelength, $F(\lambda, t)$, and the entire dataset was fit globally with a sum of exponentials decay model using

equation (3).

$$F(\lambda,t)=\sum_i A_i(\lambda)e^{-t/\tau_i} \quad (3)$$

Here, $A_i(\lambda)$ is the amplitude as a function of wavelength (called the Decay Associated Spectra, DAS) associated with a particular decay time constant τ_i. Four exponential components were required to adequately fit samples Cy3Cy5-X2 and Cy3Cy5-X4 and their DAS are depicted in Figure 38C and D, respectively. Both samples show two short lifetime DAS with positive amplitudes in the Cy3 emission wavelength region and negative amplitudes in the Cy5 emission wavelength region. This DAS shape is a classic signature of Cy3-to-Cy5 energy transfer. There are apparently two kinetic components involved in the energy transfer process, one with a lifetime of 165-225 ps (black curve) and the other with a lifetime of about 750 ps (red curve). The global fitting also returns 2 components with longer, nanosecond lifetimes, both with positive amplitudes across the entire wavelength region, and these presumably represent the decay of Cy3 that does not undergo energy transfer and the decay of Cy5 after energy transfer is complete. The Cy3 to Cy5 energy transfer in the Cy3Cy5-X2C sample where both dye molecules are on the same loop exhibits a very fast component (consistent with its apparently high efficiency of energy transfer). Higher time resolution measurements will

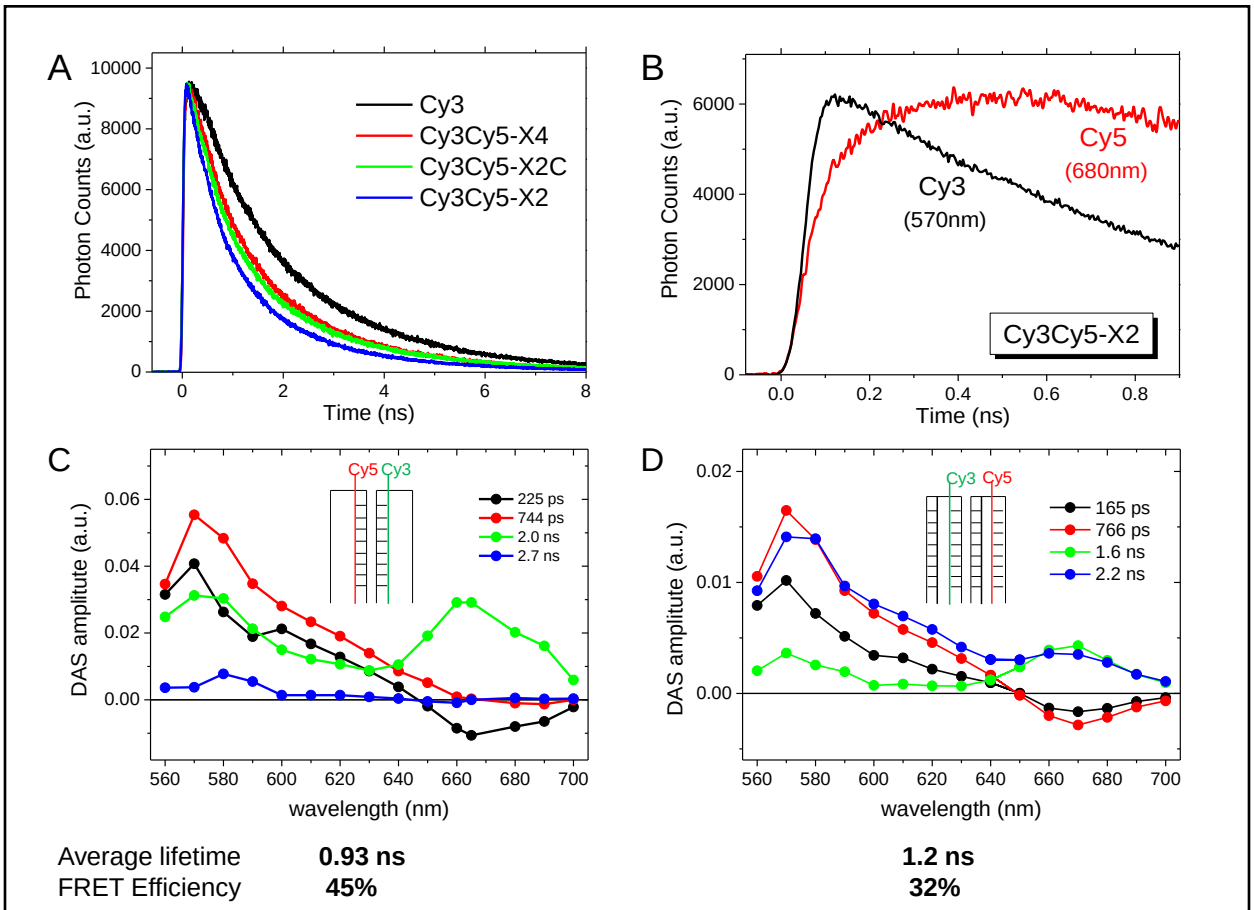


Figure 38. (A) Fluorescence decay traces at 570 nm for Cy3 (black), Cy3Cy5-X4 (red), Cy3Cy5-X2C (green), and Cy3Cy5-X2 (blue). (B) Kinetic traces of Cy3 (black) and Cy5 (red) from Cy3Cy5-X2. (C) and (D). DAS of Cy3Cy5-X2 and Cy3Cy5-X4 resulting from global analysis using 4-exponential components. The average decay lifetimes of Cy3 in the construct and the Cy3-to-Cy5 FRET efficiencies are given below each DAS plot.

be required to adequately describe the excited state kinetics in that system, and these are in progress.

One can use the excited state lifetimes to estimate the energy transfer efficiency of each sample. Because the decay kinetics in these samples is complex, amplitude-weighted average lifetimes of Cy3 and relative amplitudes were calculated using equation (4):

$$\tau_{ave} = \frac{\sum_i A_i \tau_i}{\sum_i A_i} \qquad (4)$$

and these were used to estimate the energy transfer efficiency. Here, A_i and τ_i are the amplitude at 570 nm and the associated lifetime from global analysis. Using this, the average lifetimes for Cy3Cy5-X2 and Cy3Cy5-X4 were determined to be 0.93 ns and 1.2 ns, respectively, corresponding to a 45% and 32% energy transfer efficiency. Note that the values determined from steady state measurements for these samples were also in the 30-40% range. The heterogeneity of the kinetics makes the use of average lifetimes to calculate the energy transfer efficiency somewhat inaccurate, but the fact that there is reasonable agreement is encouraging.

5. Future directions:

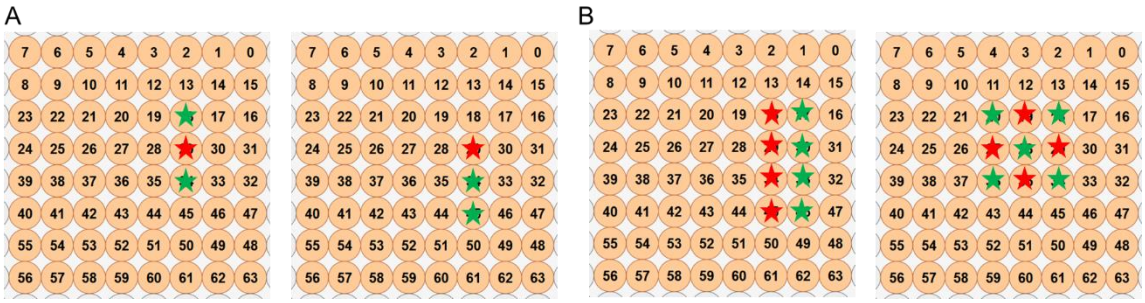


Figure 39. Future designs involve **A.** linear arrangements of Cy3, Cy5 with different ratios and **B.** 2D arrangements with 2 rows and alternative patterns.

We are using this platform now to explore a variety of possible dye geometries. A few examples of such constructs are illustrated in Figure 39. The designs in Figure 39A focus on testing the actual contribution of the position in a multi-donor situation. The designs in Figure 39B focus on studying the role of stoichiometry as well as reciprocal positioning for a multiple donors and multiple acceptors in the system. Array design, experimental analysis and modeling will be performed iteratively to generate the fundamental parameters needed to engineer increasingly complex systems.

Electrode interface of photosynthetic reaction center proteins in macroporous materials

1. Background and design concept:

The laboratories of Seo, Woodbury and Lin are exploring ways to effectively interface the light-induced redox potentials generated by photosynthetic reaction centers from purple bacteria with novel nano and meso-structured electrode materials. Interfacing redox proteins with electrodes remains a very challenging but important goal. Such an interface opens the door to a wide variety of applications involving the exchange of energy and information between biological and

electronic systems. Coupling such an interface to a biophotonic element adds an additional level of both control and energy input.

Antimony Tin Oxide (ATO) thin films can be produced on surfaces to form optically transparent and electrically conductive layers. Under certain conditions, the ATO films take on a porous structure and the dimensions of the porosity can be varied from nanometers to many microns. The focus of this work are so-called macroporous films, with features on the order of microns. The presence of the porous features have two advantages. First, they greatly increase the effective area of the surface (hundreds of fold) and second they provide protective cavities for association with macromolecules such as proteins or DNA.

Recently, Seo's lab collaborated with the laboratory of Anne Jones at ASU and demonstrated the ability to associate cytochrome c with these surfaces in such a way that the cytochrome *c* could be readily reduced by altering the potential of the electrode. The cytochrome c under these conditions had a redox potential of 207 mV (near the solution value) and they calculated an electron transfer rate between the electrode and the cytochrome of about 1 s^{-1}. This represented a significant advance, showing that stable incorporation of a common biological redox component could form a facile interface with the ATO electrode.

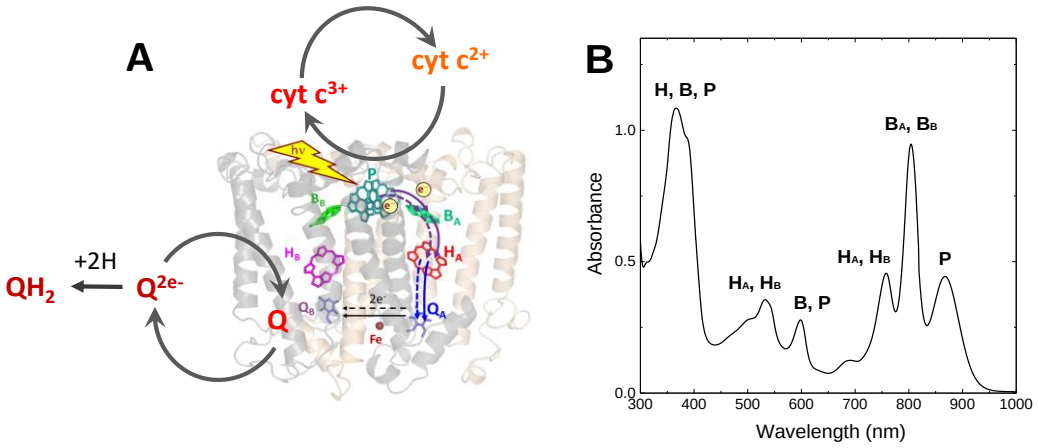


Figure 40. (A) Electron transport in the *Rhodobacter (Rb.) sphaeroides* reaction center. A special dimer of bacteriochlorophylls, denoted 'P', is promoted to an excited state by solar energy and rapidly loses an electron to an acceptor molecule, the monomeric bacteriochlorophyll 'B_A'. This electron is very quickly transferred to the bacteriopheophytin molecule 'H_A' and then on to the quinone molecule 'Q_A' to separate charge across the membrane. The electron is then passes from Q_A to another quinone molecule, 'Q_B'. This process happens twice to donate 2 electrons to Q_B, which is subsequently protonated forming a hydroquinone, QH_2, and leaves the Q_B pocket. The hydroquinone molecule diffuses through the membrane to the cytochrome b/c1 complex and is oxidized, generating a proton motive force to drive ATP synthesis. The special pair, P, is then re-reduced by donation of an electron from the mobile electron carrier, cytochrome c_2. (B) Absorption spectrum of isolated reaction center proteins. Pigments responsible to each absorption band are labeled.

One of the natural biological partners of cytochrome *c* is the bacterial photosynthetic reaction center (RC) from purple non-sulfur bacteria. The RC converts solar energy into chemical redox energy through a series transmembrane electron transfer reactions as illustrated in Figure 40A. The initial electron transfer reaction starts with excitation of the primary electron donor (P), an electron transfer cascade is initiated and continues down a redox gradient to a quinone molecule (Q_A, via cofactors at the B_A and H_A sites). In less than a nanosecond, the oxidized and reduced species in the reaction center are separated by about 30Å. The quantum yield of charge separation per photon

absorbed is almost 1. The electron then passes from Q_A to the second quinone, Q_B, which is subsequently reduced and doubly protonated and then diffuses through the membrane to the cytochrome *b/c1* complex, where it is oxidized and a proton motive force is generated for ATP production.

An important point of this process is that the second quinone acts as a two-electron gate, converting a one electron photo-induced electron transfer into a two electron reduced species able to leave the RC and participate in two electron redox chemistry. This is key as almost all of the redox chemistry that takes place during carbon and nitrogen metabolism is two electron chemistry.

Equally important is how the oxidized primary donor (P^+) is re-reduced. This takes place via electron transfer from cytochrome *c* in the bacterial system; the RC docks with the cytochrome and an electron transfer reaction takes place with a rate constant on the order of 10 microseconds. These concepts are diagramed in Figure 40A. In the work described below, we take advantage of the natural electronic interface between the RC and the cytochrome *c* as well as the one-to-two electron redox transformation carried out by the RC to create a system capable of accepting electrons from the ATO electrode, driven by the energy of light, and then creating a two-electron reduced product. The absorption spectrum of isolated reaction centers is shown in Figure 40B.

The *Rb. sphaeroides* RC has previously been attached to electrodes to generate photocurrent. However, the vast majority of the prior studies involved direct monolayer deposition of RCs on electrodes, and therefore current generated was limited to the nanoamp per square centimeter scale. Nature, however, does not rely on a monolayer. The intracytoplasmic membrane of photosynthetic purple bacteria, within which the antenna complexes and reaction centers are contained, invaginates to form 3D structures such as vesicles, tubules and lamellae (allowing thylakoid-like stacking) to maximize the surface area available for the photosynthetic machinery (Figure 41A). The few studies that have achieved µA of photocurrent have done so using RCs associated with porous TiO_2. By incorporating RCs into a porous material, greater numbers of RCs per area and thus greater photocurrents were achieved. However these studies involved the RC donating an electron to the TiO_2 and as the reduction potential of the quinones was too low to do this it was necessary to exclude quinone from the electron transport chain, limiting the usefulness of any such a bioelectrochemical device.

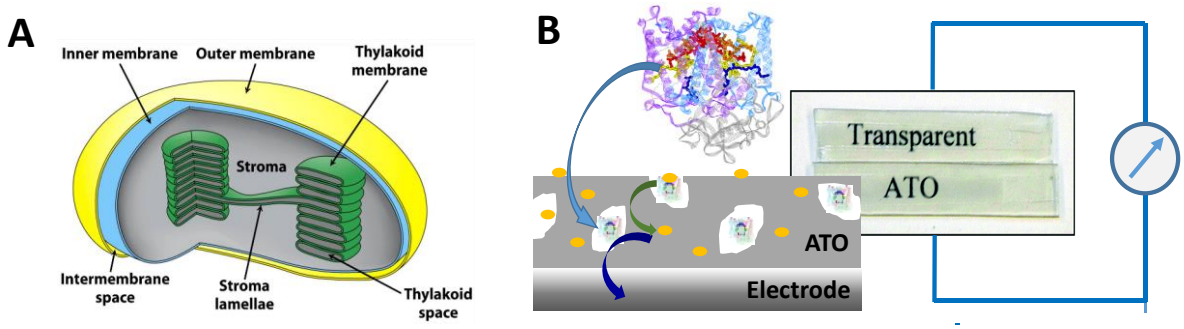


Figure 41. (A) Structure of chloroplast from plants showing stacked thylakoid membranes inside. The photosynthetic apparatus, including reaction center proteins, are embedded in the membranes. (B) Schematic illustration of RC incorporation into ATO pores and the setup for photoinduced current measurements.

Antimony-doped tin oxide (ATO) thin films are transparent, conductive electrode materials that are porous and can potentially incorporate multiple layers of RCs analogous to natural systems (Figure 41B). As described above, in contrast to the prior TiO_2 work, we have devised a system

in which the ATO acts as a cathode, providing electrons to the system and ultimately generating a two electron reductant.

2. Incorporation of *Rb. Sphaeroides* RCs into the pores of ATO films:

The first step of the work was to achieve binding of the *Rb. Sphaeroides* RCs to the ATO. RCs were isolated from cultures of *Rb. Sphaeroides* 2.4.1. and then purified using anion exchange followed by size exclusion chromatography. Macroporous ATO was synthesized by modifying a previously established sol-gel route for producing mesoporous coatings[2]. Thin films of ATO were then prepared on fluorine-doped tin oxide (FTO) glass slides using the doctor-blade method.

Initial trials to incorporate RCs within the pores of ATO were unsuccessful, hampered by aggregation of RCs in solution and a lack of binding due to the negativity of both ATO and the RC in nonionic detergent. The net surface charge of the RC at pH 8.0 is negative (pI of the RC is 6.1), resulting in an effective repulsive force between the RCs and the negatively charged surface of the ATO. This was successfully addressed by changing the detergent from nonionic Lauryldimethylamine-oxide (LDAO) to the cationic detergent dodecyltrimethylammonium bromide (DTAB) and increasing the ionic strength of the buffer by addition of KCl (250 mM) to mask the electrostatic repulsion of the charged headgroups of the detergent. The RCs were successfully incorporated into the ATO under these conditions, however, the RCs rapidly washed out of the pores when placed in electrolyte buffer for photocurrent measurements. It was possible to stabilize the system by adding a clear polymer Nafion®, however, the RCs were not stable in the cationic detergent, as shown by the depressed 'P' band at 865 nm in the absorption spectrum.

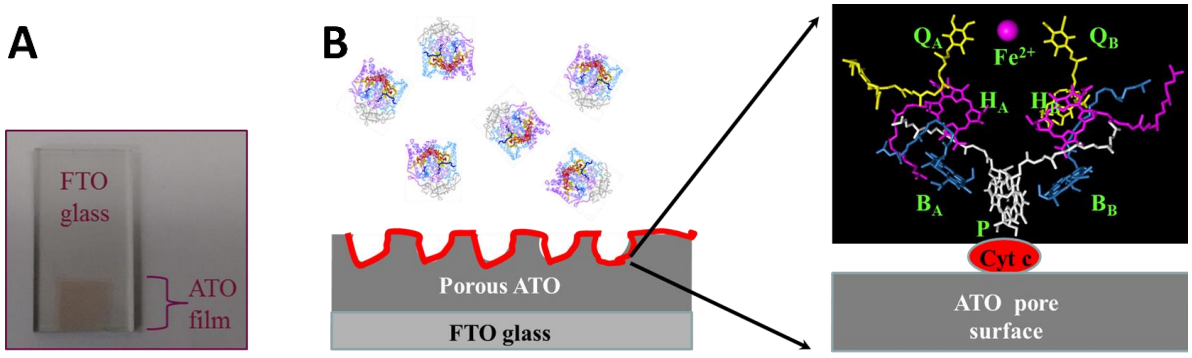


Figure 42. (A) ATO film (on FTO glass) pre-soaked in cytochrome c (shown in the purple square, the dimension is 1x1 cm); (B) Schematic illustrating the oriented binding of RCs to the surface of ATO pores via cytochrome c.

Moreover, the orientation of the RCs within the ATO pores could not be specified, which may hinder the electron transfer to ATO.

We then decided to take advantage of the previous work discussed above, interfacing a layer of cytochrome *c* in the ATO pores to which the RC would bind. Cytochrome *c* has a net positive charge and readily interacts with the ATO film. As mentioned above, it has previously been shown to immobilize in ATO pores and retain its native conformation and function. In the intracytoplasmic membrane of *Rb. Sphaeroides*, cytochrome *c* docks to the reaction center and donates an electron to the oxidized primary electron donor, P^+. Thus the cytochrome can both act as an oriented docking component and as a redox wire, connecting the RC to the ATO electrode.

Cytochrome *c* (horse heart) was adsorbed to ATO by incubating ATO slides in 150 µM protein in pure water (18.2 MΩ cm^{-1}) for 30 minutes as described in Kwan *et al* (Figure 42A). Excess protein solution was withdrawn with a pipette and ATO surfaces were washed repeatedly with pure water and left to dry. A solution of *Rb. Sphaeroides* RCs was then applied to the ATO films using a pipette. Absorption spectra of the RC-ATO slides showed that RCs were successfully incorporated within the ATO pores and retained their conformation and function (Figure 43). In this way, a density of 0.5 nmoles RCs/cm^2 (estimated from the ~0.15 optical density of the film at 800 nm) was achieved. RCs immobilized in this way are extremely stable within the ATO pores, producing photocurrent weeks after initial measurements when stored at 4ºC in the dark.

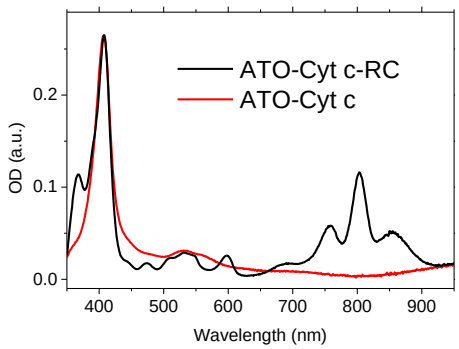


Figure 43. Absorption spectra for an ATO slide following soaking in cytochrome c (red) and a cytochrome c-soaked ATO slide following application of RC solution (black). The curves are normalized at the absorption maxima near 410 nm. Slides have been left to air dry after each step.

3. Photocurrent measurements:

To characterize the function of ATO-RC system, photocurrent generated in the RC-ATO slide was measured using the electrochemical set-up shown in Figure 44. In addition to the working electrode and counter electrode shown, an Ag/AgCl reference electrode was also included to monitor the ambient redox potential. In the initial work, the electrolyte buffer was 0.1 M Tris containing 100 µM quinone (the native ubiquinone-10). The RC-ATO slide was set as the working electrode and the measurement were run at the open potential of the system. The photocurrent generated was measured with and without illumination using a Titanium-Sapphire laser as the light source (Millennia pumped Tsunami, Spectra Physics) at an intensity of 5-10 mW/cm^2. Photocurrent was recorded using a CHI-660A electrochemistry workstation (CHI Instrument Co., USA).

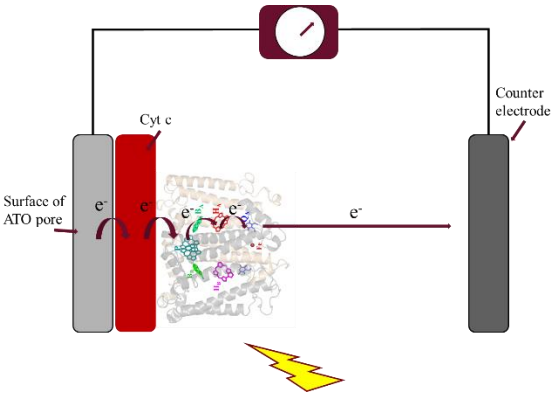


Figure 44. Schematic of electrochemical set-up and proposed electron flow indicated by arrows.

Various sample conditions were tested to understand the origin of the photocurrent generated from the ATO-RC system and the results are summarized in Figure 45.

Both the ATO slide pre-soaked in cytochrome *c* without RCs, and ATO slide with RCs without cytochrome *c* showed no detectable photocurrent within the noise (Figure 45A and B). ATO slides which were not pre-soaked in cytochrome *c* also had a tenfold lower amount of RC (determined by their absorption spectra). It is likely that any RCs present in these ATO slides had simply dried onto the ATO films and were rapidly lost in the electrolyte buffer. A photocurrent of up to 2 µA was observed from an ATO slide pre-soaked in cytochrome *c* and with RCs attached (Figure 45C). However, the initial high photocurrent rapidly dropped off to a lower level (~ 0.5 µA) which was then sustained for long time. We hypothesized that the fast decay was due to RCs with only Q_A and no Q_B. Q_A does not leave the pocket and thus once it is reduced, current ceases. The concept was that the RC Q_B site needed to be filled for the sustained current to dominate as this would allow two electron reduction of Q_B and rapid exchange with unreduced quinone in the buffer. This was not taking place very quickly due to the very limited solubility of ubiquinone-10 (the native molecule has a long hydrophobic tail with 10 isoprenoid units). To overcome this, we soaked the RCs in a tenfold molar excess of ubiquinone-0 (which has no hydrophobic tail and is thus much more water soluble) before loading onto the cytochrome *c* coated ATO film. In this case, the ubiquinone-0 occupied the Q_B pocket of the RCs. Ubiquinone-0 was also incorporated in the Tris electrolyte buffer, at a final concentration of 100 µM, to facilitate exchange for continued current flow. Under these conditions the fast decay phase was almost entirely diminished and the sustained part became dominant and was maintained at 1-2 µA level (Figure 45D).

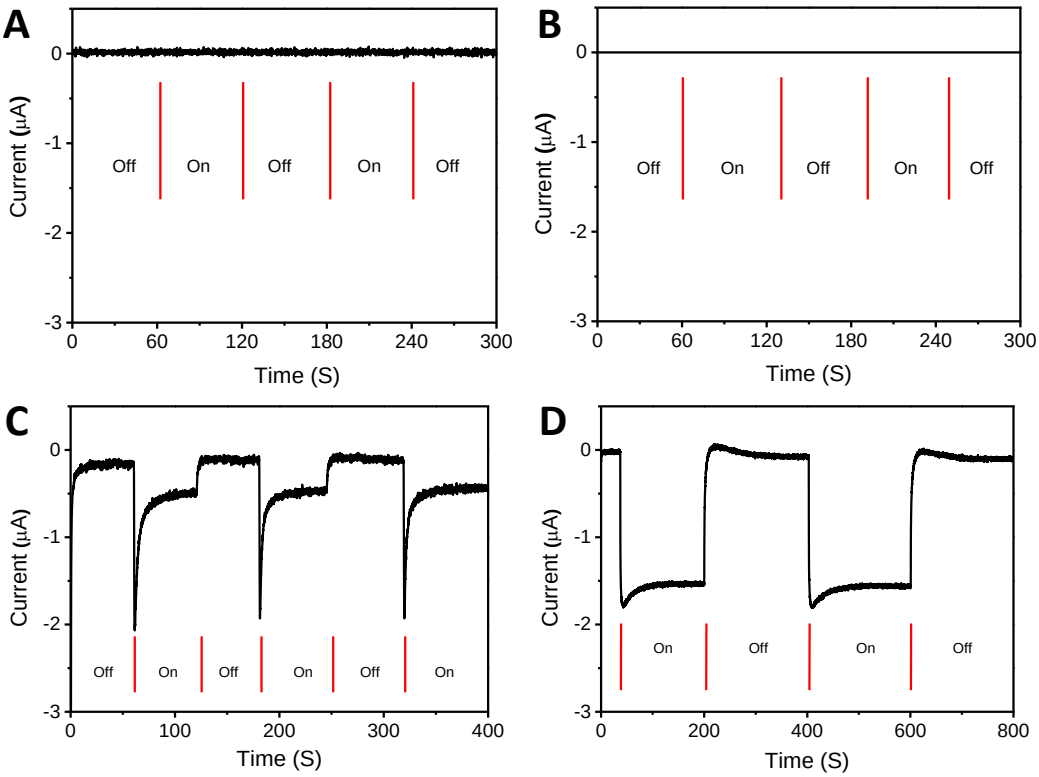
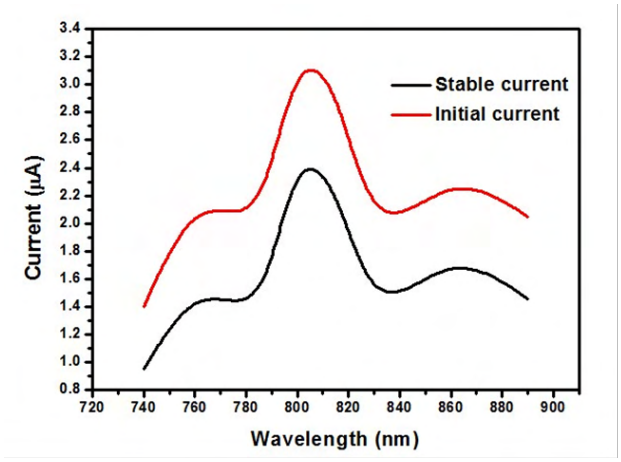


Figure 45. Photocurrent detected from the ATO films (A) ATO coated with Cytochrome c (ATO-Cyt) without RC in 100 µM Ubiquione-0, excited with Ti:S laser at 800 nm at 10 mW/cm^2; (B) ATO-RC without cytochrome c in 100 µM ubiquione-0 at 10 mW; (C) ATO-Cyt with RC and ubiquinone-10; and (D) ATO-Cyt with RC where RCs have been pre-soaked in ubiquinone-0. Red vertical lines mark the light ON/OFF times.



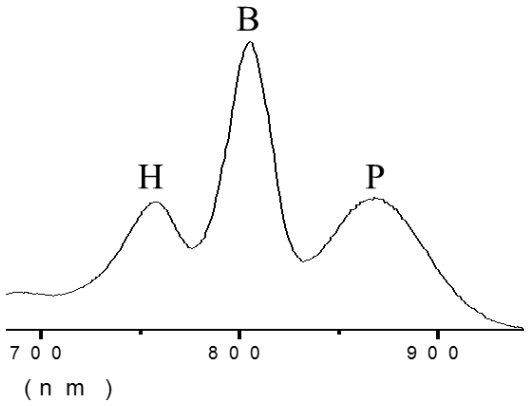


Figure 46. Left: Action spectrum collected for RC-ATO slides; Right: Absorption spectrum of *Rb. sphaeroides* RC in the Qy transition region.

To demonstrate that the observed current derives from electron transfer in the RCs, the action spectrum of the photocurrent was measured (photocurrent as a function of illumination wavelength). In this measurement, a tunable continuous-wave Titanium:Sapphire laser was used as the light source. The excitation wavelength was tuned from 700 to 880 nm and the output power was kept constant. The photocurrent as a function of excitation wavelength (the action spectrum) is shown in Figure 46 left. The spectral profile closely resembles that of the RC absorption spectrum (Figure 46 right), suggesting that the RC is indeed responsible for the observed photocurrent. Note that both the fast and slow phase of the photocurrent response had the same action spectrum.

The redox characteristics of the electrode interface were characterized by varying the potential of the anode relative to the Ag/AgCl reference from -0.15 V to +0.25 V and measuring the photocurrent. Figure 47 shows this curve (red) overlaid on the titration profile of the cytochrome *c* spectrum reported previously for the ATO/cytochrome c system without the reaction center present (shown is the potential as a function of the fraction of cytochrome reduced). As can be seen, the two curves have nearly the same midpoint potential, which is similar to that expected for horse heart cytochrome c. This is consistent with the idea that it is the cytochrome that first accepts the electron from the ATO electrode and then provides that to the RC.

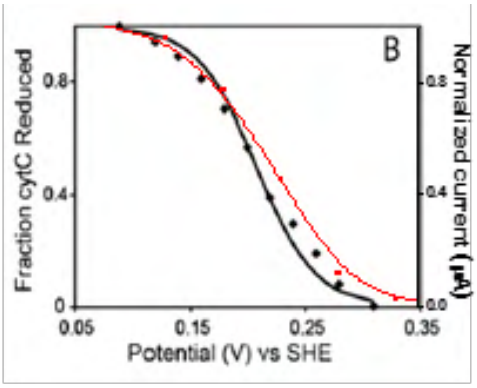


Figure 47. Photocurrent as a function of applied potential for an ATO slide soaked in cytochrome C and RCs (red) overlain on a potential titration curve reported for ATO soaked in cytochrome c in Kwan *et al*. Photocurrent data have been normalized to 1 at the maximum.

4. Summary

In this work we have demonstrated the incorporation of RCs into the pores of transparent, conductive ATO films by coupling the RC to the surface via its natural partner, cytochrome c.

This approach has several advantages: 1) RCs are naturally oriented relative to the ATO surface such that the electron-accepting 'P' end is facing the ATO surface and can directly receive electrons from the cytochrome. 2) The quinone end of the RC is available for exchange with the buffer, such that quinone can be reduced in the Q_B pocket and then released into solution to perform chemistry. 3) The reaction center in this system serves to couple a one-electron photo-induced electron transfer process into the formation of a two electron reductant, allowing interface with common two electron processes in organic chemistry. Photocurrents of ~2 $\mu A/cm^2$ were demonstrated. Both the action spectrum of the photocurrent and the potential titration curve are consistent with a system in which the electron travels from the ATO to the cytochrome and then to the RC where the quinone is reduced and released.

This work represents the first report of the incorporation of RCs into the pores of ATO and the first manuscript from this subproject is currently in preparation.

5. Future directions:

Work is continuing to improve this system by increasing the concentration of RC applied, the RC-ATO incubation times and the levels of light intensity applied to the RC-ATO slides during photocurrent measurements.

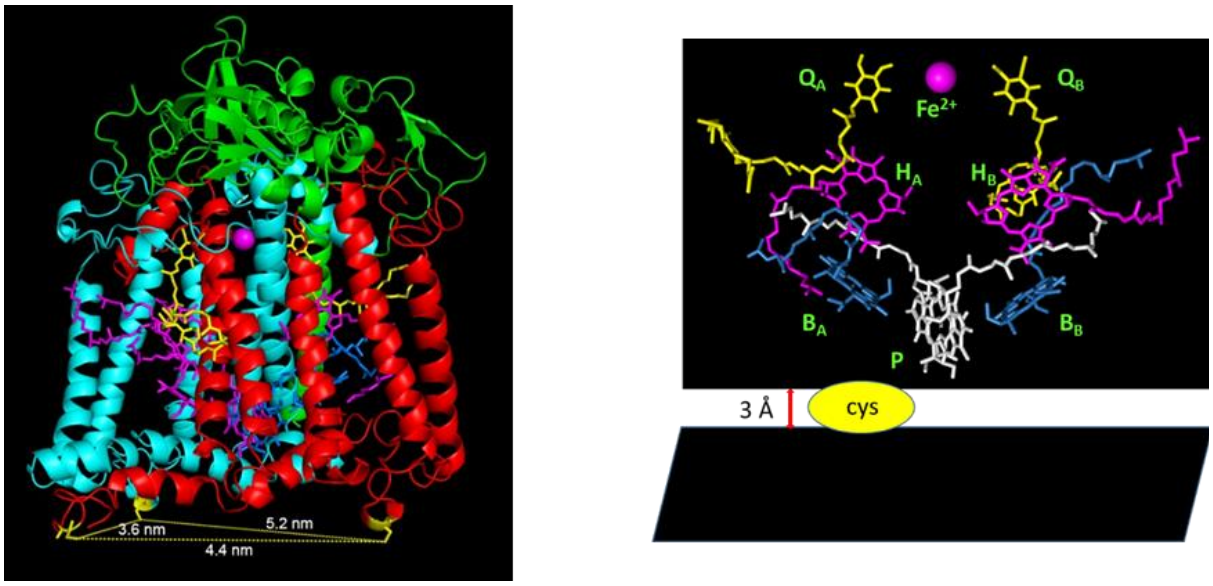


Figure 48. Schematic of the triple cysteine RC mutant used in this work. RCs modified to yield one and three external cysteines on the P side of the RC have been produced to allow orientated, direct binding to mRGO films through disulfide bond formation. This RC mutant has previously been shown to bind to the surface of a gold electrode however photocurrent was limited due to nonspecific binding between gold and protein[1].

We further plan to interface isolated reaction centers from other species of photosynthetic purple bacteria, such as *Blc. viridis* and *Alc. vinosum*, which have a tetraheme cytochrome c molecule permanently bound to the 'P' end of the reaction center (courtesy of our collaborator Prof. Richard Cogdell at the University of Glasgow). This could yield the pre-soaking with cytochrome c unnecessary and improve binding efficiency of the RCs.

Work to date has focused on isolated reaction centers, however, all natural photosynthetic organisms contain a light-gathering antenna system, which serves to increase the cross section available for light absorption. We intend to incorporate this antenna system into our biohybrid electrochemical cell design to try to increase the range of wavelengths absorbed. Two approaches will be investigated. In one approach we will investigate the addition of a natural antenna by incorporating LH1-RC systems from a range of purple bacteria (courtesy of our collaborator Prof. Richard Cogdell at the University of Glasgow). In the second approach we will incorporate DNA constructs similar to those we have generated previously containing dyes appropriately placed to transfer energy into the RC. It has been shown previously that DNA can be incorporated into the pores of ATO films.

The desire to precisely orient the RC on the electrode material has also led us to begin another subproject involving the same investigators. Multilayer reduced graphene oxide (mRGO) electrode films can be functionalized with thiol binding sites. We have a range of RCs modified with surface cysteine residues at the 'P' end of the RC to facilitate orientated binding to the thiol groups of this material through disulfide bond formation. The triple cysteine mutant illustrated in Figure 48 was provided by our collaborator Prof. Tom Beatty, at the University of British Columbia, whose group has previously reported successful binding of this modified RC to the surface of a gold electrode. Photocurrent was limited in that previous work due to nonspecific binding between gold and protein[1] and we are now working to bind these RCs to the mRGO films.

Introduction of a light-responsive photo-protective element in a photosynthetic pathway

1. Motivation and Background:

Natural light harvesting systems in photosynthetic organisms not only have efficient means of absorbing light and capturing its energy, but they also utilize critical control mechanisms as part of their function. Light is both an energy source and a destructive element; excess excitation energy leads to a variety of deleterious processes, and natural photosynthetic systems go to great lengths to avoid destructive photochemistry by employing various photoprotection mechanisms. We have begun to address this in our nanostructured hybrid light harvesting systems by exploring the utility of incorporating photoprotective components. In particular, we are focusing on a component found in cyanobacteria that involves a small orange carotenoid binding protein (OCP). OCP has the property that it is in a dimeric form in low light conditions (called OCP^{o}), but upon

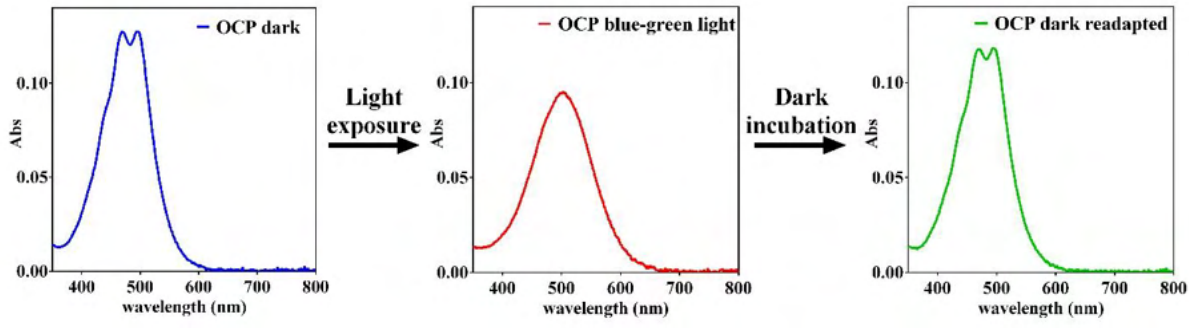


Figure 49. Spectra of OCP during a "dark-light-dark" cycle to test light-induced monomerization and spectral changes. The light used for illumination was a blue-green beam of 30 mW, centered at 430 nm and with a spectral width of 100 nm.

exposure to high light, it monomerizes. The monomeric OCP, also called OCP^r, binds to the phycobilisome (the cyanobacterial antenna) and quenches the excited states, dissipating excess light energy to avoid damage. Each of the OCP monomers contains a non-covalently bound carotenoid co-factor. The carotenoid accepts excitation energy from the pigments of the phycobilisome via energy transfer (FRET), and thermally dissipate it. A peculiar feature of OCP is the intensity dependence of the monomerization reaction: the rate, as well as the percentage of dissociation are dependent on light intensity, making OCP a facile system for the regulation of photoprotective function. The scope of this part of the project is two-fold: exploring experimental conditions required for optical control of OCP dissociation, and incorporating OCP into our DNA nanostructured phonic devices as a regulatory element.

2. Characterization of OCP

Currently, the mechanism underlying the dissociation of the OCP protein into monomers is not clear. The aim of this part of the project is to gain further insight of this mechanism and to explore the experimental conditions needed to manipulate the quenching state of the OCP. To do this, we are investigating the ability of OCP to quench the fluorescence from the types of organic fluorophores we have previously incorporated into our nanostructured light-harvesting systems to increase the overall absorption cross section.

Figure 49 shows the results of our initial tests using excitation centered at 430 nm to induce the changes in OCP photochemical and spectral properties. What can be seen is that there is a significant change in the OCP spectrum upon illumination which is completely reversible in the dark.

We then labeled the protein with different fluorescent dyes. Each OCP monomer subunit contains an exposed cysteine residue that is available for chemical modification. This cysteine can be used either to attach fluorescent dyes or to link OCP to nucleic acids structures (*vide infra*). Maleimide modified dyes were used to specifically target this cysteine residue; four dye molecules, TMR, Alexa Fluor 647, ATTO 655, and Cy7 were selected and the spectra of the modified

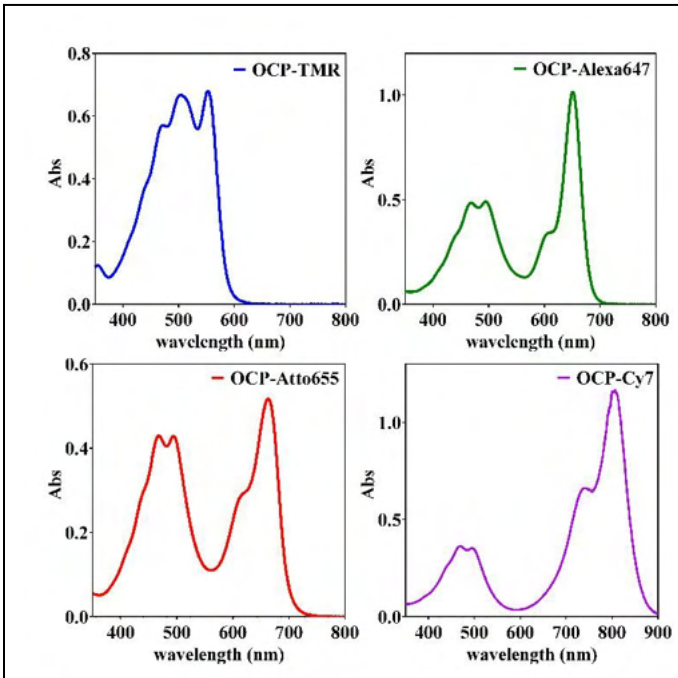
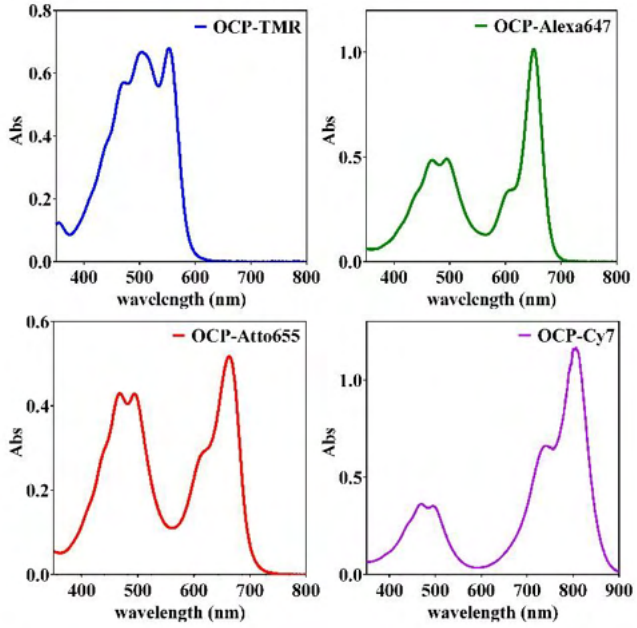


Figure 50. Spectra of OCP labeled with different organic dye molecules. A close to 1:1 OCP:dye labeling is concluded based on the calculation using the absorbance of the protein and the dyes.



OCP in each case is show in

Figure . The ratio of monomer OCP-to-dye was approximately 1 as calculated from the extinction coefficients of the protein (135 $mM^{-1}cm^{-1}$ at 495 nm) and dyes (provided by the manufacturers), indicating that the labeling efficiency of the cysteine is nearly 100%. This methodology suggests that a similar approach can be used in the future to conjugate the protein to DNA structures.

Figure 51 shows the results of illuminating TMR and ATTO 655 modified OCP samples with light in the 430 nm region. One can see that, as in Figure 49, there is a definite spectral shift similar to

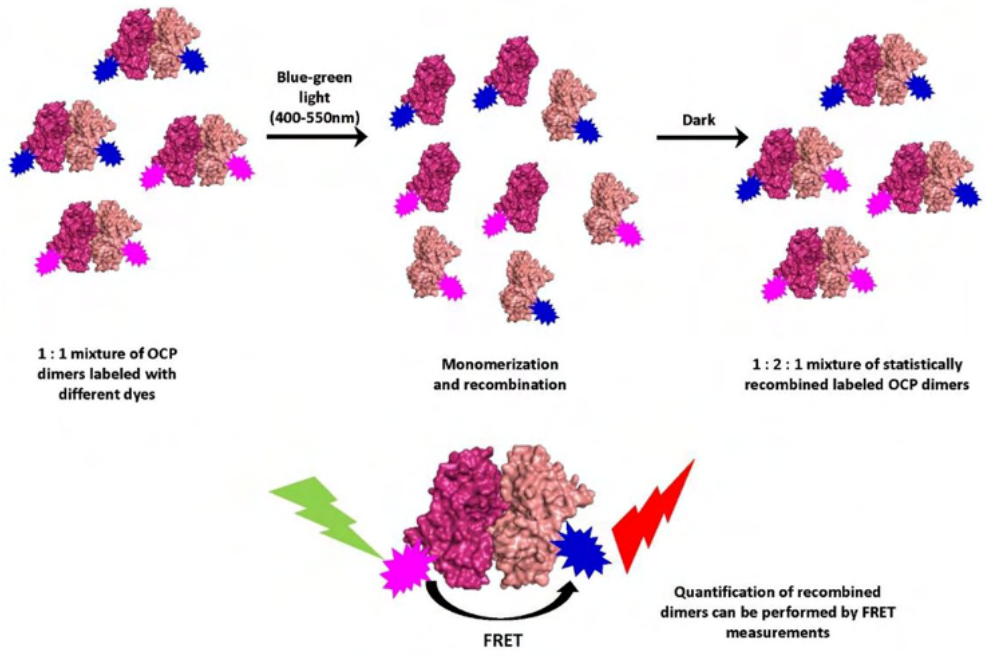


Figure 52. Proposed scheme to study the monomerization – dimerization process of OCP. Upper: OCP is labeled with two different dye molecules capable of forming a FRET pair. Lower: detection of the FRET signal.

that seen without labels present, indicating that the modified protein is still able to undergo monomerization. In this system, it is possible to study the monomer/dimer transition in more detail. To this end, we are using a FRET-based approach. The experimental concept is presented in Figure . OCP is prepared with two different dye labels, (upper left), capable of a FRET interaction. The two batches of dye-labeled OCPs are then mixed and the protein is exposed to light to induce monomerization (upper middle). Finally, the sample is transferred back into the dark to allow dimerization to take place (upper right). In principle, about 50% of the OCP dimers should contain a FRET pair if the monomerization and re-dimerization were random. By monitoring the FRET response during this process (Figure 52, lower panel), it is possible to observe the monomer exchange in solution during the light-dark cycle. This method should allow us to study the reaction directly in solution, with the possibility of exploring parameters that may influence the dynamics of the system such as protein concentration, pH, and ionic strength. Currently we are in the process of optimizing the experimental conditions for in both steady state and time-resolved fluorescence spectroscopic measurements.

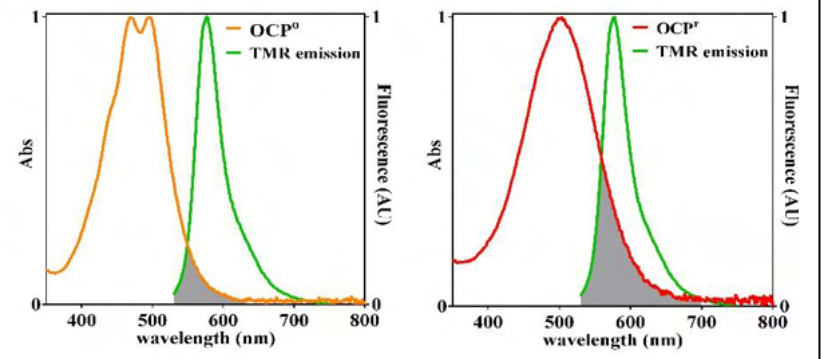


Figure 53. Overlap of the emission of the dye TMR with the absorption spectrum of OCP in the dark (left) and light (right) forms. The shaded area represents the overlap between the two spectra.

3. Modulated Quenching of Fluorophores by OCP:

In vivo, OCP quenches the excited states of the phycobilisome by direct binding; the energy from the excited pigment molecules in the phycobilisome is transferred to the carotenoid molecule in OCP. By using the same energy transfer mechanism, it is possible for the carotenoid in the protein to quench the emission of organic dyes whose emission overlaps with the carotenoid absorbance in either of its two spectral states. If the fluorophore fluorescence spectrum overlaps better with the spectrum of one spectral state of the OCP vs. the other, differential quenching controlled by light can be achieved. Here, TMR was the dye chosen to test this phenomenon due its spectral properties (

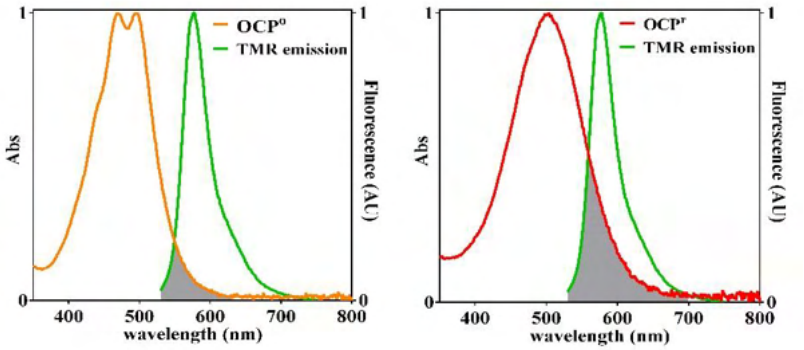
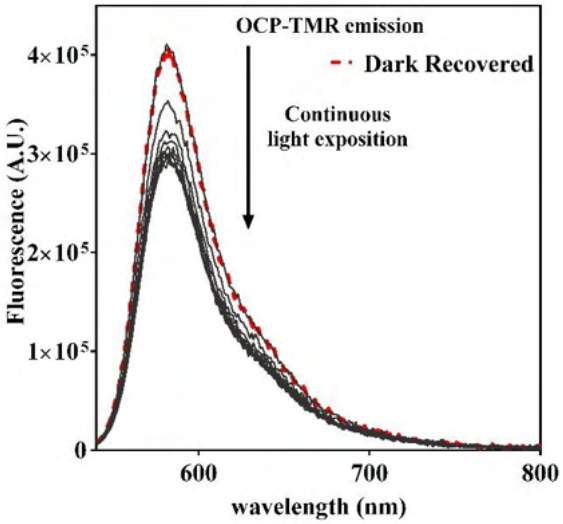


Figure). As can be seen, when OCP converts to the OCP^r form, the overlap of its absorbance with the TMR fluorescence spectrum increases. This should increase the rate of energy transfer from TMR to the OCP, quenching the TMR fluorescence.

To test this, a sample of OCP-TMR was excited at 520 nm with a light intensity of ~180 uW, which is a typical intensity used for fluorescence experiments in bulk solution. This wavelength will both excite TMR, as well as slowly induce the spectral shift in OCP. The emission spectrum of TMR was recorded every 30 seconds. As shown in Figure 54, the fluorescence steadily decreases with time during illumination. When the sample was then incubated in the dark for about 5 minutes, the fluorescence spectrum returned to its original amplitude



(

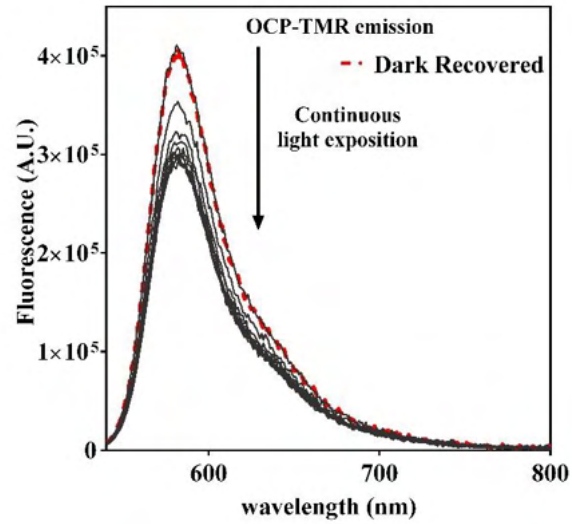


Figure 54. Emission spectra of TMR bound to OCP under green light illumination. The black traces were recorded at intervals of 30 s during continuous illumination. The red dashed line shows the emission of the same sample after a 5 minutes recovery in the dark.

Figure , red dashed line) showing that the fluorescence quenching of TMR by OCP^r is completely reversible when OCP returns to the OCP^o form.

Figure 55 shows the intensity dependence of this effect. The emission peak of TMR (580 nm) was monitored over a period of about 450 s at various light intensities. Each kinetic trace was subsequently fit to a monoexponential decay, and the rate constant at each

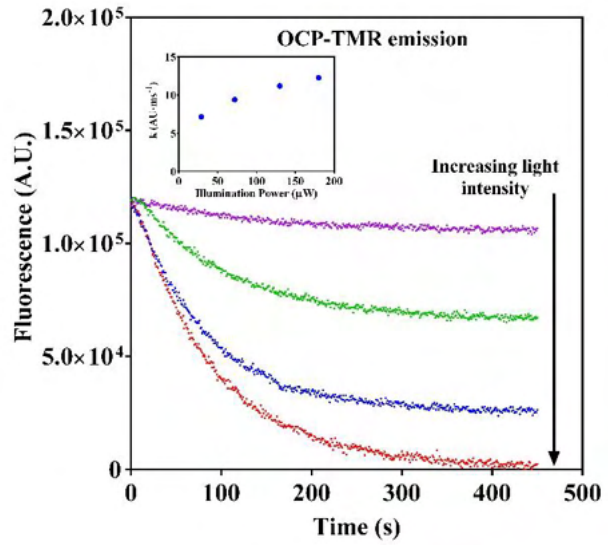


Figure 55. Fluorescence emission signal of TMR attached to OCP as a function of illumination time and excitation intensity. The inset shows the decay rate obtained from monoexponential fitting of the fluorescence data plotted versus the illumination power.

illumination power is reported in Figure 55 inset. The decay rate is proportional to the rate of production of OCP^r at that particular excitation power, again consistent with the conclusion that the increased quenching arises from the change in spectral form of OCP.

4. <u>Constructing a DNA nanostructure incorporating the light-induced photo-protective complex:</u>

As described above, OCP can be used to successfully quench the fluorescence emitted by organic dyes directly attached to it in a light-dependent fashion. We next would like to integrate the protein in a DNA nanostructured light-harvesting system where dyes and photosynthetic elements are assembled in an organized fashion, similar to the kinds of DNA-based photonic systems we have published previously. To accomplish this, we will need to incorporate OCP into the system and demonstrate light-dependent quenching of the excitation energy.

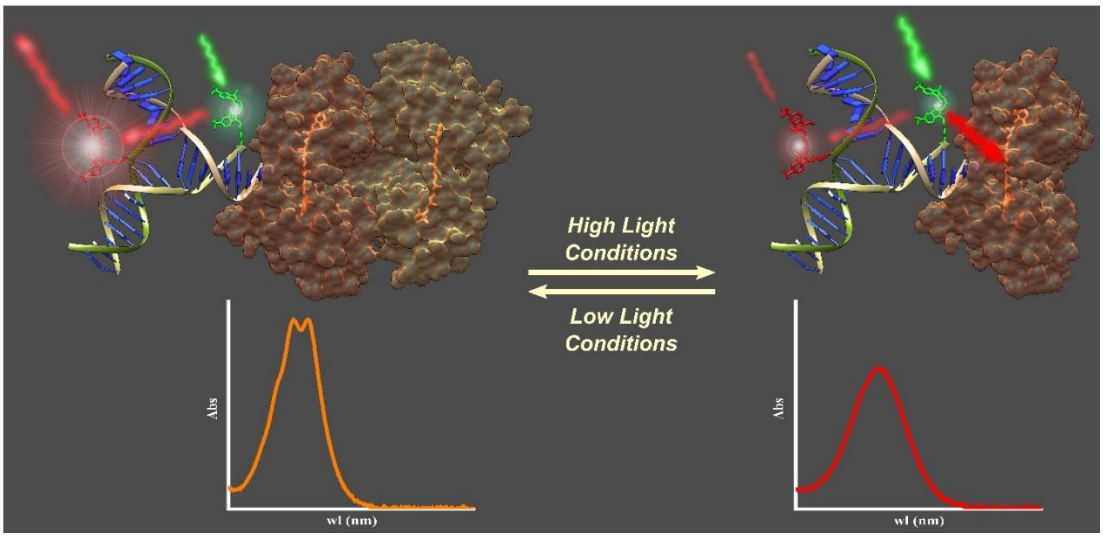


Figure 56. Concept for the application of OCP as a light-induced photo-protective element on a DNA nanostructure. The DNA nanostructure chosen here is a 3 arm junction (yellow and blue cartoon) labeled with two dyes: Cy3 (green) and Cy5 (red). Under low light conditions, left side, the OCP molecule is in its dimeric form and the spectral overlap with Cy3 is low: when exciting Cy3, energy transfer from Cy3 to Cy5 occurs, and FRET can be observed. Under high light conditions, right side, the OCP is in its monomeric form: the spectrum has undergone a transition so that has greater overlap with the emission of Cy3. In this case the energy from Cy3 is quenched by the carotenoid molecule, and FRET with Cy5 is diminished.

We have chosen to use the 3 arm DNA nanostructure we described previously as the basis for building the light regulated antenna system. The concept is depicted in

Figure . The 3 arm DNA structure is conjugated to two dyes, the FRET pair Cy3-Cy5 is here used as an example, but other FRET pairs with similar spectral characteristic could be used as well. The dye-labeled nanostructure can be then conjugated to the cysteine of OCP using SPDP mediated chemistry, as previously reported for other DNA-protein systems. The left side of Figure 56 shows the expected behavior of the system under low light conditions: OCP is present in its dimer form, and the energy of excitation of Cy3 is transferred to Cy5 with no interference due to quenching. When the excitation intensity of Cy3 is increased (right side of

Figure **)**, the situation changes: OCP separates monomerizes, a spectral shift occurs, and the excited state of Cy3 is quenched by the carotenoid due to increased spectral overlap, and a small

percentage of energy is transferred to Cy5. Beyond this test system, OCP could be incorporated into more complex photosynthetic networks, acting as an inducible photo-protection element.

Computational Design of DNA lattice-based Light-harvesting Antennas

To understand principles underlying efficient design of nanophotonic materials capable of absorbing and guiding light effectively, we are developing and applying computational models to test our quantitative understanding of optimal dye configurations on DNA-based lattices. These models provide concrete hypotheses that are tested experimentally, providing feedback to enhance

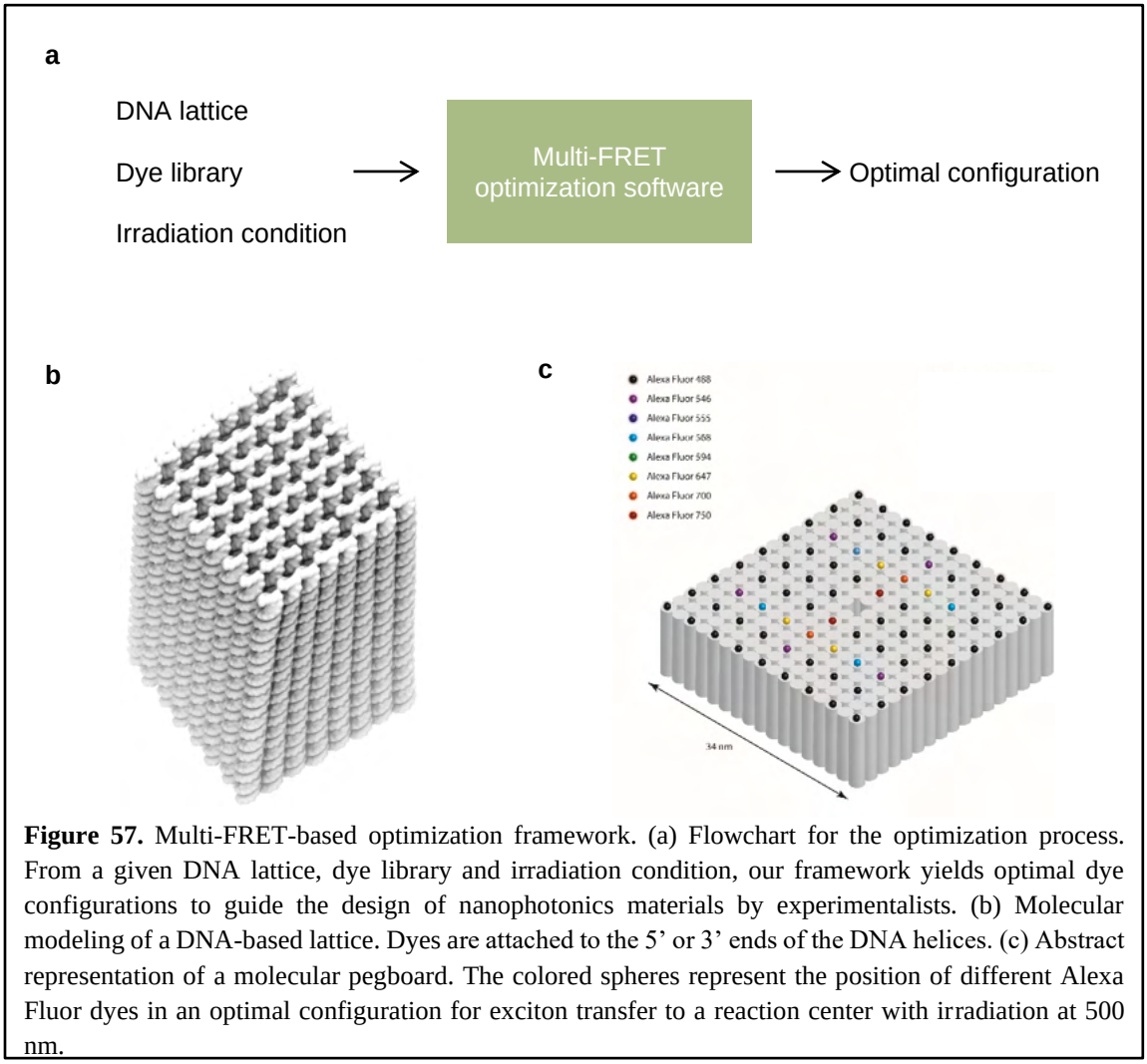


Figure 57. Multi-FRET-based optimization framework. (a) Flowchart for the optimization process. From a given DNA lattice, dye library and irradiation condition, our framework yields optimal dye configurations to guide the design of nanophotonics materials by experimentalists. (b) Molecular modeling of a DNA-based lattice. Dyes are attached to the 5' or 3' ends of the DNA helices. (c) Abstract representation of a molecular pegboard. The colored spheres represent the position of different Alexa Fluor dyes in an optimal configuration for exciton transfer to a reaction center with irradiation at 500 nm.

our molecular-level understanding of the fundamentals of energy transfer in FRET networks. Mechanical simulations based on our software CanDo (Computer-aided engineering for DNA origami) informs the ground-state conformation and rigidity of specific DNA-based antenna designs. Based on our previously published multi-FRET modeling framework that was funded by this MURI project, we developed a tool that can predict optimal dye configurations for energy harvesting and transfer. A graphical user interface enables experimentalists to rapidly and easily obtain optimized dye configurations that can be synthesized and tested. This optimization tool is based on a Monte Carlo optimization scheme that maximizes the rate of exciton transfer to a central

reaction center under arbitrary irradiation conditions, automatically choosing dyes from a user-defined library. Our previous work has shown that the irradiation wavelength and total irradiance strongly influence the optimal dye design.

We are currently working to test this optimization approach using experimental validation in order to test key parameters of the model that are empirically determined. Once validated, the modeling approach will be used to design and test computationally predicted optimal dye arrangements on DNA lattices for efficient DNA-based light-harvesting antennas.

Programming excitonic circuits on DNA nanoassemblies

Photosynthetic light-harvesting complexes feature arrays of strongly-coupled pigments that direct energy transfer to the reaction center with near-unity efficiency. A major challenge and opportunity for nanotechnology is to rationally construct nanoscale excitonic circuits from the bottom up to mimic natural light-harvesting assemblies. Structured DNA assemblies serve as chromophore scaffolds with nanometer-scale control over three-dimensional dye architectures to realize this aim. However, programmed dye aggregates that mimic the J-aggregate organization often observed in natural photosynthetic complexes have been limited to short, isolated units on

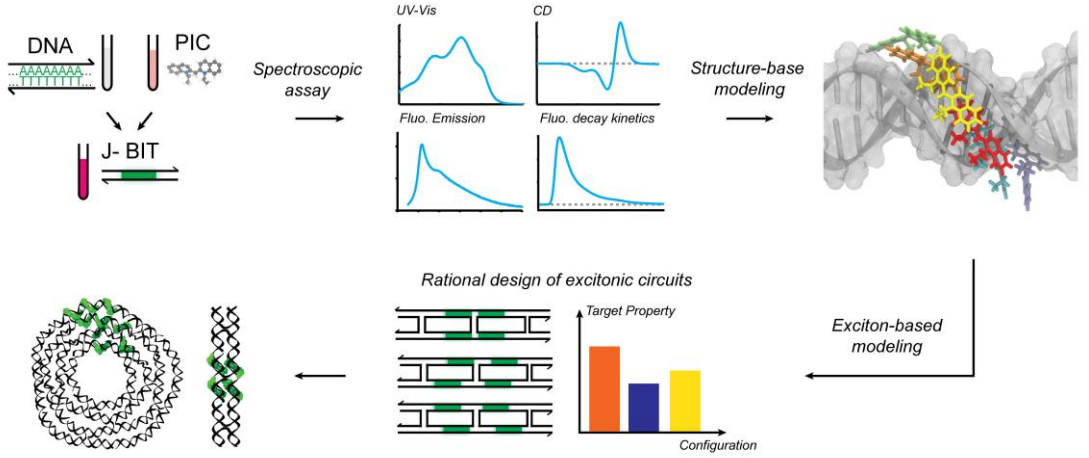


Figure 58. Schematic of programmable framework for synthetic DNA-based excitonic circuits. Chromophore J-aggregates on single DNA duplexes are assembled into higher-order assemblies using antiparallel DNA duplexes that can be organized into linear, circular, and spherical arrays. Structure-based modeling is used to guide the design of emergent optical and energy transfer properties based on the molecular conformation of DNA-dye "Jbits".

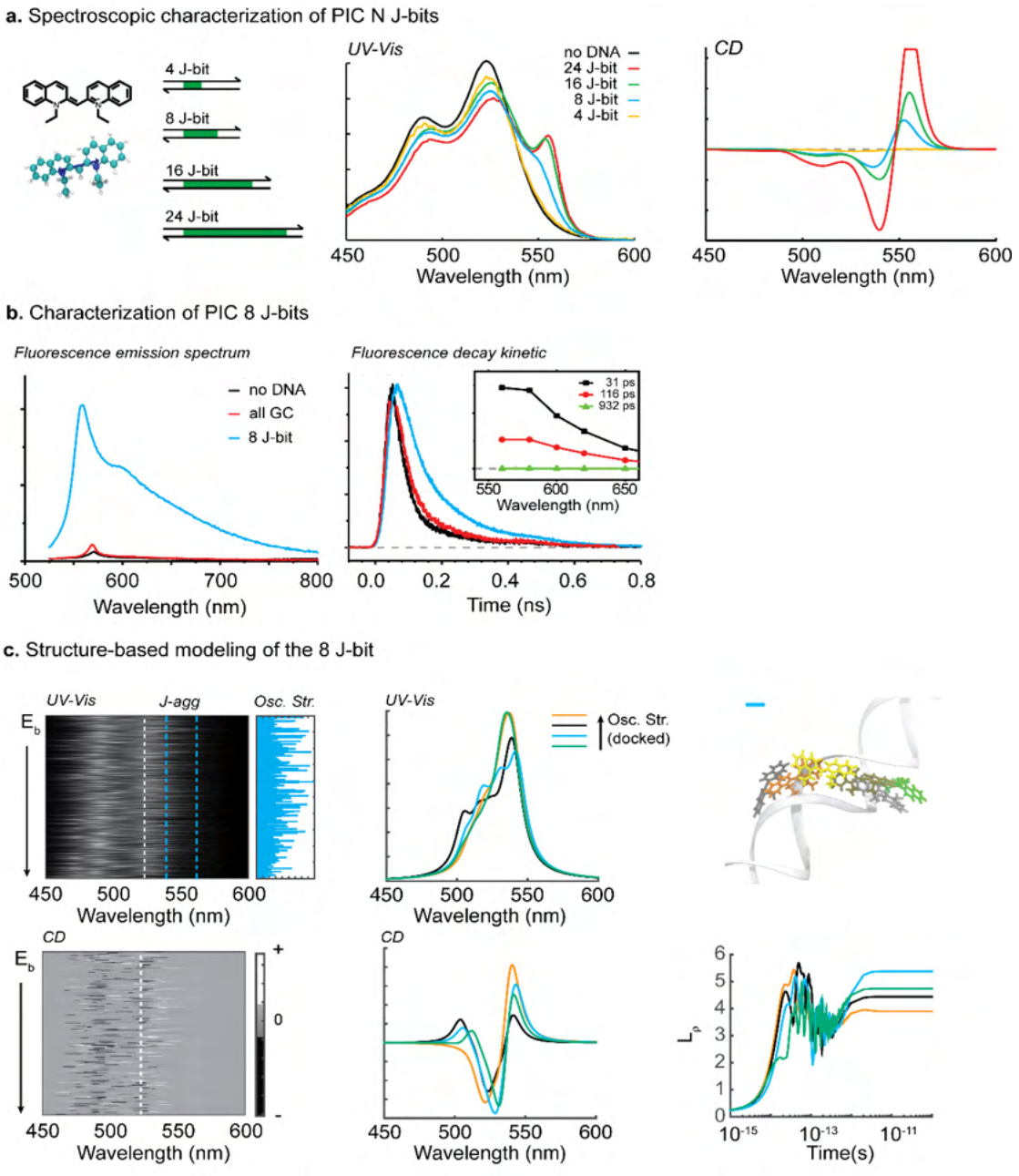


Figure 59. Designing fundamental J-aggregate building blocks from PIC molecules. a. UV-Vis and CD spectra of N-J bits, where N is the number of DNA A/T base-pairs in the binding site. The chemical and conformation of PIC monomer and calculated transition dipole is shown. b. Fluorescence emission spectrum (left), fluorescence decay kinetics (center) of the 8 J-Bit. The excitation wavelength for the emission spectra and kinetics is 520 nm. The decay associated spectra (DAS) is shown in inset of the fluorescence kinetics. c. Simulated UV-Vis and CD spectra for the top 1000 scored PIC aggregate (left). The portion of the spectra showing J-aggregation is shown with the associated oscillator strength of each aggregate. Simulated UV-Vis and CD spectra of the top four candidates that show J-aggregation and positive CD at the long wavelength (center). Molecular structure of one of these aggregates (top) and time-dependent exciton coherence length (bottom) (right).

single DNA duplexes. Further, rational control of emergent excitonic properties of these dye

aggregates has not been achieved.

In the context of this MURI, we have used structure-based computational modeling to develop a highly programmable, rational means of controlling the targeted assembly and optical properties of excitonic circuits based on synthetic DNA. We have identified a set of fundamental J-aggregate units that serve as building blocks to construct fast, coherent energy transfer in arbitrary higher-order synthetic assemblies that mimic and extend beyond natural excitonic circuits. Because our approach is based on highly programmable DNA building blocks, these design principles offer a new class of nanoscale excitonic materials for integration with programmed optical barcodes, light-harvesting antennas, and excitonic circuits for nanotechnology. Specifically, we have used the natural propensity of pseudoisocyanine dyes (PIC) to self-assemble into J-aggregates on short sequence-specific portions of DNA duplex, to create circuits in larger scale DNA nanoassemblies (Figure 58). A combination of quantum and molecular modeling and time-resolved spectroscopy enabled to characterize these J-aggregate units that we call "J-bits." UV-Vis and CD spectroscopy confirms the formation of chiral J-aggregates on the DNA duplex (Figure 59a). Time-resolved spectroscopy further reveals enhancement of the quantum yield and increase of the fluorescence lifetime, which make this material promising for energy transfer applications (Figure 59b). Finally, a structure-based modeling framework that leverages molecular docking with time-dependent density functional theory (TD-DFT) and exciton models enables us to deduce the atomic-level conformation of these J-aggregates, which is necessary to design more complex circuits with customizable optical and transport properties (Figure 59c).

Next we used the J-bit to design higher-order DNA-PIC J-aggregates with custom optical properties to demonstrate the ability to design complex excitonic circuits using our bottom-up approach. DX-Tiles are the fundamental building block of DNA origami, in which two antiparallel DNA duplexes are rigidly constrained by two crossover junctions, offering the ability to design rings, sheets, and bundles of arbitrary size on the nanometer scale. DNA sequence was chosen to introduce four 8-mer binding sites surrounding the central staple double crossover. Optical properties and transport characteristics of these circuits can be predicted from the atomic-level conformation above (Figure 60). UV-Vis and CD spectroscopy on the synthesized DX-Tile circuits confirmed the formation of a J-aggregate structure, similar to the spectra that were theoretically predicted. Time-resolved spectroscopy also showed that quantum yield enhancement and increased lifetime were also present in these assemblies.

Future work includes using these DX-Tile assemblies to demonstrate J-bit mediated transfer between a donor (ATTO390) and acceptor dyes (AF647), as well as programming J-bit circuits on larger-scale DNA origami structures including rings, sheets, tubes, and lattices. Future work will also focus on broadening the scope of chromophore molecules that can be used to design these excitonic circuits. Because our rational, structure-based design framework is general to DNA-chromophore aggregates, similar assemblies may be programmed using either covalently attached chromophores, intercalating, or base-substituting dyes. In particular, we envision using chem-informatic approaches to screen in-silico for chromophores, DNA architectures, and motifs with high absorption and exciton mobility, which can lead to the discovery of new materials for the development of high-performance excitonic circuits, inspired by recent success using similar

methodology in the field of organic electronics. The present collaborative work is under preparation for submission.

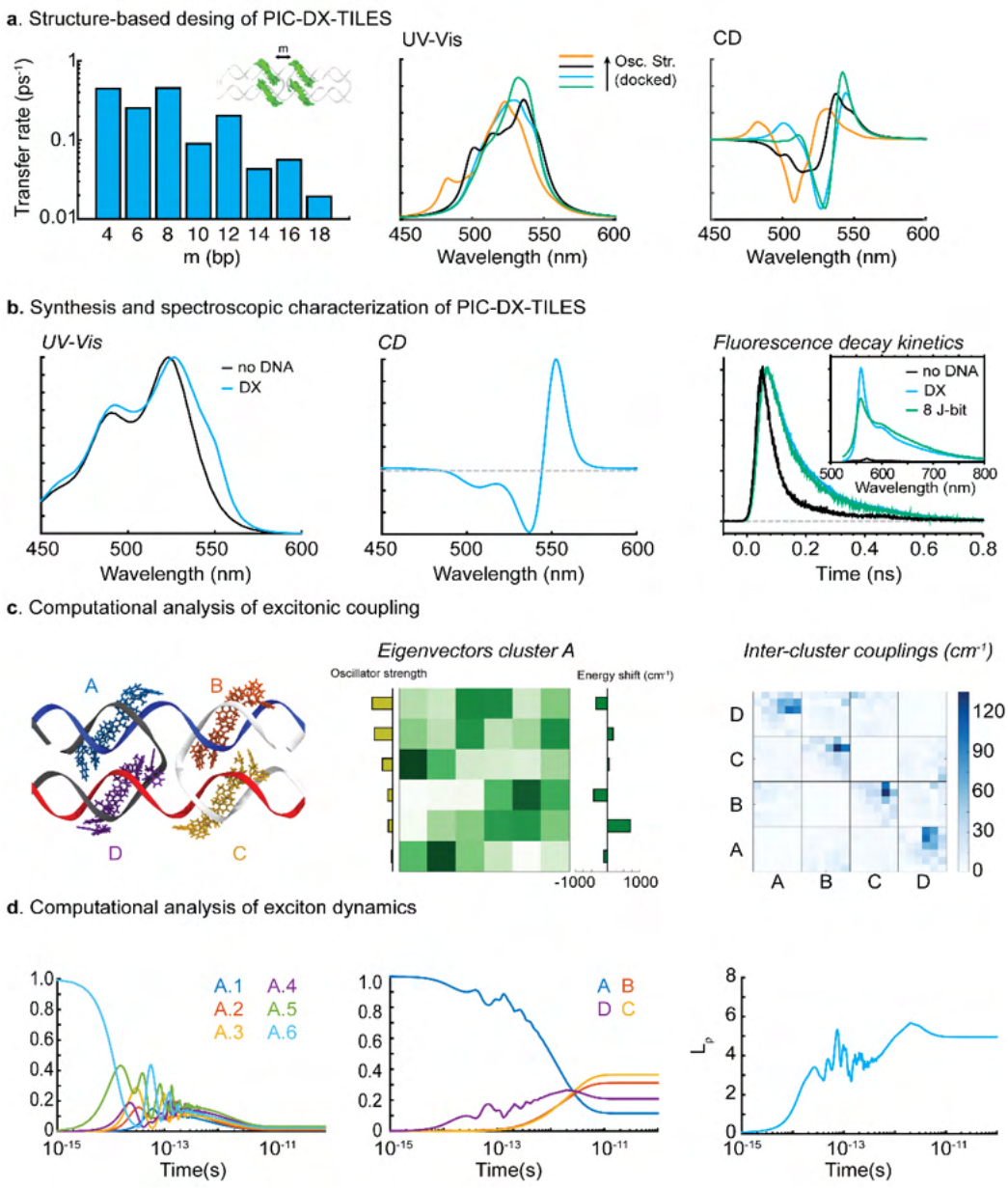


Figure 60. Structure-based design, synthesis and characterization of J-Bit DX-Tiles excitonic circuits. a. Computational design of PIC-DX-Tiles using multiple configurations of J-bits to tune transport properties by varying the distance between the J-bits (left). UV-Vis (center) and CD spectra (right) of the 4 bp configuration, using the top 4 conformations of the J-bit. b. UV-Vis (left), CD (center) and fluorescence decay kinetics (right) for the synthesized PIC-DX-Tiles. Fluorescence emission spectra are shown in the inset. Excitation wavelength is 520 nm. c. Molecular conformation (left) exciton states (center) and inter-cluster exciton coupling (right). d. Exciton dynamics following initial excitation of the A.6 monomer. Time-dependent exciton population in each of the molecules that constitute the A aggregate (left). Integrated time-dependent exciton population in each of the four aggregates in the PIC-DX-Tile. (center). Time-dependent exciton coherence length (right).

Production of materials to transfer bioelectroactive and photoelectrochemical pathways to external platforms

1. Fabrication of macroporous, transparent, conducting metal oxide (TCO) films:

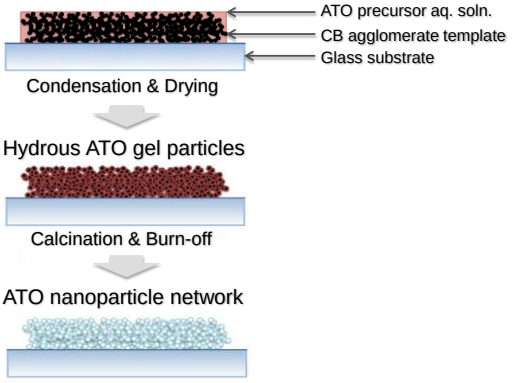


Figure 61. Schematic diagram of the synthetic procedure for the fabrication of the macroporous ATO coatings.

In last year's report, we described our preliminary results on successful development of a new synthetic method for production of macroporous films of antimony-doped tin oxide (ATO) on fluorine-doped tin oxide (FTO) substrate. The new method employs carbon black/PEG soft thixotropic gel as a self-volume-adjusting hard template and has allowed us to prepare target materials with desired structural, physical and chemical characteristics in a very reproducible manner. As shown in the previous sections of this report, the macroporous ATO coatings have been successfully employed in other MURI team members' laboratories through collaborations. Here we describe only the synthesis and characteristics of the macroporous coating material.

The synthetic route is illustrated in Figure 61, in which a mixture of the ATO/PEG precursor solution and aggregated carbon black is coated on a FTO glass substrate first. The amounts of carbon black particles and PEG are adjusted to impart a suitable viscosity to the precursor mixture for spreading the coatings, as well buttressing the inorganic gel as the solvent evaporates. Gelation takes place in the solution inside and around the high structure carbon black particles. After drying and calcination, a macroporous structure with a gel network of ATO particles is formed with the macropores as the negative replica of the packed structure of the carbon black particles. Although not shown here, profilometry studies indicate formation of uniform coatings with controllable thickness (4 – 8 μm).

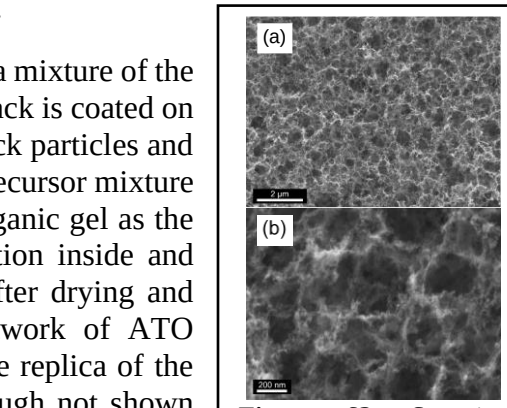


Figure 62. Scanning electron micrographs of a macroporous ATO coating. Scale bar = 2 μm (a) and 200 nm (b).

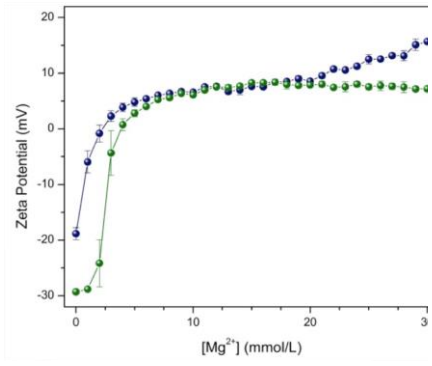


Figure 63. Zeta potential of ATO vs. Mg^{2+} concentration in water (blue curve) and in 1x TEA buffer (green curve).

Scanning electron microscope (SEM) images of the of the ATO coating (Figure 62) show macropores with sizes from 100 to 500 nm that are open at the surface. BET analysis on N_2 desorption isotherm shows a total surface area of 88 m^2/g and average pore diameter of 20 nm in the 2 – 200 nm region. Although not shown, the high surface area and presence of mesopores could be verified from transmission electron microscope (TEM) studies. Deposition of DNA nanostructures and proteins would be favored by electrostatic attraction between them and the surface of ATO. Figure 63 shows that the surface charge of ATO is highly negative in water and in 1x TEA buffer solution but increases rapidly with an increase in Mg^{2+} concentration to

become positive at $[Mg^{2+}] > 2$ or 4 m*M*. This supports our findings that in their aqueous solutions, DNA nanostructures strongly interact with ATO surface and can be easily deposited on the ATO pore surface. Although not shown here, the homogeneity of the distribution of DNA nanostructures in the macroporous ATO coating was confirmed by using confocal microscopy.

2. Fabrication of thionated reduced graphene oxides and their films:

We have continued to refine our methodologies for fabrication of Langmuir-Blodgett (LB) films of thiol-functionalized reduced graphene oxides (called "mercapto reduced graphene oxides (mRGOs)" hereafter; shown in Figure 64). Through collaborations with Yan group, our preliminary results indicate that the mRGO LB films can be an effective electrode to achieve selective deposition of DNA nanostructures through covalent cross-linking, providing bioelectroactive and photoelectrochemical pathways:

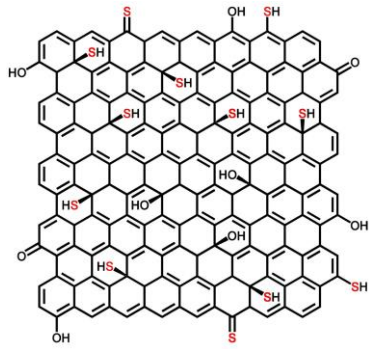


Figure 64. Schematic diagram of mercapto reduced graphene oxides (mRGOs).

2.1 Electron Transfer between mRGO and DNA Origami with Enzyme Cascades

DNA origami with glucose oxidase-horseradish peroxidase (Gox-HRP) enzyme cascade was deposited on mRGO and covalently cross-linked by forming disulfide bond between mRGO and DNA origami (Figure 65). Although not shown here, the disulfide bond formation was confirmed from the observation of an oxidation peak at ~0.9 V vs. Ag/AgCl in the CV curve which is due to oxidation of –S–S– to $–SO_3H$. In a separate set of experiments performed with DNA origami only with HRP, we first established that the deposition of DNA origami with HRP on an mRGO LB film allowed a direct detection of the oxidation state of the iron in HRP during the catalytic reduction of H_2O_2 by HRP. Compared with the free HRP in solution, our mRGO-DNA origami-HRP architecture showed 8 times higher reduction and oxidation currents, although the concentration of HRP (nM range) was lower than that of free HRP (2.5 mg/mL).



Figure 65. Schematic diagram of mRGO-DNA origami with enzyme cascade.

With the DNA origami with glucose oxidase-horseradish peroxidase (Gox-HRP) enzyme cascade deposited on an mRGO LB film (Figure65), the performance of the enzyme cascade was verified by carrying out cyclic voltammetry (CV) with and without glucose in the presence of ABTS. Without glucose, only the reduction and oxidation peaks of ABTS (~0.45 V) was observed. After adding glucose, the CV showed the reduction and oxidation peaks of iron in HRP which are located around –0.2 V (Figure 66),

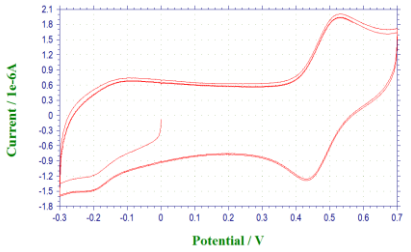


Figure 66. FCV of mRGO-DNA origami-enzyme cascade in 130 mM PBS with glucose at a scan rate of 100 mV/s.

indicating that H_2O_2 was produced by the oxidation of glucose catalyzed by Gox and could be subsequently reduced by the catalytic action of HRP.

2.2 Swinging Arm on mRGO Film

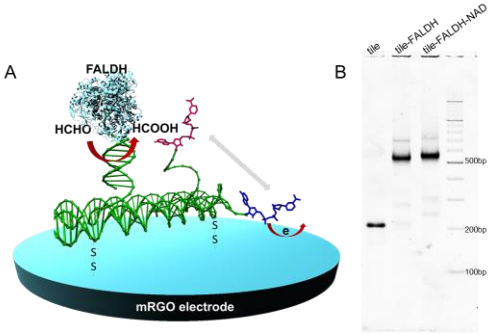


Figure 67. (A) Schematic diagram of FALDH-tile-NAD complex on mRGO LB electrode and (B) Structural characterization of FALDH-tile-NAD complex with 3% native PAGE.

A unique benefit of the covalent cross-linking between mRGO LB film and DNA origami could be seen in our electrochemical studies of the swinging arm DNA origami-enzyme complex, as the experiment has been challenging with other electrodes such as Au. Figure 67 shows the design of the tile-FALDH-NAD complex on mRGO LB film. DNA tile was functionalized with two –SH groups (-SH modified ssDNA) which was used to immobilize the complex on an mRGO LB electrode through formation of disulfide bonds. DNA tile-enzyme complex had FALDH and a NAD-swinging arm. Formaldehyde dehydrogenase (FALDH) oxidizes formaldehyde to formic acid by using NAD+ as a cofactor and has been used in biofuel cell system to convert the biofuel energy to electricity. NAD+ is reduced to NADH during the oxidation of formaldehyde and then can be effectively oxidized back to NAD+ by accepting two electrons from the electrode when it swings toward the electrode.

Figure 68 shows the CVs of the tile-FALDH-NAD complex on mRGO with and without formaldehyde (HCHO). Without the substrate, the CV exhibits only a loop due to the Faraday current. After adding the substrate, the CV shows an oxidation peak of NADH located at ~0.55 V vs. Ag/AgCl. Although not shown here, a control experiment indicated that free NADH becomes oxidized by the mRGO LB electrode with a broad oxidation peak located at ~0.6 V vs. Ag/AgCl. The oxidation potential of the swinging arm NADH is closer to the thermodynamic potential of 0.49 V at pH 6 than that of the free NADH. The lower overpotential observed for the swinging arm NADH clearly indicates the favorable effect of the swinging arm architecture. The efficiency of the swinging arm was 25% based on the peak area.

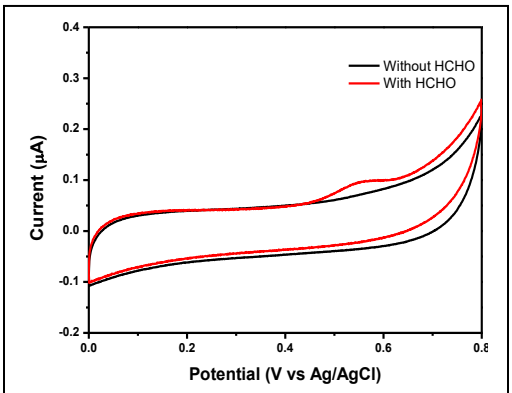


Figure 68. CV of mRGO-Enzyme in 130 mM PBS buffer with and without HCHO at a scan rate of 5 mV/s.

3. Future directions:

Having developed synthetic protocols for macroporous ATO films, the Seo lab plans to explore various methods to control the surface functionalities by modifying the surface charge or by surface functionalization with organic moieties. We have seen that Mg^{2+} ion is effective in providing a positive surface charge. Other metal ions especially with higher valency may be more effective in this regard. Organic surface functionalization with organosilanes has been popular and yet it is still challenging to achieve monolayers of the organosilanes on metal oxide surfaces.

We will explore new methodologies based on thermodynamics of the solvation of metal ions or metal slat pairs in organic solvent to overcome the challenge. In addition, we will further examine the role of the synthetic parameters for the macroporous ATO films, as the current method lead to films that become less robust when stored in air for many weeks.

Deposition of DNA structures on m-RGO LB films on various substrates has been successful as shown in this report. In our continuing effort, we plan to find optimum conditions to increase the current of HRP reduction and oxidation peaks and improve the efficiency of our design. Future effort will also be devoted to refine the deposition method in order to achieve high yield deposition and cross-linking. We will examine other cross-linking methods including thiol-ene click chemistry in order to provide flexible and more selective cross-linking. By taking advantage of the good transparency of the mRGO LB films, we will further examine new DNA-enzyme complexes that are photoelectrochemically active. This also can be complimentary for the enzyme cascade experiment as it allows us to use a UV light to detect the glucose.

Translating Biochemical Pathways to Non-Cellular Environments

Principal Investigator: Hao Yan[1]
Co-PIs: Don Seo[1], Neal Woodbury[1], Mark Bathe[2], William Shih[3], Nils Walter[4], Jinglin Fu[5]

[1]Arizona State University, [2]MIT, [3]Harvard University, [4]U of Michigan, [5]Rutgers University

Reporting period: 8/01/15-7/31/16

I. Scientific and Technical Objectives

We intend to engineer and optimize nanoscale devices and systems based on important biochemical conversion pathways, where the converted species are molecules (enzymes transforming substrates into products), or energy, as is the case for photosynthesis. The use of DNA-directed assembly allows us to control and exploit the interactions between synthetic and naturally occurring bio-materials to produce highly functional biochemical conversion systems. Regarding enzyme transformations, our primary goal is to construct artificial enzyme cascades using two- and three-dimensional DNA structures as templates, and to study the ideal number of enzymes, relative distance, spatial arrangement, diffusion behavior, and reaction kinetics of the cascades in a controlled, non-cellular environment. Towards this goal, we initially focused on a representative DNA-templated GOx/HRP enzyme cascade. We will apply the results of the initial study toward the design of more complex, bioelectroactive, NAD dependent dehydrogenase pathways, with the ultimate goal of interfacing our systems with external conductive materials. We aimed to achieve the following objectives during this reporting period: (1) systematically evaluate DNA-scaffolded enzyme networks and pathways in various conditions, (2) develop a spatially addressable DNA nanoplatform for the directional regulation of two enzyme pathways through the control of substrate channeling between the two enzyme pairs, (3) creates a programmable hybrid device containing both biochemical and electrochemical components that is capable to assemble and tune the activities of an enzymatic cascade pathway on the gold electrode, (4) construct a three-enzyme pathway with an optimised geometric arrangement to facilitate substrate transfer, (5) demonstrate DNA crowded-enzyme complexes with enhanced activities, (6) summarize a general protocol of assembling multienzyme complexes on DNA nanostructures, (7) investigate reconfiguration kinetics of DNA nanostructure and the mechanism of the walking process by single-molecule analysis, (8) establish a method to co-reconstitute multiple membrane proteins in a single size specific liposome, (9) built an all-atom model of several DNA nano-particles and perform molecular dynamics (MD) simulations. Our findings will ultimately be used to enhance local diffusion behavior, reaction kinetics, and the optical and electrical properties within the proposed devices, behavior that can be extended to other systems of interest to the DoD.

Regarding photosynthesis, our aim is to develop methods for translating energy conversion pathways to non-cellular environments where their functions can be more easily manipulated. The approach is to use rationally designed DNA nano-scaffolds to engineer light-harvesting networks containing synthetic pigments, interfaced with energy conversion proteins (photosynthetic reaction centers) from natural photosynthetic organisms. We intend to precisely position functional elements on the DNA scaffolds, generating energy and electron transfer pathways in which inter-molecular interactions can be predictably designed, and the local environment can be controlled.

We hope to engineer systems with more uniform light absorption, efficient energy transfer and conversion, and improved photo-stability for maximum performance. Here, we are exploring ways to effectively interface the light-induced redox potentials generated by photosynthetic reaction centers from purple bacteria with novel nano and meso-structured electrode materials. Toward this end, two different types of materials were utilized: nanoporous transparent metal oxides and functionalized reduced graphene oxides. We are also exploring ways to incorporate a light-responsive photo-protective element into a DNA-templated artificial antenna system to adapt its photoprotection function for light regulation. We have also used a bottom-up synthetic experimental-computational strategy to develop a highly programmable, rational means of controlling the targeted assembly and optical properties of excitonic circuits based on synthetic DNA. In line with DoD goals, the proposed research will increase our understanding of nanoscale energy transfer processes and aid in the development of robust strategies for the synthesis, characterization, and assembly of synthetic biochemical pathways for application in high-efficiency photo-energy generation, energy storage devices, sensors, or completely new capabilities that enhance war fighter and battle system capabilities.

II. Concise Accomplishments

Enzyme Pathway – We have: (a) used the artificial distance sensitive swinging arm system as a model to study how enzyme 2D network behaves compare to single-particle system and how does geometry affect the 2D enzyme network, (b) demonstrated the directional regulation of enzyme pathways in an artificial multi-enzyme network by controlling the position of the substrate channeling, (c) demonstrated the use of a self-assembled, spatially addressable DNA origami nanostructure to direct the precise positioning of protein enzymes onto a gold electrode to form a sub-monolayer of the enzyme-pairs on the DNA origami with designed inter-enzyme distances, (d) assembled a three-enzyme pathway on a series of DNA nanoscaffolds to investigate the dependence of their activities on spatial arrangement and observed the overall activity of the three-enzyme pathway relied less on inter-enzyme distance and more on the geometric patterns that arranged them within a relatively small range of 10 - 30nm, (e) developed protocols for the robust assembly, purification and characterization of multi-enzyme complexes organized by DNA nanoscaffolds, (f) investigated kinetics of DNA tile reconfiguration, 3- and 4- tile assembly using single-molecule analysis, (g) designed 2- and 3-step DNA tile assemblies as tracks and DNA walkers with different lengths of the toehold and used single-molecule fluorescence resonance energy transfer (smFRET) characterization to investigate the mechanism of the walking process, (h) established a method to co-reconstitute multiple membrane proteins in a single size specific liposome and measured the number of copies of Vdac1 associated with each nanostructure-templated vesicle at the single-particle level, via stepwise photobleaching measurements on barrel-templated Vdac1 proteoliposomes by TIRFM, and (i) built all-atom models of a DNA tetrahedron and a DNA octahedron to compare equilibrium structures from MD to the Finite Element framework present in CanDo.

Photosynthetic Pathway – We have (a) devised a system in which *Rb. sphaeroides* RCs are electrochemically coupled to transparent, porous ATO electrode films via cytochrome *c* to produce a biohybrid platform in which 2-electron reduction and release of a soluble quinone can be controlled both optically and electronically, (b) been incorporating the natural photosynthetic antenna system along with the reaction centers to increase the cross section available for light absorption and reaction centers from a species of photosynthetic purple bacteria that have a

permanently bound cytochrome c subunit, (c) been interfacing Photosystem I from the cyanobacterium *Thermosynechococcus elongatus* to ultimately generate a higher redox power in our biohybrid photoelectrochemical cell, (d) been interfacing reaction centers with a new type of electrode material, a functionalized graphene that can be applied to a variety of surfaces including flexible, transparent materials, (e) incorporated an Orange Carotenoid Protein into a DNA-templated artificial antenna system to adapt its photoprotection function for light regulation, and (f) used a bottom-up synthetic experimental-computational strategy to develop a highly programmable, rational means of controlling the targeted assembly and optical properties of excitonic circuits based on synthetic DNA.

III. Expanded Accomplishments

Enzyme Pathway

Swinging arm channeled artificial 2D protein array organized by DNA nanoscaffolds

1. Introduction:

Natural system gives us big inspiration. Cell membrane consists of the phospholipid bilayer with embedded proteins which works like a huge 2D platform packed with carefully organized functional enzymes achieving a variety of cellular processes such as cell adhesion, ion conductivity and cell signaling, etc.

One of the presentative examples is the structure of ATP synthase to facilitate the synthesis of ATP through chemiosmosis in photosynthetic membrane. Recent studies by cryoelectron microscopy and tomography have shown that this large complex forms a unique 2 row of dimers along the cristae ridges instead of distributed randomly in the membrane. The arrangement is proposed to contribute to functionality: i.e. partly responsible for shaping the cristae.

Another example is the carefully arranged photosynthetic membrane. In photosynthesis, the harvesting of solar energy and its subsequent conversion into a stable charge separation are dependent upon an interconnected macromolecular network of membrane-associated chlorophyll–protein complexes. The size, relative positions and associations of the photosynthetic complexes reveal crucial new features of the organization of the network. It has been reported that the membrane is divided into specialized domains each with a different network. The light-capture LH2 domains form linear arrays and The LH1 complex is ideally positioned to function as an energy collection hub, which are often only separated by narrow ‘energy conduits’ of LH2 just two or three complexes wide.

In order to better understand 2D enzymatic networks in nature. We use the artificial distance sensitive swinging arm system has a model to study how enzyme 2D network behaves compare to single-particle system, how does geometry affect the 2D enzyme network. Scaling up of the engineered multi-enzyme complexes better mimics the cell organization of multi-enzyme network.

2. Design and assembly of Swinging arm channeled 2D protein array:

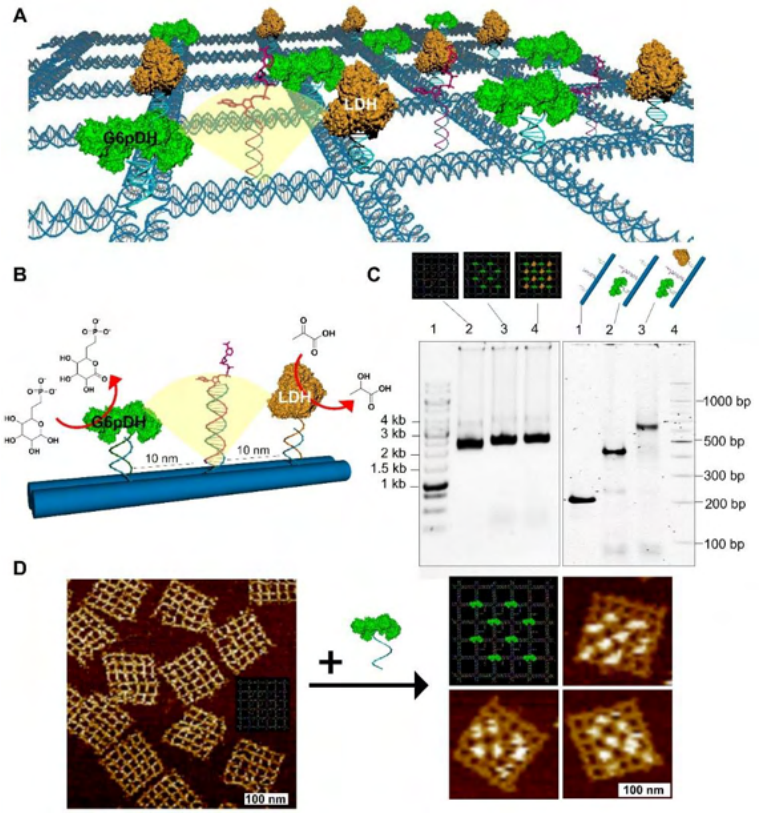


Figure 1. Design and characterization of a NAD$^+$-modified swinging arm 2D array and single particle swinging arm. Schematic illustration of the design of a **(A)** swinging arm array on a 5 × 5 lattice DNA origami and **(B)** a single-particle swinging arm organized on a DX DNA tile. The complex consists of equal number of two types of enzymes: glucose-6 phosphate dehydrogenase (G6pDH) and lactate dehydrogenase (LDH), and a NAD$^+$-modified double-stranded poly(A)$_{30}$-(T)$_{25}$ swing arm is positioned half-way between the pair of enzymes, facilitating the transfer of hydrides, enabling continued enzyme cascade. **(C)** (left) Agarose gel (0.75%) characterization of the origami-enzyme complex and (right) native PAGE characterization (3%) of the DX tile-enzyme complex: lane 1, 1 kb DNA ladder; lane 2, origami; lane 3, origami-G6PDH$_8$-NAD$_8$ complex, lane 4, origami-G6PDH$_8$-NAD$_8$-LDH$_8$ complex, lane 5, DX tile; lane 6, DX tile-G6pDH-NAD complex, lane 7, DX tile-G6pDH-NAD-LDH complex, lane 8, 100 bp DNA ladder. **(D)** Representative AFM images of the origami-enzyme complexes. Scale bar: 100 nm.

To mimic the multi-enzyme network in nature, here we use a 5 × 5 square lattice like DNA origami as a scaffold, 8 of each protein are assembled on the structure, NAD molecules are positioned between each protein, therefore 4 NAD arms are surrounding one protein instead of one in the single tile swinging arm design (**Figure 1A**). The anchor point of NAD swinging arm to both proteins are designed to be 10 nm. This origami with finite size is applied to mimic the infinite 2D array, but with better quantitate control. A double crossover (DX) DNA tile is used to assemble the single-particle swinging arm system, with the same distances between each component in the 2D system (**Figure 1B**). The complex consists of equal number of two types of enzymes: glucose-6 phosphate dehydrogenase (G6pDH) and lactate dehydrogenase (LDH), and a NAD$^+$-modified double-stranded poly(A)$_{30}$-(T)$_{25}$ swing arm is positioned half-way between the pair of enzymes, facilitating the transfer of hydrides, enabling continued enzyme cascade.

To avoid the heterogeneity generated by multiple NAD-ssDNA conjugation, a double-stranded swinging arm is used with 30T hybridized with 25A, 5 A is used as ssDNA linker to give enough

flexibility. Experimental results showed that the activity of the G6pDH-NAD^+ semi-swinging arm is enhanced after adding a poly(A)$_{15}$ strand to hybridize with the NAD^+-poly(T)$_{20}$ arm, so dsDNA swinging arm won't restrict the swinging (**Figure 2**).

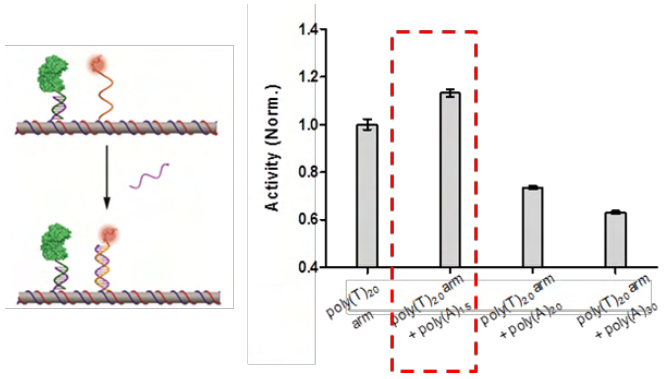


Figure 2. Activity comparison of double-stranded (dsDNA) swinging arm vs. single-stranded (ssDNA) swinging arm. Poly(T)$_{20}$-poly(A)$_{15}$ double-stranded swinging arm showed higher activity compared to ssDNA swinging arm poly(T)$_{20}$.

3. <u>Activity of Swinging arm channeled 2D protein array compare to single particle system:</u>

First, we evaluated the length dependency of both the 2D array system and single-tile system. The activities of the two designs were measured individually in bulk solution for three swinging arm lengths (polyA$_{20}$-T$_{15}$, polyA$_{30}$-T$_{25}$, polyA$_{40}$-T$_{35}$) using phenazine methosulfate (PMS) catalyzed resazurin fluorescence assays (**Figure 3AB**). As predicted, the arm with poly(A)$_{30}$ resulted in the highest activity for both origami and tile, because the length matches the distance between enzymes and swinging arm (10

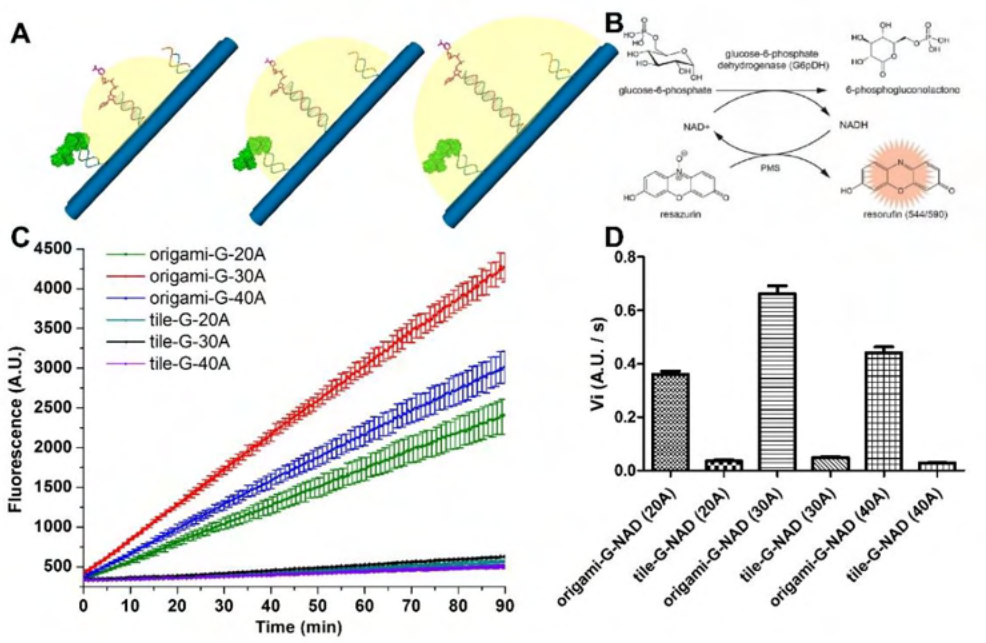
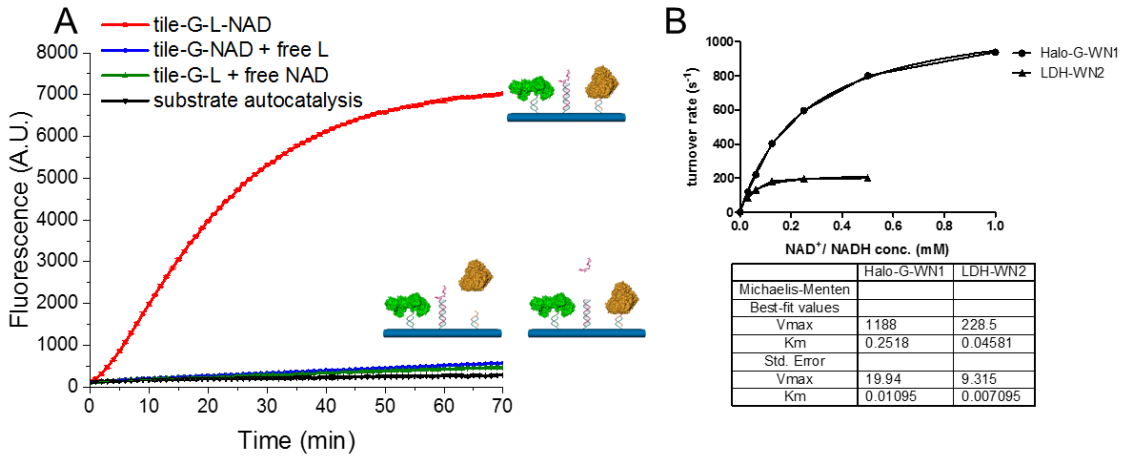


Figure 3. Optimization of the length of the double-stranded NAD+-swinging arm. (**A**) Schematic illustration of design of polyA(20) -T(15), polyA(30) -T(25), and polyA(40) -T(35). Five single stranded T bases were left unpaired at the connection point to the DNA tile to allow enough flexibility of the swing. The double stranded body of the swing arm allows a better distance control then a single stranded swing arm. (**B**) The coupled fluorescence assay for activity test. (**C** & **D**) Activity of polyA(20) -T(15), polyA(30) -T(25), to polyA(40) -T(35) double-stranded swinging arm both on origami and DX tile scaffold. On both scaffolds, the A30-T25 swinging arm show higher activities.

nm) (**Figure 3CD**) . With the optimal arm length, NAD+-modified swinging arm, origami-G6pDH-NAD$^+$ assembly showed an activity enhancement of ~4-fold compared to tile-G6pDH-NAD$^+$ with the same concentration of enzymes at 8 nM (**Figure 5AB**). The control samples with freely diffusing NAD+ shows little activity (almost same as substrate autocatalysis).

Next, using the optimized distance and parameters, a G6pDH-NAD+-LDH swinging arm structure was constructed. The activity of this complete two-enzyme nanostructure is compared to that of the partially assembled structures including a G6pDH-LDH assembly with freely diffusing NAD$^+$, a G6pDH-NAD$^+$ arm assembly with freely diffusing LDH (**Figure 4A**). For the same total NAD$^+$ and enzyme concentration (8 nM), the activity of the complete swinging arm structure is ~ 50-fold higher than Semi-assembled swinging arm complexes with G6pDH-NAD$^+$ attached and the LDH freely diffusing in solution, confirming the LDH harm arm also works. Kinetic measurements found ~5-fold higher turnover number (kcat) for the isolated G6pDH than LDH, indicating that LDH is the rate-limiting enzyme in the G6pDH-LDH cascade (**Figure 4B**).



	Halo-G-WN1	LDH-WN2
Michaelis-Menten		
Best-fit values		
Vmax	1188	228.5
Km	0.2518	0.04581
Std. Error		
Vmax	19.94	9.315
Km	0.01095	0.007095

Figure 4. Activity characterization of LDH- half arm. (**A**) G6pDH-NAD+-LDH swinging arm activity compare to that of the partially assembled structure G6pDH-NAD+ arm assembly with freely diffusing LDH. (**B**) Michaelis-Menten plot for G6pDH and LDH activity (turnover rate) vs. NAD+ concentration. Kcat of G6pDH is roughly 5 fold higher than the LDH.

We compared the 2D network with single particle of the complete origami/ tile-G6pDH-LDH-NAD complex. Overall pathway activities for origami-G6pDH-LDH-NAD compared to tile-G6pDH-LDH-NAD, with same concentration of enzymes (8 nM), showed about 4 fold activity enhancement. Indicating the network effect of enzyme cascades do benefit the overall pathway

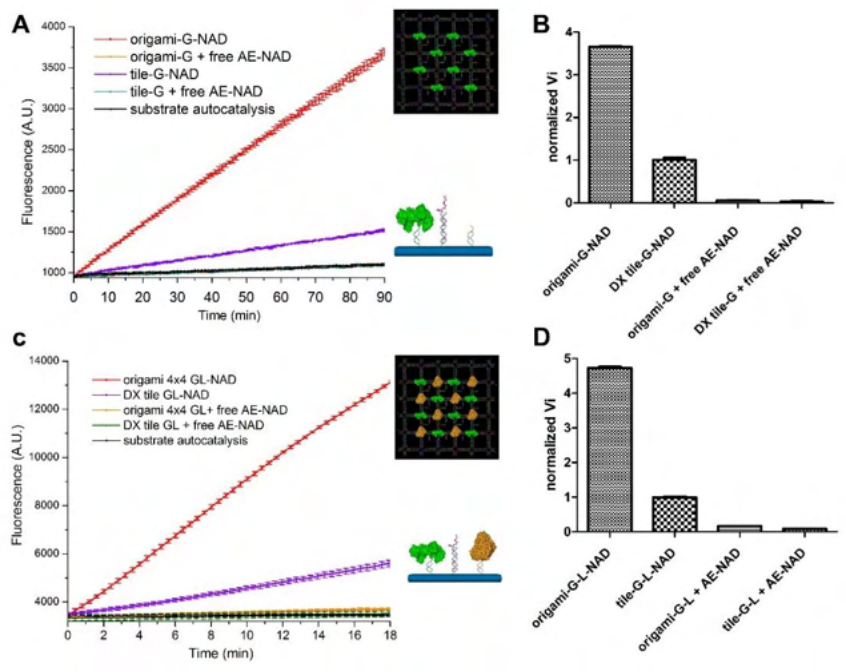


Figure 5. Characterization of enzymatic activity comparing the Origami- G_8-NAD^+_8-L_8 array and DX tile-G-NAD^+-L swinging arm structures. (**A**&**B**) Activity of Origami-G_8-NAD^+_8 (red), Origami-G_8 with free AE-NAD (orange, hidden in the back of green and black), DX tile-G-NAD^+ (purple), DX tile-G with free AE-NAD (green), and substrate autocatalysis (black). (**C**&**D**) Overall pathway activities for Origami-G_8-NAD^+_8–L_8 (red), Origami-G_8–L_8 with free AE-NAD (orange), DX tile-G-NAD^+–L (purple), DX tile-G–L with free AE-NAD (green), and substrate autocatalysis (black).

efficiency, potentially due to the accessibility of multiple swinging arms and downstream enzymes in a close distance compared to single-particle systems (**Figure 5CD**).

4. <u>Stoichiometry analysis:</u>

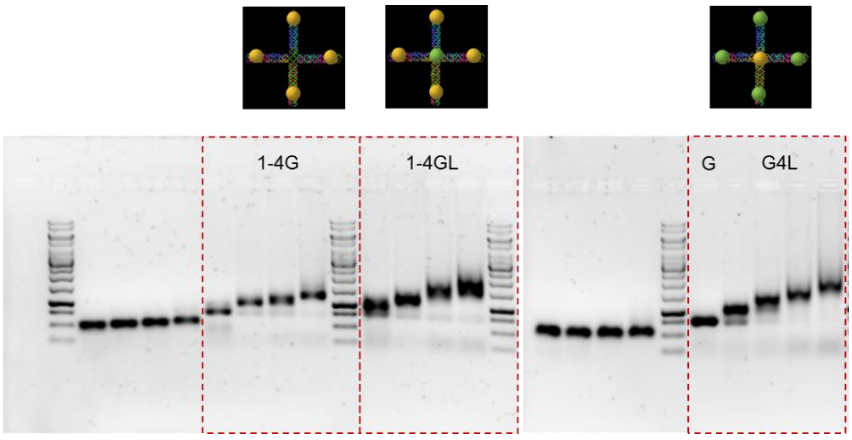


Figure 6. Agarose gel (0.75%) characterization of the tile-enzyme complex: lane 1,10,15,20, 1 kb DNA ladder; lane 2-5, 4x4 tiles; lane 6-9,16-19, 4x4 tile-G6PDH$_{1-4}$-NAD$_{1-4}$ complex; lane 11-14, 4x4 tile-G6PDH$_{1-4}$-NAD$_{1-4}$-LDH complex; lane 21, 4x4 tile-G6PDH-NAD; lane 22-25, 4x4 tile-G6PDH$_1$-NAD$_{1-4}$-LDH$_{1-4}$ complex.

To understand the correlation of enhancement fold of activity and geometry. We investigate the dependence of enzymatic activity on the number of surrounding NAD^+-modified swinging arms on a DNA-scaffolded 4 × 4 tile. Since in the 2D network, for each enzyme, there is 4 arms and 4 enzymes around it locally. Titration from 1 to 4 G6pDH around one LDH, and 1 to 4 LDH around

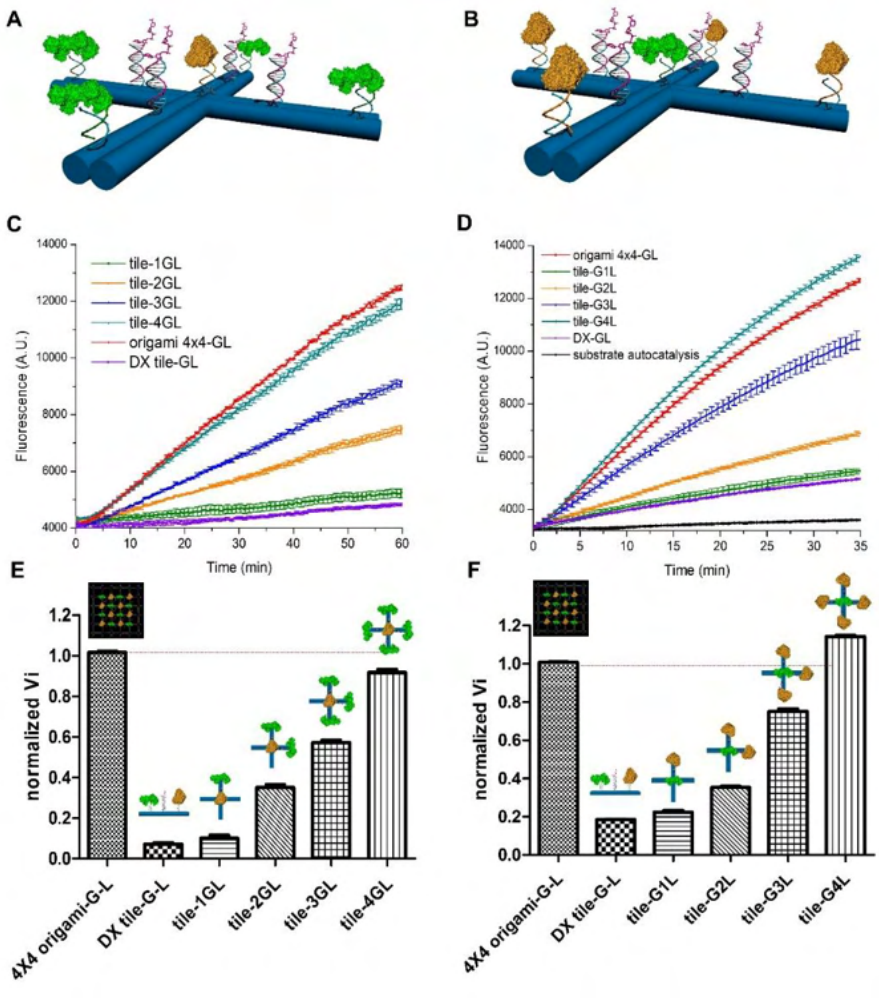


Figure 7. Comparison of enzymatic activity on the 2D array structure of an origami with the G6pDH-NAD^+_n-LDH_n/ $G6pDH_n$-NAD^+_n-LDH (n = 1, 2, 3, 4) swinging arm structures on a 4x4 tile or a DX tile. (**A** & **B**). Schematic figures of the control samples to test the relative stoichiometric dependence of enzyme activity with G6pDH or LDH at center of a 4 × 4 DNA tile and the numbers of NAD^+-modified arms and LDH or G6pDH increases from 1 to 4, respectively. (**C**&**D**) Activity results for Origami-$G6pDH_8$-NAD^+_{24}-LDH_8 construct compared to small tile based G6pDH-NAD^+_n-LDH_n (n = 1, 2, 3, 4): Origami-G_8-NAD^+_{24}-L_8 (red); 4x4 tile-G6pDH-NAD^+_1-LDH_1 (green), 4x4 tile-G6pDH-NAD^+_2-LDH_2 (orange), 4x4 tile-G6pDH-NAD^+_3-LDH_3 (blue), 4x4 tile-G6pDH-NAD^+_4-LDH_4 (canyon), and DX tile-G6pDH-NAD^+-LDH (purple). (E&F) Activity results for Origami-$G6pDH_8$-NAD^+_{24}-LDH_8 construct comparing to $G6pDH_n$-NAD^+_n-LDH (n = 1, 2, 3, 4): Origami-G_8-NAD^+_{24}-L_8 (red); 4x4 tile-$G6pDH_1$-NAD^+_1-LDH (green), 4x4 tile-$G6pDH_2$-NAD^+_2-LDH (orange), 4x4 tile-$G6pDH_3$-NAD^+_3-LDH (blue), 4x4 tile-$G6pDH_4$-NAD^+_4-LDH (canyon), and DX tile-G6pDH-NAD^+-LDH (purple).

one G6pDH has be tested. The stepwise assembly of 4 × 4 tile-enzymes has been characterized by agarose gel (**Figure 6**). Higher mobility has been observed with more enzyme assembled.

The activity of different stoichiometry of G6pDH, NAD, and LDH has been investigated. For group one, LDH is assembled at the center, from one to four NAD-LDH has been assembled in different samples (**Figure 7A).** A linear increase of activity has been observed when increasing the ratio G to L from 1 to 4. In the design. The activity of network system has comparable activity as the 4x4 tile-G6pDH$_4$-NAD$^+_4$-LDH, indicating the LDH in network system is reacting with 4 G around it locally at the same time and saving extra 3 fold of G6pDH. (in the network system, we only have 1 to 1 ratio of G: L, while in the tile we have 4:1 ratio of G: L). For group two (**Figure 7A)**, we are measuring the LDH activity increase while increasing the number of LDH around one G6pDH. The activity in 2D system is between ratio of 3 and 4 which indicates the G in network is a little less activate than the 4:1 L: G ratio, but still ~ 4 fold faster than equal number of enzymes in tile system due to more accessibility to the other enzymes.

5. Summary:

In summary, we designed and constructed artificial "swinging arm"-channeled multi-enzyme 2D network with NAD$^+$-modified molecular arms and compared to the previously developed single particle swinging arm. The benefits of enzyme networks have been discovered. To further study the geometry effects of network on enzyme activities, more pattern needs to be explored. Organizing enzyme cascades in a 3D scaffold, e.g. hosted in DNA 3D crystals is a promising direction in the future.

Directional regulation of enzyme pathways

Artificial multi-enzyme systems with precise and dynamic control over the enzyme pathway activity are of great significance in bionanotechnology and synthetic biology. Herein, we exploit a spatially addressable DNA nanoplatform for the directional regulation of two enzyme pathways (G6pDH-MDH and G6pDH-LDH) through the control of NAD$^+$ substrate channeling by specifically shifting NAD$^+$ between the two enzyme pairs.

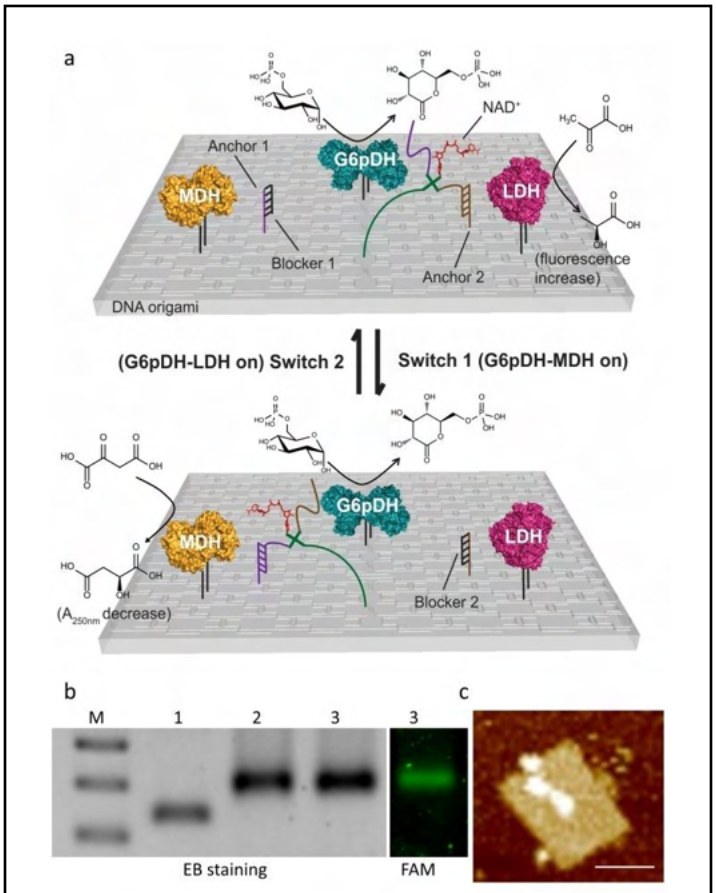


Figure 8. Design and characterization of the enzyme pathway regulation system on DNA origami. (**a**) The nanostructured complex consisting of G6pDH, MDH, LDH, and NAD$^+$-anchored HJ on a rectangular DNA origami platform. (**b**) Characterization of the assembled DNA origami complex with 1.2% fluorescence agarose gel. (**c**) AFM image of the rectangular origami with G6pDH/MDH/LDH and HJ. Scale bar: 50 nm

1. Design and characterization of the enzyme pathway regulation system:

As shown in **Figure 8a**, we constructed a model multi-enzyme system arranged on a rectangular DNA origami platform that involves three dehydrogenases (glucose-6-phosphate dehydrogenase (G6pDH), malate dehydrogenase (MDH), and lactate dehydrogenase (LDH)) and a cofactor (nicotinamide adenine dinucleotide (NAD^+)). G6pDH uses NAD^+ to oxidize glucose-6-phosphate, and the NAD^+ is turned into NADH, which can be used by both MDH and LDH as the reducing agent to reduce oxaloacetate to malate and pyruvate to lactate, respectively. The NAD^+ substrate channeling has a great influence on the activities of the two-enzyme cascade system (G6pDH-MDH or G6pDH-LDH): the two-enzyme cascade system is expected to achieve high activity when the co-substrate is tethered between the two enzymes and allowed to swing between them; a lower activity is expected when the co-substrate is far away from both enzymes. Thus by switching the position of the NAD^+ substrate channeling, the relative activities of the two two-enzyme pathways (G6pDH-MDH and G6pDH-LDH) can be regulated. As shown in **Figure 8a**, when NAD^+ is tethered to anchor 1 for substrate channeling between G6pDH and MDH, the G6pDH-MDH and G6pDH-LDH pathways are activated and deactivated, respectively. The opposite activation pattern is observed when the substrate channeling is switched to anchor 2, which is located between G6pDH and LDH.

The protein-DNA conjugates were synthesized by using a bifunctional succinimidyl 3-(2-pyridyldithio)propionate (SPDP) linker (for LDH) or a HaloTag genetically engineered on the protein (for MDH and G6pDH). Through sequence-specific hybridization of the DNA tags linked to the enzymes with the extended anchoring probes on the origami, all three enzymes were successfully attached to a rectangular DNA origami (**Figure 8c**). The assembly yield of all three enzymes on the DNA origami was estimated to be higher than 80%, based on an agarose gel mobility shift assay (Figure 1b). The successful attachment of the HJ on the DNA origami was also confirmed by the native gel electrophoresis (**Figure 8b**).

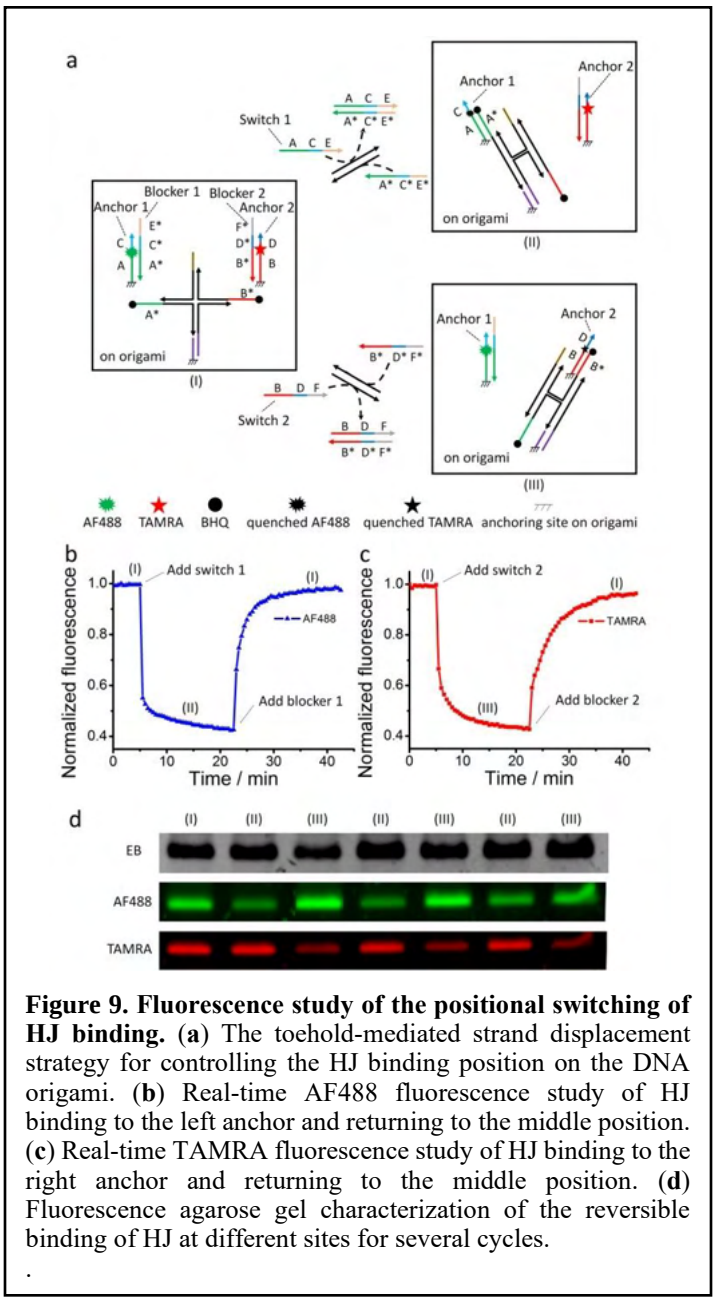


Figure 9. Fluorescence study of the positional switching of HJ binding. (**a**) The toehold-mediated strand displacement strategy for controlling the HJ binding position on the DNA origami. (**b**) Real-time AF488 fluorescence study of HJ binding to the left anchor and returning to the middle position. (**c**) Real-time TAMRA fluorescence study of HJ binding to the right anchor and returning to the middle position. (**d**) Fluorescence agarose gel characterization of the reversible binding of HJ at different sites for several cycles.

.

In a proof-of-concept experiment to demonstrate the positional switching of the HJ between the two anchoring sites on the DNA origami, we utilized fluorescence spectroscopy for the real-time monitoring of the switching process. As shown in **Figure 9a**, green (AF488) and red (TAMRA) fluorescent dyes were used to label the two anchors on the origami scaffold, respectively. On the HJ, a quencher (BHQ1) was attached to both arms that will bind with the anchors. In the presence of switch 1(ACE), blocker 1 (E*C*A*) is removed to unlock anchor 1 (AC), enabling HJ to bind with anchor 1 (via AA* pairing, status II), which brings the quencher near the green dye and decreases the green emission (**Figure 9b**). The addition of the block strand (E*C*A*) releases the HJ from anchor 1 back to the middle position (status I), and the green fluorescence is recovered. Similarly, upon addition of switch 2 (BDF) and blocker 2 (F*D*B*), the position of the HJ can be changed between anchor 2 (BD via BB* pairing, status III) and the middle position (status I), resulting in the quenching and recovery of the red emission of TAMRA, respectively (**Figure 9c**). These results also show that the switching between the binding states was relatively fast (within a few minutes, shown in **Figure 9b, c**) and reversible (**Figure 9d**).

2. <u>Directional regulation of enzyme pathway on DNA origami:</u>

The activity modulation of each enzyme pathway was first achieved through optimization of the spacer length and the distance between the enzymes. In these experiments, NAD^+ was anchored on the free arm of the HJ through a disuccinimidyl suberate (DSS) linking strategy. Taking G6pDH-MDH as an example (**Figure 10a**), this enzyme pathway was activated when the HJ binds to anchor 1, which brings the NAD^+ substrate channeling closer to MDH; however, this enzyme pathway is blocked when the HJ binds to anchor 2 so that the substrate channeling is kept further away from MDH. The normalized activity ratio of the pathway in the active and inactive states was used as the criterion for the optimization of the design parameters.

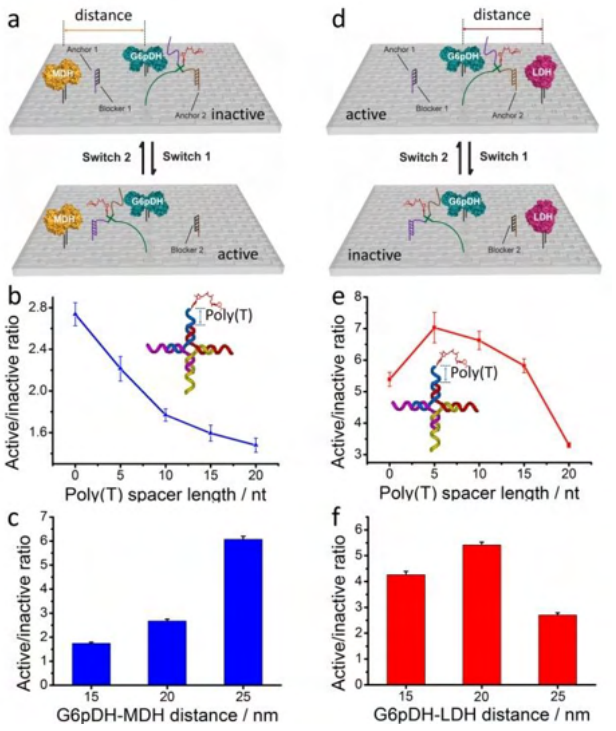


Figure 10. Optimization of the activity regulation of G6pDH-MDH (a-c) and G6pDH-LDH (d-f) by changing the substrate channeling position. The poly(T) spacer length between NAD^+ and HJ (**b, e**) and the inter-enzyme distance (**c, f**) were optimized. The normalized activity ratio of the pathway in the active and inactive states was used as the criterion for optimization.

The first parameter to be optimized was the length of the single-stranded polythymidine (T) linker between NAD^+ and HJ at a fixed inter-enzyme distance of approximately 20 nm. Poly(T) spacers with different lengths (T0, T5, T10, T15, and T20) were utilized for both pathways. The results showed that T0 spacer enabled both pathways to reliably achieve high on/off activity ratios. Furthermore, by fixing

the position of G6pDH, we also changed the position of MDH (or LDH) to control the enzyme distance (**Figure 10c** and **Figure 10f**) using the optimized NAD^+ spacer length. The activity assay results show that the best distances for G6pDH-MDH and G6pDH-LDH were 25 and 20 nm, respectively.

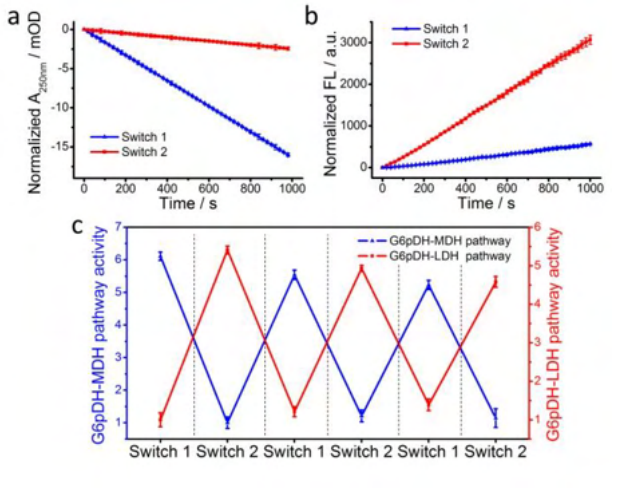


Figure 11. Directional regulation of enzyme pathways by DNA switches. (a) G6pDH-MDH pathway activity in the presence of switch 1 or 2. (**b**) G6pDH-LDH pathway activity in the presence of switch 1 or 2. (**c**) Regulatory cycling of the enzyme pathway activity. All enzyme activities were normalized to the respective activity in the initial status. A two-fold amount of switch 1 or 2 was added for each conformational change.

Finally, we achieved the directional regulation of the enzyme pathways by using short ssDNA to alternatively control the on and off switching of the G6pDH-MDH and G6pDH-LDH pathways on the DNA scaffold. As shown in **Figure 11a-b**, in the presence of switch 1, the HJ binds to anchor 1 to achieve substrate channeling between G6pDH and MDH, thus activating the G6pDH-MDH pathway (its activity can be monitored by a significant absorption decrease at 250 nm in **Figure 11a**).Simultaneously, the G6pDH-LDH pathway was blocked (indicated by the small increase in the fluorescence intensity at 590 nm in **Figure 11b**). Conversely, in the presence of switch 2, HJ binds to anchor 2 and brings the substrate channeling close to LDH, turning on the G6pDH-LDH pathway (indicated by a strong increase in the fluorescence intensity) and shutting down the G6pDH-MDH pathway (indicated by the small absorption decrease at 250 nm). The optimized on/off activity ratio for both pathways is approximately five- to sevenfold. As shown in **Figure 11c**, the reversibility of the enzyme pathway regulation was also successfully confirmed by several cycles of activity regulation.

In summary, we have demonstrated the directional regulation of enzyme pathways in an artificial multi-enzyme network by controlling the position of the substrate channeling. The artificial enzyme network exhibited different activities for the two enzyme pathways in response to different external stimuli (different regulatory DNA single strands) with fast response and good reversibility: Switch 1 activated the G6pDH-MDH pathway and shut down the G6pDH-LDH pathway whereas switch 2 activated the G6pDH-LDH pathway and reduced the G6pDH-MDH pathway. In the future, this strategy for the activity regulation of enzyme pathways through the control of substrate channeling should be applicable to the design of smart enzyme networks involved in feedback or feed-forward control and synergistic or antagonistic effects, as well as the development of functional catalytic devices for energy and material converters and regulatory biological circuits for synthetic biology and biomedicine.

Electrochemical wiring of redox enzymatic cascade pathways on sub-monolayer DNA origami assembled on gold electrode

1. Introduction:

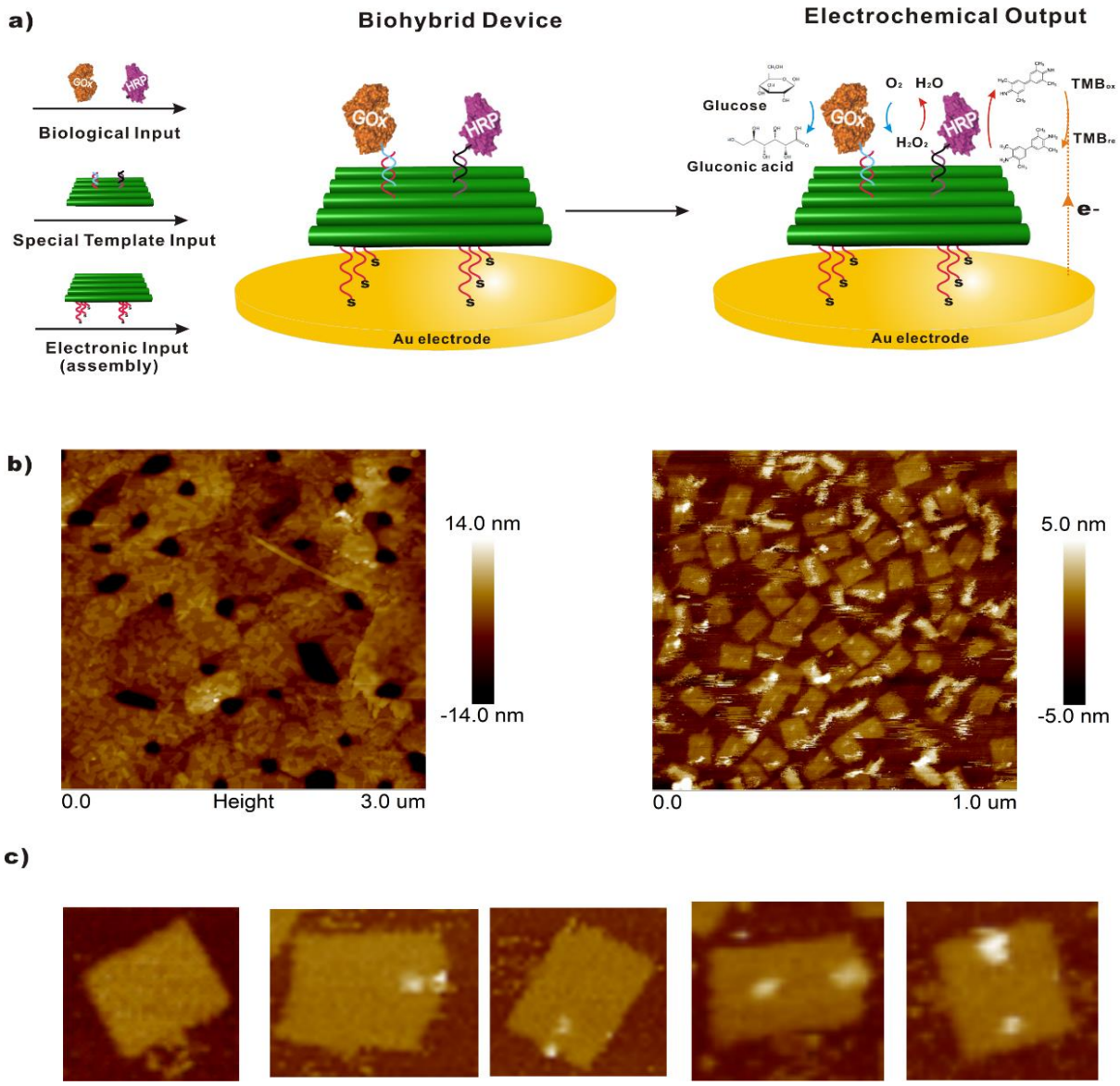


Figure 12. a) Schematic of the biohybrid device, where glucose oxidase (GOx) and horseradish peroxidase (HRP) enzyme cascade were assembled on gold electrode through thiol-modified DNA origami scaffold. The reaction schemes are also shown. The enzyme-catalyzed reactions are linked to the electrochemical reaction of TMB on the electrode to realize a cycling of the electron carrier molecule and to give the electrochemical output. The overall reaction is that for every molecule of glucose oxidized, one molecule of O_2 is reduced to H_2O molecule, and two electrons are transferred from the electrode to the system. The direction of the electron transfer is indicated by the dashed arrow. **b**) AFM image of thiol-modified rectangular origami on gold substrate. c) AFM images of rectangular origami and co-assembled GOx/HRP origami on mica with the GOx/HRP distance ranging from 10 nm, 20 nm, 45 nm to 65 nm.

The development of hybrid nanodevices that contain multiple components of different materials has gained rapidly increasing attention in recent years. New biomimetic systems are being developed as a result of continuous improvement in microelectronics technology and DNA nanotechnology, leading to improved knowledge about multi-enzymatic molecular mechanisms in a non-cellular environment. The spatial organization of enzymes catalyzing a sequence of chemical reactions can influence the specificity, controllability, and throughput of the reaction cascades, which are essential factors to mimic natural enzyme organization for optimizing the production of valuable metabolites with industrial and medical importance. Manipulation of biological routes would enable the production of a vast array of valuable compounds including commodity and specialty chemicals (e.g. biodegradable plastics), biofuels (e.g. ethanol, butanol), and therapeutic molecules (e.g. anticancer drugs, antimicrobial compounds). Furthermore, translating biochemical pathways to non-cellular environments is also one of the key goals in nanobiotechnology. Despite the importance, to date there are only very few biomimetic systems available to systematically control the biological behavior by influencing enzymatic activity in multi-enzyme systems.

Structural DNA nanotechnology has emerged as a reliable way to organize nanoscale systems because of the programmability of DNA hybridization, and the versatility of DNA-biomolecule conjugation strategies. Protein–DNA assemblies have been used to organize cascades of enzymatic reactions by controlling the relative distance and orientation of enzymatic components, or by facilitating the interface between enzymes/cofactors and electrode surfaces. By taking advantage of the sequence specificity and the resulting spatial addressability of DNA nanostructures, it is possible to mimic enzyme cascade reaction on a microelectronic device.

Here we demonstrate the use of a self-assembled, spatially addressable DNA origami nanostructure to direct the precise positioning of protein enzymes onto a gold electrode to form a sub-monolayer of the enzyme-pairs on the DNA origami with designed inter-enzyme distances. These nanostructures were assembled on gold electrode surface via either Au-S linkage or ligand-protein (biotin-avidin) interactions, while the assembly on surface was verified to be close to monolayer which ensures the efficiency of enzyme cascade and electron transfer reactions on the electrode. The enzyme cascade reactions between GOx/HRP on the electrode were monitored by electrical devices, and the flux of the enzyme reactions were enhanced by the electrochemical measurement due to efficient cycling of the electron carrier 3,3’,5,5’-tetramethylbenzidine (TMB) on the electrode (**Figure 12**). This work creates a programmable hybrid device containing both biochemical and electrochemical components that is capable to assemble and tune the activities of an enzymatic cascade pathway on the gold electrode. The reliable sub-monolayer assembly of functionalized DNA nanostructures on the gold electrode will facilitate sensitive electrochemical detection of bio-recognition and protein catalyzed reactions and will see applications for bio-sensing and disease diagnosis.

2. <u>Sub-monolayer assembly of functionalized DNA nanostructures on gold electrode:</u>

The DNA nanostructured monolayer (DNM) assembled on gold electrode could provide a superior way to examine the electrochemical effect of DNA monolayers on gold substrate, in comparison with the self-assembled monolayer (SAM) of single-stranded (ss-) DNA on gold substrates. This is due to the rigidity of origami that greatly reduces the chance of inter-strandentanglement that is often observed in ssDNA-based monolayers. Also, the presence of regularly patterned 0.5 nm wide, 7-10 nm (2-3 DNA helical turns) long cavities on the DNA nanostructures, electrons could more easily diffuse through the DNMs than the SAM of ssDNA. We tested this idea using the DNA origami modified with the electro-active molecules ferrocene (Fc) or methylene blue (MB), respectively, and deposited them on gold microelectrode. Alternating current voltammetry (ACV) scans showed peaks at ~ -0.20 V and 0.43 V, respectively (**Figure 13c and d**), which are consistent with the free molecules on the electrode. This result indicates that the electron transfer from the electro-active molecules to the electrode is not attenuated by the DNA origami tiles assembled on the microelectronic device. Therefore, DNA origami can be used as a new reliable assembly scaffold for electrochemical studies and the creation of gold surfaces modified by DNMs is suited for advanced biosensoring applications.

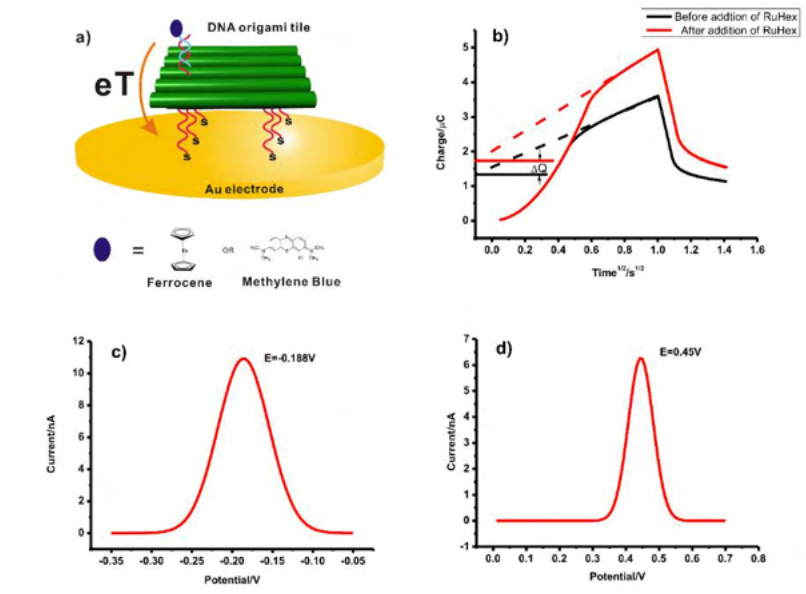


Figure 13. Directional regulation of enzyme pathways by DNA switches. (a) G6pDH-MDH pathway activity in the presence of switch 1 or 2. (**b**) G6pDH-LDH pathway activity in the presence of switch 1 or 2. (**c**) Regulatory cycling of the enzyme pathway activity. All enzyme activities were normalized to the respective activity in the initial status. A two-fold amount of switch 1 or 2 was added for each conformational change.

3. <u>Electrochemical analysis of on-device reactions on gold electrode:</u>

It was found that the SH-10nm assembled on gold surface exhibited the highest enzyme activity, which was ~20 times greater than the activity of the SH-control, which contains DNA origami assembled on electrode with free unbound enzymes in solution, even the SH-65nm exhibited ~6 folds enhancement of enzyme activity compared with the SH-control (**Figure 14d-e**). Decreasing the distance between GOx and HRP from 65 to 10 nm resulted in a gradual increase in the enzyme activity. As shown in **Figure 14d and e**, the closer the two enzymes are, the higher the activity enhancement becomes. The distance dependence of the enzyme activity enhancement shown in **Figure 14e** is consistent with previous work detected using fluorescence methods in solution, although the distance dependence is less steep on the electrode.

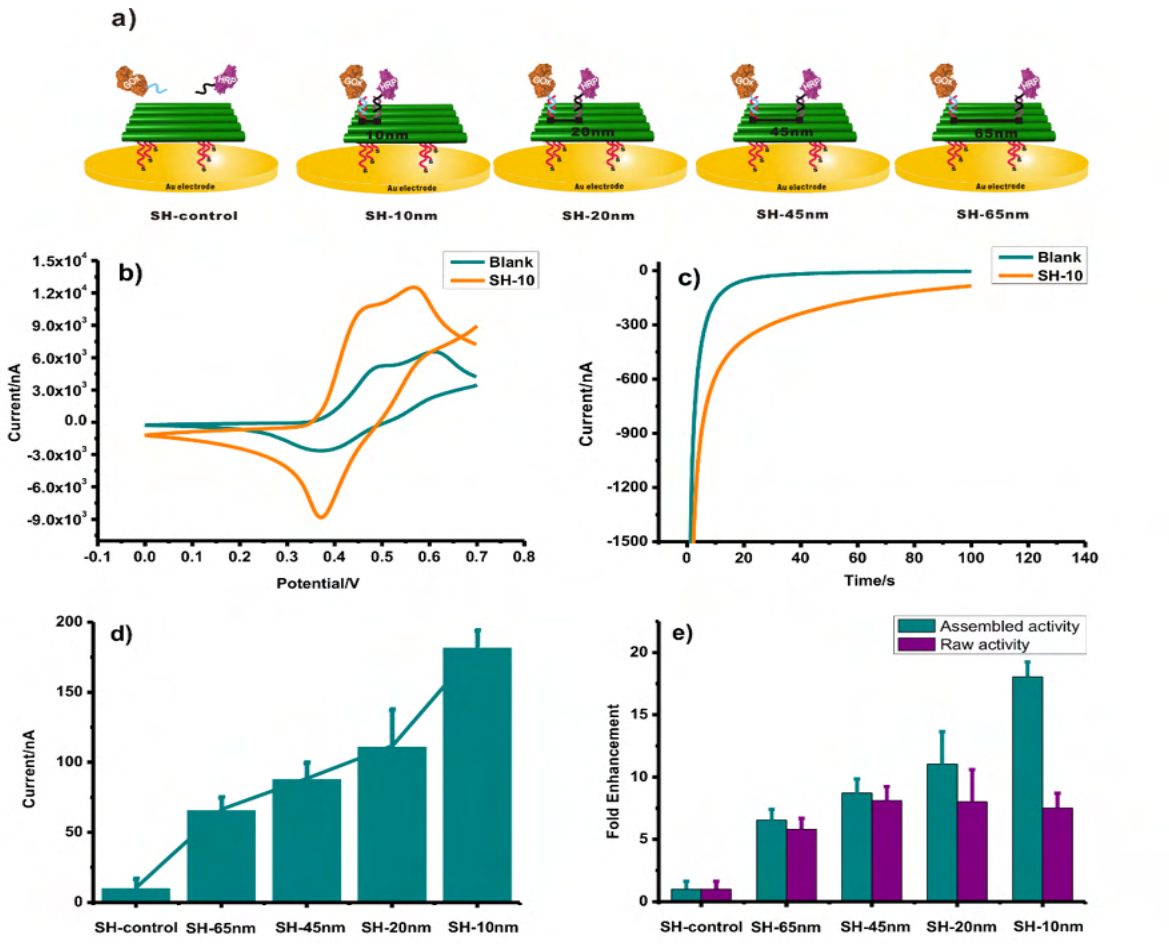


Figure 14. **Enzymatic activity for enzyme-assembled DNA origami samples on gold electrode surface was evaluated by electrochemical work-station**. **a**) Rectangular DNA origami tiles with assembled Gox/HRP enzyme pairs with inter-enzyme spacing from 10 nm to 65 nm. **b**)-**c**) Cyclic voltammograms scan (cycles between 0 to 0.70 V vs. Ag/AgCl 3M) and amperometric detection for the assembled GOx/HRP pairs on DNA origami attached on gold electrode at 150 mV. **d**) The electro-reduction current of the amperometric detection shows a strong distance-dependence of the assembled GOx/HRP pairs. **e**) Enhancement of the activity of the enzyme pairs attached on DNA origami, compared to a control sample with DNA origami on electrode surface with free enzyme-unbounded in solution (SH-control). Both the raw activity and the yield-corrected activity (corrected for the co-assembly yield of the completely assembled nanostructures) are shown.

By comparing the enzyme activity enhancement on electrode with those obtained in solution, the fold of enhancement is larger on electrode for all inter-enzyme distances. This may be explained by the enrichment effect of gold electrode for the enzyme cascade reactions, which possibly allowed the transfer of substrate molecules between multiple enzymatic active sites, both inter or intra of the origami tiles on the surface. The close to full monolayer surface assembly of DNA origami scaffold have constructed a relatively dense micro-environment that have multiple rectangular tiles near each other, which makes the diffusion of intermediate molecules from one tile to another much faster and more frequent compared with that in solution condition. So except for the direct diffusion path of intermediates between two sequential enzymes on the same DNA origami, a second diffusion pathway that delivers intermediate molecules to the second enzyme on

one of the nearby DNA origami tiles can not be neglected, because the reaction takes place on a two dimensional surface rather than in solution. The second diffusion processes becomes more frequent along the surface of gold electrode where the origami scaffold sample is densely packed with high ratio coverage, which result a 20-30 folds increase of the enzyme activity for SH-10nm on electrode instead of ~15-folds increase in solution, and even for SH-65nm that has the longest inter-enzyme distance, the activity enhancement is 5-6 folds on electrode instead of ~ 2 folds in solution.

In summary, we have developed a reliable DNA-nanostructured monolayer platform for organizing enzymes spatially onto gold electrode. With the aid of precise design ability of structural DNA nanotechnology, this electrochemical microelectronic device creates a programmable hybrid device that contains both biochemical and electronic components, which leads to pre-designed, ordered multi-enzyme nanostructures that facilitate inter-protein communication and artificial biocatalytic cascades. The activity of a GOx/HRP cascade spatially organized by a DNA nanostructure on electrode surface was studied as a function of the inter-enzyme distance, and the enhancement of enzyme activity on device is significantly better than the one in solution. This result may lead to design of future microelectronic devices for better biodetection and analysis. This study shows that redox enzymatic cascade pathway immobilized on the surface of a gold electrode results in a predictable electrochemical signal generation. The methodologies demonstrated here can become the basis for targeting and controlling biochemical fluxes of other biohybrid devices. The DNA nanostructure based biofabrication method could further facilitate the utilization of biologically inspired nanoscale processes and therefore bridges the communication and fabrication gaps between microelectronics and biological systems.

A three-enzyme pathway with an optimized geometric arrangement to facilitate substrate transfer

1. Introduction:

Cascade reactions drive and regulate a variety of metabolic activities. Efficient coupling of substrate transport between enzymes is important for overall pathway activity and also controls the depletion of intermediate molecules that drive the reaction forward. Here, we assembled a three-enzyme pathway on a series of DNA nanoscaffolds to investigate the dependence of their activities on spatial arrangement. Unlike previous studies, the overall activity of the three-enzyme pathway relied less on inter-enzyme distance and more on the geometric patterns that arranged them within a relatively small range of 10 - 30nm. Pathway intermediate detection demonstrated that the assembled enzyme systems quickly depleted the intermediate molecules through efficient reaction coupling.

In the previous report, we demonstrated the assembly of a three-enzyme pathway on a DNA nanostructure via Native PAGE electrophoresis and AFM. In this report, we observed that due to the spatial organization, the reaction intermediates between the three enzymes only need to diffuse a small distance to reach the next enzyme. We investigated the effect of substrate coupling on overall pathway activity and demonstrated that intermediate molecule depletion drives the reaction forward.

2. Optimization of the activity of assembled two-enzyme pairs:

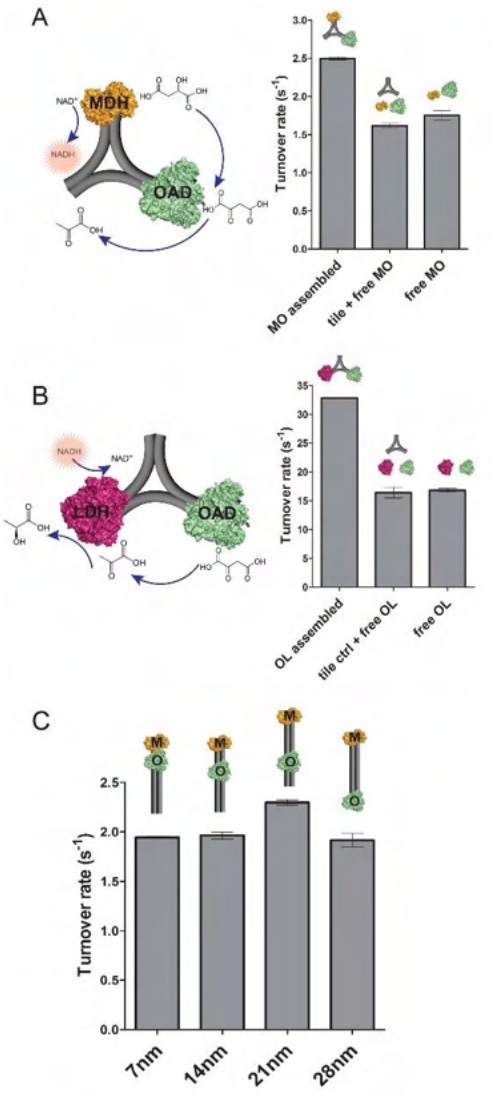


Figure 15. **Optimization of the activity of assembled two-enzyme pairs of MDH-OAD and OAD-LDH**. **A**) Left: schematics of MDH-OAD pathway; Right: activity of NADH production for the MDH-OAD pathway (MO). **B**) Left: schematics of the OAD-LDH pathway; Right: activity of NADH depletion for OAD-LDH pathway (OL). **C**) Distance-dependent activity of a MDH-OAD pair assembled on a double-crossover DNA nanostructure with 7, 14, 21 and 28 nm inter-enzyme distances. Condition: for the MDH-OAD pair, 10 nM enzyme structure is incubated with 1 mM malic acid and 1 mM NAD^+ in 100 mM HEPES buffer (pH 8.0); for the OAD-LDH pair, 10 nM enzyme structure is incubated with 1 mM OAA and 1 mM NADH in 100 mM HEPES buffer (pH 8.0).

We first evaluated the assembly and activity for the two-enzyme pairs of MDH/OAD and OAD/LDH, repectively. As shown in **Figure 15A**, the NADH production rate for an assembled MDH/OAD pair is ~2.5 s^{-1}, which is ~1.7 fold faster than the unassembled enzyme pair in the presence of the same concentration of a non-binding DNA structure (~1.5 s^{-1}). In **Figure 15B**, the NADH depletion rate for an assembled OAD/LDH pair is ~33 s^{-1}, ~2-fold faster than the unassembled enzyme pair (~ 16 s^{-1}). Since the OAD/LDH pair consumes NADH much faster (>10-fold) than the NADH production rate by the MDH/OAD pair, the reaction catalysed by the MDH/OAD pair is the rate-limiting step in the three-enzyme pathway.

To improve the NADH production rate, we next studied the distance-dependent activity of the MDH/OAD pair on a linear DNA scaffold with a series of spacing distances of 7, 14, 21, and 28 nm. As shown in **Figure 15C**, the activity variations of enzyme complexes positioned at different distances was less than 20%, which is much smaller as compared with the previously reported studies of distance-dependent enzyme cascade activities, possibly due to the rapid diffusion of OAA intermediate.

3. <u>Optimization of the geometric arrangement of assembled three-enzyme pathway for enhancing the lactate production:</u>

Next, the geometric arrangements of the three enzymes were studied to improve mass transport of molecules within the pathway. The three enzymes were arranged into a series of linear patterns and a triangular pattern (Figure 3A). Because the MDH-catalysed oxidation of malate is the rate-limiting step with rapid kinetics of the reversed reaction, efficient removal of the reaction products of NADH and OAA is critical to ensure that the reaction proceeds forwardly. Thus, the geometric arrangement of the three enzymes is important for depleting these reaction intermediates. As shown in **Figure 16A**, enzymes were first arranged into a series of linear patterns and the triangular pattern. For the linear patterns, the O-M-L (~2.5-fold

enhancement over free enzymes) showed the highest activity compared to the M-O-L (~1.4-fold enhancement) and M-L-O (~1.8-fold). For the O-M-L distance, both the linear diffusion of OAA between MDH and OAD that of NADH between MDH and LDH had the shortest distance (~14-nm). Thus, OAA and NADH were depleted faster by OAD and LDH due to the shortest diffusion distance, which promoted the MDH-catalysed reaction forward. Conversely, for the M-O-L pattern, the linear diffusion distance of OAA between MDH and OAD was ~14-nm, and the linear diffusion of NADH between MDH and LDH was ~28-nm. For the M-L-O pattern, the linear diffusion distance of OAA between MDH and OAD was ~ 28-nm, and that of NADH between MDH and LDH was ~14-nm. For enzymes assembled into a triangular pattern on the 3PS scaffold, the distances between any two enzymes were all ~12-nm. Thus, all the intermediate substrates (e.g. OAA, NADH, and pyruvate) released from the reactions traveled the same and shortest distance to reach the next enzyme partner. An additional 1.7-fold activity improvement was observed for the triangular M-O-L pattern compared to the best linear O-M-L pattern.

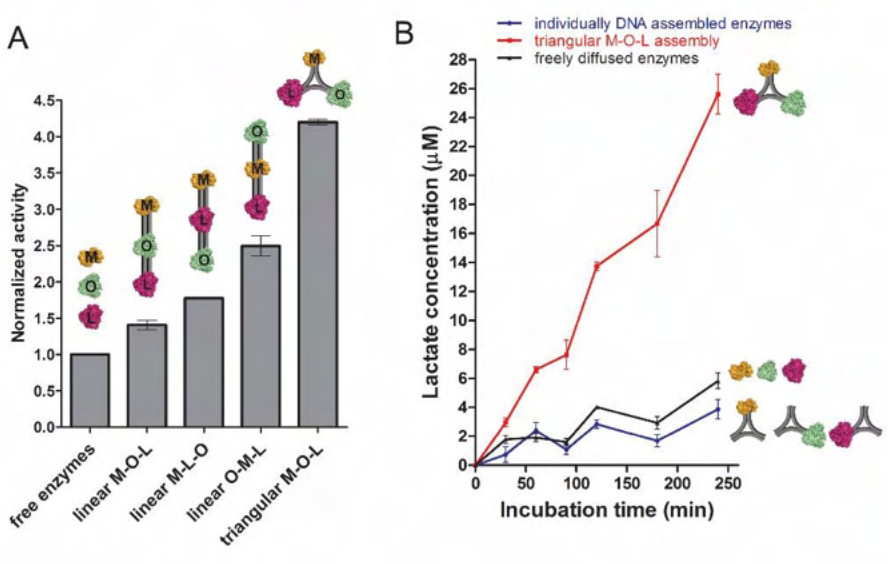


Figure 16. Optimization of the geometric arrangements of assembled three-enzyme pathway for enhancing the lactate production. A) Activity enhancement of a series of assembled three enzyme structures as compared to the activity of unassembled, free enzymes. From left to right: freely-diffused enzymes; linear M-O-L assembly with the interenzyme distance of 14 nm; linear M-L-O assembly with the interenzyme distance of 14 nm; linear O-M-L assembly with the interenzyme distance of 14 nm; triangular M-O-L assembly on a three-point star DNA nanostructure. **B**) Lactate production rate of triangular M-O-L assembly (shown in red), individually DNA-assembled enzymes (purple) and freely diffused enzymes (black).

The overall pathway activity of the assembled three-enzymes on the 3PS scaffold was evaluated for production of the end product, lactate. Using a stop-time assay as previously reported, the triangular M-O-L assembly (**Figure 16B, red**) produced lactate at a rate ~ 5-fold faster than the individual enzymes assembled on the DNA-3PS (**Figure 16B, purple**) and ~ 4.5-fold faster than freely diffused enzymes (**Figure 16C, black**).

4. <u>Accumulated NADH in the three-enzyme pathway:</u>

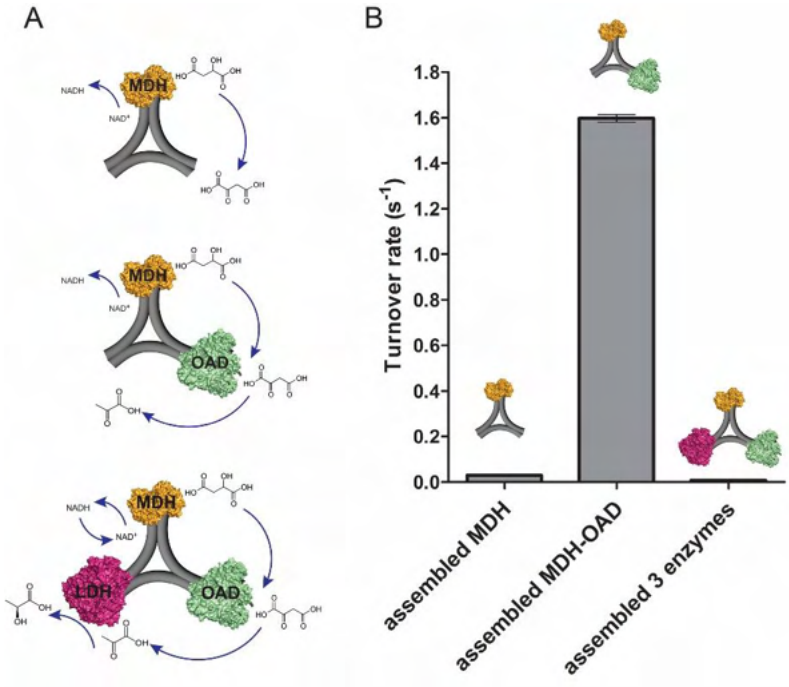


Figure 17. Accumulated NADH in the three-enzyme pathway. (**A**) Schematics of NADH accumulation in the enzyme pathway. Top: For a single MDH, NADH is produced at a very low level due to the thermally unfavored reaction; Middle: For a MDH-OAD cascade, NADH is quickly produced with the oxidation of malic acid due to the removal of OAA by an OAD; Bottom: For a MDH-OAD-LDH cascade, the NADH intermediate will be consumed by LDH to produce lactate, thus the overall accumulated NADH concentration is low. (**B**) Experimental measurement of accumulated NADH in the enzyme systems.

The depletion rate of the intermediate molecules (e.g. NADH) were also evaluated for the three-enzyme pathway. As shown in **Figure 17A (top)**, the MDH alone catalysed oxidation of malic acid to OAA and reduction of NAD^+ to NADH at a very slow rate (~0.03 s^{-1}) with 1 mM NAD^+ input. The addition of the second enzyme OAD quickly removed OAA by converting it to pyruvate, thus promoting the MDH-catalysed reaction toward more NADH production (**Figure 17A, middle**). Addition of the third enzyme LDH depleted NADH by oxidizing it back to NAD^+ (**Figure 17A, bottom**). It is predicted that an efficiently coupled enzyme pathway should quickly deplete the NADH intermediate for reducing pyruvate, leaving a low concentration of NADH detected, while a partially coupled pathway may release a large amount of the intermediate into the bulk solution. As shown in **Figure 17B**, almost no NADH production (~0.008 s^{-1}) was detected for the fully assembled MDH-OAD-LDH pathway, as compared to the much higher NADH production rate (~1.60 s^{-1}) for the assembled MDH-OAD pathway. This experiment and the stop-time assay results demonstrate that in the fully coupled reaction pathway, the overall reaction is more efficient toward the end product because the precious intermediates NADH are well-coupled between the neighbouring MDH-LDH without significant leakage to the bulk solution.

In summary, we studied the activities of a three-enzyme pathway of MDH-OAD-LDH with variable spatial distances and geometric arrangements. Unlike the previously reported two-enzyme systems, the overall activity of the three-enzyme pathway was more dependent on the geometric patterns arranging enzymes rather than the inter-enzyme spacings. By optimizing the geometric patterns of the three enzymes, a 5-fold activity enhancement was obtained for the assembled enzyme pathway compared to the unassembled free enzymes. Furthermore, the depletion of the pathway intermediates was very efficient in the assembled enzyme systems with little detectable NADH in the bulk solution, demonstrating that almost all NADH was coupled into the enzyme pathway without leakage. Our studies will help guide the design of artificial multi-enzyme systems

with optimized geometric arrangements to facilitate bioenergy production and the synthesis of high value chemicals and biofuels.

DNA crowded-enzyme complexes with enhanced activities

1. Introducing DNA crowding on enzyme surface:

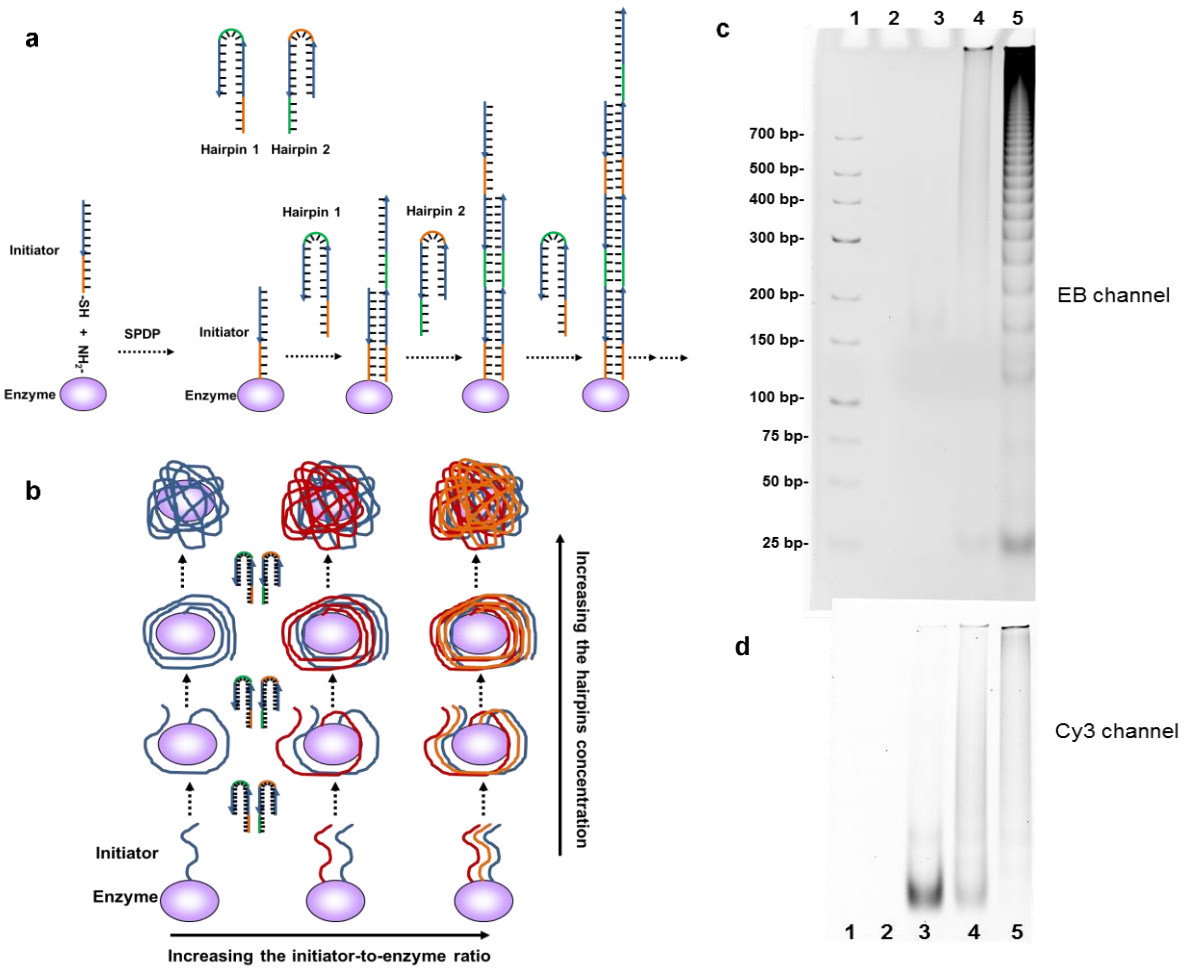


Figure 18. Design and characterization of the growth of DNA hair on enzymes using HCR. a, Schematic of the growth of DNA hair on enzymes using HCR. **b**, the formation of DNA hair with varying initiator-to-enzyme ratio and hairpins concentration. **c**, Native PAGE characterization of enzymes with DNA hair. Lane 1, DNA ladder; lane 3, 1 µM Cy3labeled G6pDH-initiator; lane 4, 1 µM Cy3labeled G6pDH-initiator with 1 µM hairpin1 and hairpin2; lane 5, 1 µM Cy3labeled G6pDH-initiator with 10 µM hairpin1 and hairpin2.

As shown in **Figure 18a**, our approach involves two steps: (1) the conjugation of initiator strands to enzymes and (2) the growth of DNA double helix on the enzyme surface by initiator-triggered hybridization chain reaction. A SPDP (N-succinimidyl 3-(2-pyridyldithio) propionate) crosslinker was used to conjugate the primary amines of the lysine residues on the enzyme surface to a thiol-modified initiator strand. When hairpin substrates are added into the solution, the initiator strand on the enzyme surface will first hybridize with one hairpin (e.g. hairpin 1), exposing a toe-hold for hairpin 2. The opened hairpin 2 will subsequently expose another toe-hold for hairpin 1, continuing

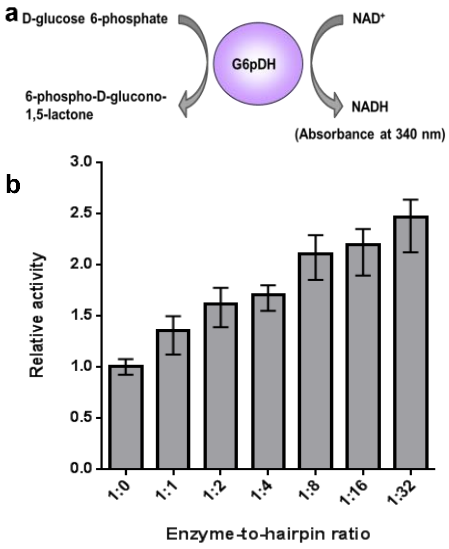
the hybridization process. Therefore, one initiator can trigger the hybridization of a long DNA duplex with alternative hybridization of hairpin 1 and 2. The size of the DNA duplex can be controlled by the imitator-to-hairpin ratio. As shown in **Figure 18b**, the HCR duplex on the enzyme surface will behave as a hair (DNA persistence distance is ~ 50 nm , 150-nt) and thus wrap around the enzyme. In this way, the enzyme is surrounded by a local DNA duplex with high density.

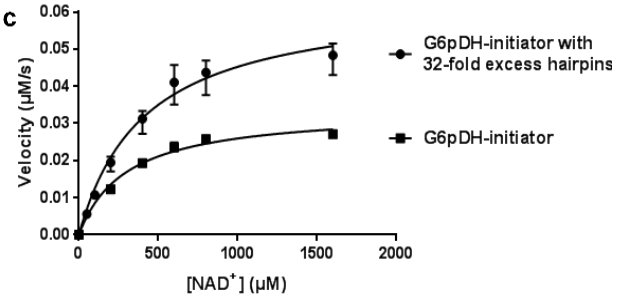
2. Characterization of the formation of DNA hair on enzymes:

As shown in **Figure 18c**, multiple DNA-crowded enzyme complexes were characterized by gel electrophoresis. G6PDH modified with an initiator (Lane 3, G6PDH-I, ~ 150 – 200 bp size) showed a faster mobility and a low EB-staining signal due to the presence of only one or two short initiator strands on the enzyme surface. The incubation of G6PDH-I with hairpin substrates at 1:1 ratio reduced in a complex (Lane 4, > 200 bp size) with slower mobility with more EB-staining signal due to the growth of DNA duplex on the enzyme surface. The incubation of G6PDH-I with hairpin substrates at 1:10 ratio resulted in large complexes (lane 5, > 700 bp) with strong EB-staining signal due to the formation of long DNA duplex on the enzyme surface. In **Figure 18d**, fluorescently labelled G6PDH showed that enzymes were migrated together with large DNA duplexes, demonstrating the DNA wrapping near the enzyme surface.

3. Activity characterization of the enzymes with DNA hair:

As shown in **Figure 19a**, DNA-crowded G6PDH was evaluated by the reduction of NAD^+ to NADH with the simultaneous oxidation of glucose 6-phosphate, resulting in an increased absorbance at 340 nm. In **Figure 19b**, the activity of G6PDH-I was increased as the addition of





Free G6pDH-initiator		G6pDH with DNA hair	
K_m (μM)	k_{cat} (s^{-1})	K_m (μM)	k_{cat} (s^{-1})
298 ± 32	33.6 ± 1.2	414 ± 63	63.9 ± 3.8

Figure 19. Activity characterization of enzymes with DNA hair. (**a**) Schematic of the enzymatic reaction. (**b**) Normalized activities of enzymes with DNA hair when varying the hairpins concentration. Sample preparation: 100 nM G6pDH-initiator was combined with 0, 0.1, 0.2, 0.4, 0.8, 1.6, or 3.2 μM hairpin1 and hairpin2 in 1×SPSC buffer. Then they were incubated at room temperature for 24 h. Assay conditions: All enzyme solutions were diluted 100 fold for activity test. The final concentration of G6pDH was 1 nM.. Substrates were1 mM G6p and 1 mM NAD^+ in 1xTBS buffer with 1 mM $MgCl_2$ (pH 7.5). (**c**) The Michaelis-Menten fitting of G6PDH-I and G6PDH-I/hairpins

more hairpin substrates, with the maximum enhancement of ~ 2.5 fold with an enzyme-to-hairpin

ratio of 32 as compared with G6PDH-I alone. In **Figure 19c**, detailed kinetic analyses showed that the *Km* varied relatively smaller between G6PDH-I and G6pDH-I/hairpin (~ 1.4 hold increase), while the turnover number of G6PDH-I/hairpin increased almost 2-fold as compared with G6PDH-I.

4. Future direction:

We will test the generality of DNA-crowded complexes for more enzyme targets. DNA crowding will also be utilized to improve multienzyme systems. The newly developed method of DNA crowding only requires a few DNA strands and can be scaled up to much higher concentration of proteins (hundreds of micromolar) as compared with the complicated and low nanomolar concentrations of DNA origami. More mechanistic studies of hydration layer will probe the nature of DNA crowding effect.

A general protocol of assembling multienzyme complexes on DNA nanostructures

Over the past four years, we have developed protocols for the robust assembly, purification and characterization of multi-enzyme complexes organized by DNA nanoscaffolds. These protocols have been successfully employed to develop a series of artificial enzyme complexes with functions such as facilitated inter-enzyme substrate diffusion, biocatalytic swinging arms, compartmentalized enzyme cascades and regulated enzyme nanoreactors. Here, we present detailed protocols for exploiting DNA nanostructures as assembly scaffolds that organize the spatial arrangements of multi-enzyme cascades with control over their relative distance, compartmentalization, and substrate diffusion paths. The protocol describes the preparation and purification of DNA-conjugated enzymes and cofactors, along with the assembly of these prepared complexes on DNA nanostructures. The architecture of assembled enzyme complexes is then readily characterized using a broad selection of techniques from routine gel electrophoresis to advanced single-molecule imaging. We also describe methods to purify these nano-assemblies and test them with functional assays based on either bulk or single-molecule fluorescence measurements. The entire assembly and characterization of a multi-enzyme complex can be completed within one to two weeks.

1. Spatially addressable DNA nanostructures for positioning enzymes:

Spatially addressable assembly is one of the most attractive features of DNA nanostructures, due to the well-defined geometry of the DNA double helix and the unique sequence of each oligonucleotide that encodes the overall architecture of the structure. As shown in **Figure 20a**, the B-form DNA double helix has well-defined structural characteristics in aqueous solution, such as a helical diameter of ~2.4 nm, a helical rise of ~3.4 nm for each of 10.5 base pairs (bps), and an ~34.3° rotation angle between two adjacent base pairs[5]. Using DNA nanostructures as the assembly templates, enzymes can be positioned with controlled parameters of spatial distance (**Figure 20b**) and relative anchor angles (**Figure 20c**), as well as the geometric arrangement and stoichiometry of the participating enzymes (**Figure 20d**). **Figure 20e-h** shows an example of positioning of a two-enzyme glucose oxidase (GOx)/horseradish peroxidase (HRP) cascade on a rectangular DNA origami with distances ranging from 10-nm, 20-nm, 45-nm to 65-nm. A statistically significant analysis of the inter-enzyme distances (anchor-to-anchor) for the enzyme pair was performed by atomic force microscope (AFM). The spatial dimensions of a scaffolding DNA nanostructure are described as following:

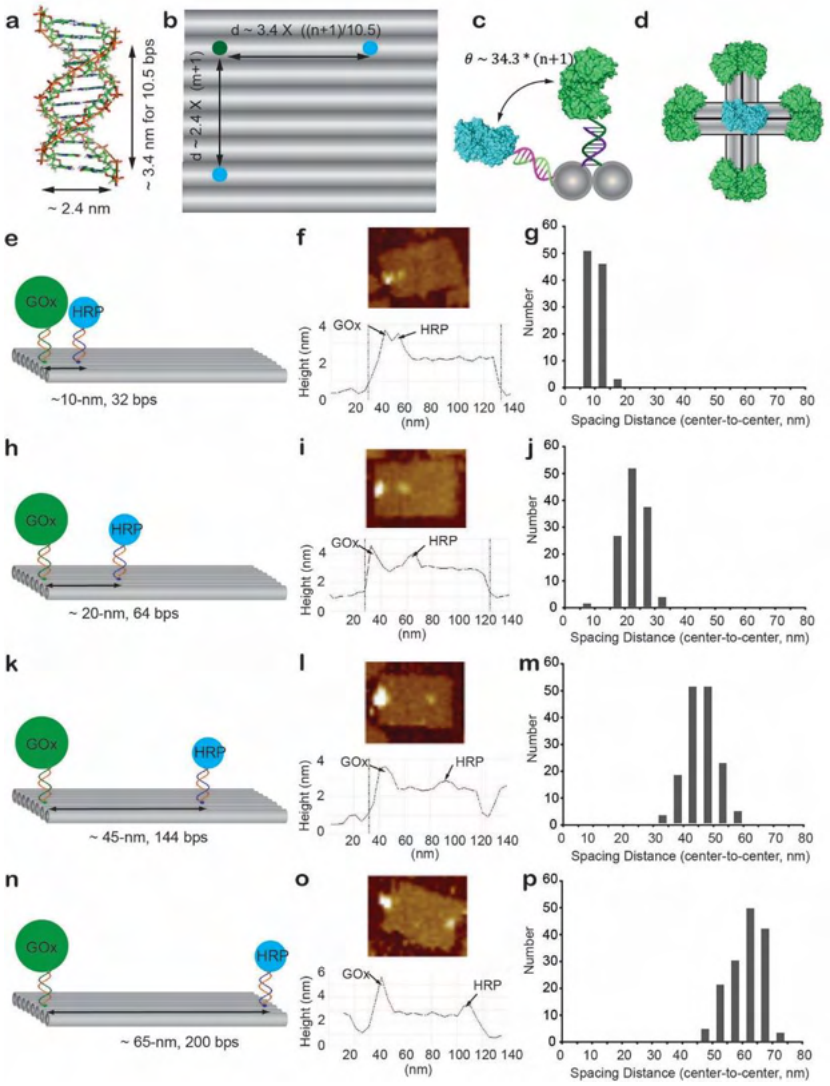


Figure 20. The assembly of enzymes on spatially-addressable DNA scaffolds. (**a**) DNA double-helix. Position of molecules on the DNA nanostructures with controlled (**b**) spacing distances, (**c**) relative angles, and (**d**) geometric arrangements. (**e**) The organization of a pair of GOx/HRP enzyme cascade on a rectangular DNA origami tile with 10-nm spacing distance, (**g**) AFM characterization of the height profile where the assembly of two enzymes results in the brighter spots due to the increased height than the surface of a DNA origami and (**h**) the statistical analysis of the observed inter-enzyme distances. The GOx/HRP pair is also assembled and characterized with the spacing distance of (**h-j**) 20-nm, (**k-m**) 45-nm and (**n-p**) 65-nm on the DNA origami tiles.

- The distance between two anchor positions along the same helix is determined by the number (p) of helical repeats between them:

  $Distance \sim 3.4\ nm \times p\ ;\ p = \frac{n+1}{10.5}$

  n is the number of spacing nucleotides.

  Note: p must be an integer number for the anchors on the same plane.
- The distance between two anchor positions perpendicular to the helix long axis can be determined by the number (m) of spacing helices between them:

$Distance \sim 2.4\ nm \times (m + 1)$

- The relative angle between two anchor positions can be controlled approximately by the rotation angle between base pairs (bps):
  $\theta \sim 34.3\ ^\circ * (n + 1)$;
  n is the number of spacing bps.
  Examples of such angles are: ~ 100° for 2 spacing bps, ~ 170° for 4 spacing bps, and ~ 270° for 7 spacing bps.

2. Protocol overview:

The general strategy of assembling enzyme complexes on DNA nanostructures is illustrated in **Figure 21a**. An enzyme is chemically conjugated to a single-stranded oligonucleotide, which serves as an anchor to hybridize with the corresponding complementary capture strand that is displayed on the surface of a DNA nanoscaffold. **Figure 21b** shows the general flow chart of the assembly, purification and characterization of the multi-enzyme complexes on the DNA nanostructures. The entire protocol includes the following key steps: (1) the preparation and purification of DNA-conjugated enzymes/cofactors; (2) the assembly of enzyme complexes onto DNA nanostructures; (3) the characterization of the assembled enzyme complexes; (4) the purification of assembled enzyme complexes; and (5) the activity evaluation at the bulk and single-molecule level. The detailed procedures will be published on *Nature Protocols* soon.

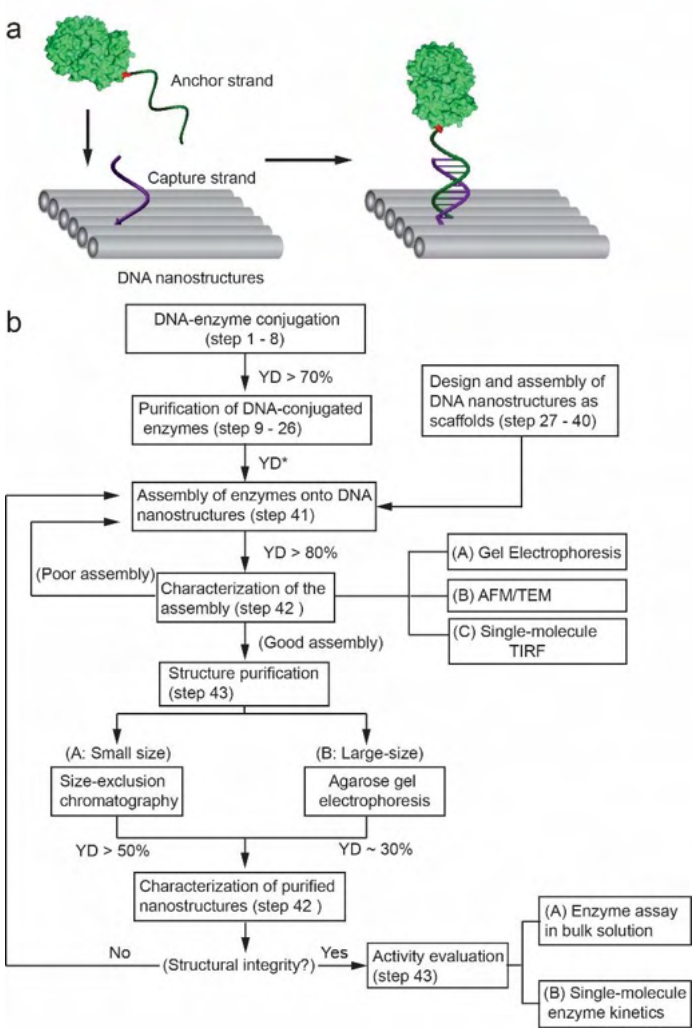


Figure 21. Overview of DNA nanostructures-scaffolded assembly of multi-enzyme complexes. (a) The assembly strategy of hybridizing a DNA-conjugated enzyme with a complementary capture strand displayed on the surface of a DNA nanostructure. **(b)** The overview protocol of the assembly, purification and characterization of multi-enzyme complexes organized by DNA nanoscaffolds. Corresponding procedure steps and estimated yields are labelled on the workflow.

Single-molecule visualization of DNA tile reconfiguration

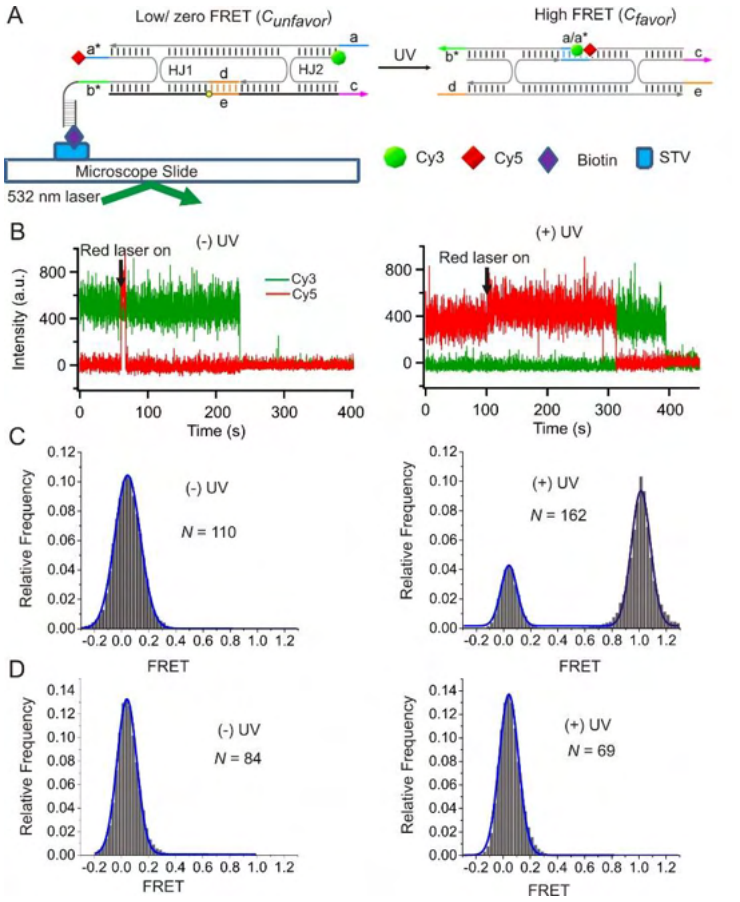


Figure 22. Single-molecule visualization of UV-triggered reconfiguration of DX tiles. (**A**) Schematic of DX tile reconfiguration triggered by UV irradiation. After photocleavage of the linker, the Holliday junctions (HJ1 and HJ2) undergo reconfiguration from unfavorable ($C_{unfavor}$) to favorable (C_{favor}) configuration. (**B**) Typical single-molecule traces before (left, (-) UV) and after (right, (+UV)) UV irradiation for 5 min. After recording the FRET movie, the red laser was turned on to confirm the presence of Cy5 fluorophore (downward arrows). (**C**) smFRET histograms for the corresponding experiments in (**B**). (**D**) A control experiment on the same DX tile lacking UV-cleavable linker.

Towards building tunable dynamic devices, we explored a DX tile design (assembled in the Yan lab, ASU) that is capable of reconfiguration driven by Holliday junction (HJ) isomerization (**Figure 22A**). A photo-cleavable site (2-nitrobenzyl group) is embedded between the two crossovers on the DX tile, opposite the central strand loop with a strategically positioned nick point. By UV exposure, cleavage of the strand creates a pair of 5-nucleotide sticky ends between the two crossovers that allow the automatic DX tile reconfiguration from Cunfavor to Cfavor, releasing the stored free energy. We hypothesized that the reconfiguration process undergoes multiple intermediate states, presenting multiple rate-limiting steps including photocleavage, cleavage site dissociation, and HJ relaxation. Routine fluorescence spectrometry is not capable of resolving the proposed mechanism at the required time scale. By contrast, FRET-based single-molecule total internal reflection fluorescence microscopy (TIRFM) confirmed the distinct conformational transition at the single-molecule level (**Figure 22**). Our preliminary results of single-molecule visualization of the DX tiles and their reconfiguration upon UV irradiation is shown in **Figure 22**. As expected, the tiles switched from a low (~0.0) to a high (~1.0) FRET state after UV irradiation as they underwent reconfiguration (**Figure 22A**). While all molecules exhibited a zero FRET state in the absence of UV, a vast majority of molecules (72%) were switched to high FRET after UV irradiation (**Figure 22C**). In contrast, control experiments with the DX tiles that lack a photocleavable linker showed only a zero FRET state both before and after UV irradiation (**Figure 22D**). These results confirmed that the tiles were properly assembled to their thermodynamically unfavorable configuration (the zero FRET state) and underwent a conformational switch to then more favorable conformation (the high FRET state) upon photocleavage of the backbone and reconfiguration of the covalently linked HJs.

Investigation of reconfiguration kinetics of DX tiles by single-molecule analysis

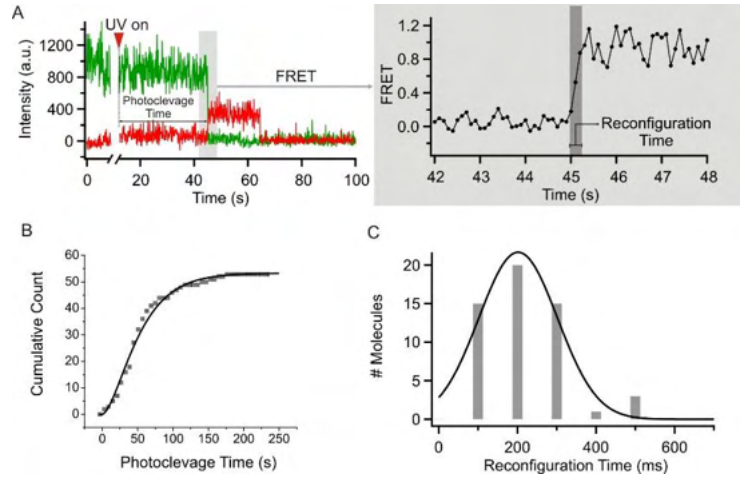


Figure 23. Photocleavage and reconfiguration kinetics of DX tiles. (**A**) Typical single-molecule trace showing Cy3 (green) and Cy5 (red) fluorescence intensities. Right panel shows the zoomed-in FRET trace of the shadowed section in the left panel. Estimation of reconfiguration time (≈ time spent to increase FRET from zero to 1.0, shadow) is highlighted at the right. (**B**) Estimation of photocleavage time. (**C**) Distribution of the reconfiguration time after photocleavage.

To monitor the tile reconfiguration kinetics at the single-molecule level, we recorded both the Cy3 and Cy5 fluorophore intensity of the tiles +/- UV irradiation. We measured the time lapse between onset of UV irradiation and tile reconfiguration, which we assigned as photocleavage time (**Figure 23A**). Interestingly, when the photocleavage time was plotted as a cumulative count, it followed a double-exponential pattern, suggesting that the tile has to undergo at least two underlying processes before reconfiguration (**Figure 23B**). The two time constants extracted from the fitting were t1 = 23.0±0.2 and t2 = 30.9±0.2 sec. While more experiments are needed to confirm these results, the shorter (t1) and longer (t2) time constants may represent the photophysical process itself, followed by the conformational change. These results also suggest the existence of at least one conformational intermediate. We further measured an actual reconfiguration time of the tiles from smFRET traces (as highlighted in Fig. Walter2A, right) and plotted as a histogram (**Figure 23C**). The mean reconfiguration time obtained by Gaussian fitting of the histogram is 202±13 ms. In the future, we anticipate that a higher time-resolution would allow more precise determination of the reconfiguration kinetics of this tile as well as that of other sequence designs.

Single-molecule fluorescence characterization of a 3-tile assembly

Along the lines of building ever-larger, dynamic DNA nanostructures, we designed DNA tiles to use them as building blocks—an alternative but robust strategy for making large structures with tunable dynamic properties. Understanding the kinetics of tiles assembly is the first key step towards this goal. Therefore, we designed and assembled (in the Yan lab, ASU) and investigated the binding of DNA tiles containing sticky ends (**Figure 24A**). Proper fluorophore labeling of the tiles allowed monitoring association/dissociation of the tiles by recording the fluorescence intensity over time (**Figure 24B**). From the dwell time analysis of the traces using a Hidden Markov Modeling (HMM) fitting algorithm, we determined the association (ON time: t_{on}) and dissociation (OFF time: t_{off}) of the tiles. Interestingly, both t_{on} and t_{off} are longer for T2. We

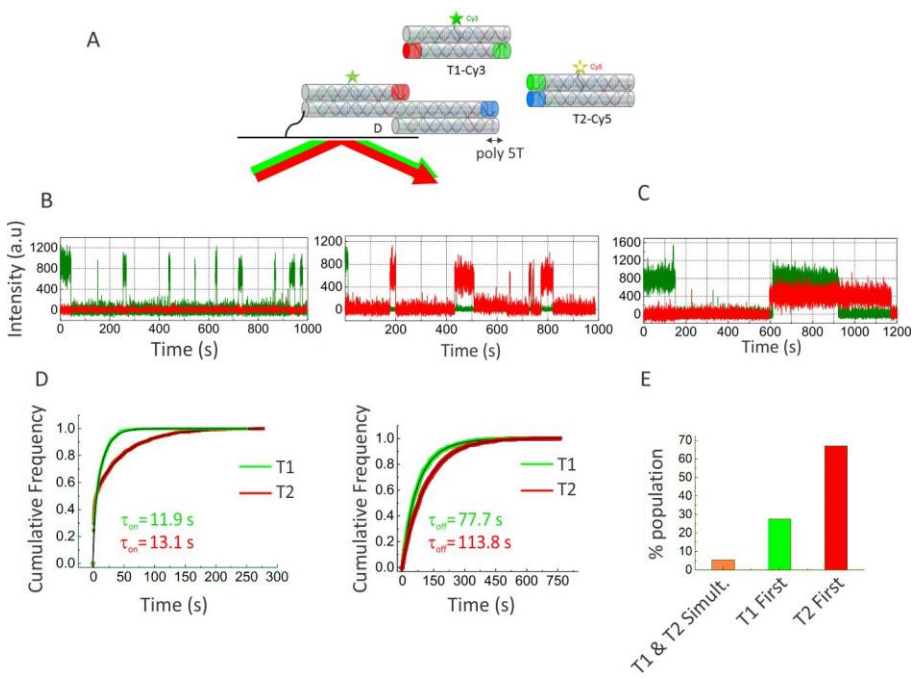


Figure 24. Single-molecule kinetic analysis of a 3-tile system. (**A**) Schematic of the tiles design. Dimer tile (D) is Cy3 labeled and is surface immobilized using a biotin-modified poly 20A DNA linker that is pre-hybridized with its complementary strand. The complementary sequences in the tiles are highlighted in matching colors. The tiles T1 and T2 are labeled with Cy3 and Cy5, respectively. (**B**) Typical intensity time traces for T1-Cy3 (left) and T2-Cy5 (right) binding to the Dimer. (**C**) Typical single-molecule traces when both T2 and T3 are present in the solution at 10 nM concentrations. (**D**) Dwell time analysis for the tiles (left panel: ON time; right panel: OFF time). (**E**) Population analysis for the preference of binding of T2 and T3 to the dimer when both of the tiles are present in the imaging solution.

attribute this observation to the different extent of electrostatic repulsion (due to the negative charge of the DNA backbone) between the tiles and the Dimer. Contrary to T2, which binds on the side of the Dimer, T1 experiences a higher electrostatic repulsion as it has a larger contact area with the Dimer. The longer t_{on} for T2 can be attributed to the stabilized microenvironment such as local crowding due to the presence of an extra poly 5T sequence (introduced to avoid tile dimerization, **Figure 24A**) at the adjacent helix. These observations lead us to a hypothesis that the extra poly 5T is responsible for the decreased accessibility of binding with T2. However, our results suggest that such local crowding stabilizes the assembly once binding has occurred. We are currently planning to test this hypothesis systematically in control experiments using DNA tiles that do not have such extra poly 5T sequences.

Interestingly, we found that T2 binds first and recruits T1 to form a stable 3-tile complex (**Figure 24C**). The preferential binding of T2 over T1 is again consistent with our hypothesis that there is a lower electrostatic repulsion for T2. Furthermore, we performed a control experiment in the presence of 200 mM NaCl in addition to the regular 12.5 mM Mg^{2+} in the imaging buffer to minimize electrostatic repulsion between the Dimer and tiles. We found that the preference of binding was not altered. However, the added NaCl dramatically decreased the population of 3-tile complex (by ~50%), possibly by destabilizing the sticky-end hybridization due to the large excess of NaCl mitigating the effect of Mg^{2+}.

Single-molecule fluorescence characterization of a 4-tile assembly

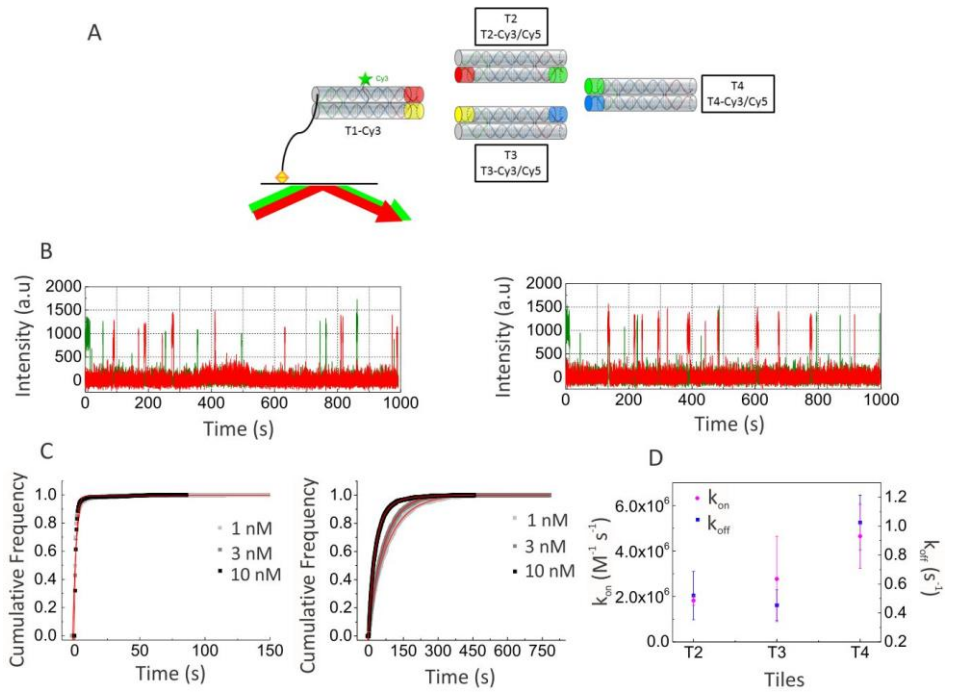


Figure 25. Single-molecule kinetic analysis of a 4-tile system. (**A**) Schematic of the tiles design. Tile T1 is Cy3 labeled and is surface immobilized using a protruding 20nt biotin-modified DNA linker (random sequence) that is pre-hybridized with its complementary strand. The complementary sequences in the tiles are highlighted in matching colors. The tiles T2, T3, and T4 are either labeled with Cy3, Cy5, or unlabeled. (**B**) Typical intensity time traces for T2-Cy3 and T3-Cy5 binding (left) and swapped labeling (Right). (**C**) Dwell time analysis of T2 binding at three different concentrations (1, 3, and 10 nM)—k_{off} (left) and k_{on} (right) panel. (**D**) Comparison of k_{on} and K_{off} among three tiles.

Using similar approaches as described above for the 3-tile system, we scaled up to a 4-tile system. In these experiments, we left one type of tile unlabeled while the other three were labeled (**Figure 25A**). The tile T1 was surface immobilized and the kinetic parameters for binding of the other three tiles to T1 were determined by using a combination of labeled and unlabeled tiles (**Figure 25B**).

First, to understand the effect of DNA-tile concentration on the assembly, we performed experiments with varying concentrations of DNA tiles. For example, **Figure 25C** shows the kinetics of association (t_{on}) and dissociation (t_{off}) of T2 at three different concentrations. While t_{on} is similar for the three concentrations tested, t_{off} is concentration dependent, suggesting that the tile attachment is a nucleation-limited process. Since 10 nM tiles showed evidence of frequent binding without compromising the signal-to-noise ratio, we used this concentration of tiles to further investigate the binding kinetics (**Figure 25D**). A comparison of kinetic parameters (k_{on} and k_{off}) among the three tiles shows that the k_{on} values are not significantly different (notice the overlap of error bars). This observation is consistent with our expectation that kinetics of association for these two tiles should be similar since the sticky-end sequences were chosen to be energetically similar (Yan lab, ASU). While k_{on} is not significantly different between the tiles, the higher k_{off} for T4 is expected. As shown in the experimental design (**Figure 25A**), T4 must wait until either T2

or T3 binds to T1, which explains its shorter t_{on} ($k_{off} = 1/t_{on}$) for T4. We also noticed that due to transient association, some of the binding events are too short to be detected by our fitting algorithm, which introduces a bias on the kinetic constants. Currently, we are performing experiments with a higher Mg^{2+} concentration (30 mM instead of the regular 12.5 mM) in the imaging buffer to prolong the association time and determine the kinetic parameters more reliably. In summary, we anticipate that our elucidation of kinetic parameters for the reconfiguration of the DX tile and the DNA-tile assembly at the single-molecule level will contribute to future improvement and optimization of dynamic DNA devices and other nucleic acid-based nanosystems.

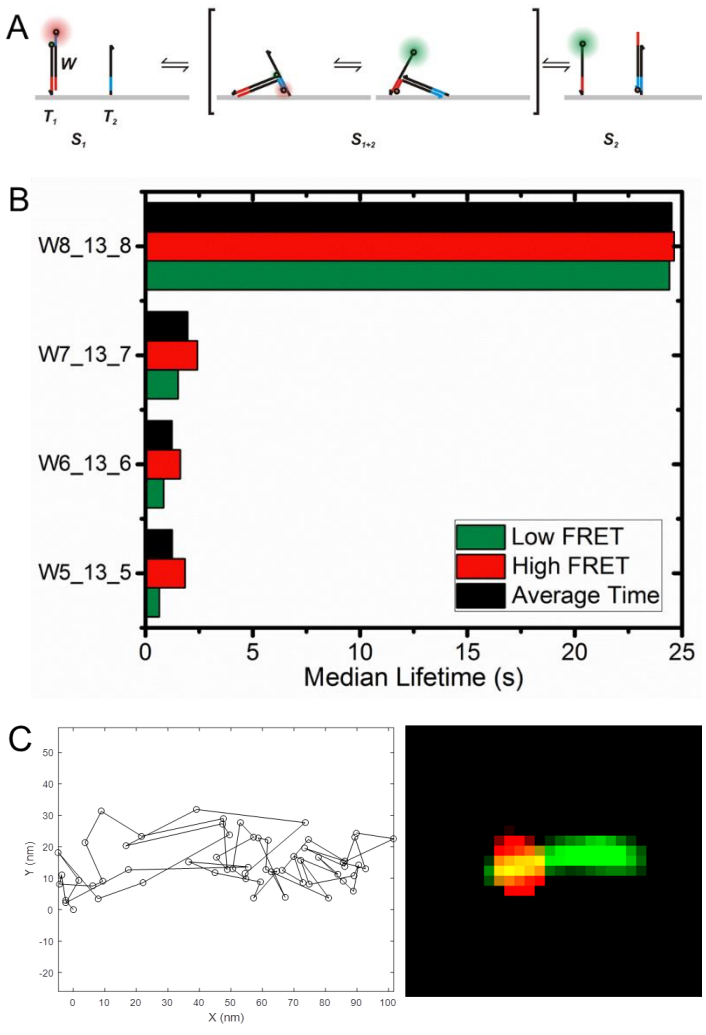


Figure 26. Single-molecule characterization of a fast DNA walker. (**A**) Schematic of walking mechanism on a two-stranded DNA track tile. (**B**) Median lifetimes in the high- and low-FRET states and averaged lifetime for walkers with varying toehold lengths (8 to 5 nucleotide). (**C**) Representative trajectory from single particle tracking analysis (left) and overlaid image of DNA walker and DNA origami (right).

A DNA walker utilizing toehold exchange

Ever since the step-by-step (hand-over-hand) movement of molecular motors such as the dynein, myosin and kinesin super families was mechanistically characterized, attempts have been made to mimic their dynamic behavior in the form of synthetic molecular walkers. Several DNA-based molecular walkers have been synthesized, motivated by the long-term goal of controlling molecular transport processes with the programmability and structural robustness of DNA nanotechnology. Previous studies have shown that DNA walkers can walk directionally along a track upon sequential addition of a DNA strand as chemical “fuel”. Despite all this progress, the DNA walkers reported so far have been constrained by slow translocation rates, which are typically on the order of a few nm/min. By comparison, natural protein motors have translocation rates of ~1μm/s under saturating ATP conditions, a 3-4 orders of magnitude faster rate. It is desirable to reduce this gap if synthetic DNA walkers are to serve as useful agents of molecular transport. Based on prior investigations, the translocation rate of many DNA walkers is believed to be limited by

slow catalytic steps or the release of cleavage products. In contrast, the displacement of one strand DNA duplex by another can be catalyzed by the nucleation of short single-strand overhangs, or "toeholds", a process that can be very rapid when the reagents are present at high concentrations. Since DNA scaffolds can be used to generate local effective reagent concentrations in excess of 100 μM in bimolecular reactions, a DNA walker using toehold exchange reactions for locomotion may be able to realize higher translocation rates than any previously reported DNA walkers.

We therefore designed 2- and 3-step DNA tile assemblies as tracks and DNA walkers with different lengths of the toehold. We used single-molecule fluorescence resonance energy transfer (smFRET) characterization to investigate the mechanism of the walking process. So far, the fastest rate constant of stepping approaches 1 s^{-1}, which is ~100-fold higher than current DNA-based transporters. We present evidence that the walking occurs by a rapid branch migration step followed by slower dissociation and rebinding of toehold sequences, in which the branch migration is rapid and may be treated as a rapid equilibrium process (**Figure 26A**). Consistent with this notion, we showed that the rate constant of stepping between adjacent step sites is dependent on the toehold length. The dwell time spent on the two observed, low-FRET and high-FRET states decreases when the toehold becomes shorter (**Figure 26B**). In the 3-step system, thus, the fastest FRET transitions are observed for the $W_{6_13_6}$ walker, with median dwell times of 1.2 s and 1.5 s in the low- and high-FRET states, respectively. To test our hypothesis further, we changed the length of the middle domain to create the fastest walker, $W_{6_13_6}$. As expected, the longer middle domain did not lengthen the stepping time. In summary, we have created a rapid, directionless single-stranded DNA walker that utilizes a toehold exchange mechanism to traverse oligonucleotide tracks repeatedly in a head-over-heels fashion.

Based on this systematic mechanistic study, we employed this DNA walker on a long, polymerized DNA origami track to test its potential application as a long-range molecular transporter (**Figure 26C**). With the help of single particle tracking, we observed an obvious movement of the W6_13_6 walker on the one-row-track DNA origami over a typical distance of about 100 nm. We view this as a very promising result for the further use of simple, efficient toehold exchange walkers to transport molecules on DNA nanoassemblies.

Designer proteoliposomes scaffolded by DNA nanostructures

1. DNA barrel scaffolded membrane protein Vdac1 assembly after chemically conjugated with oligonucleotide:

Proteoliposome reconstitution is a standard method to stabilize purified transmembrane proteins in membranes for structural and functional assays. After a membrane protein is reconstituted into a liposome, its activity is affected by many factors, including liposome size and geometry and membrane protein co-reconstitution efficiency, a random process that is adversely affected by several factors, including protein aggregation. Previously, we present an approach to solving this problem by using spatial addressable DNA nanostructures to control liposome size and geometry. Here we establish a method to co-reconstitute multiple membrane proteins in a single size specific liposome. The temporary attachment of designated "signal" oligonucleotides to individual membrane proteins permits them to assemble on complementary "address" sites on the DNA nanostructure template, thus facilitating the insertion of the membrane protein complexes into liposome with defined stoichiometry and composition. As a proof of principle, proteoliposomes

containing six membrane proteins were reconstituted using a voltage-gated anion channel (VDAC1) as a model system (**Figure 27a**).
A single-cysteine mutant version of Vdac1 was expressed as described previously, and two

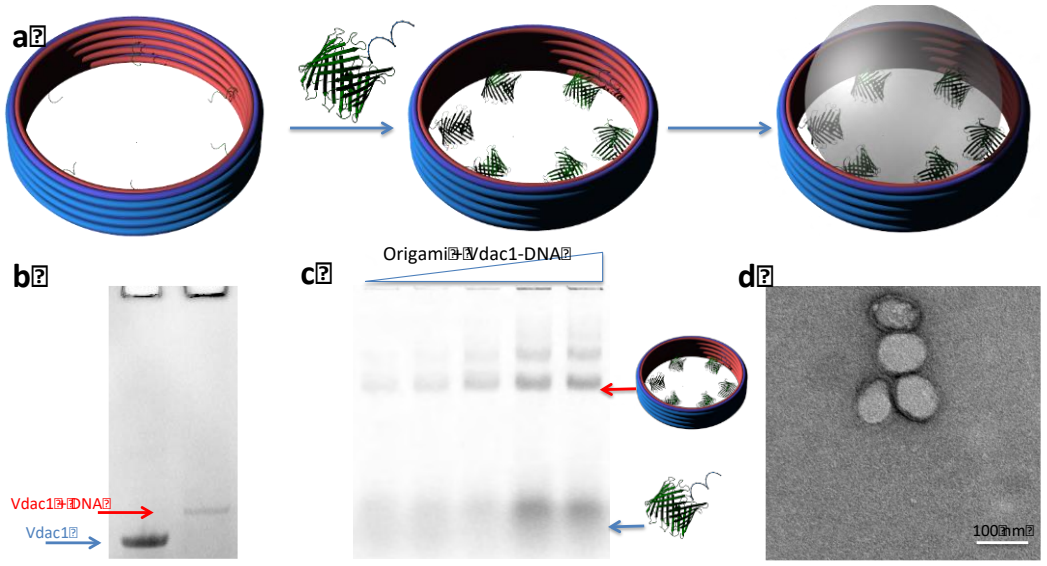


Figure 27. DNA Origami scaffolded liposome with controllable number of membrane protein Vdac1. **a**) Schematic of liposome reconstitution using DNA Origami with 6 Vdac1 protein. **b**) SDS-PAGE of Sulfo-SMCC crosslinking Vdac1(one cysteine mutant) and short DNA oligo. **c**) SDS-AGE of DNA Origami assembled Vdac1-DNA conjugates with increasing Vdac1-DNA amount from left to right side. **d**) Negative staining TEM of liposome reconstituted inside DNA Origami pre-assembled with 6 Vdac1-DNA conjugates.

different cross-linkers, sulfo-SMCC and DBCO-PEG4-maleimide, were used to conjugate Vdac1 to amine- or azide-modified DNA, respectively. SDS-PAGE (**Figure 27b**) showed that both linkers conjugate the oligonucleotide to Vdac1 with >95% yield. After conjugation, DNA-Vdac1 was utilized to assemble with DNA barrel through oligonucleotide hybridization, confirmed by agarose gel electrophoresis fluorescence co-localization (**Figure 27c**). TEM analysis showed successful formation of uniformly sized liposomes inside the DNA barrel after recosntitution (**Figure 27d**).

2. <u>DNA barrel scaffolded Vdac1 directed liposome reconstitution:</u>

We tested reconstitution of barrel-templated liposomes with Vdac1 hexamers both in the presence and absence of the 36 interior lipid handle modifications. DNA barrel was used to assemble with Vdac1-DNA (labeled with AF647), in the presence and absence of extra lipid anti-handles, then was combined with a mixture of lipid (0.8% labeled with Rhodamine B), surfactant, and lipid-decorated DNA barrel, and reconstituted into barrel-templated proteoliposomes by removal of detergent *via* dialysis. To estimate the liposome reconstitution efficiency for both methods, two-colour TIRF microscopy was used to quantify the fluorescence co-localization of an AF647-labelled Vdac1 and a Rhodamine B-labelled lipid within biotin-modified DNA barrels that were anchored to a streptavidin-modified glass surface for TIRF visualization (**Figure 28**). Without the help of lipid molecule decoration, the liposome reconstitution yield is around 29 +/- 6%, while with lipid decoration, the liposome reconstitution yield increases to 64 +/- 6% (**Figure 28**). Thus, while Vdac1 alone is sufficient to seed some liposome growth, the presence of additional

hydrophobic molecules on the inner cavity of the barrel considerably improves the yield of the reconstitution process.

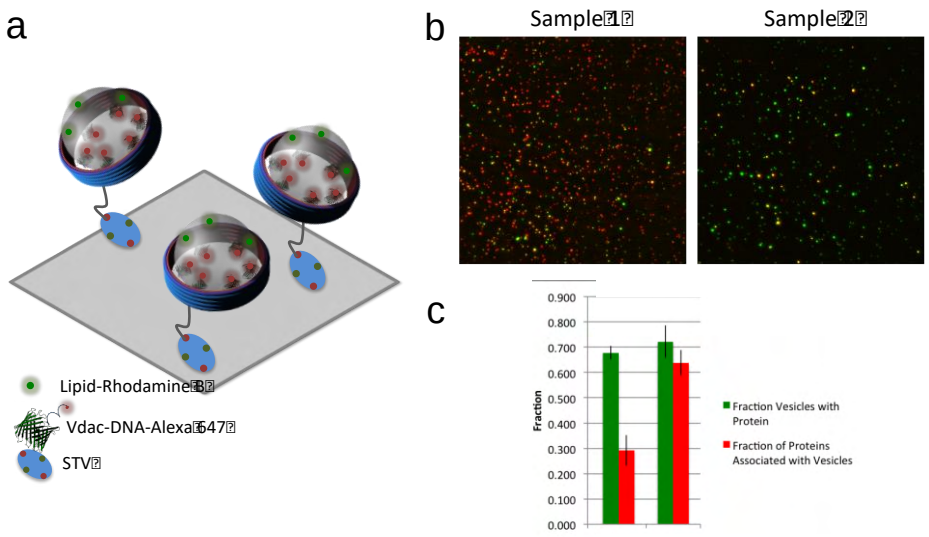


Figure 28. DNA barrel scaffolded Vdac1 proteoliposome with 2 reconstitution methods. **a**) Schematic of fluorescence co-localization of barrel scaffolded proteoliposome using TIRF; **b**) Representative field of view of barrel scaffolded proteoliposome under TIRF microscope; **c**) Fluorescence co-localization analysis for both methods.

3. <u>DNA barrel scaffolded proteoliposome with precisely controllable membrane protein stoichiometry:</u>

To measure the number of copies of Vdac1 associated with each nanostructure-templated vesicle at the single-particle level, we carried out stepwise photobleaching measurements on barrel-templated Vdac1 proteoliposomes by TIRFM. We first prepared two types of Vdac1-DNA conjugate, each bearing a different oligonucleotide sequence and fluorophore (Vdac1-a-AF555 and Vdac1-b-AF647). Next, DNA barrels were reconstituted with a 27-fold excess (relative to handle sites) of each of these two Vdac1-oligonucleotide conjugates, and immobilized the complexes on a glass coverslip via biotin modifications on the DNA barrel (**Figure 29a**). Fluorescence intensity traces (λ_{ex}: 640 nm or 561 nm) for each particle showed a discrete number of photobleaching steps (**Figure 29c**) which were counted to determine the number of copies of Alexa 647/555-labeled Vdac1 associated with each barrel/liposome particle. We observed that, for the barrel designed to carry 3 copies of Vdac1-a-AF555 and 3 copies of Vdac1-b-AF647, more than 76% of particles had 3 or fewer photobleaching steps for each fluorophore, despite the 27-fold excess of Vdac1. The mean number of photobleaching steps per particle was 3.3 +/- 1.0 (*s.d.*) and 1.7 +/- 0.9 for Vdac1-a-AF555 and Vdac1-b-AF647, respectively. In the case of Vdac-1-a-AF555, over 65% of particles had exactly 3 photobleaching steps, indicating that the number of Vdac1 inside one proteoliposome particle is quite precisely controlled by the number of handle sites per barrel template. The fact that Vdac1-b-AF647 exhibited fewer than 3 photobleaching steps on average is likely due to bleaching of AF647 during synthesis and purification of the Vdac1-DNA conjugates, since a control experiment with the fluorescently labeled DNA oligonucleotides (without Vdac1 conjugation) revealed that ~79% of barrels exhibited exactly 3 photobleaching steps for AF555, and ~70% for AF647 (**Figure 29d**). The small fraction of

particles with more than 3 photobleaching steps (24% for Vdac1-a-AF555, 4% for Vdac1-b-AF47) may have resulted from a moderate amount of untemplated aggregation of Vdac1 subunits, or from two or more unresolved DNA barrels that were interpreted as a single barrel in the TIRFM measurement. Through the above quality control experiments, we have demonstrated that the DNA-origami barrel serves as a template to control the size of liposome (<100 nm in diameter) and the number of externally oriented Vdac1 per vesicle (6 particles).

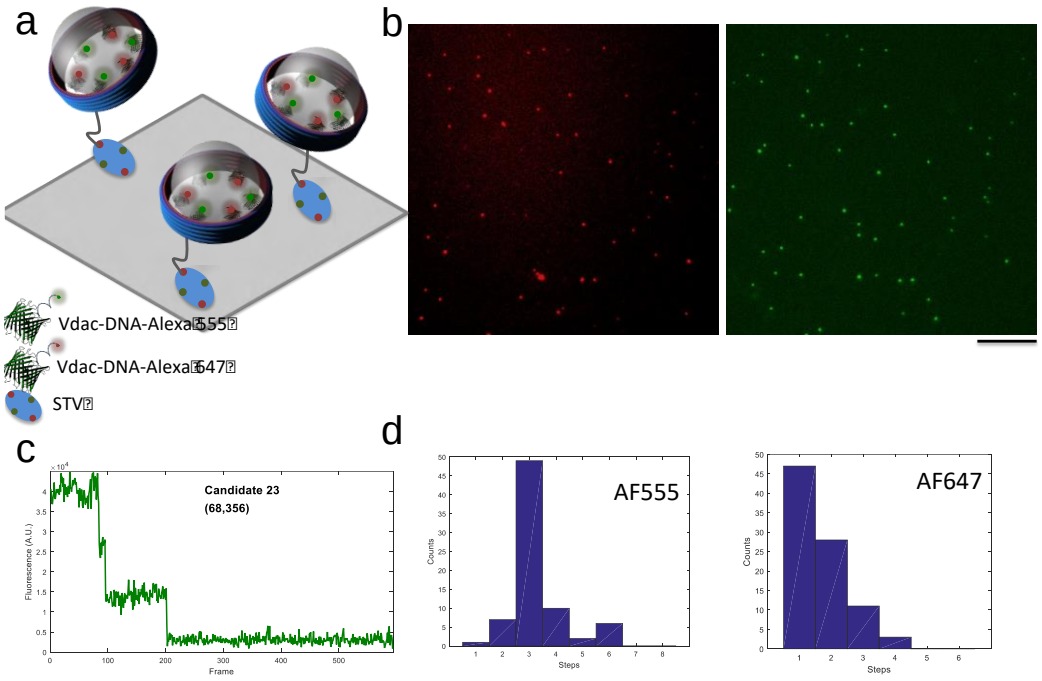


Figure 29. DNA barrel scaffolded Vdac1 proteoliposome with 6 proteins. **a**) Schematic of fluorescence co-localization of barrel scaffolded proteoliposome using TIRF; **b**) Representative field of view of barrel scaffolded proteoliposome under TIRF microscope; **c**) Fluorophore photobleaching trajectories with three photobleaching steps. Photobleaching steps were quantitatively analysed by fitting the trajectories by HMM in QUB program. (**d**) Photobleaching statistics for DNA barrel scaffolded Vdac1 proteoliposome.

4. Future directions:

Work in now in progress to (a) trigger membrane protein release after reconstitution to study membrane protein self-assembly process through FRET; b) DNA barrel scaffolded CD4/CCR5 proteoliposome for HIV-1 infection process study.

Structure-based modeling of large-scale DX-based assemblies

The preceding work was limited to isolated duplexes and a single DX tile, whereas full control over excitonic energy transfer in 2D and 3D requires higher-ordered programmed DNA assemblies to scaffold strongly coupled chromophores. The utilization of higher-ordered programmed DNA assemblies to control excitonic energy transfer requires intimate knowledge of the atomic-level details of these structures. These applications require the Angstrom-level positioning accuracy at the scale of individual DNA bases. Structural information gained from all-atom simulations can

be applied to improving FE models for DNA nanoassemblies which will lead to an increase in knowledge regarding chromophore placement on DNA-dye assemblies.

To aid in prediction of equilibrium 3D structures of DNA nano-assemblies as used in software such as caDNAno and CanDo, an all-atom model of several DNA nano-particles were built and molecular dynamics (MD) simulations were performed. All-atom models of a DNA tetrahedron and a DNA octahedron were built to compare equilibrium structures from MD to the Finite Element framework present in CanDo, as shown in **Figure 30**.

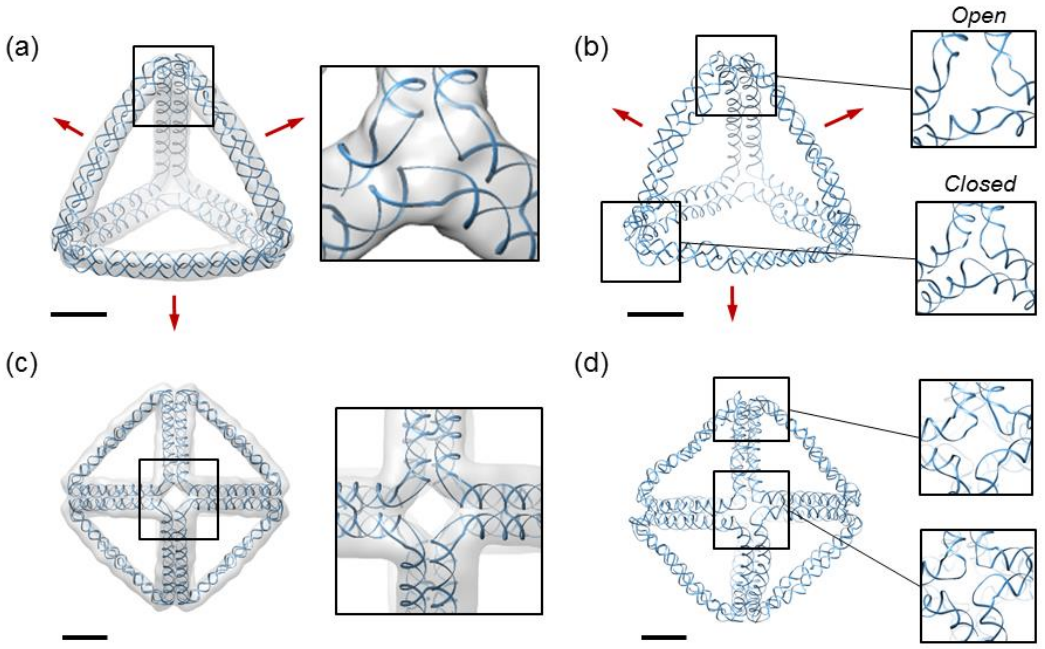


Figure 30. Equilibrium structures of the tetrahedral and octahedral nanoparticles generated by the FE framework and the MD simulations. The FE equilibrium structures, colored in blue, were fit into the reconstructed cryo-EM map using the software UCSF Chimera. The FE structure (**a**) and the MD structure (**b**) of the tetrahedral nanoparticle both show an outward bowing of each edge, which is represented by the red arrows. Vertices with the absence and presence of interactions between unpaired bases are termed as "open vertices" and "closed vertices", respectively. The FE structure (**c**) and the MD structure (**d**) of the octahedral nanoparticle are rendered in the same way. All scale bars are 5nm.

As the FE model of the tetrahedron and octahedron DNA nanoparticles cannot reproduce atomic level structural details, and cannot reproduce details seen in cryo-EM reconstructed maps, such as the outward bowing of the edges in a tetrahedron, or the right-handed twisting of the vertices in an octahedron, the all-atom MD model is important in determining how structure determines function in these systems. For example, in the DNA tetrahedron, as seen in **Figure 31**, molecular dynamics simulations can provide insight into the global effect of the bowing of the edges and twisting at the vertices of DNA polyhedral. The 100 ns MD simulation of the tetrahedron confirms an outward bowing angle of near 14 degrees, and a similar MD simulations of the octahedron confirms a right-handed vertex twisting angle of near 10 degrees, similar to the estimated 15 degree right-handed vertex twisting angle seen in the reconstructed cryo-EM map. These atomic level details from MD simulations can also potentially inform the improvement of the coarse-grained FE model in CanDo.

To do this, several MD simulations of unconstrained DNA nano-particles were performed, including those of a duplex bulge, a 3-arm vertex, and a 4-arm vertex as seen in **Figure 32**.

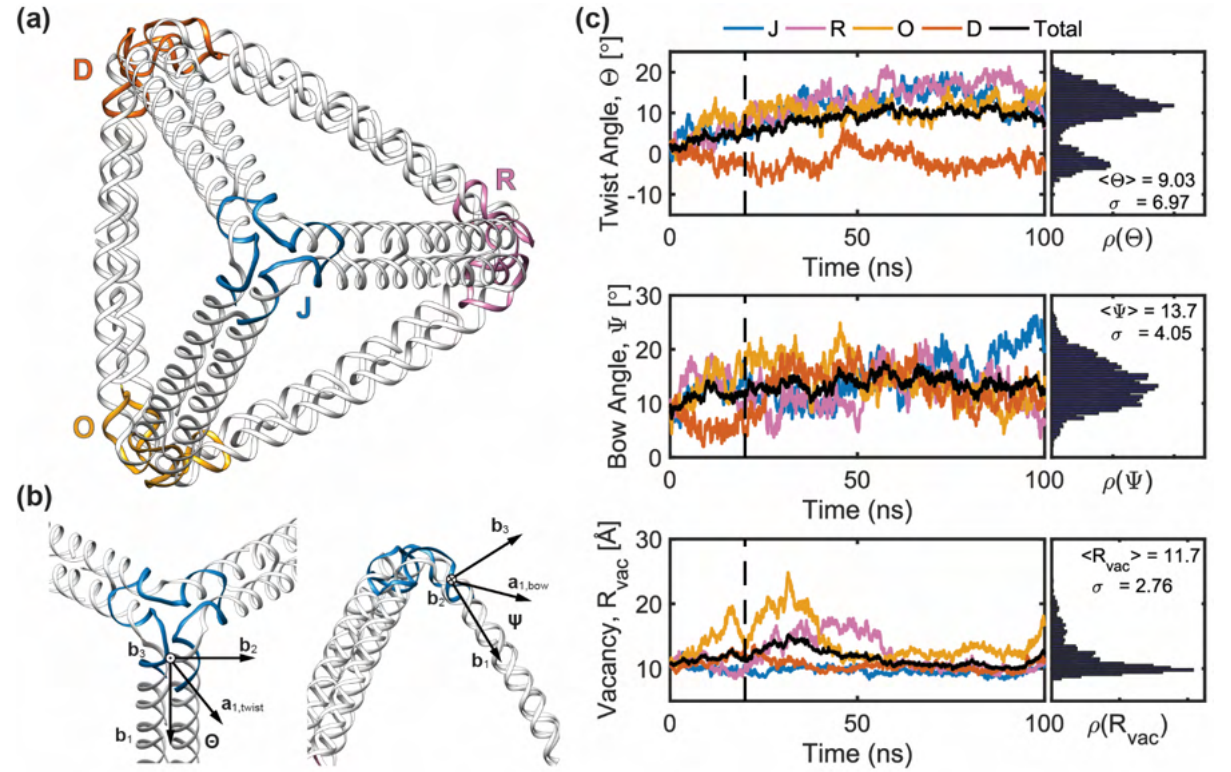


Figure 31. Geometric analysis of a tetrahedron nanoparticle. (**a**) Location of each vertex on the tetrahedron according to its pdb chain identifier. (**b**) Definition of twisting and bowing angles at each vertex in relation to the orthonormal basis. (**c**) Twisting angles in degrees, bowing angles in degrees, and radial vacancies in Ångstroms at each distinct vertex (J, R, O, D) during a 100 ns MD simulation. The distribution of the (**c**) twisting angle, bowing angle, and radial vacancy are shown separately in the right panel, along with the mean and standard deviation.

During the course of these all-atom MD simulations of unconstrained DNA nanoparticles, several features are observed. First, the relative rigidity of the 3-arm and 4-arm vertex as compared to the duplex bulge is noticeable in the analysis of the duplex bending angle, and the duplex torsional twisting angle. Second, both the 3-arm and 4-arm vertex show a distinct out-of-plane bending angle away from the bulge regions of the vertex. These geometric features seen by analyzing the MD trajectories of unconstrained DNA nanoparticles can inform future FE models when building DNA nanoparticles, especially constrained polyhedral, so that the building blocks such as bulges and vertices are used in their lowest energy conformations, avoiding unnecessary DNA nanoparticle strain and assisting stability.

Future work on this project includes the derivation of FE model parameters directly from MD simulations of unconstrained DNA nanoparticles, to improve the predictive capability of coarse-grained DNA modeling. Also, potential energy surfaces of the DNA origami “building blocks”, such as bulges and vertices using different sequences / lengths of ssDNA at the bulge region will be scanned to determine the optimal design of the vertex regions. In particular, we envision that the use of all-atom MD models of DNA nanoparticles will be used in conjunction with coarse-

grained FE models to improve upon and explain structural features. The present work is under preparation for submission.

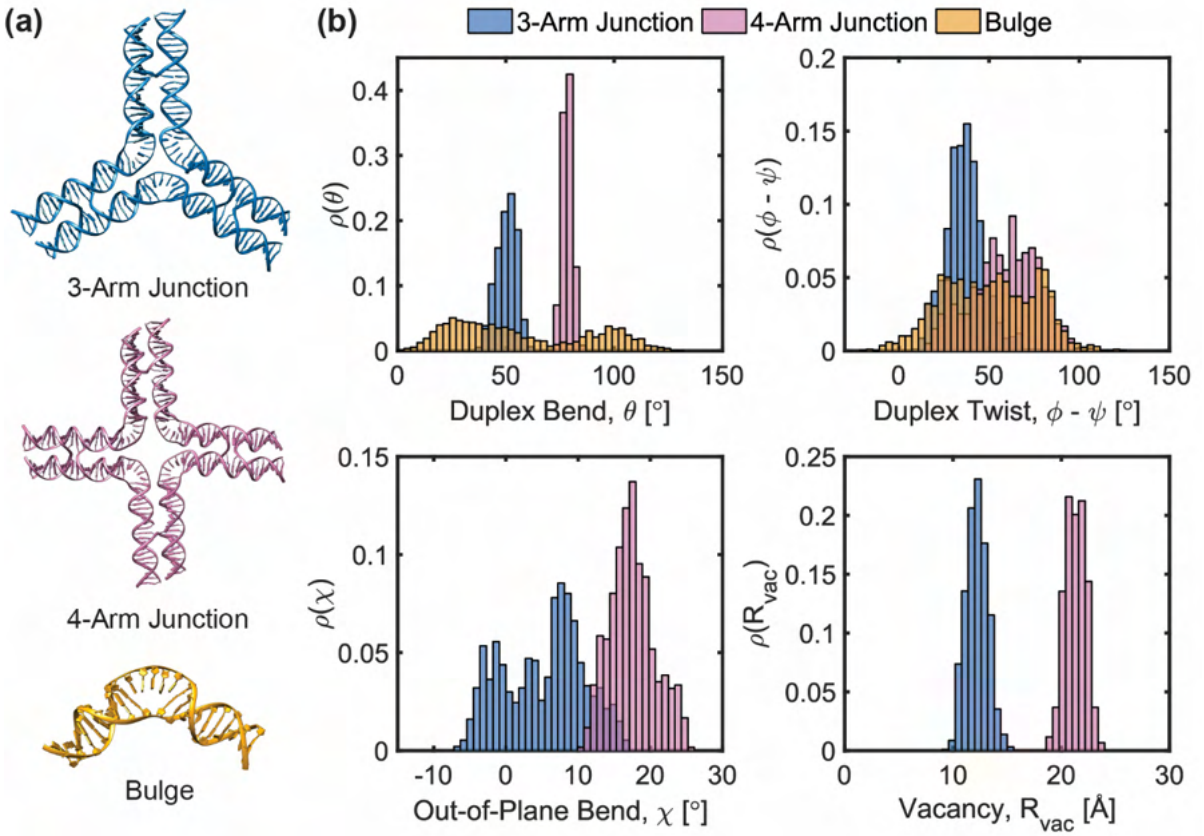


Figure 32. Geometric analysis of an unconstrained DNA 3-arm junction, 4-arm junction, and duplex bulge. (**a**) All-atom models of the 3-arm junction (top), 4-arm junction (middle), and duplex bulge (bottom). (**b**) Histogram of various geometric values calculated from MD trajectories. Duplex bending angles in degrees (top left), duplex torsional twisting angles in degrees (top right), out-of-plane bending angles in degrees (bottom left), and radial vacancies in Ångstroms (bottom right) during 100 ns (3-arm junction, 4-arm junction) or 200 ns (duplex bulge) MD simulations.

Photosynthetic Pathway

Electrode interface of photosynthetic reaction center proteins in macroporous materials

1. Background and design concept:

The laboratories of Seo, Woodbury and Lin are exploring ways to effectively interface the light-induced redox potentials generated by photosynthetic reaction centers from purple bacteria with novel nano and meso-structured electrode materials. Generating a facile interface between redox-active biochemical complexes and electronic materials is challenging for a number of reasons. The attachment of biological complexes to surfaces is often nonspecific and unstable, with the current exchange limited due to a poor connection to the electrode, and such systems are frequently difficult to assemble, control and monitor. Historically, the majority of work interfacing redox proteins with conductive materials has focused on pyrolitic graphite and alkanethiol/alkylthiol-modified gold. Limitations arising from monolayer deposition, denaturation of the protein(s) of interest and the lack of optical transparency of the substrate (which precludes both spectroscopic analysis and limits optoelectronic applications) prompted the development of transparent (semi)conductive oxides (TCOs). TCOs were a significant step forward allowing spectroelectrochemistry of immobilized redox proteins and, from an applied perspective, electrochromic and optoelectronic applications of the biohybrid system. Novel nano- and mesostructured porous TCOs are becoming increasingly available. The 3D architecture of porous TCO materials greatly increases the effective surface area (hundreds of fold) and provides protective cavities for association with macromolecules such as proteins or DNA. This serves to both concentrate the redox protein of interest (and thus increase the optical density for spectroscopic investigations and applications) and to promote functional stability by providing protective encapsulation. Although proteins have been incorporated into other porous transparent conductive oxides, such as WO_3TiO_2 and SnO_2, the excellent transparency and optical properties of porous indium tin oxide (ITO) have made it the favored TCO. Incorporation of high concentrations of the small redox protein cytochrome *c* into ITO has been reported (on the order of hundreds of pmol/cm^2 rather than the tens of pmol/cm^2 reported for monolayer studies), with the redox properties intact. Porous antimony-doped tin oxide (ATO) is now emerging as a preferred alternative to porous ITO due to its lower cost and very high optical transparency and conductivity. The incorporation of functionally intact DNA nanostructures into ATO pores has been demonstrated. More recently the redox proteins cytochrome *c* and azurin were successfully interfaced with the porous ATO surfaces and shown to retain their redox activity. In Kwan *et al.* (2011), the authors reported extremely high loading of cytochrome *c* into porous ATO (over 1000 pmol/cm^2 for cytochrome *c*, an order of magnitude greater than that reported previously for cytochrome *c* in porous in ITO) and used spectroelectrochemistry techniques to demonstrate that cytochrome *c* had retained its redox activity upon adsorption on ATO pore surfaces.

Photosynthetic reaction centers (RCs) perform light-driven reduction of a terminal acceptor molecule that is then available for subsequent chemistry. This makes them an ideal photonic element for interfacing with electrodes and controlling local redox chemistry in time and space via optical and electronic signals. Because the redox reactions are light driven, as opposed to requiring a substrate, the control of turnover rate is directly and instantaneously connected to light level at a particular time and place. The reaction centers from the bacterium *Rhodobacter (Rb.) sphaeroides* are well suited for this purpose. The structure of these RCs is known, their electron transfer reactions have been well characterized and they are very stable. Furthermore, *Rb. sphaeroides*

RCs are amenable to protein engineering and easily expressed in large quantities when grown in the dark chemoautotrophically.

The conversion of absorbed solar energy into chemical redox energy is initiated in *Rb. sphaeroides* RCs by excitation of the primary electron donor, P, which is an excitonically coupled pair of bacteriochlorophylls. A series of electron transfer reactions takes place down a redox gradient from the excited state of P, through a monomeric bacteriochlorophyll (B_A) and a bacteriopheophytin (H_A) resulting in reduction of a molecule of ubiquinone, 'Q_A' with near unity quantum yield on a time scale of about 200 ps. The electron then passes from Q_A to the second ubiquinone, Q_B, forming the semiquinone anion of this cofactor. A second photoinduced electron transfer to Q_B completes the two electron reduction forming a dihydroquinone which leaves the binding pocket and diffuses through the membrane to the cytochrome b/c1 complex where it drives proton pumping and ultimately ATP production. The oxidized primary donor (P^+) is then re-reduced via electron transfer from a soluble cytochrome *c*; cytochrome *c* docks with the RC and an electron transfer reaction takes place with a rate constant on the order of 10 microseconds.

There have been a number of previous reports of bacterial RCs interfaced with electrodes for use in integrated optical electronic devices, photovoltaics and biosensors. In the field of molecular electronics, for example, RCs isolated from *Rb. sphaeroides* have been inserted into nanogaps between gold electrodes to act as a switch, which can be controlled by the voltage applied across the electrodes. In addition, the sensitivity of RCs to certain herbicides, such as triazines (which block electron transfer by displacement of the secondary quinone) has been used to develop herbicide sensors based on inhibition of the measured photocurrent.

A major issue in many of the previous studies has been the connection between the reaction center and the electrode. Lebedev *et al.* (2006) demonstrated that cytochrome *c* could be employed as a redox wire, reducing the electron tunneling distance to P and thus improving the connection between P and the electrode surface. Photocurrents generated by HIS-tagged RCs interfaced with an NTA-terminated SAM on a gold electrode were improved by an order of magnitude when cytochrome *c* was incorporated into the system. Another key limitation is monolayer deposition of RCs on the electrode surface. Typically, a monolayer of reaction centers can only produce nanoamps of current per cm^2 (in terms of a reduced product formed by the RC, 1 nanoamp/cm^2 = ~10 femtomoles reduced product per cm^2). Lu *et al*. (2005) and Lukashev *et al*. (2008) achieved photocurrents on the $\mu A/cm^2$ scale (picomoles/cm^2 of reduced product) by interfacing RCs with a porous titanium oxide electrode (doped with tungsten trioxide in the case of Lu *et al*. 2005) to achieve multiple layers of RCs. However, the later studies involved the RC donating an electron to the doped tin oxide electrode (rather than receiving an electron as described below).

We have devised a system in which *Rb. sphaeroides* RCs are electrochemically coupled to transparent, porous ATO electrode films via cytochrome *c* to produce a biohybrid platform in which 2-electron reduction and release of a soluble quinone can be controlled both optically and electronically. This work has resulted in a publication submitted to ACS Applied Materials & Interfaces, and initiated a new area of research which is summarized in section 4 of this report.

2. Incorporation of photosynthetic reaction center protein into ATO films:

2.1. Preparation of ATO film on FTO glass

A previously established sol-gel route for producing highly mesoporous ATO coatings was adapted for the fabrication of macroporous ATO coatings. Briefly, 1.00 g of $SnCl_4 \cdot 5H_2O$ (Alfa Aesar, 98%) and 1.00 g of deionized water were added to a solution of 0.05 g $SbCl_3$ (Alfa Aesar, ≥99.9%) in 6.50 g of *n*-BuOH (J.T. Baker, 99.9%) in an Ultra-Turrax tube drive with a rotor-stator element. A separate mixture containing 12.4 wt.% carbon black, acetylene (Alfa Aesar, 50% compressed ≥99.9%, surface area = 75 m^2/g, bulk density of 0.095 – 0.103 g/cm^3), 25.8 wt.% polyethylene glycol bisphenol A, epichlorohydrin copolymer (PEG) (Sigma-Aldrich, 15-20 kDa) and 61.8 wt.% ±-epichlorohydrin (Fluka, ≥99.9%) was homogeneously blended in a separate bottle. From this mixture, 6.15 g was transferred to the metal salt solution in the tube drive. The tube drive was run on speed 3 for 10 seconds, followed by vigorous shaking. Subsequently, the mixing was carried out with a setting of six for one minute followed by vigorous shaking, and finally the tube drive run on the maximum setting for one minute to produce the reaction mixture.

For producing coatings, fluorine-doped tin oxide (FTO, Hartford Glass, sheet resistance 8 Ω/sq.) was washed with soapy water and sonicated in an acetone bath. Two opposing edges were masked by applying double-thick tape (Scotch Transparent Tape) to cover 1 mm of the FTO face, and a single layer of tape was applied to a third edge. About 0.25 mL of the reaction mixture was pipetted on the single tape layer, and was drawn smoothly and quickly across the entire slide length with a Pasteur pipette. After drying for one hour under ambient conditions, the tubes were placed in a tube furnace that was flushed with oxygen for one hour before increasing the temperature to 500 °C. The initially black coatings were calcined at 500 °C for four hours under an oxygen flow to yield translucent, pale blue coatings.

2.2. Incorporation of bacterial reaction centers into ATO films

RCs were isolated from anaerobically grown cultures of *Rb. sphaeroides* 2.4.1 and purified. Harvested cells were re-suspended in 20mM Tris.HCl (pH 8.0) and broken by three passes through a French Press (15,000 kpsi) in the presence of a small amount of DNase and $MgCl_2$. Unbroken material was removed by low speed centrifugation (2700 g, 10min) and membranes were pelleted with high speed ultracentrifugation (250,000 g, 90min). Membranes were adjusted to OD 50 and solubilized in 20mM Tris.HCl (pH 8.0) containing 0.25% LDAO, in the presence of 150 mM NaCl to preferentially solubilize the RC from the chromatophores, for 60 min at 20ºC. The solubilized RCs were centrifuged at 250,000 g for 60 min to pellet unsolubilized material and the supernatant was then dialyzed overnight to remove NaCl. Solubilized RCs were purified by ammonium sulphate precipitation followed by anion exchange and size exclusion chromatography.

ATO slides were pre-soaked in cytochrome *c* to facilitate oriented binding of the RC at the electron-accepting P end. In the intracytoplasmic membrane of *Rb. sphaeroides* cytochrome *c* docks at the P end of the reaction center and donates an electron to the specialized pair of Bchls to re-reduce the reaction center. It can thus act both as an oriented docking component and as a redox wire, connecting the RC to the ATO electrode as illustrated in **Figure 34A**. Cytochrome *c* has previously been shown to retain its conformation and redox properties within ATO pores, and has been used to orient RCs on a SAM-coated gold electrode. Lebedev and coworkers reported a significant improvement in photocurrent when equine cytochrome *c* was included in their system, which was independent of the initial redox state of the cytochrome *c*. Cytochrome *c* (equine heart, Sigma) was adsorbed to ATO by incubating ATO slides in a solution of 150 μM cytochrome *c* in nanopure water (18.2 $M\Omega\ cm^{-1}$) for 30 minutes as described in Kwan *et al*. (2011). Excess solution

was withdrawn by pipette and ATO surfaces were then washed repeatedly with nanopure water and left to air dry under cover. A solution of *Rb. sphaeroides* RCs was then applied to the ATO films using a pipette and the slides were again left to air dry under cover. Steady-state absorption spectra were collected before and after RC application.

2.3. Photocurrent measurements and cyclic voltammetry

Photoelectrochemical measurements and cyclic voltammetry (CV) were performed on a CHI 650D electrochemical station electrochemistry workstation (CHI Instrument Co., USA), with a three-electrode system containing a Ag/AgCl (CHI 111) reference electrode and a platinum wire counter electrode. For each experiment, an ATO slide was set as the working electrode. The electrochemical cell was covered with black tape with a 1 cm^2 window to allow illumination and the working electrode was inserted such that the ATO side of the slide faced the cell window. ATO slides were illuminated using a Ti:Sapphire laser (5W Millennia pumped Tsunami, Spectra Physics). The light intensity immediately outside the cell was recorded using a FieldMate Laser Power Meter (Coherent) and adjusted using a neutral density filter. The electrolyte buffer was 0.1 M Tris buffer (+/- ubiquinone-0). A potential equal to the dark open circuit potential was applied to the ATO slide during each photocurrent measurement and the effect of illumination was recorded.

3. Building an optically controlled biohybrid system:

Cytochrome *c* is the natural redox partner of the RC from *Rb. sphaeroides* and exposing the ATO/cytochrome *c* electrode system (See Kwan *et al.*) to RCs results in the specific and stable assembly of RCs onto the surface. The highly porous architecture of the transparent ATO films allows multiple layers of cytochrome *c*/RCs, analogous to the invaginated membranes of natural systems. The incorporation of cytochrome *c* and *Rb. sphaeroides* RCs was confirmed with UV-vis spectroscopy (**Figure 33**). The positions and relative intensities of the Q_y absorption maxima demonstrated that the RCs retain their conformation and function when assembled in the ATO pores (**Figure 33**). Based on the extinction coefficients for cytochrome *c* (106 mM^{-1} cm^{-1} at 410 nm) and the RC (288 mM^{-1} cm^{-1} at 802 nm), the spectroscopic surface coverage was calculated to be 2.3 and 0.45 nmol/cm^2, respectively, equating to a ratio of approximately 5 molecules of cytochrome *c* for every one RC. This high incorporation of cytochrome *c* is on the same order of magnitude as that reported for cytochrome *c* in porous ATO by Kwan *et al.* (2011) and an order of magnitude higher than that reported for porous ITO.

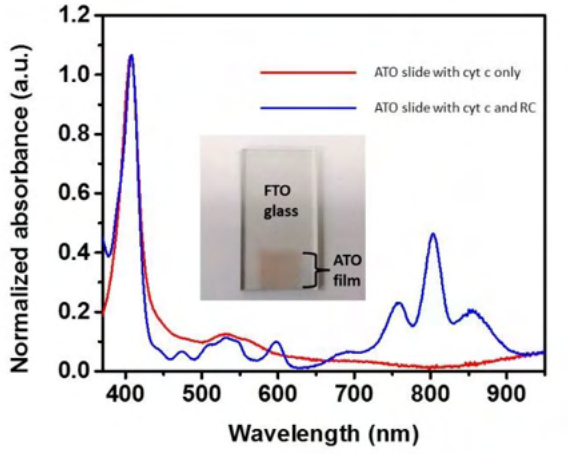


Figure 33. Steady-state absorption spectra for an ATO slide following soaking in cytochrome *c* (red) and a cytochrome *c*-soaked ATO slide following application of RC solution (blue). Data are normalized at the 407 nm Soret peak for cytochrome *c*. Slides have been left to air dry after each step. Inset shows a photo of an ATO film on FTO glass, following soaking in 150 µM cytochrome *c* and washing to remove the unbound molecules. Film dimension is 1 cm^2.

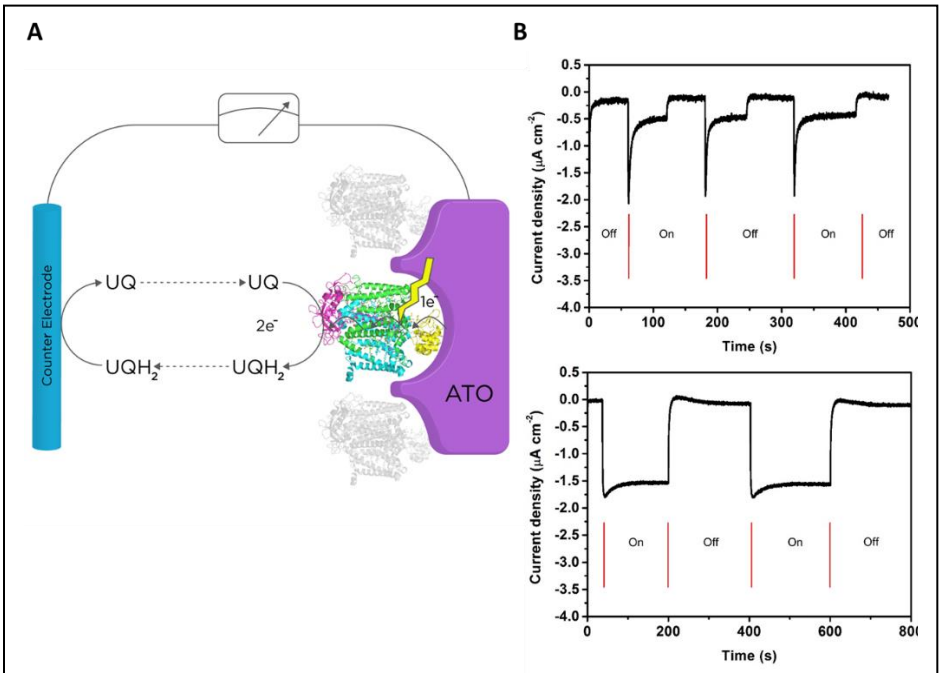


Figure 34. A Photosynthetic RCs interfaced with an ATO electrode via a cytochrome *c* bridge. The cytochrome *c* serves to both orientate the RC such that the electron-accepting P end is facing the electrode and as redox wire to facilitate electron transfer from the electrode to P. In this system, the RC performs one electron photochemistry but generates a two electron carrier (the reduced ubiquinone, which leaves the quinone binding pocket and must be replaced by another ubiquinone molecule from the electrolyte solution). **B** Photocurrent detected from ATO films containing cytochrome *c* and RCs, with either 100 μM Ubiquinone-10 (top) or 100 μM Ubiquinone-0 (bottom) in the 0.1 M Tris electrolyte buffer. For the bottom panel, RCs have also been pre-soaked overnight in a 10-fold Molar excess of Ubiquinone-0. Slides were illuminated with a continuous wave Ti:Sapphire laser set to 800 nm, with a intensity of 5 mW/cm^2.

To characterize the function of the ATO-cyt *c*-RC system, photocurrents were measured using the electrochemical set-up illustrated in **Figure 34A**. Various sample conditions were tested to understand the origin of the photocurrent generated from the ATO-cyt *c*-RC system and the results are summarized in **Figure 34B**. Only slides containing both cytochrome *c* and RCs showed detectable photocurrent (**Figure 34B**). ATO slides which had been pre-soaked in cytochrome *c* but not treated with RCs showed no detectable photocurrent and ATO slides which were not first pre-soaked in cytochrome *c* but treated with RCs also showed no detectable photocurrent. Slides not pretreated with cytochrome *c* also did not appreciably bind RCs; the RC absorbance after incubation was tenfold lower than slides that were first pre-soaked in cytochrome *c*. The ATO-cyt *c*-RC complexes proved to be extremely stable, with slides still capable of producing photocurrents weeks after initial measurements when stored under darkness at 4 °C.

When fully assembled ATO-cyt *c*-RC slides were illuminated continuously at 800nm and 5 mW/cm^2 (light intensities were intentionally kept well below saturation, see below), an initial photocurrent density of 2 μA/cm^2 was observed (**Figure 34B**). However, the initial high photocurrent rapidly decreased to a sustained level of ~ 0.5 μA/cm^2. The RCs naturally contain ubiquinone-10, which contains a long, hydrophobic isoprenoid tail, and is thus nearly insoluble in aqueous solution. Upon including 100 μM of ubiquinone-0 (no isoprenoid tail and thus considerably more soluble than ubiquinone-10) in the electrolyte buffer, a sustained photocurrent between 1.5 and 2 μA/cm^2 was obtained (**Figure 34B**). Apparently, after the initial reduction of bound quinone, the current was limited by the exchange of the reduced quinone with oxidized quinone in the solvent and subsequent migration to the counter electrode. The presence of the more soluble quinone alleviated this limitation, at least in part.

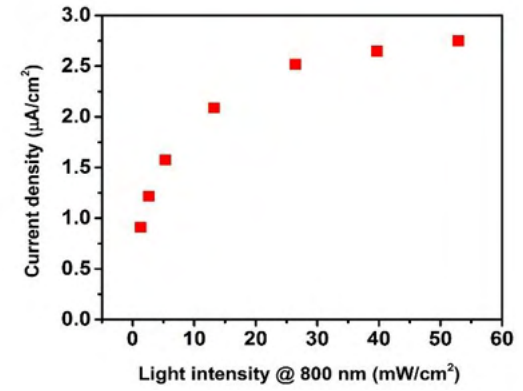


Figure 35. Photocurrent density detected from ATO films containing cytochrome *c* and RCs as a function of light intensity. The electrolyte buffer contains 0.1 M Tris and 100 μM Ubiquinone-0. Slides were illuminated with a continuous wave Ti:Sapphire laser set to 800 nm. The illumination intensities (at 800 nm) ranged from 1.3 mW/cm^2 to 53 mW/cm^2.

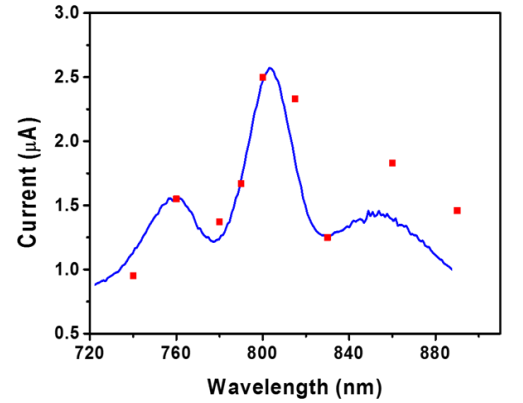


Figure 36. Action spectrum (photocurrent as a function of excitation wavelength) collected for ATO slides containing cytochrome c and *Rb. sphaeroides* RCs (red), overlain with the steady state absorption spectrum for ATO slides containing cytochrome c and *Rb. sphaeroides* RCs (blue). The light source used to excite the RCs within the ATO was a tunable continuous wave Ti:Sapphire laser (with an illumination intensity of 1.3 mW/cm2). The excitation wavelength was tuned from 740 to 890 nm, spanning the Qy transition region of the RCs absorption spectrum, with the laser illumination power kept constant.

The light intensity dependence of the system was determined by varying the power of the continuous, 800 nm Ti:Sapphire laser illumination incrementally from 1.3 to 53 mW/cm^2), and recording the resulting photocurrent (**Figure 35**). The photocurrent is half saturated at about 5 mW/cm^2 and largely saturated by 50 mW/cm^2 giving a maximum photocurrent of nearly 3 μA/cm^2. The light intensities used for the studies reported below (<3 mW/cm^2) were within the linear region of the curve.

To demonstrate that the observed current is derived from electron transfer in the RCs, an action spectrum of the photocurrent was collected (photocurrent as a function of illumination wavelength). A tunable continuous-wave Ti:Sapphire laser was used as the light source and the excitation wavelength was tuned from 740 to 890 nm with the output power kept constant at 1.3 mW/cm^2 to ensure a linear response of photocurrent to the functional absorbance cross section at each wavelength. The photocurrent as a function of excitation wavelength (the action spectrum) is shown in **Figure 36** (red symbols). The spectral profile closely resembles that of the RC absorption spectrum (**Figure 36** blue curve), confirming that the RC is indeed responsible for the observed photocurrent. Note that both the initial and sustained photocurrent (as observed in **Figure 34B**) yield the same action spectrum.

Electrochemical measurements were used to directly characterize the potential dependence of the photocurrent. The potential of the working electrode (the ATO slide containing the cytochrome *c* and RC) was varied from the dark open circuit potential (+0.0315) by -0.15 V to +0.15 V relative to the Ag/AgCl reference (equivalent to +0.08V to + 0.38V relative to SHE) using a potentiostat, and the photocurrent under constant illumination (2.6 mW/cm^2 at 800 nm) was measured. The photocurrent dropped as the working potential was

increased, with a half maximum potential of 0.22V (SHE) (**Figure 37**), in good agreement with the expected midpoint potential for the cytochrome c^{3+} /cytochrome c^{2+} reduction of horse heart cytochrome *c* (0.25 V, as well as with measurements of cytochrome *c*-soaked on ATO electrodes in the absence of RCs. In addition, fitting of the data in **Figure 37** to a Nernst relationship resulted in n=1, indicating that a one-electron transport is taking place at the electrode interface. These results are consistent with reduction of the cytochrome *c* by the ATO electrode as a required intermediate step in the transfer of an electron from the electrode to the photo-oxidized donor of the RC as suggested in the diagram of **Figure 34A**.

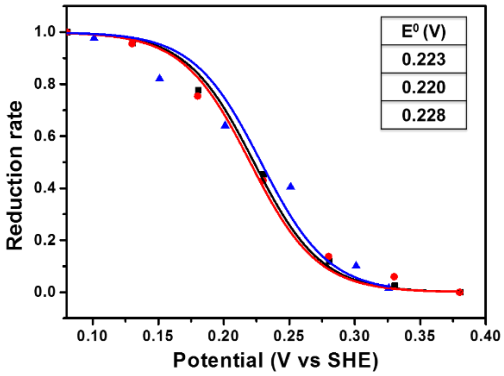


Figure 37. Nernst curves generated for three separate ATO slides, each containing cytochrome c and *Rb. sphaeroides* RCs. The potential dependence of the photocurrent was measured by varying the potential applied at the anode relative to the Ag/AgCl reference electrode and recording the photocurrent. Nernst curves generated by fitting this data are all n=1, indicating a one electron system, have midpoint potentials, E0 (inset), close to the value 0.25 V expected for cytochrome c in solution. This supports the concept that cytochrome c accepts the electron from ATO and then provides it to the RC.

The dependence of the sustained photocurrent in **Figure 34B** on addition of ubiquinone-0 implies that the current can be limited by the amount of electron carrier in solution and suggests that ubiquinone-0 is accepting two electrons (via two sequential photoexcitations) from the second quinone binding site (the Q_B site). However, in principle, the electrons could be leaving the RC by a different pathway. One can test this by adding an inhibitor that acts specifically at the Q_B site such as terbutryn. Terbutryn is a triazide herbicide well known for its inhibition of photosynthesis in plants and bacteria. It readily displaces the quinone molecule in the Q_B pocket and has previously been employed to inhibit electron transfer to the quinone at this site in many studies of the electron transfer kinetics in *Rb. sphaeroides* RCs. **Figure 38** shows the photocurrent for an ATO slide containing cytochrome *c* and RCs in the absence and presence of 100 µM terbutryn. In the

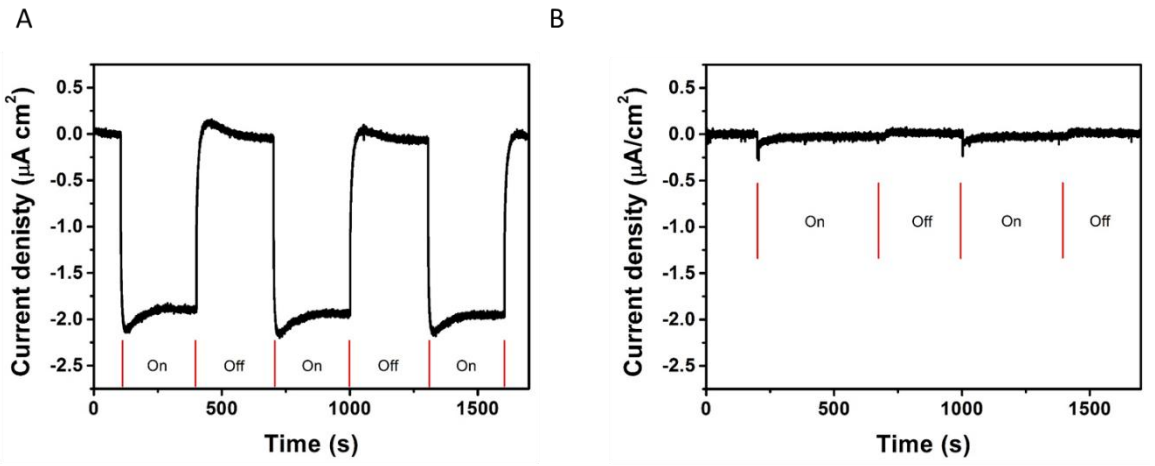


Figure 38. Photocurrent detected for an ATO film pre-soaked in cytochrome c and treated with RCs in **A** 0.1 M Tris containing 100 µM Ubiquinone-0 and **B** 0.1 M Tris containing 100 µM Ubiquinone-0 and 100 µM Terbutryn, which blocks electron transport to the QB quinone.

presence of terbutryn, the photocurrent drops to almost zero (**Figure 38B**). The little remaining photocurrent can be attributed to RCs in which terbutryn has not displaced quinone in the Q_B site or where terbutryn has been exchanged for ubiquinone-0 present in the electrolyte buffer. This marked attenuation of photocurrent confirms that electron transfer to the quinone in the Q_B pocket. Presumably, absorbance of two successive photons by the reaction center results in formation of the dihydroquinone in the Q_B pocket, which is then released and exchanged with an oxidized quinone in solution. While it is formally possible that the quinone in the Q_B site only transfers protons and electrons to an exterior quinone, and is not replaced, this is not the mode of action seen in Nature, and it would be difficult to imagine the structure of a complex that would allow such a transfer. The role of quinone in the Q_B site also points out an important functional aspect of the system. One-electron photochemistry is used to generate two-electron reduced compounds. Most bond formation in organic chemistry takes place using two electron redox reactions.

A sustained photocurrent of 11 $\mu A/cm^2$ was obtained by applying a 0.1 V potential, SHE, to the working electrode along with a saturating light intensity and a saturating concentration of ubiquinone-0 in the buffer. Note that at 0.1 V SHE the cytochrome *c* is completely reduced (**Figure 37**). This photocurrent translates into 0.13 doubly reduced quinone molecules released per reaction center per second (0.26 electrons per RC per second reach the counter electrode). This is much slower than the intrinsic rate that the reaction center is able to reduce quinones and oxidize cytochrome. What is limiting the photocurrent? The rate of photon absorbance by the RC is about 4 photons per second for every $1mW/cm^2$ of 800 nm light. This means that at a light intensity that gives rise to only half the photocurrent at saturation (~1.25 $\mu A/cm^2$ at 5mW, **Figure 35**), the reaction center is absorbing about 20 photons per second, which equates to approximately 10 photons per second once polarization of the laser beam is taken into account, but the photocurrent reaching the counter electrode is only about 0.03 electrons per RC per second. Thus there are more than 300 times as many photons absorbed as electrons contributing to the photocurrent, yet the RC is not in light saturation. This means the limitation must occur after electron transfer in the RC. The vast majority of the electrons transferred by the RC are not arriving at the counter electrode. In terms of quinones reduced, each RC at that light level is presumably reducing 5 quinones per second (~20 nanomoles quinone per cm^2 per second), yet only 0.015 quinones per reaction center per second (~0.06 nanomoles quinone per cm^2 per second) reach the counter electrode. The most likely explanation is that >99% of the doubly reduced ubiquinone molecules released by the RC, which have a potential near 0V, SHE, are simply donating their electrons back to the working electrode (which for the experiments described has a potential $\geq$ 0.1V, SHE). Thus the amount of reduced quinone produced in the vicinity of the working electrode, and thus potentially available for further chemistry, is likely in the many nanomole per cm^2 per second range.

We conclude from this work that layering cytochrome *c* on porous ATO electrodes allows the assembly of RCs onto the surface and provides a specific binding configuration and electrical connection between the electrode and the RC initial electron donor. The high effective surface area of the transparent macroporous electrode greatly increases the number of RCs that can absorb light and generate reduced quinones. The resulting photocurrent (~ 2 $\mu A/cm^2$ with no applied potential and >10 $\mu A/cm^2$ when a small negative potential is applied) represents a convenient measure that is proportional to the amount of redox activity taking place. Perhaps most importantly from a systems perspective, each component can be individually and quantitatively controlled and monitored. The level of cytochrome *c* reduction can be controlled by potential. The rate of reaction center photoexcitation can be controlled by light intensity. The rate of exchange between

the final electron acceptor in the reaction center and the soluble quinones which carry electrons to the counter electrode is sensitive to both the concentration of free quinone and to specific inhibitors of the secondary quinone pocket. This represents a prototype for a type of integrated biohybrid system in which 2-electron redox chemistry can be controlled in time and space both optically and electronically.

This work has now been submitted as '*Photocurrent generation by photosynthetic purple bacterial reaction centers interfaced with a porous antimony-doped tin oxide (ATO) electrode*' to Applied Materials and Interfaces.

4. New progress:

Since the work detailed above we have now expanded this project in a number of areas:

4.1 incorporating the natural photosynthetic antenna system along with the reaction centers to increase the cross section available for light absorption and reaction centers from a species of photosynthetic purple bacteria that have a permanently bound cytochrome c subunit;
4.2 interfacing Photosystem I from the cyanobacterium *Thermosynechococcus elongatus* to ultimately generate a higher redox power in our biohybrid photoelectrochemical cell;
4.3 interfacing reaction centers with a new type of electrode material, a functionalized graphene that can be applied to a variety of surfaces including flexible, transparent materials.

4.1. Incorporating the antenna system to increase cross section of light absorption

Our previous work was focused on using isolated reaction centers to build a biohybrid system for generating photocurrent which can be controlled optically or electronically. In nature, all photosynthetic organisms contain a light-gathering antenna system, which serves to increase the cross section available for light absorption. We have now moved on to include this antenna system into our biohybrid photoelectrochemical cell. Two approaches are being investigated so far. In one approach we have used a natural antenna system, the light-harvesting system 1 (LH1), as the additional light-absorbing component. As illustrated in the inset of **Figure 38**, LH1 is the core antenna surround RC protein which can be isolated as a co-protein complex, LH1-RC. The LH1-RC systems were isolated from a range of purple bacteria in the lab of our collaborator Prof. Richard Cogdell at the University of Glasgow. In the second approach, we are incorporating biomimetic artificial light-harvesting antenna into the RC system using either dye molecules or DNA-templated dye conjugates with the dyes appropriately placed

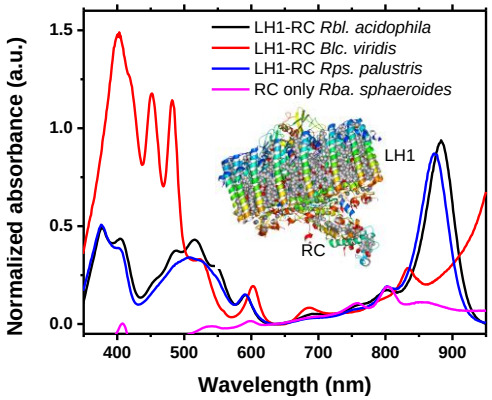


Figure 39. Absorption spectra for cytochrome *c*-soaked ATO slides following pipette application of either RCs from *Rba. sphaeroides* (pink), LH1-RC from *Rbl. acidophila* (black), LH1-RC from *Blc. viridis* (red) or LH1-RC from *Rps. palustris* (blue). The curves are normalized at 650 nm. Slides have been left to air dry after each step.

to transfer energy to the reaction center. Efficient excitation energy transfer from dye molecules and DNA-templated dye conjugates to RC proteins has been demonstrated successfully in our previous work. It has also been shown previously that DNA can be incorporated into the pores of ATO films.

In addition, we are interfacing the LH1-RC systems from species of photosynthetic purple bacteria, such as *Blc. viridis* and *Alc. vinosum*, which have a tetraheme cytochrome *c* molecule permanently bound to the 'P' end of the reaction center. These samples were also isolated in Prof. Richard Cogdell's lab at the University of Glasgow. These samples may improve binding efficiency of the RCs and further enhance the electronic communication between the electrode and the reaction center.

Thus far, we have successfully interfaced the LH1-RC complexes (the natural antenna system, Light-harvesting complex 1, together with the reaction center to which it is intimately connected) from *Rhodopseudomonas (Rps.) palustris*, *Rhodoblastus (Rbl.) acidophila* and *Blastochloris (Blc.) viridis* with ATO via horse heart cytcochrome *c*. The performance of these ATO-cyt *c*-LH1-RC systems have then been compared to concomitantly prepared ATO-cyt *c*-RC systems. The absorption spectra for cytochrome *c*-soaked ATO slides following pipette application of those LH1-RC complexes and the isolated RCs are shown in **Figure 39**, where strong absorption increases in the wavelengths below 550 nm and above 850 nm are evident. The electrochemical cell was as described above for the initial ATO-cyt *c*-RC work. All RC and LH1-RC samples were applied to the ATO film at an OD of 25 at the peak corresponding to the Qy maxima of the monomeric Bchls. Electrolyte buffers contained 0.1 M Tris and 250 µM ubiquinone-0 and a potential bias of 0.1 V (SHE) was applied to all slides to ensure all ATO-bound cytochrome *c* was reduced. A broadband white light source was used to test the photocurrent generated in response to different light intensities. As expected, light intensity experiments show that when illuminated with white light the ATO-cyt *c*-LH1-RC systems perform better at lower intensities, and reach light saturation more quickly, than the ATO-cyt *c*- RC systems without antenna (**Figure 40**). ATO-cyt *c*-LH1-RC receives the excitation energy captured by the light-gathering antenna in addition to those directly received by the RC and are therefore work more efficiently and get saturated at a lower light level than those systems containing RC alone.

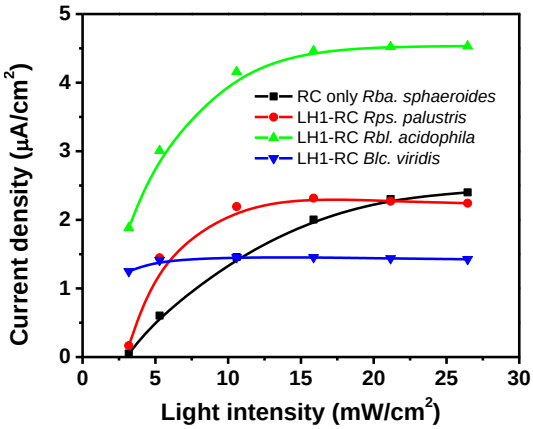


Figure 40. Photocurrent detected for an ATO films pre-soaked in cytochrome *c* and treated with either RCs (black) or LH1-RCs (red, blue and green), 0.1 M Tris containing 250 µM Ubiquinone-0. The light source used to excite the RCs/LH1-RCs within the ATO was a white light, with the power density increased incrementally.

We have also successfully interfaced *Blc. viridis* and *Rbl. acidophila* LH1-RCs directly with the ATO. The RC within these complexes have a permanently bound tetraheme cytochrome *c* (THC) subunit. The four heme groups are arranged in a linear sequence of alternating high and low potential hemes that is conserved in all THCs, however, the potentials of the individual hemes do

vary across species. It has been shown for *Blc. viridis* that when the two high-potential hemes are reduced prior to light excitation, one directly reduces the photo-oxidized P^+ (and is itself subsequently reduced by the other). Within the intracytocplasmic membrane the photo-oxidized THC is reduced by either cytochrome c2 or cytochrome c8, or in some cases, a high-potential iron-sulfur protein (HiPIP), depending on the bacterial species. It is therefore reasonable to compare the performance of such complexes on both ATO only and ATO-cyt *c* slides.

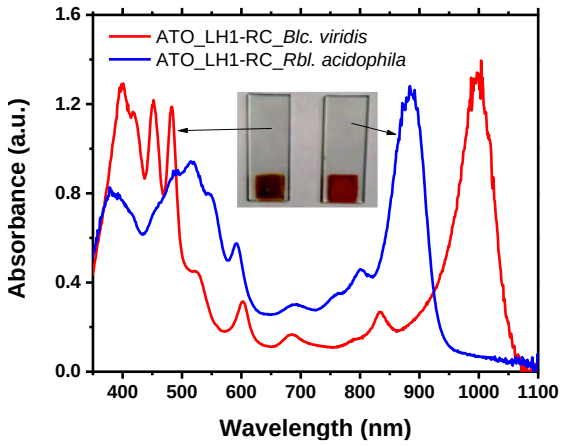


Figure 41. Steady-state absorption spectra (left) and photo images (right) of ATO slides to which either *Blc. viridis* or *Rbl. acidophila* LH1-RCs have been applied with a pipette. The absorption of each sample were recorded at different spots. Slides have been left to air dry after each step. Film dimensions are 1 cm^2.

As shown in **Figure 41**, LH1-RC samples containing a permanently attached cytochrome *c* subunit can be directly bound to the ATO surface and produce photocurrent (**Figure 42**). However for *Rbl. Acidophila*, ATO-LH1-RC system the performance is markedly poorer than that observed when ATO has been pre-soaked in cytochrome *c*. This will be presented in the results shown in **Figure 44**.

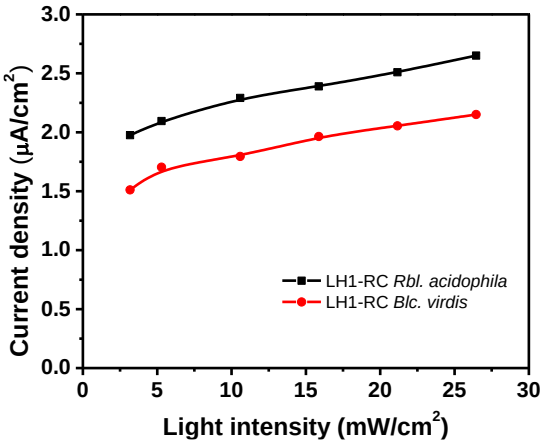


Figure 42. Photocurrent detected for ATO films treated with LH1-RCs from *Rbl. acidophila* (black) and *Blc. viridis* (red), both in 0.1 M Tris containing 250 μM Ubiquinone-0. A while light source was used to illuminate the samples.

The differential stability of ATO films pre-soaked in cytochrome *c* and treated with various proteins was surveyed by taking recurrent measurements over a period of 50 days, with slides stored under darkness at 4°C in between measurements (**Figure 43**). The results indicate that these systems are relatively stable, still capable of producing photocurrents 50 days after initial measurements. It is also interesting to notice that, for all except the ATO-cyt *c*-LH1-RC from *Rbl. Acidophila*, the highest photocurrent was achieved 21 days after samples were prepared, suggesting that these systems actually take time to settle down. It is possible that these systems require certain time to achieve optimal connectivity or that the measurements themselves (specifically the repeated applications of a negative potential) assist in optimization. We now are in the process of testing the optimized incubation time period for these systems.

The same comparative stability was also carried out for the LH1-RCs from *Blc. viridis* and *Rbl. acidophila*, both contain the THC subunit, with and without pre-soaking the ATO in cytochrome *c* (**Figure 44**). For the LH1-RCs from *Rbl. Acidophila*, the markedly higher photocurrent initially

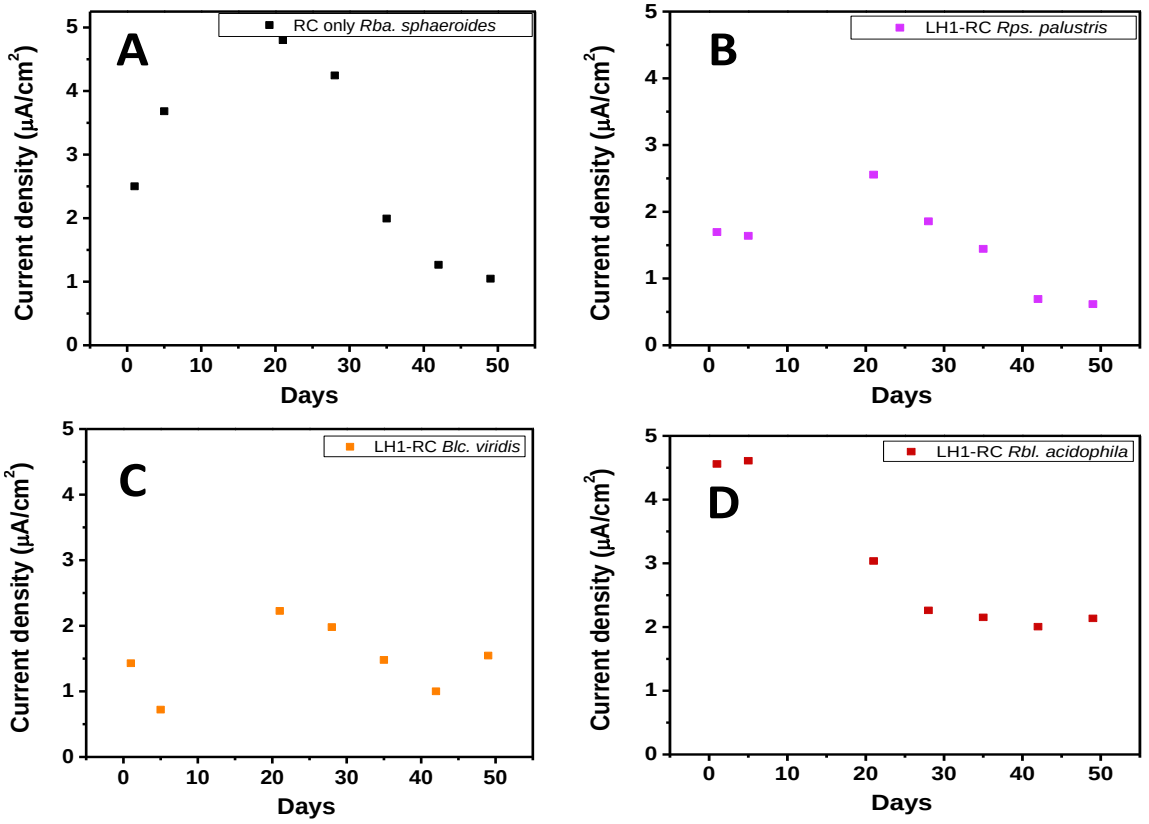


Figure 43. Photocurrent detected over a period of 50 days for ATO films pre-soaked in cytochrome *c* and treated with either RCs from *Rba. sphaeroides* (**A**), LH1-RCs from *Rps. palustris* (**B**), LH1-RCs from *Blc. viridis* (**C**) or LH1-RCs from *Rbl. acidophila* (**D**). Electrolyte buffers contained 0.1 M Tris and 250 μM Ubiquinone-0. A white light with an illumination intensity of 35 mW/cm^2 was used in all measurements. A 0.1 V (SHE) potential bias was applied to all slides. Slides were stored under darkness at 4 ºC in between measurements.

observed for the cytochrome *c* soaked ATO slides drops off to match that observed for those directly interfaced with the ATO (**Figure 44A**). Over time however the ATO- cyt *c*- LH1-RC systems perform better that the ATO- LH1-RC systems, consistently yielding higher photocurrent. For LH1-RCs from *Blc. viridis* (**Figure 44B**), differences are less noticeable but the ATO-cyt *c*- LH1-RC systems do appear to perform better. It is likely that presence of horse heart cytochrome *c* on ATO surfaces enhances the electronic connection between

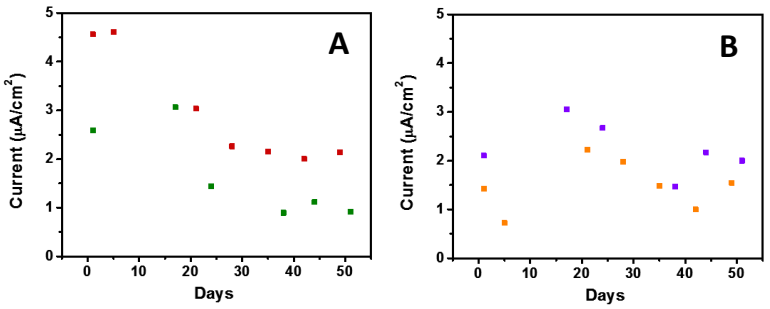


Figure 44. (A) Photocurrent detected over a period of 50 days for ATO films containing LH1-RCs from *Rbl. acidophila* with (red) and without (green) pre-soaking in cytochrome *c*; **(B)** Photocurrent detected over a period of 50 days for ATO films containing LH1-RCs from *Blc. viridis* with (orange) and without (purple) pre-soaking in cytochrome *c*. Electrolyte buffers contained 0.1 M Tris and 250 μM Ubiquinone-0. The light source used to excite the RCs/LH1-RCs within the ATO was a white light with an illumination intensity of 35 mW/cm^2. A potential bias of 0.1 V (SHE) was applied to all slides. Slides were stored under darkness at 4 ºC in between measurements.

RCs and ATO, and deliver electrons to reduce P^+, but that is affected by the potentials of the hemes within their respective tetraheme cytochrome *c* subunits.

In addition to adding natural antenna to the ATP-cyt *c*-RC system, we have also worked on synthetic analogues of these natural antenna systems. Thus far we have successfully labeled the lysine residues of *Rba. sphaeroides* RC complexes with Cy5 dye which absorbs around 620 nm and interfaced these dye-labelled RCs with ATO that has been pre-soaked in cytochrome *c*. The absorption spectra and a photo of slides of ATO-cyt *c* containing RCs with and without CY5-labels are shown in **Figure 45**. Significant enhansements of photocurrents for these systems were obtained (**Figure 46**). Under white light excitation the Cy5 dye-labelled ATO-cyt *c*-RC systems exhibits a 40% increase of photocurrent compared to that of the unlabeled ATO-cyt *c*-RC systems Cy5 dye (**Figure 46A**). When selective excitation at 650 nm is used, a 10-fold photocurrent increase is observed, confirming that the dye is serving as a light-harvesting component that delivers photon energy to the RC efficiently. We have now begun work to conjugate a 3-arm-DNA 'antenna' to the cysteine mutant RCs, which has been modified to include external cysteine residues surrounding the primary donor, P, following the work of Dutta et al. This will allow specific attachment of the artificial antenna systems the RCs and subsequent optimization of their function as biomimetic antenna-RC systems.

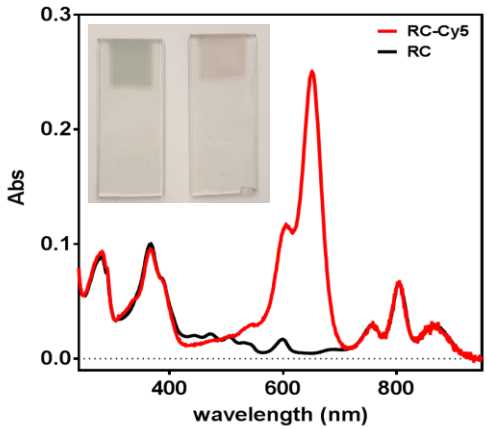


Figure 45. Steady-state absorption spectra for unlabeled (black) and Cy5-labelled RC samples (red). Inset shows a photo of ATO slides, pre-treated with cytochrome *c* and containing RCs without (left) and with Cy5-labelled (right). Data are normalized at the 800 nm. Slides have been left to air dry after each step. Film (inset) dimensions are 1 cm^2.

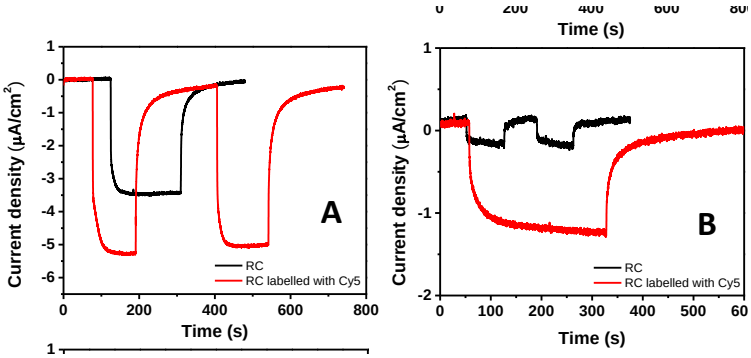


Figure 46. Photocurrent detected for a ATO films pre-soaked in cytochrome *c* and treated with either RCs (black) or RCs labelled with Cy5 (red) under white light excitation (left) or 650 nm excitation (right). The electrolyte buffer is 0.1 M Tris containing 250 μM Ubiquinone-0.

4.2. Incorporating photosystem I to harvesting more redox power from ATO-cyt c system

Another project is focused on increasing the redox power that we are capable of harvesting from our biohybrid photoelectrochemical cell with the ultimate goal of utilizing the doubly reduced product to perform redox chemistry. We have targeted Photosystem I (PSI) from the thermophilic cyanobacterium *Thermosynechococcus elongatus* to interface with the ATO electrode films based on the following considerations. Unlike purple bacterial reaction centers, which have a quinone molecule as their terminal electron acceptor, the terminal electron acceptor in PSI is an iron sulfur protein with a low enough redox potential to reduce $NADP^+$ (to NADPH). Such a biohybrid photoelectrochemical cell would therefore be capable of performing useful redox chemistry in solution. All electron transfer reaction kinetics are well characterized spectroscopically and temporally, and our collaborators from Prof. Petra Fromme's lab are experts in handling these proteins. Furthermore, this project could be coupled to the enzyme cascade produced in Prof. Hao Yan's group. Thus far we have successfully interfaced the PSI with the ATO films via horse heart cytochrome *c* (**Figure 47**). Electrochemical measurements were performed on these ATO-cyt *c*-PSI systems, as we had done previously for the purple bacterial RC systems. The electrolyte buffer used was 5 mM phosphate (pH 7) and measurements were conducted under white light excitation (with an illumination intensity of 35 mW/cm^2). Photocurrents of 1 $\mu A/cm^2$ were observed, even in the absence of an additional electron acceptor (**Figure 48**) since oxygen within the buffer is capable of oxidizing the iron sulfur center.

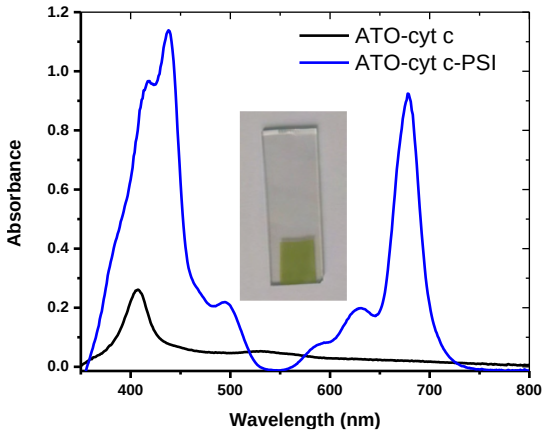


Figure 47. Steady-state absorption spectra for an ATO slide following soaking in cytochrome *c* (black) and a cytochrome *c*-soaked ATO slide following application of PSI solution (blue). Slides have been left to air dry after each step. Inset shows a photo of an ATO film on FTO glass, which has been pre-soaked in 50 µM cytochrome *c*, washed repeatedly to remove the unbound molecules and then treated with a pipette application of PSI. Film dimension is 1 cm^2.

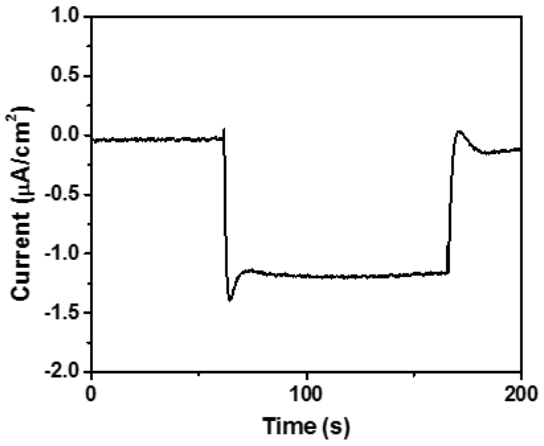


Figure 48. Photocurrent from ATO films containing cytochrome *c* and PSI, in 5 mM phosphate electrolyte buffer under white light illumination.

The system was then tested with the addition of a commonly used external electron acceptor, methyl viologen (MV^{2+}) and the result is given in **Figure 49**. It was expected that this would

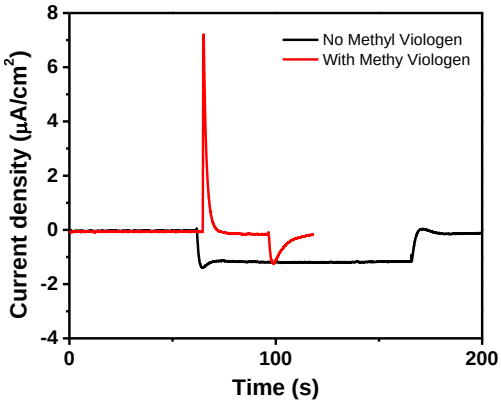


Figure 49. Photocurrent detected from ATO films containing cytochrome *c* and PSI in 5 mM phosphate electrolyte buffer with (red) and without (black) methyl viologen. Slides were illuminated with white light of 35 mW/cm^2.

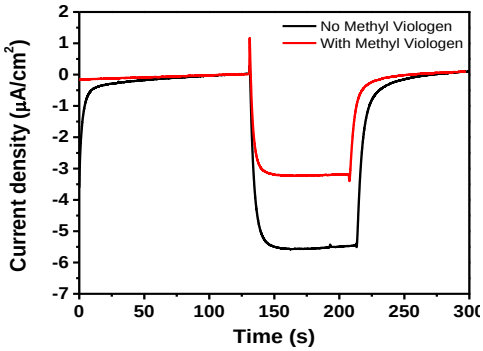


Figure 50. Photocurrent detected from ATO films containing cytochrome *c* and PSI in 5 mM phosphate electrolyte buffer with (red) and without (black) methyl viologen and a potential bias of 0 V (SHE) applied to the ATO. Slides were illuminated with white light of 35 mW/cm^2.

increase the observed photocurrent, however inclusion of methyl viologen in the electrolyte buffer had the opposite effect. The positive signal observed for the ATO-cyt *c*-PSI system in the presence of MV^{2+} indicates that it is donating the electron receives from PSI back to the oxidized cytochrome *c* and thereby short-circuiting the system. The current rapidly drops to zero as the electrons are not going to the counter electrode. In order to optimize the electron flow by reducing all the cytochrome *c* molecules on the ATO, a negative potential bias of 0 V (SHE) was applied to ATO-cyt *c*-PSI slides. This increased photocurrents to 3 μA/cm^2 in the presence of MV^{2+} and to 5.5 μA/cm^2 in the absence of methyl viologen (**Figure 50**).

It has previously been shown that applying a mixture of cytochomre *c* molecules and PSI to an electrode can improve photocurrents. The ATO-cyt c-PSI system is already a multilayered one due to the porous nature of the electrode, however we have tested the effect of applying a PSI:cyt *c* mixture to ATO films. ATO films were pre-soaked in cytochrome c as previously and were then treated with either mixture of PSI and buffer or PSI and cytochrome *c*. Solutions were left to incubate for three hours and then applied to the ATO films by pipette. The absorption spectrum for the ATO-cyt *c*-PSI:cyt *c* mix (**Figure 51**) shows a marked increase in absorption around 410 nm, due to the elevated levels of cytochrome *c*. Electrochemical measurements were performed as previously, with only 5 mM phosphate (pH 7) as the electrolyte buffer and with white light excitation. The observed photocurrent was higher for those slides containing the PSI:cyt *c* mix than for those containing PSI:buffer. The differential stability tests were performed on slides stored under darkness at 4 ºC for

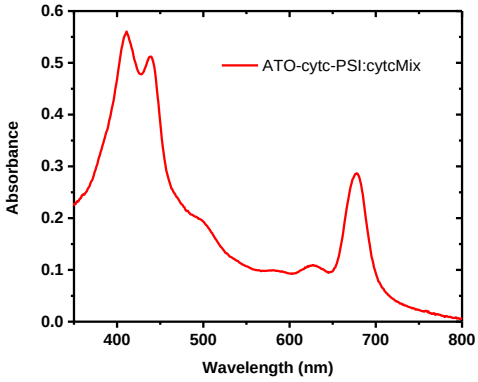


Figure 51. Steady-state absorption spectra for an ATO slide following soaking in cytochrome *c* and pipette application of a mixture of PSI and cytochrome *c*.

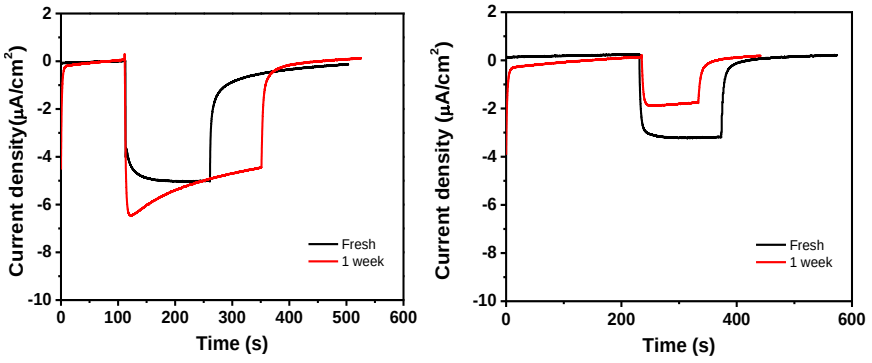


Figure 52. Photocurrent from **A.** ATO-cyt c-PSI:cyt *c* mix and **B**. ATO-cyt c-PSI:buffer for samples that was freshly prepared (black) and one week later following storage under darkness at 4ºC (red). A potential bias of 0 V (SHE) was applied to the slide and were illuminated with white light (35 mW/cm^2).

7 days and measured repeatedly. The results in **Figure 52** indicates that the ATO-cyt *c*-PSI:cyt *c* mix had survived relatively well (**Figure 52A**) while the ATO-cyt c-PSI:buffer (**Figure 52B**) system showed a marked drop in photocurrent.

Our next step is to include the natural electron acceptor, ferredoxin, and $NADP^+$ to produce NADPH. Since the reduction of $NADP^+$ to NADPH is reversible, an enzyme that will irreversibly consume the NADPH produced. Ferredoxin is a strong reductant but can only function in one electron reductions, while $NADP^+$ can only accept 2 electrons in the form of a hydride. We therefore require an intermediary to facilitate the electron transfer. The transfer of electrons from reduced ferredoxin to $NADP^+$ is catalyzed by the flavoprotein, ferredoxin-NADP+ reductase (FNR). This complex accepts the electrons one at a time from ferredoxin and then transfers a hydride to $NADP^+$ to form NADPH. Since FNR is a reversible enzyme, it will also reduce ferredoxin in presence of NADPH, potentially generating a short circuit in our system and we therefore intend to use an enzyme (for example glutamate dehydrogenase, which catalyzes conversion of glutamate linked to oxidation of NADPH), to recycle NADPH back to $NADP^+$.

4.3. Interfacing RCs with mercapto-reduced graphene oxide (mRGO) Langmuir Blodgett films

The desire to precisely orient the RC on the electrode material has led us to begin another subproject involving the same investigators. Mercapto-reduced graphene oxide (mRGO) has been functionalized with thiol binding sites. As an initial step, however, the RCs were deposited on mRGO Langmuir Blodgett films without the disulfide formation like in the case of the ATO electrode studies.

The preparation of mRGO LB films on ITO-PET is shown in **Figure 53A**. mRGO was synthesized by solvothermal reduction of graphene oxides in pyridine in the presence of P_4S_{10}. The thiol groups substantially improve the dispersibility of mRGO in ethanol even after 3 min centrifugation at 3000 rpm (**Figure 53A**). The ITO/PET substrate was placed in a perforated petri dish, sitting in a larger petri dish. After adding deionized water to the petri dish, the mRGO ethanol dispersion was slowly pipetted onto the surface of the water in the small petri dish. mRGO Langmuir films gradually formed on the water surface due to the differential dispersibility of mRGO in ethanol and water and self-assembly of the mRGO sheets. The films were then transferred onto the substrate by carefully draining the water from the larger petri dish. This equipment-free LB deposition method is highly scalable, which allows mRGO LB films to be

deposited onto virtually any substrate, regardless of its shape, size or flexibility. The resulting mRGO slide exhibited excellent flexibility and transparency (**Figure 53A**). Although not shown here, the immobilization of RCs on mRGO was confirmed by atomic force microscopy (AFM). RC features are observed over a size range between 7 and 15 nm immobilized on the mRGO films.

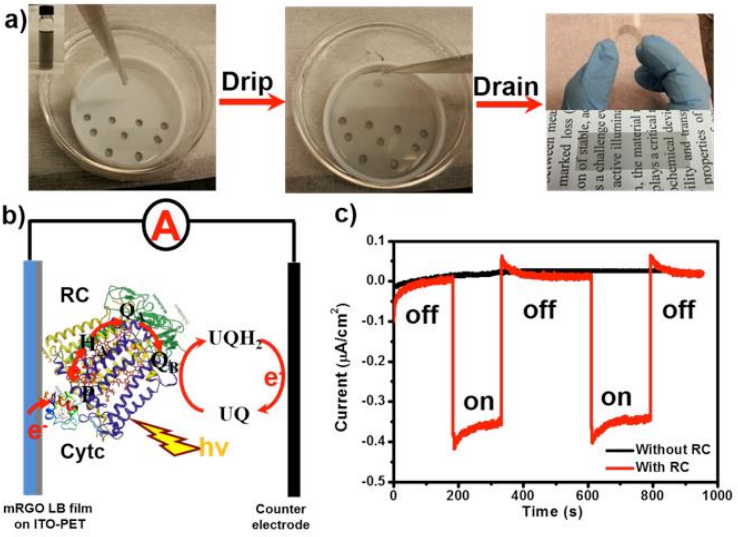


Figure 53. A The preparation of mRGO LB films on ITO/PET; **B** Schematic illustration of the electrochemical cell for RCs/mRGO; **C** Photocurrent of mRGO slide with/without RCs.

Photocurrents were measured using the electrochemical set-up shown in **Figure 53B**. The conversion of absorbed light into chemical redox energy is initiated in *Rb. sphaeroides* RCs by excitation of the primary electron donor, 'P', a coupled pair of bacteriochlorophylls. An electron transfer cascade is activated and continues down a redox gradient to a quinone molecule, 'Q_A', via intermediary cofactors (a monomeric bacteriochlorophyll, 'B_A', and a bacteriopheophytin, 'H_A'). The electron then passes from Q_A to a second quinone, Q_B, forming the semiquinone anion. A second photon completes the reduction of Q_B, forming dihydroquinone which then diffuses to the counter electrode. Cytochrome c serves as an electron transfer mediator passing the electron from mRGO to P^+, re-reducing the primary donor. With this set-up and applying a potential of 0.125 V vs SHE, a photocurrent density up to 0.40 μA/cm^2 is observed for the RC/mRGO system with 5.0 mW/cm^2 illumination at 800 nm (**Figure 53C**). No detectable photocurrent is observed for mRGO slides which have not been soaked in RCs. The nega tive photocurrent indicates that the RCs are preferentially orientated with the P-side facing the mRGO surface. A photocurrent density of 0.20 μA/cm^2 can be achieved when only the open circuit potential (OCP) ~0.230 V vs SHE is applied (**Figure 54**).

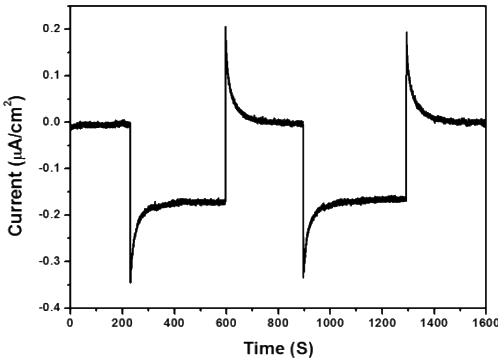


Figure 54. Photocurrent of RCs/mRGO when open circuit potential is applied.

It appears that cytochrome c mostly acts as a diffusible electron transfer mediator between the electrode and the RCs in this system (**Figure 55A**). Washing out unbounded cytochrome c after the photocurrent reached saturation (by rinsing the electrode with fresh buffer and replacing the electrolyte with cytochrome c-free electrolyte), dramatically decreases the photocurrent density from 0.20 to 0.04 μA/cm^2. Although not shown here, this photocurrent was recovered by injecting cytochrome c into the electrolyte, confirming that cytochrome c is mostly serving as a diffusible charge mediator in this system.

The inclusion of a tenfold molar excess of ubiquinone-0 (UQ:RCs=10:1) during the overnight incubation with the RC solution significantly (threefold) improves the photocurrent (**Figure 55B**). This is somewhat unexpected as ubiquinone-0 is included in the electrolyte buffer. As the terminal electron acceptor for the RC, the dihydroquinone formed by photochemical reduction is released and must therefore be exchanged with an oxidized quinone. It may be that the replacement of insoluble ubiquinone-10 in the QB pocket by the soluble ubiquione-0 during incubation, facilitates the quinone exchange.

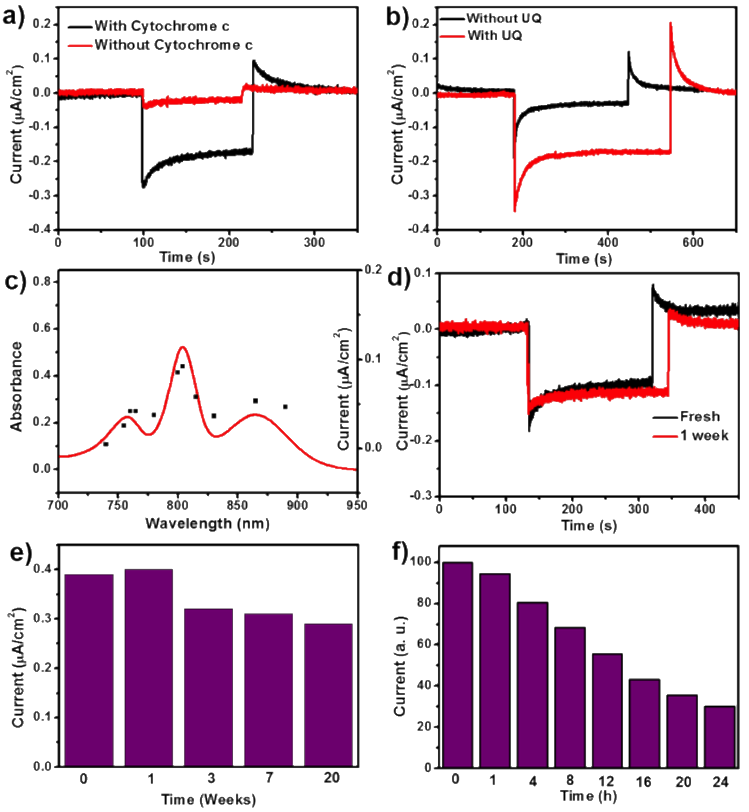


Figure 55. a) Photocurrent of the RC/mRGO system with/without free cytochrome c in the electrolyte; **b**) Photocurrent of the RC/mRGO system with/without ubiquinone-0 (UQ) during incubation; **c**) Action spectrum of RCs/mRGO (dotted line) and absorption spectrum (red line) of RCs in solution before incubation; photocurrent of RCs/mRGO after one-week storage under light at room temperature **d**), twenty-weeks storage at 4 ºC in dark **e**) and 24 h continuous illumination f).

To demonstrate that the observed current is due to photo-induced electron transfer in the RCs, an action spectrum of the photocurrent was collected (photocurrent as a function of illumination wavelength). A tunable continuous-wave Ti:Sapphire laser was used as the light source and the excitation wavelength was tuned from 740 to 890 nm holding the output power constant (1.3 mW/cm^2). The resulting spectral profile closely resembles that of the RC absorption spectrum, confirming that the RC is indeed responsible for the observed photocurrent (**Figure 55C**).

The stability of RCs on mRGO LB films was evaluated by measuring the photocurrent of the same slide over a period of time. The RCs/mRGO slides showed no photocurrent degradation after one-week storage under ambient light at room temperature in air (**Figure 55D**). The photocurrent from a RCs/mRGO slide was monitored for 20 weeks, during which time the slide was stored in the electrolyte at 4 ºC in the dark. After one-week storage, the RCs-mRGO slide exhibited the same photocurrent as the freshly made slide (**Figure 55E**). About 70% of initial photocurrent remained even after twenty-week storage in air. Furthermore, even after 1 h continuous illumination with white light at high intensity (35 mW/cm^2), the photocurrent decreased by only 5% (**Figure 55F**), which is less than the 15% reported previously. Even after 24 h of continuous illumination 30% of the original photocurrent remained. Moreover, 50% of the RCs remained active after three-week storage under ambient light.

In summary, *Rb. sphaeroides* RCs have been successfully immobilized on flexible transparent mRGO LB films for biomimetic solar energy transduction. These RCs display a relatively high stability, retaining 70% of their activity after 20 weeks when stored in the dark at 4ºC, and 30% of their activity after 24 hours of continuous 35 mW/cm^2 illumination. Photocurrent densities up to 0.4 μA/cm^2 can be achieved using 5.0 mW/cm^2 light intensity at 800 nm. The remarkable stability of RCs on mRGO LB film offers great potential for the development of a flexible biomimetic device. Why the RCs are particularly stable after immobilization on the mRGO electrode is unclear and further studies in terms of the surface properties including the presence of surface thiols, hydrophobicity and morphology are required.

Our next step is move on to a set of RC proteins modified with surface cysteine residues at the 'P' end of the RC to facilitate orientated binding to the thiol groups of this material through disulfide bond formation. We have prepared a RC mutant with a single cysteine residue. The triple-cysteine mutant has been provided by our collaborator Prof. Tom Beatty, at the University of British Columbia, whose group has previously reported successful binding of this modified RC to the surface of a gold electrode. We will accomplish direct attachment of single cysteine and triple cysteine mutant RCs to the mRGO and generate photocurrent.

Electrode interface of photosynthetic reaction center proteins in macroporous materials

1. Motivation and background:

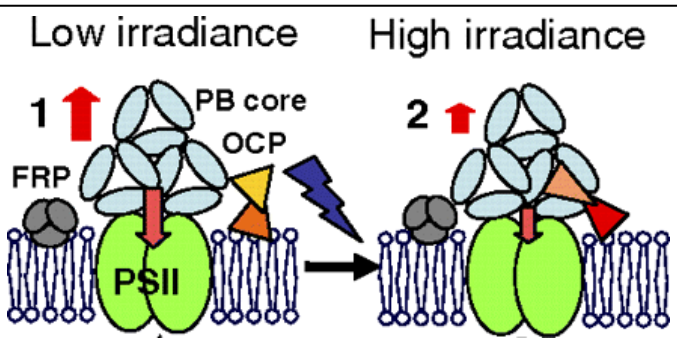


Figure 56. Working model for OCP photoprotection in cyanobacteria. (**1**) In darkness and under low irradiance the OCP (double triangle) is mostly orange and not (or weakly) attached to the phycobilisome (PB). Only the core of the PB is presented in the figure. (**2**) Absorption of blue-green light induces changes in the carotenoid and the protein converting OCP^o to OCP^r. The OCP^r will bind to the APC trimers of the core of the PBs and fluorescence quenching will be induced. The red arrows in 1 and 2 illustrated the relative amount of fluorescence from PB. (Image adapted from http://www.pnas.org/content/107/25/11620/F6.full)

The laboratories of Woodbury, Lin, and Yan are exploring ways to incorporate an Orange Carotenoid Protein into a DNA-templated artificial antenna system to adapt its photoprotection function for light regulation. Natural light harvesting systems in photosynthetic organisms not only have efficient means of absorbing light and capturing its energy, but they also utilize critical control mechanisms as part of their function. Light is both an energy source and a destructive element; excess excitation energy leads to a variety of deleterious processes, and natural photosynthetic systems go to great lengths to avoid destructive photochemistry by employing various photoprotection mechanisms. We have addressed this in our nanostructured hybrid light harvesting systems by exploring the utility of incorporating photoprotective components. In particular, we are focusing on a component found in cyanobacteria that involves a small orange carotenoid binding protein (OCP). OCP has the property that it is in an orange form in low light conditions (OCP^o), but upon exposure to high light, it switches into a red form (OCP^r). The red form is able to quench excess excited

energy absorbed by light-harvesting antenna and dissipate it as heat as illustrated in the working model shown in **Figure 56**. Furthermore, when the protein is isolated from cyanobacteria in dim light conditions, it is found to be in a dimer form. Upon light activation, and subsequent transition $OCP^O \rightarrow OCP^R$, the protein dimer dissociates into monomers. The monomerization reaction has been found to be a reversible process, though the relationship between the orange-to-red and the dimer-to-monomer transitions has not been described yet. It has been shown that the red form of OCP is able to bind to the phycobilisome (the cyanobacterial antenna), and it quenches the excited states, dissipating excess light energy to avoid damage. OCP contains a non-covalently bound carotenoid co-factor. Apparently, the carotenoid accepts excitation energy from the pigments of the phycobilisome via energy transfer (FRET) and thermally dissipate it. A peculiar feature of OCP is the intensity dependence of the conversion reaction: the rate and the percentage of dissociation are dependent on incident light intensity, making OCP a facile system for the regulation of photoprotective function. The scope of this part of the project is two-fold: exploring experimental conditions required for optical control of OCP monomerization reaction, and incorporating OCP into DNA nanostructured photonic devices, as a regulatory element.

2. Optical control of OCP monomerization reaction:

Currently, the mechanism underlying the dissociation of the OCP protein into monomers is not completely understood. The aim of this part of the project is to gain further insight into this mechanism and to explore the experimental conditions needed to manipulate it. To do this, we have investigated the ability of OCP to quench the fluorescence from the types of organic fluorophores we have previously incorporated into our nanostructured light-harvesting systems to increase the overall absorption cross section.

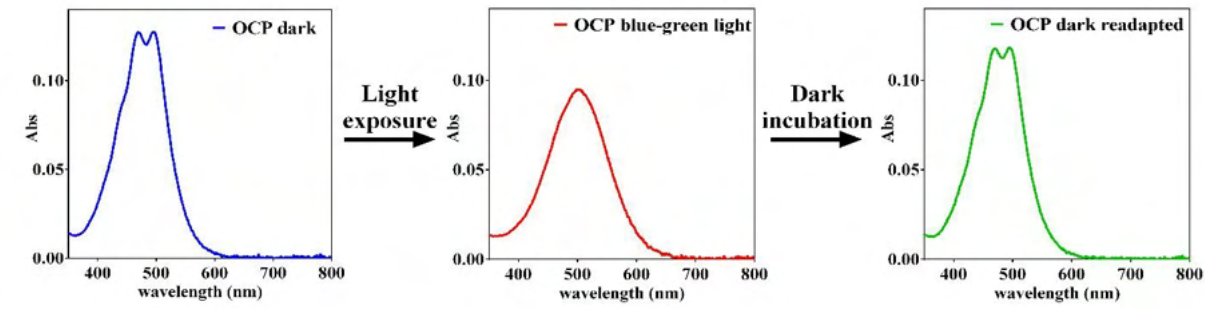


Figure 57. Absorption spectra of OCP during a "dark-light-dark" cycle. The light used for illumination was a blue-green beam of 30 mW, centered at 430 nm and with a spectral width of 100 nm.

Figure 57 shows the results of our initial tests using excitation centered at 430 nm to induce the changes in OCP photochemical and spectral properties. What can be seen is that there is a significant change in the OCP spectrum upon illumination which is completely reversible in the dark. We then labeled the protein with different fluorescent dyes. Each OCP monomer subunitcontains an exposed cysteine residue that is available for chemical modification. This cysteine can be used either to attach fluorescent dyes or to link OCP to nucleic acids structures (*vide infra*). Maleimide modified dyes were used to specifically target this cysteine residue: four dye molecules, TMR, Alexa Fluor 647, ATTO 655, and Cy7 were selected and the spectra of the

modified OCP in each case is shown in **Figure 58**. The ratio of monomer OCP-to-dye was approximately 1 as calculated from the extinction coefficients of the protein (132 $mM^{-1}cm^{-1}$ at 495 nm) and dyes (provided by the manufacturers), indicating that the labeling efficiency of the cysteine is nearly 100%. This methodology suggests that a similar approach can be used in the future to conjugate the protein to DNA structures. **Figure 59** shows the results of illuminating TMR and ATTO 655 modified OCP samples with light in the 430 nm region. One can see that, as in **Figure 57**, there is a definite spectral shift similar to that seen without labels present, indicating that the modified protein is still able to undergo monomerization. In this system, it is possible to study the monomer/dimer transition in more detail. To this end, we are using a FRET-based approach. The experimental concept is presented in **Figure 60**. OCP is prepared with two different dye labels, (upper left), capable of a FRET interaction. The two batches of dye-labeled OCPs are then mixed and the protein is exposed to light to induce monomerization (upper middle). Finally, the sample is transferred back into the dark to allow dimerization to take place (upper right). In principle, about 50% of the OCP dimers should contain a FRET pair if the monomerization and re-dimerization were random. By monitoring the FRET response during this process (**Figure 60**, lower panel), it is possible to observe the monomer exchange in solution during the light-dark cycle. This method should allow us to study the reaction directly in solution, with the possibility of exploring parameters that may influence the dynamics of the system such as protein concentration, pH, and ionic strength. Currently we are in the process of optimizing the experimental conditions for in both steady state and time-resolved fluorescence spectroscopic measurements.

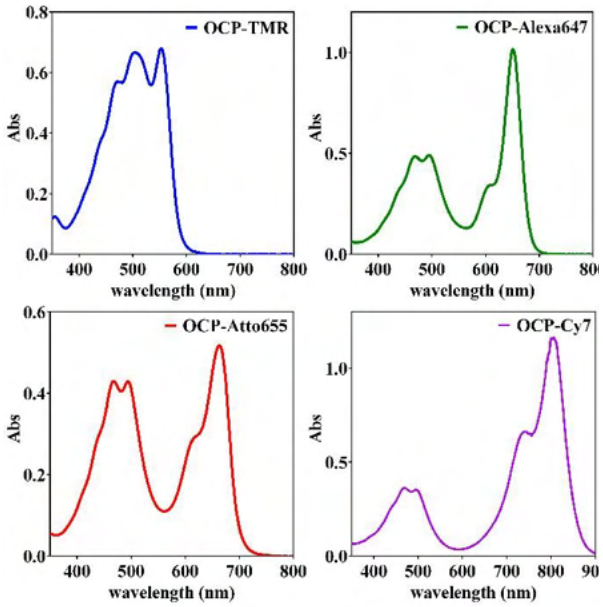


Figure 58. Spectra of OCP labeled with different organic dye molecules. A close to 1:1 OCP:dye labeling is achieved.

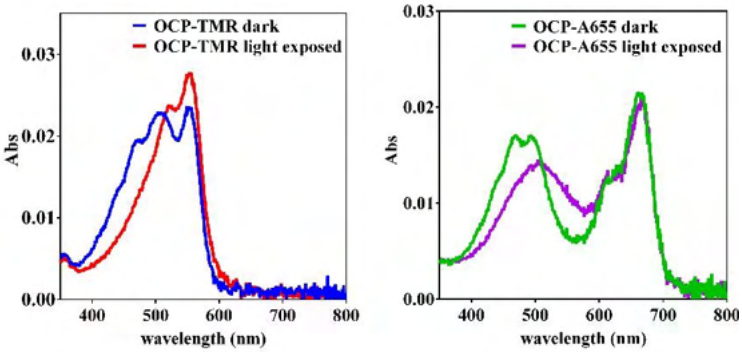


Figure 59. Examples of light-induced spectral shift of OCP samples labeled with TMR (left) and ATTO 655 (right). In both cases a clear spectral shift of the carotenoid absorbance toward longer wavelengths was observed.

The experimental design illustrated in **Figure 60** was realized using, separately, three pairs of fluorescent dyes capable of FRET: tetramethylrhodamine (TMR) and Atto655, Atto655 and Cy7, and Alexa647 and Cy7. Samples were prepared with a 1:1 molar ratio of OCP carrying the first

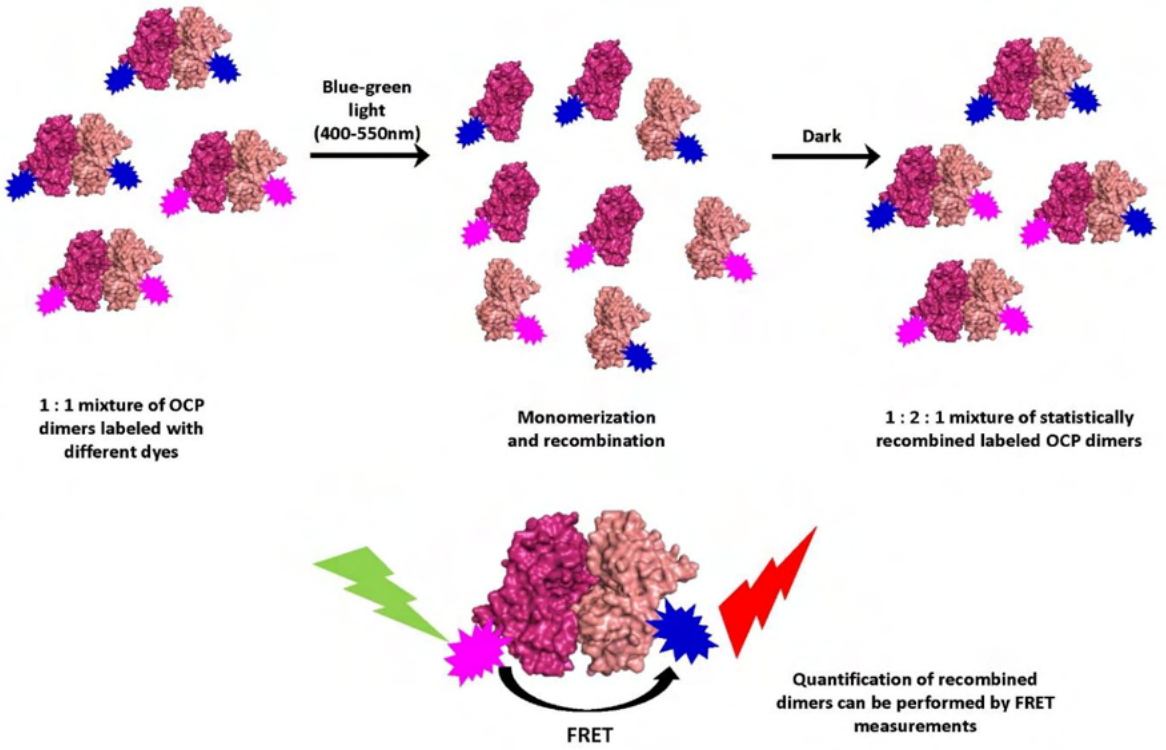


Figure 60. Proposed scheme to study the monomerization – dimerization process of OCP. Upper: OCP is labeled with two different dye molecules capable of forming a FRET pair. Lower: detection of the FRET signal.

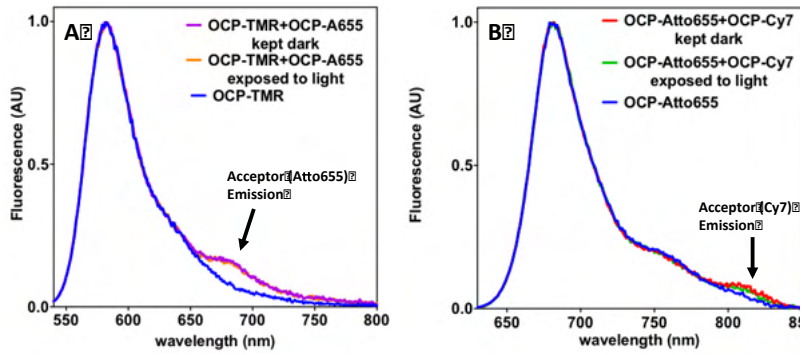


Figure 61. A. Emission Spectra of mixtures of OCP-TMR and OCP-Atto655 kept in the dark (purple) or exposed to light (red) to induce monomerization: the spectra was recorded exciting TMR, and the changes between samples were expected to occur in the emission of the acceptor (Atto655, indicated by the arrow). The emission of OCP-TMR is reported as a reference (blue). **B**. Emission Spectra of mixtures of OCP-Atto655 and OCP-Cy7 kept in the dark (red) or exposed to light (green) to induce monomerization: the spectra was recorded exciting Atto655, and the changes between samples were expected to occur in the emission of the acceptor (Cy7, indicated by the arrow). The emission of OCP-Atto655 is reported as a reference (blue).

dye (energy donor) and OCP carrying the second dye (energy acceptor). The mixture was then split in two equal parts: one sample was kept in the dark, the second sample was exposed for 10 minutes to the same light used to convert OCP from orange to red form in **Figure 57**. Steady state fluorescence spectra of dark and light treated samples for each of the 3 dye-labeled OCP proteins were compared with excitation into the donor dye molecule. The focus was fluorescence intensity increase at the emission wavelength of the energy acceptor dye, which should provide evidence for the formation of OCP dimer with different dyes labeled on each monomer as

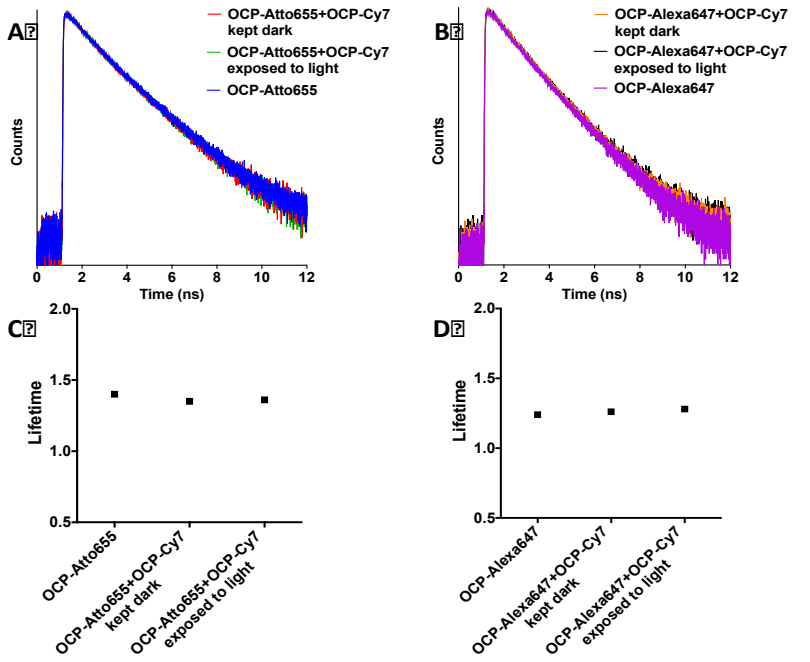


Figure 62 A. Fluorescence decay of Atto655 in sample mixtures containing OCP-Atto655, and OCP-Cy7, kept either in the dark or exposed to light. The emission of OCP-Atto655 alone is reported for reference. **B.** Emission decay of Atto655 in sample mixtures containing OCP-Alexa647, and OCP-Cy7. Samples were either kept in the dark or exposed to light. The emission of OCP-Alexa647 alone is reported for reference. **C.** Average lifetime of Atto655 obtained from fitting the emission decays presented in panel **A. D.** Average lifetime of Alexa647 obtained from fitting the emission decays presented in panel **B.**

illustrated at the bottom part of **Figure 60**. Fluorescence spectra from the recombination experiment using OCP-TMR and OCP-Atto655 pair, and OCP-Atto655 and OCP-Cy7 pair are shown in **Figure 61A** and **Figure 61B**, respectively. The arrows in the plots indicate the spectral region where the acceptor dye emits. If the situation illustrated in **Figure 60** occurred, an increase in the emission of the acceptor dye is expected. As can be seen in **Figure 61**, it seems quite clear that no difference is shown from the light treated samples. The results are similar for both dye pairs, therefore excluding an influence of the dye chosen. As a further test, the fluorescence lifetime of the of the donor dye was measured using time correlated single photon counting techniques and the kinetic traces are plotted in **Figure 62A** for the dye Atto655 in samples containing OCP-Atto655 + OCP-Cy7. It is clear that no difference between the sample kept in the dark and the sample exposed to light occurs, and both are similar to the decay of OCP-Atto655 alone. The value of the average lifetime for each sample, obtained by data fitting, is reported in **Figure 62C**, and it confirms that all three samples have the same emission decay lifetime, suggesting that there is no energy transfer from Atto655 to Cy7 in the sample exposed to light. The data for samples containing OCP-Alexa647 + OCP-Cy7 are presented in **Figure 62B** and **Figure 62D**. The analysis of these data results in a similar outcome as for the samples OCP-Atto655 + OCP-Cy7, i.e. the mixture of two differently labeled OCP does not change its emission properties after

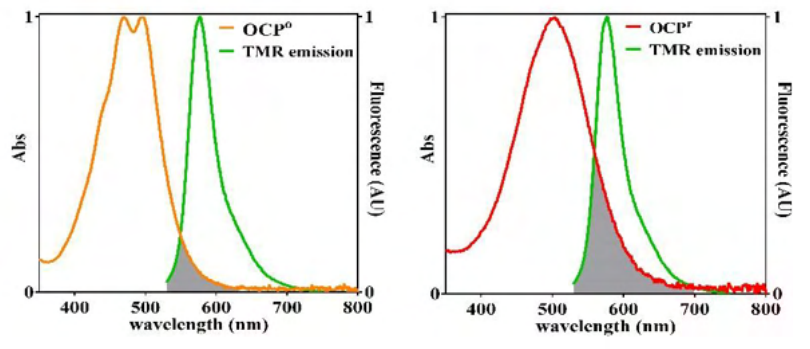


Figure 63. Overlap of the emission of the dye TMR with the absorption spectrum of OCP in the dark (left) and light (right) forms. The shaded area represents the overlap between the two spectra.

exposure to light. The results presented here indicate that under the current experimental conditions, most likely the submicromolar concentration of protein, there is no significant amount of recombination of OCP monomers. This does not exclude the possibility that recombination may occur in different conditions, and it might be a process that can be tuned by other factors, such as ionic strength and pH of the buffering solution. Further experiments need to be performed.

3. Modulated quenching of fluorophores by OCP:

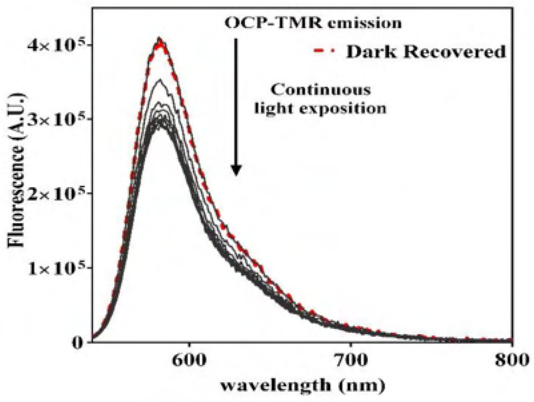


Figure 64. Emission spectra of TMR bound to OCP under green light illumination. The black traces were recorded at intervals of 30 s during continuous illumination. The red dashed line shows the emission of the same sample after a 5 minutes recovery in the dark.

In vivo, OCP quenches the excited states of the phycobilisome by direct binding; the energy from the excited pigment molecules in the phycobilisome is transferred to the carotenoid molecule in OCP. By using the same energy transfer mechanism, it is possible for the carotenoid in the protein to quench the emission of organic dyes whose emission overlaps with the carotenoid absorbance in either of its two spectral states. If the fluorophore fluorescence spectrum overlaps better with the spectrum of one spectral state of the OCP *vs* the other, differential quenching controlled by light can be achieved. Here, TMR was the dye chosen to test this phenomenon due its spectral properties (**Figure 63**). As it can be seen, when OCP converts to the OCP^r form, the overlap of its absorbance with the TMR fluorescence spectrum increases. This should increase the rate of energy transfer from TMR to the OCP, quenching the TMR fluorescence.

To test this, a sample of OCP-TMR was excited at 520 nm with a light intensity of ~180 µW, which is a typical intensity used for fluorescence experiments in bulk solution. This wavelength will both excite TMR, as well as slowly induce the spectral shift in OCP. The emission spectrum of TMR was recorded every 30 seconds. As shown in **Figure 64**, the fluorescence steadily decreases with time during illumination. When the sample was then incubated in the dark for about 5 minutes, the fluorescence spectrum returned to its original amplitude (**Figure 64,** red dashed line) showing that the fluorescence quenching of TMR by OCP^r is completely reversible when OCP returns to the OCP^o form.

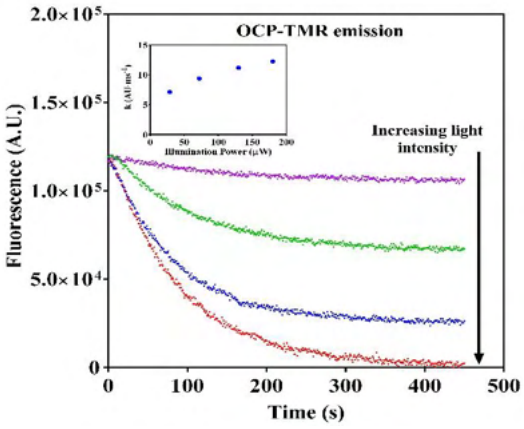


Figure 65. Fluorescence emission signal of TMR attached to OCP as a function of illumination time and excitation intensity. The inset shows the decay rate obtained from monoexponential fitting of the fluorescence data plotted versus the illumination power.

Figure 65 shows the intensity dependence of this effect. The emission peak of TMR (580 nm) was monitored over a period of about 450 s at various

light intensities. Each kinetic trace was subsequently fit to a monoexponential decay, and the rate constant at each illumination power is reported in **Figure 65** inset. The decay rate is proportional to the rate of production of OCP^r at that particular excitation power, again consistent with the conclusion that the increased quenching arises from the change in spectral form of OCP.

4. Constructing a DNA nanostructure incorporating the light-induced photo-protective complex:

As described above, OCP can be used to successfully quench the fluorescence emitted by organic dyes directly attached to it in a light-dependent fashion. Our next approach was to integrate the

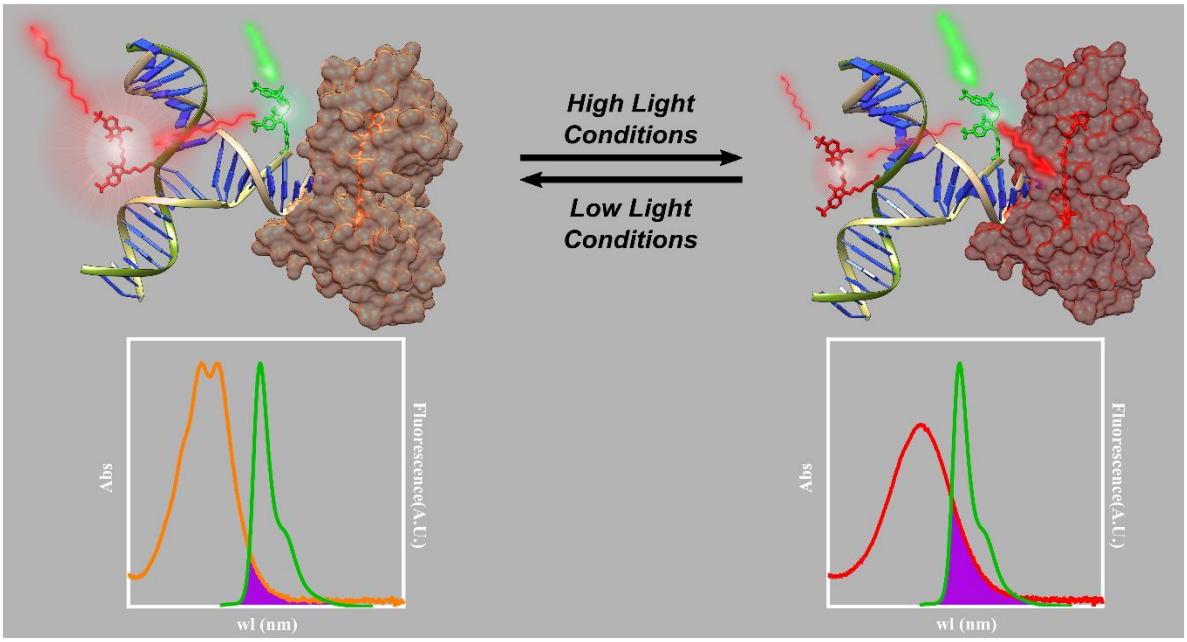


Figure 66. Concept for the application of OCP as a light-induced photo-protective element on a DNA nanostructure. The DNA nanostructure chosen here is a 3 arm junction (yellow and blue cartoon) labeled with two dyes: Cy3 (green) and Cy5 (red). Left: under low light conditions, the OCP is in its inactive form and the spectral overlap with Cy3 is low. When Cy3 is excited, energy transfer from Cy3 to Cy5 occurs, resulting in a strong fluorescence emitted from Cy5. Right: under high light conditions, the OCP is in its active form: the spectrum has undergone a transition so that has greater overlap with the emission of Cy3. In this case the energy from Cy3 is quenched by the carotenoid molecule, and energy transfer from Cy3 to Cy5 is reduced.

protein in a DNA nanostructured light-harvesting system where dyes and photosynthetic elements are assembled in an organized fashion, similar to the kinds of DNA-based photonic systems we have published previously. To accomplish this, we have first incorporated OCP into the system and demonstrated light-dependent quenching of the excitation energy.

We have chosen to use the 3arm DNA nanostructure we described previously as the basis for building the light regulated antenna system. The concept is depicted in **Figure 66**. The 3 arm DNA structure is conjugated to two dyes, the FRET pair Cy3-Cy5 is here used as an example, but other FRET pairs with similar spectral characteristic could be used as well. The dye-labeled nanostructure can be then conjugated to the cysteine of OCP using SPDP or other maleimide mediated chemistry, as previously reported for other DNA-protein systems. The left side of **Figure**

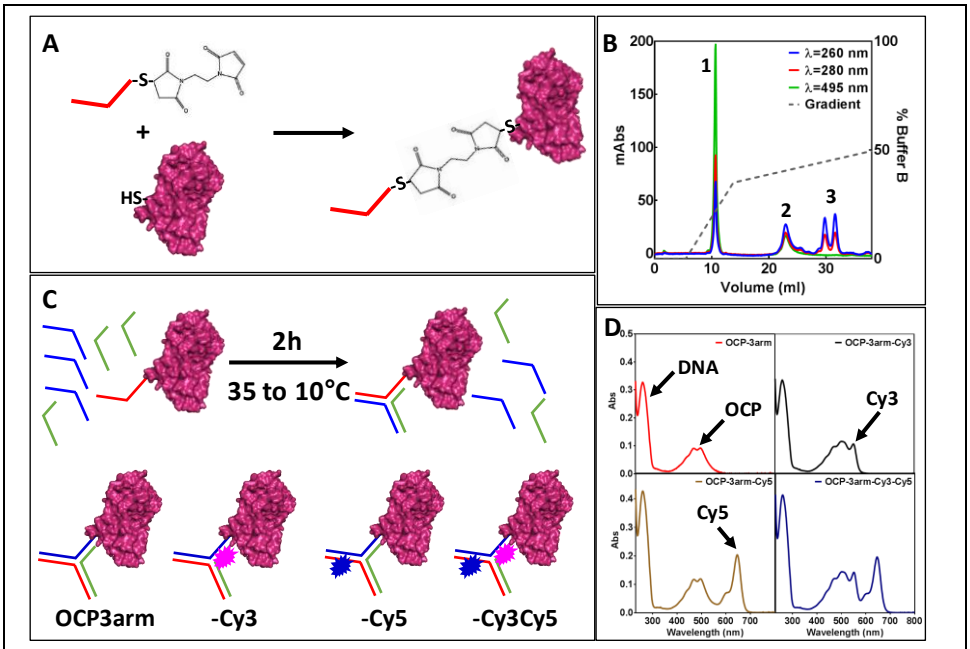


Figure 67 A. Modification of OCP using a DNA strand modified with a *bis*-maleimide linker. **B.** Ion exchange chromatography elution profile from the separation of the products of the coupling reaction of OCP with DNA. Three wavelengths are used to monitor the elution from the column: 260, 280, and 495 nm, corresponding to the absorbance of DNA, protein, and carotenoid, respectively. Peak 1 is the unmodified OCP. Peak 2 corresponds to OCP-DNA. Peak 3 is DNA alone. **C.** Schematics of the procedure used to anneal the 3arm DNA structure, with indication of the thermal gradient used. The different combinations of dyes arranged on the DNA 3arm are presented in the bottom part of the panel. D. UV-Vis spectra of the OCP-3arm assembled samples showing the spectral features of DNA, OCP, Cy3, and Cy5.

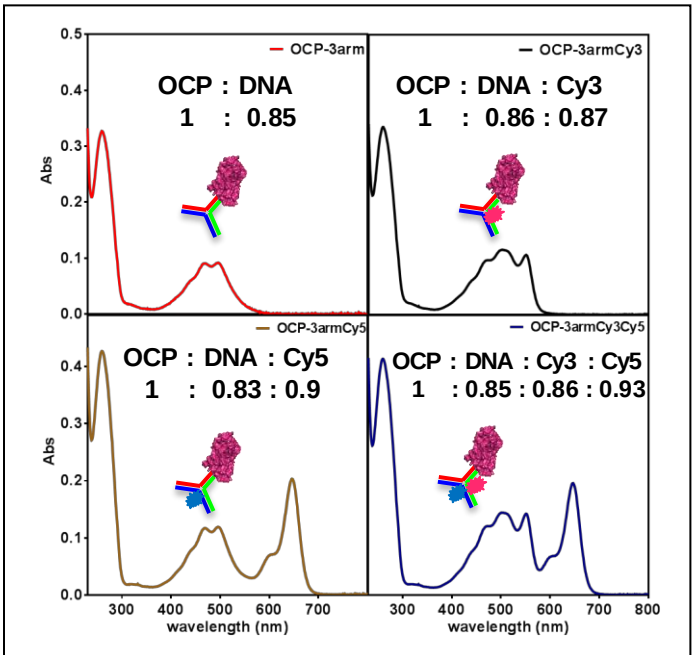


Figure 68. UV-Vis spectra of the OCP-3arm samples with calculated stoichiometry of various components presented.

66 shows the expected behavior of the system under low light conditions: OCP is present in its orange form, and the energy of excitation of Cy3 is transferred to Cy5 with little interference from OCP. An increase in excitation intensity should convert OCP into the red form (right side of **Figure 66)**, enhancing spectral overlap between the OCP and the excited state of Cy3. Part of the Cy3 fluorescence should thus be quenched by the carotenoid inside OCP, resulting in a decrease of energy transfer to Cy5. Beyond this test system, OCP could be incorporated into more complex photosynthetic networks, acting as an inducible photo-protection element.

We performed the conjugation of OCP to a single strand of DNA, St1, as illustrate in **Figure 67A** modifying the DNA first with a *bis*-maleimide linker and then reacting it with the protein at an available surface cysteine. The product of this reaction, named OCP-St1, was purified using ion exchange chromatography. The results are shown in **Figure 67B**: the unmodified OCP (peak 1), the OCP-St1 (peak 2) and St1 alone (peak 3) elute at very different retention volumes in the gradient. The purified OCP-St1 was then used to anneal the OCP-3arm sample by

mixing a stoichiometric amount of the other two DNA strands required to assemble the 3arm structure. The modularity of DNA makes it possible to prepare four different samples where different combinations of labeled and unlabeled DNA strands can be used, as illustrated in **Figure 67C**. The assembled samples were further purified using size exclusion chromatography, and then characterized with UV-Vis spectroscopy to identify the spectral features of the individual components, as presented in **Figure 67D**. The ratio of the components in each assembly was calculated based on their extinction coefficients, and are shown in **Figure 68**, where the stoichiometry of the components is reported with each spectrum. To ensure the correct formation of the OCP-3arm complex, the samples were run on a polyacrylamide gel under native conditions to preserve the conformation of the protein and the DNA 3arm junction. The samples were compared to the 3arm DNA assembled in the same combinations without the protein linked to the strand St1. In **Figure 69** we report the gel results recorded by different imaging methods to visualize all the components in the system, left to right: the first image shows the fluorescence of Cy3 and Cy5, the second image was obtained staining specifically the DNA, and the third image was obtained staining specifically the protein. It is evident from **Figure 69** that the samples corresponding to the 3arm junction only run further into the gel than the samples containing OCP-3arm, indicating that a larger assembly is present when the protein is linked to St1. Furthermore, comparison of OCP-St1 with OCP-3arm shows that the former runs slightly further into the gel than the latter: this indicates that a bulkier structure is attached to OCP, and thus the formation of the 3arm junction. As an additional check, the samples were separately run on an analytical gel filtration column (**Figure 70**). It is shown that the 3arm junction, OCP-St1 and OCP-3arm elute at different retention

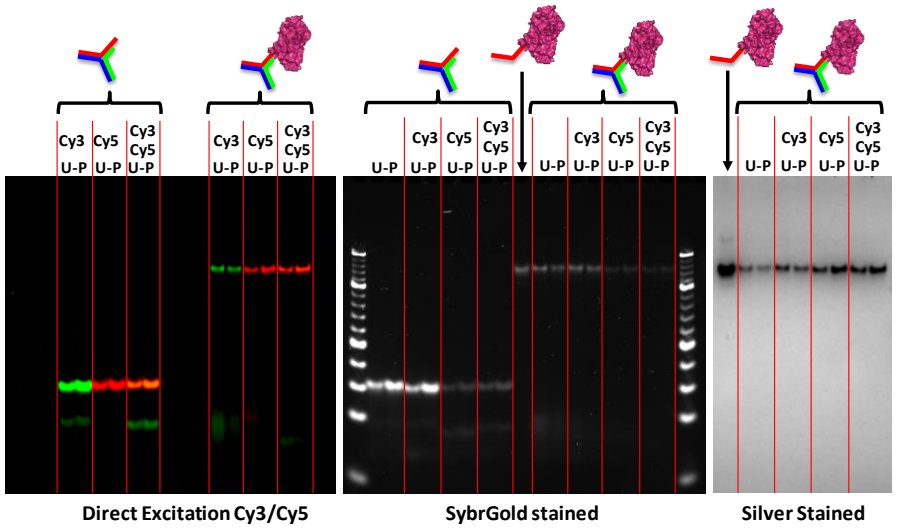


Figure 69. Native polyacrylamide gel electrophoresis results that show the formation of the 3arm and OCP-3arm complexes after annealing and purification (U = unpurified sample, P = purified sample). Left: the gel was imaged to visualize Cy3 and Cy5 by exciting the dyes directly. Center: the gel was stained with SybrGold, which binds to DNA, to visualize the bands containing DNA on the gel. Right: the gel was treated with Silver stain to visualize the presence of protein in the bands.

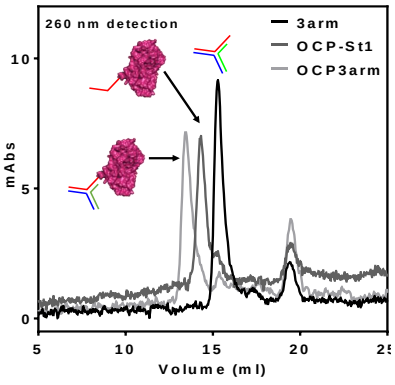


Figure 70. Size exclusion chromatography elution profile for 3arm, OCP-St1, and OCP-3arm samples monitored at 260 nm.

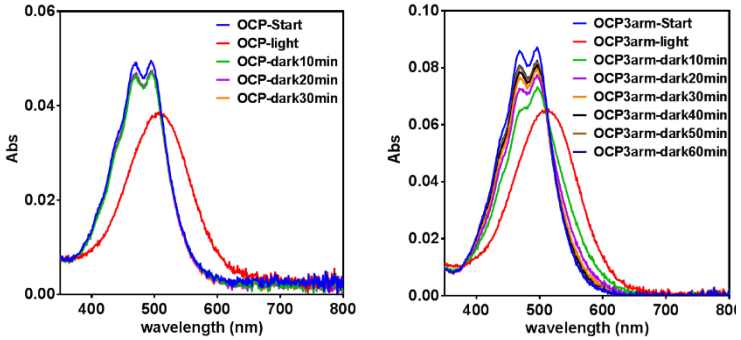


Figure 71. Light activation and dark recovery of the OCP, left, and OCP-3arm sample, right. The initial OCP sample (blue spectrum) was illuminated for 5 min with strong white light to convert it into OCP^R (red spectrum). The samples absorbance was monitored every ten minutes to observe the conversion of OCP^R back to OCP^O.

volumes, further confirming the formation of a correctly assembled OCP-3arm sample where the DNA is in a 3 way junction conformation.

We then tested whether the function of OCP was retained after modification with DNA and assembly of the 3arm structure. The photoactivation of OCP^O into OCP^R was monitored using UV-Vis spectroscopy and the results are shown in **Figure 71** (Left: OCP, Right: OCP-3arm). For each sample, an initial spectrum in the dark was taken, the protein was then illuminated for 5 min with intense white light. Subsequently, a spectrum of the red form was taken, and the recovery was monitored recording spectra every 10 min in the dark. As shown in **Figure 71**, OCP and OCP-3arm convert from the orange to the red

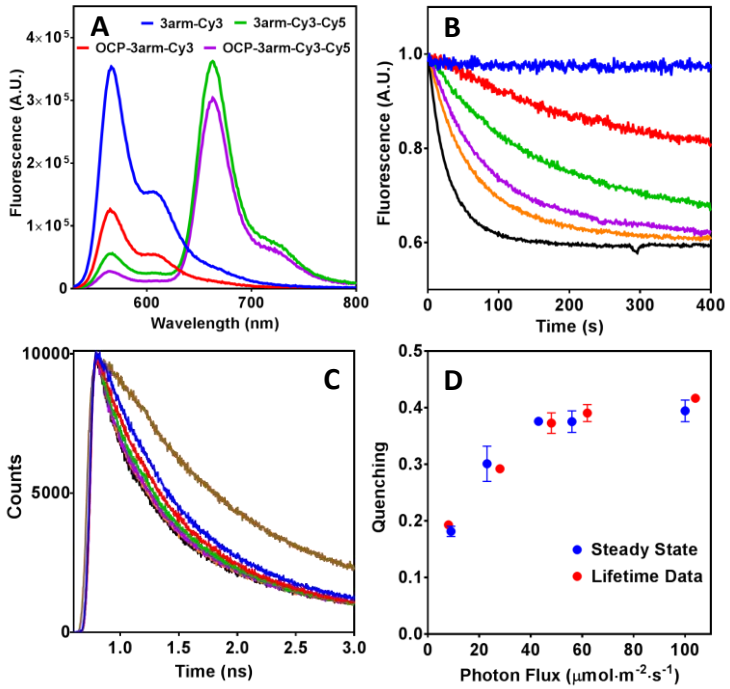


Figure 72 A. Fluorescence Emission spectra of 3arm-Cy3, OCP-3arm-Cy3, 3arm-Cy3-Cy5, and OCP-3arm-Cy3-Cy5 used to calculate the energy transfer efficiencies from Cy3 to OCP^O and to Cy5. **B.** Fluorescence intensity change of OCP-3arm-Cy3 sample as a function of exposure time monitored at 560 nm (Cy3 emission). The OCP-3arm-Cy3 was excited at 520 nm with photon fluxes of 9 (blue), 9 (red), 23 (green), 43 (magenta), 56 (orange) and 100 (black) $mmol \cdot m^{-2} \cdot s^{-1}$, and the curves were normalized at the maximum intensity at time zero. The blue trace is recorded in the presence of FRP. **C.** Emission decay curves (exc: 520 nm, em: 560 nm) showing the effect of light activation of OCP on the lifetime of the Cy3 dye. The brown curve is the decay kinetics of Cy3 in the 3armCy3 sample. The blue, red, green, magenta, orange and black traces were recorded with excitation densities of 8, 8, 28, 48, 62, 104 $mmol \cdot m^{-2} \cdot s^{-1}$, respectively. The blue trace was measured in the presence of FRP. **D.** Level of quenching of Cy3 induced by OCP calculated from the data in panel B (blue) and C (red).

form and back, albeit with different time courses. The OCP recovers in about 10 minutes or less, whereas the full recovery of OCP-3arm took about 1 hour. Nevertheless, the protein retained its ability to respond to light, transition from the orange to the red form, and transition back when incubated in the dark.

We then tested the OCP quenching in its orange form on the OCP-3arm-Cy3 and OCP-3arm-Cy3-Cy5 systems. We recorded the fluorescence emission spectra of the samples at low excitation power and in the presence of the Fluorescence Recovery Protein (FRP), which quickly converts OCP^R back to OCP^O, thus keeping the equilibrium concentration of OCP^R negligible.[46, 47] The spectra were compared with the emission spectra of the 3arm-Cy3 and 3arm-Cy3-Cy5 without OCP. The results are shown in **Figure 72A**. It is evident that OCP in the orange form receives energy from Cy3 in the OCP-3arm-Cy3 construct, thus resulting in a decreased fluorescence emission (red line) compared to the 3arm-Cy3 sample (blue line). A similar decrease of emission of Cy3 is observed in the OCP-3arm-Cy3-Cy5 construct (purple line), compared to the 3arm-Cy3-Cy5 (green line), where also a decrease in the emission of Cy5 (peak at 662 nm) occurs. The energy transfer from Cy3 to OCP^O in OCP-3arm-Cy3 was estimated to be 60%.

In the absence of FRP, OCP can be converted under constant illumination. Excitation of Cy3 at 520 nm will also excite the OCP and thus initiate the photoconversion OCP^O->OCP^R. We tested this by monitoring the emission of Cy3 in OCP-3arm-Cy3 under constant illumination at different power intensities, and the results are shown in **Figure 72B**. The blue line is the control where OCP-3arm-Cy3 was illuminated at low power in the presence of FRP to maintain OCP in the orange form. No changes in the emission at 566 nm are observed in this case. When FRP is not present in the sample, the emission at 566 nm decreases in time until it reaches a plateau. The rate of decrease, as well as the final plateau level, both vary as a function of illumination power, as show in **Figure 72B** (see figure legend for details on the illumination intensity level). To confirm that this effect is indeed caused by the accumulation of OCP^R in the sample, we measured the lifetime of the dye Cy3 as a function of illumination power (**Figure 72C**). As expected, a decrease in the lifetime of the dye is observed, indicating that there is energy transfer from Cy3 to OCP^R. The fraction of fluorescence quenched by OCP^R was calculated using the data shown in **Figure 72B** and **C**, and the results are shown in **Figure 72D**. The plot shows that the amount of Cy3 fluorescence quenched by OCP increases with the illumination power, reflecting the activation of OCP to its red form.

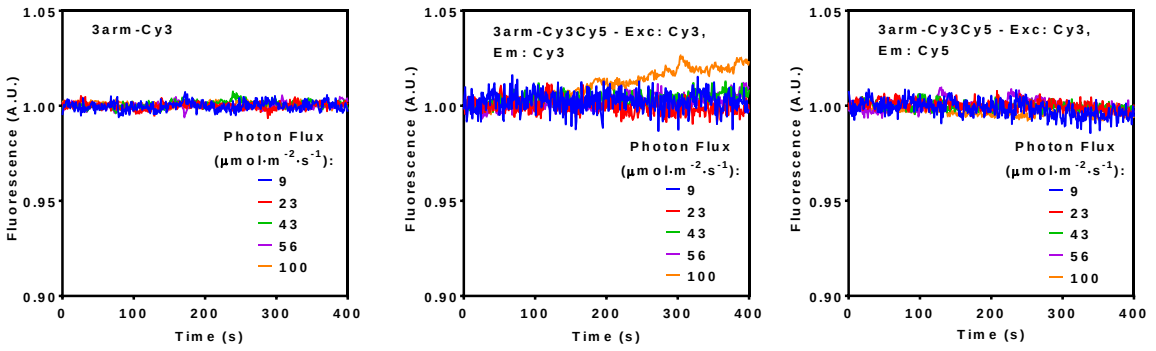


Figure 73. Fluorescence intensity changes of the 3 configurations of the dye-labeled 3arm samples under continuous illumination. Left: excitation of 3armCy3 at 520 nm and detection at 566 nm for Cy3 emission. Center: excitation of 3armCy3Cy5 at 520nm and detection of the emission at 566 nm. Right: 3armCy3Cy5 was excited at 520 nm, and the emission at 662 nm to monitor the emission from Cy5.

As a control, fluorescence intensity changes of the 3 configurations of the dye-labeled 3arm samples were monitored under continuous illumination. No decrease in fluorescence is observed when OCP is not present in the system (**Figure 73**).

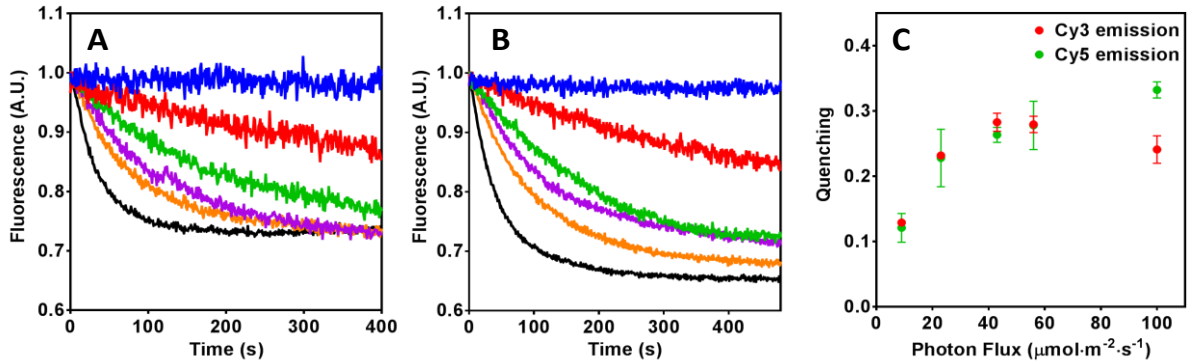
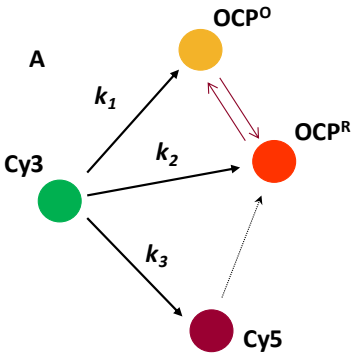


Figure 74. A. Emission of Cy3 in OCP-3arm-Cy3-Cy5 sample recorded at 560 nm upon excitation at 520 with photon fluxes of 9 (blue), of 9 (red), 23 (green), 43 (magenta), 56 (orange) and 100 (black) mmol·m^{-2}·s^{-1}. The blue curve was recorded in the presence of an excess of FRP. **B.** Fluorescence intensity of Cy5 at 662 nm in OCP3armCy3Cy5 upon excitation at 520 nm at various intensity levels. The color coding is the same as for panel A. **C.** Quenching of the emission of Cy3 (red) and Cy5 (green) extracted from the data in panel A and B, and reported as a function of illumination intensity of the sample.

The results shown above clearly demonstrate that the OCP protein acts, in OCP-3arm-Cy3, as a light intensity activated quenching element, and the amount of fluorescence quenched depends on the intensity used to illuminate the sample.

In Cyanobacteria, the role of OCP is to quench the excess excited state of donor pigments in an antenna complex, and dissipate the energy as heat, resulting in a decreased amount of energy flow downstream through the antenna. The system we designed to mimic the photo-protection function of OCP in nature systems, OCP-3arm-Cy3-Cy5, can be used as a model for this situation. In this model, Cy5 is the acceptor dye. Its fluorescence intensity is monitored in order to follow the amount of energy transfer from Cy3 to Cy5. We tested the construct under continuous illumination at 520 nm, which preferentially excites Cy3. Fluorescence intensity changes of Cy3 and Cy5 as a function of time were recorded and presented in **Figure 74.** The intensity change of Cy3, at 566 nm (**Figure 74A**) resembles the data presented in **Figure 72B** from OCP-3arm-Cy3. The time dependence of the Cy5 emission at 662 nm closely follows the emission of Cy3 (**Figure 74B**). To quantify this, we used the blue curve in each plot as a reference, which was measured in the presence of FRP to maintain OCP in the orange state, and calculated the percentage of quenching at the end point of the time traces. The data are shown in **Figure 74C**. It is clear that the fraction of total fluorescence quenched for Cy3 and Cy5 follows the same trend as a function of illumination power. This means that the amount of energy transferred from Cy3 to the acceptor Cy5 decreases with the increase of excitation light intensity, a consequence of a lower population (presumably shorter lifetime) of excited Cy3.

The investigation of the OCP-3arm-Cy3 and OCP-3arm-Cy3-Cy5 system, both by steady state and lifetime measurements allowed us to analyze the energy transfer pathways between Cy3, OCP^{O}, OCP^{R} and Cy5. The diagram presented in **Figure 75A** shows these pathways and the associated



B

k_1 ($\times 10^9$ s^{-1})	k_2 ($\times 10^9$ s^{-1})	k_3 ($\times 10^9$ s^{-1})
1.2	2.5	5.5

Figure 75. A. Schematics of the energy transfer pathways in the OCP-3arm-Cy3-Cy5 system. The Cy3 dye is the donor, and OCP^O, OCP^R and Cy5 are the acceptors. The black arrows represent the energy transfers, and the associated rate constants are indicated on them. The red arrows shows the interconversion between the two forms of the protein. The dashed arrow from Cy5 to OCP^R represents the negligible transfer from the Cy5 dye to the protein. **B.** Rate constants extracted from the data.

kinetic rate constants, whose values were calculated from the measurements discussed above and reported in **Figure 75B**. The knowledge of these parameters is fundamental for the design of future antenna systems that will use OCP as a quenching element.

The experiments performed and the data presented here have demonstrated that it is possible to incorporate OCP in a DNA-based antenna complex, and retain the functionality of the protein. In the OCP-3arm-Cy3-Cy5 complex, OCP acts as a light-responsive element that is activated under high light conditions and quenches the fluorescence of the dye molecule in the antenna. We successfully characterized the energy transfer rate constants in the system, and we are now understand more completely the parameters necessary to design larger and more complex networks of photonic elements incorporating OCP. OCP can be exploited for photoprotection, as it operates in natural systems, in case of high intensity illumination conditions, or it can be used as a regulatory element that can deviate energy from selected branches of a photonic network and be activated by tuning the intensity, or wavelength, of the excitation light.

Programmed coherent coupling in a DNA-based excitonic circuit

Natural light-harvesting complexes use protein scaffolds to spatially organize arrays of strongly-coupled pigments that direct energy transfer to the reaction center with near-unity efficiency. A major challenge and opportunity for nanotechnology is to rationally construct nanoscale excitonic circuits from the bottom-up to mimic natural light-harvesting assemblies by programming densely packed dye aggregates, such as cyanines. Structured DNA assemblies serve as chromophore scaffolds with nanometer-scale control over three-dimensional dye architectures to realize this aim. However, programmed dye aggregates that mimic the J-aggregate organization often observed in natural photosynthetic complexes have been limited to short, isolated units on single DNA duplexes. Further, rational control of emergent excitonic properties of these dye aggregates has not been achieved, including structure-based modeling to predict the emergent excitonic properties of multi-dye aggregates.

In the context of this MURI, we have used a bottom-up synthetic experimental-computational strategy to develop a highly programmable, rational means of controlling the targeted assembly and optical properties of excitonic circuits based on synthetic DNA. As detailed in last year's report, we have identified a set of fundamental J-aggregate units that serve as building blocks to construct fast, coherent energy transfer in arbitrary higher-order synthetic assemblies that mimic and extend beyond natural excitonic circuits. Specifically, we have used the natural propensity of

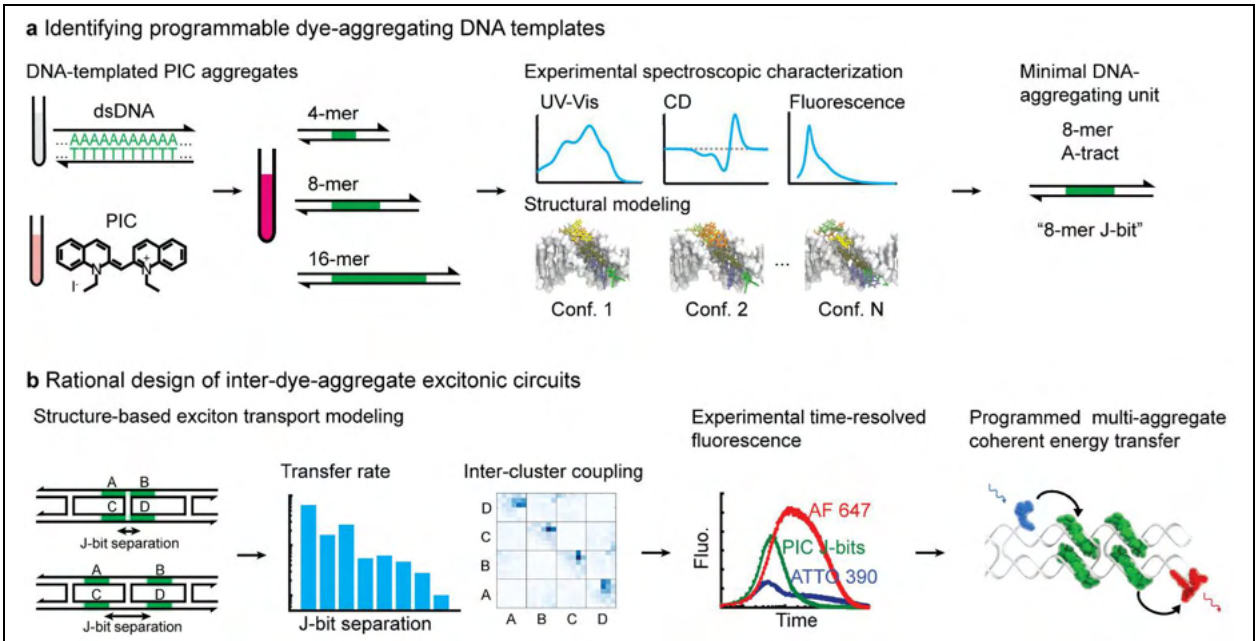


Figure 76. Schematic of programmable framework for synthetic DNA-based excitonic circuits. (**a**) pseudoisocyanine (PIC) dyes self-assemble on the minor groove of DNA A/T-tracts, forming a minimal dye-aggregating unit termed a "J-bit". (**b**) Rational design of inter-dye-aggregate excitonic circuits, formed by assembling J-bits into higher-order assemblies using anti-parallel DNA duplexes.

pseudoisocyanine dyes (PIC) to self-assemble into J-aggregates on short sequence-specific portions of DNA duplex, to create circuits in larger scale DNA nanoassemblies (**Figure 76**).

Next, we used the PIC J-bit to design higher-order DNA-PIC J-aggregates with custom optical properties to demonstrate the ability to design complex excitonic circuits using our bottom-up approach. DX-Tiles are the fundamental building block of DNA origami, in which two antiparallel DNA duplexes are rigidly constrained by two crossover junctions, offering the ability to design rings, sheets, and bundles of arbitrary size on the nanometer scale. DNA sequence was chosen to introduce four 8-mer A/T-tract binding sites surrounding the central staple double crossover. Optical properties and transport characteristics of these circuits can be predicted from the atomic-level conformation as predicted by molecular docking simulations. UV-Vis and CD spectroscopy on the synthesized DX-Tile circuits confirmed the formation of a J-aggregate structure, similar to the spectra that were theoretically predicted. Time-resolved spectroscopy also showed that quantum yield enhancement and increased lifetime were also present in these assemblies.

Finally, we used these DX-Tile assemblies to demonstrate J-bit mediated transfer between donor (ATTO390) and acceptor dyes (AF647), using both a two-step (**Figure 77a**), and three-step (**Figure 77b**) energy transfer pathway. In the two-step energy transfer experiment, steady-state fluorescence emission and relaxation kinetics measurements suggest strong transfer from the J-bits to AF647, with an estimated ~34-40% FRET efficiency. In the three-step energy transfer experiment, a ~10-fold increase in AF647 fluorescence was reported when including the PIC J-bits as an intermediate in the ATTO390 – AF647 chromophore system. Both of these results support the specific role of PIC J-bits in mediating efficient excitonic energy transfer.

We are currently extending this preliminary work in many research directions which will utilize the advantages of programming excitonic energy transfer circuits using DNA nanostructures. First,

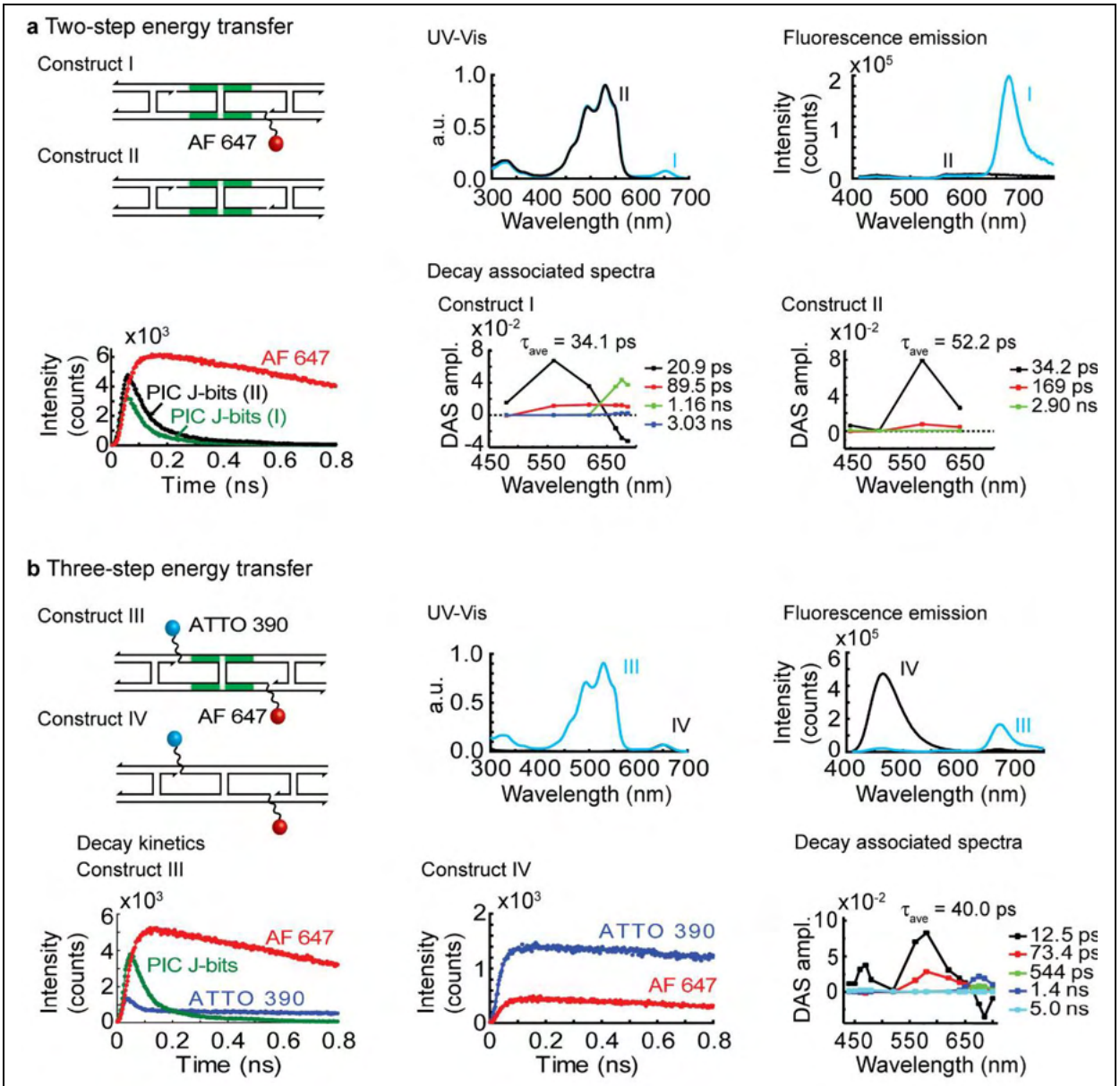


Figure 77. Programming two- and three-step energy transfer within the PIC DX-tile. (**a**) Two-step energy transfer from PIC-DX-tile to a single dye acceptor. The PIC DX-tile is excited with a 400 nm laser. The exciton is transferred to the Alexa Fluor 647 acceptor dye (I). Results are compared with a control structure without the final acceptor (II). (**b**) Three-step energy transfer mediated with PIC DX-tile. A donor dye (ATTO 390) is excited with a 400 nm laser. The exciton is subsequently transferred to the PIC DX-tile's J-bits, and to an Alexa Fluor 647 acceptor dye (III). Results are compared with a control structure with no PIC to mediate transfer (IV).

larger-scale DNA origami structures including rings, sheets, tubes, and lattices will be designed, taking advantage of the myriad of structural possibilities inherent in DNA nanotechnology. An automated framework to build DNA nanostructures of various shapes with user-programmed A/T-tract sequences is currently in development, and will allow the design of more complicated and potentially useful excitonic circuits. In **Figure 78**, we show an example of a larger DX-tile based DNA-dye assembly patterned for long-range excitonic transport. We can use excitonic models in

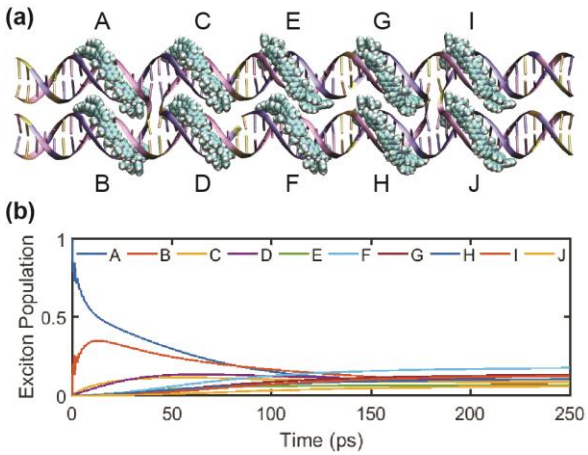


Figure 78. Excitonic transport in a 1D DNA-dye assembly. (**a**) Patterned DX-tile with 10 programmed A/T-tracts for binding of PIC J-bits. (**b**) Excitonic transport using the stochastic Schrodinger equation (SSE) formalism where the exciton is initially localized on J-bit A.

conjunction with an automated framework to screen DNA-dye assemblies for useful excitonic transport properties.

In the future we will also focus on broadening the scope of chromophore molecules that can be utilized in these excitonic circuits. Since our rational, structure-based design framework is general to DNA-chromophore aggregates, similar assemblies may be programmed using either covalently attached chromophores, intercalating, or base-substituting dyes. In particular, we envision using chem-informatic approaches to screen in-silico for chromophores, DNA architectures, and motifs with high absorption and exciton mobility, which can lead to the discovery of new materials for the development of high-performance excitonic circuits, inspired by recent success using similar methodology in the field of organic electronics. The present collaborative work is submitted and under revision.

Report Documentation Page, Standard Form SF298 – Enclosure 1

1. PERIOD COVERED BY REPORT: August 1, 2016 - July 31, 2017

2. PROPOSAL TITLE: Translating Biochemical Pathways to Non-Cellular Environments

3. CONTRACT/GRANT NUMBER: W911NF-12-1-0420

4. AUTHOR OF REPORT: Hao Yan

5. PERFORMING ORGANIZATION NAME AND ADDRESS:

Principal Investigator: Hao Yan
Arizona State University
PO Box 875601
Tempe, AZ 85287-1604

Administrative Contact: Patricia McGlynn
Office for Research and Sponsored Projects Administration
PO Box 876011
Tempe, AZ 85287-6011

6. AMSRD-ARL-RO-SI Proposal Number: 61781-LS-MUR

Report Documentation Page, Standard Form SF298 – Enclosure 2

1. SUBMISSIONS/PUBLICATIONS UNDER ARO SPONSORSHIP FOR THIS REPORTING PERIOD

(a) Total number of papers published in peer reviewed journals: 14

1. Carey, A-M, Zhang H-J, Mieritz D, Volosin A, Gardiner AT, Cogdell RJ, Yan H, Seo D-K, Lin S and Woodbury NW (2016) "Photocurrent generation by photosynthetic purple bacterial reaction centers interfaced with a porous antimony-doped tin oxide (ATO) electrode", *ACS Appl. Mater. Interfaces*, **2016**, 8 (38), pp 25104–25110

2. Zhang H-J, Carey, A-M, Jeon, K-W, Liu M, Murrell TD, Locsin J, Lin S, Yan H, Woodbury NW and Seo D-K (2016), "Highly Stable and Scalable Photosynthetic Reaction Centers-Mercapto Reduced Graphene Oxide System for Solar Energy Transduction", *J. Mater. Chem. A*, **2017**, **5**, 6038-6041

3. Zhang, H.; Jeon, K.-W.; Seo, D.-K. 'Equipment-free Deposition of Graphene-Based Molybdenum Oxide Nanohybrid Langmuir Blodgett Films for Flexible Electrochromic Panel Application' *ACS Appl. Mater. Interfaces*, **2016**, *8* (33), pp 21539–21544

4. Zhao, R.; Mieritz, D. G.; Chan, C.; Seo, D.-K. 'New NASICON-Type Hydrogen Titanium Phosphate Sulfate Electrodes for Li-ion and Na-ion Batteries' *J. Power Sources* **2017**, 10, 197-206.

5. Mieritz, D.; Li, X.; Volosin, A.; Liu, M.; Yan, H.; Walter, N. G.; Seo, D.-K. 'Tracking Single DNA Nanodevices in Hierarchically Meso-Macroporous Antimony-Doped Tin Oxide Demonstrates Finite Confinement' *Langmuir*, **2017**, *33* (25), 6410–6418.

6. Andreoni A., Lin S., Liu H., Blankenship R., Yan H., Woodbury N.W., An Orange Carotenoid Protein as a quenching element in a DNA based light harvesting antenna *Nano Lett.* **2017** Feb 8; 17(2):1174-1180.

7. Jinglin Fu, Gabriele Stankeviciute*, Sung Won Oh*, John Collins*, Yinghui Zhong and Ting Zhang "Self-assembled Nucleic Acid Nanostructures for Cancer Theranostics Medicines", *Current Topics in Medicinal Chemistry* **2017**, 17, 1-14.

8. Jinglin Fu, Renee Yang, Soma Dhakal, Zhao Zhao, Minghui Liu, Ting Zhang, Nils Walter and Hao Yan "Assembly of Multi-Enzyme Complexes on DNA Nanostructures", *Nature Protocol*, **2016**, 11,2243–2273.

9. Jinglin Fu and Tianran Li "Spatial Organization of Enzyme Cascade on a DNA Origami Nanostructure", invited book chapter for "3D DNA Nanostructures — Methods and Protocols", *Methods in Molecular Biology*, **2016**, Humana Press.

10. Scott Huston, John Collins, Fangfang Sun, Ting Zhang, Timothy D. Vaden, Y. –H. Percival Zhang and Jinglin Fu* "An Activity Transition from NADH Dehydrogenase to NADH Oxidase during Protein Denaturation", *BioTechnology and Applied Biochemistry*, **2017** accepted.

11. Pan, K.; Bricker, W. P.; Ratanalert, S.; Bathe, M. Structure and conformational dynamics of scaffolded DNA origami nanoparticles. *Nucleic Acids Res.* 45, 6284-6298 (**2017**).

12. Ponnuswamy N, et al. Oligolysine-based coating protects DNA nanostructures from low-salt denaturation and nuclease degradation. *Nature Communications* 8, 15654, (**2017**)

13. Iwaki M, Wickham SF, Ikezaki K, Yanagida T, Shih WM. A programmable DNA origami nanospring that reveals force-induced adjacent binding of myosin VI heads. *Nature Communications* 7, 13715, (**2016**)

14. F. Hong, S. Jiang, T. Wang, Y. Liu*, H. Yan*, 3D Framework DNA origami with Layered Crossovers, *Angew Chem Int Ed*. 128, 13024–13027, (**2016**).

(b) Total number of papers published in non-peer-reviewed journals: N/A

(c) Total number of presentations: 22

1. "DNA-crowded enzyme nanoparticles with improved activity and stability", oral presentation, The 6th International Conference on DNA Nanotechnology 2017, Beijing, China (presented by Jinglin Fu)

2. "Assembly of Bio-mimetic Multienzyme Complex on DNA Nanoscaffolds", oral presentation, 254th ACS National Meeting 2017, Washington DC. (presented by Jinglin Fu)

3. "Develop DNA-crowded enzyme nanoparticles for promoting activity and stability", oral presentation, ACS Middle Atlantic Regional Meeting 2017, Hershey. (presented by Jinglin Fu)

4. "Spatially Interactive Biomolecular Networks Organized by Nucleic Acids Nanostructures", invited talk, East Lake International Forum for Outstanding Overseas Young Scholars 2016, Wuhan, China. (presented by Jinglin Fu)

5. "DNA-crowded enzyme complexes with improved activity and stability", oral presentation, 252nd ACS National Meeting 2016, Philadelphia. (presented by Jinglin Fu)

6. “Assembly of multi-enzyme complexes on DNA nanoscaffolds”, oral presentation, 252nd ACS National Meeting 2016, Philadelphia. (presented by Jinglin Fu)

7. “Lego-Style Construction of Future Therapeutics From DNA”, 19th IUPAB congress, Edinburgh, UK, Invited Speaker, July 16-20, 2017 (Presented by William Shih)

8. “Lego-Style Construction of Future Therapeutics From DNA”, DNATEC17, Dresden, Germany, Invited Speaker, May 29- June 2, 2017 (Presented by William Shih)

9. “Lego-Style Construction of Future Therapeutics From DNA”, Gates-Ragon Global Health Innovation Partnership workshop, Cambridge, MA, Invited Speaker, April 24, 2017 (Presented by William Shih)

10. “Lego-Style Construction of Future Therapeutics From DNA”, GRC RNA nanotechnology, CA, Invited Speaker, January 22-27, 2017 (Presented by William Shih)

11. “Lego-Style Construction of Future Therapeutics From DNA”, Shanghai Institute of Applied Physics, Chinese Academy of Sciences, Shanghai, China (2016 September) (Presented by William Shih)

12. “Lego-Style Construction of Future Therapeutics From DNA”, Aarhus University, Aarhus, Denmark (2016 November) (Presented by William Shih)

13. “3D Digital Nanofabrication via DNA Self-Assembly”, Draper Programmable Assembly Workshop, Needham, MA, USA (2017 January) (Presented by William Shih)

14. “What Can RNA Nanotechnology Learn From DNA Nanotechnology?”, GRC RNA Nanotechnology, Ventura, CA, USA (2017 January) (Presented by William Shih)

15. “Lego-Style Construction of Future Therapeutics From DNA”, Rice University, Houston, TX, USA (2017 April) (Presented by William Shih)

16. “Lego-Style Construction of Future Therapeutics From DNA”, Yale Chemical Biology Symposium, New Haven, CT, USA (2017 May) (Presented by William Shih)

17. "DNA Actuated Enzyme Nanoreactors", SRC/IBM Workshop on Biological pathways for electronic nanofabrication and materials, San Jose, Nov. 17-18, 2016. (Presented by Hao Yan)

18. "Programmable Molecular and Material Systems" NSF Workshop on Midscale Instrumentation, November, 2016, Arlington, VA, (Presented by Neal Woodbury)

19. "Photocurrent Generation by Photosynthetic Bacterial Reaction Centers Interfaced with a Porous Antimony-Doped Tin Oxide (ATO) Electrode" 26th Western Photosynthesis Conference, Jan. 2017, CA, (Presented by Anne-Marie Carey)

20. "Porous Sol-Gel Metal Oxides for Sustainability Applications" Iowa State University, Oct. 21, 2016 (Presented by Don Seo).

21. "Porous Sol-Gel Metal Oxides for Sustainability Applications - From Bio/Nano Hybrid-based Solar Energy Conversion to Carbon Capture" Pohang Institute of Technology, South Korea, March 2, 2017 (Presented by Don Seo)

22. "Porous Sol-Gel Metal Oxides for Sustainability Applications - From Bio/Nano Hybrid-based Solar Energy Conversion to Carbon Capture" Arizona State University, Sept 1, 2017 (Presented by Don Seo)

(d) Total number of manuscripts:

Submitted: 2

1. Boulais, E.; Sawaya, N.; Veneziano, R.; Andreoni, A.; Banal, J.; Kondo, T.; Mandal, S.; Lin, S.; Schlau-Cohen, G.; Woodbury, N.; Aspuru-Guzik, A.; Bathe, M. Programmed coherent coupling in a synthetic DNA-based excitonic circuit. *Nat. Mater*. In Review.

2. Anne-Marie Carey, HaoJie Zhang, Minghui Liu, Daiana Sharaf, Natalie Akram, Hao Yan, Su Lin, Neal W. Woodbury, and Dong-Kyun Seo "Enhancing photocurrent generation in photosynthetic reaction center-based photoelectrochemical cells with biomimetic DNA antenna", submitted

In Preparation: 6

1. Bricker, W. P.; Bathe, M. Computational study of psuedoisocyanine dye aggregation behavior in solution. In Preparation Andreoni A., Lin S., Liu H., Blankenship R., Yan H., Woodbury N.W., An Orange Carotenoid Protein as a quenching element in a DNA based light harvesting antenna, *in preparation*

2. Adendorff, M. R.; Bricker, W. P.; Bathe, M. Sequence effects in immobile DNA four-way junctions: A computational study. *In Preparation*.

3. Andreoni A., Sedeh R.S., Cheng H., Enderlein J., Yan H., Bathe M., Woodbury N.W., Modeling and measurements of the diffusion properties of DNA nanostructures, *in preparation*

4. Daniel Mieritz, Runli Liang, Haojie Zhang, Anne-Marie Carey, Shaojiang Chen, Alex Volosin, Su Lin, Neal W. Woodbury, Dong-Kyun Seo "Effect of film thickness of meso-macroporous antimony-doped tin oxide on the performance of reaction center-based bio/nanohybrid photoelectrochemical cells", *in preparation*

5. Li, J., Johnson-Buck, A., Yang, Y.R., Yan, H., and Walter, N.G. Exploring the speed limit of toehold exchange with a cartwheeling DNA Walker. *To be submitted soon.*

6. Pal, N., Dhakal, S., Jiang, S., Yan, H., Liu, Y., and Walter, N.G. Characterizing Double Crossover DNA Tile Assembly at the Single Molecule Level Reveals Cooperativity. *In preparation*

(e) Total number of books: N/A

(f) Total number of honors and awards: 1

Ph.D.s Awarded: Nichole Michelotti, Matthew Marek, Vishalakshi Krishnan, Paul Lund, Corey Custer

(g) Title of patents disclosed during the reporting period: 2

1. "Nanocaged enzymes with enhanced catalytic activity and increased stability", US Provisional Patent. App. No. 62361884
2. "Assembly of large lipid nanodiscs stabilized by more than two MSP proteins" provisional patent filed in 2017

(h) Total number of patents awarded during the reporting period: N/A

2. STUDENT/SUPPORTED PERSONNEL METRICS FOR THIS REPORTING PERIOD

(a) Total number of graduate students: 3

Institution	Name	FTE	% Supported
ASU	Yu Zhou		5.83
U Mich	Jieming Li		100

(b) Total number of post doctorates: 10

Institution	Name	FTE	% Supported
ASU	Alessio Andreoni		1
ASU	Anne-Marie Carey		99.1
ASU	Zhilei Ge		100
ASU	Minghui Liu		53.4
ASU	Haojie Zhang		100
ASU	Xiaodong Qi		22.4
MIT	William Bricker		91.7
Harvard	Zhao Zhao		50
ASU	Sarthak Mandal		24.2
U Mich	Nibedita Pal		100

(c) Total number of faculty: 6

Institution	Name	FTE	% Supported
ASU	Hao Yan		15.6
ASU	Neal Woodbury		0
ASU	Don Seo		9.2
Harvard	William Shih		23
Rutgers	Jinglin Fu		0
MIT	Mark Bathe		5.8 summer

(d) Total number of undergraduate students: 2

Institution	Name	FTE	% Supported
ASU	Angela Christine Denton-Parrish		4.2
Rutgers	Gabriele Stankeviciute		0

(e) Graduating undergraduate metrics: N/A

(f) Total number of Master's degrees awarded: N/A

(g) Total number of Ph.D.'s awarded: N/A

(h) Total number of other research staff: 3

Institution	Name	Title	FTE	% Supported
ASU	Su Lin	Res Scientist		19.3
ASU	Chad Simmons	Asst Res Professional		61.6
MIT	Leila Bellou	Senior Research Support Associate		0.3

3. TECHNOLOGY TRANSFER

Remylop, LLC, one of the two spin-off startups from Don Seo's technologies, is currently commercializing its nanomaterials technologies. LG Chem, the largest chemical company in South Korea, has validated Remylop's proprietary material production technology and successfully completed pilot-testing of the new nanoporous materials for an undisclosed application with a market size over $600M/yr. In Phase II project, Remylop and LG Chem plan to bring the technology into commercial scale production and testing. In addition, Remylop is in talk with its Russian collaborators, companies and local government to bring its materials to Russian market for medical and household applications. Remylop is also in negotiation with a company in Sweden for commercialization of a different type of nanoporous materials for a different application with a market size over $20M.

4. SCIENTIFIC PROGRESS AND ACCOMPLISHMENTS (see technical report)

Translating Biochemical Pathways to Non-Cellular Environments

Principal Investigator: Hao Yan[1]
Co-PIs: Don Seo[1], Neal Woodbury[1], Mark Bathe[2], William Shih[3], Nils Walter[4], Jinglin Fu[5]

[1]Arizona State University, [2]MIT, [3]Harvard University, [4]U of Michigan, [5]Rutgers University

Reporting period: 8/01/16-7/31/17

I. Scientific and Technical Objectives

We intend to engineer and optimize nanoscale devices and systems based on important biochemical conversion pathways, where the converted species are molecules (enzymes transforming substrates into products), or energy, as is the case for photosynthesis. The use of DNA-directed assembly allows us to control and exploit the interactions between synthetic and naturally occurring bio-materials to produce highly functional biochemical conversion systems. Regarding enzyme transformations, our primary goal is to construct artificial enzyme cascades using two- and three-dimensional DNA structures as templates, and to study the ideal number of enzymes, relative distance, spatial arrangement, diffusion behavior, and reaction kinetics of the cascades in a controlled, non-cellular environment. Towards this goal, we initially focused on a representative DNA-templated GOx/HRP enzyme cascade and a more complex, bioelectroactive, NAD dependent dehydrogenase pathways, with the ultimate goal of interfacing our systems with external conductive materials. We aimed to achieve the following objectives during this reporting period: (1) develop DNA-crowded enzyme complexes with enhanced activity, (2) develop a general protocol of assembling multienzyme complexes on DNA nanostructures, (3) establish a method to produce large sized nanodisc for Poliovirus infection study using DNA origami as modular scaffold, (4) investigate the application of finite element methods to DNA nanotechnology and develop a general approach to calculate 3D solution shapes of arbitrary DX-based polyhedral designs, (5) develop a highly programmable, rational means of controlling the targeted assembly and optical properties of excitonic circuits based on synthetic DNA, (6) use single-molecule fluorescence resonance energy transfer (smFRET) to monitor a DNA tile reconfiguration process mimicking microtubules, (7) investigate the designed DNA walker on 2- and 3-step DNA tile walking systems, 2D high-density DNA-strand modified surface and the mechanism of walking through smFRET.

Regarding photosynthesis, our aim is to develop methods for translating energy conversion pathways to non-cellular environments where their functions can be more easily manipulated. The approach is to use rationally designed DNA nano-scaffolds to engineer light-harvesting networks containing synthetic pigments, interfaced with energy conversion proteins (photosynthetic reaction centers) from natural photosynthetic organisms. We intend to precisely position functional elements on the DNA scaffolds, generating energy and electron transfer pathways in which inter-molecular interactions can be predictably designed, and the local environment can be controlled. We hope to engineer systems with more uniform light absorption, efficient energy transfer and conversion, and improved photo-stability for maximum performance. Here, we are exploring ways to effectively interface the light-induced redox potentials generated by photosynthetic reaction centers from purple bacteria with novel nano and meso-structured electrode materials. Toward

this end, two different types of materials were utilized: nanoporous transparent metal oxides and functionalized reduced graphene oxides. We are also exploring ways to incorporate a light-responsive photo-protective element into a DNA-templated artificial antenna system to adapt its photoprotection function for light regulation. We have also used a bottom-up synthetic experimental-computational strategy to develop a highly programmable, rational means of controlling the targeted assembly and optical properties of excitonic circuits based on synthetic DNA. In line with DoD goals, the proposed research will increase our understanding of nanoscale energy transfer processes and aid in the development of robust strategies for the synthesis, characterization, and assembly of synthetic biochemical pathways for application in high-efficiency photo-energy generation, energy storage devices, sensors, or completely new capabilities that enhance war fighter and battle system capabilities.

II. Expanded Accomplishments

Enzyme Pathway

DNA crowded-enzyme complexes with enhanced activities

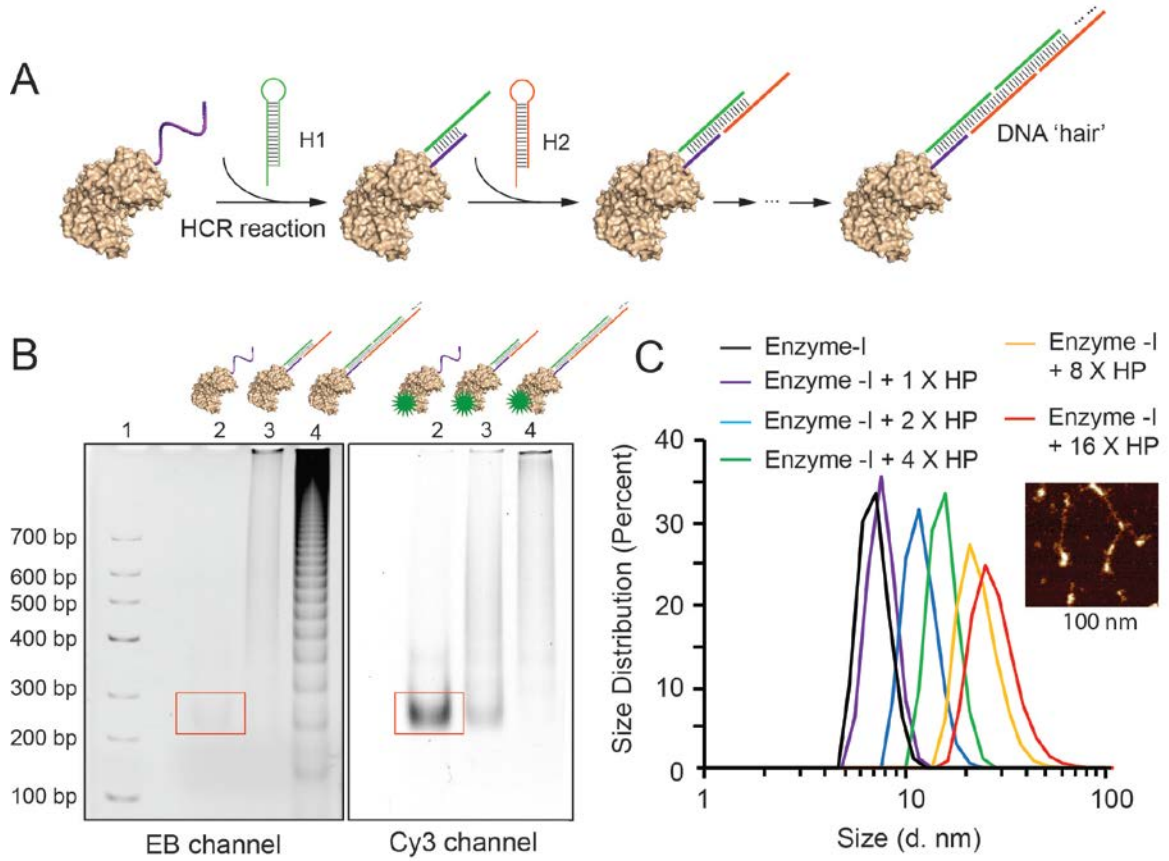


Figure 1. The design and characterization of DNA-crowded enzymes. (A) The construction of long DNA duplex on an enzyme surface by HCR. (B) (3%) PAGE characterization of DNA-crowded enzymes with EB staining (left) of DNA and fluorescent imaging (right) of Cy3-labelled G6PDH. Lane 1: DNA ladder; Lane 2: 1 μM initiator-conjugated G6PDH (G6PDH-I); Lane 3: 1 μM G6PDH-I + hairpins (1×); Lane 4: 1 μM G6PDH-I + hairpins (10 ×). (C) DLS analysis of DNA-crowded enzyme sample with the titration of HPs-to-enzyme ratios. Inset: AFM imaging of DNA-crowded enzyme complex.

As shown in **Figure 1A**, the construction of DNA-crowded enzyme complex involves two steps: (1) the conjugation of an initiator strand to an enzyme (enzyme-I) and (2) the growth of double-strand DNA (dsDNA) on the enzyme surface by the initiator-triggered hybridization chain reaction (HCR). One initiator on the enzyme surface can trigger the growth of a long dsDNA with the alternative hybridization of hairpin 1 and 2. The relative length of dsDNA was determined by the initiator-to-hairpin ratio, where excess hairpins resulted in longer dsDNA by HCR. The long HCR duplex on the enzyme surface behaves as a flexible 'DNA hair' to crowd the enzyme (Non-nick dsDNA's persistence length is ~ 50 nm. But a HCR duplex has many nick points that make it easier to bend). As shown in **Figure 1B**, the gel electrophoresis was used to characterize the growth of dsDNA on the enzyme surface, where larger dsDNA with slower mobility was observed with the addition of more hairpins. The fluorescent imaging of Cy3-labelled enzyme showed that the enzyme was migrated together with the large dsDNA. As shown in **Figure 1C**, dynamic light scattering (DLS) was used to characterize the hydrodynamic diameters of multiple enzyme-HCR complexes in solution phase. An enzyme-initiator conjugate showed a peak diameter ~ 7 nm. The diameter of enzyme-HCR complexes was increased from ~ 8 nm to ~ 30 nm with the addition of hairpins from 1-fold to 16-fold excess. We also used atomic force microscopy (AFM) to directly visualize DNA-crowded enzymes on mica surface, where long DNA "hairs" were observed with the attachment of bright spots of proteins.

Next, we evaluate the enzyme activities depending on the growth of long dsDNA on the enzyme surface. As shown in **Figure 2A**, G6PDH-initiator (G6PDH-I) conjugate was incubated with excess hairpins from 1 to 128-fold for initiating the growth of dsDNA on the enzyme surface by HCR. The activity of G6PDH-I/HCR complex was increased as the addition of more hairpins, with more than 200% enhancement when G6PDH-I was incubated with 16-fold or more hairpins. As a control, non-initiator conjugated enzymes were also incubated with excess hairpins, but these enzymes only showed slightly increased (< 20%) activities. Similar results were also observed for HRP- HRP-HCR complex which showed more than 300% enhanced activity by adding 32-fold or more HPs (**Figure 2B**). These results demonstrated the enzyme activity was significantly boosted when a long dsDNA was grown on the enzyme surface. To evaluate the effect of labelled numbers for initiator strands, we conjugated and purified HRP with 1, 2 and 3 initiators. Activities of HRP were affected little by conjugating to DNA strands. As shown in **Figure 2C**, HRP-I_2/HCR and HRP-I_3/HCR showed higher activities than HRP-I_1/HCR, possibly due to the fact that more

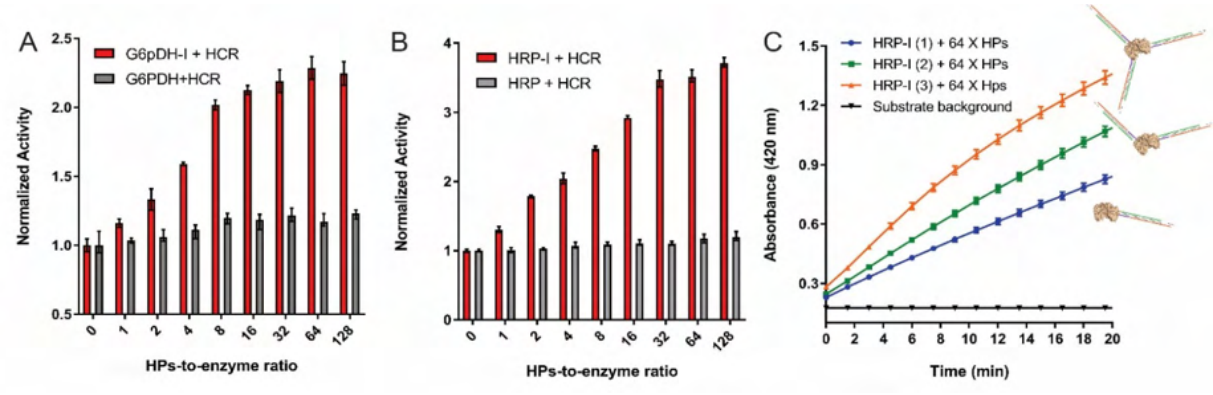


Figure 2. Evaluation of DNA-crowded enzyme complexes. (A) Titration of HPs-to-enzyme ratio for affecting DNA-crowded G6PDH activity; (B) Titration of HPs-to-enzyme ratio for affecting DNA-crowded HRP activity. (C) Titration of labelled initiators per enzyme for affecting DNA-crowded HRP activity. Error bar: range of data.

dsDNA duplexes were induced to grow on the enzyme surface. However, many enzymes may show reduced activities as conjugating more DNA molecules (> 3) to the enzyme surface (e.g. G6PDH-I_3) To avoid the significantly damaged activities, we suggested conjugating two initiator strands to one enzyme for triggering dsDNA growth on the enzyme surface.

To gain more mechanistic insight of the enhanced enzyme activities, we tested the Michaelis-Menten kinetics for HRP-I_x/HCR and G6PDH-I_x/HCR complexes. As shown in **Table 1**, HRP-I_1/HCR, HRP-I_2/HCR and HRP-I_3/HCR all showed increased turnover numbers as compared with none-HCR enzymes of HRP-I_1, HRP-I_2, and HRP-I_3, indicating an inherently higher catalytic activity of the enzymes. HRP-I_2/HCR and HRP-I_3/HCR showed ~ 2.7-hold enhancement of k_{cat} values, whereas HRP-I_1/HCR showed less enhancement, ~ 1.6-hold. The difference of enhanced turnover numbers is consistent with the observation that enzymes labelled with more initiator strands produced more activity (**Figure 2C)**. Similarly, G6PDH-I_x/HCR complexes also showed higher turnover numbers (~ 2 -3 fold) than non-HCR enzymes. However, G6PDH-I_3/HCR ($k_{cat, NAD}$~ 210 s^{-1}) was less active than G6PDH-I_1/HCR ($k_{cat, NAD}$~ 327 s^{-1}) and G6PDH-I_2/HCR ($k_{cat, NAD}$~ 378 s^{-1}), which could be resulted from the low activity of G6PDH-I_3. In contrast, K_m (Michaelis-Menten constant) values varied little between enzyme-HCR and free enzyme-initiator for most substrates, suggesting that the HCR duplex does not substantially hinder diffusion of small-molecule substrates.

Enzyme	pI	Molecular Weight	Substrate	Enzyme-I		Enzyme-HCR	
				K_m (μM)	k_{cat}(s^{-1})	K_m (μM)	k_{cat}(s^{-1})
HRP-I(1)	8.8	44 kD	H_2O_2	19±2	84±2	19±1	137±2
HRP-I(2)	8.8	44 kD	H_2O_2	21±2	74±1	23±1	203±2
HRP-I(3)	8.8	44 kD	H_2O_2	19±1	77±1	24±1	225±3
G6PDH-I(1)	4.3	100 kD	G6P	335±44	105±5	333±30	289±9
			NAD^+	627±63	129±5	625±35	326±8
G6PDH-I(2)	4.3	100 kD	G6P	446±49	83±3	447±42	285±10
			NAD^+	673±78	133±7	673±68	378±16
G6PDH-I(3)	4.3	100 kD	G6P	602±52	48±2	519±42	144±5
			NAD^+	785±60	61±2	711±51	210±6

Table 1. Enzyme kinetic data (values of K_m and k_{cat}) for each individual enzyme-HCR complex in comparison with the values for enzyme-initiator conjugates. The Michaelis-Menten plots of each enzyme and the conditions of the enzyme activity measurements can be found in the method. The pI values of the enzymes were obtained from brenda-enzymes.org.

In addition to enhanced turnover numbers for catalysis, the enzyme-HCR complex also showed increased stability against various denaturation conditions, such as long-term storage, freeze-thaw cycles and thermal incubation. As shown in **Figure 3A**, we tested the stability of enzyme solutions against long-term storage at room temperature (25 °C). All HRP-HCR complexes showed more

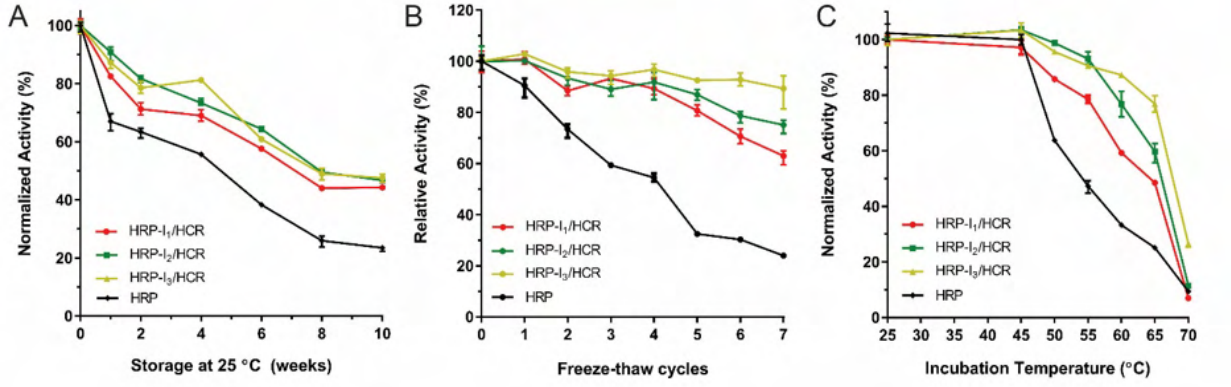


Figure 3. Evaluating the stability of DNA-crowded enzyme against (A) long-term storage under room temperature; (B) freeze-thaw cycles and (C) thermal incubation.

stable activities as compared with HRP wildtype. For example, at the 10th week, HRP-HCR complexes retained ~ 50% of original activities, whereas individual HRP only retained ~20% of original activities. In **Figure 3B**, HRP-HCR complexes were more stable against multiple freeze-thaw cycles than wildtype HRP. It was also noticed that HRP-I_3/HCR (retain~ 90% activity at 10th cycle) was more stable than HRP-I_1/HCR (retain~ 63% activity at 10th cycle) and HRP-I_2/HCR (retain~ 75% activity at 10th cycle), as well as HRP wildtype (retain~ 24% activity at 10th cycle). To rule out the potential absorption of enzymes onto the tube walls during the incubation, we used a Cy3-labelled enzyme to monitor the solution fluorescence during the incubation period. The Cy3-labelled enzyme solution did not show significant decrease of fluorescence during either long-term storage or freeze-thaw cycles, which suggested that the concentration of solution enzymes did not alter significantly during the incubation. In **Figure 3C**, HRP-HCR complexes showed an increased thermal stability of enzyme from 45 – 70 °C.

In summary, we have developed a simple and robust method for assembling DNA-crowded enzyme complex with promoted enzyme activity and increased stability. By conjugating an initiator strand to an enzyme, we were able to initiate the growth of long dsDNA on the enzyme surface to increase local DNA crowding. The number and length of DNA duplexes were controlled by the copies of labelled DNA initiators and the addition of hairpins. The enzyme-HCR complexes exhibited increased turnover numbers of 2- to 3-fold higher than that of the free enzymes. Conversely, the K_m values remain similar between enzyme-HCR complexes and free enzymes, indicating an uninterrupted diffusion of small-molecule substrates and products through the surface-grown DNA duplexes. The enhanced activities of enzyme-HCR complexes were consistent with recently reported enzyme/DNA hybrid nanostructures, which might be attributed to the local DNA crowding with high density of negatively charged phosphate groups. This effect appears consistent with recent independent evidence that many conserved metabolic enzymes are stabilized by polyphosphate and associate non-specifically with nucleic acids through cryptic

binding sites, thus taking advantage of the high polyanionic DNA and RNA contents of the cell. Unlike DNA origami nanocages with application limit of low achievable concentration, the small production scale and the high cost of complex oligonucleotides, the assembly of DNA-crowded enzyme particles only involved three strands of one initiator and two hairpin substrates. The concentration and production of enzyme particles can be easily scaled up to high micro-molar concentrations for practical use. In the future, it may be feasible to crosslink multiple DNA-crowded enzyme particles into nanocrystals and hydrogels which can stabilize enzymes against various denaturations, as well as facilitating the multi-enzyme catalysis. The DNA-crowded enzyme particles may also find utility in theranostic applications as therapeutic agents and drug delivery.

A general protocol of assembling multienzyme complexes on DNA nanostructures.

Over the past four years, we have developed protocols for the robust assembly, purification and characterization of multi-enzyme complexes organized by DNA nanoscaffolds. These protocols have been successfully employed to develop a series of artificial enzyme complexes with functions such as facilitated inter-enzyme substrate diffusion, biocatalytic swinging arms, compartmentalized enzyme cascades and regulated enzyme nanoreactors. Here, we present detailed protocols for exploiting DNA nanostructures as assembly scaffolds that organize the spatial arrangements of multi-enzyme cascades with control over their relative distance, compartmentalization, and substrate diffusion paths. The protocol describes the preparation and purification of DNA-conjugated enzymes and cofactors, along with the assembly of these prepared complexes on DNA nanostructures. The architecture of assembled enzyme complexes is then readily characterized using a broad selection of techniques from routine gel electrophoresis to advanced single-molecule imaging. We also describe methods to purify these nano-assemblies and test them with functional assays based on either bulk or single-molecule fluorescence measurements. The entire assembly and characterization of a multi-enzyme complex can be completed within one to two weeks.

1. Spatially addressable DNA nanostructures for positioning enzymes:

Spatially addressable assembly is one of the most attractive features of DNA nanostructures, due to the well-defined geometry of the DNA double helix and the unique sequence of each oligonucleotide that encodes the overall architecture of the structure. As shown in **Fig. 4a**, the B-form DNA double helix has well-defined structural characteristics in aqueous solution, such as a helical diameter of ~2.4 nm, a helical rise of ~3.4 nm for each of 10.5 base pairs (bps), and an ~34.3° rotation angle between two adjacent base pairs. Using DNA nanostructures as the assembly templates, enzymes can be positioned with controlled parameters of spatial distance (**Fig. 4b**) and relative anchor angles (**Fig. 4c**), as well as the geometric arrangement and stoichiometry of the participating enzymes (**Fig. 4d**). **Fig. 4 e-h** shows an example of positioning of a two-enzyme glucose oxidase (GOx)/horseradish peroxidase (HRP) cascade on a rectangular DNA origami with distances ranging from 10-nm, 20-nm, 45-nm to 65-nm. A statistically significant analysis of the inter-enzyme distances (anchor-to-anchor) for the enzyme pair was performed by atomic force microscope (AFM). The spatial dimensions of a scaffolding DNA nanostructure are described as following:

- The distance between two anchor positions along the same helix is determined by the number (p) of helical repeats between them:
  $Distance \sim 3.4\ nm \times p\ ;\ p = \frac{n+1}{10.5}$
  n is the number of spacing nucleotides.
  Note: p must be an integer number for the anchors on the same plane.
- The distance between two anchor positions perpendicular to the helix long axis can be determined by the number (m) of spacing helices between them:
  $Distance \sim 2.4\ nm \times (m+1)$
- The relative angle between two anchor positions can be controlled approximately by the rotation angle between base pairs (bps):
  $\theta \sim 34.3\ ^\circ * (n+1)$;
  n is the number of spacing bps.

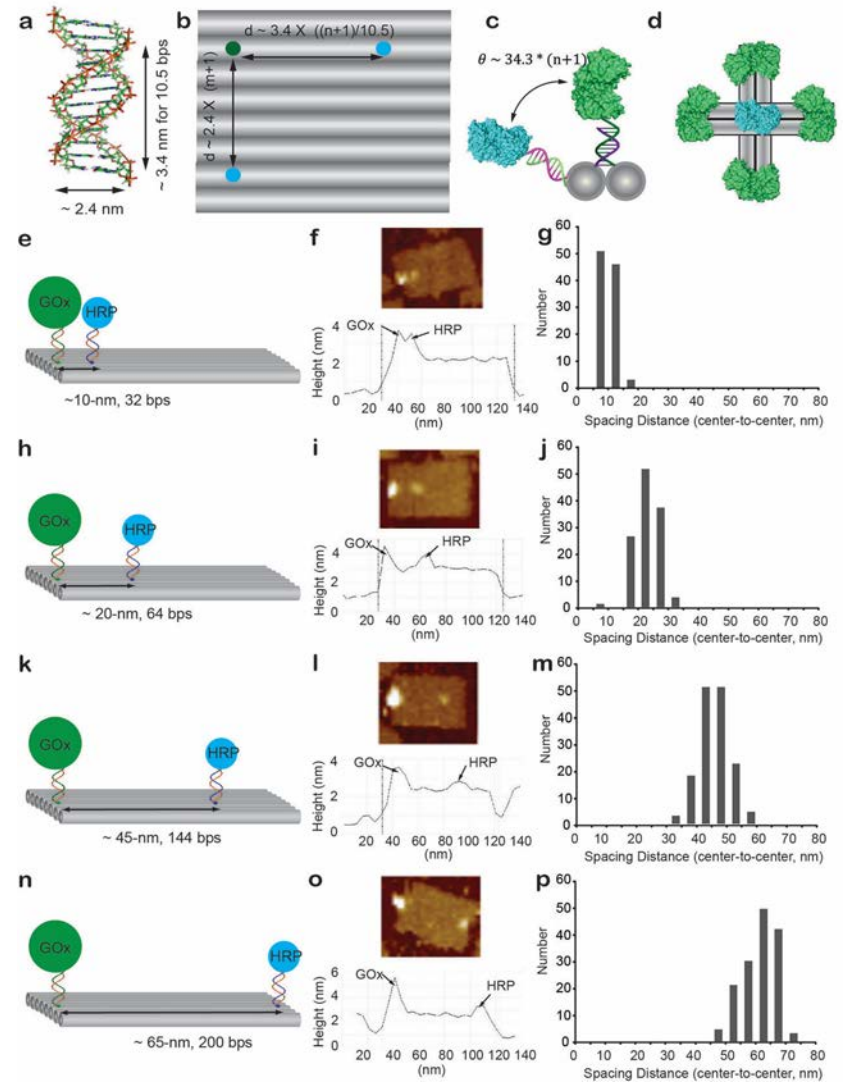


Figure 4. The assembly of enzymes on spatially-addressable DNA scaffolds. (a) DNA double-helix. Position of molecules on the DNA nanostructures with controlled (b) spacing distances, (c) relative angles, and (d) geometric arrangements. (e) The organization of a pair of GOx/HRP enzyme cascade on a rectangular DNA origami tile with 10-nm spacing distance, (g) AFM characterization of the height profile where the assembly of two enzymes results in the brighter spots due to the increased height than the surface of a DNA origami and (h) the statistical analysis of the observed inter-enzyme distances. The GOx/HRP pair is also assembled and characterized with the spacing distance of (h-j) 20-nm, (k-m) 45-nm and (n-p) 65-nm on the DNA origami tiles.

Examples of such angles are: ~ 100° for 2 spacing bps, ~ 170° for 4 spacing bps, and ~ 270° for 7 spacing bps.

2. Protocol overview:

The general strategy of assembling enzyme complexes on DNA nanostructures is illustrated in **Fig. 5a**. An enzyme is chemically conjugated to a single-stranded oligonucleotide, which serves as an anchor to hybridize with the corresponding complementary capture strand that is displayed on the surface of a DNA nanoscaffold. **Fig. 5b** shows the general flow chart of the assembly, purification and characterization of the multi-enzyme complexes on the DNA nanostructures. The entire protocol includes the following key steps: (1) the preparation and purification of DNA-conjugated enzymes/cofactors; (2) the assembly of enzyme complexes onto DNA nanostructures; (3) the characterization of the assembled enzyme complexes; (4) the purification of assembled enzyme complexes; and (5) the activity evaluation at the bulk and single-molecule level. The detailed procedures was published on *Nature Protocols*.

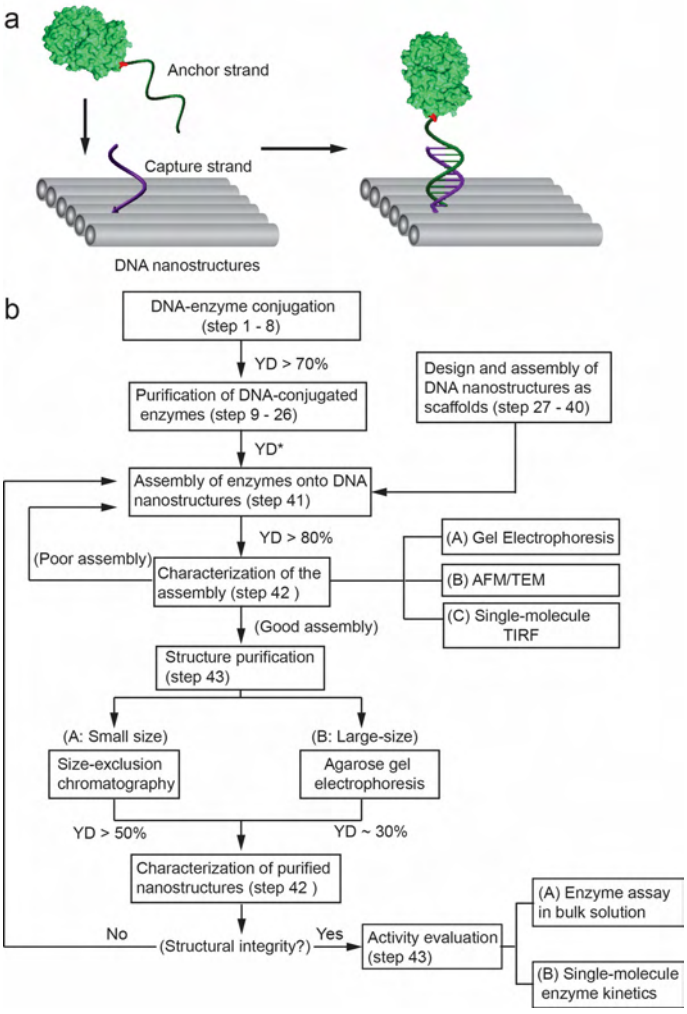


Figure 5. Overview of DNA nanostructures-scaffolded assembly of multi-enzyme complexes. (a) The assembly strategy of hybridizing a DNA-conjugated enzyme with a complementary capture strand displayed on the surface of a DNA nanostructure. **(b)** The overview protocol of the assembly, purification and characterization of multi-enzyme complexes organized by DNA nanoscaffolds. Corresponding procedure steps and estimated yields are labelled on the workflow.

DNA origami as modular scaffold to produce large sized nanodisc

1. DNA barrel scaffolded 60-nm sized nanodisc production:

Phospholipid bilayer nanodiscs provide a detergent-free lipid bilayer model, enabling biochemical and biophysical characterization of membrane proteins in a physiologically relevant environment. A traditional nanodisc is composed of a nanometer-sized phospholipid bilayer patch encircled by two copies of an alpha helical, amphipathic membrane scaffold protein (MSP). To date, however, the utility of this system for structural studies has been limited by the heterogeneity in size and the number of membrane proteins enclosed, and only small nanodiscs can be constructed with currently available protein scaffolds. To overcome these limitations we developed a modular method using DNA origami barrel as scaffold to produce nanodiscs with much larger homogenous sizes.

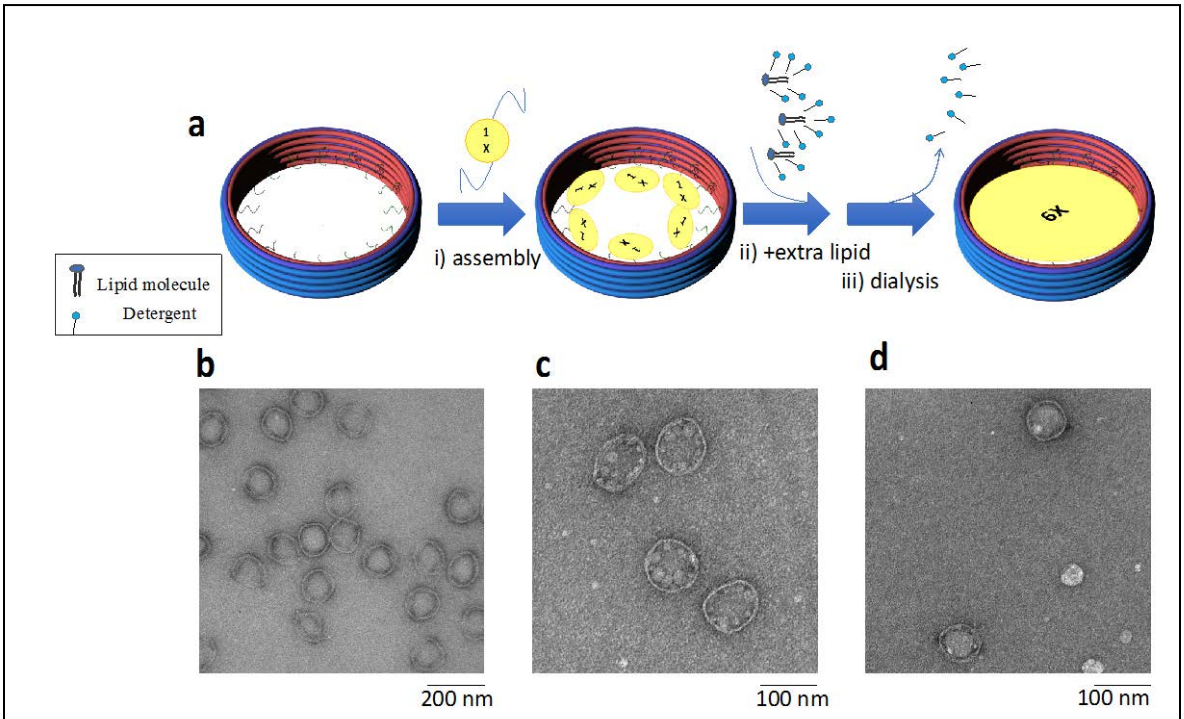


Figure 6. DNA Origami scaffolded reconstitution of large sized nanodisc. A) Schematic of large sized nanodisc reconstitution using DNA Origami through three steps procedure: i) DNA Origami directed 10-nm nanodisc assembly through hybridization between DNA handles from origami nner face and ssDNA conjugated onto nanodisc; followed by ii) incubation with extra amount of lipid molecules and iii) dialysis to remove detergent to reconstitute large sized nanodisc. B), C), D) represent negative staining TEM images of DNA origami after each steps.

As shown in Figure 6, Oligonucleotide-conjugated 10-nm diameter nanodisc are site-specifically placed onto the interior surface of a DNA-origami barrel, which create a high local concentration of 10-nm diameter nanodisc. After adding extra lipid and detergent to disrupt lipid membrane, a large sized (60-nm diameter) nanodisc can be formed during a reconstitution procedure. The growth of the 60-nm diameter nanodisc is confined by the surrounding double-stranded DNA

helices, so the final geometry of the lipid nanodisc is complementary to hollow cavity within the DNA barrel.

To assemble 10-nm nanodisc with DNA barrel, MSP with 3 cysteine mutant (equally ditributed equally on protein structure) was expressed, and utilized to reconstitute nanodisc, followed by chemically conjugating with amine-modified DNA through cross-linkers, sulfo-SMCC. The DNA-origami barrel, 75 nm in inner diameter, constituted as three layers of DNA helix rings and 36 ssDNA extensions as handles, was designed using the software caDNAno, and folded in a one-pot reaction by combining single-stranded viral DNA (p7308) with ~250 synthetic oligonucleotide strands using a 20 h thermal annealing program. Correctly folded structures were isolated by glycerol-gradient centrifugation28 and verified by negative-stain transmission electron microscopy (TEM) (Fig. 6b). Through hybridization between DNA extension from origami inner face and ssDNA on nanodisc, 10-nm diameter nanodisc can be assembled into origami barrel, as shown in Figure 6c. Statistic counting showed that roughly 6-10 nanodisc was assembled onto each barrel. To make larger sized nanodisc, we first add extra lipid and detergent to disrupt lipid membrane. Next, dialysis method was utlized to remove detergent for homogenous large sized nanodisc formation. As shown in Figure 6d, a thin white layer formed inside barrel, with roughly 70% efficiency.

2. DNA barrel scaffolded large sized nanodisc for Poliovirus infection study:

Next, we used DNA scaffolded nanodiscs as model membranes to study the question of how simple nonenveloped viruses transfer their genomes across membranes to initiate infection. Although there are now several model systems being used to study this process, the mechanism of genome translocation remains poorly understood, and a more detailed structural analysis of the membrane-associated forms of the cell-entry intermediates is required. So far, mechanistic insights have been limited, due in part to technical difficulties involved in direct visualization of viral gene delivery

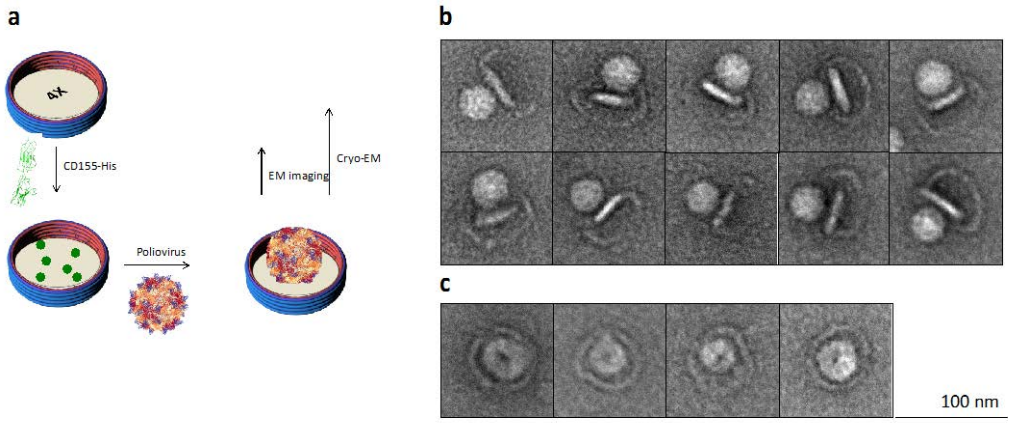


Figure 7. DNA origami scaffolded nanodisc for Poliovirus entry study. A) Schematic of experiment design, DNA Origami scaffolded nanodisc was decorated with CD155 first, then incubate with Poliovirus at 37 °C for 10 min before checking with negative staining TEM. B) Negative staining TEM image of step 1: poliovirus bind with nanodisc; C) Negative staining TEM image of step 2: pore formation on nanodisc by poliovirus infection. (Scale bar: 100 nm)

and size heterogeneity of liposomes.

Poliovirus (~30-nm diameter) is the prototype member of the enterovirus genus of the picornavirus family. Viral infection is mediated by a specific receptor, CD155. The receptor catalyzes a conformational rearrangement and expansion of the virus particle. The expanded virus is then endocytosed by a noncanonical, actin-independent pathway, and the RNA is released across the endosomal membrane. The 60-nm nanodisc is sufficiently large to accommodate multiple CD155 copies and has enough surface area to act as a surrogate membrane for the RNA-translocation complex during viral uncoating.

To prepare large sized nanodisc for Poliovirus infection study, we first added 2% NTA-lipid during reconstitution process, which can induce binding of CD155 through His-tag NTA interaction. CD155 decorated large nanodisc then incubated with Poliovirus at 37 °C for 10 min before negative staining TEM imaging, as shown in Figure 7. Initially, virus bind with nanodisc (shown in Figure 7b), followed by a potential hole punching on membrane surface (shown in Figure 7c).

3. Future directions:

Work in now in progress to (a) Cryo-EM imaging of nanodisc-poliovirus sample for structure determination; b) Test of a new virus, Rotavirus using 60-nm sized nanodisc to study infection process.

Structure-based modeling of large-scale DX-based assemblies

A recent paper (Veneziano et al. 2016) demonstrated an arbitrary scaffolding procedure for designing DX-based polyhedral nanoparticles based on a geometric design, and showed distinct geometrical features of these nanoparticles using cryo-EM imaging. We apply a new bulge and open nick motif to our off-lattice CanDo implementation, so that these polyhedral DX-based nanoparticles can be accurately modeled using a finite element procedure.

We have continued our investigation of the application of finite element methods to DNA nanotechnology and developed a general approach to calculate 3D solution shapes of arbitrary DX-based polyhedral designs based on a coarse-grained finite element model using a lattice-free sequence and topology design. The sequence and topology of a DNA nanostructure is designed using computer-aided design (CAD) software such as Tiamat (Williams et al. 2009) for the off-lattice design, and caDNAno (Douglas et al. 2009), for the on-lattice design. The design file is then read by a parser that interprets the design as a graph with bases modeled as vertices and phosphodiester bonds and Watson-Crick basepairing modeled as edges. We extend our previous implementation of off-lattice CanDo (Pan et al. 2014), which predicts structural, mechanical, and thermodynamic properties of a programmed DNA assembly by developing an improved bulge and open nick motif. Our current implementation of off-lattice CanDo is capable of modeling the following design motifs shown in Figure 8: duplexes, nicks, single-stranded DNA (ssDNA) regions, double crossovers, single crossovers, open nicks, and bulges (Pan, Bricker, et al. 2017).

Rotational stiffness coefficients [pN nm rad^{-1}]	Double crossover	Single crossover	Open nick	Bulge
About axis **x**	1353	1353	13.53	13.53
About axis **y**	1353	1353	0	0
About axis **z**	135.3	13.53	13.53	13.53

Table 2. Rotational stiffness coefficients of the double crossover, the single crossover, the open nick, and the bulge.

In Figure 8, an isolated duplex has the geometry of a straight-line segment of length L_0N, where L_0 = 0.34 nm per nucleotide. The duplex has an empirical stretch modulus of 1,100 pN, a bend modulus of 230 pN nm^2, and a twist modulus of 460 pN nm^2 (Kim et al. 2012). The connection of

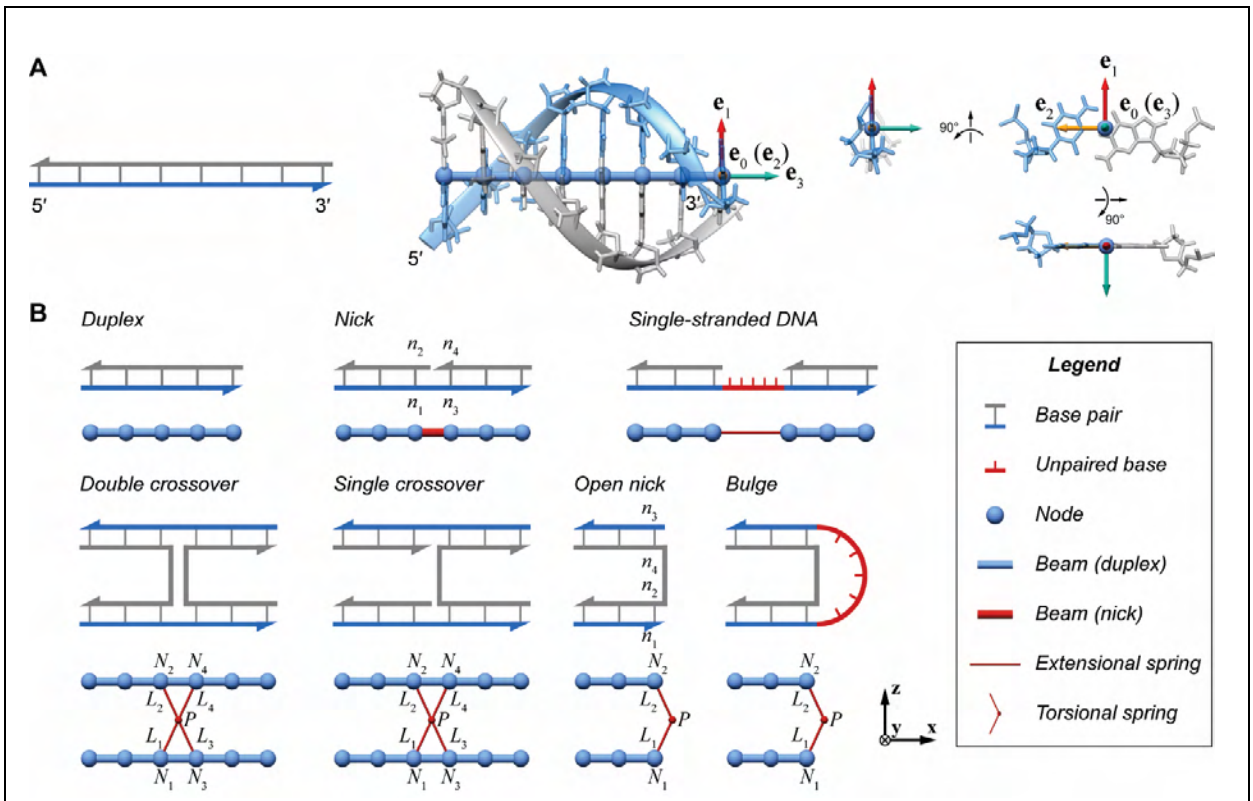


Figure 8. Mechanical models of secondary structural motifs for programmed DNA assemblies. A Each base pair in the secondary structure of a programmed DNA assembly (left) is modeled as a FE node, which corresponds to the all-atom model (center, right). **B** A set of secondary structural motifs and their corresponding FE models in programmed DNA assemblies.

two stacking base pairs in a duplex is modeled as a beam element with geometric and mechanical properties from experimental values of B-form DNA. Duplexes with a nick between two stacked base pairs are assumed to have the same ground-state geometric and mechanical properties as B-form DNA, thus, they are modeled using the same beam element as a duplex (Kim et al. 2012). Unstacked, or open nicks, are modeled using a 100-fold reduced bending and twisting stiffness factor, as shown in Table 2, and ssDNA is modeled to have nonlinear spring-like mechanical properties of an extensible worm-like chain (Kim et al. 2012).

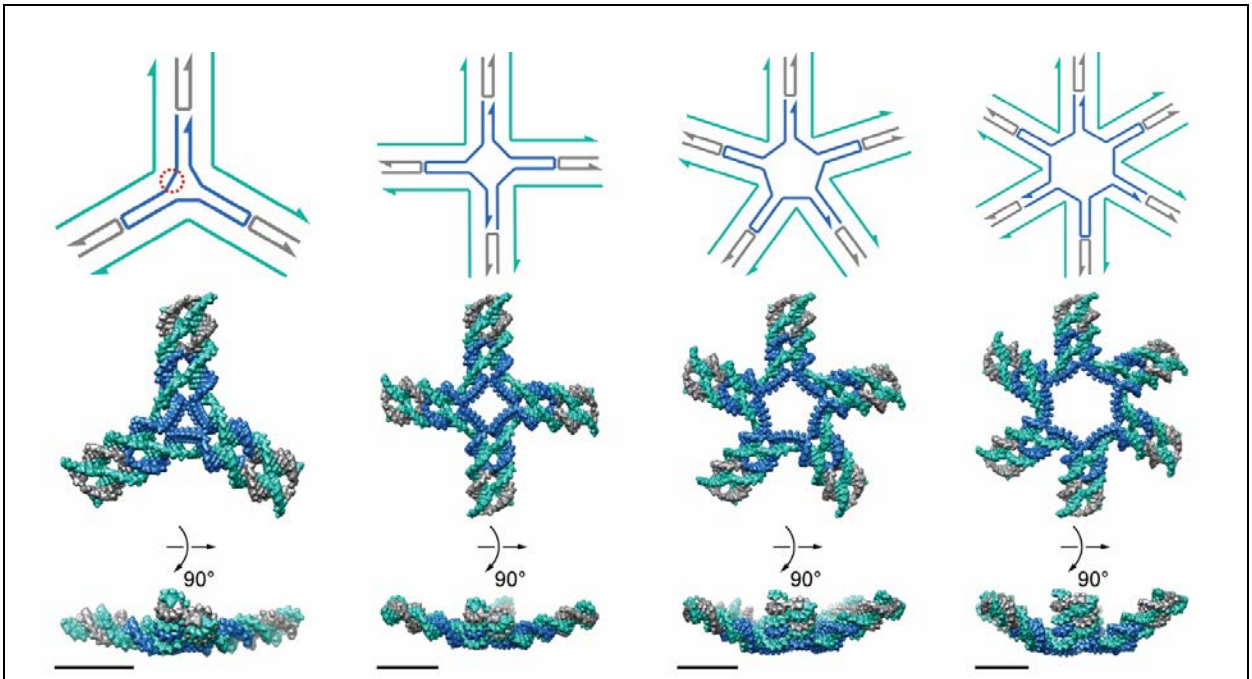


Figure 9. Mechanical models of unconstrained multi-arm vertices. Secondary structures and corresponding FE models (top) at the ground-state mechanical free energy (bottom) of 3-arm, 4-arm, 5-arm, and 6-arm vertices consisting of duplexes, double crossovers, single crossovers, and bulges.

Double crossovers and single crossovers are modeled similarly, and for arbitrary polyhedral nanoparticles have a ground-state geometry defined by two antiparallel duplexes with an interhelical distance of 1.85 nm and a right-handed interhelical angle of 0°. The mechanical properties of a double crossover are represented by a torsional spring with linear stiffness connecting two duplexes. Single crossovers are assumed to have an identical ground-state geometry to double crossovers, except that the rotational stiffness about axis **z** is reduced by a factor of 10 (Table 2). The ground-state geometry of open nicks and bulges is similar to that of a double crossover, except that the base pairs on one side of the pivot point, *P*, are removed. Compared to double crossovers, the rotational stiffness coefficients of bulges about axes **x** and **z** are reduced by factors of 100 and 10, respectively. We assume the three rotational stiffness coefficients of open nicks are identical to those of bulges, due to their similar secondary structure (Table 2) (Pan, Bricker, et al. 2017).

As unconstrained *N*-arm vertices are the building blocks of DX-based polyhedral nanoparticles, we utilize the off-lattice CanDo model to generate ground-state solution shapes for 3-, 4-, 5-, and 6-arm vertices (Fig. X2). Due to the chirality, each unconstrained vertex shows significant out-of-plane bending towards the major groove of the DNA at the bulges, which has been previously observed by He *et al.* for DNA tiles (He et al. 2010). This model is then extended to geometrically distinct DNA origami nanoparticles which have been recently imaged using cryo-EM (Veneziano et al. 2016). In Figure 10, the off-lattice CanDo model is extended to study the tetrahedron, octahedron, icosahedron, cuboctahedron, and reinforced cube polyhedral nanoparticles. The FE model using the improved bulge motif (in blue) is able to accurately model the experimental solution shape from the reconstructed cryo-EM map (white). Molecular dynamics (MD)

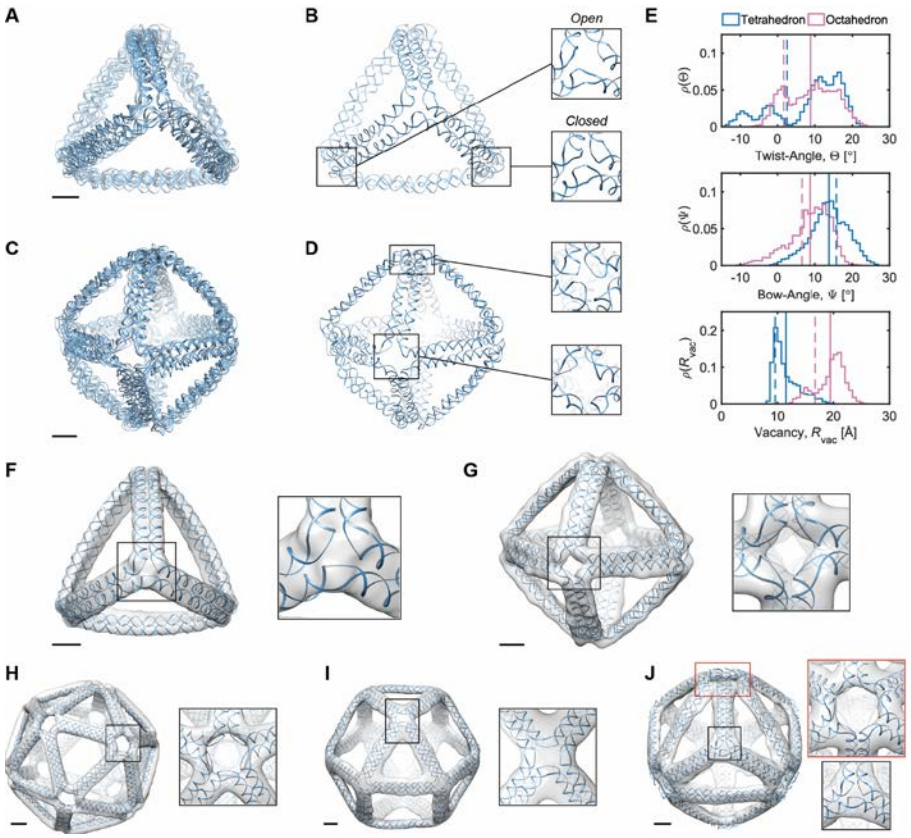


Figure 10. Equilibrium structures of the polyhedral nanoparticles generated by the FE framework and the MD simulations. A Four aligned snapshots at 25 ns, 50 ns, 75 ns, and 100 ns of the MD trajectory of the tetrahedron. **B** The snapshot at 25 ns of the tetrahedron with vertices with the absence and presence of interactions between unpaired bases termed as "open vertices" and "closed vertices", respectively. **C** Four snapshots at 25 ns, 50 ns, 75 ns, and 100 ns of the MD trajectory of the octahedron are rendered in the same way as in (a). **D** The snapshot at 25 ns of the octahedron. **E** The distribution of the twist-angle, bow-angle, and radial vacancy during the MD simulations of the tetrahedral and octahedral nanoparticles. Each angle is averaged over the four vertices of the tetrahedron or the six vertices of the octahedron. Solid lines indicate the mean value during the MD trajectory and dashed lines indicate the value obtained from the ground-state FE model. **F**-**J** FE equilibrium structures, colored in blue, of the tetrahedron, the octahedron, the icosahedron, the cuboctahedron, and the reinforced cube were fit into the reconstructed cryo-EM map.

simulations show atomic-level details of global polyhedral structure, such as twisting at the vertices (Fig. 10e), which is not seen in the coarse-grained FE model.

Lastly, the FE model is further extended to compute the equilibrium structures of 45 DNA origami nanoparticles of diverse geometric shapes (Fig. 11) designed in a recent work (Veneziano et al. 2016). Since experimental cryo-EM data does not exist for all 45 nanoparticles, we compare each ground-state structure to an idealized 3D geometric model assuming all DNA duplexes are straight (Veneziano et al. 2016). The ground-state solution structure of all 45 nanoparticles are presented, as well as close-ups of four structures which have very low RMSD values compared to the geometric model, as well as close-ups of four structures which have relatively higher RMSD values compared to the geometric model.

This work has been published this year as an article in *Nucleic Acids Research* (Pan et al., 2017).

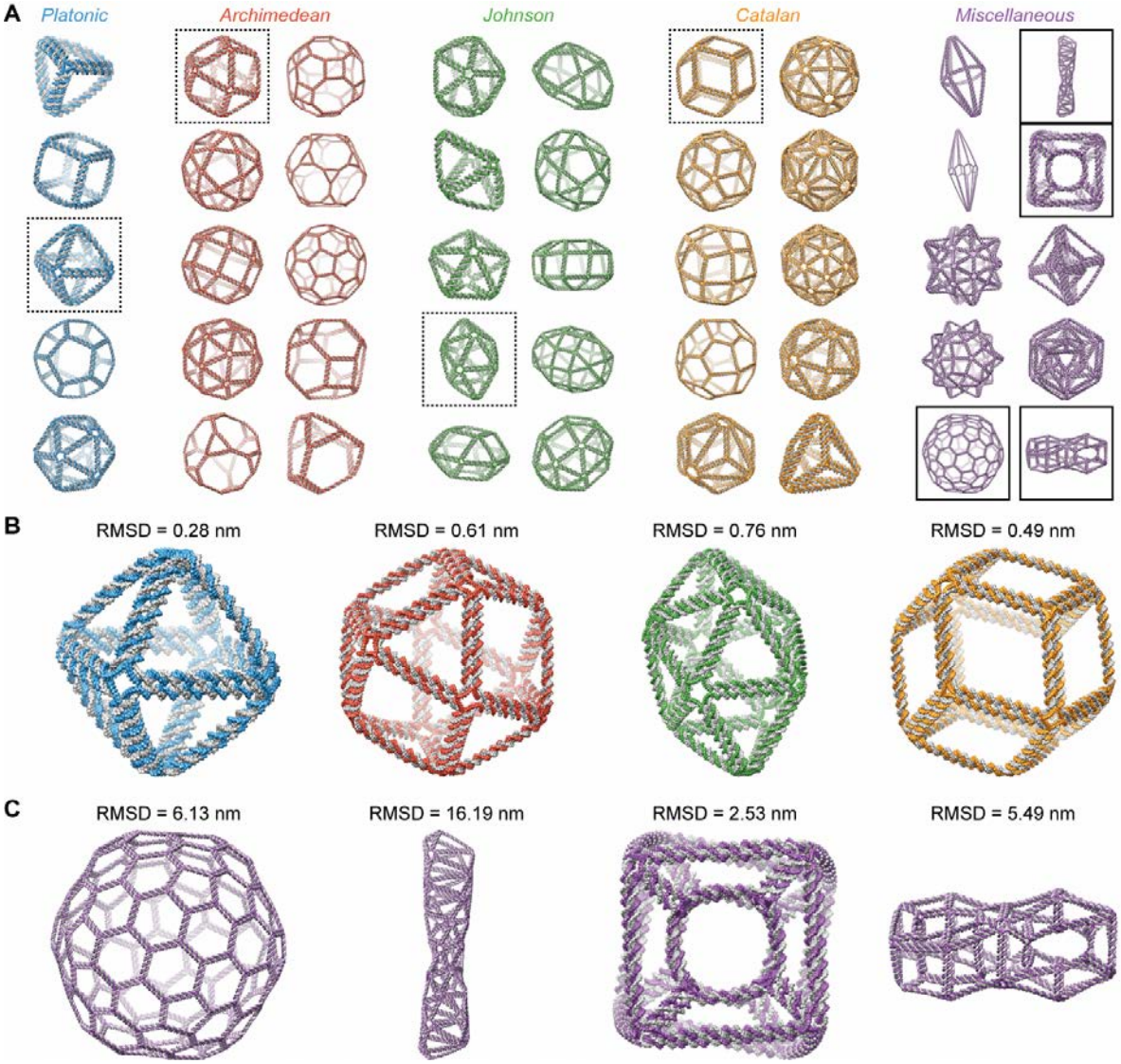


Figure 11. Equilibrium structures of 45 nanoparticles generated by the FE framework. A Structures of the 45 nanoparticles generated by the FE model. **B** The octahedron, cuboctohedron, gyroelongated square bipyramid, and rhombi dodecahedron are zoomed in due to small RMSD values. **C** The Goldberg polyhedron, double helix, nested cube, and double torus are zoomed in due to relatively larger RMSD values.

Single-molecule visualization of DNA tile reconfiguration

Towards building tunable dynamic devices, we explored a DX tile design (assembled in the Yan lab, ASU) that is capable of reconfiguration driven by Holliday junction (HJ) isomerization (**Fig. 12A**). A photo-cleavable site (2-nitrobenzyl group) is embedded between the two crossovers on the DX tile, opposite the central strand loop with a strategically positioned nick point. By UV exposure, cleavage of the strand creates a pair of 5-nucleotide sticky ends between the two crossovers that allow the automatic DX tile reconfiguration from $C_{unfavor}$ to C_{favor}, releasing the stored free energy. We hypothesized that the reconfiguration process undergoes multiple intermediate states, presenting multiple rate-limiting steps including photocleavage, cleavage site

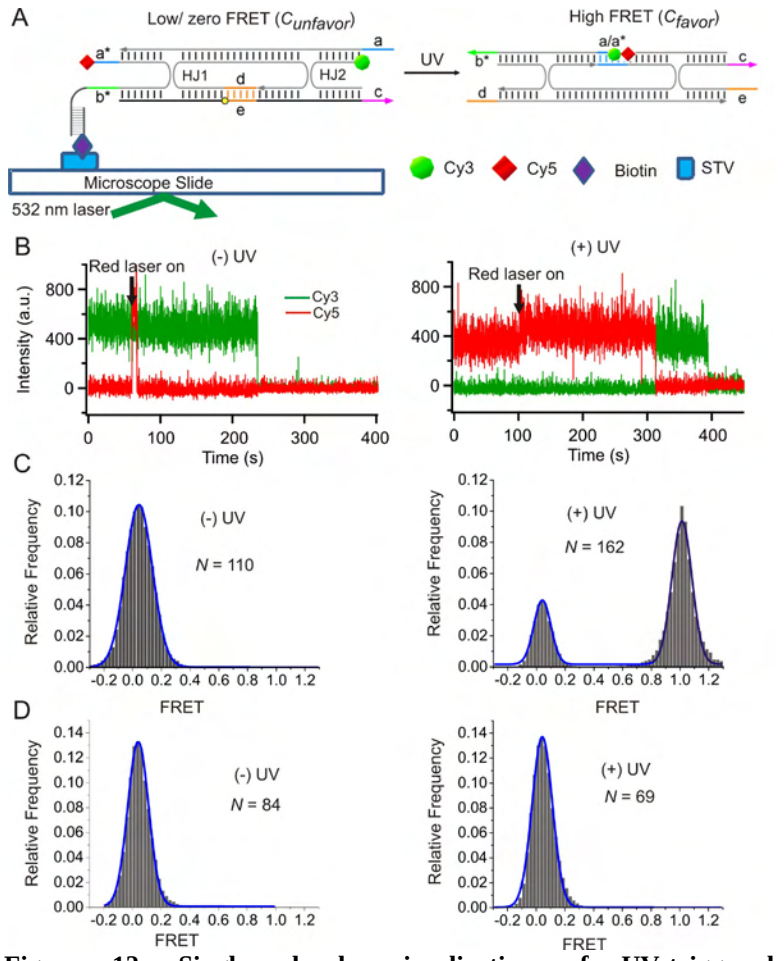


Figure 12. Single-molecule visualization of UV-triggered reconfiguration of DX tiles. (A) Schematic of DX tile reconfiguration triggered by UV irradiation. After photocleavage of the linker, the Holliday junctions (HJ1 and HJ2) undergo reconfiguration from unfavorable ($C_{unfavor}$) to favorable (C_{favor}) configuration. (B) Typical single-molecule traces before (left, (-) UV) and after (right, (+UV)) UV irradiation for 5 min. After recording the FRET movie, the red laser was turned on to confirm the presence of Cy5 fluorophore (downward arrows). (C) smFRET histograms for the corresponding experiments in (B). (D) A control experiment on the same DX tile lacking UV-cleavable linker.

dissociation, and HJ relaxation. Routine fluorescence spectrometry is not capable of resolving the proposed mechanism at the required time scale. By contrast, FRET-based single-molecule total internal reflection fluorescence microscopy (TIRFM) confirmed the distinct conformational transition at the single-molecule level (**Fig. 12**). Our preliminary results of single-molecule visualization of the DX tiles and their reconfiguration upon UV irradiation is shown in **Fig. 12**. As expected, the tiles switched from a low (~0.0) to a high (~1.0) FRET state after UV irradiation as they underwent reconfiguration (**Fig. 12A**). While all molecules exhibited a zero FRET state in the absence of UV, a vast majority of molecules (72%) were switched to high FRET after UV irradiation (**Fig. 12C**). In contrast, control experiments with the DX tiles that lack a photocleavable linker showed only a zero FRET state both before and after UV irradiation (**Fig. 12D**). These results confirmed that the tiles were properly assembled to their thermodynamically unfavorable configuration (the zero FRET state) and underwent a conformational switch to then more favorable conformation (the high FRET state) upon photocleavage of the backbone and reconfiguration of the covalently linked HJs.

Investigation of reconfiguration kinetics of DX tiles by single-molecule analysis

To monitor the tile reconfiguration kinetics at the single-molecule level, we recorded both the Cy3 and Cy5 fluorophore intensity of the tiles +/- UV irradiation. We measured the time lapse between onset of UV irradiation and tile reconfiguration, which we assigned as photocleavage time (**Fig. 13A**). Interestingly, when the photocleavage time was plotted as a cumulative count, it followed a

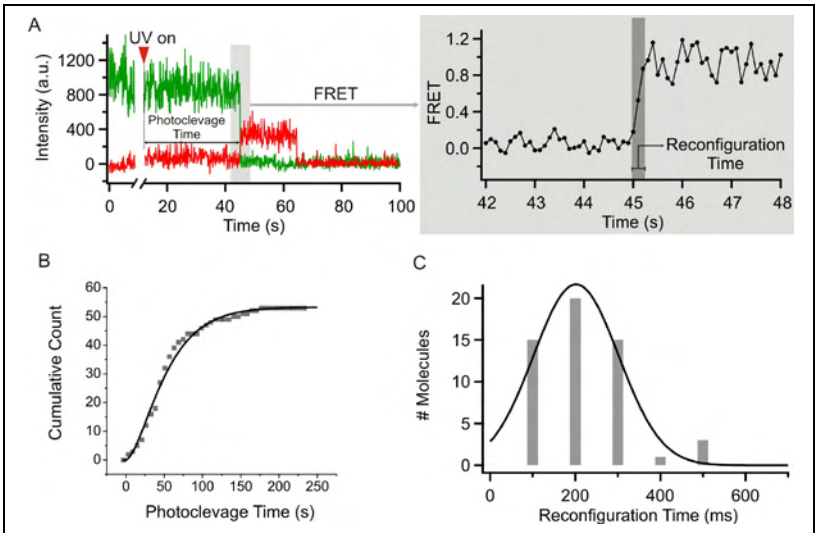


Figure 13. Photocleavage and reconfiguration kinetics of DX tiles. (A) Typical single-molecule trace showing Cy3 (green) and Cy5 (red) fluorescence intensities. Right panel shows the zoomed-in FRET trace of the shadowed section in the left panel. Estimation of reconfiguration time (≈ time spent to increase FRET from zero to 1.0, shadow) is highlighted at the right. (B) Estimation of photocleavage time. (C) Distribution of the reconfiguration time after photocleavage.

double-exponential pattern, suggesting that the tile has to undergo at least two underlying processes before reconfiguration (**Fig. 13B**). The two time constants extracted from the fitting were $t_1 = 23.0 \pm 0.2$ and $t_2 = 30.9 \pm 0.2$ s. While more experiments are needed to confirm these results, the shorter (t_1) and longer (t_2) time constants may represent the photophysical process itself, followed by the conformational change. These results also suggest the existence of at least one conformational intermediate. We further measured an actual reconfiguration time of the tiles from smFRET traces (as highlighted in **Fig. 13A**, right) and plotted as a histogram (**Fig. 13C**). The mean reconfiguration time obtained by Gaussian fitting of the histogram is 202 ± 13 ms. In the future, we anticipate that a higher time-resolution would allow more precise determination of the reconfiguration kinetics of this tile as well as that of other sequence designs.

Single-molecule fluorescence characterization of DX tile assembly

Even though large number of DNA nanostructures of varying shapes and sizes are synthesized over time, but employing DNA nanostructures as building blocks for biomimetics is a fairly new concept. A very recent study used DNA based nanotubes to mimic the dynamic instability of cytoskeleton. Towards this goal, understanding the kinetics of tiles self-assembly is the first key step to get a comprehensive picture about the kinetics of DNA nanotubes polymerization at single molecule/tile level. However, significantly less amount of investigation has been performed to understand the kinetics of DNA tile based self-assembly. Towards that goal we used double crossover (DX) DNA tiles (designed and assembled in Yan lab, ASU) as building blocks for making large structures with tunable dynamic properties. In the work presented here, we wanted to address some fundamental questions: What type of initial structure is more suitable for efficient growth of nanostructures? What are the factors that might positively/negatively affect the self-assembly? What role is played by microenvironment? To what extent the kinetics is affected by the sticky end sequence? Can these insights be used to build dynamic/reconfigurable

nanostructures? From the perspective of DNA nanoengineering, these knowledges are highly desirable to design, predict and implement dynamic DNA tile based self-assembly. We have employed TIRFM to observe real time association and dissociation kinetics of tile assembly.

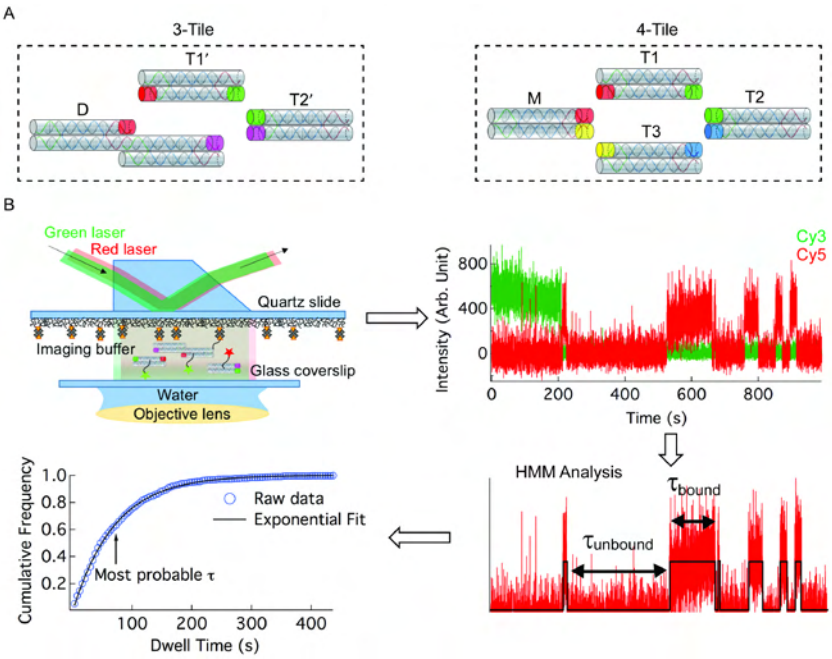


Figure 14. Single-molecule kinetic analysis of a DX tile system. (A) Schematic of the tiles design. Dimer tile D and monomer M are Cy3 labeled and is surface immobilized using a biotin-modified DNA linker that is pre-hybridized with its complementary strand. The complementary sequences in the tiles are highlighted in matching colors. The incoming tiles T1', T2', T1, T2 and T3 are labeled with either Cy3 or Cy5. (B) Schematic for instrumental set-up and data analysis procedure.

We have investigated two DNA tile based nanostructure named as 3-Tile system and 4-Tile system (**Fig. 14A**). The association of the DX tiles can be precisely controlled by the choosing appropriate complimentary sticky end sequence (color coded regions). With suitable fluorophore (Cy3 and Cy5) labeling of the tiles we monitored association and dissociation of the tiles by recording the fluorescence intensity over time. Using hidden-Markov modeling fitting algorithm, dwell times as τ_{bound} and $\tau_{unbound}$ were extracted from the idealized fluorescent intensity traces. Cumulative distributions of dwell times were fitted with double exponential function to extract the most probable dwell time. The weighted average of the dwell time was used to calculate the forward and reverse reaction rates, k_{asso} ($=1/(\tau_{unbound}*C)$) and k_{disso} ($=1/\tau_{bound}$). Finally the equilibrium association constant ($K_{eq}= k_{asso}/k_{disso}$) and free energy change ($\Delta G=-RTlnK_{eq}$) was calculated. All the data were acquired at room temperature in 1X-TAE buffer with 30 mM $MgCl_2$. The concentration of immobilized tile (D in 3-Tile system and M in 4-Tile system) were kept at 20 pM whereas that for freely floating tiles were maintained at 10 nM in all the cases. Cy3 labeled D and M tiles were surface immobilized by protruding 20nt biotin-modified DNA linker of random DNA sequence pre-hybridized with its complementary strand. The complementary sticky end sequences in the tiles were highlighted in matching colors. The tiles T1' and T2' were labeled with Cy3 and Cy5 respectively. T1, T2 and T3 were labeled with either Cy3, Cy5, or unlabeled.

Single-molecule fluorescence characterization of 3-Tile system

The kinetic parameters for 3-Tile system at four different conditions in presence of 30 mM $MgCl_2$ are given in **Table 3**. The second order association rates k_{asso} for our systems are found to be ~ $(0.7\text{-}2)\text{x}10^6$ $M^{-1}s^{-1}$ which is comparable to the DNA base hybridization rate. As can be seen from

	τ_{bound} (s)	k_{disso} (s^{-1})	$\tau_{unbound}$ (s)	K_{asso} ($M^{-1}s^{-1}$)	K_{eq} (M^{-1})	ΔG (kcalmol^{-1})
T1'-Cy3 only	17.7±0.3	0.056±0.001	57.2±0.9	(1.75±0.03)x10^6	(3.12±0.1)x10^7	-10.2±0.02
T2'-Cy5 only	24.2±3.0	0.041±0.005	147.8±6.6	(0.68±0.03)x10^6	(1.64±0.1)x10^7	-9.8±0.05
T1'-Cy3 in presence of T4-Cy5	33.9	0.029	62.4	1.6x10^6	5.4x10^7	-10.5
T2'-Cy5 in presence of T3-Cy3	21.1	0.047	101.5	0.99x10^6	2.1x10^7	-9.9

Table 3. The kinetic parameters of T1'-Cy3 and T2'-Cy5 in 3-Tile system in presence of 30 mM $MgCl_2$.

the table, when only T1' or T2' is present in the imaging buffer, τ_{bound} is slightly higher for T2'. We attributed this observation to different extent of electrostatic repulsion experienced between incoming tiles and D. Compared to T2' which binds sidewise to D, T1' is expected to experience higher electrostatic repulsion from D due to larger contact area. This might contribute to decreased τ_{bound} in comparison to T2'. However efficient screening of negatively charged DNA backbone by 30 mM $MgCl_2$ helps to circumvent this repulsion as can be observed from significantly long τ_{bound}. Interestingly, T1' has almost three times smaller $\tau_{unbound}$ than T2'. We speculate that D is providing T1' an extended platform for easy landing and therefore facilitates binding. However, for T2' the flanking 5-thymine (introduced to avoid inter-tile stacking) from the neighboring helix can create

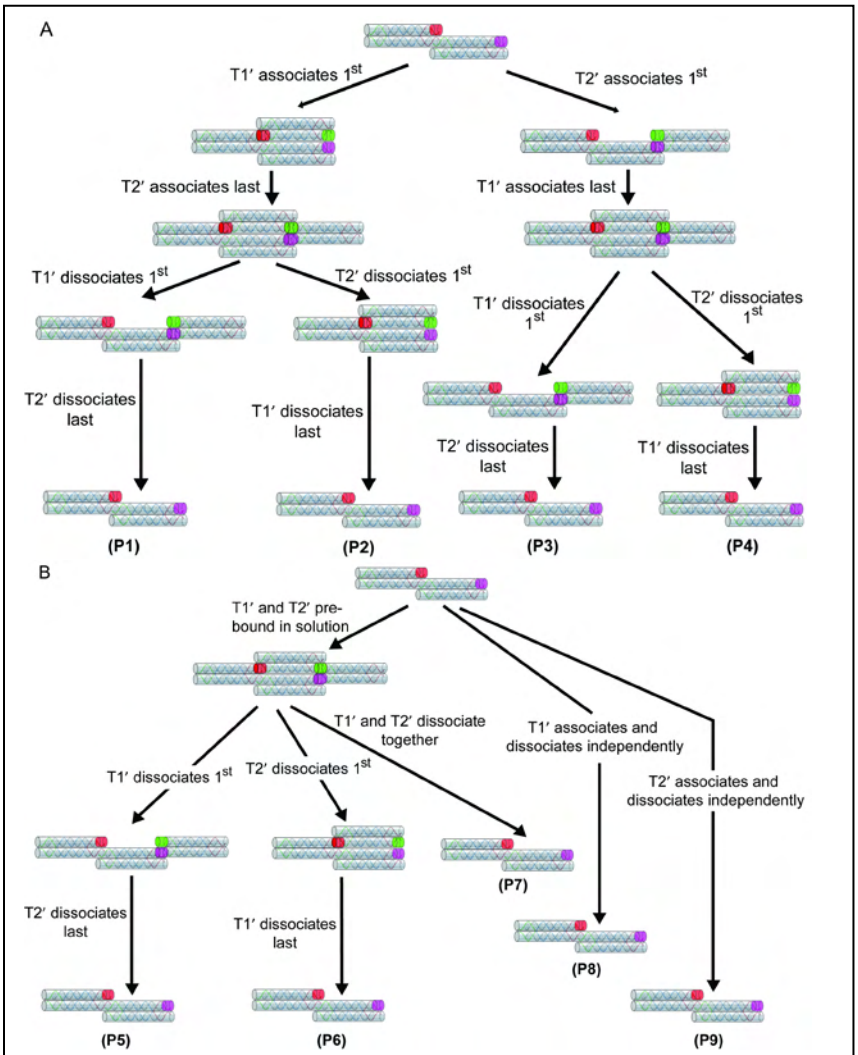


Figure 15. Flow chart of association and dissociation order of tiles in 3-Tile system.

some steric hindrance and additional crowding thereby decreasing the accessibility of binding site for T2'. However, higher τ_{bound} suggest that such local crowding stabilizes the assembly once the binding occurred. Interestingly, when T2' tile is also present in the solution, τ_{bound} for T1' increases almost two times but $\tau_{unbound}$ does not change significantly. Thus the presence of T2' introduces cooperativity in T1' association. However, no significant change in the kinetic parameters for T2' was observed in presence of T1'. At this juncture, we wanted to investigate the presence of any preferential association order when both T1' and T2' are present in the solution. Meticulous investigation of the trajectories revealed that the presence of another type of tile (e.g, T1' in presence of T2' or vice versa) gave rise to the various association and dissociation possibilities, e.g., T1' can bind first to D and then T2' binding follows or vice versa etc. We found 9 different possibilities of association and dissociation and summarized them in **Fig. 15A** and **B**. We observed that type P2 (i.e., T1' associates 1st and dissociates last) has highest % of population (44%) followed by 30% of P3 (i.e., T2' associates 1st and dissociates last). This finding also reinforced our hypothesis that D offers itself as a larger landing platform for easy landing and successive binding of T1'. Once T2' is bound, association of T1' becomes difficult due to steric hindrances and aligning the two sticky ends at two opposite ends. The percentage of occurrence for association and dissociation orders for T1' and T2' are summarized in **Fig. 16**. Although T1' shows higher possibility of association prior to T2', possibility of dissociating first is similar for both T1' and T2' tiles. It should be noted that when both T1' and T2' are bound to D, both have to unzip two sticky ends for dissociation thus making the dissociation order of equal probability. K_{eq} and ΔG for T1' where it associates 1st to D and dissociates last (P2, highest % of occurrence) were found to be 2.01×10^8 M^{-1} and -11.3 $kcalmol^{-1}$ respectively which is strongest association observed among all the various types. This also corroborates that along with a larger base provided by D, presence of T2' induces further stronger binding of T1'.

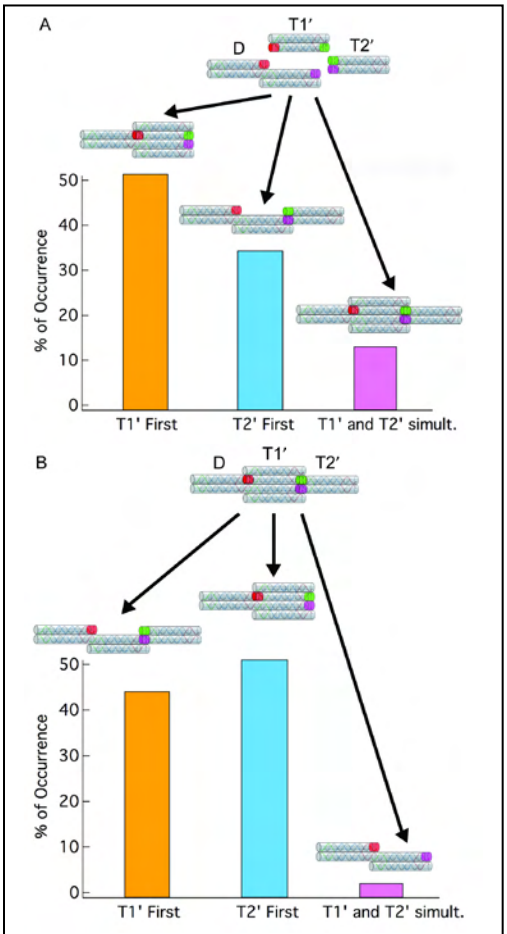


Figure 16. Percentage of occurrence of (A) association and (B) dissociation orders for T1' and T2' in 3-Tile system.

Significantly strong binding observed in 3-Tile system motivated us to investigate further the possible aspects facilitating stable growth. Towards that objective we systematically introduced changes in 3-tile system. Firstly, we changed the sequence of the purple sticky end keeping the GC content same. Other sticky end sequences remained same. However, the 5′-3′ direction of green sticky end sequences has been changed and the red sticky end sequences have been interchanged between D and T1′ keeping the hybridized sequence between D and T1′ same. The modified 3-Tile system is renamed as D* 3-Tile system and T1′ and T2′ have been renamed as T1 and T2. The old 3-Tile system is mentioned as D 3-Tile system from here on.

The kinetic parameters for D* 3-Tile system is presented in Table 4. As expected, the τ_{bound} value for T1 remained

Table 4. Kinetic parameters of T1-Cy3 and T2-Cy5 in D* 3-Tile system in presence of 30 mM $MgCl_2$.

	τ_{bound} (s)	k_{disso} (s^{-1})	$\tau_{unbound}$ (s)	k_{asso} ($M^{-1}s^{-1}$)	K_{eq} (M^{-1})	ΔG (kcalmol^{-1})
T1-Cy3 only	14.4±0.7	0.070±0.003	70.3±3.0	(1.4±0.06)x10^6	(2.1±0.1)x10^7	-10.0±0.1
T2-Cy5 only	29.7±3.1	0.034±0.004	85.6±0.3	(1.2±0.04)x10^6	(3.5±0.4)x10^7	-10.3±0.1
T1-Cy3 in presence of T2-Cy5	14.6±3.1	0.071±0.020	78.5±12.5	(1.3±0.2)x10^6	(1.5±0.2)x10^7	-9.9±0.1
T2-Cy5 in presence of T1-Cy3	30.3±3.7	0.033±0.004	91.9±10.8	(1.1±0.1)x10^6	(3.2±0.5)x10^7	-10.2±0.1

similar as T1′ because the sticky end hybridization sequence remained same except the directionality. For T2, τ_{bound} increases marginally and has ~2 times lower $\tau_{unbound}$ and ~2 times higher K_{eq} than T2′. This increment in K_{eq} or subsequently more negative ΔG signifies that the sticky end sequence might play a role towards building large DNA nanostructures. However, as the sticky end sequences were designed using nearest-neighbor model in such a way that they have similar binding energies, we did not observe any strong effect of sticky end sequence on the kinetics. Nonetheless, higher $\tau_{unbound}$ of T2 compared to T1 reinforced the hypothesis further that the flanking poly-thymine from neighboring helix can create steric hindrance towards accessing the binding sight.

Previous study reported reduced nucleation barrier for DNA tile self-assembly in presence of a seed. The study established that the nucleation seed significantly accelerates the nucleation process and the presence of seed not only increases the number of growing nanotubes but also the total length of the nanotubes. Motivated by this study, we investigated the effect of seed size on the binding kinetics. Towards that goal we decreased the size of the initial seed size from a dimer (D/D*) to a monomer (M) DX tile and number of floating tiles in the imaging buffer increased from 2 to 3. The new system is named as 4-Tile system. A simpler way to look at 4-Tile system as a modified 3-Tile system where D is divided into two parts M and T3. T3 is labelled with either Cy3 or Cy5 and Cy3 labelled tile M is immobilized on the microscope slide (**Fig. 12A, Right panel**) for single molecule data acquisition. With the new design, T1 and T2 tiles now can be shared among D* 3- and 4-Tile systems and any observed difference in the kinetics of T1, T2 and T3 can be directly attributed to the change in initial seed size provided to the floating incoming tiles.

Single Molecule Data for 4-Tile system

In our single molecule experiments for the 4-Tile system, the imaging buffer contained three tiles and two of them were fluorescently labelled with either a Cy3 or Cy5 and third one is left unlabelled. The kinetic parameters of all of the tiles determined at 30 mM $MgCl_2$ are presented in Table 5. We observed that the dissociation rates for any of the tiles in 4-Tile system are significantly faster compared to both 3-Tile systems. τ_{bound} and hence K_{eq} in 4-Tile system are order of magnitude shorter than 3-Tiles system. Less negative ΔG for 4-Tile system also indicates that 4-Tile system is kinetically much less stable than 3-Tile system. Our results also showed a large standard deviation of in all parameters compared to the 3-Tile system. This indicates that

Table 5. The kinetic parameters of T1-Cy3/Cy5, T2-Cy3/Cy5 and T3-Cy3/Cy5 in 4-Tile system in presence of 30 mM $MgCl_2$.

	τ_{bound} (s)	k_{disso} (s^{-1})	$\tau_{unbound}$ (s)	k_{asso} ($M^{-1}s^{-1}$)	K_{eq} (M^{-1})	ΔG (kcalmol^{-1})
T1 only	4.3±0.2	0.23±0.01	74.9±1.6	(1.3±0.03)x10^6	(5.8±0.3)x10^6	-9.2±0.04
T3 only	0.8±0.02	1.32±0.04	27.8±1.9	(3.6±0.3)x10^6	(2.7±0.1)x10^6	-8.8±0.02
T1 in presence of T2 and T3	2.9±0.9	0.34±0.10	51.8±18.3	(1.9±0.7)x10^6	(5.6±2.6)x10^6	-9.2±0.3
T2 in presence of T3 and T1	2.7±2.0	0.37±0.28	60.4±44.0	(1.7±1.2)x10^6	(4.4±4.7)x10^6	-9.1±0.6
T3 in presence of T1 and T2	1.6±0.6	0.61±0.21	56.8±14.0	(1.8±0.4)x10^6	(2.9±1.2)x10^6	-8.8±0.2

association/dissociation processes in the 4-Tile system are much more heterogeneous than that in 3-Tile systems possibly due to increased complexity. We observed a stark difference in dissociation rate and hence in kinetic parameters between 3- and 4-Tile systems. T2 when used in 4-tile system, exhibited very high dissociation rate and much less negative ΔG value. Similar trend was also observed for T1. Surprisingly, with the same sticky end sequences, T1 and T2 show ~10 times higher τ_{bound} and one order of magnitude increment in K_{eq} when used in D* 3-Tile system compared to 4-Tile system (**Fig. 17**). We reason that a larger nucleation structure provided in D* 3-Tile system attributed to stronger association of DNA tiles. In D* 3-Tile system, T1 and T2 was provided with a larger nucleation structure compared to the same T1 tile used in 4-Tile system and the data evidenced that in presence of a larger initial nucleation structure T1 and T2 exhibit one order of magnitude stronger binding thereby facilitating the nanostructure growth.

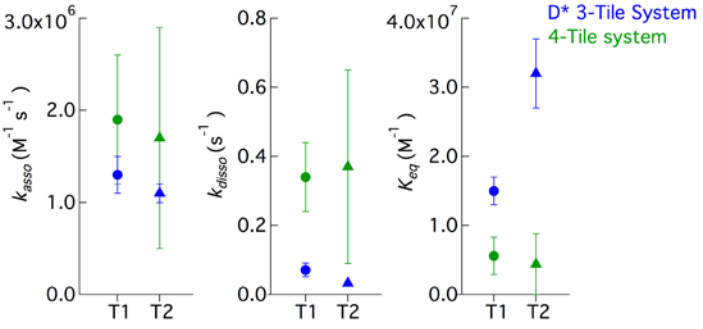


Figure 17. Comparison of kinetic parameters between D* 3-Tile and 4-Tile system.

Additionally, motivated by previous studies showing that the divalent cations accelerate the folding of multi-layered DNA origami whereas monovalent cations antagonize compaction, we investigated the tile-assembly kinetics in presence of competing monovalent counter ion. As 3-Tile system exhibited much stronger association, we chose 3-Tile system. Towards that goal we externally added 100 mM NaCl in the imaging buffer in presence of 30 mM $MgCl_2$. Interestingly, we did not observe any effect of NaCl on the kinetics. Even having similar ionic strength (0.10 M@100 mM NaCl and 0.09 M@30 mM $MgCl_2$) NaCl did not show any noticeable change on the kinetics. When compared the fractional surface density of ions on the DNA tile, it was much higher for Mg^{2+} at 30 mM $MgCl_2$ than that for 100 mM NaCl (see SI for calculation). Therefore, we believe that the fractional surface charge density of Mg^{2+} on DNA tile surface circumvent any

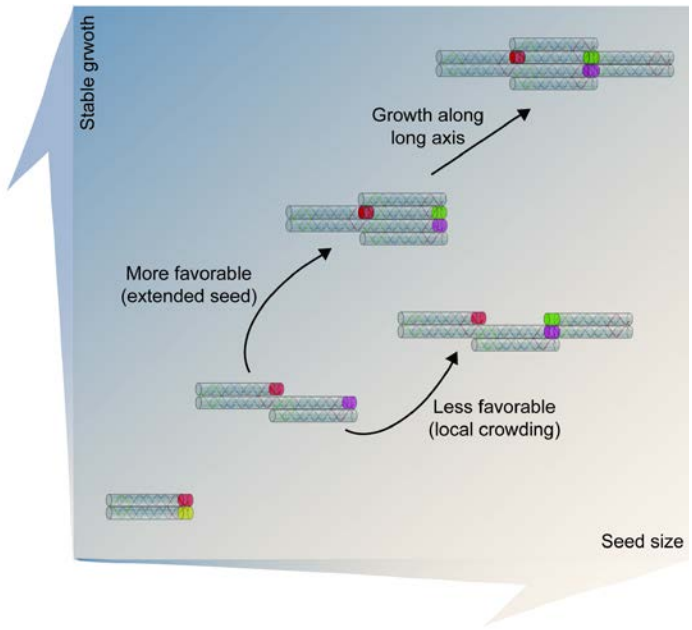


Figure 18. Stable growth mechanism for DX tile assembly.

effect of NaCl even at low bulk concentration of $MgCl_2$. Thus we speculate that for the specific application of DNA based self-assembly, where high concentration of monovalent counter ions are needed, our finding should give important direction about the ratio of monovalent to divalent counter ions to be used without significantly altering the kinetics.

Our comparative kinetic analyses of D 3-, D* 3- and 4-Tile systems suggest that initial nucleation structure, sticky end sequence, and change in the ionic environment around the sticky end hybridization site, all can have determinant effect on the kinetics of tile-tile assembly. **Fig. 18** depicts a possible mechanism or pathway for stable growth of DX tile based assembly. We observed that although the association rates in the three systems studied here remain largely unaffected, the dissociation rates are strongly dependent on the structure of the system. The larger starting nucleation seed favored longer association thereby decreased dissociation by one of order of magnitudes. Comparing the ΔG values for different systems, we concluded that the extended nucleation structure facilitates nanostructure growth by providing an easy landing for incoming tiles and promoting stronger binding. The sequences of the sticky ends and their locations on the tile produced noticeable change however, further detailed and systematic study is required to observe any systematic effect. The change in microenvironment around sticky end hybridization site (e.g., steric hindrance created by flanking poly-thymine) significantly affected both association and dissociation rates. We anticipate that the results presented here will provide important steps toward having better control over DNA self-assembly. It will be interesting to observe if the insights obtained in this study can translated to build dynamic/reconfigurable nanostructures. In summary, we expect that our elucidation of kinetics of DX DNA-tile assembly at the single-molecule level will contribute to further development and optimization of dynamic DNA devices and biomimetics using DNA tiles as building blocks.

Investigating the DNA walker on 2- and 3-step DNA tile walking systems through single molecule fluorescence resonance energy transfer (smFRET)

To mechanistically characterize and optimize the stepping behavior of the transporter, we started with a simple DNA tile system bearing two adjacent footholds for the walker to step between. This *2-Foothold* system consists of a 4-helix DNA tile decorated with single-stranded DNA overhangs F_1 and F_2 as well as a biotin label for surface immobilization in TIRF measurements. The tile was assembled by thermal annealing of synthetic DNA oligonucleotides and characterized by native PAGE. The footholds are spaced by ~7 nm to match the 17-21 nucleotide length of the duplex

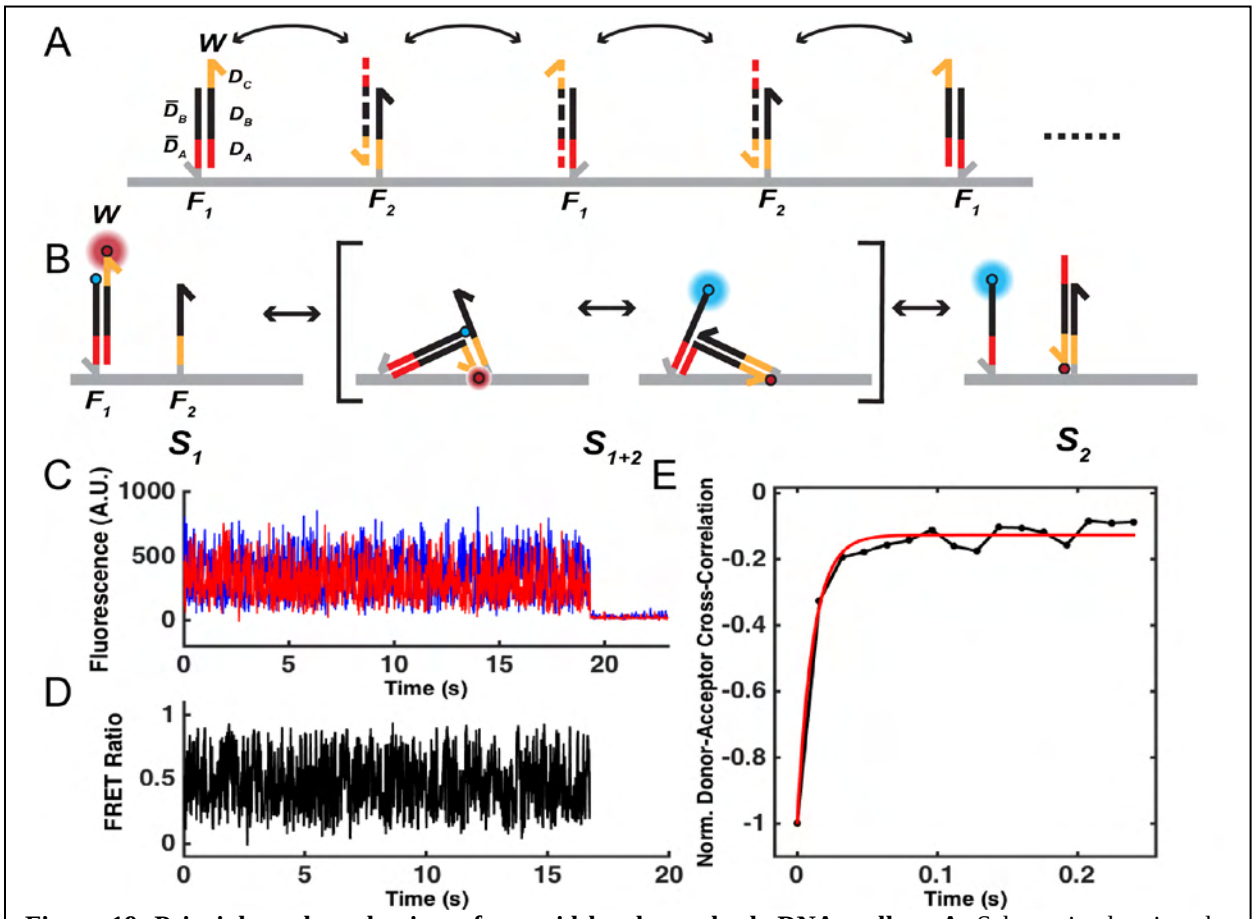


Figure 19. Principle and mechanism of a rapid head-over-heels DNA walker. A, Schematic showing the designed walking mechanism of a toehold exchange DNA walker**. B**, Schematic of smFRET measurement of stepping kinetics of a Cy5-labeled DNA walker on a 2-Foothold DNA tile in which one foothold is labeled with Cy3. **C,** Rapid anti-correlated fluctuations in Cy3 (blue) and Cy5 (red) intensity fluorescence for a single walker-tile complex, suggesting branch migration in hybrid state $\mathbf{S}_{1+2}$. **D**, FRET ratio versus time for the trajectory shown in **c**. **E,** Cross-correlation analysis of Cy3 and Cy5 signal in **c**, with a single-exponential fit indicating an anti-correlation time constant of 11.4 ms for this trajectory.

formed by binding of the walker to a foothold, and equipped with $(dT)_3$ linkers to provide conformational flexibility. The DNA walker $W_{a_b_c}$ consists of a middle branch migration domain D_B of length b (generally 13 nucleotides) flanked by two toehold domains D_A and D_C with lengths a and c (a = c = 4 to 8 nucleotides). The sequence of the walker was chosen to allow for comparison with prior studies of toehold exchange kinetics. To permit measurement of stepping kinetics by single-molecule fluorescence resonance energy transfer (smFRET), the 5′-end of F_1 is labeled with the FRET donor Cy3, and the 3′-end of $W_{a_b_c}$ is labeled with FRET acceptor Cy5. Thus, any stepping of W between F_1 and F_2 through toehold exchange is expected to give rise to a time-dependent change in FRET efficiency between Cy3 and Cy5 (**Fig. 19B**). First, we characterized by smFRET the behavior of a walker bearing 8-nucleotide toehold domains ($W_{8_13_8}$). While a significant fraction of walkers exhibited static high- or low-FRET efficiency behavior, the largest fraction of walkers (35-40%) exhibited a FRET efficiency varying between 0.3 and 0.7 (**Fig. 19C, D**). On close inspection, this mid-FRET state contained rapid anti-correlated fluctuations of Cy3 and Cy5 fluorescence intensity, indicating rapid changes in the distance between Cy3 and Cy5 (**Fig. 19E**). The cross-correlation function between Cy3 and Cy5 decays with a time constant of

12 ± 3 ms. Due to the rapidity of these fluctuations and the fact that the apparent FRET efficiency occupies a continuum of values rather than discrete states, we hypothesized that these fluctuations are predominantly due to reversible branch migration of domain D_B, with only transient dissociation of either toehold from its respective foothold strand. That is, instead of occupying either state S_1 or S_2 (**Fig. 19B**), the walker exists primarily in a hybrid dynamic equilibrium state S_{1+2} in which it is partially base-paired to both F_1 and F_2. This is consistent with expectations based on the local effective concentration of 250 μM measured in a similar tile system, where the equilibrium is expected to strongly favor hybridization of the 8-nucleotide toehold sequences. The toehold-dissociated states S_1 and S_2 are not typically observed because of their low occupancy and short lifetimes. Changing the toehold length to 7-, 6-, or 5-nucleotides gives similar kinetic behavior, consistent with the presence of the same branch migration domain length b = 13. Monte Carlo simulations of branch migration within a 13-nucleotide domain suggest that an anti-correlation time constant of ~12 ms will occur when the lifetime of an individual base pair step along the duplex is ~400 μs, which is somewhat shorter than the ~2.5 ms previously estimated for this sequence based on kinetic modeling from bulk fluorescence measurements but longer than earlier estimates of 10-100 μs from three-stranded branch migration of genomic-length DNA sequences.

To further test our hypothesis of a hybrid S_{1+2} state, a third foothold strand F_1' with the same sequence as T_1 was added to assemble a *3-Foothold* DNA tile. The addition of this third foothold is expected to enable the walker to occupy a second hybrid state $S_{2+1'}$ (**Fig. 20A**), resulting in a new low-FRET state in addition to the mid-FRET state observed for the *2-Foothold* system. Indeed, most mid-FRET trajectories for $W_{8_13_8}$ showed slow transitions to and from an additional FRET state of ~0.3 on the 3-Foothold tile (**Fig. 20B**), suggesting a new, slower process limited by toehold dissociation. Based on these results, we predicted that decreasing the length of the toehold would yield dramatically faster stepping behavior of walkers, since the rate of dissociation of short DNA duplexes increases exponentially with decreasing length. Indeed, walkers with 7-, 6-, and 5-nucleotide toeholds showed two-state FRET behavior with much more rapid transitions between states (**Fig. 20B-I**). The median lifetimes of the mean of high-FRET and low-FRET states decrease from 31.3 s (interquartile range, or IQR, 52.1-16.5 s) for $W_{8_13_8}$ to 1.4 s (IQR 3.7-1.1 s) for $W_{5_13_5}$, yielding rate constants of stepping that range from 0.03 s^{-1} to 0.72 s^{-1} (**Fig. 20N**). Given the step size of 7 nm, the fastest walker has an average (undirected) translocation speed of ~300 nm min^{-1}. While the stepping rate increases dramatically when the toehold length is decreased to 7 nucleotides, further increases are marginal, and the stepping rate of $W_{5_13_5}$ is very similar to that of $W_{6_13_6}$. Given these observations, it is likely that a step other than toehold dissociation has become rate-limiting for walkers with toehold lengths $\leq$ 6 nucleotides. Since hybridization nucleation has been shown to slow down dramatically for very short stretches of contiguous base pairs (*e.g.*, less than seven complementary nucleotides), it is plausible that toehold binding and/or initiation of branch migration has become rate-limiting for short toeholds. In addition, as the length of toeholds decreases, the difference in apparent FRET efficiency between the two main states increases (**Fig. 20J-M**). This observation is consistent with the decrease in the distance between the donor and acceptor dyes in the S_{1+2} state, as well as an increase in the donor-acceptor distance in the $S_{2+1'}$ state, when a shorter toehold is present.

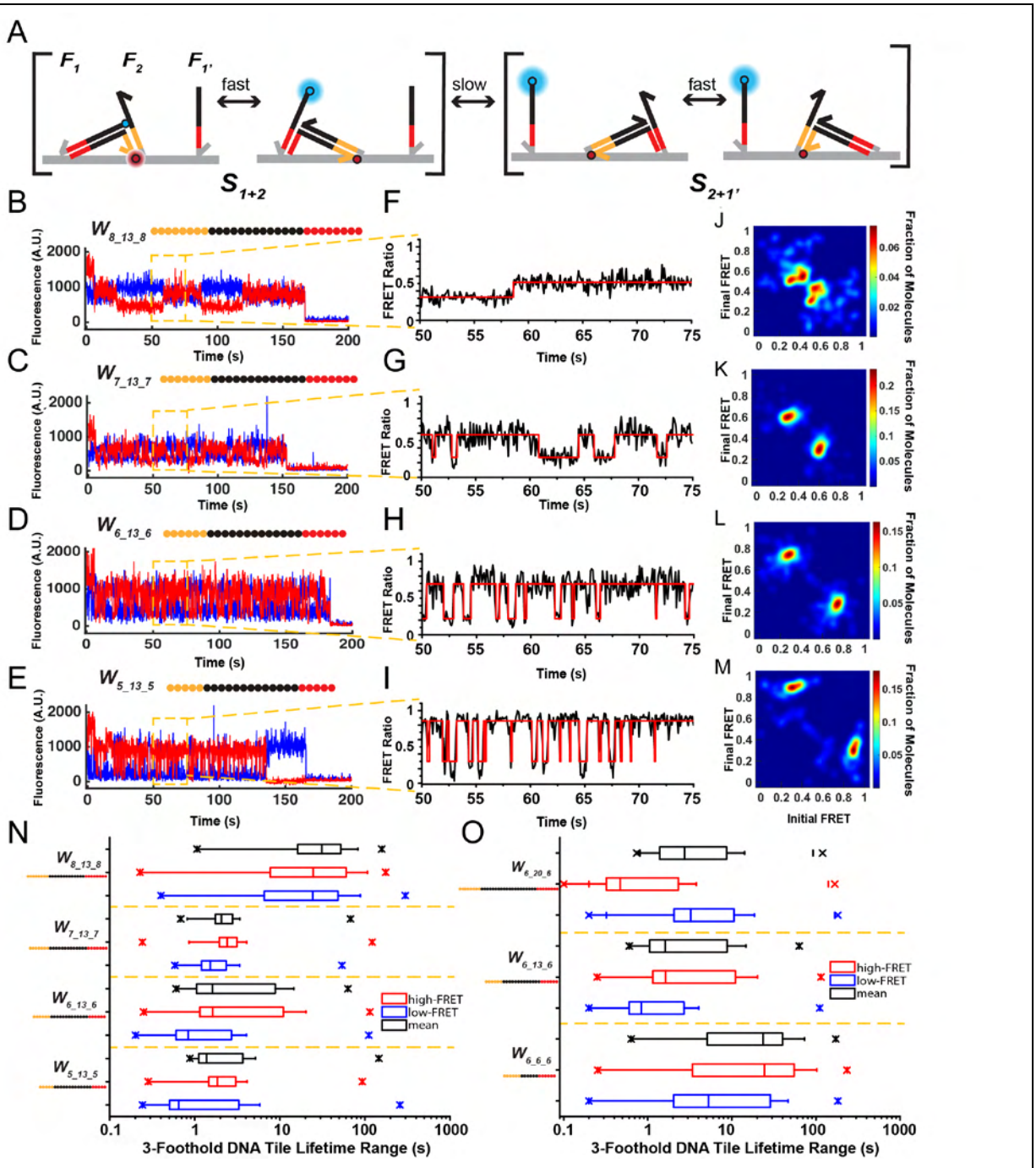


Figure 20. Single-molecule FRET characterization of walkers with varying toehold lengths. A, Kinetic model of stepping and associated FRET transitions for Cy5-labeled DNA walker on Cy3-labeled ***3-Foothold*** DNA tile. **B-E**, Representative single-molecule FRET trajectories of walkers with varying toehold length on a ***3-Foothold*** DNA tile. Cy3 fluorescence is shown in blue, while Cy5 fluorescence is shown in red. The elevated Cy5 signal in the first ~10 seconds of each trace results from direct excitation at 640 nm to confirm the presence of an active acceptor on each walker-tile complex. **F-I,** Zoomed-in trajectories showing FRET transitions for 25-s segments of the molecules depicted in **B-E**. **J-M,** Transition occupancy density plots (TODPs) illustrating the most common FRET transitions for each walker. N = 87, 96, 107, and 109 for $\boldsymbol{W_{5_13_5}}$, $\boldsymbol{W_{6_13_6}}$, $\boldsymbol{W_{7_13_7}}$, *and* $\boldsymbol{W_{8_13_8}}$, respectively. **n,** Box-and-whisker plot of stepping kinetics in the high- and low-FRET states for walkers with varying toehold domain ($\boldsymbol{D_A}$ and $\boldsymbol{D_C}$) lengths. **o,** Box-and-whisker plot for walkers with varying middle domain ($\boldsymbol{D_B}$) lengths. N = 105 and 132 for $\boldsymbol{W_{6_6_6}}$, $\boldsymbol{W_{6_20_6}}$. The box includes the population of all molecules from 25th percentile to 75th percentile. The whisker corresponds to the outlier

To investigate the possibility that branch migration kinetics are rate-limiting for walkers with shorter toeholds, we investigated walkers with different lengths of domain D_B, with accompanying changes in the foothold sequences to maintain complementarity with each walker. Since branch migration can be approximated as a one-dimensional random walk, the time required for one strand to displace another strand in a duplex is expected to be proportional to the square of the number of base pairs to be broken and reformed. Thus, if the branch migration kinetics were rate-limiting, increasing b from 13 to 20 nucleotides would be expected to slow the stepping rate by a factor of $20^2/13^2 = 2.4$, while decreasing b from 13 to 6 nucleotides would be expected to accelerate stepping by a factor of $13^2/6^2 = 4.7$. However, when the middle domain increases to 20 nucleotides (walker $W_{6_20_6}$), the median stepping lifetime is 2.7 s (IQR 8.7-1.4 s), which is similar to that of $W_{6_13_6}$ (1.6 s, IQR 8.7-1.1 s), and the median lifetime in the high-FRET state is even shorter for $W_{6_20_6}$ (0.47 s, IQR 2.3-0.3 s) than for $W_{6_13_6}$ (1.62 s, IQR 10.7-1.2 s). Furthermore, when D_B is decreased to 6 nucleotides (walker $W_{6_6_6}$), the median stepping lifetime increases to 23.6 s (IQR 39.4-5.2) (**Fig. 20O**), contrary to expectations if branch migration were rate-limiting. $W_{6_6_6}$ also yields more heterogeneous kinetic behavior compared to $W_{6_20_6}$ (**Fig. 20O**). An important complication arises from the fact that, since the distance between adjacent foothold strands is fixed at 7 nm, altering the length of the branch migration domain may introduce an incongruity between the walker-foothold duplex length and the spacing between foothold strands. However, the $(dT)_3$ ssDNA spacers between the foothold strands and the tile are expected to provide sufficient flexibility to compensate for the difference of ±2.3 nm from the addition or subtraction of 7 nucleotides from D_B. In any case, the lack of a positive correlation between the length of D_B and the stepping lifetime suggests that any impact of branch migration kinetics upon the stepping rate is overshadowed by other factors, such as toehold binding kinetics and/or geometric compatibility between the walker length and foothold spacing.

Investigating the toehold exchange DNA walker on a 2D oligo strands modified surface through super-resolved single particle tracking

Based on smFRET measurements, the DNA walker with the fastest stepping rate and most homogeneous behavior is $W_{6_13_6}$. To test the performance of this optimized DNA walker as a long-distance 2D transporter, we developed a surface modification method that yields a high density of DNA footholds on a glass coverslip. In this method, alkyne-functionalized F_1 and F_2 are attached to an azide-modified coverslip through copper-free click chemistry, resulting in random, high-density deposition of the two different foothold strands on the surface (**Fig. 21A, B**). Using TIRF microscopy, we measured an average oligonucleotide surface density of 1.67×10^4 /μm^2, corresponding to an average distance between nearest-neighbor F_1 and F_2 strands of ~10.5 nm (**Fig. 21C**). This estimate should be interpreted as an upper bound on the average spacing between footholds, since our measurements may underestimate the true density if a significant fraction of probe fluorophores are photobleached prior to the measurement. To confirm that this larger inter-foothold distance is compatible with rapid stepping by the walker, we repeated our smFRET measurements of stepping in a *3-Foothold* system constructed from a distinct DNA origami scaffold. Despite the larger distance between adjacent foothold sites on this DNA origami (10.44 nm on average, assuming 0.33 nm/nucleotide) compared to the previous tile system (~7 nm), smFRET characterization revealed a similar stepping rate constant of ~0.5 s^{-1} (IQR 0.6-0.1 s^{-1}) for $W_{6_13_6}$ on this new scaffold, suggesting that the stepping rate is robust to small perturbations in foothold spacing.

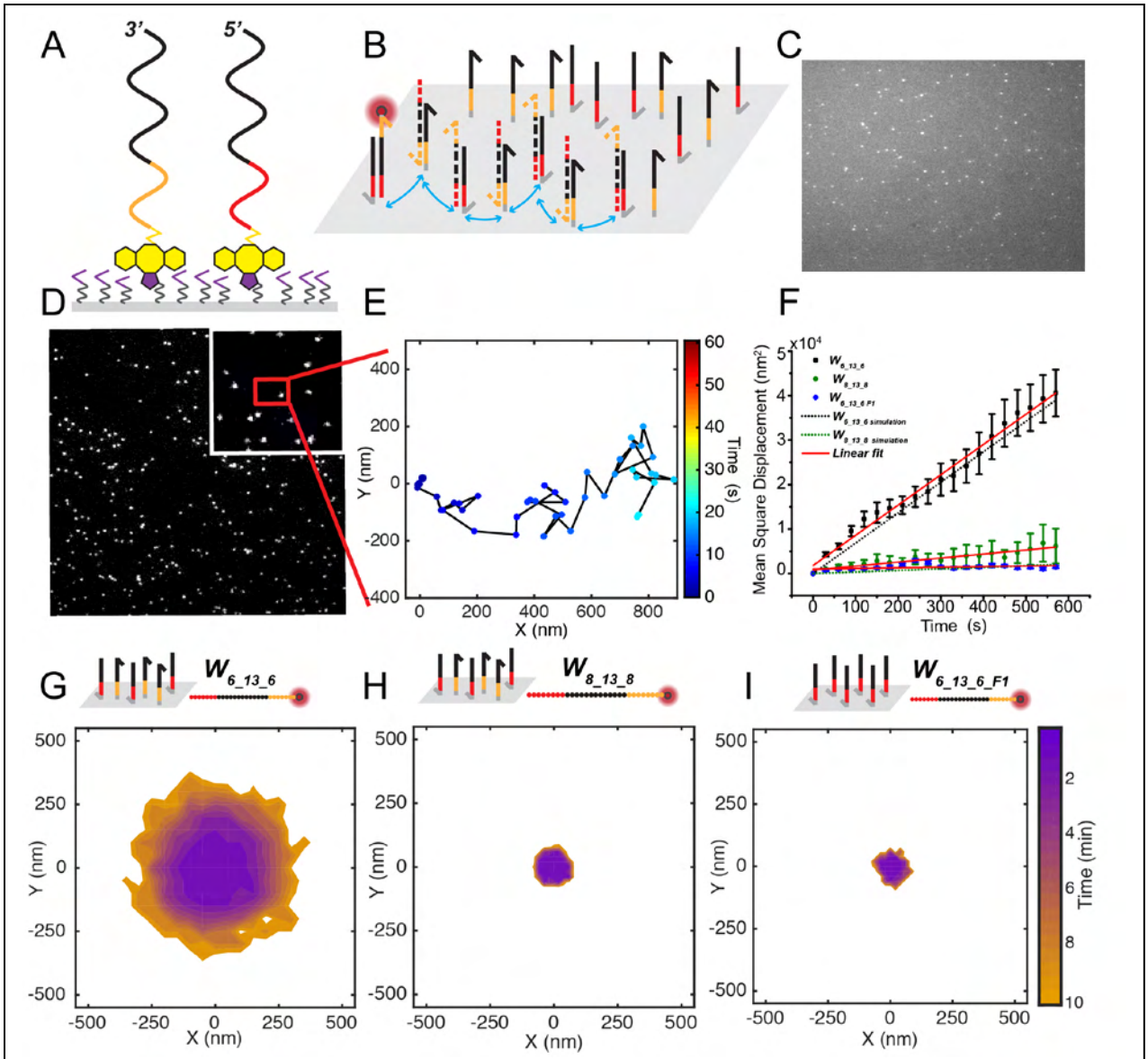


Figure 21. Characterization of 2D foothold arrays and long-range walker movement. A, Schematic of ***F₁*** and ***F₂*** DNA conjugated to glass coverslip surface at high density *via* copper-free click chemistry. Surface azides are shown in orange-grey curve lines and DBCO in yellow. **B,** Schematic of walker movement over a 2D array of footholds. **C,** TIRF image of complementary oligonucleotides bound to footholds on coverslip surface at a ratio of 1 fluorescently labeled oligo: 1 million unlabeled fluorescent oligonucleotides. **D-E,** TIRF image of Cy5-labeled $W_{6_13_6}$ on ***F₁*** and ***F₂*** coated quartz slide (**D**) and one representative fast-moving trajectory of $W_{6_13_6}$ (**E**). **F**, Mean square displacement (MSD) *versus* time plot for $\boldsymbol{W_{6_13_6}}$, $\boldsymbol{W_{8_13_8}}$, and $\boldsymbol{W_{6_13_6}}$ control (***F₁*** only). The diffusion coefficient fit from MSD is 17, 2.3, and 0.33 (nm^2/s) respectively. The predicted diffusion coefficient (dot line in green and black) from smFRET measurement of DNA tile is compared with single particle tracking result. **G-I**, Comparison of extent of diffusion of $\boldsymbol{W_{6_13_6}}$, $\boldsymbol{W_{8_13_8}}$ and $\boldsymbol{W_{6_13_6}}$ ***F₁***-only control over a 10-minute period of observation.

Next, we characterized the long-range movement of optimized walker $W_{6_13_6}$ by 2-dimensional single-particle tracking using TIRF microscopy (**Fig. 21D, E**). Most of the molecules travel >200 nm from their starting position within 10 minutes (**Fig. 21F**), resulting in a measured diffusion 2D coefficient of 17±0.5 $nm^2\ s^{-1}$ (R^2= 0.99), and some molecules are observed to travel nearly 1 µm before photobleaching (**Fig. 21D**). In contrast, particle tracking of $W_{8_13_8}$ indicates a much smaller

diffusion coefficient of 2.2±0.2 nm^2 s^{-1} (R^2= 0.89) (**Fig. 21F, H**), consistent with predictions based on its ~10-fold slower stepping rate as measured by smFRET. For comparison, a random walk model with step size 10.5 nm and stepping rates taken from smFRET measurements on 3-Foothold DNA tiles predicts diffusion coefficients of 17.1 nm^2 s^{-1} and 0.9 nm^2 s^{-1} for $W_{6_13_6}$ and $W_{8_13_8}$, respectively. This close agreement with predictions from measurements of stepping kinetics and foothold density suggests that the optimized walker functions as designed, even on a different substrate and over substantially longer distances. Moreover, a surface coated with only a single foothold type (F_1) results in no significant diffusion of $W_{6_13_6}$ (D ~ 0.33±0.2 nm^2/s (R^2= 0.09), standard deviations in position σ_x = 16.4 nm, σ_y = 15.2 nm), indicating that the observed diffusion is indeed the result of the designed walking mechanism involving both footholds (**Fig. 21G, I**).

Photosynthetic Pathway

Building a DNA-scaffold light-responsive photo-protective element in a photosynthetic pathway

1. Motivation and Background

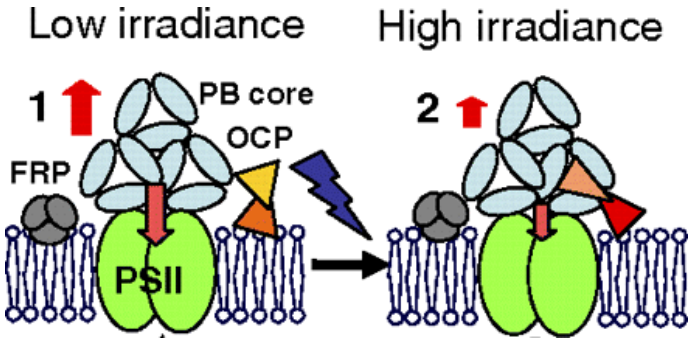


Figure 22 Working model for OCP photoprotection in cyanobacteria. (1) In darkness and under low irradiance the OCP (double triangle) is mostly orange and not (or weakly) attached to the phycobilisome (PB). Only the core of the PB is presented in the figure. (2) Absorption of blue-green light induces changes in the carotenoid and the protein converting OCP^o to OCP^r. The OCP^r will bind to the APC trimers of the core of the PBs and fluorescence quenching will be induced. The red arrows in 1 and 2 illustrated the relative amount of fluorescence from PB. (Image adapted from http://www.pnas.org/content/107/25/11620/F6.full)

Natural light harvesting systems in photosynthetic organisms not only have efficient means of absorbing light and capturing its energy, but they also utilize critical control mechanisms as part of their function. Light is both an energy source and a destructive element; excess excitation energy leads to a variety of deleterious processes, and natural photosynthetic systems go to great lengths to avoid destructive photochemistry by employing various photoprotection mechanisms. While most attempts to mimic photosynthetic light harvesting functions using engineered systems have focused on optimizing the energy transfer efficiency, spectral coverage and absorbance cross section of the apparatus, we have addressed the photo-protection issues in our nanostructured hybrid light harvesting systems by exploring the utility of incorporating photoprotective components. In particular, we are focusing on a component found in cyanobacteria that involves a small orange carotenoid binding protein (OCP). OCP has the property that it is in an orange form in low light conditions (OCP^o), but upon exposure to high light, it switches into a red form (OCP^r). The red form is able to quench excess excited energy absorbed by light-harvesting antenna and dissipate it as heat as illustrated in the working model shown in **Figure 22**. Furthermore, when the protein is isolated from cyanobacteria in dim light conditions, it is found to be in a dimer form. Upon light activation, and subsequent transition $OCP^O \rightarrow OCP^R$, the protein dimer dissociates into monomers. The monomerization reaction has been found to be a reversible process, though the relationship between the orange-to-red and the dimer-to-monomer transitions has not been described yet. It has been shown that the red form of OCP is able to bind to the phycobilisome (the cyanobacterial antenna), and it quenches the excited states, dissipating excess light energy to avoid damage. OCP contains a non-covalently bound carotenoid co-factor. Apparently, the carotenoid accepts excitation energy from the pigments of the phycobilisome via energy transfer (FRET) and thermally dissipates it. A peculiar feature of OCP is the intensity dependence of the conversion reaction: the rate and the percentage of dissociation are dependent on incident light intensity, making OCP a facile system for the regulation of photoprotective function. The scope of this part of the project is two-fold: exploring

experimental conditions required for optical control of the OCP monomerization reaction, and incorporating OCP into DNA nanostructured photonic devices, as a regulatory element.

Taking inspiration from photosynthetic mechanisms in natural systems, we have introduced OCP as a light-sensitive photo protective quenching element into an artificial light-harvesting antenna model to control the flow of energy as a function of light intensity excitation. The artificial antenna model is made of organic dyes (Cy3, Cy5) templated with a DNA-scaffold to be assembled with OCP on it as a modulated quenching element. By controlling the illumination intensity it is possible to switch the direction of excitation energy transfer from the donor Cy3 to either of two acceptors (**Figure 23**). Under low light conditions energy is transferred from Cy3 to Cy5, and under intense illumination, energy is transferred to OCP. These results demonstrate the feasibility of controlling the pathway of energy transfer using light intensity in an engineered light-harvesting system. This work has been published in the journal Nano Letters in 2017.

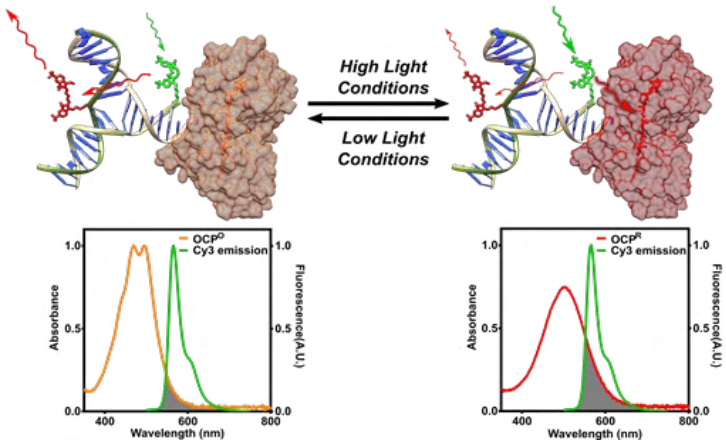


Figure 23 Top: schematics depicting the conceptual design of the OCP-DNA-dyes system used in this work. The arrows indicate the energy flow between the components. On the left, the system is represented under low light illumination, and on the right under high light conditions. Bottom: the two panels show the spectra overlap between the emission of Cy3 and the absorption of OCP^O (left), and OCP^R (right). The spectral overlap between the Cy3 emission and OCP absorption is shaded in gray for clarity.

2. Constructing a DNA nanostructure incorporating the light-induced photo-protective complex

As mentioned above, the role of OCP in Cyanobacteria is to quench the excess excited state of donor pigments in an antenna complex, and dissipate the energy as heat, resulting in a decreased amount of energy flow downstream through the antenna. The system we designed to mimic the photo-protection function of OCP in natural systems, OCP-3arm-Cy3-Cy5, can be used as a model for this situation. In this model, Cy5 is the acceptor dye. Its fluorescence intensity is monitored in order to follow the amount of energy transfer from Cy3 to Cy5. To utilize OCP as a regulatory element for quenching the fluorescence emitted by organic dyes in a light-dependent fashion, we integrated the protein in a DNA nanostructured light-harvesting system where dyes and photosynthetic elements are assembled in an organized fashion, similar to the kinds of DNA-based photonic systems we have published previously. To accomplish this, we have first incorporated OCP into the system and demonstrated light-dependent quenching of the excitation energy.

We have chosen to use the 3arm DNA nanostructure we described previously as the basis for building the light regulated antenna system. The concept is depicted in **Figure 23**. The 3 arm DNA structure is conjugated to two dyes, the FRET pair Cy3 (green)-Cy5 (Red) is here used as an example, but other FRET pairs with similar spectral characteristic could be used as well. The dye-labeled nanostructure can be then conjugated to the cysteine of OCP using SPDP or other

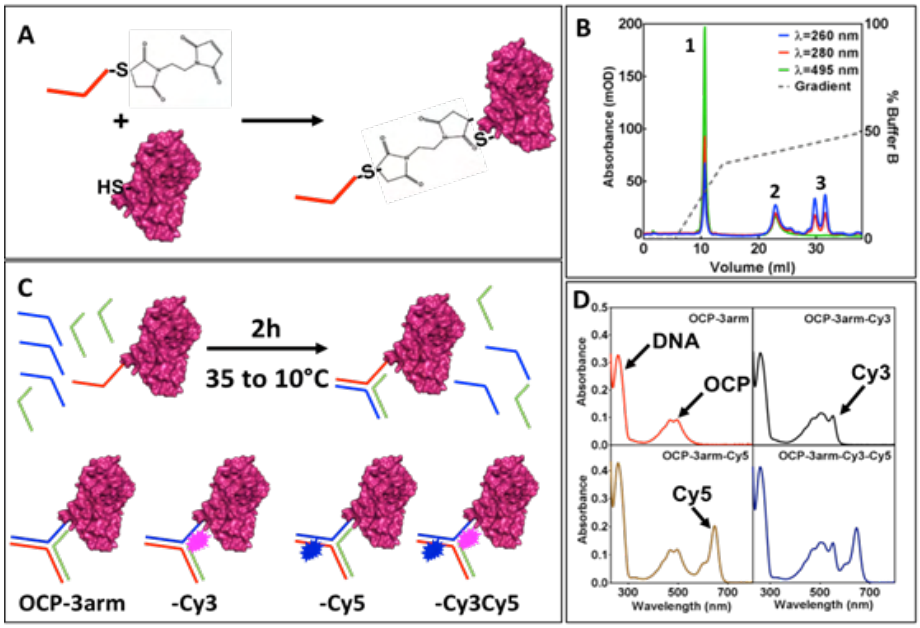


Figure 24 A) Scheme of the coupling reaction used to link the DNA strand St1 with OCP. The maleimide-modified strand is reacted with the protein to form a stable, covalently attached, protein-DNA bioconjugate. **B**) Anion exchange chromatography results for the purification of OCP-St1 after the conjugation reaction. The wavelength monitored at 260, 280, and 495 nm show the presence of DNA (blue), protein (red), and protein-DNA (green) in the eluate, respectively. The dashed line indicates the elution gradient. **C**) Upper part: scheme illustrating the annealing of the DNA 3arm junction on the OCP-St1 construct. Lower part: the four OCP-3arm construct that were separately produced by substituting the strands St2 and St3 with their labeled counterpart. **D**) Absorption spectra of the four OCP-3arm samples after purification. The spectral signatures of DNA (3arm), OCP, Cy3 and Cy5 are clearly visible and were used to calculate the ratio between the components, as indicated in the main text.

maleimide mediated chemistry, as previously reported for other DNA-protein systems. The left side of **Figure 23** shows the expected behavior of the system under low light conditions: OCP is present in its orange form, and the energy of excitation of Cy3 is transferred to Cy5 with little interference from OCP. An increase in excitation intensity should convert OCP into the red form (right side of **Figure 23)**, enhancing spectral overlap between the OCP and the excited state of Cy3. Part of the Cy3 fluorescence should thus be quenched by the carotenoid in OCP, resulting in a decrease of energy transfer to Cy5. Beyond this test system, OCP could be incorporated into more complex photosynthetic networks, acting as an inducible photo-protection element.

We performed the conjugation of OCP to a single strand of DNA, St1 (Red), as illustrated in **Figure 24A,** modifying the DNA first with a *bis*-maleimide linker and then reacting it with the protein at an available surface cysteine. The product of this reaction, named OCP-St1, was purified using ion exchange chromatography and the results are shown in **Figure 24B** (peak 2). The purified OCP-St1 was then used to anneal the OCP-3arm sample by mixing a stoichiometric amount of the other two DNA strands required to assemble the 3arm structure. The modularity of DNA makes it possible to prepare four different samples where different combinations of labeled and unlabeled DNA strands can be used, as illustrated in **Figure 24C**. The assembled samples were further purified using size exclusion chromatography, and then characterized with UV-Vis spectroscopy

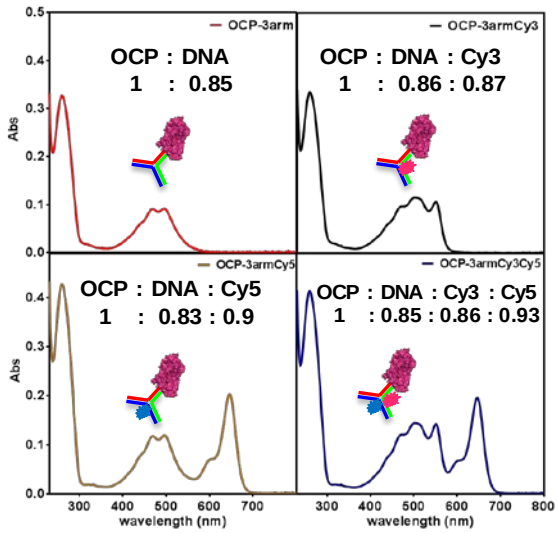


Figure 25 UV-Vis spectra of the OCP-3arm samples with calculated stoichiometry of various components presented.

to identify the spectral features of the individual components, as presented in **Figure 24D**. The ratio of the components in each assembly was calculated based on their extinction coefficients, and are shown in **Figure 25**, where the stoichiometry of the components is reported with each spectrum.

3. Exploring the functional incorporation of the OCP into an artificial antenna system

We then tested the OCP quenching in its orange form on the OCP-3arm-Cy3 and OCP-3arm-Cy3-Cy5 systems. We recorded the fluorescence emission spectra of the samples at low excitation power and in the presence of the Fluorescence Recovery Protein (FRP), which quickly converts OCP^R back to OCP^O, thus keeping the equilibrium concentration of OCP^R negligible.[13, 14] The spectra were compared with the emission spectra of the 3arm-Cy3 and 3arm-Cy3-Cy5 without OCP. The results are shown in **Figure 26A**. It is evident that OCP in the orange form receives energy from Cy3 in the OCP-3arm-Cy3 construct, thus resulting in a decreased fluorescence emission (red line) compared to the 3arm-Cy3 sample (blue line). A similar decrease of emission of Cy3 is observed in the OCP-3arm-Cy3-Cy5 construct (purple line), compared to the 3arm-Cy3-Cy5 (green line), where also a decrease in the emission of Cy5 (peak at 662 nm) occurs. The energy transfer from Cy3 to OCP^O in OCP-3arm-Cy3 was estimated to be 60%.

In the absence of FRP, OCP can be converted under constant illumination. Excitation of Cy3 at 520 nm will also excite the OCP and thus initiate the photoconversion $OCP^O \rightarrow OCP^R$. We tested this by monitoring the emission of Cy3 in OCP-3arm-Cy3 under constant illumination at different power intensities, and the results are shown in **Figure 26B**. The blue line is the control where OCP-3arm-Cy3 was illuminated at low power in the presence of FRP to maintain OCP in the orange form. No changes in the emission at 566 nm are observed in this case. When FRP is not present in the sample, the emission at 566 nm decreases in time until it reaches a plateau. The rate of decrease, as well as the final plateau level, both vary as a function of illumination power, as show in **Figure 26B** (see figure legend for details on the illumination intensity level). To confirm that this effect is indeed caused by the accumulation of OCP^R in the sample, we measured the lifetime of the dye Cy3 as a function of illumination power (**Figure 26C**). As expected, a decrease

in the lifetime of the dye is observed, indicating that there is energy transfer from Cy3 to OCP^R. The fraction of fluorescence quenched by OCP^R was calculated using the data shown in **Figure 26B** and **C**, and the results are shown in **Figure 26D**. The plot shows that the amount of Cy3 fluorescence quenched by OCP increases with the illumination power, reflecting the activation of OCP to its red form.

These results clearly demonstrate that the OCP protein acts, in OCP-3arm-Cy3, as a light intensity activated quenching element, and the amount of fluorescence quenched depends on the intensity used to illuminate the sample.

The ability of OCP to quench the excited state of the donor in competition with energy transfer to an acceptor was investigated further in the OCP-3arm-Cy3-Cy5 system. As shown in **Figure 26,** illumination at 520 nm induces photoconversion of OCP^O to OCP^R and quenches the emission from Cy3 in the OCP-3arm-Cy3 construct. In the OCP-3arm-Cy3-Cy5 construct, emission from Cy3 is light dependent as well (**Figure 27**), at least partially due to quenching by OCP^R as observed in the OCP-3arm-Cy3 system. The intensity change of Cy3, at 566 nm (**Figure 27A**) resembles the data presented in **Figure 26B** from OCP-3arm-Cy3. The time dependence of the Cy5 emission at 662 nm closely follows the emission of Cy3 (**Figure 27B**). To quantify this, we used the blue curve in each plot as a reference, which was measured in the presence of FRP to maintain OCP in the orange state, and calculated the percentage of quenching at the end point of the time traces. The data are shown in **Figure 27C**. It is clear that the fraction of total fluorescence quenched for Cy3 and Cy5 follows the same trend as a function of illumination power. This means that the amount of energy

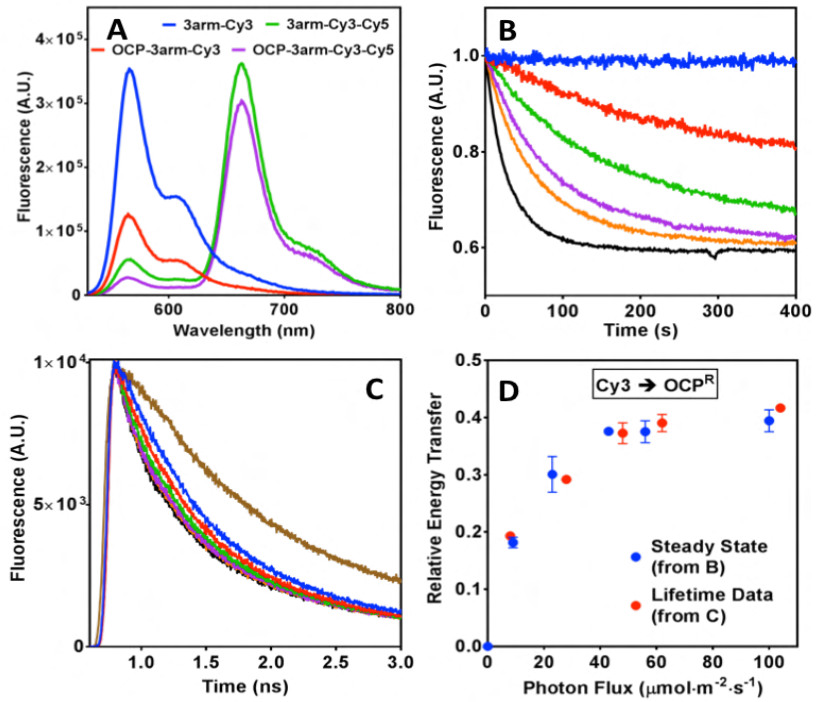


Figure 26 A. **Fluorescence emission spectra of samples used to calculate the energy transfer efficiency from Cy3 to Cy5 and OCP**. To calculate the efficiency between different components within a complex, the emission spectra were recorded at low illumination intensity with addition of FRP to maintain OCP in the orange state. **B**. Fluorescence intensity change of OCP-3arm-Cy3 sample as a function of exposure time monitored at 560 nm (Cy3 emission). The OCP-3arm-Cy3 was excited at 520 nm with photon fluxes of 9 (blue), 9 (red), 23 (green), 43 (magenta), 56 (orange) and 100 (black) □mol·m^{-2}·s^{-1}, and the curves were normalized at the maximum intensity at time zero. The blue trace was recorded in the presence of FRP. **C**. Emission decay curves at 560 nm showing the effect of light activation of OCP on the lifetime of the Cy3 dye. The brown curve is the decay kinetics of Cy3 in the 3arm-Cy3 sample. The blue, red, green, magenta, orange and black traces were recorded with excitation densities of 8, 8, 28, 48, 62, 104 μmol·m^{-2}·s^{-1}, respectively. The blue trace was measured in the presence of FRP. **D.** Relative emission of Cy3 calculated from the data in panel B (blue circles) and C (red circles) as a function of excitation intensity. The OCP+FRP sample was used as a reference to calculate the data point at a Photon Flux of 0 μmol·m^{-2}·s^{-1}. Excitation was at 520 nm for all measurements.

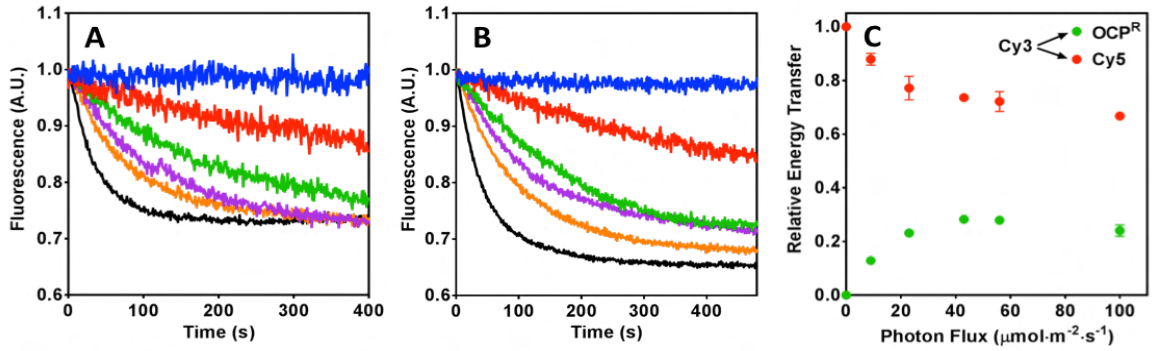


Figure 27. **A** Fluorescence intensity of Cy3 in OCP-3arm-Cy3-Cy5 sample recorded at 560 nm upon excitation at 520 with photon fluxes of 9 (blue), 9 (red), 23 (green), 43 (magenta), 56 (orange) and 100 (black) μmol·m^{-2}·s^{-1}. The blue curve was recorded in the presence of an excess of FRP. **B** Fluorescence intensity of Cy5 at 662 nm in OCP-3arm-Cy3-Cy5 upon excitation at 520 nm at various intensity levels. The color coding is the same as for panel A. **C** Energy transfer from Cy3 to OCP (green) and from Cy3 to Cy5 (red) extracted from the data in panel **A** and **B**, as a function of illumination intensity.

transferred from Cy3 to the acceptor Cy5 decreases with the increase of excitation light intensity, a consequence of a lower population (presumably shorter lifetime) of excited Cy3.

The investigation of the OCP-3arm-Cy3 and OCP-3arm-Cy3-Cy5 system, both by steady state and lifetime measurements allowed us to analyze the energy transfer pathways between Cy3, OCP^O, OCP^R and Cy5. The diagram shown these pathways and the associated kinetic rate constants, whose values were calculated from the measurements discussed above and reported in **Figure 28**. The knowledge of these parameters is fundamental for the design of future antenna systems that will use OCP as a quenching element.

In **Figure 28A,** a model for the energy transfer pathways between the donor and the acceptors is presented with each transfer represented by a black arrow, and the interconversion of OCP in its two forms represented by two red equilibrium arrows. The dashed arrow from Cy5 to OCP^R indicates that the transfer between the dye and the active form of the protein appears to be small enough not to affect the final results of the calculations. The rate constants k_1, k_2, and k_3 represent the microscopic energy transfer rate constants in the system, and they can be calculated from the lifetime and energy transfer efficiency data. Their values are reported in **Figure 28B**. The data indicates that the energy transfer rate from Cy3 to OCP increases about 2.2-fold upon conversion of the protein from the inactive (OCP^O) to the active (OCP^R) state. The ~2 fold increase of k_2 compared to k_1 takes it closer to the Cy3 → Cy5 transfer rate, k_3 (**Figure 28B**), and allows energy transfer to the OCP's carotenoid to be more effective. The results that a decrease of Cy5 emission is seen to behave in the same way as for Cy3, illustrate that OCP^R competes with Cy5 as an energy transfer acceptor more effectively than it does in the OCP^O form. For the OCP-3arm-Cy3 sample, the Cy3 fluorescence lifetime data provide an average lifetime that results from a contribution of k_1, k_2, and the relative populations of OCP in either the OCP^O or OCP^R states. **Figure 28C** shows the apparent rate constant k_1' ($= 1/\tau_{avg}$) as extracted from the fluorescence lifetime measurements. We can calculate the fraction of OCP in the OCP^O and OCP^R forms by using the equation: $k_1' = (1-\alpha)k_1 + \alpha k_2$, where α is the fraction of OCP^R, and (1-α) represent the fraction of OCP^O.

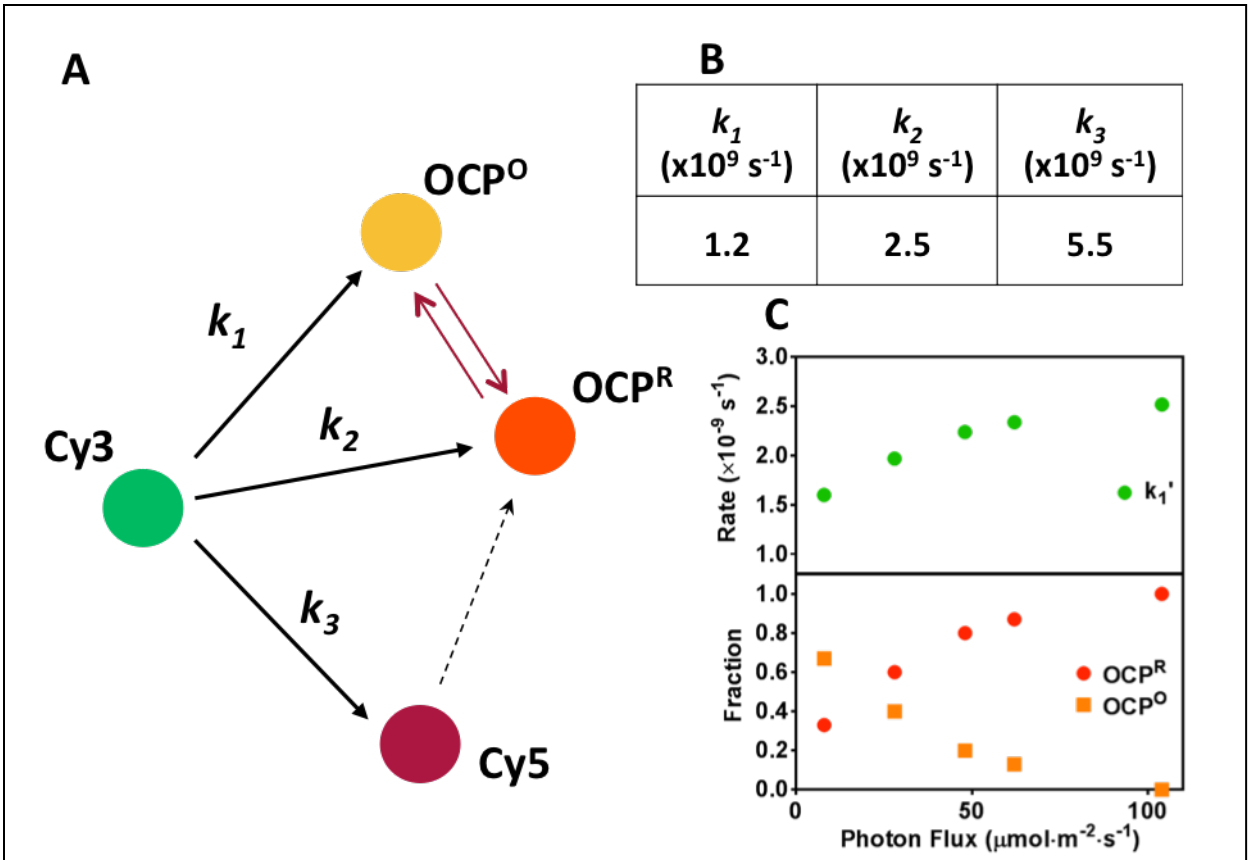


Figure 28. A. Scheme of the energy transfer pathways in the OCP-3arm-Cy3-Cy5 system. The Cy3 dye is the main donor when 520-nm excitation light is used, and OCP^O, OCP^R and Cy5 are the possible acceptors. The black arrows represent the energy transfer paths with the associated rate constants (see main text for details). The red arrows represent the interconversion between the two forms of the protein. The dashed arrow from Cy5 to OCP^R represents the negligible transfer from the Cy5 dye to the protein. **B.** Rate constants extracted from the TCSPC data. **C.** Upper: the apparent rate constant k_1' as a function of excitation intensity, calculated from the data in Figure 2C. Lower: the relative populations of OCP in the orange (OCP^O, solid square) and red (OCP^R, solid circle) states.

In summary, this study has demonstrated that the Orange Carotenoid Protein from cyanobacteria can be incorporated as a light-regulating component into an artificial antenna system using DNA as a scaffold. When conjugated to DNA, OCP retains its capability to switch back and forth from the orange to the red form in response to light activation, and it does so with an intensity dependent behavior that is subject to FRP regulation. The data presented show that the protein is able to quench the fluorescence of a proximal dye donor, Cy3, and as a consequence competes for energy transfer to Cy5. Therefore, OCP can be used as a quenching element in an artificial antenna to regulate energy transfer pathways in response to light intensity changes. It is possible to foresee the incorporation of the protein into more complex energy transfer networks, organized for example on larger DNA origami structures. In a network of light harvesting elements, OCP could provide photoprotection by limiting the excited state lifetime at high intensity illumination, while preserving efficient energy capture at low to moderate illumination intensity. The short lifetime of the carotenoid (few ps) should allow OCP to efficiently quench several fluorophores in its proximity, therefore limiting the number required in the system: the complexity of designs can thus be reduced. Ultimately, the integration of other photochemically responsive elements, such as reaction center proteins that perform charge separation upon light activation, would open the

possibility to design artificial photosystems for specific purposes and with a safety mechanism mimicking the natural one.

We now understand more completely the parameters necessary to design larger and more complex networks of photonic elements incorporating OCP. OCP can be exploited for photoprotection, as it operates in natural systems, in case of high intensity illumination conditions, or it can be used as a regulatory element that can deviate energy from selected branches of a photonic network and be activated by tuning the intensity, or wavelength, of the excitation light.

Electrode interface of photosynthetic reaction center proteins in macroporous materials

1. Background and previous results

The laboratories of Seo, Woodbury and Lin are exploring ways to effectively interface the light-induced redox potentials generated by photosynthetic reaction centers with novel nano and meso-structured electrode materials. Generating a facile interface between redox-active biochemical complexes and electronic materials is challenging for a number of reasons. The attachment of biological complexes to surfaces is often nonspecific and unstable, with the current exchange limited due to a poor connection to the electrode, and such systems are frequently difficult to assemble, control and monitor. Historically, the majority of work interfacing redox proteins with conductive materials has focused on pyrolitic graphite and alkanethiol/alkylthiol-modified gold. Limitations arising from monolayer deposition, denaturation of the protein(s) of interest and the lack of optical transparency of the substrate (which precludes both spectroscopic analysis and limits optoelectronic applications) prompted the development of transparent (semi)conductive oxides (TCOs). TCOs were a significant step forward allowing spectroelectrochemistry of immobilized redox proteins and, from an applied perspective, electrochromic and optoelectronic applications of the biohybrid system. Novel nano- and mesostructured porous TCOs are becoming increasingly available. The 3D architecture of porous TCO materials greatly increases the effective surface area (hundreds of fold) and provides protective cavities for association with macromolecules such as proteins or DNA. This serves to both concentrate the redox protein of interest (and thus increase the optical density for spectroscopic investigations and applications) and to promote functional stability by providing protective encapsulation. Although proteins have been incorporated into other porous transparent conductive oxides, such as WO_3, TiO_2 and SnO_2, the excellent transparency and optical properties of porous indium tin oxide (ITO) have made it the favored TCO. Incorporation of high concentrations of the small redox protein cytochrome *c* into ITO has been reported (on the order of hundreds of pmol/cm^2 rather than the tens of pmol/cm^2 reported for monolayer studies), with the redox properties intact. Porous antimony-doped tin oxide (ATO) is now emerging as a preferred alternative to porous ITO due to its lower cost and very high optical transparency and conductivity. The incorporation of functionally intact DNA nanostructures into ATO pores has been demonstrated. More recently the redox proteins cytochrome *c* and azurin were successfully interfaced with the porous ATO surfaces and shown to retain their redox activity. In Kwan *et al.* (2011), the authors reported extremely high loading of cytochrome *c* into porous ATO (over 1000 pmol/cm^2 for cytochrome *c*, an order of magnitude greater than that reported previously for cytochrome *c* in porous in ITO) and used spectroelectrochemistry techniques to demonstrate that cytochrome *c* had retained its redox activity upon adsorption on ATO pore surfaces.

Photosynthetic reaction centers (RCs) perform light-driven reduction of a terminal acceptor molecule that is then available for subsequent chemistry. This makes them an ideal photonic element for interfacing with electrodes and controlling local redox chemistry in time and space via optical and electronic signals. Because the redox reactions are light driven, as opposed to requiring a substrate, the control of turnover rate is directly and instantaneously connected to light level at a particular time and place. The reaction centers from the bacterium *Rhodobacter (Rb.) sphaeroides* are well suited for this purpose. The structure of these RCs is known, their electron transfer reactions have been well characterized and they are very stable. Furthermore, *Rb. sphaeroides* RCs are amenable to protein engineering and easily expressed in large quantities when grown in the dark chemoautotrophically.

The conversion of absorbed solar energy into chemical redox energy is initiated in *Rb. sphaeroides* RCs by excitation of the primary electron donor, P, which is an excitonically coupled pair of bacteriochlorophylls. A series of electron transfer reactions takes place down a redox gradient from the excited state of P, through a monomeric bacteriochlorophyll (B_A) and a bacteriopheophytin (H_A) resulting in reduction of a molecule of ubiquinone, 'Q_A' with near unity quantum yield on a time scale of about 200 ps. The electron then passes from Q_A to the second ubiquinone, Q_B, forming the semiquinone anion of this cofactor. A second photoinduced electron transfer to Q_B completes the two electron reduction forming a dihydroquinone which leaves the binding pocket and diffuses through the membrane to the cytochrome b/c1 complex where it drives proton pumping and ultimately ATP production. The oxidized primary donor (P^+) is then re-reduced via electron transfer from a soluble cytochrome *c*; cytochrome *c* docks with the RC and an electron transfer reaction takes place with a rate constant on the order of 10 microseconds. There have been a number of previous reports of bacterial RCs interfaced with electrodes for use in integrated optical electronic devices, photovoltaics and biosensors. In the field of molecular electronics, for example, RCs isolated from *Rb. sphaeroides* have been inserted into nanogaps between gold electrodes to act as a switch, which can be controlled by the voltage applied across the electrodes. In addition, the sensitivity of RCs to certain herbicides, such as triazines (which block electron transfer by displacement of the secondary quinone) has been used to develop herbicide sensors based on inhibition of the measured photocurrent.

A major issue in many of the previous studies has been the connection between the reaction center and the electrode. Lebedev *et al*. (2006) demonstrated that cytochrome *c* could be employed as a redox wire, reducing the electron tunneling distance to P and thus improving the connection between P and the electrode surface. Photocurrents generated by HIS-tagged RCs interfaced with an NTA-terminated SAM on a gold electrode were improved by an order of magnitude when cytochrome *c* was incorporated into the system. Another key limitation is monolayer deposition of RCs on the electrode surface. Typically, a monolayer of reaction centers can only produce nanoamps of current per cm^2 (in terms of a reduced product formed by the RC, 1 nanoamp/cm^2 = ~10 femtomoles reduced product per cm^2). Lu *et al*. (2005) and Lukashev *et al*. (2008) achieved photocurrents on the $\mu A/cm^2$ scale (picomoles/cm^2 of reduced product) by interfacing RCs with a porous titanium oxide electrode (doped with tungsten trioxide in the case of Lu *et al*. 2005) to achieve multiple layers of RCs. However, the later studies involved the RC donating an electron to the doped tin oxide electrode (rather than receiving an electron as described below).

In the past few years of this research, we have successfully devised a system in which *Rb. sphaeroides* RCs are electrochemically coupled to transparent, porous ATO electrode films via

cytochrome *c* (cyt *c*) to produce a biohybrid platform in which 2-electron reduction and release of a soluble quinone can be controlled both optically and electronically (**Figure 29**).

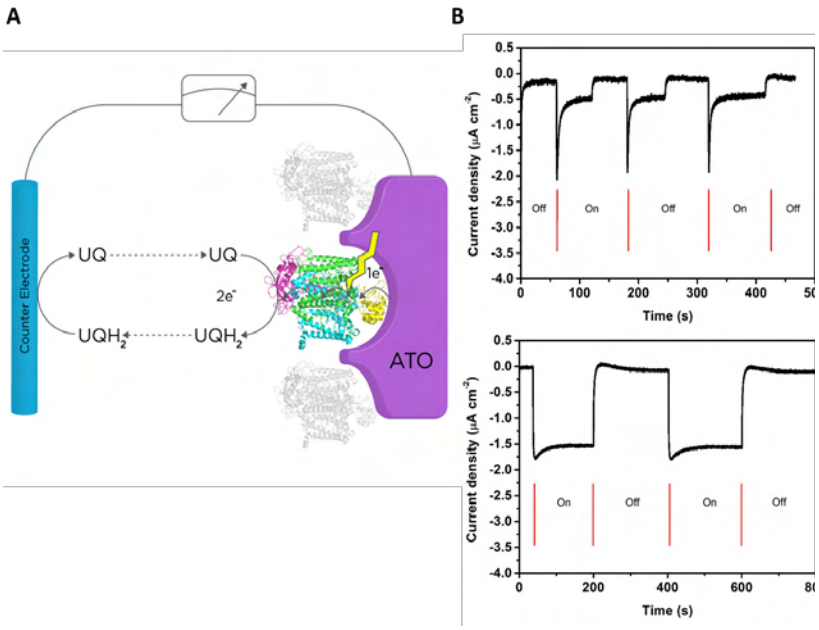


Figure 29. A Photosynthetic RCs interfaced with an ATO electrode via a cytochrome *c* bridge. The cytochrome *c* serves to both orientate the RC and as redox wire to facilitate electron transfer from the electrode to P. In this system, the RC performs one electron photochemistry but generates a two electron carrier (the reduced ubiquinone, which leaves the quinone binding pocket and must be replaced by another ubiquinone molecule from the electrolyte solution). **B** Photocurrent detected from ATO films containing cytochrome *c* and RCs, with either 100 μM Ubiquinone-10 (top) or 100 μM Ubiquinone-0 (bottom) in the 0.1 M Tris electrolyte buffer. For the bottom panel, RCs have also been pre-soaked overnight in a 10-fold Molar excess of Ubiquinone-0. Slides were illuminated with a continuous wave Ti:Sapphire laser set to 800 nm, with an intensity of 5 mW/cm^2.

Cytochrome *c* is the natural redox partner of the RC from *Rb. sphaeroides* and exposing the ATO/cytochrome *c* electrode system (See Kwan *et al.*) to RCs results in the specific and stable assembly of RCs onto the surface. The highly porous architecture of the transparent ATO films allows multiple layers of cytochrome *c*/RCs, analogous to the invaginated membranes of natural systems. The incorporation of cytochrome *c* and *Rb. sphaeroides* RCs was confirmed with UV-vis spectroscopy (**Figure 30**). The positions and relative intensities of the Q_y absorption maxima demonstrated that the RCs retain their conformation and function when assembled in the ATO pores (**Figure 30**).

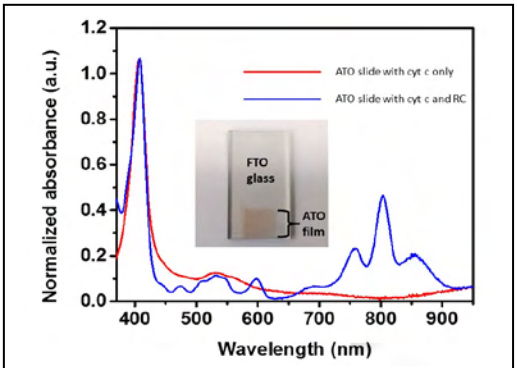


Figure 30. Steady-state absorption spectra for an ATO slide following soaking in cyt *c* (red) and a cyt *c*-soaked ATO slide following application of RC solution (blue). Data are normalized at the 407 nm peak for cyt *c*. Inset: photo of an ATO film on FTO glass, following soaking in 150 μM cyt *c* and washing to remove the unbound molecules (dimension 1x1 cm^2).

Photocurrents were measured using the electrochemical set-up illustrated in **Figure 29A**. The conversion of absorbed light into chemical redox energy is initiated in *Rb. sphaeroides* RCs by excitation of the primary electron donor, 'P', a coupled pair of bacteriochlorophylls. An electron transfer cascade is activated and continues down a redox gradient to a quinone molecule, 'Q_A', via intermediary cofactors (a monomeric bacteriochlorophyll, 'B_A', and a bacteriopheophytin, 'H_A'). The electron then passes from Q_A to a second quinone, Q_B, forming the semiquinone anion. A second photon completes the reduction of Q_B, forming dihydroquinone which then diffuses to the counter electrode. Cytochrome *c* serves

as an electron transfer mediator passing the electron from ATO to P^+, re-reducing the primary donor. Various sample conditions were tested to understand the origin of the photocurrent generated from the ATO-cyt *c*-RC system and the results shows that only slides containing both cytochrome *c* and RCs generate detectable photocurrent (**Figure 29B**).

We conclude from this work that layering cytochrome *c* on porous ATO electrodes allows the assembly of RCs onto the surface and provides a specific binding configuration and electrical connection between the electrode and the RC initial electron donor. The high effective surface area of the transparent macroporous electrode greatly increases the number of RCs that can absorb light and generate reduced quinones. The resulting photocurrent (~ 2 $\mu A/cm^2$ with no applied potential and >10 $\mu A/cm^2$ when a small negative potential is applied) represents a convenient measure that is proportional to the amount of redox activity taking place. Perhaps most importantly from a systems perspective, each component can be individually and quantitatively controlled and monitored. The level of cytochrome *c* reduction can be controlled by potential. The rate of reaction center photoexcitation can be controlled by light intensity. The rate of exchange between the final electron acceptor in the reaction center and the soluble quinones which carry electrons to the counter electrode is sensitive to both the concentration of free quinone and to specific inhibitors of the secondary quinone pocket. This represents a prototype for a type of integrated biohybrid system in which 2-electron redox chemistry can be controlled in time and space both optically and electronically. This work has been published in the journal of Applied Materials and Interfaces.

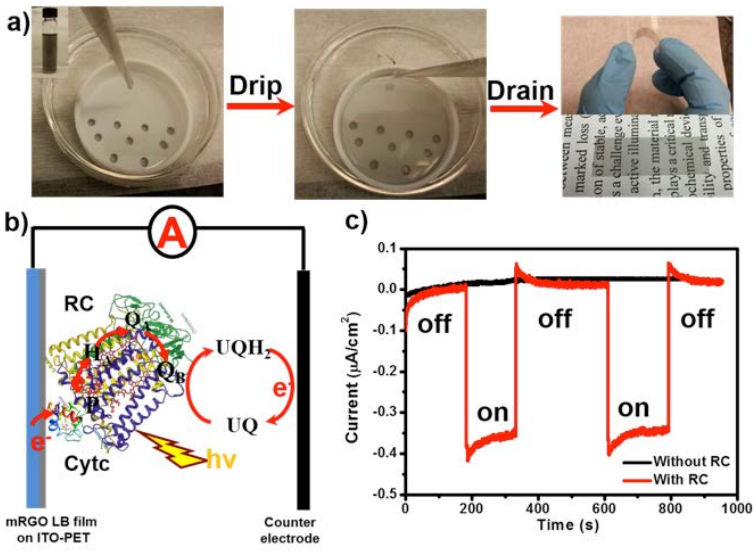


Figure 31. a) The preparation of mRGO LB films on ITO/PET; b) Schematic illustration of the electrochemical cell for RCs/mRGO; c) Photocurrent of mRGO slide with/without RCs.

The desire to precisely orient the RC on the electrode material has led us to begin another subproject involving the same investigators. We have interfaced reaction centers with a new type of electrode material, a functionalized graphene that can be applied to a variety of surfaces including flexible, transparent materials. Mercapto-reduced graphene oxide (mRGO) has been functionalized with thiol binding sites. This equipment-free LB deposition method is highly scalable, which allows mRGO LB films to be deposited onto virtually any substrate, regardless of its shape, size or flexibility. The resulting mRGO slide exhibited excellent flexibility and transparency (**Figure 31a**). The immobilization of RCs on mRGO was confirmed by atomic force microscopy (AFM, not shown). RC features are observed over a size range between 7 and 15 nm immobilized on the mRGO films. Photocurrents were measured using the electrochemical set-up shown in **Figure 31b**, based on the same principle as described for the ATO-cyt *c*-RC system. With this set-up and

applying a potential of 0.125 V vs SHE, a photocurrent density up to 0.40 μA/cm^2 is observed for the RC/mRGO system with 5.0 mW/cm^2 illumination at 800 nm (**Figure 31c**).

In summary, *Rb. sphaeroides* RCs have been successfully immobilized on flexible transparent mRGO LB films for biomimetic solar energy transduction. These RCs display a relatively high stability, retaining 70% of their activity after 20 weeks when stored in the dark at 4 ºC, and 30% of their activity after 24 hours of continuous 35 mW/cm^2 illumination. Photocurrent densities up to 0.4 μA/cm^2 can be achieved using 5.0 mW/cm^2 light intensity at 800 nm. The remarkable stability of RCs on mRGO LB film offers great potential for the development of a flexible biomimetic device. This work has been published in the Journal of Materials Chemistry.

2. Incorporating the antenna system to increase cross section of light absorption

Our previous work was focused on using isolated reaction centers to build a biohybrid system for generating photocurrent which can be controlled optically or electronically. Inspired by how natural photosynthesis work, we have expanded the project by adding additional light collecting elements into the RC system. The purpose is to gain further control of the device under various light conditions. In nature, all photosynthetic organisms contain a light-gathering antenna system, which serves to increase the cross section available for light absorption. We have now included this antenna system in our biohybrid photoelectrochemical cell. Two approaches have been investigated so far. In one approach, we have used a natural antenna system, the light-harvesting system 1 (LH1), as the additional light-absorbing component. As illustrated in the inset of **Figure 32**, LH1 is the core antenna surrounding the RC protein in the membrane and can be isolated as a complex, LH1-RC. The LH1-RC systems were isolated from a range of purple bacteria in the lab of our collaborator Prof. Richard Cogdell at the University of Glasgow. In the second approach, we have incorporated biomimetic artificial light-harvesting antenna into the RC system using DNA-templated dye conjugates with the dyes appropriately placed to transfer energy to the reaction center. Efficient excitation energy transfer from dye molecules and DNA-templated dye conjugates to RC proteins has been demonstrated successfully in our previous work.

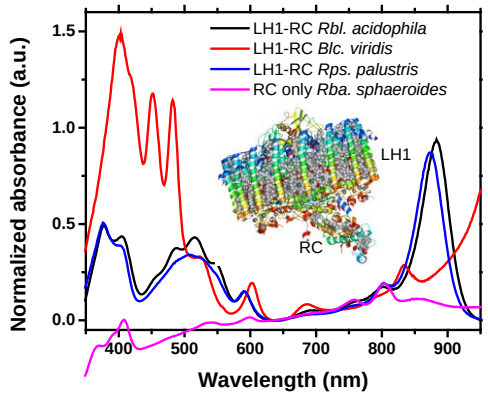


Figure 32. Absorption spectra for cytochrome *c*-soaked ATO slides following pipette application of either RCs from *Rba. sphaeroides* (pink), LH1-RC from *Rbl. acidophila* (black), LH1-RC from *Blc. viridis* (red) or LH1-RC from *Rps. palustris* (blue). The curves are normalized at 650 nm. Slides have been left to air dry after each step.

We have successfully interfaced the LH1-RC complexes from *Rhodopseudomonas (Rps.) palustris, Rhodoblastus (Rbl.) acidophila* and *Blastochloris (Blc.) viridis* with ATO via horse heart cytcochrome *c*. The performance of these ATO-cyt *c*-LH1-RC systems have then been compared to ATO-cyt *c*-RC systems. The absorption spectra for cytochrome *c*-soaked ATO slides following pipette application of those LH1-RC complexes and the isolated RCs are shown in **Figure 32**, where strong absorption increases in the wavelengths below 550 nm and above 850 nm are evident. The electrochemical cell was as described above for the initial ATO-cyt *c*-RC work. All RC and

LH1-RC samples were applied to the ATO film at an OD of 25 at the peak corresponding to the Qy maxima of the monomeric Bchls. Electrolyte buffers contained 0.1 M Tris and 250 µM ubiquinone-0 and a potential bias of 0.1 V (SHE) was applied to all slides to ensure all ATO-bound cytochrome *c* was reduced. A broadband white light source was used to test the photocurrent generated in response to different light intensities. As expected, light intensity experiments show that when illuminated with white light the ATO-cyt *c*-LH1-RC systems perform better at lower intensities, and reach light saturation more quickly, than the ATO-cyt *c*- RC systems without antenna (**Figure 33**). ATO-cyt *c*-LH1-RC complexes receive the excitation energy captured by the light-gathering antenna in addition to that directly received by the RC and they therefore work more efficiently and saturate at a lower light level than those systems containing RC alone.

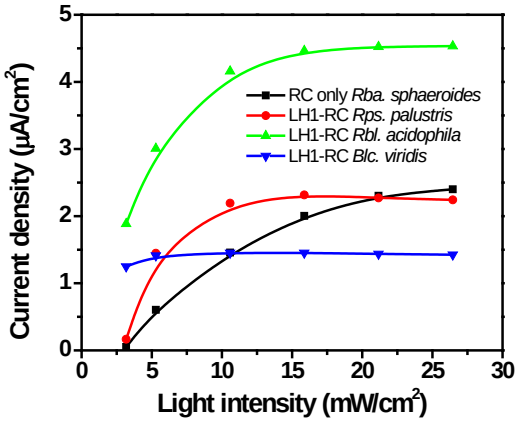


Figure 33. Photocurrent detected for an ATO films pre-soaked in cytochrome *c* and treated with either RCs (black) or LH1-RCs (red, blue and green), 0.1 M Tris containing 250 µM Ubiquinone-0. The light source used to excite the RCs/LH1-RCs within the ATO was a white light, with the power density increased incrementally.

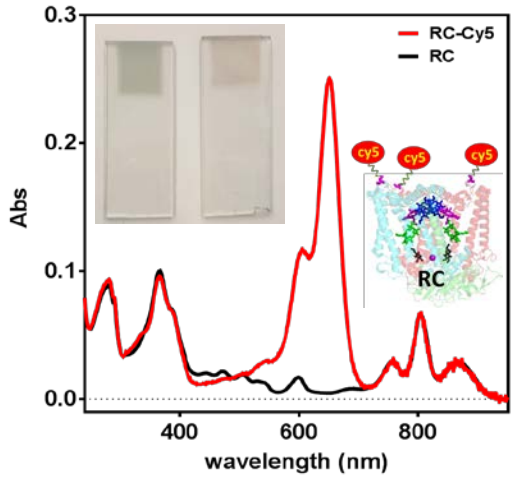


Figure 34. Steady-state absorption spectra for unlabeled (black) and Cy5-labelled RC samples (red). Inset shows a photo of ATO slides, pre-treated with cytochrome *c* and containing RCs without (left) and with Cy5-labelled (right). Data are normalized at the 800 nm. Slides have been left to air dry after each step. Film (inset) dimensions are 1 cm^2. The schematic on the right shows a RC with 3 cy5 dyes attached.

We then investigated RC proteins in which surface cysteine residues engineered near the 'P' end of the RC to facilitate orientated binding of dye or DNA-dye complexes to the thiol groups. We have prepared both RC mutants with a single cysteine residue in this region and with three. The triple-cysteine mutant was provided by our collaborator Prof. Tom Beatty, at the University of British Columbia, whose group has previously reported successful binding of this modified RC to the surface of a gold electrode. We have labeled both the single and triple cysteine residues of *Rb. sphaeroides* RC complexes with Cy5 dye which absorbs around 620 nm and interfaced these dye-labelled RCs with ATO that has been pre-soaked in cytochrome *c*. The absorption spectra and a photo of slides of ATO-cyt *c* containing triple cysteine RCs with and without CY5-labels are shown in **Figure 34**.

Significant enhancement of photocurrent for these systems compared to reaction centers without dye were obtained (**Figure 35**). Under white light excitation the Cy5 dye-labelled ATO-cyt *c*-RC system exhibits a 40% increase of photocurrent compared to that of the unlabeled ATO-cyt *c*-RC system Cy5 dye (**Figure 35A**). When selective excitation at 650 nm is used, a 10-fold photocurrent increase is observed (**Figure 35B**), confirming that the dye is serving as a light-harvesting component that delivers photon energy to the RC efficiently.

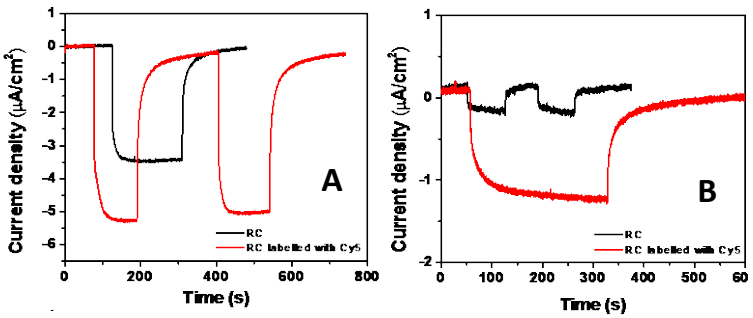


Figure 35. Photocurrent detected for a ATO films pre-soaked in cytochrome *c* and treated with either RCs (black) or RCs labelled with Cy5 (red) under white light excitation (**A**) or 650 nm excitation (**B**). The electrolyte buffer is 0.1 M Tris containing 250 μM Ubiquinone-0.

We then worked to conjugate a 3-arm-DNA 'antenna' containing multiple dyes to the cysteine mutant RCs to allow specific attachment of the artificial antenna systems to the RCs and subsequent optimization of their function as biomimetic antenna-RC systems. Two synthetic dyes are chosen and strategically placed in the antenna in such a way that they can collect additional light energy in two different spectral regions of the solar spectrum and transfer their energy to RC through Förster resonance energy transfer (FRET). Three of those antennae are conjugated through disulfide bonds to each *Rb. sphaeroides* RC near the primary donor, P, to facilitate the energy transfer process. A schematic illustration with one antenna complex is shown in the inset of **Figure 36A.** The distinct advantage of this antenna, constructed with the previously characterized 3arm DNA superstructure is in allowing the attachment of more than one dye, and the tunability offered by the capacity to alter those dyes. For our experiments, we selected the dyes Cy3 and Cy5, which absorb in the visible region of the solar spectrum (around 450 – 580 and 550 – 700 nm, respectively) where the RC absorbance is very low (**Figure 36A**), and have sufficient spectral overlap to allow a cascade of excitation energy transfer from Cy3 to Cy5 to the RC. That is, based on their absorption and emission spectra RC can be

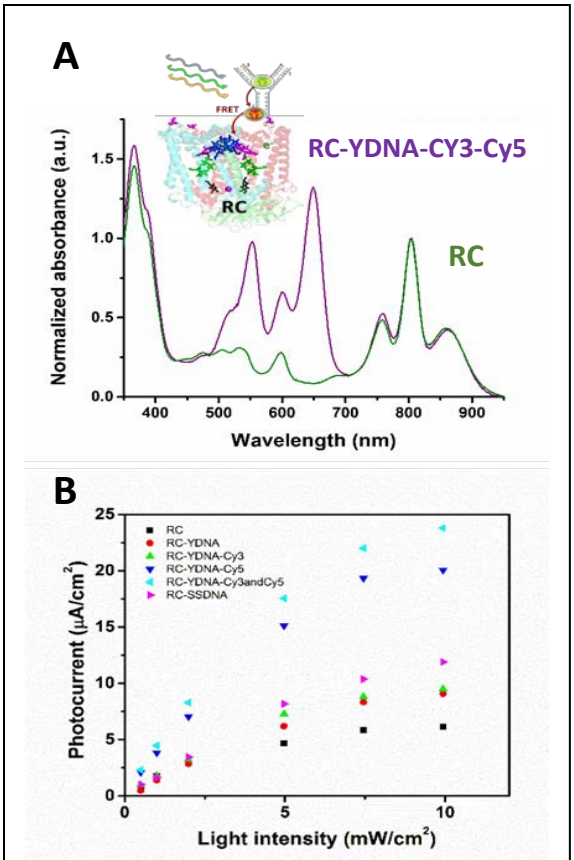


Figure 36. A. Steady-state absorption spectra for the RC (green) and the RC-YDNA-Cy3Cy5 (magenta) samples. Spectra are normalized at 804 nm. **B.** Photocurrent densities for ATO films containing cytochrome *c* and RC-DNA conjugates (applied as 15 ul of 7 uM RC) as a function of light intensity. The electrolyte buffer contains 0.1 M Tris and 500 μM ubiquinone-0 (UQ). Slides were illuminated with a broad spectrum fiber optic white lamp. The illumination intensities (at 800 nm) ranged from 0.5 mW/cm^2 to 10 mW/cm^2.

excited through energy transfer from Cy5 to the RC as well as through an energy transfer cascade from Cy3 to Cy5 to the RC, as reported by Dutta *et al.* for RC-YDNA-Cy3Cy5 samples in solution.

DNA-based biomimetic antenna incorporating a single dye, either Cy3 (RC-YDNA-Cy3) or Cy5 (RC-YDNA-Cy5), and both Cy3 and Cy5 (RC-YDNA-Cy3Cy5) were prepared and covalently attached to the surface cysteines of triple cysteine mutant of *Rb. sphaeroides* RCs. The cysteine residues of the RC mutant are more than 3.5 nm apart from each other to limit self-quenching of the excited state and to avoid intramolecular disulfide bond formation. They are also optimally placed for energy transfer relative to the electron donor, P, in the RC, with distances from each cysteine to P ranging from 3.0 to 3.7 nm. Fast protein liquid chromatography (FPLC) was used to select RCs that had DNA antenna conjugated to all three cysteine residues (i.e. DNA: RC = 3:1). Triple cysteine mutant RCs with the 3arm Y DNA-based biomimetic antenna but no dye molecules (RC-YDNA) and triple cysteine mutant RCs with no DNA antenna (RC), were also prepared as control samples.

Following the general processes in our previous work, the RC-DNA conjugates were then incorporated into macroporous antimony-doped tin oxide (ATO) films, which had been impregnated with cytochrome *c*, on fluorine tin oxide (FTO) glass slides. The RCs are interfaced with the ATO pore surface via a cytochrome *c* bridge, which serves as a redox wire. Dutta *et al.* showed that the DNA antenna does not hinder cytochrome *c* oxidation. Each slide was placed into an electrochemical cell containing 0.1 M Tris buffer with 500uM ubiquinone-0 (UQ), using a platinum counter electrode, a Ag/AgCl reference electrode, and ATO set as the working electrode, to construct a biohybrid photoelectrochemical cell with the same setup as shown in **Figure 29A**.

Upon illumination, the RC performs charge separation within the cell, generating a two-electron reductant (UQH_2) and photocurrent. The photocurrent was recorded for each system tested under white light illumination at different light intensities from 0.5 to 10 mW/cm^2; intensity was varied by using a neutral density filter. Photocurrents recorded for the RC-YDNA-Cy3Cy5 and RC-YDNA-Cy5 systems were 4- and 3-fold greater, respectively, than those achieved for the unmodified RC system (**Figure 36B**). Both RC-YDNA-Cy3 and RC-YDNA systems performed slightly better than the system with RC alone, with about 0.5-fold relative increase.

The highest photocurrent was observed for the RC-YDNA-Cy3Cy5 system as one might expect because the double-dye antenna provides the largest spectral coverage through both energy transfer from Cy5 to the RC and the energy transfer cascade from Cy3 to Cy5 to the RC. The large photocurrent for RC-YDNA-Cy5 indicates that the energy transfer from Cy5 to RC is highly efficient. Because of the distance and spectral overlap, there should be little energy transfer directly from Cy3 to RC, it is thus reasonable that the RC-YDNA-Cy3 system performed only slightly better than the unmodified RC system. Photocurrent measurements at selective excitation wavelengths support this explanation. When illuminated at 650 nm (**Figure 37B**), both the RC-YDNA-Cy3Cy5 and RC-YDNA-Cy5 systems showed the same 3-fold increase in photocurrent. As Cy3 has no absorbance at 650 nm, it cannot contribute here, while Cy5 transfers excitation directly to the RC in both systems. Using 550 nm light that selectively excites Cy3, there is a 2-fold enhancement in the photocurrent generated by the RC-YDNA-Cy3Cy5 system, while RC-YDNA-Cy3 shows a much smaller increase (**Figure 37A**).

It is notable that both RC-YDNA-Cy3 and RC-YDNA systems perform more or less the same (**Figure 37A**). This indicates that the increased photocurrent of the former with respect to RC system may not be all due to the energy transfer from Cy3 to RC but rather that the presence of the Y DNA itself is important. Indeed, the spectral overlap between Cy3 and the RC is rather small compared to Cy5 and thus energy transfer would not be as efficient. In the literature, it has been reported that redox proteins, such as cytochrome *c*, can interact electrostatically with DNA to take part in long distance redox reactions. Given the plentiful availability of cytochrome *c* inside the pores of the ATO electrode, it is plausible that the DNA double strands of the RC-YDNA strongly interact with the small proteins and form a more redox-conductive medium on the electrode pore surface. Somewhat similar observations have been made in a previous report where photocurrents generated by a photosystem I/gold electrochemical cell were significantly improved by the creation of multiple electroactive layers of photosystem I and cytochrome *c* using a DNA matrix.

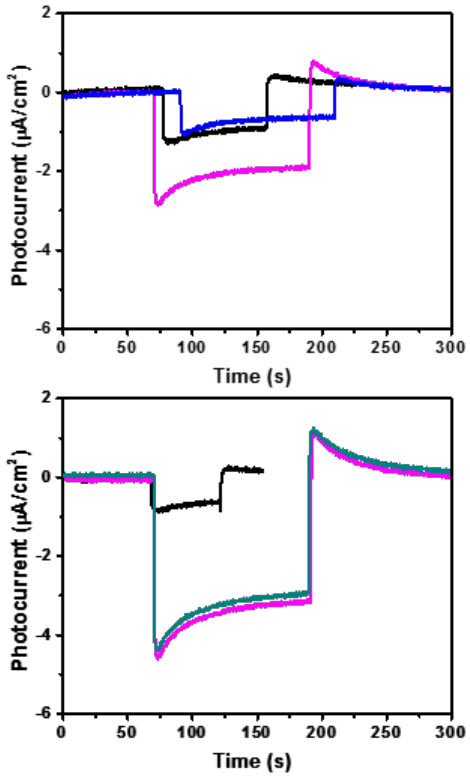


Figure 37. A Photocurrents observed for RC-YDNA conjugates with Cy3 only (blue), Cy3 and Cy5 (magenta) or no dyes (black) under selective excitation using a 20 W fiber optic lamp and a 550 nm (+/- 8 nm) bandpass filter. **B** Photocurrents observed for RC-YDNA conjugates with Cy5 only (cyan), Cy3 and Cy5 (magenta) or no dyes (black) under selective excitation using a 20 W fiber optic lamp and a 650 nm (+/- 8 nm) bandpass filter. The electrolyte buffer contains 0.1 M Tris and 500 μM Ubiquinone-0.

In consideration of the structural organization between the Y DNA and cytochrome *c* proteins, one might think that the stability and flexibility of the DNA structure is important in achieving the minimal energy complex of those different molecules via electrostatic forces. When bound to DNA in the proper position, cyanine dyes can intercalate in dsDNA and thus affect the stability of the DNA structure to which they are attached. However, that may not be the case because both RC-YDNA-Cy3 and RC-YDNA systems perform similarly. In order to see the effect of the structural flexibility, we tested the system with single stranded DNA, RC-ssDNA, in which only Strand 1 of the Y DNA nanostructure was attached to each of the cysteines. As the light intensity increased the system outperformed the RC-YDNA system (**Figure 29**). At the lowest light intensities, the RC-ssDNA produces similar photocurrents to the RC-YDNA and the RC-YDNACy3 but as the light intensity increases, and so the requirement for efficient electronic communication with the electrode surface becomes greater, the RC-ssDNA substantially outperforms the others.

In summary, a DNA-based biomimetic antenna containing the synthetic dyes Cy3 and Cy5 has been covalently conjugated to the surface cysteines of a modified *Rb sphaeroides* RC, which was then incorporated into an ATO-based photoelectrochemical cell. The antenna substantially enhances the RC's absorption in the visible region of the solar spectrum, which improves the overall absorbance cross section of the RCs and thus, the performance of the photoelectrochemical

cell in which they are incorporated. In addition, we have found that DNA conjugation alone can improve the cell performance. While it is tempting to suggest that the DNA nanostructure could be facilitating the electrochemistry of cytochrome *c* within our photoelectrochemical cell, we have no direct evidence of this and the reason behind this enhancement remains to be determined. Since this DNA-based biomimetic antenna is essentially a tunable template onto which different dyes, and different numbers of dyes, can be incorporated, it provides a new platform for designing modular light-harvesting antennae which can optimize spectral coverage to improve the performance of photoelectrochemical cells. This work has been submitted to the journal of ChemSusChem recently.

3. Incorporating Photosystem I to harvesting more redox power from ATO-cyt c system.

In this project, we focused on increasing the redox power harvested from our biohybrid photoelectrochemical cell with the ultimate goal of utilizing the doubly reduced product to perform redox chemistry. We have targeted Photosystem I (PSI) from the thermophilic cyanobacterium *Thermosynechococcus elongatus* to interface with the ATO electrode films based on the following considerations. Unlike purple bacterial reaction centers, which have a quinone molecule as their terminal electron acceptor, the terminal electron acceptor in PSI is an iron sulfur protein with a low enough redox potential to reduce $NADP^+$ to NADPH via ferredoxin. NADPH has a midpoint potential of -0.32 V, almost 400 mV lower than ubiquinone, and is used in numerous enzymatic reactions that reduce carbon. Indeed, biofuels and many industrially important chemicals (e.g. drug precursors and biodegradable plastics) require NADPH-dependent enzymes for their production.

The reaction path for generating NADPH is illustrated in the red frame in **Figure 38.** All electron transfer reaction kinetics are well characterized spectroscopically and temporally, and our collaborators from Prof. Petra Fromme's lab are experts in handling these proteins. Furthermore, this project can be coupled to enzyme cascades produced in Prof. Hao Yan's group. Another important reason for using Photosystem I from the thermophilic cyanobacterium *Thermosynechococcus elongatus* to interface with the ATO electrode films is that the *elongates* PSI binds to, and takes electrons from, horse heart cytochrome *c*, just as does the *Rb. sphaeroides* reaction center. Therefore we used essentially the same

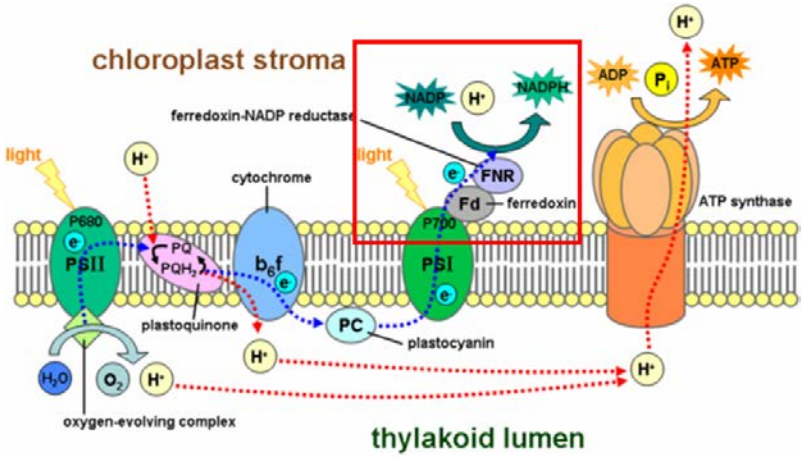


Figure 38. A typical photosynthetic membrane from an oxygenic photosynthetic organism, such as the thermophilic cyanobacterium *Thermosynechococcus elongates* that we have selected for our studies, illustrating photosystem I (PSI). The terminal electron acceptor in PSI is an iron sulfur protein with a low enough redox potential to reduce $NADP^+$ to NADPH.

electrochemical set up and incubated the PSI complexes with the ATO films coated with horse heart cytochrome *c*. A typical absorption spectrum of PSI on ATO film is shown in **Figure 39A** (blue curve). The electrolyte buffer used was 5 mM phosphate (pH 7) and electrochemical measurements were performed on the PSI with the ATO under white light excitation (with an illumination intensity of 35 mW/cm^2). Photocurrents of 1 μA/cm^2 were observed (**Figure 39B**) even in the absence of an additional electron acceptor since oxygen within the buffer is capable of oxidizing the iron sulfur center.

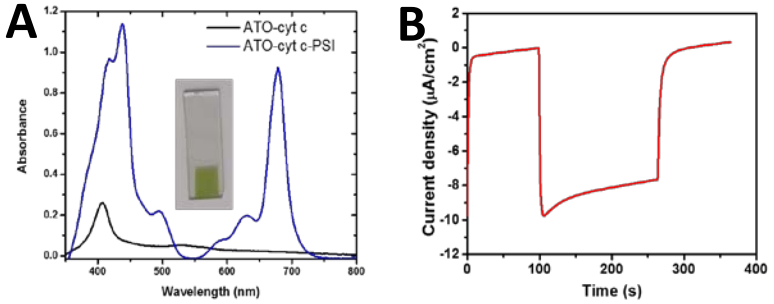


Figure 39. A. Steady state absorption spectra for ATO slides containing cytochrome c (black) and cytochrome c and PSI (blue). Inset shows an ATO slide treated with cytochrome c and PSI. **B**. Photocurrent generated by a biohybrid photoelectrochemical cell containing an ATO slide with cytochrome *c* and PSI. The electrolyte buffer used was 5 mM phosphate (pH 7) and measurements were conducted under white light excitation (with an illumination intensity of 35 mW/cm^2) with an applied potential of 0V (SHE).

Our next step was to include the natural electron acceptor, ferredoxin, and $NADP^+$ to produce NADPH. The reaction scheme is illustrated in the top part of **Figure 40A**. Since the reduction of $NADP^+$ to NADPH is reversible, an enzyme which can irreversibly consume the NADPH produced was also added. Ferredoxin is a strong reductant but can only function in one electron reductions, while $NADP^+$ can only accept 2 electrons in the form of a hydride. We therefore require an intermediary to facilitate the electron transfer. The transfer of electrons from reduced ferredoxin to NADP+ is catalyzed by the flavoprotein, ferredoxin-NADP+ reductase (FNR). This complex accepts the electrons one at a time from ferredoxin and then transfers a hydride to $NADP^+$ to form NADPH. Since FNR is a reversible enzyme, it will also reduce ferredoxin in the presence of NADPH, potentially generating a short circuit in our system and we therefore use an enzyme (for example glutamate dehydrogenase, which reduces glutamate and oxidizes NADPH), to recycle NADPH back to $NADP^+$.

In order to detect the steady state concentrations of NADPH generated from the photoelectrical experiment, a commonly used assay based on diaphorase reaction was employed as shown in the lower half of **Figure 40A**,. In this assay, diaphorase converts NADPH to $NADP^+$ and simultaneously converts the nonfluorescent compound resazurin to highly fluorescent resorufin. A dramatic increase of fluorescence around 580 nm when resazurin is converted to resorufin is shown in **Figure 40C** (blue and red curve, respectively). One can therefore monitor NADPH production by observing the rise in the resorufin fluorescence peak in the electrolyte buffer. Some of the results showing the effect of sequential addition of the reaction components on the photocurrent for an ATO-cytc-PSI system are shown in **Figure 40B**. While ferredoxin addition appears to short circuit the system, with the photocurrent reducing as ferredoxin likely donates electrons to the cytochrome *c*, the photocurrent recovers upon the addition of $NADP^+$. It appears that this is not sustained upon addition of the diaphorase, as the NADPH is converted back to $NADP^+$. However we believe the presence of the dye is complicating the system. The resorufin fluorescence peak obtained for the electrolyte buffer for an ATO-cyt c slide that has been treated

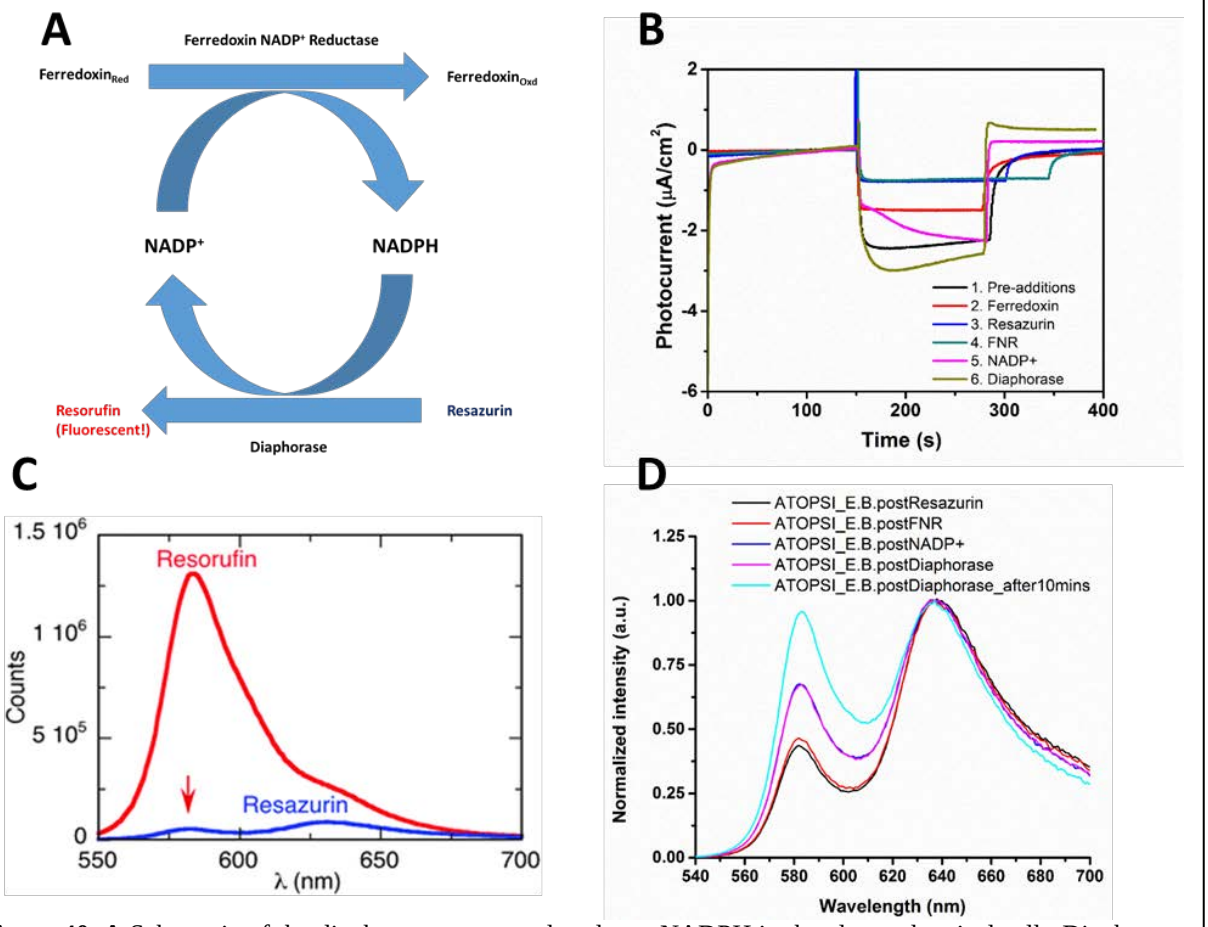


Figure 40. A Schematic of the diaphorase assay used to detect NADPH in the electrochemical cell. Diaphorase converts NADPH to $NADP^+$ and simultaneously converts the nonfluorescent compound resazurin to the highly fluorescent resorufin (reactions shown in the bottom half of **A**). **B**. Photocurrents achieved for an ATO-cytc-PSI slide with sequential addition of each of the reaction components shown in the legend. The electrolyte buffer used was 5 mM phosphate (pH 7) and measurements were conducted under white light excitation (with an illumination intensity of 35 mW/cm^2) with an applied potential of 0V (SHE). **C**. Resazurin (blue curve) and resorufin (red curve) fluorescence spectra in solution. **D**. Fluorescence spectra collected for the electrolyte buffers for ATO-cytc-PSI slides after each experiment shown in **B**.

with PSI is significantly greater than that obtained from a system in which the PSI is absent indicating that we have successfully produced resorufin within the electrochemical cell (**Figure 40D**), but it does appear that some resorufin is produced even in the absence of PSI and our most recent experiments indicate that resazurin can also be reduced by the ferredoxin. The system is chemically complicated and we are continuing to conduct control experiments and to better understand the detailed flow of electrons through the system. We are now employing a simpler assay for NADPH by directly measuring fluorescence from NADPH in the electrolyte buffers.

4. Tracking diffusion of DNA superstructures in meso-macroporous ATO coatings

In fabrication of the bio/nano hybrid photoelectrochemical systems, it is important to understand how the large biomolecules can be incorporated in the pores of the inorganic electrode materials. However, there have been few reports on how their pore structure physically interacts with

biomacromolecules as a characteristic critical for designing 'smart' hybrid materials. By taking advantage of single particle tracking (SPT) expertise of Walter's lab, we thus studied the diffusion dynamics of DNA superstructure molecules (fluorophore-labeled DNA nanotweezers probes) inside the meso-macroporous ATO host and thus yielded fruitful insights into the interactions of host and guest.

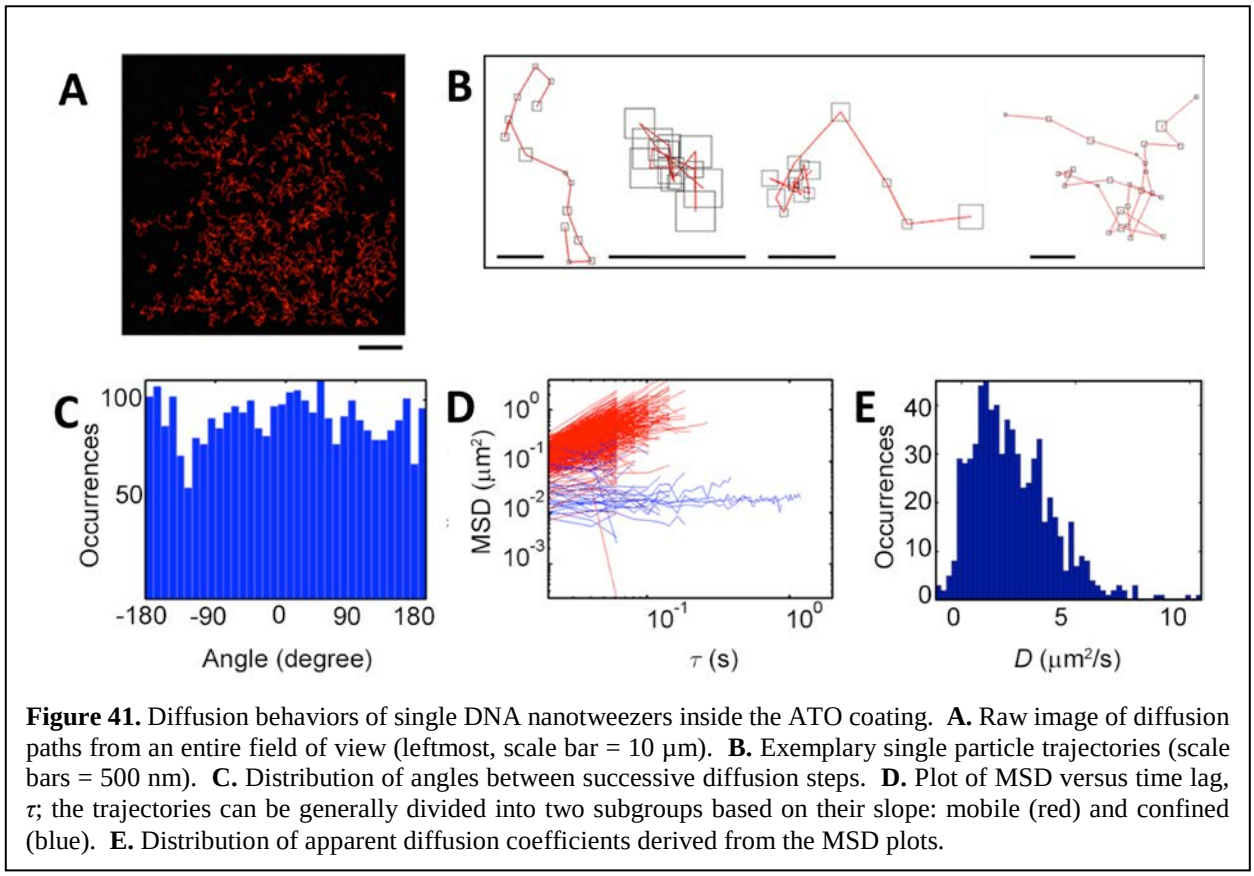


Figure 41. Diffusion behaviors of single DNA nanotweezers inside the ATO coating. **A.** Raw image of diffusion paths from an entire field of view (leftmost, scale bar = 10 μm). **B.** Exemplary single particle trajectories (scale bars = 500 nm). **C.** Distribution of angles between successive diffusion steps. **D.** Plot of MSD versus time lag, τ; the trajectories can be generally divided into two subgroups based on their slope: mobile (red) and confined (blue). **E.** Distribution of apparent diffusion coefficients derived from the MSD plots.

A representative field of view with observed tracks is shown in **Figure 41A**. The DNA probes appear to diffuse randomly, but a closer inspection reveals different types of individual diffusion trajectories (**Figure 41B**). Most of the trajectories behave like the Brownian diffusion expected in an open space (e.g., the far left and right ones in **Figure 41B**), while some traces indicate the tracked probes as temporarily confined (e.g., the second one from the left in **Figure 41B**). The confinement is not permanent (finite confinement) and some trajectories show free diffusion of the probe after a brief confinement (e.g., the second one from the right in **Figure 41B**). To extract kinetic information, further track analyses were carried out using custom MATLAB codes. In a given focal plane, 2D random walks were observed from an analysis of the distribution of angles between successive diffusion steps, as evident from the equal distribution of angles in each direction (**Figure 41C**). This result is expected since the observed 2D trajectories are projections of the 3D random motions of the probes inside the ATO coating. Moreover, most of the observed tracks had fewer than 10 steps, owing to the fast 3D diffusion in and out of the imaging plane, further supporting fast 3D random motion behavior. The diffusion coefficients (D) of individual

particles were calculated from the Einstein-Smoluchowski equation: MSD (τ) = 2n$D\tau$, where n is the dimensionality of motion, by plotting their mean square displacement (MSD) versus the time lag (τ), with n = 2 in this case (**Figure 41D**). The DNA probes can be generally divided into two major groups based on the slopes of their linear fits, with red color used for average slopes >0.1 $\mu m^2/s$ (fast diffusion, **Figure 41D**) and blue color for average slopes $\leqslant$0.1 $\mu m^2/s$ (slow diffusion). The distribution of calculated diffusion coefficients is shown in **Figure 41E**, with a major peak around ~2 $\mu m^2/s$.

In summary, we could unveil a detailed view of the multimodal diffusion dynamics of biomacromolecules inside this hierarchically porous architecture by using SPT studies with fluorophore-labeled DNA nanotweezers. We found two diffusion regimes, one corresponding to free diffusion in the large macropores (diffusion constant D = 2.2 $\mu m^2/s$), and the other reflecting partially confined diffusion within the macropores (~200 nm) that are inhibited by the physical interaction with the gel network walls (D = 0.12 $\mu m^2/s$). Overall, we have concluded that the hierarchically porous ATO coating is a promising substrate to incorporate large guest molecules such as DNA nanostructures while supporting their molecular integrity, monodispersity and free diffusion. This work has been published in journal *Langmuir* recently.

5. Controlling thickness of the meso-macroporous ATO coatings for the best photoelectrochemical performance.

Our previous development of a new carbon-black template method allows an easy preparation of meso/macroporous ATO coatings. We decided to see if we could produce coatings with different thicknesses in order to examine the efficiency of the ATO-cyt *c*-RC system. The efficiency would depend on the quality of thick coatings and the efficiency of light penetration/scattering among others. For the thick coating production, we sought to understand the viscous behavior of the precursor mixture with carbon black, and measured the viscosities of mixtures with various polymer and CB amounts. Identifying the compositional boundary that marks a sol-gel transition of CB aggregates from Newtonian fluidity to Bingham plasticity allowed us to identify the template blends of interest. ATO coatings were produced first by doctor-blading with multiple layers of Scotch tape as the side wall to control the thickness. They were characterized using scanning electron microscopy (SEM) to image the surface pore structure, stylus profilometry to measure the coating thickness, and UV/Vis, current-voltage and photovoltaic studies to understand

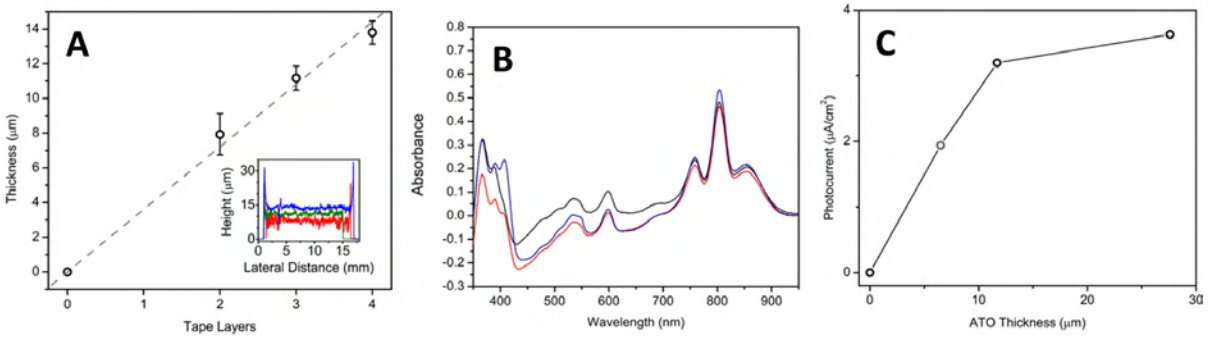


Figure 42. A Stylus profilometry measurements of meso-macroporous ATO coatings with tape layers of 1x (black), 2x (red), 3x (green) and 4x (blue) with the best fit linear curve (dashed line). **B**. Absorbance spectra of the RC-treated ATO coatings, with tape layers of 1x (black), 2x (red), and 4x (blue). **C**. Photocurrent measurements of *Rb. sphaeroides* RC attached to cyt *c* modified ATO coatings with various thicknesses.

the dependence between coating thickness and photocurrent generated from photosynthetic RC attached through cytochrome *c* (cyt *c*).

Figure 42A summarizes the stylus profile thickness measurements of the best coatings made using masks of varying thicknesses (inset; 2x (red), 3x (green) and 4x (blue)). While the 1x coating is scraped off by the stylus, the integrity of the coatings increases with the thickness. The coating thickness is almost directly proportional to the mask thickness up to at least 15 μm, but the fluidity of the reaction mixture is likely responsible for an increasing amount of the volume flowing out with thicker tape masks, reflected by the better fit of the quadratic equation. Non-uniformities in the height appear on two length scales. Shallow peaks and valleys (~ 2 – 3 μm) appear across a lateral distance of ~ 5 mm from streaking, and the local height variation decreases from ~ 4 μm for 2x coatings to ~ 1 – 2 μm for 3x and 4x coatings. **Figure 42B** shows the absorbance spectra of the electrodes, whose characteristic peak positions and relative intensity ratios indicate the structural integrity of the RC proteins. The maxima at 365 nm and 390 nm correspond to the Soret bands of the RC Bchls, while the peak at 408 nm corresponds to cyt *c*. As the thickness of the ATO is increased, the absorption at 408 nm increases relative to the absorption by the RC, indicating that the relative amount of bound cyt *c* increases as the thickness of the ATO film is increased. There are no significant differences in the intensity at the absorption maxima relating to the RCs. This is likely because the spectra of these slides were collected prior to the measurement during which unbound RCs are washed away. Therefore, the absorbance indicates the total RC uptake rather than only RCs that are bound to incorporated cyt *c* molecules, which are responsible for generating photocurrent. Longer incubation times may result in greater incorporation of RCs into the deeper ATO pores and this should be explored.

The absorbed light was partially converted to a photocurrent, summarized in **Figure 42C** for the ATO electrodes of varying thicknesses. The photocurrent increased with the coating thickness, nearly linearly up to ~ 12 μm, and then with a diminishing gain for thicker coatings; the photocurrent levels off approaching 4 $\mu A/cm^2$, as the coating with ~ 12 μm thickness yielded 3.2 $\mu A/cm^2$ and that with ~ 30 μm thickness yielded 3.6 $\mu A/cm^2$ of photocurrent. Increasing the intensity of the light source resulted in a direct increase in the photocurrent, in that increasing the intensity by five times typically increased the photocurrent by two to three times. It is not clear to what extent the leveling-off of photocurrent with thicker coatings could be avoided by increasing the concentrations of RC and/or quinone, increasing the incubation time, or by increasing the intensity of the incident light. Another limitation may be that back-transfer of the electrons to the porous ATO electrode becomes more severe further from the FTO glass substrate. We are now in the process of writing a manuscript from this work.

Programmed coherent coupling in a DNA-based excitonic circuit

Natural light-harvesting complexes use protein scaffolds to spatially organize arrays of strongly-coupled pigments that direct energy transfer to the reaction center with near-unity efficiency. A major challenge and opportunity for nanotechnology is to rationally construct nanoscale excitonic circuits from the bottom-up to mimic natural light-harvesting assemblies by programming densely packed dye aggregates, such as cyanines. Structured DNA assemblies serve as chromophore scaffolds with nanometer-scale control over three-dimensional dye architectures to realize this aim. However, programmed dye aggregates that mimic the J-aggregate organization often observed in natural photosynthetic complexes have been limited to short, isolated units on single DNA

duplexes. Further, rational control of emergent excitonic properties of these dye aggregates has not been achieved, including structure-based modeling to predict the emergent excitonic properties of multi-dye aggregates.

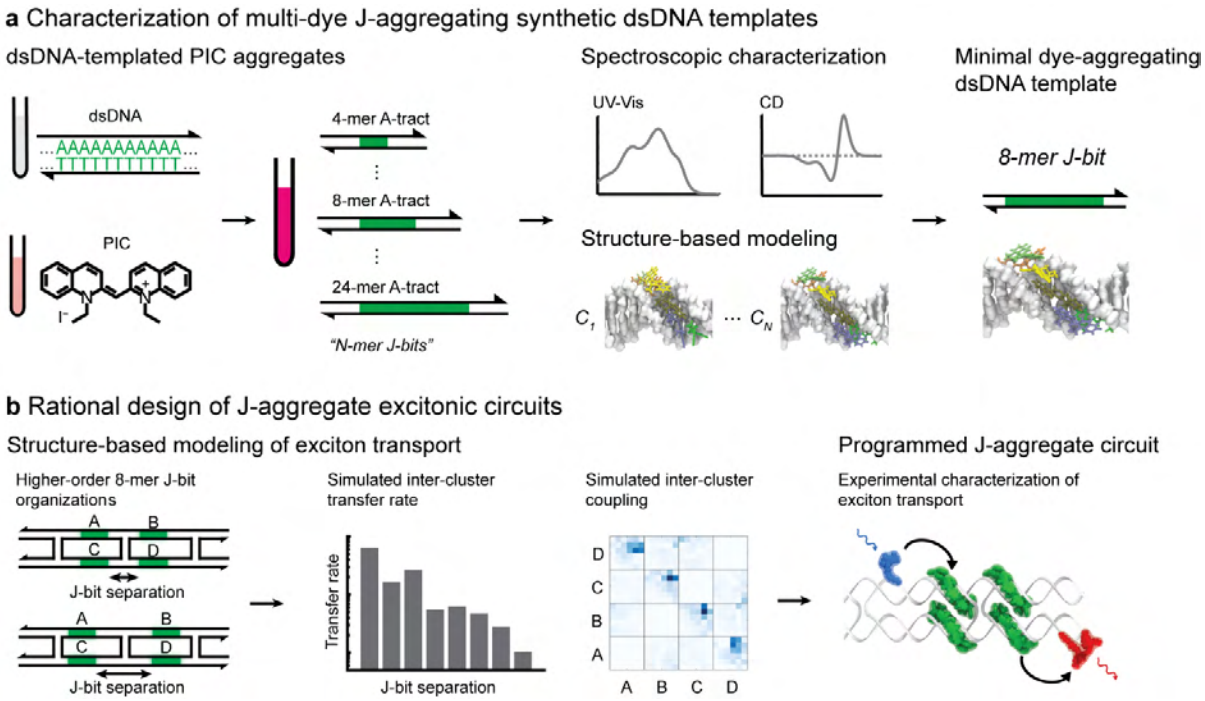


Figure 43. Schematic overview of the overall design and validation framework of DNA-based excitonic circuits with enhanced energy transport. (a) Pseudoisocyanine (PIC) molecules self-assemble on B-form DNA A-tracts as multi-dye complexes with UV-Vis and CD signatures that are characteristic of J-aggregates. The minimal J-aggregating synthetic DNA template (an 8-mer "J-bit") was first determined experimentally using UV-Vis and CD. The length of the templating A-tract was varied systematically to identify the minimal length required to form a stable J-aggregate, found to be 8 base pairs. The molecular conformations of the bound PIC dyes were inferred computationally using structure-based modelling of the experimental spectroscopic signatures of the DNA-dye complexes, as indicated schematically in the figure. (b) Rational design of multiple interacting multi-dye aggregates was then performed using structure-based modeling of inter-dye-aggregate energy transfer. J-bits were organized into higher-order assemblies using cross-linked, antiparallel DNA duplexes known as DX-tiles. J-bit conformations templated on DX-tiles were explored computationally in order to identify sequence designs that exhibit fast exciton transport, as illustrated schematically in the figure. The optimal computationally designed circuit was then synthesized and its energy transfer was characterized experimentally using steady-state and time-resolved fluorescence spectroscopy.

In the context of this MURI, we have used a bottom-up synthetic experimental-computational strategy to develop a highly programmable, rational means of controlling the targeted assembly and optical properties of excitonic circuits based on synthetic DNA. As detailed in last year's report, we have identified a set of fundamental J-aggregate units that serve as building blocks to construct fast, coherent energy transfer in arbitrary higher-order synthetic assemblies that mimic and extend beyond natural excitonic circuits. Specifically, we have used the natural propensity of pseudoisocyanine dyes (PIC) to self-assemble into J-aggregates on short sequence-specific portions of DNA duplex, to create circuits in larger scale DNA nanoassemblies (Fig. 43).

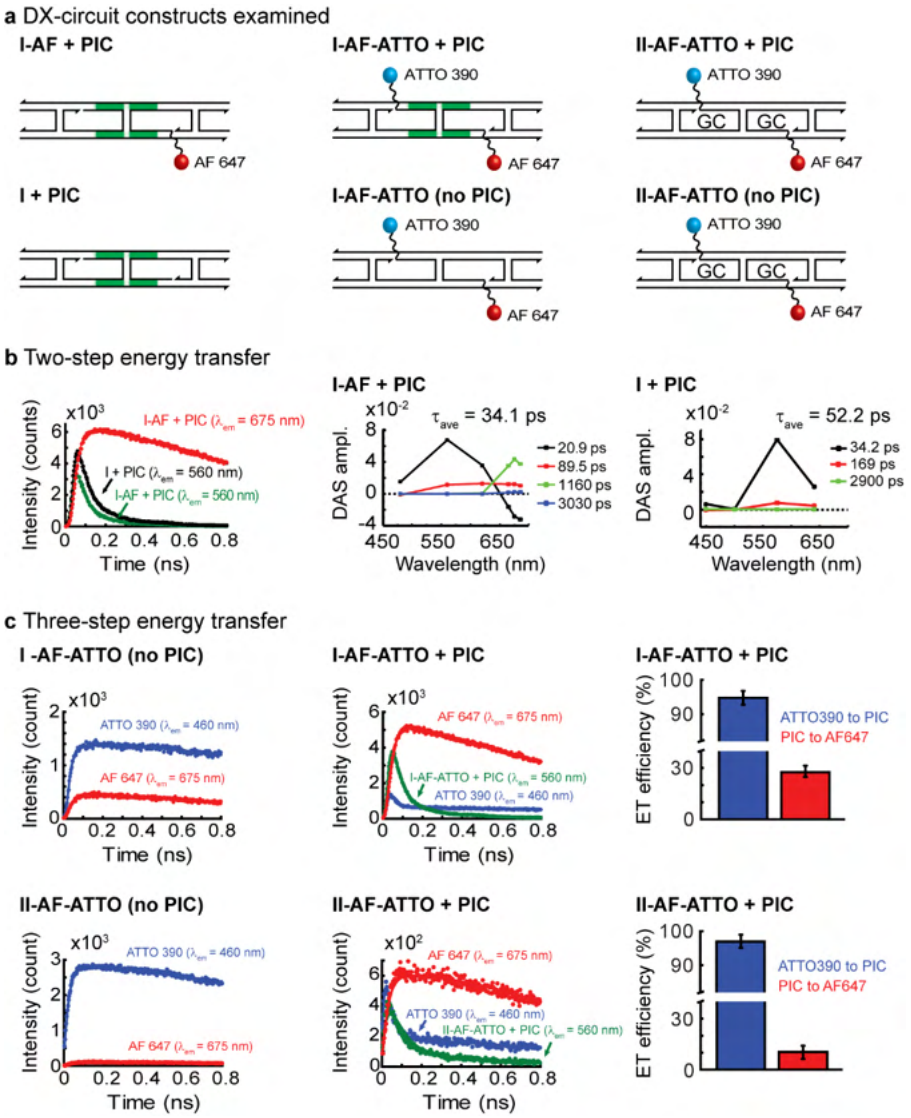


Figure 44. Programming two- and three-step energy transfer within the multi-J-bit excitonic circuit. (a) Schematic diagrams depicting the DX-tile constructs used to program multi-J-bit excitonic circuits with two-step and three-step energy transfer. (b) Two-step energy transfer from the Construct I + PIC to a single dye acceptor, Construct I-AF + PIC. The sample is excited with a 400 nm laser. The energy is transferred to the Alexa Fluor 647 acceptor dye (I-AF + PIC). Results are compared with a control construct without the acceptor (I + PIC). Fluorescence decay kinetics at wavelengths corresponding to AF 647 (675 nm) and PIC J-bits (560 nm) (left). Fluorescence decay-associated spectra resulting from fits of the fluorescence kinetic data for Construct I-AF + PIC (center) and Construct I + PIC (right). Average lifetimes at 560 nm and 575 nm from global analysis at the PIC J-bit band are indicated for Constructs I-AF + PIC and I + PIC, respectively. (c) Three-step energy transfer mediated by the multi-J-bit excitonic circuit. The ATTO 390 donor dye is excited with a 400 nm laser. Energy is subsequently transferred to the J-bits templated by the DX-tiles, and onwards to the Alexa Fluor 647 acceptor dye: I-AF-ATTO + PIC. Results are compared with a control construct with no PIC mediating transfer: I-AF-ATTO (no PIC) (top, left). Fluorescence decay kinetics at wavelengths corresponding to AF 647 (675 nm), ATTO 390 (460 nm) (left, top and bottom) and the J-bits and non-specifically bound PIC (560 nm) (center, top, bottom). The energy transfer efficiency of ATTO to PIC and PIC to AF 647 (right, top and bottom) calculated using average fluorescence lifetimes of ATTO 390 (460 nm) and PIC (560 nm) from Construct I-ATTO-AF + PIC or no PIC and Construct II-ATTO-AF + PIC or no PIC.

Next, we used the PIC J-bit to design higher-order DNA-PIC J-aggregates with custom optical

properties to demonstrate the ability to design complex excitonic circuits using our bottom-up approach. DX-Tiles are the fundamental building block of DNA origami, in which two antiparallel DNA duplexes are rigidly constrained by two crossover junctions, offering the ability to design rings, sheets, and bundles of arbitrary size on the nanometer scale. DNA sequence was chosen to introduce four 8-mer A/T-tract binding sites surrounding the central staple double crossover. Optical properties and transport characteristics of these circuits can be predicted from the atomic-level conformation as predicted by molecular docking simulations. UV-Vis and CD spectroscopy on the synthesized DX-Tile circuits confirmed the formation of a J-aggregate structure, similar to the spectra that were theoretically predicted. Time-resolved spectroscopy also showed that quantum yield enhancement and increased lifetime were also present in these assemblies.

Finally, we used these DX-Tile assemblies to demonstrate J-bit mediated transfer between donor (ATTO390) and acceptor dyes (AF647), using both a two-step (Fig. 44a), and three-step (Fig. 44b) energy transfer pathway. In the two-step energy transfer experiment, steady-state fluorescence emission and relaxation kinetics measurements suggest strong transfer from the J-bits to AF647, with an estimated ~34-40% FRET efficiency. In the three-step energy transfer experiment, a ~10-fold increase in AF647 fluorescence was reported when including the PIC J-bits as an intermediate in the ATTO390 – AF647 chromophore system. Both of these results support the specific role of PIC J-bits in mediating efficient excitonic energy transfer.

We are currently extending this preliminary work in many research directions which will utilize the advantages of programming excitonic energy transfer circuits using DNA nanostructures. First, a theoretical physical model of PIC J-aggregation in solution and bound to DNA is in progress, as detailed in the following section. Second, larger-scale DNA origami structures including rings, sheets, tubes, and lattices will be designed, taking advantage of many structural possibilities inherent in DNA nanotechnology. An automated framework to build DNA nanostructures of various shapes with user-programmed A/T-tract sequences is currently in development, and will allow the design of more complicated and potentially useful excitonic circuits. This present collaborative work is submitted and currently under review.

Aggregation of psuedoisocyanine dye in solution

Based on previous results showing J-aggregation behavior of psuedoisocyanine (PIC) dye in A/T-tracts, we further investigate the physical aggregation behavior of PIC dye in solution and bound to DNA from a theoretical perspective. These results incorporate quantum mechanics (QM) and molecular mechanics (MM) simulations to determine accurate interaction energies and binding energies.

First, we investigate the initial dimerization step of J-aggregation of PIC in solution by scanning the interaction energy surfaces of two PIC chromophores as seen in Figure 45. Interaction energy calculations are performed using dispersion-corrected DFT at the B3LYP/6-31+G (d) level of theory with implicit water solvation. These results show distinct π-π stacking interactions with significant energy minima near γ rotation angles -80, 0, 45, and 80 degrees (Fig. 45a). Rotation around the α rotation angle away from 0 degrees does not result in favorable interaction energies between the PIC dimers (Fig. 45c).

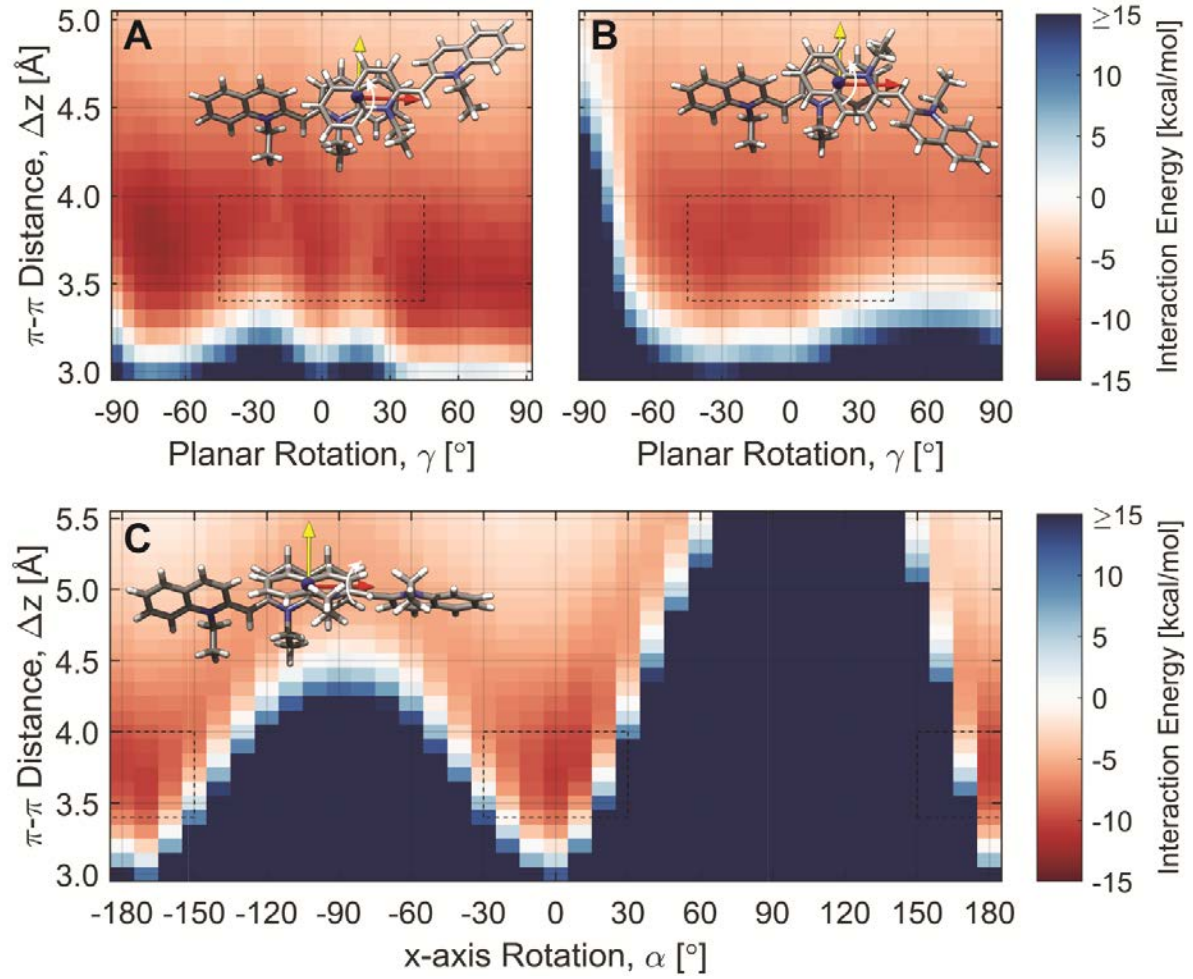


Figure 45. Interaction energies between rotated PIC dimers. A Interaction energy surface of PIC dimers based on π-π stacking distance, Δz, and planar rotation, γ, where α = 0°. **B** Interaction energy surface of PIC dimers based on π-π stacking distance, Δz, and planar rotation, γ, where α = 180°. **C** Interaction energy surface of PIC dimers based on π-π stacking distance, Δz, and x-axis rotation, α. Interaction energies are calculated using dispersion-corrected DFT [DFT-D3/B3LYP/6-31+G(d)] with implicit water solvation using COSMO.

We utilize the data from PIC dimerization interaction energies (Fig. 45) to build linear J-aggregated models of potential PIC structures in solution. Figure X2 shows six possible structured J-aggregate combinations of PIC molecules. To calculate downstream photophysical properties of these linear J-aggregate structures, the Coulombic couplings for each PIC dimer pair are calculated using the transition density cube (TDC) method, and a site-based Hamiltonian is subsequently built (Fig. 46, right) to compare excitonic energy transfer between the linear models.

In solution, PIC forms J-aggregate structures which are rod-like in character as seen in Cryo-TEM experiments (von Berlepsch et al., *J. Phys. Chem. B* **37**, 2000). We show a model of a rod-like PIC linear aggregate in Figure 47, along with its calculated site-basis Hamiltonian and simulated absorption and circular dichroism spectra, which are compared to the experiment. It is likely that PIC adopts this aggregate conformation in solution due to favorable interaction energies upon

dimerization, potentially with ionic charge stabilization around the outer portion of the rod structure. This work is currently being documented in a manuscript that is in preparation.

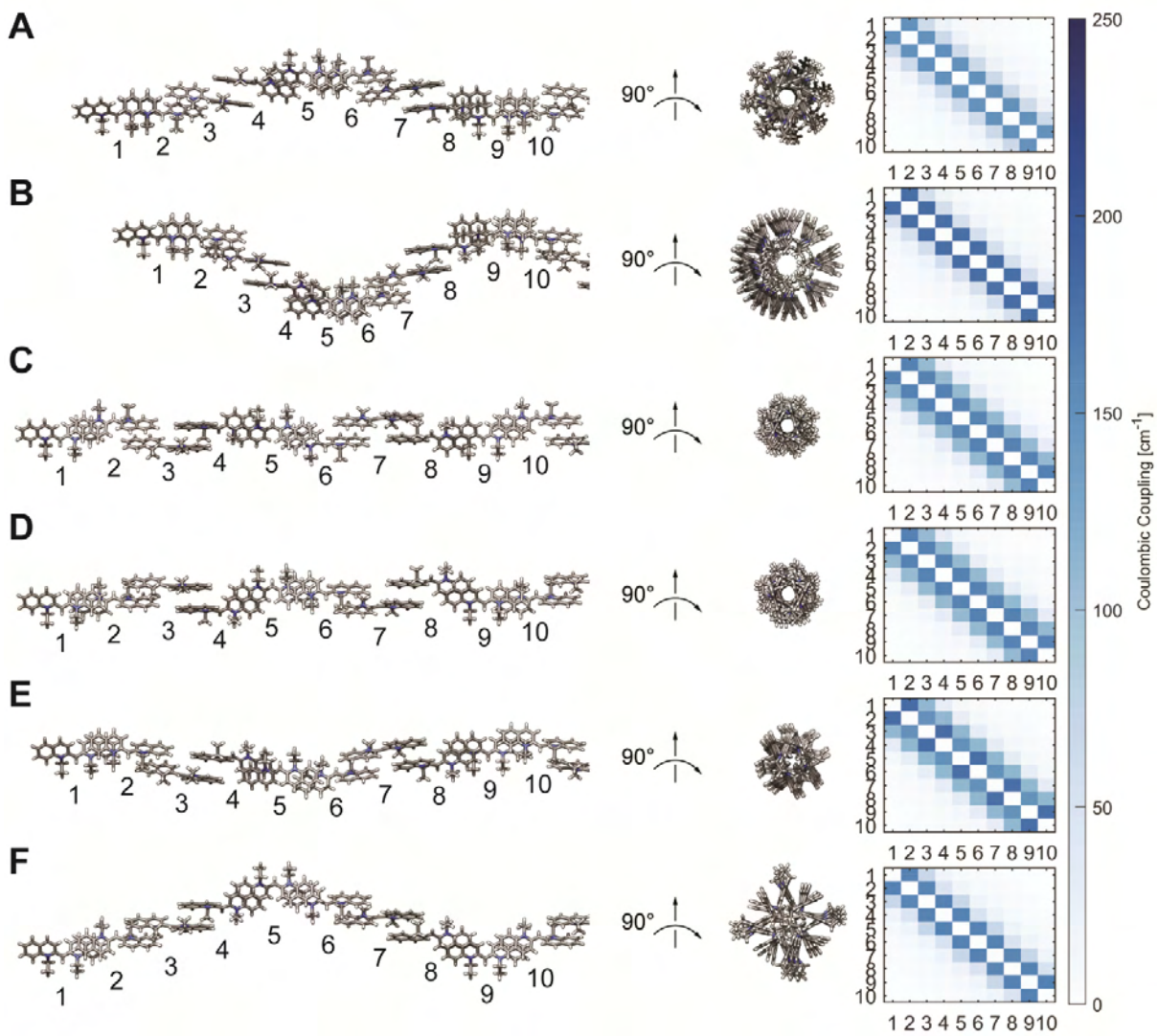


Figure 46. Right-handed PIC Aggregation Models. A PIC sequential aggregation using Δx = 1.2 Å, Δz = 3.7 Å, and β = 180°. **B** PIC sequential aggregation using Δx = 1.2 Å, Δz = -3.7 Å, and β = 180°. **C** PIC sequential aggregation using Δx = 1.2 Å, Δz = 3.7 Å, α = 180°, and β = 180°. **D** PIC sequential aggregation using Δx = 1.2 Å, Δz = -3.7 Å, α = 180°, and β = 180°. **E** PIC sequential aggregation using Δx = 1.2 Å and β = 180°, and alternating between Δz = 3.7 Å and -3.7 Å. **F** PIC sequential aggregation using Δx = 1.2 Å, α = 180°, and β = 180°, and alternating between Δz = 3.7 Å and -3.7 Å. All models use the right-handed stereoisomer of PIC. Exciton sites are labeled sequentially from 1 to 10. (right) Site-basis Hamiltonian for each PIC aggregate model.

Next, we plan to study the binding interaction energies between PIC and sequence specific DNA duplexes, to determine why AT-tracts show increased J-aggregation behavior over other DNA sequences, such as GC or ATA. This study will combine quantum mechanics (QM) of the PIC molecule(s) due to their important electronic properties with molecular mechanical (MM) simulations of the DNA region and surrounding solvent where PIC binds.

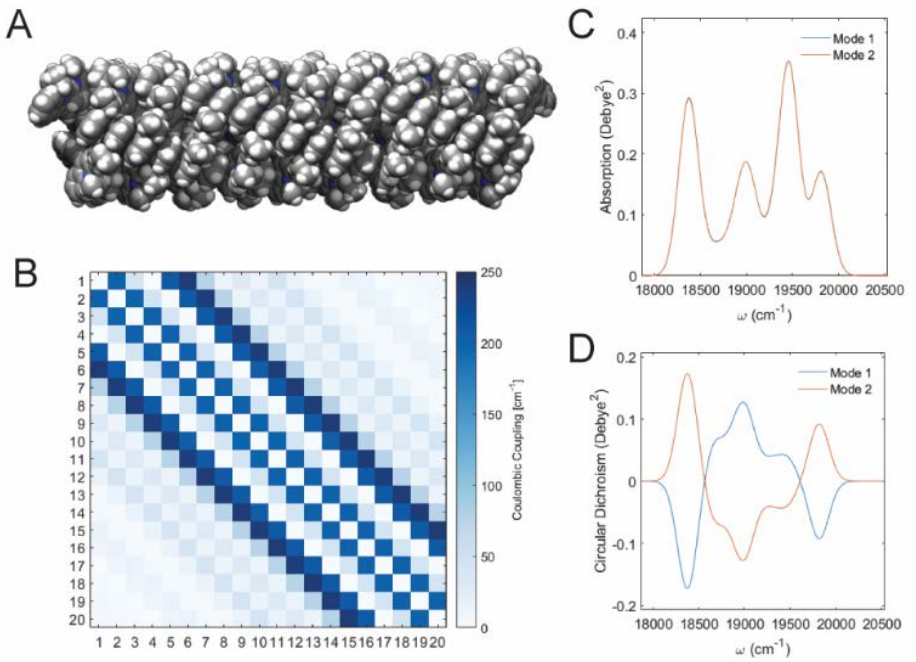


Figure 47. A rod-like model for PIC aggregation in solution. A. Model of right-handed PIC rod-like J-aggregate structure. **B.** Site-basis Hamiltonian for rod-like structure with couplings calculated using TD-DFT and the transition density cube (TDC) method. **C.** Excitonic absorption spectra of rod-like PIC. **D.** Excitonic circular dichroism spectra for rod-like PIC showing difference between right- and left-handed chirality.

Translating Biochemical Pathways to Non-Cellular Environments

Principal Investigator: Hao Yan[1]

Co-PIs: Don Seo[1], Neal Woodbury[1], Mark Bathe[2], William Shih[3], Nils Walter[4], Jinglin Fu[5]

[1]Arizona State University, [2]MIT, [3]Harvard University, [4]U of Michigan, [5]Rutgers University

Reporting period: 8/01/17-7/31/18

I. Scientific and Technical Objectives of Overall MURI Project

Our goal is to engineer and optimize nanoscale devices and systems based on important biochemical conversion pathways, where the converted species are molecules (enzymes transforming substrates into products), or energy, as is the case for photosynthesis. The use of DNA-directed assembly allows us to control and exploit the interactions between synthetic and naturally occurring bio-materials to produce highly functional biochemical conversion systems. Regarding enzyme transformations, our primary goal is to construct artificial enzyme cascades using two- and three-dimensional DNA structures as templates, and to study the ideal number of enzymes, relative distance, spatial arrangement, diffusion behavior, and reaction kinetics of the cascades in a controlled, non-cellular environment. Towards this goal, we initially focused on a representative DNA-templated GOx/HRP enzyme cascade and a more complex, bioelectroactive, NAD dependent dehydrogenase pathways, with the ultimate goal of interfacing our systems with external conductive materials. We aimed to achieve the following objectives during this reporting period: (1) develop DNA-crowded enzyme complexes with enhanced activity, (2) develop a 2D enzyme cascade network with efficient substrate channeling on DNA nanostructures, (3) establish a method to produce large sized nanodisc for Poliovirus infection study using DNA origami as modular scaffold, (4) develop a highly programmable, rational means of controlling the targeted assembly and optical properties of excitonic circuits based on synthetic DNA, (5) investigate the designed DNA walker on 2- and 3-step DNA tile walking systems, 2D high-density DNA-strand modified surface and the mechanism of walking through smFRET.

Regarding photosynthesis, our aim is to develop methods for translating energy conversion pathways to non-cellular environments where their functions can be more easily manipulated. The approach is to use rationally designed DNA nano-scaffolds to engineer light-harvesting networks containing synthetic pigments, interfaced with energy conversion proteins (photosynthetic reaction centers) from natural photosynthetic organisms. We intend to precisely position functional elements on the DNA scaffolds, generating energy and electron transfer pathways in which inter-molecular interactions can be predictably designed, and the local environment can be controlled. We hope to engineer systems with more uniform light absorption, efficient energy transfer and conversion, and improved photo-stability for maximum performance. Here, we are exploring ways to effectively interface the light-induced redox potentials generated by photosynthetic reaction centers from purple bacteria and PS1 with novel nano and meso-structured electrode materials. Toward this end, two different types of materials were utilized: nanoporous transparent metal oxides and functionalized reduced graphene oxides. We are also exploring ways to incorporate a light-responsive photo-protective element into a DNA-templated artificial antenna system to adapt its photoprotection function for light regulation. We have also used a bottom-up synthetic experimental-computational strategy to develop a highly programmable, rational means of controlling the targeted assembly and optical properties of excitonic circuits based on synthetic DNA. In line with DoD goals, the proposed research will increase our understanding of nanoscale energy transfer processes and aid in the development of robust strategies for the synthesis, characterization, and assembly of synthetic biochemical pathways for application in high-efficiency photo-energy generation, energy storage devices, sensors, or completely new capabilities that enhance war fighter and battle system capabilities.

II. Accomplishments in the Past Year:

Engineer and optimize nanoscale devices and systems based on important biochemical conversion pathways

We have achieved the following objectives during this reporting period: (1) develop DNA-crowded enzyme complexes with enhanced activity, (2) develop a 2D enzyme cascade network with efficient substrate channeling on DNA nanostructures, (3) establish a method to produce large sized nanodisc for Poliovirus infection study using DNA origami as modular scaffold, (4) develop a highly programmable, rational means of controlling the targeted assembly and optical properties of excitonic circuits based on synthetic DNA, (5) investigate the designed DNA walker on 2- and 3-step DNA tile walking systems, 2D high-density DNA-strand modified surface and the mechanism of walking through smFRET.

1. DNA-crowded enzyme complexes with enhanced activities and stabilities

We present a robust and simple method to prepare DNA-crowded enzyme complexes by directly assembling long DNA duplexes on the enzyme surface. DNA-crowded enzyme complexes show boosted substrate turnover numbers, and increased stabilities against various storage conditions. They could be potentially scaled up for applications in biomaterials and biotechnology.

As shown in Fig. 1A, the construction of a DNA-crowded enzyme complex involves two steps: (1) the conjugation of an initiator strand to an enzyme (enzyme-I) and (2) the growth of dsDNA on the enzyme surface by the initiator-triggered hybridization chain reaction (HCR). One initiator on the enzyme surface can trigger the growth of a long dsDNA with the alternative hybridization of hairpin 1 and hairpin 2. The relative length of dsDNA was determined by the initiator-to-hairpin ratio, where excess hairpins resulted in longer dsDNA by HCR. The long HCR duplex on the enzyme surface behaves as a flexible 'DNA hair' to crowd the enzyme because a HCR duplex has many nick points that make it easier to bend (non-nick dsDNA may also bend when it is longer than the persistence length of ~50 nm). As shown in Fig. 1B, gel electrophoresis was used to characterize DNA-crowded enzymes, where the longer dsDNA with slower mobility was observed with the addition of more hairpins. The

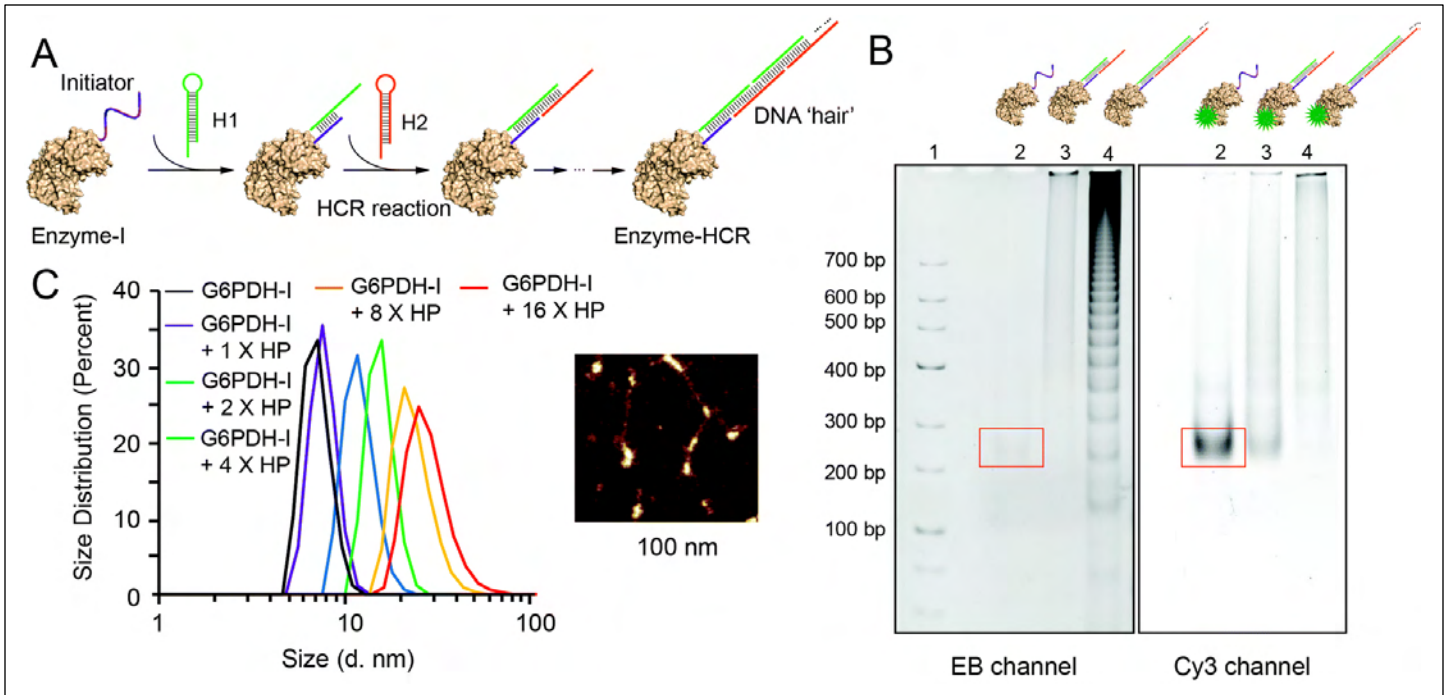


Figure 1: The concept and characterization of DNA-crowded enzymes. (A) The construction of a long DNA duplex on an enzyme surface by HCR. (B) (3.5%) PAGE characterization of DNA-crowded enzymes with EB staining (left) of DNA and fluorescent imaging (right) of Cy3-labelled G6PDH. Lane 1: DNA ladder; Lane 2: 1 µM initiator-conjugated G6PDH (G6PDH-I); Lane 3: 1 µM G6PDH-I + hairpins (1×); Lane 4: 1 µM G6PDH-I + hairpins (10×). Red circle highlights G6PDH-I. (C) DLS analysis of a DNA-crowded enzyme sample with the addition of excess hairpins. Inset: AFM imaging of a DNA-crowded enzyme with the addition of 16× hairpins (scale: 100 nm).

fluorescent imaging of Cy3-labelled enzyme showed that the enzyme migrated together with a large dsDNA complex. As shown in Fig. 1C, dynamic light scattering (DLS) was used to characterize the hydrodynamic diameters of multiple enzyme-HCR complexes in a solution phase. An enzyme–initiator conjugate showed a peak diameter of ~7 nm. The diameter of enzyme–HCR complexes was increased from ~8 nm to ~30 nm with the addition of hairpins from 1-fold to 16-fold excess. We also used atomic force microscopy (AFM) to directly visualize DNA-crowded enzymes on a mica surface, where long DNA "hairs" were observed with the attachment of bright spots of proteins (Fig. 1C inset).

Next, we evaluated the catalytic activities of DNA-crowded enzymes depending on the growth of long dsDNA on the enzyme surface. As shown in Fig. 2A, the G6PDH-initiator (G6PDH-I) conjugate was incubated with excess hairpins from 1 to 128-fold for initiating HCR. The activity of the G6PDH-I/HCR complex increased with the addition of more hairpins, resulting in more than 200% enhancement when 16-fold or more hairpins were added. As a control, non-initiator conjugated enzymes were not observed for significant activity enhancement (<20%) with the addition of hairpins. Similar results were also observed for the HRP-I/HCR complex which showed a >300% enhanced activity by adding 32-fold more hairpins (Fig. 2B). To evaluate the labelled numbers of initiator strands, we conjugated and purified HRP with 1, 2 and 3 initiators (HRP-I_1, HRP-I_2 and HRP-I_3. As shown in Fig. 2C, HRP-I_2/HCR and HRP-I_3/HCR showed higher activities than HRP-I_1/HCR, possibly due to more dsDNA duplexes on the enzyme surface. However, many enzymes may show decreased activities after conjugating to multiple DNA molecules (>3). To avoid damaged activities, we suggested conjugating one or two initiator strands to one enzyme for triggering dsDNA growth on the enzyme surface.

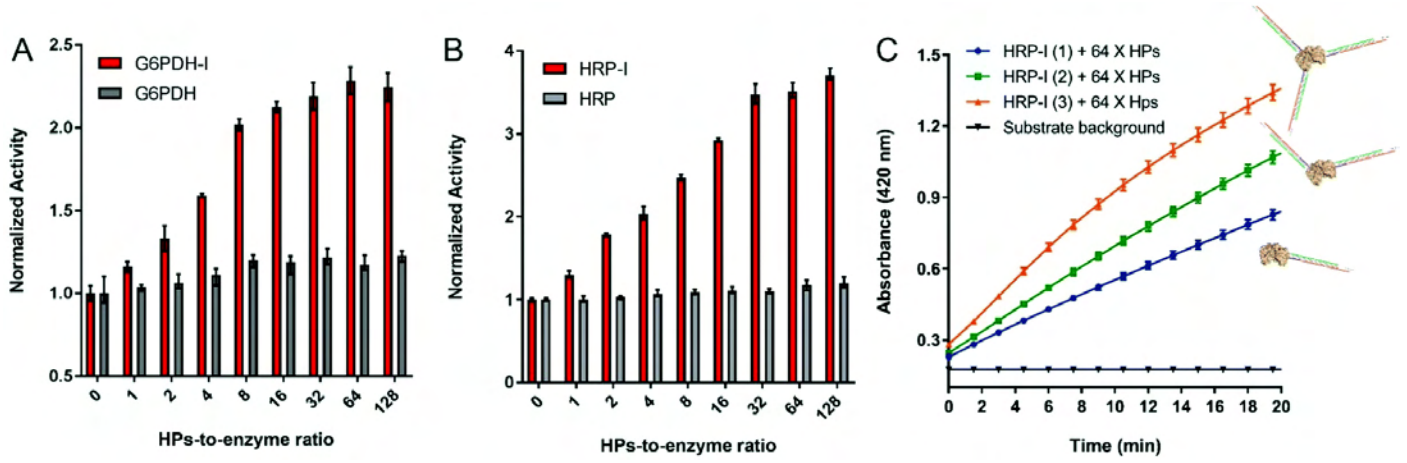


Figure 2: Evaluation of DNA-crowded enzyme complexes. (A) Titration of HPs-to-enzyme ratio for affecting DNA-crowded G6PDH activity. (B) Titration of HPs-to-enzyme ratio for affecting DNA-crowded HRP activity. (C) Titration of labelled initiators per enzyme for affecting DNA-crowded HRP activity. Error bar: range of data.

The boosted activities of the enzyme–HCR complexes were consistent with the recently reported activity enhancement for enzyme/DNA hybrid nanostructures. These enhanced activities were suggested to be relevant with the high density of negatively charged phosphate groups on DNA nanostructures or the attraction of substrate molecules onto DNA scaffolds. Furthermore, the closely spaced backbone phosphates of DNA molecules could modify the local nanoenvironment, such as stabilized hydrogen-bonded water structures by kosmotropic phosphates and decreased pH near the DNA surface. Experimental and modelling studies have shown that proteins are more stable and active in an ordered, hydrogen-bonded water solvent, possibly due to the decreased hydrogen bonding ability of water with proteins, and hence the stabilization of hydrophobic interactions and inner hydrogen-bonding of a folded protein. The effect of DNA nanoscaffolds on enzymes

appears to be similar to recent studies of the primordial chaperone for polyphosphate, which stabilizes enzymes under stressed conditions. It is also noticed that many conserved metabolic enzymes are non-specifically associated with nucleic acids through cryptic binding sites.

In addition to enhanced turnover numbers for catalysis, the enzyme–HCR complex also showed increased stability against various denaturation conditions, such as long-term storage, freeze–thaw cycles and thermal incubation. As shown in Fig. 3A, we tested the stability of enzyme solutions against long-term storage at room temperature (25 °C). The DNA-crowded enzyme complex of HRP-I_2/HCR showed more stable activities than HRP-I_2 and HRP wildtype. For example, in the 10th week, HRP-I_2/HCR retained ~50% of its original activity, whereas HRP-I_2 and wildtype HRP only retained ~10% and ~20% of their original activities, respectively (ESI,† Fig. S10–S12). Further studies showed that HRP-I_2/HCR and HRP-I_3/HCR were slightly more stable than HRP-I_1/HCR over long-term incubation (ESI,† Fig. S13). As shown in Fig. 3B, HRP–HCR complexes (retained ~80% activity at the 7th cycle) were more stable against multiple freeze–thaw cycles than HRP-I conjugates and wildtype HRP (retained ~25% activity at the 7th cycle). It was also noticed that HRP-I_3/HCR (retained >90% activity at the 7th cycle) was more stable than HRP-I_1/HCR (retained ~65% activity at the 7th cycle) and HRP-I_2/HCR (retained ~80% activity at the 7th cycle). More detailed data are shown in ESI,† Fig. S15–S18. To rule out the potential absorption of enzymes onto the tube walls during the incubation, we used a Cy3-labelled enzyme to monitor the solution fluorescence during the incubation period. The Cy3-labelled enzyme solution did not show significant decrease of fluorescence during either long-term storage or freeze–thaw cycles, which suggested that the concentration of solution enzymes did not alter significantly during the incubation (ESI,† Fig. S14 and S19). As shown in Fig. 3C, HRP–HCR complexes showed an increased thermal stability in the range of 45–65 °C.

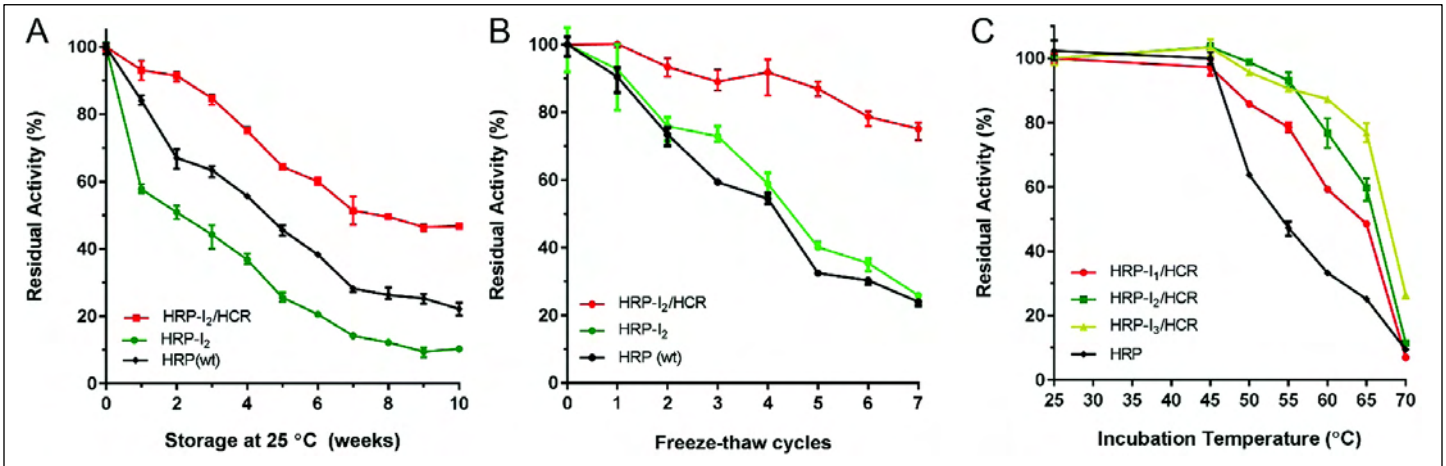


Figure 3: Evaluation of the stability of DNA-crowded enzymes against (A) long-term storage at room temperature (25 °C), (B) freeze–thaw cycles and (C) thermal incubation. Error bar: range of data.

In summary, we have developed a simple and robust method for assembling DNA-crowded enzyme complexes with promoted enzyme activity and increased stability. By conjugating an initiator strand to an enzyme, we were able to initiate the growth of long dsDNA on the enzyme surface to increase local DNA crowding. The number and length of DNA duplexes were controlled by the copies of labelled DNA initiators and the addition of hairpins. The enzyme–HCR complexes exhibited increased turnover numbers of 2- to 3-fold higher than those of enzymes without surface dsDNA crowding. Conversely, the Km values remained similar between enzyme–HCR complexes and free enzymes, indicating an uninterrupted diffusion of small-molecule substrates and products. Unlike DNA origami nanocages, which require a complex set of oligonucleotide staples with low production scale, the assembly of DNA-crowded enzyme complexes only involved three strands of one initiator and two hairpin strands. With the future improvement of large-scale DNA synthesis, the concentration and production of enzyme complexes could be scaled up to high micro-molar concentrations for practical use. In the future, it may

be feasible to crosslink multiple DNA-crowded enzyme particles into nanocrystals and hydrogels which can stabilize enzymes against various denaturation conditions, as well as facilitating multi-enzyme catalysis. The DNA-crowded enzyme particles may also find utility in theranostic applications and drug delivery.

2. 2D enzyme cascade network with efficient substrate channeling by swinging arms

In living cells, compartmentalized or membrane-associated enzymes are often assembled into large networks to cooperatively catalyze cascade reaction pathways essential for cellular metabolism. Here, we report the assembly of an artificial 2D enzyme network of two cascade enzymes—glucose-6-phosphate dehydrogenase (G6PDH) and lactate dehydrogenase (LDH)—on a wireframe DNA origami template. Swinging arms were used to facilitate the transport of the redox intermediate of NAD+/NADH between enzyme pairs on the array. The assemblies of 2D enzyme networks were characterized by gel electrophoresis and visualized by atomic force microscopy (AFM). The spatial arrangements of multiple enzyme pairs were optimized to facilitate efficient substrate channeling by exploiting the programmability of DNA origami to manipulate the key parameters of swinging arm length and stoichiometry. Compared with a single enzyme pair, the 2D organized enzyme systems exhibited higher reaction efficiency due to the promoted transfer of intermediates within the network.

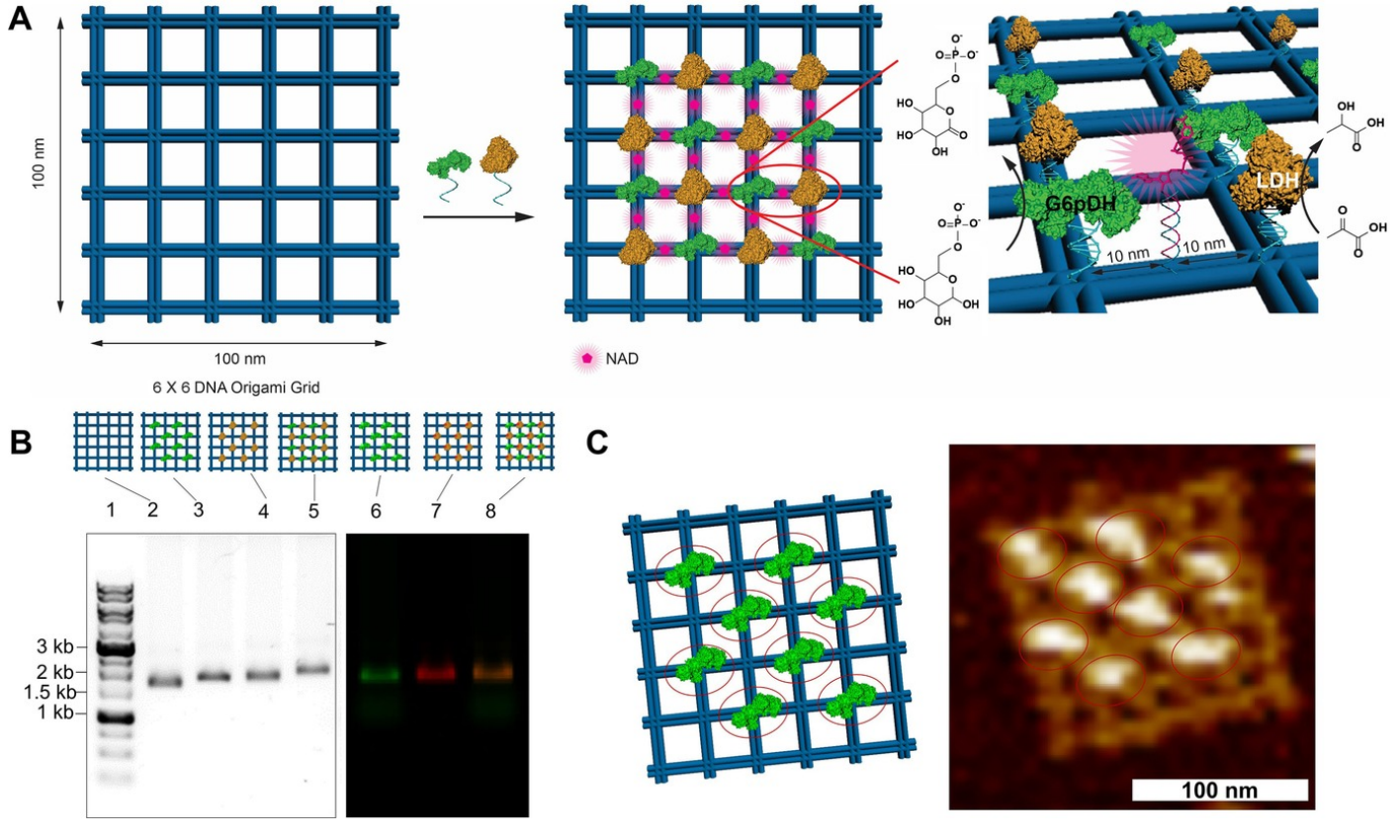


Figure 4: Design and characterization of a 2D enzyme network. A) Schematic illustration of the enzyme network on a 6×6 lattice DNA origami. B) Agarose gel (0.75 %) electrophoresis of assembled structures: lane 1, 1 kb DNA ladder; lane 2, origami; lane 3, origami-G8-NAD+ complex; lane 4, origami-L8-NAD+ complex, lane 5, origami-G8-NAD+-L8 complex; lane 6, origami-G8 (AlexFluor-555-labeled)-NAD+ complex; lane 7, origami-L8 (AlexaFluor-647-labeled)-NAD+ complex; and lane 8, dual-color image of origami-G8 (AlexFluor-555-labeled)-NAD+-L8 (AlexaFluor-647-labeled) complex. C) Representative AFM image of origami-G8 complex. Scale bar: 100 nm.

As shown in Figure 4A, a 2D enzyme network of glucose-6-phosphate dehydrogenase (G6PDH) and lactate dehydrogenase (LDH) was positioned on a square lattice-like DNA origami template consisting of 6×6 four-point

star junctions (overall dimensions ≈100 nm×100 nm) through DNA linkers. The square lattice-like DNA origami was designed and assembled by using an approach we previously reported. The protein network consisted of eight pairs of G6PDH and LDH, with each enzyme anchored at the junction point of the square lattice, so that each enzyme can interact with 2, 3, or 4 of the other enzyme that is located ≈ 20 nm away. In this enzyme cascade, G6PDH first catalyzes the oxidation of glucose-6-phosphate (G6P), with the concurrent reduction of nicotinamide adenine dinucleotide (NAD+) to NADH. Subsequently, LDH catalyzes the reduction of pyruvate to lactic acid by using the NADH produced by G6PDH. To facilitate substrate channeling, a double-stranded DNA swinging arm carrying an NAD+ cofactor at the tip was positioned halfway between each pair of G6PDH and LDH (≈10 nm away from each enzyme) to transfer the hydride intermediate. In total, 24 of these swinging arms were

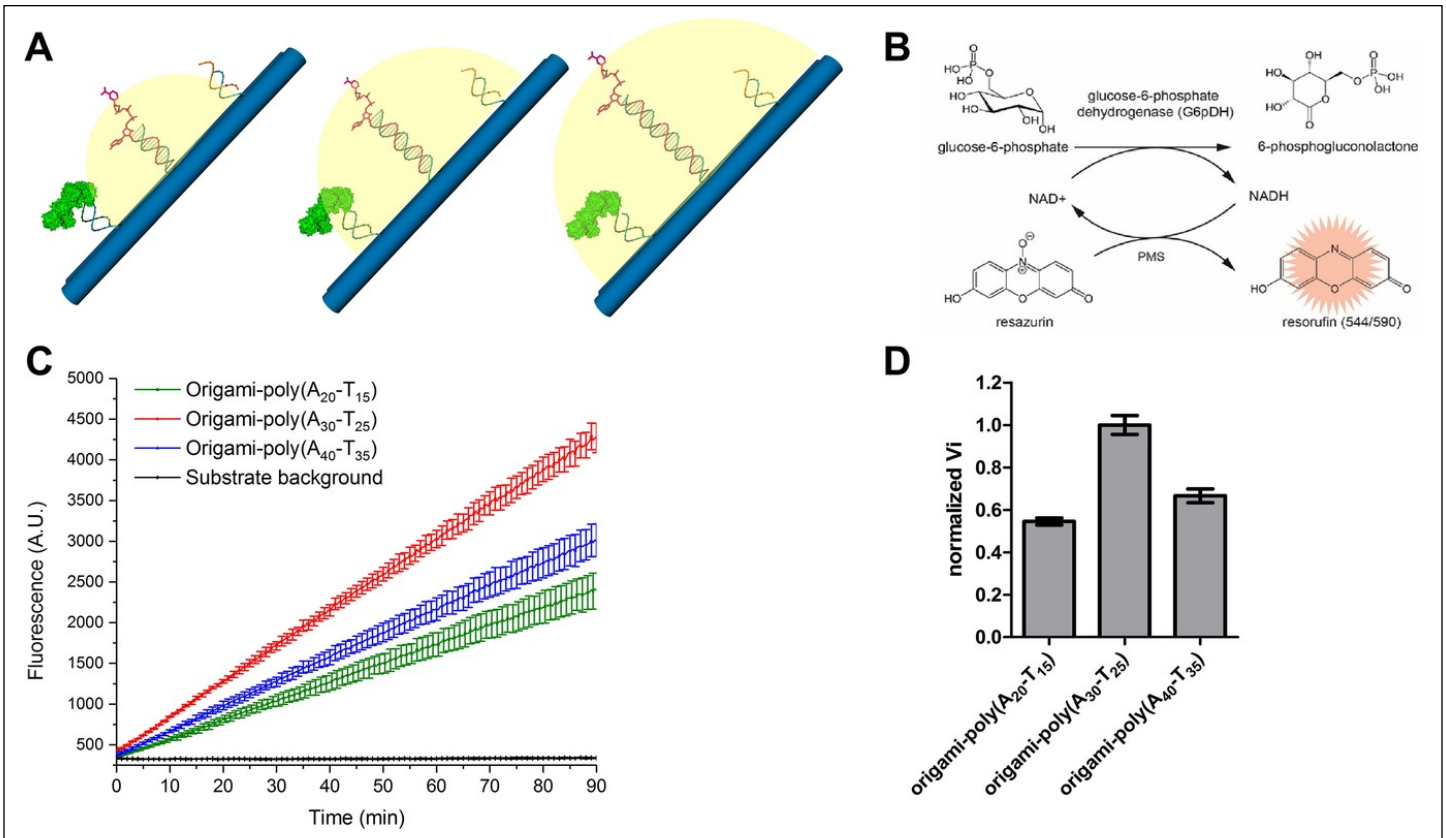


Figure 5: Optimization of the length of the double-stranded NAD+-swinging arm. A) Schematic illustration of designed duplex swinging arms composed of polyA20-T15, polyA30-T25, and polyA40-T35; B) Coupled fluorescence assay for determining enzyme activity of G6PDH; C) Enzyme activity of origami-G8-NAD+ with polyA20-T15 swinging arms (green), polyA30-T25 swinging arms (red), and polyA40-T35 swinging arms (blue), with the background of substrate autocatalysis (black). D) Normalized activity of the three scenarios in C. Assay conditions: Enzyme–origami complex (final concentration 1 nm) is added into a substrate solution of G6P (1 mm), resazurin (1 mm), and phenazine methosulfate (PMS; 1 mm) in standard 1× TBS buffer (50 µL per well, pH 8). All shown concentrations are the final concentrations in the assay. Error bars represent the standard deviations of at least three replicates.

assembled on the 6×6 lattice origami.

In Figure 5 B, agarose gel electrophoresis was used to characterize the assembled protein networks, with the stepwise addition of the two types of proteins onto the DNA origami scaffold gradually resulting in a slower mobility. Fluorescence gel imaging of dye-labeled proteins also confirmed the co-assembly of G6PDH and LDH on the DNA origami. As shown in Figure 5 C, the protein network was also directly visualized by atomic force microscopy (AFM), in which the assemblies of the proteins on the DNA origami were confirmed by the increased height (brighter spots) as compared with the DNA origami alone.

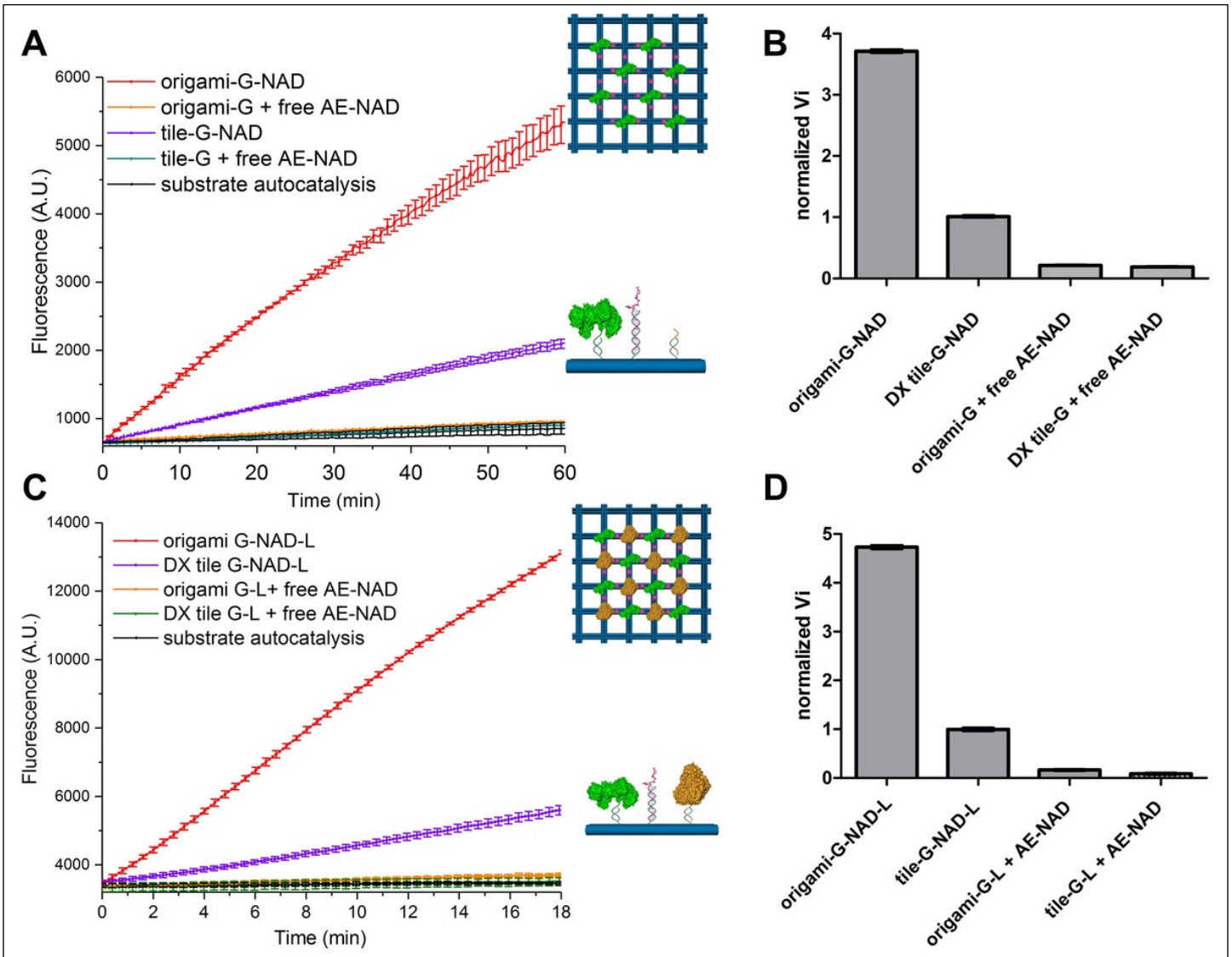


Figure 6: Characterization of enzymatic activity comparing the origami-G8-NAD+-L8 array and DX tile-G-NAD+-L swinging arm structures. A) Raw activity of origami-G8-NAD+ (red), origami-G8 with free AE-NAD+ (orange, hidden behind the green and black curves), DX tile-G-NAD+ (purple), DX tile-G with free AE-NAD+ (green), and substrate autocatalysis (black). B) Normalized activities. C) Raw activities for overall pathway for origami-G8-NAD+-L8 (red), origami-G8-L8 with free AE-NAD+ (orange), DX tile-G-NAD+-L (purple), DX tile-G-L with free AE-NAD+ (green), and substrate autocatalysis (black). D) Normalized activity. Assay conditions: origami–enzyme complex (1 nm) or DX tile-enzyme complex (8 nm) with G6P (1 mM) and pyruvate (1 mm), LOX and HRP (10 nm each), and Amplex Red (200 µm), in 1× Tris-buffered saline (TBS; pH 8). Error bars were generated by standard deviation of at least three replicates.

The double-stranded swinging arm carrying the NAD molecule was constructed by hybridizing a NAD+-modified poly(A) strand with a poly(T) anchor strand that extended from the surface of the origami lattice, located at the middle position of the arm between two neighboring junctions (Figure 5 A). As shown in Figure 5 A, the duplex length of the swinging arm was varied from 15 to 25 to 35 bp in order to find the optimal enzyme activity. A 5 nt single-stranded portion was left unpaired on the strand carrying the NAD+ in order to leave sufficient rotational flexibility for the molecule to interact with both enzymes (see also Figure S8 D in the Supporting Information). Enzyme activity was determined by a phenazine methosulfate-catalyzed resazurin fluorescence assay (Figure 5 B).6e, As expected, the activity of the enzyme with the swinging arms was found to be dependent on the duplex length of the swinging arm, with the 25 bp duplex giving the highest level of activity (Figure 5 C

and D). This duplex length of the swinging arm matches the half length of the DNA origami grid (5 turns of DNA per side), which means the NAD^+ located at the tip of the swing arm that is anchored in the middle position of the grid arm just has the optimal swing radius to reach both enzymes located at the junctions of the grid. Therefore the 25 bp duplex was used for all enzyme networks described later. Within the enzyme network, each enzyme (e.g., G6PDH) could interact with up to four NAD^+ arms. This geometry was expected to improve the reaction efficiency as compared with a single swinging arm complex on a double-crossover (DX) DNA tile.11b To test this, we first compared the activity of G-NAD+ half-arms on the 6×6 origami lattice (G6PDH/NAD+, 8:24) with that on a DX DNA title (G6PDH/NAD+, 1:1) with an eightfold higher tile concentration.

As shown in Figure 6 A and B, the activity of the half-arm network on an origami lattice (origami-G8-NAD+24) was roughly fourfold that of the half-arm on a DNA DX tile (DX-G-NAD+ at 8-fold concentration). The two systems contained the same concentration of the enzyme G6PDH, but the complex on the origami had more swinging arm NAD^+ available near each of the enzymes, which might explain the higher activity. Next, we tested the effect of organized networks of a full enzyme network of G8-NAD+-L8. As shown in Figure 6 C and D, the organized enzyme network of G8-NAD+-L8 showed more than fourfold higher activity than the single enzyme complex of G-NAD+-L (1:1) on a DX tile when using the same concentration of total enzymes (i.e., the concentration of DX tile-based enzyme complex is approximately eight times the concentration of the origami-based enzyme network). The enhanced activity of the G8-NAD+-L8 network could be attributed to the fact that each individual G6PDH or LDH interacted with up to four enzyme partners through the swinging arms; also, even though the overall ratio of G6PDH and LDH was ≈1, an average of threefold more NAD+ were present. In contrast, for the single complex of G-NAD+-L, only one enzyme interacted with only one of the other enzyme partners through one swinging arm. Moreover, compared with the enzyme pairs without swinging arms, the overall activity of the G8-NAD+-L8 network was ≈100-fold more than that of the same enzymes on the origami tile with freely diffusing NAD+ (Figure 6 C and D). This largely boosted activity was attributed to the effect of substrate channeling by swinging arms on the network and significant increase in the local concentration of the substrate by tethering to the same complex structure.

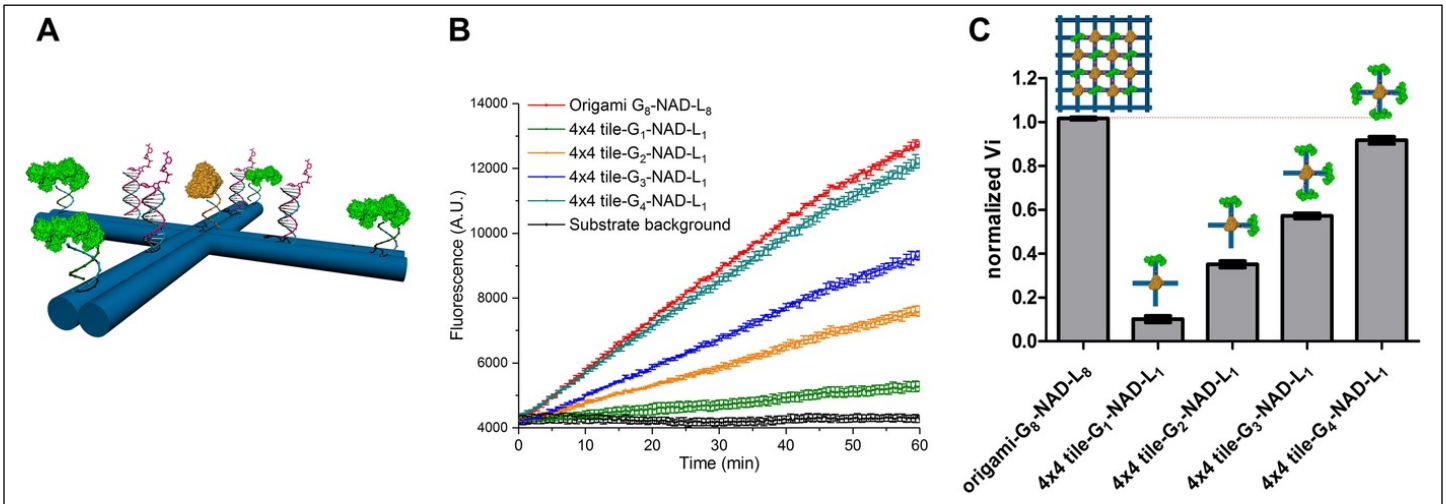


Figure 7: Comparison of enzyme activities for the G-NAD+-L swinging arm, patterned after various DNA nanoscaffolds. A) Schematic figures of control samples to test the relative stoichiometric dependence of enzyme activity with LDH at the center of a 4×4 DNA tile as the numbers of G6PDH and NAD+ increase from 1 to 4, respectively. B) Activity results for origami-G8-NAD+24-L8 construct compared with Gn-NAD+n-L (n=1, 2, 3, 4) on 4×4 tile or G-NAD+-L on DX tile. C) Normalized activity. Assay conditions: Origami–enzyme complex (1 nm) or tile–enzyme complex (8 nm) with G6P (1 mm), pyruvate (1 mm), LOX (10 nm), HRP (10 nm), and Amplex Red (200 µm) in 1× TBS (pH 8) buffer. Error bars represent standard deviations of at least three replicates.

To further probe the substrate transport between enzymes on the network, we used a planer four-arm tile (4×4) that mimicked the isolated junctions within the origami lattice. As shown in Figure 7 A, an LDH was positioned on the middle of the four-arm tile, and the number of swinging arms and G6PDH was altered from 1 to 4 on the four arms. In Figure 7 B and C, the activity of the series of Gn-NAD+n-L1 (n=1 to 4) complexes showed an almost linear increase as n increased from 1 to 4. Similar results were also observed for the series of G1-NAD+-L1–4 complexes in which the number of LDH was altered from 1 to 4 while positioning G6PDH at the center and keeping it as 1 (Figure S9). The maximal activities of G4-NAD+-L1 or G1-NAD+-L4 were similar to that of the origami scaffold enzyme network (at the same concentration of the limiting enzyme). This demonstrated our design hypothesis that each individual enzyme in the 2D network could interact with up to four enzyme partners to promote the efficient transport of substrates and intermediates for more active catalysis.

In summary, we have designed and demonstrated an artificial 2D enzyme network with efficient substrate channeling by swinging arms. The organized enzyme network increased the frequencies of catalytic interactions between enzymes, coupled with fast and effective intermediate transport by swinging arms, thus achieving much higher cascading enzyme activities than that of individual, unorganized enzyme pairs with freely diffusing substrates. These studies provide insights into the programmable frameworks for creating patterns of enzymes on 2D surfaces. The 2D enzyme networks could also be extended to 3D crystals by using recently developed tools in DNA nanotechnology.

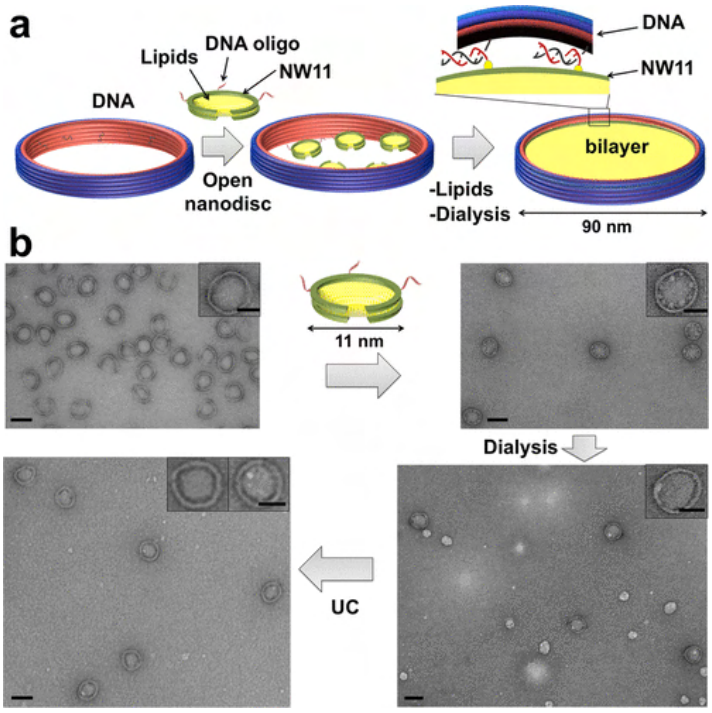


Figure 8: DNA-corralled nanodisc reconstitution. (a) Addition of detergent and lipids (POPC/POPG plus 10% cholesterol) to small nanodisc-decorated barrels (90 nm outer diameter) followed by dialysis results in the reconstitution of DCND. Each DNA barrel is decorated with ssDNA overhang as handles to hybridize with ssDNA chemically conjugated small nanodisc. (b) Negative-stain TEM images of DNA-origami barrel, with 90 nm outer diameter, before (top left) and after (top right) assembly with small nanodiscs. TEM images after dialysis to remove detergent, forming integrated large sized nanodiscs (bottom right) and after ultracentrifugation (UC) to remove free lipid vesicles (bottom left). Scale bar, 100 nm (top insets with 50 nm scale bar). Each step is imaged at lower magnification in Figures S1–S5.

3. DNA-corralled nanodiscs for the structural and functional characterization of membrane proteins and viral entry

Here we present a modular method for manufacturing large-sized nanodiscs using DNA-origami barrels as scaffolding corrals. Large-sized nanodiscs can be produced by first decorating the inside of DNA barrels with small lipid-bilayer nanodiscs, which open up when adding extra lipid to form large nanodiscs of diameters ~45 or ~70 nm as prescribed by the enclosing barrel dimension. Densely packed membrane protein arrays are then reconstituted within these large nanodiscs for potential structure determination. Furthermore, we demonstrate the potential of these nanodiscs as model membranes to study poliovirus entry.

Scaffolded DNA origami employs folding of a long scaffold strand with hundreds short staple strands to achieve self-assembly of custom shapes. Using DNA origami, each component strand can be uniquely addressed, providing a molecular billboard to arrange biomolecules with prescribed compositions and stoichiometries for biofunctional study. The mechanical stiffness of self-assembled DNA nanostructures also can confine the precise morphology and dimensions of nanomaterials,

including hard inorganic and soft biomaterials, through casting growth. Each DNA barrel we used in this study recruits a number of ~11 nm diameter nanodiscs that are circumscribed by a pair of noncircularized, oligonucleotide-functionalized scaffold proteins (3C-NW11), and directs their reconstitution into a single large nanodisc with a diameter prescribed by the dimension of the enclosing barrel (Figure 8). We employed two different sized barrels: 90 and 60 nm outer diameter to reconstitute ~70 or ~45 nm DNA-corralled nanodiscs (DCNDs) nanodiscs, respectively (Figure 8, Figures S2, S4 and S5). The final yield for the properly formed DCND is between 40 and 70% for both nanodiscs.

Our DNA-origami barrels were designed using the software caDNAno. (Figures S6 and S7) and folded in a one-pot reaction using a 20-h thermal annealing program. Correctly folded structures were isolated by glycerol-gradient centrifugation and verified by negative-stain transmission electron microscopy (TEM) (Figure 8b and Figure S3) and native agarose gel electrophoresis (Figures S8). The 11 nm nanodiscs were first covalently coupled to oligonucleotides through Sulfo-SMCC cross-linkers (Figure S9), and then assembled onto the DNA-origami barrels through hybridization to the single-stranded DNA handles (36, 24 handles for 90 nm, 60 nm barrel respectively) preimmobilized onto the nanostructure (Figure 8a). The successful hybridization with 11 nm sized nanodiscs was confirmed by negative stain-EM. As shown in Figure 1b and Figure S1, the DNA-origami barrel inner face is lined with small white disk-shaped structures along the interior face of the barrels. Most of the internalized nanodiscs have sizes around 11 nm in diameter, while some nanodiscs have sizes bigger than 11 nm, which can result from the heterogeneity of uncircularized nanodiscs.

In order to direct the reconstitution of the 11 nm nanodiscs into one single large nanodisc, we added excess lipids solubilized in detergent followed by dialysis. After dialysis, we performed isopycnic ultracentrifugation through a sucrose gradient to separate the DNA-barrel-scaffolded lipid nanodiscs from free vesicles on the basis of their differences in density (Figure 8b).

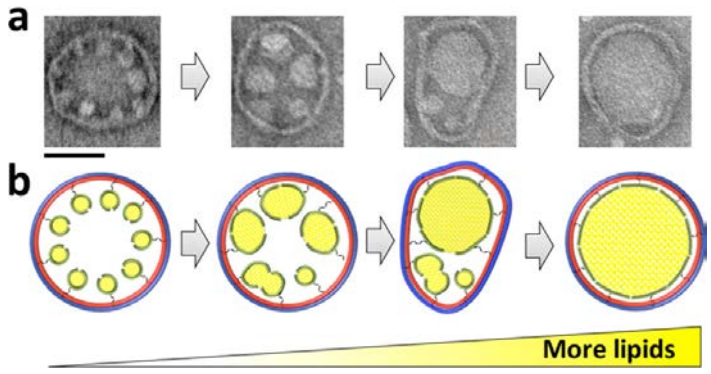


Figure 9: Proposed model for the assembly of the large bilayer within DNA-origami barrels (90 nm outer diameter). Bringing the 11 nm nanodiscs close to each other to within several nanometers is a critical first step. Adding excess lipids solubilized in detergent destabilizes and induces fusion of the neighboring nanodiscs. Next, the intermediate-sized nanodiscs fuse, perhaps aided by transient deformation of the barrel into an ellipsoid contour, to yield a single large bilayer nanodisc. Scale bar, 50 nm.

In Figure 9, we propose a model to explain the formation of the large bilayer. We hypothesize that bringing the 11 nm nanodiscs to within several nanometers, achieved here by DNA-origami templating, is an important first step for the successful assembly of the larger bilayer. Second, a destabilization must be developed at some point between the neighboring 11 nm nanodiscs to induce a highly localized rearrangement/fusion of the adjacent bilayers, resulting in one interconnected structure. This destabilization step is facilitated by the detergent that is used to solubilize the lipid mixture. The detergent destabilizes the interaction of MSP with its enclosed lipids, thus allowing the merge of neighboring nanodiscs. Third, fusion of smaller nanodiscs should initially create ellipsoid larger nanodiscs, until additional lipids can be recruited. Therefore, flexibility in the DNA-origami barrel (i.e., ability to distort into an ellipsoid as in Figure 9a,b, third panels) may help facilitate later fusion events. Lastly, additional lipids are needed to inflate ellipsoid larger nanodiscs into circular larger nanodiscs. All these factors together contribute to the success of the reconstitution of large bilayer nanodiscs.

We were able to assemble DCNDs using different lipids including the neutral lipid DOPC and the negatively charged lipid mixture POPC/POPG with or without cholesterol (Figure 8b, Figure S2). We obtained the best yield when we used POPC/POPG with 10% cholesterol as the cholesterol molecule is believed to increase the membrane mechanical stability. Interestingly, the yield did not improve after adding more cholesterol molecules. With the barrel acting as a bumper case to prevent aggregation, the enclosed nanodiscs were stable for at least 6 weeks when stored at 4 °C (Figures S10 and S14). Also, these nanodiscs show good tolerance to a broad range of pH and divalent ion concentration (Figures S11 and S12), representing a great improvement in large nanodisc stability.

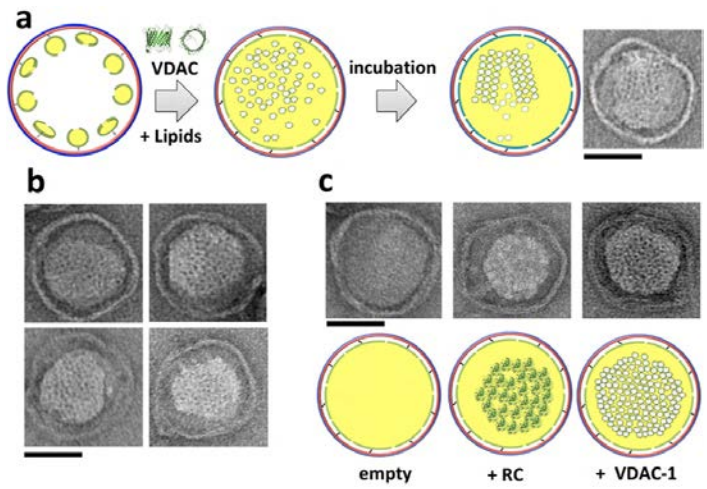


Figure 10: Reconstruction of hVDAC-1 and RC clusters within DCND. (a) Addition of lipids solubilized in detergent and hVDAC-1 to small nanodisc-decorated DNA-origami barrels (90 nm outer diameter), followed by dialysis, leads to reconstitution of hVDAC1 clusters within DCND. Multimeric assemblies of VDAC can be formed within the nanodiscs (right). (b) Typical DCND containing multimeric assemblies of VDAC. (c) Comparison of empty, RC and VDAC containing DCND. Scale bar, 50 nm.

Having established a modular method to reconstitute large stable nanodiscs using DNA barrel, we proceeded to examine whether this nanodisc platform could be used for membrane-protein incorporation for further structural and/or functional studies. Here we chose two model proteins that are known to establish functional assemblies with or without other proteins and cofactors: human Voltage-Dependent Anion Channel 1 (hVDAC-1) and the Rhodobacter sphaeroides photosynthetic reaction center protein (RC). hVDAC-1, a β barrel protein, is known to oligomerize on the surface of the outer mitochondrial membrane in apoptosis induction.Early EM and AFM studies of mitochondria from Neurospora grassa or potato tubers showed dense packing of VDAC pores or even hexagonal spindle-like arrangements. It is therefore hypothesized that oligomer interactions of VDAC may play a role for its function. On the other hand, RC is a mostly α-helical protein that plays a key role in the photochemical conversion of light into chemical energy.

Purified hVDAC1 and RC in detergent were added to the 11 nm nanodisc-decorated DNA origami along with lipids before the dialysis step (Figure 10a). After dialysis and purification of hVDAC1- and RC-loaded DCND by density gradients, we performed EM and SDS-PAGE analysis (silver-stain) to confirm the incorporation. As shown in Figure 10b,c and Figure S13, EM images and SDS-PAGE analysis verify the incorporation of both RC and hVDAC1 respectively into nanodiscs. We also showed that multimeric assemblies are formed (Figure 10a) within many of the nanodiscs when we added excess amount of either protein before the dialysis step.

Presenting membrane proteins at high density, both in freely diffusing as well as crystalline contexts, may prove useful to investigate both structural and functional rearrangements directly from the very same membranes. Often proteins are found functional in 2D crystals allowing a number of studies to collect electron diffraction data and yielding high resolution structures. Our method could be further developed to a general platform for membrane-protein structure determination by subatomic averaging using cryo-electron tomography, electron diffraction or by X-ray free electron laser (XFEL).

We next explored whether our nanodiscs could be used as a model membrane system to study early steps in viral entry. Poliovirus (~30 nm diameter) is the prototype member of the enterovirus genus of the picornavirus

family, which are positive-sense, single-stranded RNA viruses with ~7500-base genomes enclosed by an icosahedral capsid, missing an envelope. CD155 (also known as the poliovirus receptor, PVR) is the receptor to induce poliovirus infection, which catalyzes a conformational rearrangement and expansion of the virus particle, eventually leading to RNA release across the membrane.

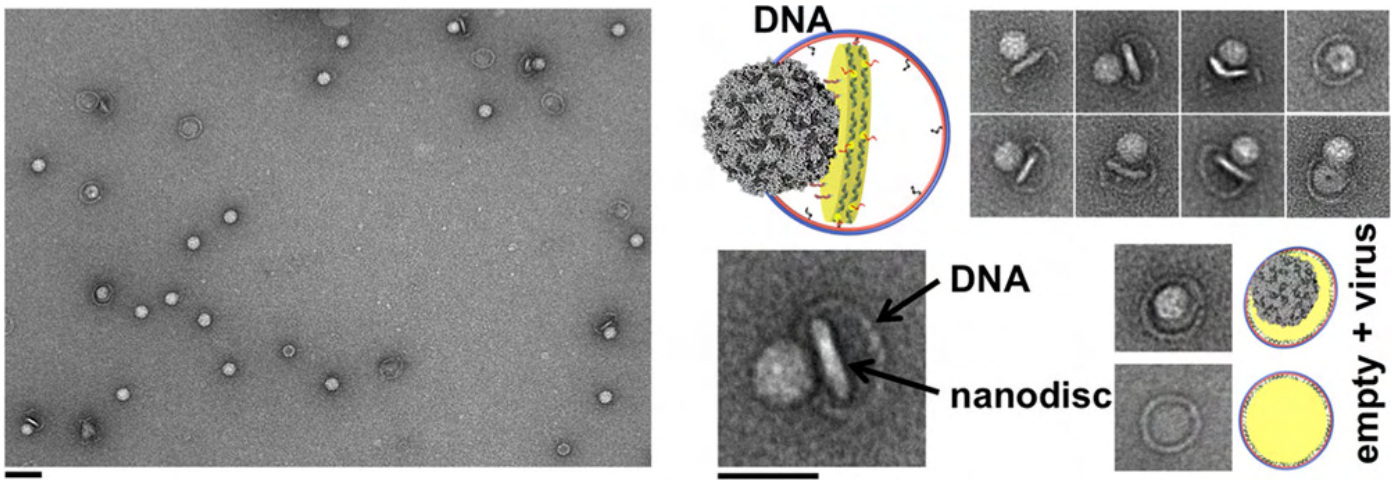


Figure 11: Poliovirus interactions with DCND containing CD155 receptor. (Left) Negative-stain TEM images of DCND (60 nm outer diameter) containing CD155 ectodomain interacting with poliovirus. Scale bar, 100 nm. (Right) TEM images showing individual viral particles tethered to DCND. Some images show the bending of the bilayer and the creation of a pore in nanodisc by the poliovirus (top right). Scale bar, 50 nm.

We prepared the 45 nm DCNDs (hosted by 60 nm outer-diameter DNA-origami barrels) containing lipids derivatized with a nitrilotriacetate (NTA) nickel-chelating headgroup. These DCND were functionalized with the His-tagged CD155 ectodomain. Next, the receptor-decorated nanodiscs were incubated with poliovirus for 5 min at 4 °C. The complex was then heated to 37 °C for 15 min to initiate receptor-mediated viral uncoating. Negative-stain EM confirmed the binding of the virus to DCND (Figure 11, Figure S14); in some cases, we observed apparent pore formation in the nanodiscs after the virus initial binding. We also observed by negative-stain and cryo-EM that many of the nanodiscs were partially released from their DNA scaffolds after binding the virus (Figure 11 and Figure S14 and S15). One potential explanation is the creation of extra membrane tension after receptor binding, which causes dsDNA dissociation between 3C-NW11 and DNA barrel. These partially detached nanodiscs are likely stabilized due to the hydrophobic interactions between 3C-NW11 and the acyl chains of the lipid bilayer (i.e., the 3C-NW11 get detached from the DNA barrel and stay with the bilayer).

In conclusion, we have developed a modular method to produce stable nanodiscs with sizes up to ~70 nm diameter using DNA-origami barrel as scaffold. We postulate our system can potentially create much larger nanodiscs, with more complicated geometry. Additionally, site-specific functionalization of DNA-origami provides a tool to precisely control membrane protein insertion, potentially with precisely controlled stoichiometry and transmembrane orientation. Therefore, our platform could provide an excellent tool for producing homogeneous membrane protein complexes in native-like environment with designed composition, stoichiometry, and orientation. We have demonstrated the utility of this model system to reconstitute membrane protein 2D clusters for potential structure determination. We used two membrane proteins, hVDAC-1 and RC, which are known to form functional oligomeric arrays in native membranes. Furthermore, we have established this system to probe an outstanding virology problem of viral entry through host membranes.

4. *Programmed coherent coupling in a synthetic DNA-based excitonic circuit*

Natural light-harvesting systems spatially organize densely packed chromophore aggregates using rigid protein scaffolds to achieve highly efficient, directed energy transfer. Here, we report a synthetic strategy using rigid DNA scaffolds to similarly program the spatial organization of densely packed, discrete clusters of cyanine dye aggregates with tunable absorption spectra and strongly coupled exciton dynamics present in natural light-harvesting systems. We first characterize the range of dye-aggregate sizes that can be templated spatially by A-tracts of B-form DNA while retaining coherent energy transfer. We then use structure-based modelling and quantum dynamics to guide the rational design of higher-order synthetic circuits consisting of multiple discrete dye aggregates within a DX-tile. These programmed circuits exhibit excitonic transport properties with prominent circular dichroism, superradiance, and fast delocalized exciton transfer, consistent with our quantum dynamics predictions. This bottom-up strategy offers a versatile approach to the rational design of strongly coupled excitonic circuits using spatially organized dye aggregates for use in coherent nanoscale energy transport, artificial light-harvesting, and nanophotonics.

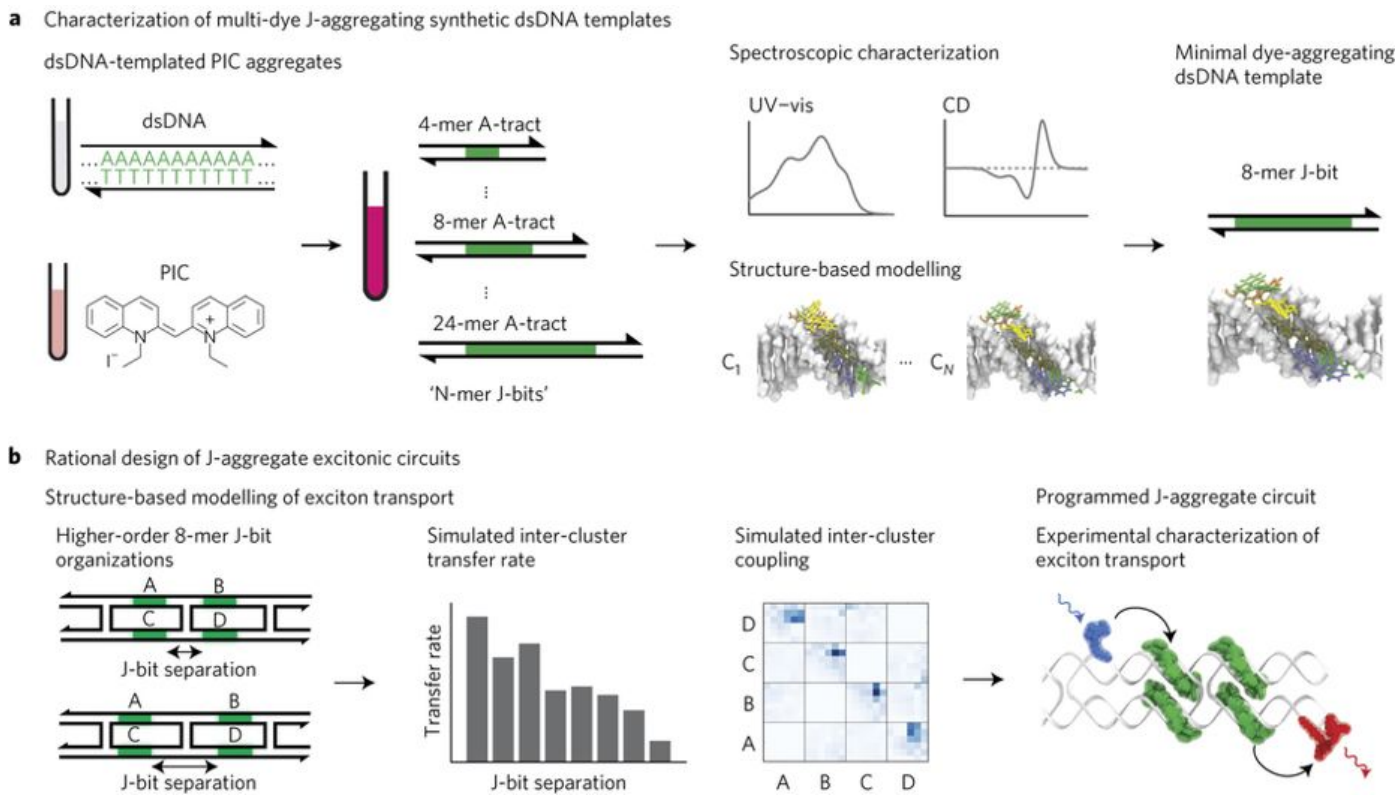


Figure 12: a, Pseudoisocyanine (PIC) molecules self-assemble on B-form DNA A-tracts as multi-dye complexes with UV–vis and CD signatures that are characteristic of J-aggregates. The minimal J-aggregating synthetic DNA template (an 8-mer 'J-bit') was first determined experimentally using UV–vis and CD. The length of the templating A-tract was varied systematically to identify the minimal length required to form a stable J-aggregate, found to be 8 base pairs. The molecular conformations of the bound PIC dyes were inferred computationally using structure-based modelling of the experimental spectroscopic signatures of the DNA-dye complexes, as indicated schematically in the figure. b, Rational design of multiple interacting multi-dye aggregates was then performed using structure-based modelling of inter-dye-aggregate energy transfer. J-bits were organized into higher-order assemblies using crosslinked, antiparallel DNA duplexes known as DX-tiles. J-bit conformations templated on DX-tiles were explored computationally to identify sequence designs that exhibit fast exciton transport, as illustrated schematically in the figure. The optimal computationally designed circuit was then synthesized and its energy transfer was characterized experimentally using steady-state and time-resolved fluorescence spectroscopy.

To achieve spatial programmability of strongly coupled dye aggregates, here we report a bottom-up synthetic experimental–computational strategy (Fig. 12) to spatially organize discrete clusters of strongly coupled pseudoisocyanine (PIC) aggregates in a manner that is consistent with the canonical double-crossover motif, which is the elemental building block of programmed synthetic DNA assemblies. We establish the size of dye aggregates that can be templated robustly within DNA duplexes of contiguous, non-alternating sequences of dA and dT dinucleotide base pairs (bp) of B-form DNA (A-tracts) while retaining coherent energy transfer (Fig. 12a), and then construct higher-order circuits using DNA duplexes constrained by antiparallel double crossovers (DX) in the canonical DX-tile motif18 to test the viability of their integration into functional architectures that still exhibit coherent energy transport (Fig. 12b). Comparison of their excitonic properties with control DNA sequences demonstrates clearly the specificity of A-tract-templating of PIC dyes into J-like aggregates, which we term 'J-bits' due to their photophysical characteristics that are reminiscent of the LH1/LH2 natural light-harvesting antennas from purple bacterium with red-shifted absorption spectrum and head-to-tail transition dipole organization. In contrast to previous DNA-based design strategies for exciton transfer that are limited to non-coherent, weakly coupled FRET-based transport mediated by dyes that are either intercalated or covalently attached to DNA using flexible linkers or low quantum yield H-aggregates that lack the strongly coupled head-to-tail transition dipole arrangement of J-aggregates (Supplementary Section 1), we demonstrate that J-bits host a low-energy delocalized, superradiant exciton state that provides a larger effective transition dipole moment and significantly stronger long-range interactions with neighbouring dye aggregates, analogous to the LH1/LH2 architecture. Given that J-bits are templated non-covalently by the underlying nucleotide sequence of DNA, they may in principle be integrated into synthetic structured DNA origami architectures of diverse geometries and energy-funnelling properties, offering the opportunity to control both the position and orientation of their effective transition dipoles.

PIC dyes have previously been shown to self-assemble into chiral J-aggregates on templates of natural, calf thymus DNA of uncontrolled sequence at a critical dye concentration of ∼450 μM with ∼250 μM DNA bases in 10 mM NaCl buffer29. To engineer custom synthetic assemblies of these dye aggregates we first sought to identify the sequence specificity of PIC J-aggregates on synthetic double-stranded DNA (dsDNA) templates of controlled sequences. Ultraviolet–visible (UV–vis) and circular dichroism (CD) spectroscopy revealed the formation of chiral J-aggregates specifically templated by DNA duplexes with A-tracts in similar 10 mM NaCl, pH 7.0 buffer (Fig. 13a and Supplementary Sections 2–4 and Supplementary Table 1 and Supplementary Figs 1 and 2). A PIC monomer concentration of 90 μM with DNA concentration of 75 μM dA · dT base pair concentration [bp] was found to optimally induce the J-aggregate absorption signal (Supplementary Fig. 1). To evaluate our ability to control J-bit optical and energy transfer properties determined by aggregate size, as well as test their geometric compatibility with antiparallel double-crossover motifs used to program structured DNA assemblies, we systematically varied the size of the aggregation template using A-tract domain lengths of 4 to 24 bp positioned between two tails of the 3 bp sequence CGC. UV–vis and CD spectroscopy revealed a tunable red-shifted J-aggregate absorption peak and circular dichroism with a positive Cotton effect at ∼550 nm for J-bits equal to or larger than the 8-mer, setting this lower bound on the minimal J-aggregate size (Fig. 13a). Specific binding of PIC monomers to 8-mer and 24-mer A-tracts assayed using isothermal titration calorimetry (ITC) revealed dissociation constants of 20 μM and 25 μM, respectively, and a binding site occupancy of ∼0.7 at the chosen PIC and DNA concentrations (Supplementary Table 2 and Supplementary Figs 3 and 4).

To exploit individual J-bits in programming higher-order exciton transport in rationally designed circuits where the position and orientation of their effective transition dipole moment is controlled, we first sought to characterize in detail their excited-state properties within isolated DNA duplexes. Steady-state fluorescence spectroscopy of the minimal 8-mer J-bit excited at 490 nm exhibited a 1.3-fold enhancement in its fluorescence quantum yield and a concomitant 1.4-fold decrease in its fluorescence lifetime compared with PIC monomers that were bound to DNA duplexes that instead contained control AT-tracts (Fig. 13b and Supplementary Figs 5

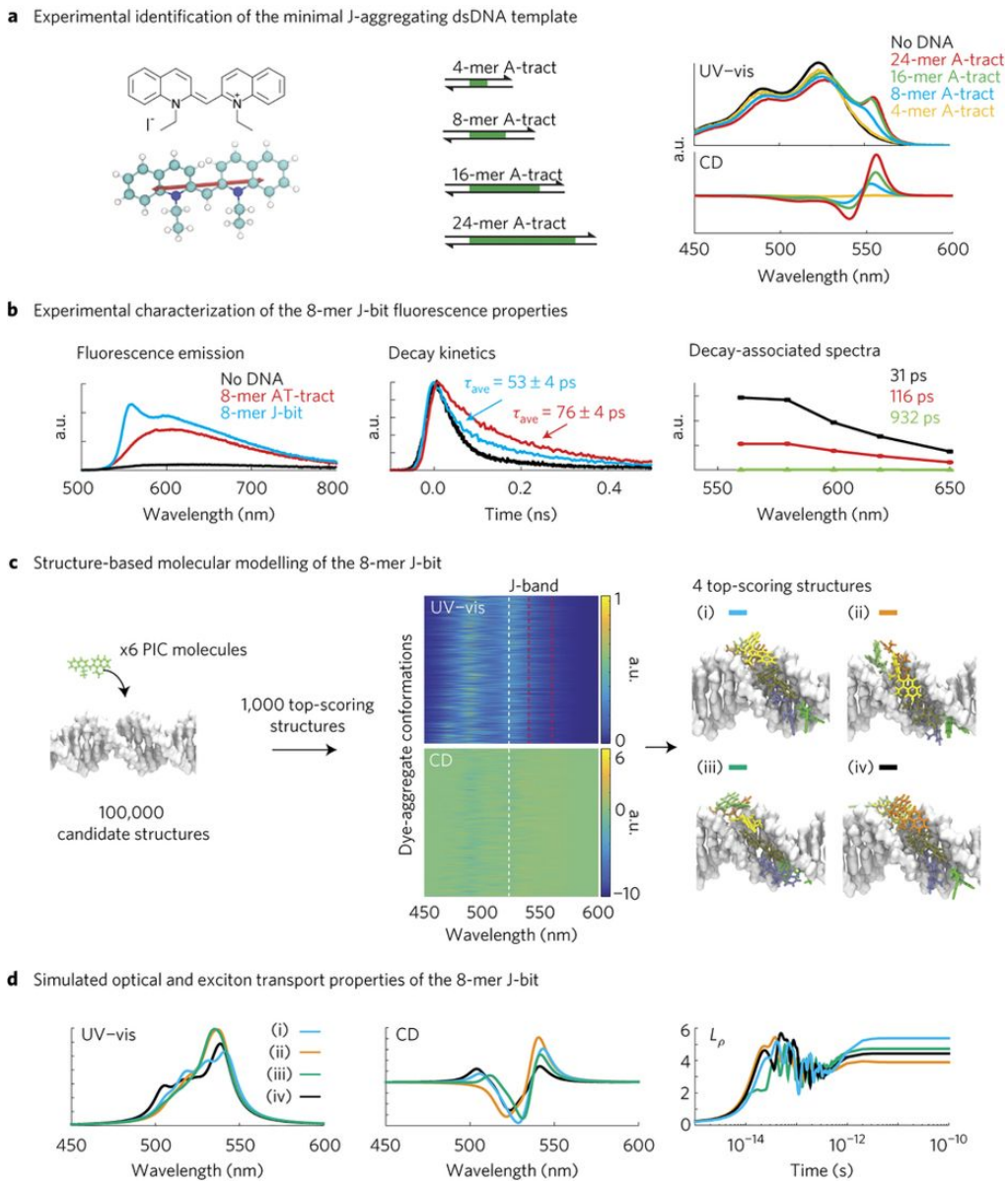


Figure 13: a, Experimental UV–vis and CD spectra of N-mer J-bits consisting of aggregated PIC molecules, where N is the number of consecutive DNA dA · dT base pairs within the templating site. The chemical structure and conformation of a single PIC monomer and its calculated transition dipole are shown on the left. b, Experimental fluorescence characterization of the 8-mer J-bit. Comparison of the fluorescence emission spectrum of the 8-mer J-bit duplex (blue curve) with that of isolated PIC in solution without any dsDNA template present (black curve), and PIC in solution with the control 8-mer AT-tract duplex template duplex present (red curve) (left). Fluorescence decay kinetics measured at λem = 560 nm for the 8-mer J-bit (blue curve), PIC solution without duplex template present (black curve) and PIC solution with the control 8-mer AT-tract duplex template (red curve) (centre). Excitation wavelength was measured at λex = 520 nm and the calculated average lifetimes for the 8-mer J-bit and 8-mer AT-tract duplexes are shown. Decay-associated spectra obtained from the global fitting of fluorescence decay kinetics of the 8-mer J-bit duplex (right). c, Structure-based dsDNA-dye aggregate conformations are inferred computationally for the 8-mer J-bit using molecular docking. 100,000 candidate duplex-dye complexes are first generated computationally (left). Simulated UV–vis and CD spectra of the 1,000 top-scoring candidate structures are then calculated and compared with the experimental spectra (centre) to yield the four top-scoring structures (right). d, Simulated UV–vis and CD spectra and the time-dependent exciton coherence length of the four top-scoring structures are shown.

and 6), indicative of superradiance. This suggests that these dyes are coherently coupled within the 8-mer J-bit

exhibiting a superradiance enhancement factor of 2.0 ± 0.3 (Supplementary Section 7) due to exciton delocalization that should yield considerably longer-range coupling in higher-order multi-aggregate assemblies, similar to the LH1/LH2 light-harvesting antenna (Supplementary Section 7).

To rationally design extended excitonic circuits that exploit the coherent energy transport within this minimal J-bit, we next sought to characterize the detailed molecular organization of chromophores within an individual J-bit. Because structures determined from nuclear magnetic resonance (NMR) or X-ray crystallography are unavailable for these cyanine-DNA conjugates, we used structure-based molecular modelling with quantum mechanical simulations instead to infer candidate supramolecular architectures for use in the design of larger-scale circuits (Fig. 13c and Supplementary Figs 8–14). Given an estimated aggregate size of six PIC molecules per 8-mer A-tract of B-form DNA, which is consistent with the 8–12 PIC molecules per turn of B-form DNA found previously, we used molecular docking and mechanics to generate over 100,000 candidate structures of PIC-DNA aggregates. In contrast to previous work29, dyes were modelled to reside in the DNA minor groove to be consistent with their strong preference for aggregation on dA · dT base pairs and in analogy with detailed NMR and X-ray crystal structures of DNA-dye complexes using synthetic polyamides and cyanine dyes similar to PIC (Supplementary Section 4). Excitonic coupling within each candidate structure was calculated from its transition density using the TrEsp method (Supplementary Section 9). UV–vis and CD stick-spectra were obtained from the diagonalization of the Frenkel Hamiltonian, which enabled classification of the candidate structures by comparison with experimental spectra (Methods and Fig. 13c, d). Notably, top-scoring multi-dye conformations consisted of head-to-tail dipole organizations similar to those found in natural LHCs, albeit with a right-handed chirality due to templating on B-form DNA (Supplementary Table 6 and Supplementary Figs 12 and 13). Further, quantum dynamics simulations using the non-secular Redfield theory predicted an exciton coherence length of 3 to 5 dyes (Fig. 13d), corresponding to a superradiance enhancement factor of 2.1 ± 0.2 that is consistent with our experimental measurement of 2.0 ± 0.3 noted above. These structural results on the prospective architecture of the isolated multi-chromophore J-bit aggregate templated by DNA A-tracts offered the application of structure-based modelling and quantum dynamics simulation to rationally design higher-order synthetic DNA-based circuits that operate beyond the classical regime.

To realize a larger-scale, synthetic excitonic circuit consisting of multiple interacting dye clusters, we chose to position four discrete J-bits within a canonical DX-based tile18. The DX-based tile is the fundamental structural unit of DNA nanotechnology that rigidly constrains parallel DNA duplexes using antiparallel crossover motifs to self-assemble large-scale nanostructures of nearly arbitrary geometry. To test our ability to rationally design such a functional higher-order excitonic circuit, we designed six synthetic single-stranded DNA oligonucleotides to fold into a DX-tile with three antiparallel crossovers in which four J-bits were positioned on A-tracts that spanned the central immobile four-way junction. (4WJ) (Fig. 14a and Supplementary Fig. 14 and Supplementary Table 7).

We used our computational framework to perform a systematic evaluation of discrete axial separations of J-bits across the central 4WJ and investigate the rate of transfer and excitonic coupling between the four J-bits with separations of 2 to 16 bp (Fig. 14a). Using the Frenkel Hamiltonian and a stochastic Schrödinger equation (SSE) approach, our calculations revealed that separations of 2 bp retained substantial excitonic couplings between individual J-bits, with inter-cluster transfer on picosecond timescales (∼1.6 ps), while weakly affecting the absorption and CD spectra (Fig. 14a, b). The coherence length of approximately five chromophores and superradiance enhancement factor of 1.5 simulated with the non-secular Redfield theory for the DX-tile are in addition similar to those that we predicted in this work for isolated J-bits (computed coherence length of 3–5 chromophores and superradiance enhancement of 2.1 ± 0.2). This result suggests that exciton delocalization and coherent transport remains in this DX-tile construct, with a timescale of ∼14 fs (Fig. 14c and Supplementary Figs 15 and 16). These computational results offered evidence for the prospective utility of this DX-tile circuit as

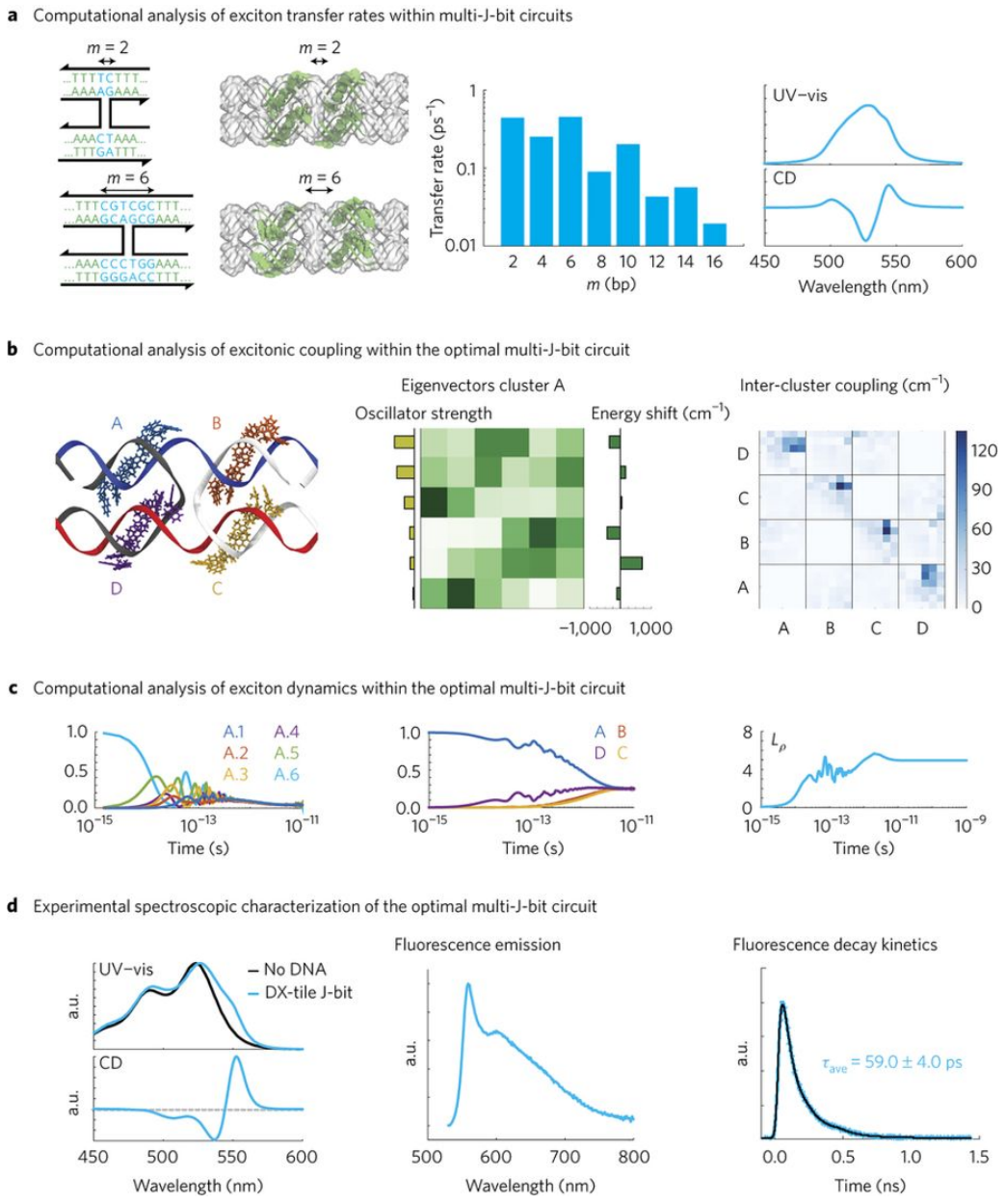


Figure 14: a, Synthetic DX-tiles are designed using immobile four-way junctions and four discrete A-tracts across the central junction (left). The number of base pairs separating the A-tracts is varied systematically to analyse computationally the impact on exciton transfer rate using the inferred J-bit molecular conformation from Fig. 13c and the SSE formalism (centre). Simulated UV–vis and CD spectra are computed for the circuit design with highest exciton transfer rate (m = 2), which is also used for synthesis (right). b, Predicted molecular conformation (left) with corresponding simulated exciton states (centre) and inter-cluster exciton coupling (right) for the optimal J-bit circuit design. c, Simulated exciton dynamics following initial excitation of the A.6 monomer. Time-dependent exciton population in each of the molecules that constitute the A-aggregate, calculated with an SSE method (left). Integrated time-dependent exciton population in each of the four J-bit aggregates templated by the DX-tile J-bit (centre). Time-dependent exciton coherence length, calculated with the non-secular Redfield method (right). d, Experimental UV–vis and CD spectra (left), fluorescence emission (centre), and fluorescence decay kinetics at 580 nm (right) for the synthesized PIC DX-tile. Excitation wavelength is 520 nm for fluorescence spectroscopy. The average lifetime of kinetics at 580 nm is calculated based on results of a global analysis.

an intermediate 'building block' in the construction of more complex excitonic circuits and antennas that operate beyond the classical regime, with the 2 bp separation resulting in the strongest coupling between the

J-bits examined. Additionally, these results suggest the possibility to tune the exciton transfer rate between J-bits by modulating their position within the DNA template, which should offer control over the relative orientations and distances between their transition dipoles both along individual DNA duplexes as well as across neighbouring DNA duplexes within two-dimensional (2D) and three-dimensional (3D) assemblies.

To test whether J-bits maintained their aggregated structural state and excitonic properties in a functional excitonic circuit, we synthesized this computationally designed DX-tile and characterized in detail its excited-state properties, which we compared with those of the 8-mer J-bits on the isolated DNA duplexes (Fig. 14d and Supplementary Figs 18 and 19). UV–vis and CD spectroscopy yielded absorption red shift and circular dichroism similar to the isolated J-bits, which suggests the formation of coherently interacting dye complexes. ITC further confirmed specific binding of the PIC dye to DNA A-tracts with a dissociation constant of ∼66 μM, resulting in a binding site occupancy of ∼0.4 at the optimal concentration of 90 μM PIC and 0.72 μM DX-tile (Supplementary Table 2 and Supplementary Fig. 14). Analysis of the steady-state fluorescence and fluorescence decay kinetics of the DX-tile based circuit also yielded similar results compared with the J-bit templated by the isolated DNA duplexes. Specifically, a superradiance enhancement factor of 1.5 ± 0.3 was measured for the DX-tile (Fig. 14d and Supplementary Section 7), in agreement with the predicted value of 1.5. Comparison with the superradiance enhancement measured for isolated J-bits (2.0 ± 0.3) suggests that exciton delocalization, coherent coupling, and superradiance were only weakly affected by integration of the J-bit into the higher-order DX-tile assembly, despite their proximities to the central crossover, consistent with predictions of computational modelling. These results indicate that J-bits templated within the rigid DX-tile structural scaffold retain their J-aggregate structure and coherent energy transfer, which may in principle be exploited to build extended excitonic circuits scaffolded using rigid DNA origami assemblies.

To further evaluate their application to the design of a modular excitonic circuit, we coupled an acceptor molecule (AF 647) to demonstrate energy transfer from the J-bits to an acceptor chromophore (Fig. 15a, b and Supplementary Section 16). Monitoring steady-state fluorescence emission (Supplementary Fig. 23) and relaxation kinetics upon excitation at 400 nm suggested a strong transfer from the J-bits to AF 647 due to their spectral overlap and the superradiant properties of the excited state of the J-bits (Fig. 15b). Excitation energy transfer from PIC to AF 647 in construct I-AF + PIC is supported by the shape of the ∼21 ps component of the fluorescence decay-associated spectra (DAS) (Fig. 15b, centre), which showed a broad positive band in the PIC emission wavelength region and a negative band in the wavelength region dominated by the AF 647 emission. We estimated a 37.3 ± 3.1% FRET efficiency based on the decrease of the J-bit fluorescence lifetime (from 52.2 ps to 34.1 ps), of the fast DAS component (from 34.2 ps to 20.9 ps), and of the integrated time-resolved fluorescence at the J-bit band in the presence of AF 647 on the DX-tile construct (Supplementary Table 14). To highlight how the programmable sequence of DNA may be utilized for designing more complex excitonic circuits, we characterized the energy transfer mediated by non-specifically bound PIC dyes in a DX-tile designed with high GC content and no contiguous A-tracts (construct II-AF + PIC and construct II + PIC; Supplementary Table 13 and Supplementary Figs 27 and 28 and Supplementary Section 17). Compared with construct I, time-resolved and steady-state fluorescence spectroscopy indicated a 4-fold lower energy transfer efficiency of PIC to AF 647 within the GC control DX-tile of 9.5 ± 0.4% compared with PIC within the DX-tile J-bit to AF 647 of 37.3 ± 3.1%. These results support the specific role of J-bits in mediating efficient exciton transport and suggest the possibility of using alternate sequences of contiguous A-tracts and high-GC-content DNA segments to program complex excitonic circuits within synthetic structured DNA assemblies.

To test whether energy transfer mediated by J-bits can be realized along both donor and acceptor pathways, we next investigated three-step energy transfer in which energy is initially absorbed by an ATTO 390 chromophore prior to transfer to J-bit intermediates and finally a terminal acceptor AF 647 chromophore located ∼9 nm away, well beyond the 4.6 nm Förster radius of the ATTO 390–AF 647 chromophore pair (Fig. 15c

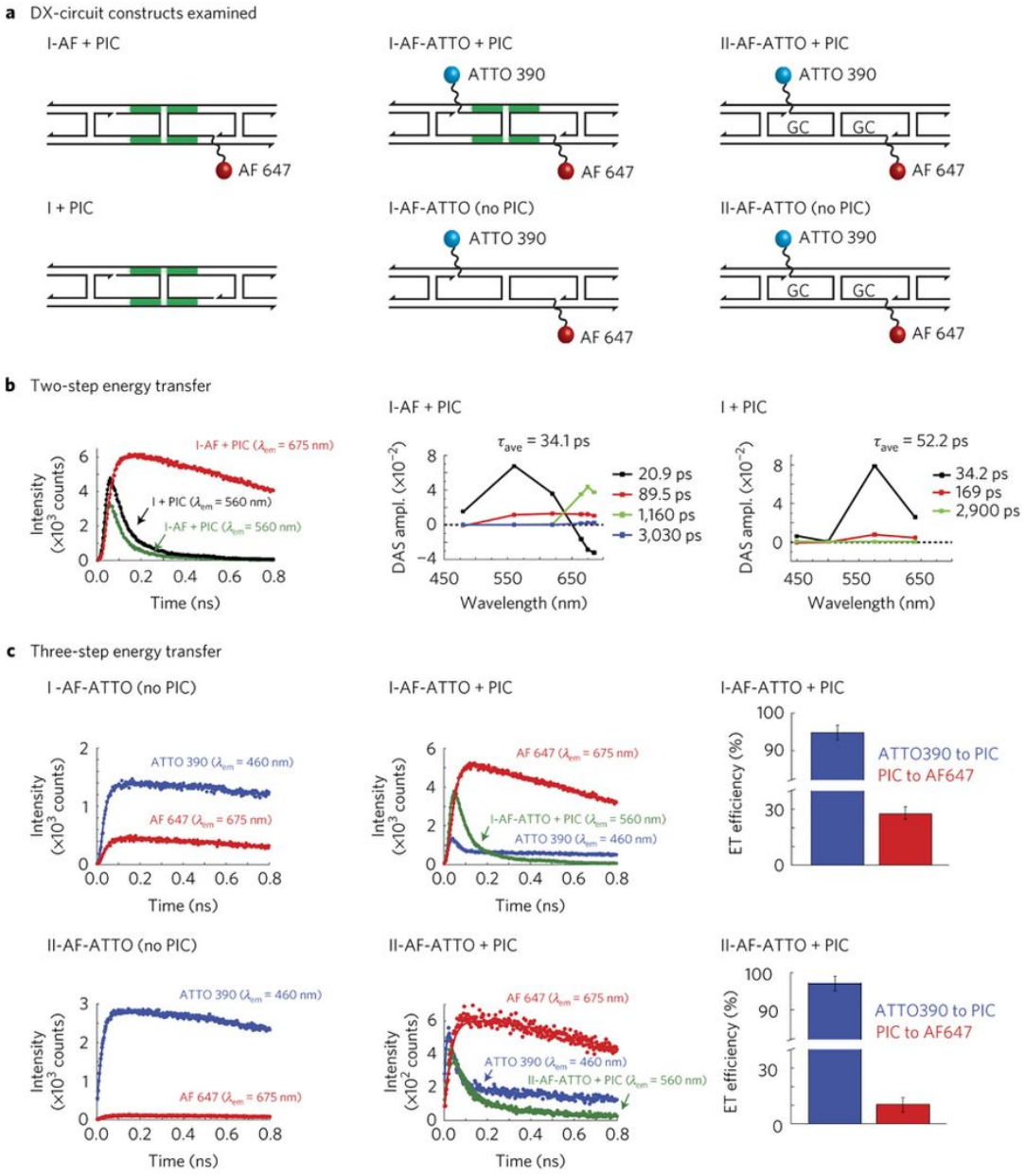


Figure 15: a, Schematic diagrams depicting the DX-tile constructs used to program multi-J-bit excitonic circuits with two-step and three-step energy transfer. b, Two-step energy transfer from the construct I + PIC to a single dye acceptor, construct I-AF + PIC. The sample is excited with a 400 nm laser. The energy is transferred to the Alexa Fluor 647 acceptor dye (I-AF + PIC). Results are compared with a control construct without the acceptor (I + PIC). Fluorescence decay kinetics at wavelengths corresponding to AF 647 (675 nm) and PIC J-bits (560 nm) (left). Fluorescence decay-associated spectra resulting from fits of the fluorescence kinetic data for construct I-AF + PIC (centre) and construct I + PIC (right). Average lifetimes at 560 nm and 575 nm from global analysis at the PIC J-bit band are indicated for constructs I-AF + PIC and I + PIC, respectively. c, Three-step energy transfer mediated by the multi-J-bit excitonic circuit. The ATTO 390 donor dye is excited with a 400 nm laser. Energy is subsequently transferred to the J-bits templated by the DX-tiles, and onwards to the Alexa Fluor 647 acceptor dye: I-AF-ATTO + PIC. Results are compared with a control construct with no PIC mediating transfer: I-AF-ATTO (no PIC) (left, top). Fluorescence decay kinetics at wavelengths corresponding to AF 647 (675 nm), ATTO 390 (460 nm) (left, top and bottom) and the J-bits and non-specifically bound PIC (560 nm) (centre, top and bottom). The energy transfer efficiency of ATTO to PIC and PIC to AF 647 (right, top and bottom) calculated using average fluorescence lifetimes of ATTO 390 (460 nm) and PIC (560 nm) from construct I-ATTO-AF + PIC or no PIC, and construct II-ATTO-AF + PIC or no PIC.

and Supplementary Figs 25, 26, 29 and S30). Strong quenching of the ATTO 390 steady-state fluorescence

emission in addition to the presence of a fast decay component at the ATTO 390 emission band (average lifetime reduced from 4.7 ns to 240 ps) both support significant transfer from ATTO 390 to the J-bits in construct I-AF-ATTO + PIC. We observed an energy transfer efficiency for ATTO 390 to PIC of 94.8 ± 2.0% in construct I, which is comparable to the observed energy transfer efficiency of ATTO 390 to PIC of 97.2 ± 2.0% observed in construct II (Fig. 15c, right). There was a ∼3-fold increase in energy transfer efficiency from PIC to AF 647 when PIC was templated by the DX-tile J-bit that mediated energy transfer to AF 647 (27.5 ± 3.3%), compared with PIC bound to the control DX-tile GC (10.4 ± 3.7%) (Fig. 15c, right). Enhanced energy transfer is further supported by the 12.5 ps DAS for construct I-AF-ATTO + PIC, which shows broad positive bands in the ATTO 390 and PIC emission wavelength regions coupled to a negative band in the AF 647 emission wavelength region (Supplementary Fig. 31). The excited-state lifetime at 580 nm (40.0 ps) that was measured using construct I-AF-ATTO + PIC (Supplementary Fig. 31) is comparable to the excited-state lifetime at 580 nm in construct I-AF + PIC, indicating a similar rate of transfer from the J-bits to the terminal AF 647 acceptor (Fig. 15b, centre). These experimental results highlight the specific role of the J-bits in mediating efficient energy transfer and demonstrate a proof of concept in the programmable sequence design of synthetic structured DNA assemblies can be leveraged to design complex excitonic circuits with enhanced energy transfer that operates beyond the classical Förster regime.

These spectroscopic data demonstrate significant exciton transfer from a delocalized excitonic state to an acceptor molecule in these two excitonic circuits. Because the coherently interacting dye clusters are integrated into the rigid DX-tile that is the elemental building block of programmed DNA nanostructures, future designs may test diverse geometric architectures that mimic light-harvesting strategies of protein-based antennas that operate beyond the classical regime previously achieved using programmed DNA self-assembly. Interesting avenues to explore as natural extensions of the current DX-based motif include rigid filaments32 to test long-range exciton transport mediated by coherently coupled dye aggregates, and 2D discs and 3D lattices and spheres to test directional nanoscale exciton-funnelling strategies. These designs may be realized using purely synthetic single-stranded DNA that is now commonly available for arbitrary placement of A-tracts within programmed DNA assemblies of nearly arbitrary geometric form, as well as coupled to functional nanoscale materials and polymers, including quantum dots and plasmonic nanoparticles. The proposed J-bit-DX-tile with controllable size of the dye cluster and relative positions of effective transition dipoles within these assemblies can additionally be used to realize architectures that optimize exciton transport rate as coherence length and topological network properties of interacting J-bits are tuned, which cannot be achieved using alternative synthetic approaches. One possibility includes extended DX-tile circuits that utilize templated J-bits of decreasing lengths to act as an energy transfer diode to funnel energy transfer towards an energy trap while PIC monomers on alternating GC-tracts operate as energy transfer resistors. Although powerful theoretically, practical implementation of such assemblies may require the development of alternative dye templating strategies such as covalent conjugation to reduce the relatively high free PIC dye concentration required to form the J-bit. Although the use of non-covalently associated, commercially available PIC dyes may directly offer the self-assembly of complex multi-chromophore aggregates templated by synthetic DNA, future work may additionally seek to broaden the diversity of chromophore molecule types that can be used to program such biomimetic spatially organized J-aggregate assemblies, which have been designed, synthesized, and characterized here. Integration of H-aggregates into rationally designed excitonic circuits would also be interesting to explore due to their strongly increased radiative lifetimes, which can contribute to long-range transport. The highly programmable and reproducible nature of programmed DNA self-assembly, together with the quantitative structure-based and quantum dynamics modelling presented here in an integrated manner, further offers an efficient, powerful, and generalized means of exploring both geometric questions as well as dye photophysical properties to speed the discovery and design of next-generation nanoscale excitonic materials, similar to the strategies used in the field of organic photovoltaics.

5. *Exploring the speed limit of toehold exchange with a cartwheeling DNA acrobat*

Dynamic DNA nanotechnology has yielded nontrivial autonomous behaviours such as stimulus-guided locomotion, computation and programmable molecular assembly. Despite these successes, DNA-based nanomachines suffer from slow kinetics, requiring several minutes or longer to carry out a handful of operations. Here, we pursue the speed limit of an important class of reactions in DNA nanotechnology—toehold exchange—through the single-molecule optimization of a novel class of DNA walker that undergoes cartwheeling movements over a field of complementary oligonucleotides. After optimizing this DNA 'acrobat' for rapid movement, we measure a stepping rate constant approaching 1 s^{-1}, which is 10- to 100-fold faster than prior DNA walkers. Finally, we use single-particle tracking to demonstrate movement of the walker over hundreds of nanometres within 10 min, in quantitative agreement with predictions from stepping kinetics. These results suggest that substantial improvements in the operating rates of broad classes of DNA nanomachines utilizing strand displacement are possible.

Dynamic DNA nanotechnology exploits the programmable reconfiguration of Watson–Crick base pairing to carry out nontrivial autonomous functions inspired by both biology and macroscopic engineering, resulting in systems such as molecular walkers, assembly lines, computers and robots. Unlike their naturally occurring counterparts, the top-down design and transparent relationship between the sequence and function of DNA nanodevices provides rich opportunities for programmable specificity and dynamics. A fundamental process in nearly all such systems is strand displacement. This process involves the stepwise replacement of one strand of a double helix with another invading strand, a process often catalysed by short overhangs of unpaired nucleotides called toeholds. A class of strand displacement reactions called toehold exchange involves competition between two toeholds of similar length. Toehold exchange has found widespread use in dynamic DNA nanotechnology due to its robust ability to accelerate the exchange of nearly isoenergetic DNA double helices by several orders of magnitude. Indeed, toehold-mediated strand displacement reactions can have second-order rate constants in excess of 10 M^{-1} s^{-1}. Thus, DNA nanomachines with local effective strand concentrations in the micromolar range may be able to execute individual operations in seconds or quicker if branch migration and toehold dissociation are sufficiently rapid.

Despite this theoretical rapidity, in current practice, most DNA nanomachines require several seconds to several hours to complete a single operation. For instance, a recently reported cargo-sorting DNA robot utilizing toehold exchange for locomotion was found to take approximately one step every 5 min despite an only 6-nm gap between neighbouring footholds. This speed is comparable with the reported speeds of other autonomous DNA walkers. In one notable exception, a translocation rate of ~1 μm min^{-1} was achieved for DNA-functionalized nanoparticles, though this system utilized a burnt-bridge mechanism involving the degradation of complementary RNA strands by an external RNase H enzyme. By comparison, natural protein motors have translocation rates of ~1 μm s^{-1} under saturating ATP conditions. We hypothesized that the sluggish performance of DNA nanomachines is not due to a fundamental limitation of strand displacement reactions, but is instead the result of designs not optimized for speed.

To test this hypothesis, we designed a DNA walker with the express purpose of rapid locomotion. We then used single-molecule fluorescence resonance energy transfer (smFRET) to characterize its translocation mechanism and kinetics, and optimized its stepping rate by varying the lengths of its toehold and branch-migration domains. These optimizations resulted in stepping rate constants of more than an order of magnitude faster than existing DNA walkers. Following optimization of the design with smFRET, we used single-particle tracking to observe the movement of toehold exchange DNA walkers over distances as long as ~1 μm on a two-dimensional (2D) array of footholds. The performance of the walkers on 2D arrays was quantitatively consistent with predictions based on the stepping kinetics measured by smFRET on DNA tile substrates. This result demonstrates that this

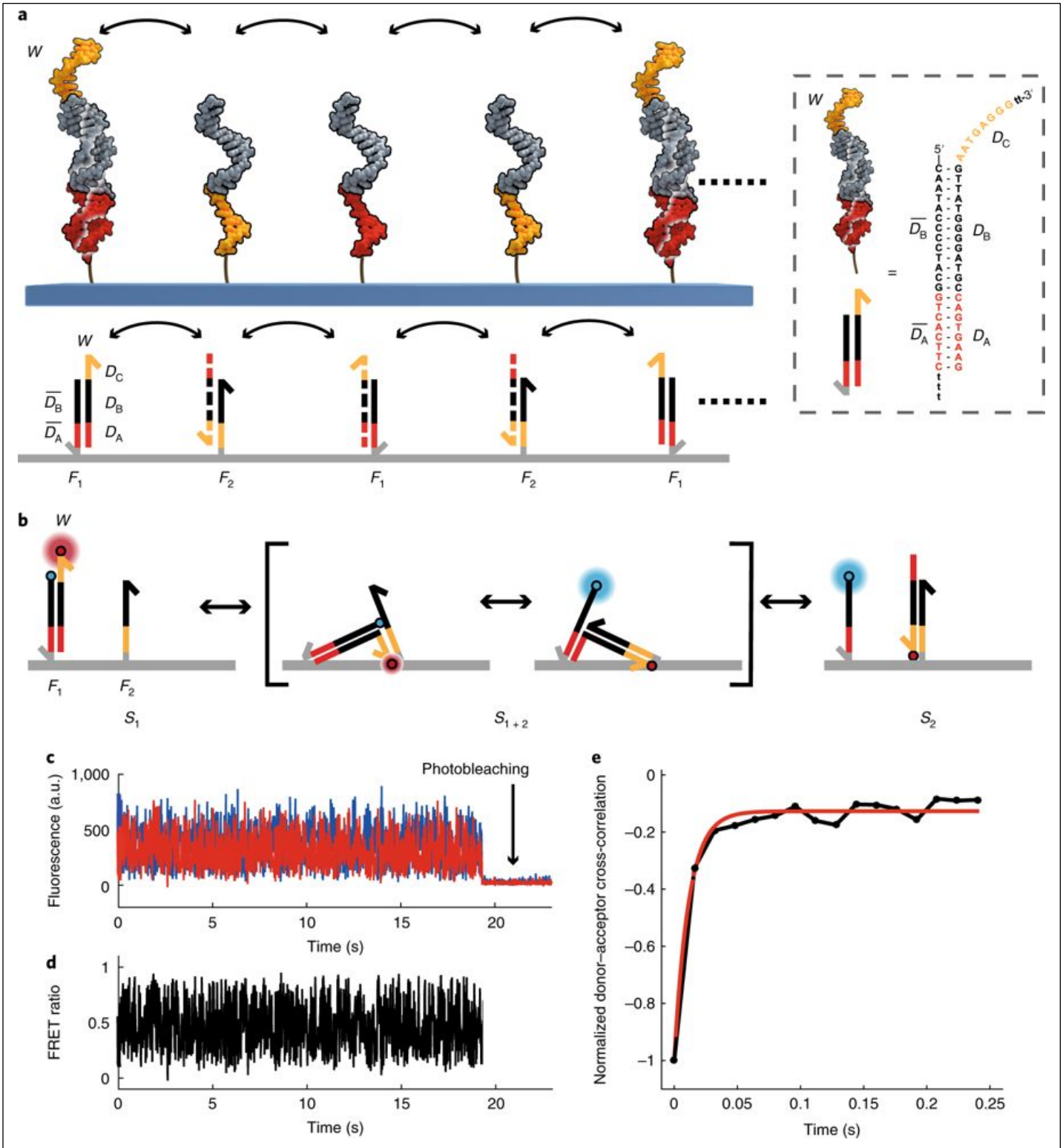


Figure 16: a, Schematic showing the intended mechanism of locomotion. b, Schematic of smFRET measurement of the stepping kinetics of a Cy5-labelled (red) DNA walker on a two-foothold DNA tile in which one foothold is labelled with Cy3 (blue). c, Rapid anticorrelated fluctuations in Cy3 (blue) and Cy5 (red) fluorescence intensity for a single walker–tile complex, suggesting branch migration in the hybrid state S1 + 2. d, FRET ratio versus time for the trajectory shown in c. e, Cross-correlation analysis of the Cy3 and Cy5 signal in c, with a single-exponential fit indicating an anticorrelation time constant of 11.4 ms for this trajectory.

mechanism of locomotion is generalizable to different substrate types and conducive to long-range movement

requiring hundreds of steps.

The DNA walker (Fig. 16a) was designed with speed, simplicity and robust performance as the primary objectives. Thus, we avoided the need for strand cleavage by protein or DNA enzymes because these pose the risk of creating kinetic traps for DNA walkers and would prevent observations of repeated stepping. Instead, we chose a mechanism based purely on toehold exchange, which permits the walker to step an indefinite number of times between two competing foothold DNA sequences. Notably, the walker undergoes rapid sequence-guided movement over long distances while remaining stably bound to at least one foothold at all times. Furthermore, we chose a cartwheeling mode of locomotion so that the free toehold is always distally located and can pivot about its anchor point. This design enables the walker to rapidly search for an unoccupied complement to bind, yielding comparable reaction rates for each step. As depicted in Fig. 1a, the single-stranded DNA (ssDNA) walker W undergoes head-over-heels movement over a surface of two different foothold sequences, F1 and F2, by toehold-mediated strand displacement. The two foothold sequences comprise a common middle branch migration domain $DB^-$and toehold domains $DA^-$and DC^-, which are unique to each foothold sequence. The walker is complementary to all three domains, with nearly identical free energy of hybridization to $DA^-$and DC^-. Thus, in a field of both F1 and F2, the walker is expected to alternate between binding to each of the footholds, resulting in an indefinite number of steps over the field of footholds.

To mechanistically characterize and optimize the stepping behaviour of the transporter, we began with a simple DNA tile system bearing two adjacent footholds for the walker to step between. This two-foothold system consists of a four-helix DNA tile decorated with ssDNA overhangs F1 and F2 as well as a biotin label for surface immobilization in total internal reflection fluorescence (TIRF) measurements (see Supplementary Methods and Supplementary Figs. 1–3). The footholds are spaced by ~7 nm to match the 17–21 nucleotide length of the duplex formed by the binding of the walker to a foothold and equipped with (dT)3 linkers to provide conformational flexibility. The DNA walker Wa_b_c consists of a middle branch migration domain DB of length b (generally 13 nucleotides) flanked by two toehold domains DA and DC (Supplementary Fig. 1) with lengths a and c (a = c = 5–8 nucleotides). The sequence of the walker was chosen to allow for comparison with prior studies of toehold exchange kinetics. To permit measurement of stepping kinetics by smFRET, the 5'-end of F1 is labelled with the FRET donor Cy3, and the 3'-end of Wa_b_c is labelled with the FRET acceptor Cy5. Thus, any stepping of W between F1 and F2 through toehold exchange is expected to give rise to a time-dependent change in FRET efficiency between Cy3 and Cy5 (Fig. 16b). To reduce the likelihood of analysing multiple walkers bound to one DNA tile, we combined the walker with a 1.5-fold molar excess of DNA tile, and our smFRET analysis filtered out complexes with > 1 photobleaching step in the donor or acceptor channel.

First, we characterized by smFRET the behaviour of a walker bearing 8-nucleotide toehold domains (W8_13_8). Less than 30% of walkers exhibited static high- or low-FRET efficiency behaviour, which may result from only one of the footholds being present or accessible. However, the largest fraction of walkers (60–70%) exhibited a FRET efficiency varying between 0.3 and 0.7 (Fig. 16c,d). On close inspection, this mid-FRET state contained rapid anticorrelated fluctuations of Cy3 and Cy5 fluorescence intensity, indicating rapid changes in the distance between Cy3 and Cy5 (Fig. 16e). The cross-correlation function between Cy3 and Cy5 decays with a time constant of 12 ± 3 ms. These fluctuations were rapid in nature and the apparent FRET efficiency occupied a continuum of values rather than discrete states. Thus, we hypothesized that these fluctuations are predominantly due to reversible branch migration of domain DB, with only transient dissociation of either toehold from its respective foothold strand. That is, instead of occupying either state S1 or S2 (Fig. 16b), the walker exists primarily in a hybrid dynamic equilibrium state S1 + 2 in which it is partially base-paired to both F1 and F2. This result is consistent with expectations based on the local effective concentration of 250 μM measured in a similar tile-based system, whereby the equilibrium is expected to strongly favour hybridization of the 8-nucleotide toehold sequences. The toehold-dissociated states S1 and S2 are not typically observed

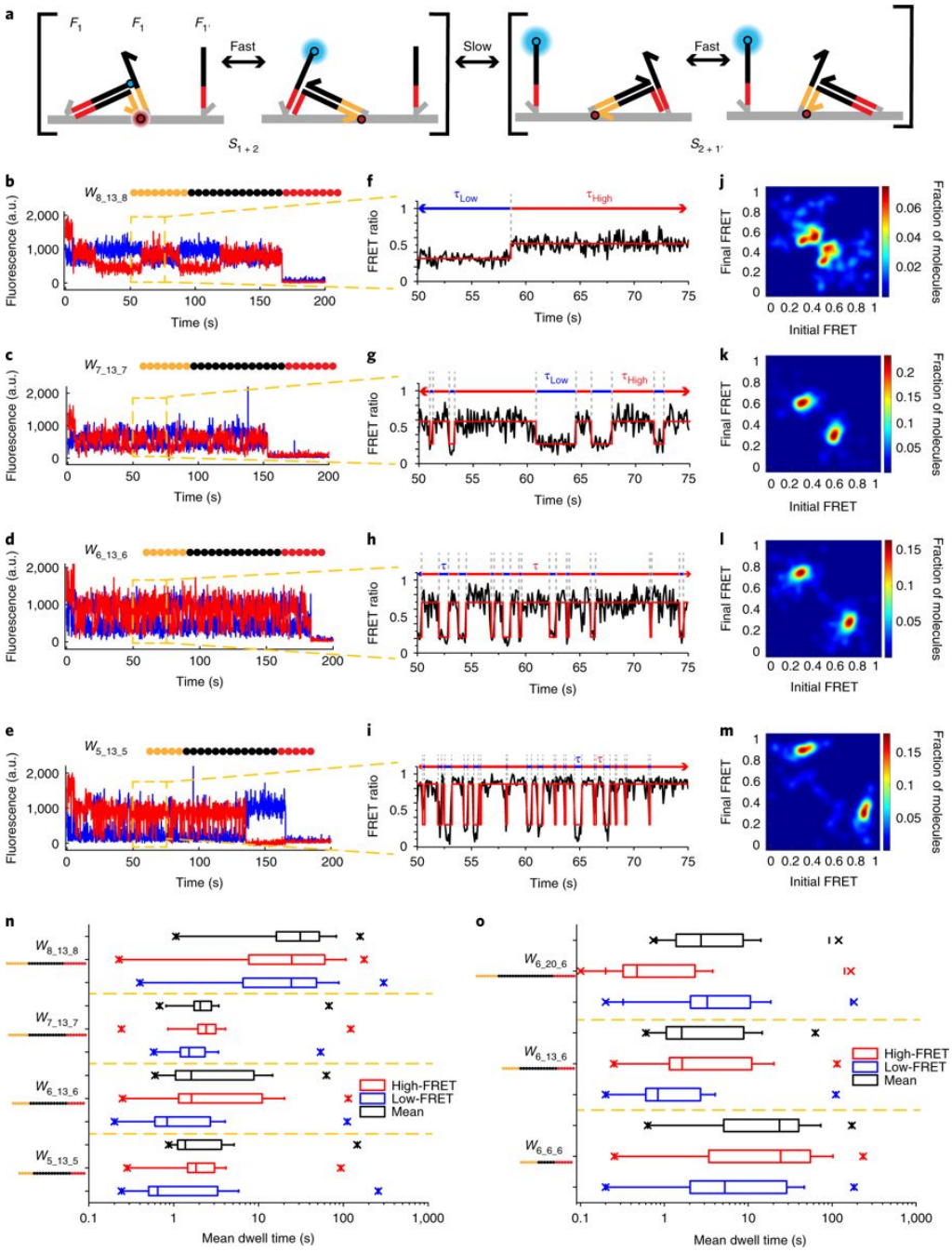


Figure 17: a, Kinetic model of stepping and associated FRET transitions for a Cy5-labelled (red) DNA walker on a Cy3-labelled (blue) three-foothold DNA tile. b–e, Representative smFRET trajectories of walkers with varying toehold lengths on a three-foothold DNA tile. Cy3 fluorescence is shown in blue, while Cy5 fluorescence is shown in red. The elevated Cy5 signal in the first ~10 s of each trace results from direct excitation at 640 nm to confirm the presence of an active acceptor on each walker–tile complex. f–i, Zoomed-in trajectories showing FRET transitions for 25-s segments of the molecules depicted in b–e. j–m, Transition occupancy density plots illustrating the most common FRET transitions for each walker. N = 87, 96, 107 and 109 for W5_13_5, W6_13_6, W7_13_7 and W8_13_8, respectively. n, Box-and-whisker plot of stepping kinetics in the high- and low-FRET states for walkers with varying toehold domain (DA and DC) lengths. o, Box-and-whisker plot for walkers with varying middle domain (DB) lengths. N = 105 and 132 for W6_6_6 and W6_20_6, respectively. The box includes the population of all molecules from the 25th percentile to 75th percentile; whiskers correspond to 0 and 100th percentiles, excluding outliers. Crosses denote the lower and upper bounds, inclusive of outliers.

because of their low occupancy and short lifetimes. Changing the toehold length to 7, 6 or 5 nucleotides

produced a similar kinetic behaviour, consistent with the presence of the same branch migration domain length b = 13 (Supplementary Fig. 4). Monte Carlo simulations of branch migration within a 13-nucleotide domain (Supplementary Note 1 and Supplementary Fig. 5) suggest that an anticorrelation time constant of ~12 ms will occur when the lifetime of an individual base pair step along the duplex is ~100 μs. This result is similar to previous estimates based on kinetic modelling from bulk fluorescence measurements and from three-stranded branch migration of genomic-length DNA sequences.

To further test our hypothesis of a hybrid S1 + 2 state, a third foothold strand F1′ with the same sequence as F1 was added to assemble a three-foothold DNA tile (Supplementary Figs. 1 and 6). The addition of this third foothold is expected to enable the walker to occupy a second hybrid state S2 + 1′ (Fig. 17a), resulting in a new low-FRET state in addition to the mid-FRET state observed for the two-foothold system. Indeed, most mid-FRET trajectories for W8_13_8 showed slow transitions to and from an additional FRET state of ~0.3 on the three-foothold tile (Fig. 17b), suggesting a new, slower process limited by toehold dissociation. Based on these results, we predicted that decreasing the length of the toehold would yield dramatically faster stepping behaviours of walkers, since the rate of dissociation of short DNA duplexes increases exponentially with decreasing length. Indeed, walkers with 7-, 6- or 5-nucleotide toeholds showed two-state FRET behaviours with much more rapid transitions between states (Fig. 17b–i). The median lifetimes (calculated from the per-molecule mean of both high- and low-FRET state lifetimes) decreased from 31.3 s (interquartile range (IQR) 52.1–16.5 s) for W8_13_8 to 1.4 s (IQR 3.7–1.1 s) for W5_13_5, yielding rate constants of stepping between 0.03 and 0.72 s−1 (Fig. 17n). Given the step size of 7 nm, the fastest walker exhibited an average (undirected) translocation speed of ~300 nm min−1. While the stepping rate increased by more than an order of magnitude when the toehold length was decreased to 7 nucleotides, further increases where marginal, and the apparent stepping rate of W5_13_5 was very similar to that of W6_13_6. In contrast, kinetic Monte Carlo simulations of stepping on a three-foothold tile predicted an exponential decrease in the stepping time as a function of toehold length, in direct proportion to the toehold dissociation rate constants (Supplementary Note 1, Supplementary Fig. 5). One possible explanation for this discrepancy is that as toehold nucleotides are removed from the walker, base pairs in the rigid walker–foothold duplex are replaced by unpaired nucleotides near the base of the foothold. This process may influence binding and/or dissociation kinetics of toehold DA by virtue of the much smaller persistence length of ssDNA30. For example, if the topology of the DNA tile positions F2 at slightly different distances from F1 and F1′, the replacement of duplex with single-stranded DNA may result in different binding rates of toehold DA to F1 and F1′. Our simulations suggest that such an asymmetry, combined with the finite time resolution of our measurements, could yield measured dwell times that deviate from the predicted exponential dependence in a manner consistent with our smFRET observations (Supplementary Note 1, Supplementary Fig. 5). This deviation occurs because a toehold DA may dissociate from, and re-associate with, F1 several times before binding to F1′. This effect gives the appearance of a single long-lived high-FRET state because the unbound state of the toehold is too short to resolve experimentally. Consistent with this hypothesis, smFRET measurements did reveal an increasing bias towards high-FRET states as the toehold length decreased (Fig. 17b–e,n), a bias that was intriguingly reversed when the DNA tile was replaced by a DNA origami substrate. In addition, as the length of the toeholds decreased, the difference in apparent FRET efficiency between the two main states increased (Fig. 17j–m). This observation is consistent with the expected decrease in the distance between the donor and acceptor dyes in the S1 + 2 state, as well as an increase in the donor–acceptor distance in the S2+1′ state, when a shorter toehold is present.

To investigate the role of branch migration in the stepping kinetics of walkers with shorter toeholds, we performed smFRET measurements on walkers with different lengths of domain DB, with accompanying changes in the foothold sequences to maintain complementarity with each walker. As with previous walker designs, smFRET transitions were observed for W6_6_6 and W6_20_6 (Supplementary Fig. 7). Kinetic Monte Carlo simulations predicted that stepping dwell times will increase linearly in proportion to the length of DB, since

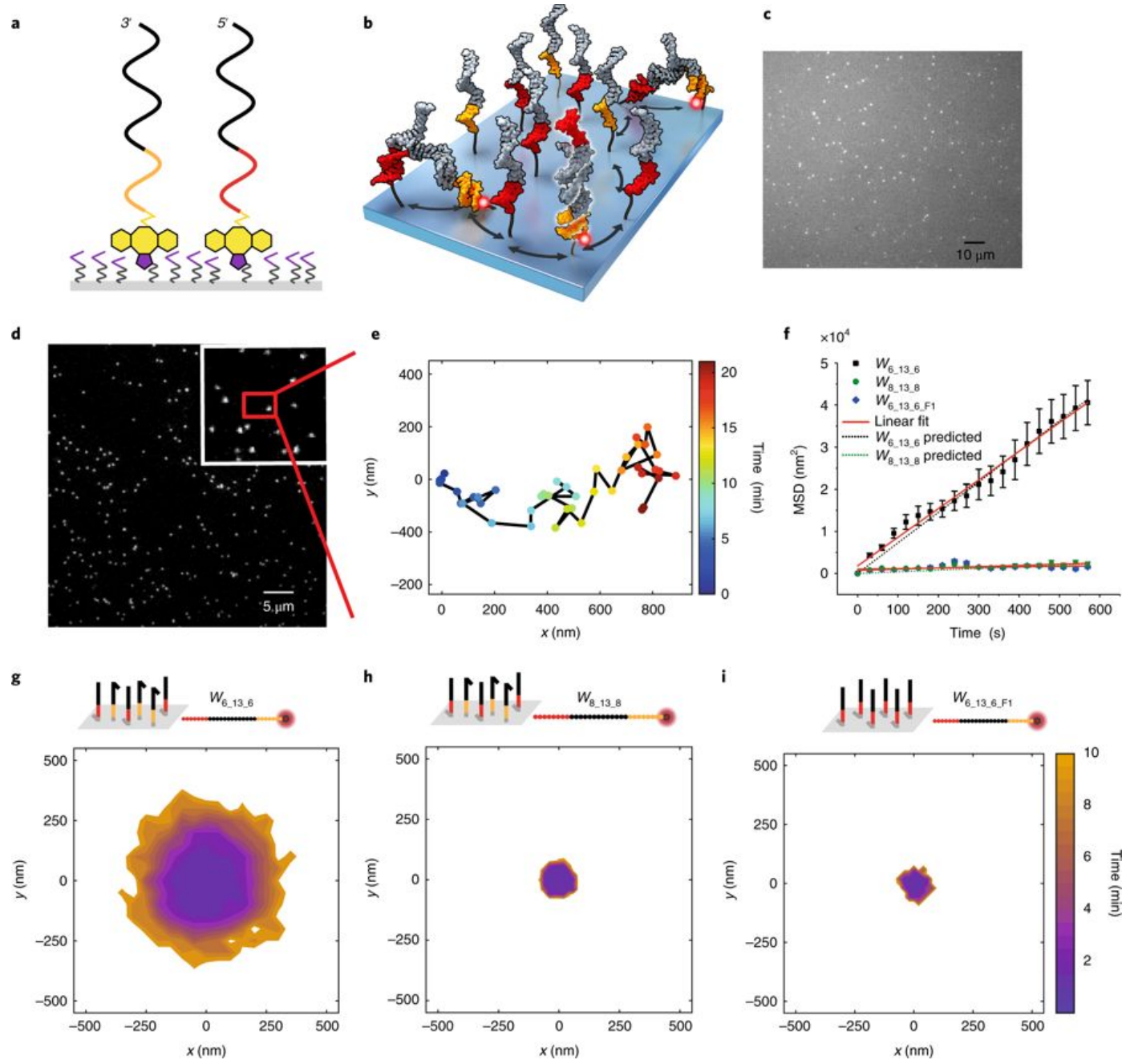


Figure 18: a, Schematic of F1 and F2 DNA conjugated to a glass coverslip surface at high density via copper-free click chemistry. Surface azides are shown in purple and dibenzocyclooctyne (DBCO) in yellow. b, Schematic of walker movement over a 2D array of footholds. c, TIRF image of complementary oligonucleotides bound to footholds on a coverslip surface at a ratio of 1 fluorescently labelled oligonucleotide:1 million unlabelled fluorescent oligonucleotides. d,e, TIRF image of Cy5-labelled W6_13_6 on a quartz slide coated with F1 and F2 (d) and a representative fast-moving trajectory of W6_13_6 (e). f, Mean square displacement (MSD) versus time plot for W6_13_6, W8_13_8 and W6_13_6_F1 (control with F1 only). Error bars represent one standard deviation. The diffusion coefficients derived from linear regression fits to the MSD versus time data are 17, 2.3 and 0.33 nm2 s–1, respectively. The MSD curves predicted from the stepping kinetics measured by smFRET on DNA tiles (broken lines in green and black) are also shown for comparison. g–i, Comparison of the extent of diffusion (region comprising 95% of trajectories, with all starting at the origin) of W6_13_6, W8_13_8 and W6_13_6_F1 (control with F1 only) over a 10-min period of observation.

walkers will spend more time in branch migration intermediates from which toehold dissociation is difficult as

impossible (Supplementary Note 1). Indeed, when the middle domain increased to 20 nucleotides (walker W6_20_6), the median stepping lifetime was 2.7 s (IQR 8.7–1.4 s), which is slightly longer than that of W6_13_6 (1.6 s, IQR 8.7–1.1 s). However, when DB was decreased to 6 nucleotides (walker W6_6_6), the median stepping lifetime increased to 23.6 s (IQR 39.4–5.2) (Fig. 17o). This result was contrary to the predictions of a simple branch migration model, suggesting that the structural details of the walker–tile complex (such as the match between walker length and foothold spacing) may play a role. The (dT)3 ssDNA spacers between the foothold strands and the tile are expected to provide sufficient flexibility to compensate for the difference of ± 2.3 nm from the addition or subtraction of 7 nucleotides from DB. However, altering the length of the branch migration domain may still introduce an incongruity between the reach of the walker and the spacing between foothold strands, since the distance between adjacent foothold strands is fixed at ~7 nm. In any case, the lack of a positive correlation between the length of DB and the stepping lifetime suggests that any impact of branch migration on the stepping rate for values of b between 6 and 20 nucleotides is overshadowed by other factors. Such factors include toehold binding and dissociation kinetics and the match between walker length and foothold spacing.

Based on smFRET measurements, the DNA walker with the fastest stepping rate and most homogeneous behaviour was W6_13_6. To test the performance of this optimized DNA walker as a long-distance 2D transporter, we developed a surface modification method that yields a high density of DNA footholds on a glass coverslip. In this method, alkyne-functionalized F1 and F2 are attached to an azide-modified coverslip through copper-free click chemistry. This process results in random, high-density conjugation of the two different foothold strands to the surface (Fig. 18a,b; see Methods). Using TIRF microscopy, we measured an average oligonucleotide surface density of 1.67 × 104 μm−2. This density is predicted to yield distances between nearest-neighbour F1 and F2 strands varying from ~2 to 13 nm, assuming a completely random distribution of footholds on the slide surface (Fig. 18c, Supplementary Fig. 8 and Methods). This estimate should be interpreted as an upper bound on the average spacing between footholds, since our measurements may underestimate the true density if a significant fraction of probe fluorophores are photobleached prior to the measurement. To confirm that larger inter-foothold distances are compatible with rapid stepping by the walker, we repeated our smFRET measurements of stepping in a three-foothold system constructed from a distinct DNA origami scaffold (Supplementary Fig. 9, Supplementary Table 1). In addition, a dT6 linker instead of a dT3 linker between the footholds and the origami was used for added flexibility. Despite the larger distance between adjacent foothold sites on this DNA origami (~10.5 nm on average, assuming 0.332 nm per nucleotide) compared with the previous tile system (~7 nm), smFRET characterization revealed a similar stepping rate constant of ~0.5 s−1 (IQR 0.6–0.1 s−1) for W6_13_6 on this new scaffold. This result suggests that the stepping rate is robust against small perturbations in foothold spacing.

Next, we characterized the long-range movement of the optimized walker W6_13_6 by 2D single-particle tracking using TIRF microscopy (Fig. 18d,e). Most of the molecules travelled > 200 nm from their starting position within 10 min (Fig. 18f), resulting in a measured 2D diffusion coefficient of 17 ± 0.5 nm2 s−1 (R2 = 0.99). Some molecules were observed to travel nearly 1 μm before photobleaching (Fig. 18d; see Supplementary Fig. 10 for other trajectories of this walker). In contrast, particle tracking of W8_13_8 indicated a much smaller diffusion coefficient of 0.7 ± 0.1 nm2 s−1 (R2 = 0.73) (Fig. 18f,h), or 2.2 ± 0.2 nm2 s−1 (R2 = 0.89) if a single extremely fast-moving outlier is included (Supplementary Fig. 11). This result was consistent with predictions based on its ~10-fold slower stepping rate as measured by smFRET. For comparison, a random walk model with predicted step sizes of 10.8 and 11.1 nm for W6_13_6 and W8_13_8, respectively (see Methods and Supplementary Fig. 8), and stepping rates taken from smFRET measurements on three-foothold DNA tiles predicted diffusion coefficients of 18.1 nm2 s−1 and 0.99 nm2 s−1 for W6_13_6 and W8_13_8, respectively. This close agreement with the predictions suggests that the optimized walker functions as designed, even on a different substrate and over substantially longer distances. Moreover, a surface with only a single foothold type (F1) resulted in insignificant diffusion of W6_13_6 (D ~0.33 ± 0.20 nm2 s–1 (R2 = 0.09), standard deviations in position

σx = 16.4 nm, σy = 15.2 nm), consistent with the designed walking mechanism involving both footholds (Fig. 18f,i; Supplementary Fig. 12).

We created a new class of ssDNA walker that exploits a toehold exchange mechanism to traverse arrays of specific oligonucleotide sequences in a cartwheeling fashion. The directionally unbiased movement of the walker has useful precedents in both nature and nanotechnology. For example, the kinesin MCAK utilizes undirected, one-dimensional diffusion to rapidly locate the ends of microtubules for depolymerization, resulting in faster searching over short distances than would be possible with direct binding from solution31. In the field of nanotechnology, synthetic biochemical cascades have exploited undirected, two-way transport to promote reagent channelling between coupled enzymes using a swinging arm over short distances (~10 nm). Moreover, a cargo-sorting robot was recently reported to use unbiased diffusion to transfer payloads over distances of tens of nanometres in a period of hours. It is likely that the cartwheeling mode of locomotion of the DNA acrobat plays an important role in generating the rapid stepping relative to similar systems studied previously, since some of these employed similar domain lengths and yet still exhibited stepping orders of magnitude slower than our system. One advantage of the cartwheeling geometry is that a rigid double-stranded segment always bridges between adjacent footholds, ensuring rapid toehold binding if there is a good match between the walker length and foothold spacing. Second, it has been suggested that the cargo-sorting robot may exhibit slow branch migration when strand displacement is initiated at the distal end of a foothold and proceeds towards the surface due to the entropic cost of stretching the ssDNA away from the surface. If this suggestion is true, the DNA acrobat overcomes this issue by virtue of the fact that branch migration always proceeds away from the point of attachment. Also of note is that most of our DNA acrobat designs remain bound to their footholds at all times by at least 18 nucleotides. This result indicates that they should be highly processive at room temperature, a prediction that is consistent with our single-particle tracking measurements, which suggest that the W6_13_6 walker may take hundreds of steps without dissociating.

The present study of a cartwheeling DNA walker also shows that the speed and range of similar DNA-based systems may be improved with careful optimization. The fastest of our toehold exchange walkers can search among ~43 foothold sites per minute with a stepping distance of ~10 nm. While still much slower than many natural motor proteins (for example, 0.38 μm2 s^{-1} for MCAK31), the stepping rate of this cartwheeling walker is more than an order of magnitude higher than that of other DNA-only walker systems. This improvement in performance was enabled by detailed single-molecule analyses of stepping kinetics as a function of key design parameters, an approach that is likely to be generalizable to many other systems in nanotechnology. While decreasing the toehold length from 8 to 5 nucleotides yields faster stepping rates as predicted, the marginal improvements in stepping rate appear to diminish below ~6 nucleotides, in contrast to the predictions of our kinetic modelling. These results, as well as those for the shortened walker W6_6_6, suggest that optimizing the mechanical properties of the system (for example, the reach of the walker and the entropic tension in single-stranded linker segments) may also be important, and could yield further improvements.

Finally, the present characterization of toehold exchange reactions at very high local effective reagent concentrations in a variety of contexts suggests that it may be challenging to obtain rate constants significantly faster than 1 s^{-1} for conventional strand displacement operations in DNA nanomachines. To surpass this apparent speed limit, dynamic DNA nanotechnology may need to incorporate further innovations inspired by natural systems, such as more precise control of local DNA mechanics and conformational changes, as well as judicious coupling to (rapid) exergonic processes.

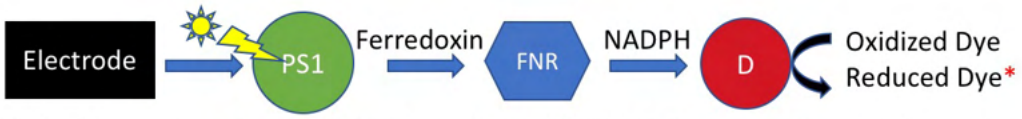
Integrating photosystem 1 into transparent, macro-porous electrodes and reducing organic compounds.
A major aspect of the MURI work in general, and the focus of the ongoing effort, involves interfacing the photosystem 1 reaction center (PS1) of cyanobacteria with macroporous antimony doped tin oxide (ATO) electrodes. The reducing power generated by PS1 is then used to initiate the transfer of electrons through an electron transfer chain, reducing nicotinamide adenine dinucleotide phosphate ($NADP^+$) to NADPH which is then used to reduce an organic molecule. This is based on our prior MURI work with reaction centers from purple nonsulfur bacteria which reduce quinones. Unfortunately the reduced quinones do not have the needed redox potential to power most dehydrogenase reactions of interest. In contrast, the NADPH produced from PS1 can be used to drive a large variety of dehydrogenases including those involved in carbon assimilation.

As will be described below, we have demonstrated that PS1 will indeed incorporate into the ATO electrodes and that upon illumination will use light to reduce $NADP^+$ to NADPH. This in turn can be used by a reductase. However, much of the light-generated electron transfer is currently not resulting in reductase activity. Most of it is wasted, either in the reduction of molecular oxygen in solution or through back reactions with the ATO electrode. The focus of our work now is to use DNA nanostructures to organize the system, much as biology does, in such a way that these unwanted reactions are avoided and a much larger fraction of the photoelectrons end up being used to power dehydrogenase activity.

1. The photoelectrochemical system

A bio-photoelectrochemical cell has been developed incorporating PSI into an electron transfer pathway involving ferredoxin (Fd), ferredoxin NADP reductase (FNR), NADP+ and the reductase diaphorase that converts the unfluorescent compound resazurin to resorufin, which is fluorescent:

In its original configuration, PS1 is connected to the ATO surface via cytochrome c, which acts and a conduit for electrons from the electrode, rereducing the primary electron donor in PS1. The remaining components are free in solution. Figure 1 shows the layout of the electrochemical circuit and also provides a snap shot of the



PS1 = Photosystem 1; FNR = Ferredoxin-NADP reductase; D = Diaphorase

data generated from it in its original form. ATO donates an electron to cytochrome c (Cyt-c) which in turn re-reduces the P_{700} of PSI after light absorption and subsequent electron transfer. The photoelectron transfer ultimately reduces Ferredoxin (Fd) which in turn acts as a co-factor for the Ferredoxin-NADP reductase (FNR) reaction, reducing $NADP^+$ to NADPH. NADPH is used by diaphorase to reduce resazurin to resorufin. Both photocurrent (Figure 1 upper right) and resorufin production (Figure 1 bottom panels) have been demonstrated.

2. Understanding the Limiting Steps

Based on past literature involving PS1 action in vitro, it seemed likely that PS1 was not only reducing Fd but also molecular oxygen. This is problematic both because it makes the system less efficient in terms of its ability to power dehydrogenase action, but also because the reactive oxygen species generated can destroy the PS1 and

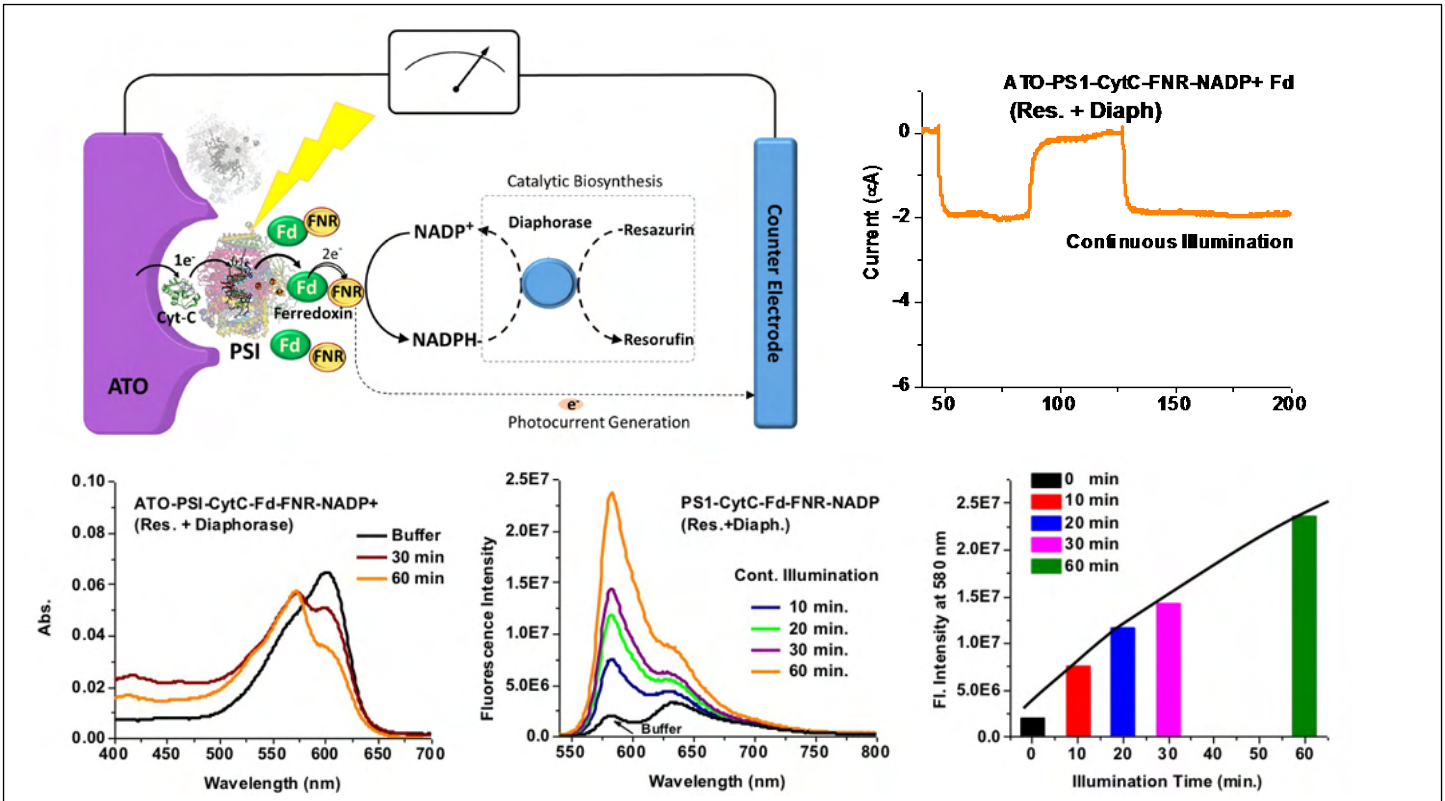


Figure 1: (Upper Left Panel) Light absorbed by photosystem 1 (PS1) results in an electron transfer reaction that oxidizes cytochrome c (Cyt-c) which in turn accepts an electron from a transparent, macroporous antimony tin oxide (ATO) electrode. Photosystem 1 (PS1) reduces Ferredoxin (Fd) which then acts as a cofactor for Ferredoxin-NADP reductase (FNR), which in turn reduces $NADP^+$ to NADPH. NADPH is a cofactor for an enzyme that reduces a substrate to a product (here, diaphorase reduces resazurin to the fluorescent dye resorufin). (Upper Right Panel) Light dependent photocurrent upon illumination. (Lower Left Panel) Change in the absorbance spectrum due to resorufin accumulation in the presence of light. (Lower Middle Panel) Increase in fluorescence due to resorufin accumulation. (Lower Right Panel) Bar chart of the increase in fluorescence from resorufin accumulation.

other components of the system over time. Figure 2, upper panels, show results from depleting the oxygen. With just cytochrome c and PS1 present on the ATO surface, and in the presence of O_2, one sees a strong photocurrent upon illumination. When O_2 is mostly removed (in our cell, complete removal is not feasible), a substantial decrease in photocurrent is observed. As one adds back the electron acceptors that compete for electrons from PS1 with O_2, the current decreases further. This strongly supports the concept that at least one of the major side reactions that we need to compete with is O_2 reduction. It is interesting that adding $NADP^+$ in addition to Fd and FNR reduces the current more than just Fd and FNR. Either reduced Fd can give rise to reduction of O_2 (or some other side reaction) or NADPH is being formed but passing electrons preferentially back to the ATO electrode. Consideration of the potentials involved suggests that NADPH passing electrons back to the electrode is the most likely reaction. This will be discussed in more detail below. The bottom panels of Figure 2 show the effect of removing most of the oxygen on the ability of the system to reduce resazurin. Recall from Figure 1 that it took more than an hour to reduce all the resazurin to resorufin in the presence of oxygen. With most of the competing oxygen removed, the process takes only about 5 minutes, again consistent with the notion that O_2 strongly competes for electrons from PS1 with Fd.

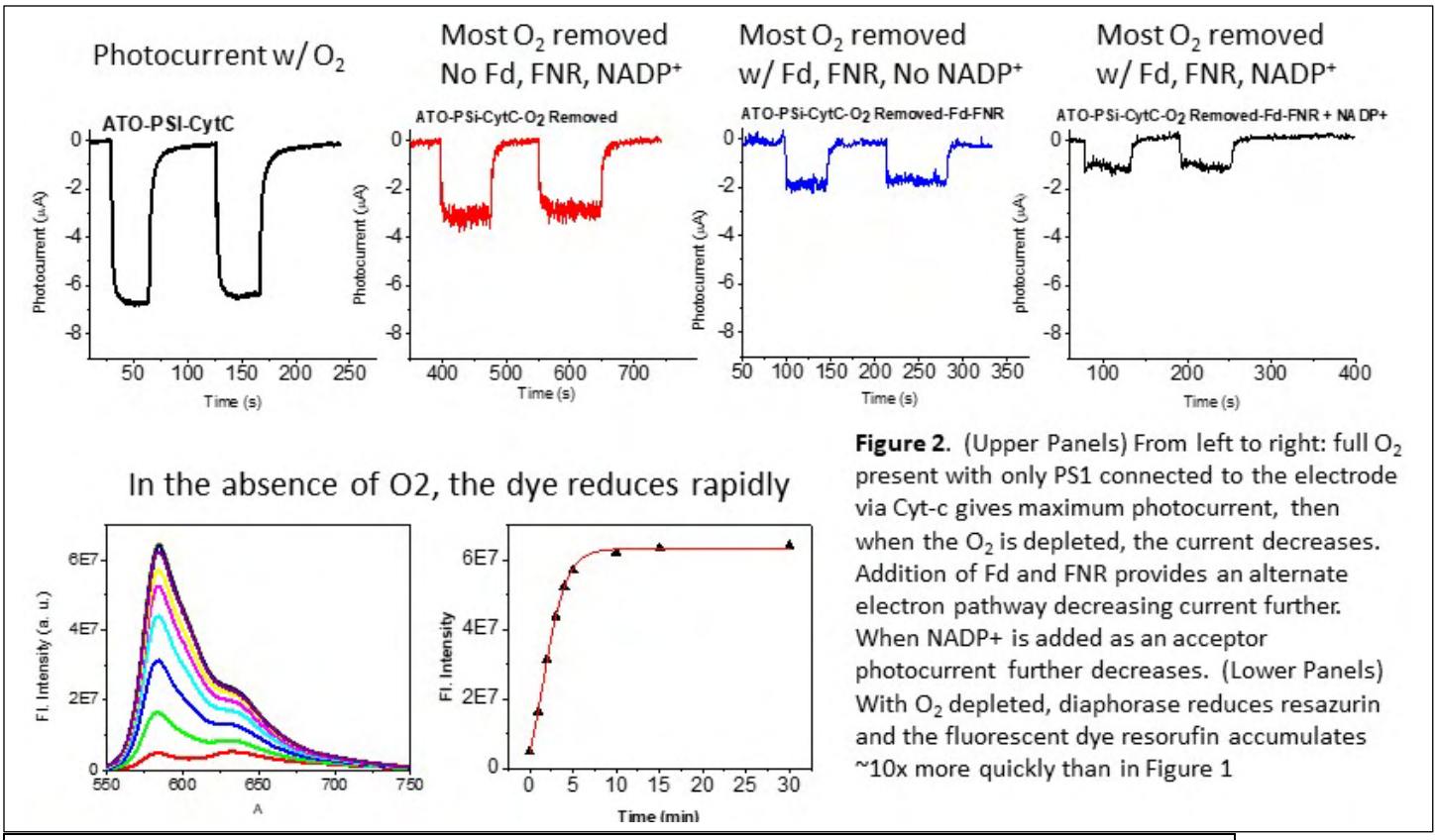


Figure 2. (Upper Panels) From left to right: full O_2 present with only PS1 connected to the electrode via Cyt-c gives maximum photocurrent, then when the O_2 is depleted, the current decreases. Addition of Fd and FNR provides an alternate electron pathway decreasing current further. When NADP+ is added as an acceptor photocurrent further decreases. (Lower Panels) With O_2 depleted, diaphorase reduces resazurin and the fluorescent dye resorufin accumulates ~10x more quickly than in Figure 1

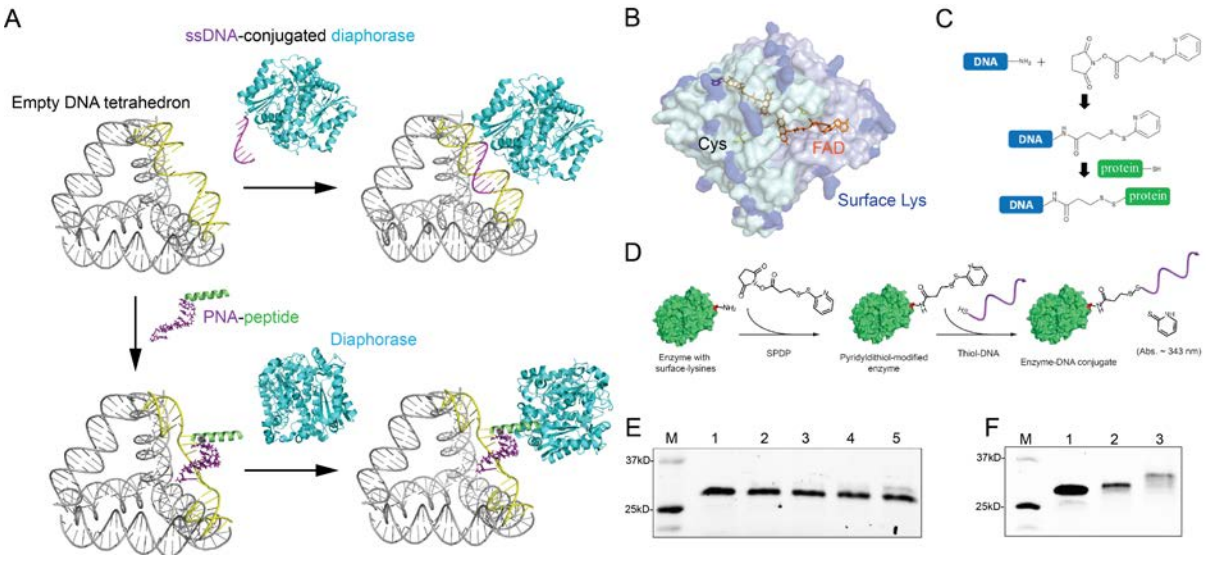


Figure 3. DNA tetrahedron-scaffolded diaphorase assembly and conjugation chemistry. A Schematics of DNA tetrahedron-assisted diaphorase assembly. **B** Crystal structure of NQO1human diaphorase including surface lysines (blue), cysteine (yellow) and FAD cofactor (orange). **C** Conjugation strategy using amine-DNA and cysteine on protein. **D** Conjugation strategy using thiolated DNA and lysine on protein. **E** SDS-PAGE gel showing conjugation yield in C. Lane 1: free diaphorase (DI); lane 2: DI + 0.5×SPDP-DNA; lane 3: DI + 1×SPDP-DNA; lane 4: DI + 2×SPDP-DNA; lane 5: DI + 4×SPDP-DNA. **F** SDS-PAGE gel showing conjugation yield in D. Lane 1: free DI; lane 2: DI-SPDP; lane 3: DI-SPDP-DNA

3. *Using DNA Nanostructures to Promote Efficient Use of Redox Potential.*

Accounting for all the photoelectrons in the system, and considering the low oxygen system performance, it is very likely that in addition to competition with O_2 reduction one or more freely diffusible components of the system are simply passing electrons back to the electrode. We first decided to explore this possibility by trying to localize diaphorase on a DNA nanostructure that we had previously shown enters and localizes in the ATO electrode pores. In this way, we should be able to put the diaphorase at high concentration where the NADPH is being formed, generating resorufin from resazurin rapidly before back transfer to the electrode can occur. For this subproject, and for all of the subprojects going forward that involve attaching protein components to DNA nanostructures, we approached attachment of the protein component to the nanostructure in two ways simultaneously. One is a method we have used a number of times before that involves a covalent attachment of the protein to a single stranded piece of DNA and then hybridization of this conjugated system into the DNA nanostructure. The second approach involves using PNA-peptide conjugates (PNA = peptide nucleic acid) that have been selected from libraries such that the peptide portion binds to the target protein. The PNA again is complementary to a single stranded region of the DNA nanostructure.

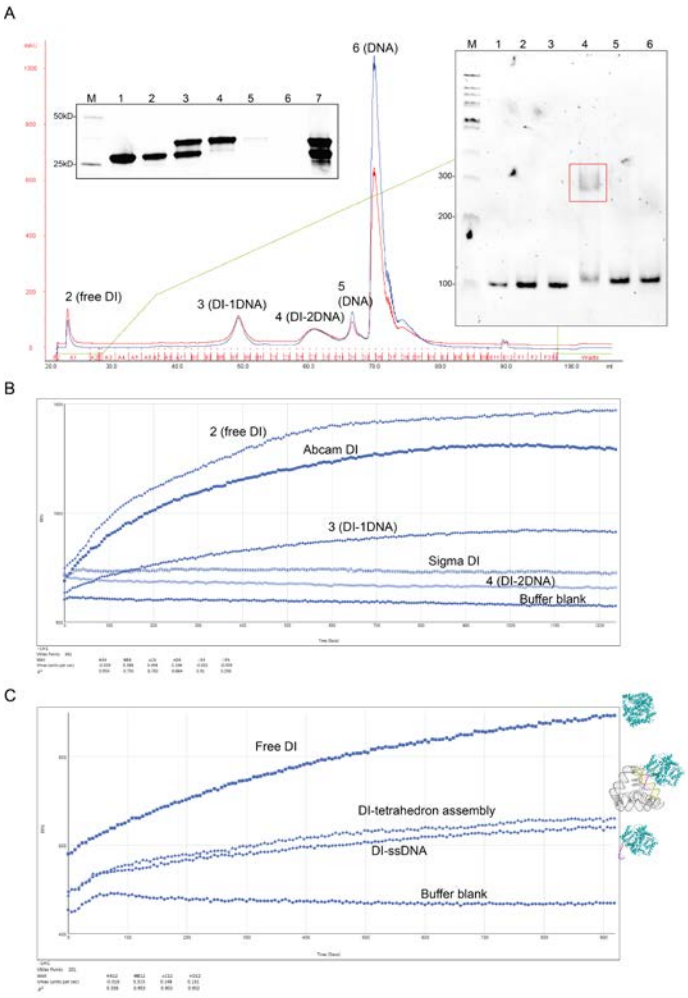


Figure 4. ssDNA-diaphorase purification, assembly and activity. A FPLC purification of ssDNA-diaphorase and assembly with DNA tetrahedron on native PAGE gel. Left gel: SDS-PAGE, lane 1: free DI; lane 2: A1; lane 3: B6-10; lane 4: C5-11; lane 5: C12-D2; lane 6: D4-7; lane 7: crude sample before FPLC. Right gel: native PAGE stained by ethidium bromide, lane 1: empty tetrahedron; lane 2: tetrahedron + fraction 2 incubated at room temperature; lane 3: tetrahedron + fraction 2 annealed with a program from 37°C; lane 4: tetrahedron + fraction 3 annealed with a program from 37°C; lane 5: tetrahedron + fraction 4 incubated at room temperature; lane 6: tetrahedron + fraction 4 annealed with a program from 37°C. **B** Enzyme activity of ssDNA conjugated diaphorase fractions; **C** Enzyme activity of DNA tetrahedron assembled diaphorase.

Figure 3A shows a schematic of the two approaches as they were applied to the first subproject, concentrating diaphorase on a DNA nanostructure in the ATO pores. In this case, the nanostructure is a tetrahedron and it has been shown previously to concentrate in the ATO pores. Figure 3B-F show the details of the first approach: covalent conjugation of single-stranded DNA to the diaphorase and subsequent verification of the construct on gels. We were able to make the tetrahedron, conjugate the ssDNA to the diaphorase, purify the conjugate, hybridize the complex to the tetrahedron and see the expected gel shifts. Figure 4 shows the results of purifying the entire tetrahedron-diaphorase complex as well as enzyme assays using the complex (not associated with the ATO electrode). We were able to generate the pure diaphorase tetrahedron complex and enzyme assays show that the complex retains about half of the native activity of the diaphorase. The activity loss in this case is

associated with conjugation of the ssDNA to the diaphorase and subsequent purification.

The diaphorase-tetrahedron complex was then used in place of free diaphorase in the electrochemical cell. The initial results of this work are shown in Figure 5. The experiment was done in such a way that the measured activity of the diaphorase (regardless of free or conjugated) was held constant. What one can see is that the initial rise is ~60% faster when the enzyme is attached to the DNA nanostructure. This is a tricky experiment to control perfectly (we need to be certain that we are really comparing the same enzyme activities and that the only effect is the concentration near the surface). We are currently working on repeating this multiple times with an internal control for the activity prior to illumination, but the effect appears to be quite significant, suggesting that the hypothesis was correct: concentrating diaphorase at the electrode surface increases the efficiency of light dependent rezasurin reduction.

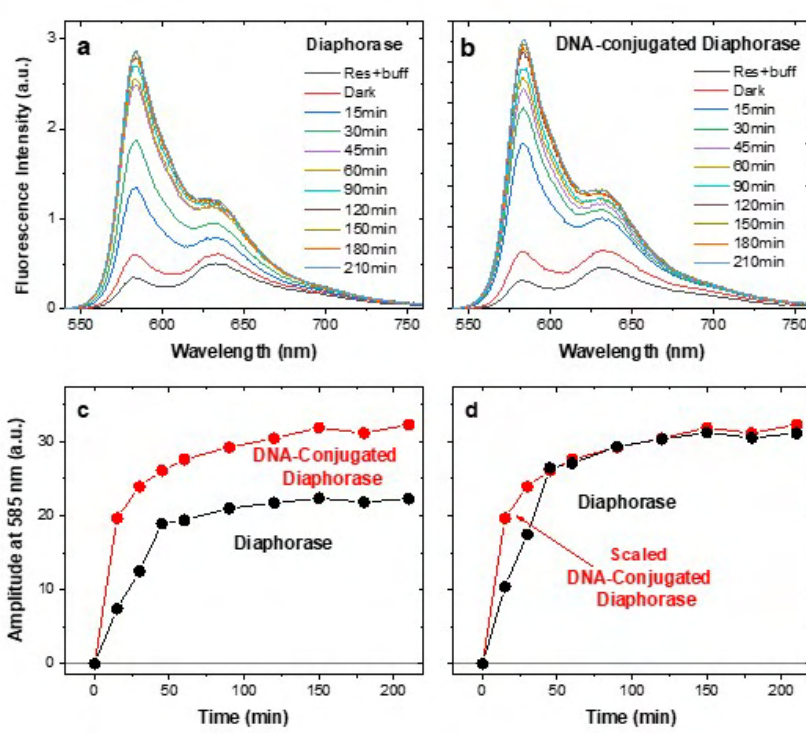


Figure 5. Photochemical experiments using the ATO PS1 system to reduce resazurin to resorufin (fluorescent) with diaphorase. Top panels show the time resolved spectra for reduction of rezasurin to resorufin using diaphorase alone (left) and diaphorase incorporated into a DNA tetrahedron and then associated with the ATO porous electrode. The nanostructured system increases more rapidly. The bottom panels plot the kinetics of reduction. Black is the diaphorase alone and red is the diaphorase associated with the DNA tetrahedron. The left picture is the raw data with the zero point subtracted. The right picture shows the two traces normalized to approach the same value.

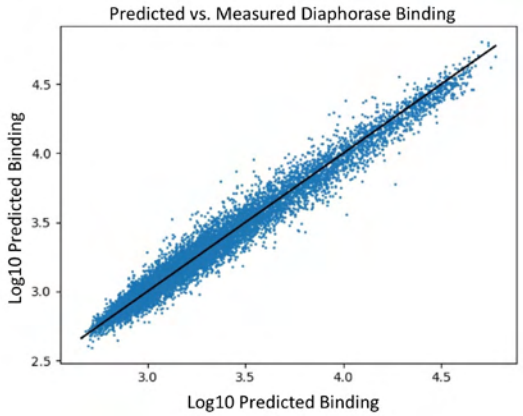


Figure 6. A machine learning algorithm was used to determine a relationship between ~113,000 unique peptide sequences and the binding signal from diaphorase. The relationship was used to predict the binding strength of ~13,000 unique test sequences. Predicted vs. measured fluorescence (binding) values are shown. The correlation coefficient was 0.98.

As noted above, we also used a second approach to assemble the diaphorase-tetrahedron complexes. The other approach involves binding diaphorase to a large peptide array and then using machine learning algorithms to design the best peptide binding sequence for diaphorase. This peptide is then synthesized with a PNA tail that is complementary to the single stranded region of the DNA tetrahedron nanostructure. The resulting PNA-peptide is incorporated into the DNA nanostructure and mixed with the native enzyme, presumably providing a much gentler approach to incorporating the enzyme into the nanostructure (avoiding the activity loss seen in Figure 4) and also allowing for self-repair; the noncovalent bond allows occasional replacement of protein components occasionally.

This peptide-based approach started with binding diaphorase to a peptide array of ~125,000 unique peptide sequences. The binding results were then used as input for a machine learning algorithm relating sequence to binding. The algorithm was quite accurate at predicting binding for sequences not used to train the algorithm (Figure 6). Based on this, two types of peptides were selected, 1) peptide sequences from the array itself that showed strong binding to diaphorase and lower binding to other proteins and 2) sequences not on the array that were predicted by the algorithm to show strong binding to diaphorase and weak binding to background proteins (all 69 billion possible sequences were evaluated). 24 sequences were selected, synthesized and scanned by surface plasmon resonance (Figure 7). Six appeared to give substantial binding. Four of these came from the original sequences on the array and two were from the predicted sequences. Two of these peptides were synthesized with a PNA tail for attachment to the tetrahedron.

Figure 8 shows the results of current experiments to perform the self-assembly. The gel shows that the PNA-peptide conjugates assembled as expected onto the DNA tetrahedron. Because the binding is not covalent, it was not possible to detect the diaphorase assembly onto the structure with gel shift assays. However, upon assaying the enzyme activity of diaphorase incubated with the PNA-peptide conjugates, both of the peptide sequences used actually <u>increase</u> the enzyme activity,

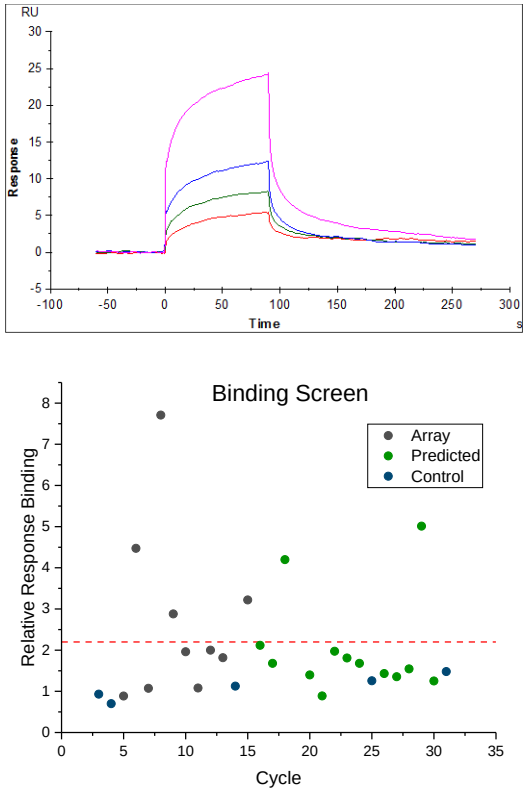


Figure 7. Top panel, a surface plasmon resonance scan of the peptide PWELYFWRD. This appears to bind with a 1-2 micromolar binding constant. Bottom panel: SPR binding screen of 24 peptides. Six peptides were selected for further analysis.

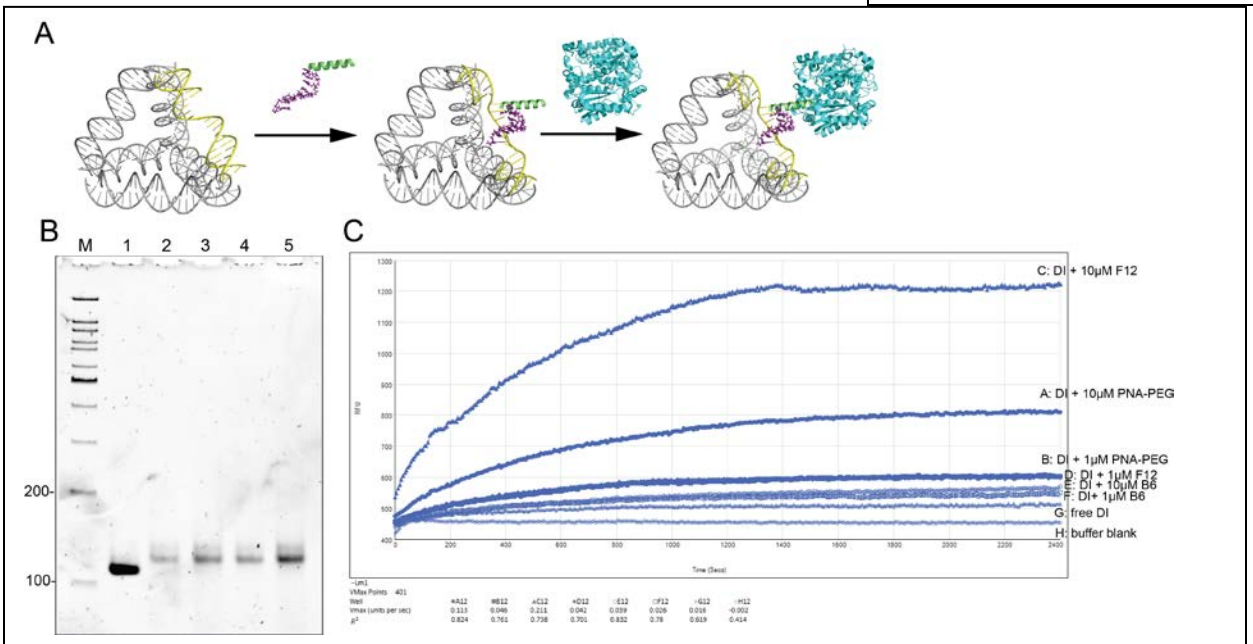


Figure 8. Recruitment of diaphorase using PNA-directed peptides on a DNA**.** **<u>A</u>** A Scheme showing recruitment of diaphorase by a DNA tetrahedron assembled PNA-peptide. **<u>B</u>** Native PAGE gel stained by ethidium bromide. Lane 1: empty DNA tetrahedron; lane 2: tetrahedron + B6; lane 3: tetrahedron + B6 + DI; lane 4: tetrahedron + F12; lane 5: tetrahedron + F12 + DI. **<u>C</u>** Enzyme activity of diaphorase incubated with 1 or 10 µM PNA-PEG, B6 and F12.

demonstrating that they do not have detrimental effects on activity and that they do in fact bind in the micromolar range. We have not yet used these constructs in the electrochemical cell, but will shortly.

III. Future Work

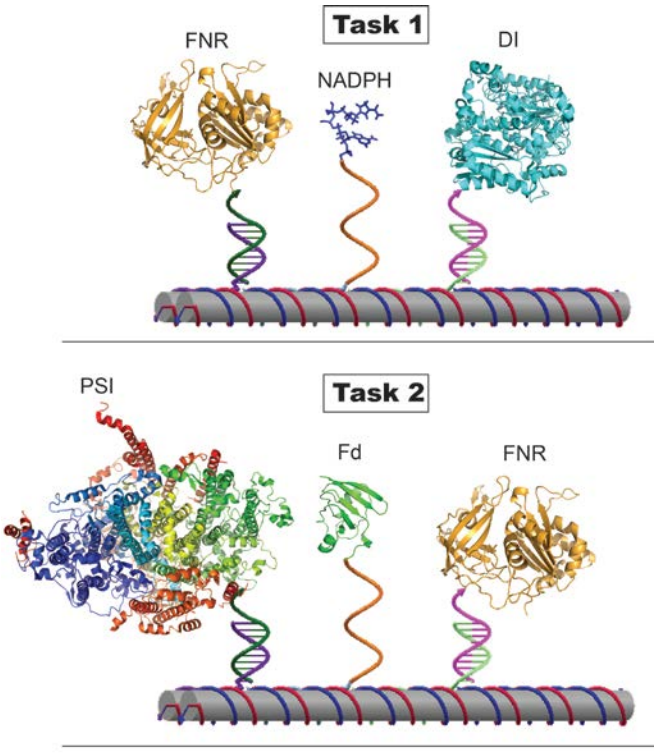


Figure 9. Task1: create a nanostructure connecting FNR and diaphorase (DI) using a flexible linker with NADPH attached to transfer electrons from PS1 to FNR. Task 2: create a nanostructure connecting PS1 and FNR, utilizing FD on a flexible linker with FD to transfer electrons from PS1 to FNR.

We recently were awarded an extension of the MURI funding to explore further the effects of using DNA nanostructured organization in order to increase the efficiency of the electrode-PS1-enzymatic reduction system. A summary of the four tasks associated with this work are:

Task 1. ***Eliminate diffusible NADPH***: Design a DNA nanostructure that directly couples FNR and diaphorase using a flexible arm with NADPH, as we have done previously for coupling dehydrogenase enzymes. This will keep NADPH from diffusing to the working electrode and unproductively becoming re-oxidized.

Task 2. ***Decrease oxygen reduction and eliminate diffusible Ferredoxin***: Though we can deplete oxygen from the system, this is difficult to implement in most practical applications. It would be better to couple specific transfer between PS1 and Ferredoxin-NADP reductase (FNR) via Fd more efficiently. We will build a nanostructure that links these three complexes with Ferredoxin on a flexible arm, as was done for NADPH in Task 1. This both makes transfer more efficient and eliminates the need for diffusible Ferredoxin.

Task 3. ***Replace diaphorase with another NADP-dependent dehydrogenase or reductase***: We will test two commercial enzymes that form alcohols from aldehydes/ketones.

Task 4. ***Integrate Task 1 - 3 to create a complete electron transfer chain:*** This will result in an electron transfer chain with no freely diffusing elements and an optimized interface with the electrode substrate.

To date, we have focused on Tasks 1 and 2 (Figure 9). We are still assembling the parts, but thus far we have:

- Designed the DNA nanostructures
- Sourced the enzymes that will be needed for larger scale preparations of DNA-conjugated enzymes
- Performed the binding of Fd and FNR to peptide arrays to select for binding peptides

MURI Supplements
Translating Biochemical Pathways to Non-Cellular Environments
Developing an photoelectrochemical system based on photosystem I

Hao Yan, PI (Hao.Yan@asu.edu)
Arizona State University
Work Performed 8/01/17-7/31/19

There were two supplements to the MURI proposal focused on developing a photosystem I (PSI) based photoelectrochemical system in which light absorbed by PSI results in NADPH production and is subsequently used by a dehydrogenase to reduce a compound.

There were two tasks in the first supplement:

Task 1. ***Link the light-driven production*** of reductants by the reaction center/electrode systems with the action of a dehydrogenase enzyme (diaphorase) on DNA nanostructures

Task 2. ***Further enhance the system*** through the use of dynamic self-assembly of unmodified enzymes on the DNA nanostructures instead of assembly based on enzymes covalently modified with DNA strands

There were four tasks in the second supplement:

Task 1. ***Eliminate diffusible NADPH***: Design a DNA nanostructure that directly couples FNR and diaphorase using a flexible arm with NADPH, as we have done previously for coupling dehydrogenase enzymes. This will keep NADPH from diffusing to the working electrode and unproductively becoming re-oxidized.

Task 2. ***Decrease oxygen reduction and eliminate diffusible Ferredoxin***: Though we can simply remove oxygen from the system, this is difficult to implement in most practical applications. It would be better to couple specific transfer between PS1 and Ferredoxin-NADP reductase (FNR) via Fd more efficiently. We will build a nanostructure that links these three complexes with Ferredoxin on a flexible arm, as was done for NADPH in Task 1. This both makes transfer more efficient and eliminates the need for diffusible Ferredoxin.

Task 3. ***Replace diaphorase with another NADP-dependent dehydrogenase or reductase***: We will test two commercial enzymes that form alcohols from aldehydes/ketones.

Task 4. ***Integrate Task 1 - 3 to create a complete electron transfer chain:*** This will result in an electron transfer chain with no freely diffusing elements and an optimized interface with the electrode substrate.

Combined Report on Supplement 1 and 2

Creating Self-assembly Components. Tasks 1 and 2 of Supplement 1 and Tasks 1 and 2 of Supplement 2 all hinged on first creating components that would allow self-assembly of enzymes onto DNA scaffolds. We chose to use peptides for this purpose. In the process of developing methods for creating and optimizing these peptides, an entirely new method for peptide sequence development was created, with the remarkable discovery that measurement of target binding to very sparse sampling all possible peptide sequences allowed us to predict binding to ALL possible peptide sequences with statistical accuracy. This was published {Taguchi, 2020 #726}. The publication involves a set of 9 different protein targets (Table 1), which included the enzymes of interest here (Diaphorase, ferredoxin NADPH reductase or FNR, and ferredoxin). Each target protein was incubated separately with a peptide array of ~125,000 nearly random peptide sequences and binding of the protein to each sequence was recorded. This was fed into a neural network (Figure 1). The result was a quantitative relationship between the level of binding and the amino acid sequence of a peptide. To test the generality of the relationship, only 90% of the sequences (~113,000) were used to train the network and the remainder were predicted by it. The predictions were remarkably

good as can be seen in Figure 2 and Table 2. Indeed, the correlation coefficients between the predicted and measured values of binding were mostly about 0.95 and in most cases there was little difference between the predicted vs. measured correlation and the correlation between two measurements (i.e., the prediction was good to within the noise in the measurement in many cases). Furthermore, the prediction were specific. As shown in Figure 3, it was not only possible to predict binding but also differential binding with high statistical accuracy.

Table 1. Protein Targets

Protein*	MW (kDa)	Protein Format
Diaphorase	30.1	Full Length
Ferredoxin	11.1	Full Length
FNR	35.3	Full Length**
PD1	42.7	ECD-Fc***
PDL1	52	ECD-Fc***
TNFα	17.5	Full Length
TNFR	20	ECD****
Transferrin	80	Full Length
Fc	26	Digested IgG

*FNR = Ferredoxin-NADP reductase, PD1 = Programmed Cell Death protein 1, PDL1 = Programmed Cell Death protein 1 Ligand, TNFα = Tumor Necrosis Factor alpha, TNFR = Recombinant Human TNF RII, Fc = Fragment Cystallizable region of an IgG antibody
**Provided by Prof. Kevin Redding, Arizona State University
***Fc-fused extracellular domain
****Extracellular domain

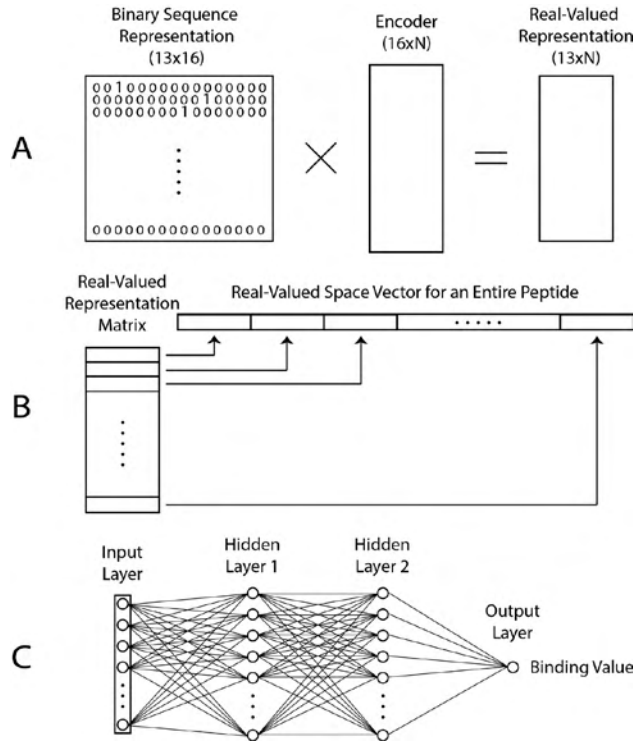


Figure 1. Neural network architecture for predicting binding value from peptide sequence. (A) The sparse binary representation of the peptide undergoes a linear transformation into the dense real-valued space representation by matrix multiplication with the encoder matrix that utilizes N descriptors in the vector representation of each amino acid. (B) The matrix representation is concatenated row-by-row, resulting in a real-valued space vector representation of the peptide. (C) The real-valued space representation of the peptide is passed through a feedforward neural network with two hidden layers to perform a non-linear prediction of the binding value from the sequence.

Table 2. Pearson Correlation Coefficients of Target Fits

Protein	Correlation Coefficient	# Technical Reps. (Corr)*
Diaphorase	0.985 ± 0.001	3 (0.99)
Ferredoxin	0.983 ± 0.001	3 (0.99)
FNR	0.994 ± 0.001	3 (0.99)
PD1	0.959 ± 0.002	2 (0.94)
PDL1	0.965 ± 0.003	2 (0.98)
TNFα	0.960 ± 0.002	3 (0.95)
TNFR	0.973 ± 0.001	3 (0.98)
Transferrin	0.979 ± 0.001	2 (0.98)
Fc	0.924 ± 0.007	2 (0.97)

*The correlation shown is the average correlation between technical replicates +/- the error in the mean

The goal with regard to applying this approach to design peptide binding components was to be able to predict peptides that bind both tightly and specifically. Often neural networks are quite good at interpolating function; in this case finding sequences with similar values as the training set, but we wanted peptides that had enhanced function, and thus needed the neural network to extrapolate to sequences that would bind more tightly than the training set. The ability of the neural network

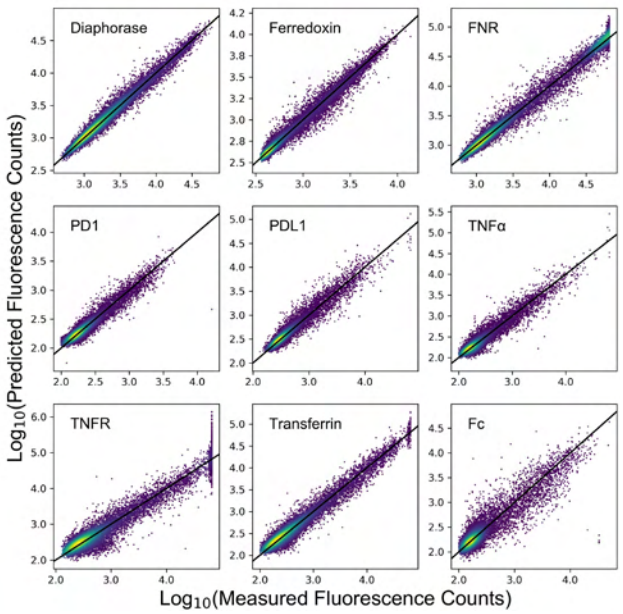


Figure 2. Predicted vs. measured binding values on a logarithmic scale for the nine proteins studied in this work. Each point of the scatter plot is colored by the density of points occupying the same region. In each case 90% of the unique peptide sequence/binding value pairs on the array were used to train the network and the remainder were used as validation. Only the validation set is shown in the plots above; these are predictions of sequences that were never seen during the training and are effectively random samples from the 10^{12} sequences that make up the entire combinatorial space.

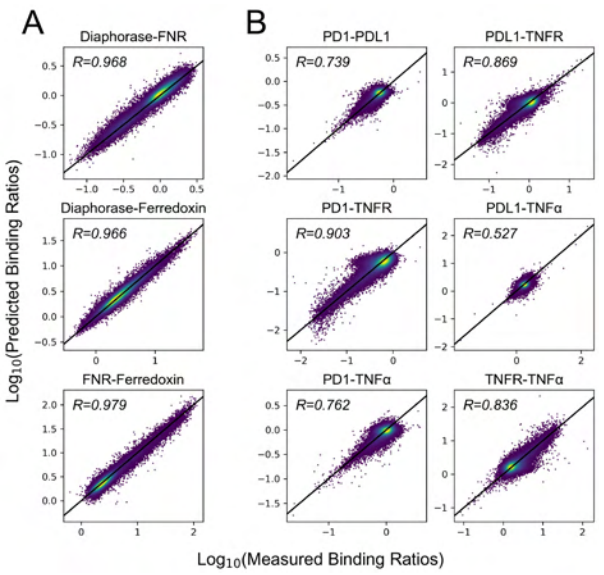


Figure 3. Predicted vs. measured binding specificities. Binding specificity is defined as $\log_{10}$ of the ratio of binding values between the two targets listed in the subplot title. Measured values are along the X-axis, and predicted values along the Y-axis. Binding specificity calculations require that the two targets are measured under identical conditions, which is true for diaphorase, FNR, and ferredoxin (**A**), and for PD1, PDL1, TNFα, and TNFR (**B**). For each target, a neural network was trained on 90,000 peptide sequence/binding values, and the predicted and measured values for the remaining ~36,000 validation set were used for plotting. Each point of the scatter plot is colored by the density of points occupying the same region.

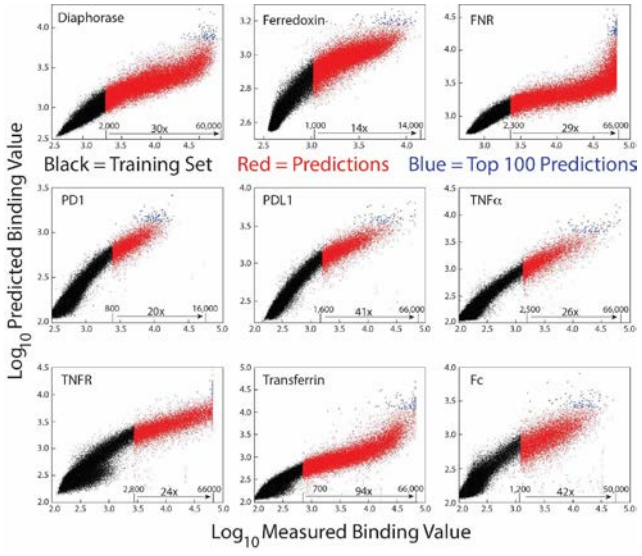


Figure 4. Binding data for each protein target was trained only on sequence/binding value pairs less than a factor of five times the lowest binding values (black) and used to predict binding of sequences with measured values up to 60,000 counts (red). The top 100 predicted sequences are shown in blue and average 40,000 counts.

used to do this is shown in Figure 4. Here, the weak binding peptides (black dots) were used to predict the binding of stronger binding peptides (red and blue dots). This worked well (note the binding scales are log scales, so it was possible to predict binding more than an order of magnitude stronger).

We then used this to design strong and specific binding peptides to diaphorase, FNR and ferredoxin. We initially built a DNA nanostructure designed to hold FNR and diaphorase close to one another in order to see if that would allow a more efficient use of NADPH. We have demonstrated previously that if you tie two enzymes onto the same DNA strand, one that reduces NAD+ and one that oxidizes NADH, there is a substantial increase in the rate of the coupled system. Surprisingly, when we introduced the coupled system into the electrochemical cell, no increase in efficiency was observed. We also tried using

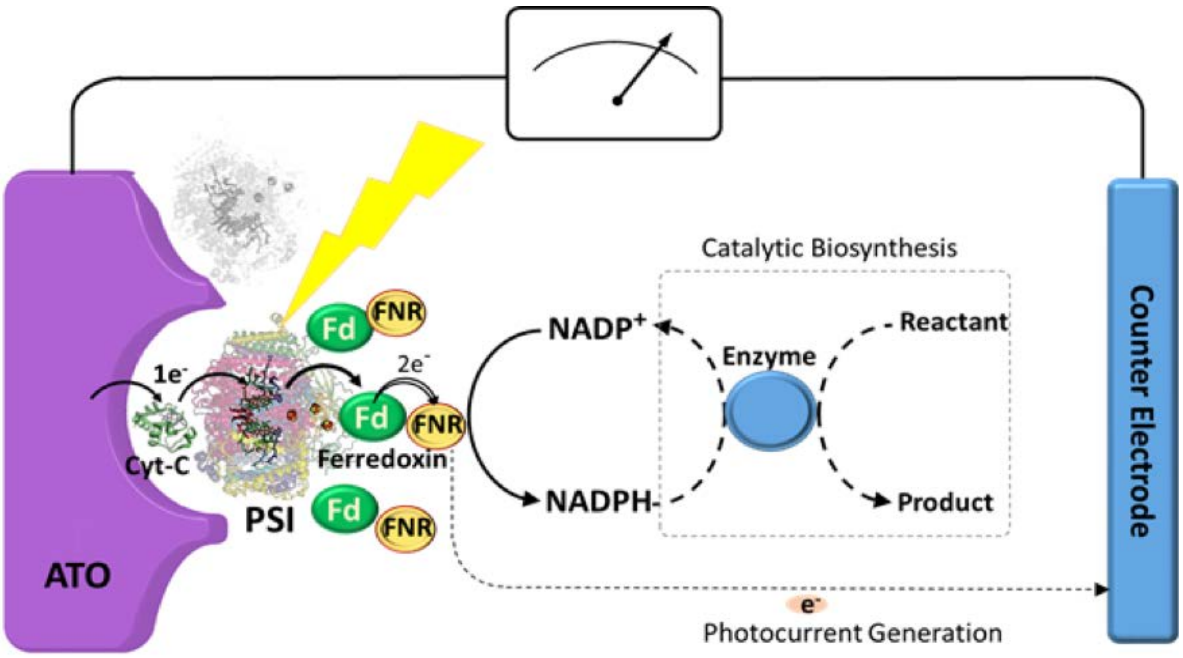


Figure 5. Schematic illustration of the PSI-based bio-photoelectrochemical cell on a porous ATO electrode for photocurrent generation and catalysis. PSI is integrated on the ATO surface via a cytochrome c bridge to facilitate electron transfer. When the cell is exposed to light, a series of electron transfer steps take place to reduce $NADP^+$ to NADPH. A dehydrogenase, such as diaphorase, can then use the NADPH produced for reduction of other compounds (in this case a reporter dye). The system is run in a potentiostat, allowing measurement of the resulting photocurrent.

DNA constructs to simply localize the diaphorase near the surface and use up the locally produced NADPH, but again that surprisingly did not have a big effect. These results caused us to look more closely at how the electron transfer from PSI to NADPH to the dye being reduced by diaphorase was taking place which led to the study described below.

The path of electron transfer in the complete photoelectrochemical system. Task 3 and 4 of Supplement 2 focused on building complete systems for light driven reduction, either using diaphorase or another dehydrogenase. This work led to the submission of a manuscript which is now under review. The total system is shown in Figure 5. When the enzyme is diaphorase and the reactant is resazurin, one sees the light dependent reduction to resorufin take place as shown in Figure 6. However, when we removed diaphorase from the system, there was only a small decrease in the rate of reduction. Indeed, even without FNR present, the system much of the activity remained. NADP+ was required as was ferredoxin, but the two enzymes had only modest effects. This explained what localizing the diaphorase either close to FNR or near the surface did not increase the efficiency of NADPH utilization for dye reduction. This prompted a whole series of experiments which showed that the canonical pathway for reduction of NADP+ was only one possible pathway. In addition, NADP+ can be reduced directly in some light dependent reaction that requires ferredoxin. It is not clear if that is direct transfer from ferredoxin or not. Recall that ferredoxin is a one electron carrier while NADP+ requires two electrons for reduction. In addition NADPH can directly reduce resazurin to resorufin, but only in the presence of light. Apparently the excited state of resazurin interacts directly with NADPH and undergoes a two electron reduction.

We did try introducing another dehydrogenase into the system, lactate dehydrogenase, in order to test this enzyme and detect the product (lactate), we needed to produce NADPH in the photoelectrochemical cell and transfer it to a separate cell to drive the reduction. However, we were unable to build up sufficient concentrations of NADPH in the bulk solution to produce enough lactate to measure. It is clear that the NADPH is produced and used right at the surface of the electrochemical system.

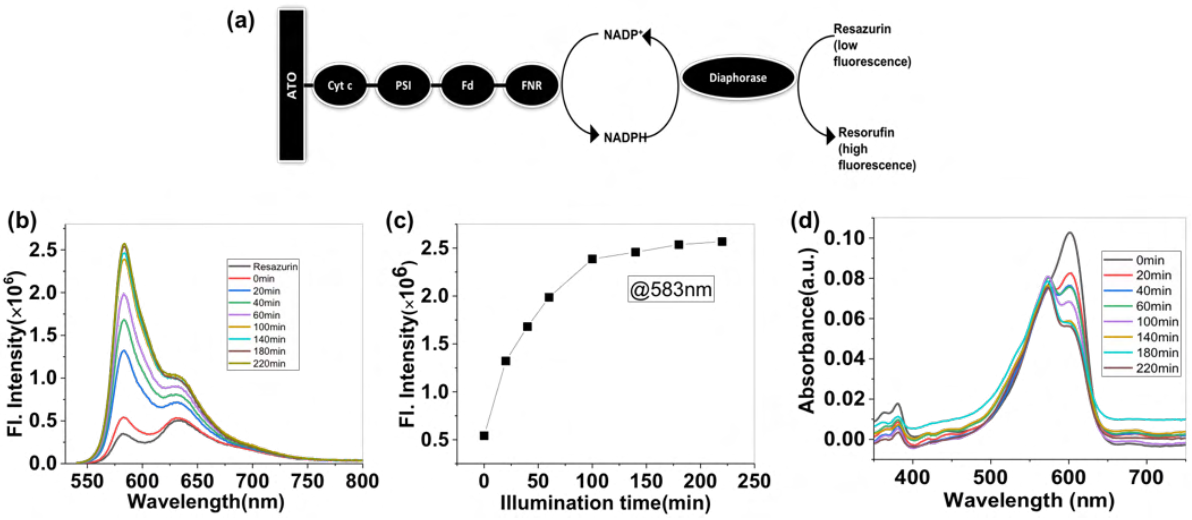


Figure 6. (a) Schematic of the complete bio-electrical system, combined with diaphorase to perform light-driven reduction of weakly-fluorescent resazurin to strongly-fluorescent resorufin using the NADPH produced by photoreduction as a substrate. (b) Fluorescence emission spectra as a result of resorufin formation in the system. With continuous illumination weakly fluorescent resazurin is being reduced by diaphorase and NADPH to resorufin that fluoresces strongly at 583 nm. The excitation wavelength is 530 nm. (c) Plot of resorufin emission intensity at 583 nm vs illumination time. Emission intensity increases with time and reaches saturation after 100-150 minutes. (d) UV-Vis absorption spectra of the same samples showing a decrease in resazurin absorbance at 571 nm and appearance of a new peak corresponding to resorufin at 600 nm.